Julius-Maximilians-Universität Würzburg

Institut für Theoretische Physik und Astrophysik
Lehrstuhl für Astronomie

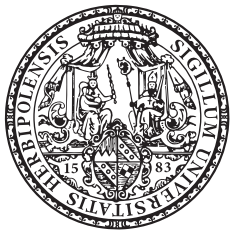

Multi-Wavelength Observations of the high-peaked BL Lacertae objects 1ES 1011+496 and 1ES 2344+514

Dissertation zur Erlangung des
naturwissenschaftlichen Doktorgrades der
Julius-Maximilians-Universität Würzburg

eingereicht von

Stefan Rügamer

aus Dettelbach

Würzburg, Dezember 2012

Eingereicht am

bei der Fakultät für Physik und Astronomie

1. Gutachter: Prof. Dr. K. Mannheim

2. Gutachter: Prof. Dr. M. Kadler

3. Gutachter:

der Dissertation

1. Prüfer: Prof. Dr. K. Mannheim

2. Prüfer: Prof. Dr. M. Kadler

3. Prüfer

im Promotionskolloquium

Tag des Promotionskolloquiums:

Doktorurkunde ausgehändigt am:

Abstract

BL Lacertae objects belong to the most luminous sources in the Universe. They represent a subclass of active galactic nuclei with a spectrum that is dominated by non-thermal emission, extending from radio wavelengths to tera electronvolt (TeV) energies. The emission is strongly variable on time scales of years down to minutes, and arises from relativistic jets pointing at small angles to the line of sight of the observer, which is the reason for naming them "blazars". Blazars are the dominant extragalactic source class in the radio, microwave and gamma-ray regime, are prime candidates for the origin of the Cosmic Rays and excellent laboratories to study black hole and jet physics as well as relativistic effects. Despite more than 20 years of observational efforts, the physical mechanisms driving their emission are not yet fully understood. So far, studies of their broad-band continuum emission were mostly concentrated on bright, flaring states. However, for a better understanding of the central engine powering the jets, the bias from flux-limited observations of the past must be overcome and their long-term average continuum spectral energy distributions (SEDs) must be determined.

This work presents the first simultaneous multi-wavelength campaigns from the radio to the TeV regime of two high-frequency peaked BL Lacertae objects known to emit at TeV energies. The first source, 1ES 1011+496, was observed between February and May 2008, the second one, 1ES 2344+514, between September 2008 and February 2009. The extensive observational campaigns were organised independently from an external trigger for the presence of a flaring state. Since the duty cycle of major flux outbursts is known to be rather low, the campaigns were expected to yield SEDs representative of the long-term average emission.

Central for this thesis is the analysis of data obtained with the MAGIC Cherenkov telescope, measuring energy spectra and light curves from ~ 0.1 to ~ 10 TeV. For the remaining instruments, observation time was proposed and additional data was organised by collaboration with the instrument teams by the author of this work. Such data was obtained mostly in a fully reduced state. Individual light curves are investigated as well as combined in a search for inter-band correlations. The data of both sources reveal a notable lack of a correlation between the emission at radio and optical wavelengths, indicating that the radio and short-wavelength emission arise in different regions of the jet.

Quasi-simultaneous SEDs of two different flux states are observationally determined and described by a one-zone as well as a self-consistent two-zone synchrotron self-Compton model. First approaches to model the SEDs by means of a χ^2 minimisation technique are briefly discussed. The SEDs and the resulting model parameters, characterising the physical conditions in the emission regions, are compared to archival data. Though the models can describe the data well, for 1ES 1011+496 the model parameters

indicate that in addition to the synchrotron and inverse-Compton emission of relativistic electrons, emission due to accelerated protons seems to be required. The SEDs of 1ES 2344+514 reveal one of the lowest activity states ever detected from the source. Despite that, the model parameters are not indicative of a distinct quiescent state, which may be caused by the degeneracy of the different parameters in one-zone models. Moreover, indications accumulate that the radiation can not be attributed to a single emission region.

The results disfavour some of the current blazar classification schemes and the so-called "blazar sequence", emphasising the need for a more realistic explanation of the systematics of the blazar SEDs in terms of fundamental parameters.

Kurzzusammenfassung

BL Lacertae-Objekte sind mit die leuchtkräftigsten Quellen im Universum. Sie stellen eine Unterklasse der Galaxien mit aktiven Kernen dar. Ihr Spektrum erstreckt sich von Radio-Wellenlängen bis in den Tera-Elektronvolt (TeV)-Bereich und ist dominiert durch nicht-thermische Strahlung. Ihre Emission is stark variabel, auf Zeitskalen von Jahren bis Minuten, und entsteht in relativistischen Jets, welche mit einem geringen Winkel zur Sichtlinie beobachtet werden. Daher werden diese Objekte "Blazare" genannt. Blazare sind die dominierende extragalaktische Quellpopulation im Radio-, Mikrowellen- und Gamma-Regime, gehören zu den favorisierten Quellen der Kosmischen Strahlung und bieten ausgezeichnete Bedingungen, um die Physik schwarzer Löcher, Jets sowie relativistische Effekte zu untersuchen. Trotz mehr als 20 Jahre andauernder Beobachtungen sind die physikalischen Mechanismen, welche für die Emission verantwortlich sind, noch nicht völlig verstanden. Bisher konzentrierten sich die Untersuchungen der Breitband-Kontinuumsstrahlung der Quellen hauptsächlich auf deren helle Ausbrüche. Um jedoch die zentrale Komponente der Jetenergetik zu verstehen, muss die in der Vergangenheit aufgebaute Tendenz zu flusslimitierten Beobachtungen überwunden werden, und die über lange Zeiträume gemittelten spektralen Energieverteilungen bestimmt werden.

Die vorliegende Arbeit präsentiert die ersten simultanen Multiwellenlängenkampagnen vom Radio- bis in den TeV-Bereich für zwei BL Lacertaue Objekte, welche als TeV-Emitter bekannt sind. Die erste der beiden Quellen, 1ES 1011+496, wurde zwischen Februar und Mai 2008 beobachtet, 1ES 2344+514, die zweite Quelle, von September 2008 bis Februar 2009. Die umfangreichen Beobachtungskampagnen wurden unabhängig von externen Benachrichtigungen über hohe Flusszustände organisiert. Da starke Ausbrüche der Quellen relativ selten sind, wurde von den Kampagnen erwartet, dass eine spektrale Energieverteilung erbringen würden, welche repräsentativ für ein Langzeitmittel der Emission wäre.

Die Analyse der Daten des MAGIC-Cherenkov-Teleskops, welches im Bereich von $\sim 0.1 - 10\,\mathrm{TeV}$ beobachtet, nahm in dieser Arbeit ein zentrale Rolle ein. Daten der übrigen Instrumente wurde entweder über Anträge auf Beobachtungszeit oder Kooperationen mit den Instrumententeams vom Autor dieser Arbeit eingeworben. Entsprechende Daten wurden hauptsächlich in einer finalen Form übermittelt. In dieser Arbeit werden die individuellen Lichtkurven untersucht sowie für die Suche nach Korrelationen zwischen den verschiedenen Bändern verwendet. Für beide Quellen konnte keine Korrelation zwischen dem Radio- und optischen Bereich gefunden werden, was darauf hindeutet, dass deren Strahlung in unterschiedlichen Regionen des Jets produziert wird.

Mit Hilfe der gewonnenen Daten wurden quasi-simultane spektrale Energieverteilungen in je zwei unterschiedlichen Flusszuständen ermittelt und mit Hilfe eines Ein-Zonen- sowie eines selbst-konsistenten Zwei-Zonen-Synchrotron-Selbst-Compton-Modells beschrie-

ben. Erste Versuche, die Energieverteilungen mit Hilfe einer χ^2-Minimisierungsstrategie zu untersuchen werden kurz erläutert. Die gewonnen Modellparameter, welche die physikalischen Eigenschaften der Emissionsregionen charakterisieren, werden mit Archivdaten verglichen. Obwohl die Modelle die spektralen Energieverteilungen gut beschreiben können, deuten die Modellparameter darauf hin, dass neben der Synchrotron- und invers-Compton-Strahlung relativistischer Elektronen auch Protonen zur Emission beitragen. Im Fall von 1ES 2344+514 konnte einer der niedrigsten jemals gemessenen Flusszustände beobachtet werden, welcher jedoch nicht durch Modellparameter gegeben ist, die auf einen Grundzustand der Quelle hindeuten würden. Eine Ursache hierfür könnte in der Entartung der Modellparameter der ein-Zonen-Modelle liegen. Zusätzlich zeichnet sich ab, dass mehrere Regionen für die beobachtete Emission verantwortlich sind.

Die gewonnenen Ergebnisse sind schwer mit aktuellen Szenarien der Klassifikation der Blazare sowie der sogenannten "Blazar-Sequenz" vereinbar. Diese Erkenntnisse verdeutlichen, dass eine realistischere, auf grundlegenden Parametern basierende Interpretation der Systematiken der spektralen Energieverteilungen von Nöten ist.

Contents

1 Introduction

The comparably young field of ground-based gamma-ray astronomy was established with the detection of the first source, the Crab Nebula, in 1989 by the Whipple telescope (Weekes *et al.* 1989). Mrk 421, the second source discovered in that energy range in 1992, was at the same time the first extragalactic object to be detected (Punch *et al.* 1992). Until 2003, further observations revealed the existence of ~ 10 new sources, though their number was still small compared to the hundreds of sources (271 or possibly 188; Hartman *et al.* 1999; Casandjian & Grenier 2008) detected at high gamma-ray energies (HE, $\sim 0.1 - 100\,\mathrm{GeV}$) by the EGRET satellite (1991 – 2000).

However, the HE regime was no longer covered from 2000 on until the start of regular observations by the AGILE and *Fermi* satellites in December 2007 and August 2008, respectively. VHE gamma-ray astronomy progressed considerably during that time, with the advent of the new generation of imaging air Cherenkov telescopes H.E.S.S. and MAGIC in 2003/2005 as well as VERITAS in 2007. Their greatly increased sensitivity and reduced energy threshold with respect to their predecessors enlarged the number of known VHE sources to more than 60 until the end of 2007, among which less than one third were of extragalactic origin[1].

Particularly these were puzzling though. All but one of them (viz. M 87) belonged to the class of blazars, active galactic nuclei which constitute one of the most luminous sources in the Universe, achieving luminosities up to $10^{49}\,\mathrm{erg\,s^{-1}}$ during outbursts. Their broadband spectral characteristics, reaching from the radio up to the VHE regime, as well as their pronounced variability on time scales of years down to minutes with flux amplitudes of up to one order of magnitude posed serious challenges for extracting interpretable results from observations conducted simultaneously. These characteristics prevent until today a clear identification of the physical mechanisms responsible for the observed emission.

Meaningful measurements, i.e. measurements yielding data that can be used to constrain theoretical models and by that extract physical parameters of the sources, have to be conducted simultaneously at all energy regimes, requiring large organisational efforts and coordination of multiple international observatories. Due to the comparably low sensitivity of the gamma-ray instruments, such observations were and still are conducted dominantly during high activity states of the sources, leaving the underlying low or quiescent state basically unexplored. "Simultaneous data" in the context of this work is defined as data taken on time scales smaller than the typical variability time scale in the different energy regimes, representing a true snapshot of the state of the source. However, measurements may also be representative of the activity state of the source if clear variability was not present in the corresponding energy regime throughout the

[1] see e.g. http://tevcat.uchicago.edu/

observations. SEDs composed of such data are coined here "quasi-simultaneous".

The sparsity of available simultaneous multi-wavelength (MW) campaigns, especially in low activity states, led the author of this work to organise such observations for seven blazars. Four sources were observed in 2006, using the high sensitivities of the MAGIC instrument and the recently launched *Suzaku* X-ray satellite. Further three campaigns, conducted in 2008, took advantage of the first public observation period of the AGILE satellite, and by that the first opportunity to achieve simultaneous coverage at HE since eight years. The goal was not only to shift the focus of such campaigns from the few (Mrk 421, Mrk 501, PKS 2155−304, 1ES 1959+650, PKS 2005−489) already well-studied and mostly bright objects to hardly studied ones, increasing the number statistics of blazars studied in that way. Moreover, the campaigns were organised independently of the activity state of the source, in order to obtain measurements of the hardly explored low or quiescent flux state. Previous campaigns were mostly concentrating on high flux states and flares, introducing a bias in the available data sets. The quiescent state allows to determine the underlying physics of the emission region, which cannot be derived from flaring states. Correlations between the light curves obtained in the different energy bands during the campaign may shed light on the time evolution and location of flares, as well as on the question if the MW emission arises from the same region. Simultaneous SEDs may identify or rule out theoretical models and by that concepts of the physical mechanisms at work in the emission region.

Two of the campaigns incorporating AGILE will be reported here, having targeted the blazars 1ES 1011+496 and 1ES 2344+514. The first one had been just discovered by MAGIC and was back then the most distant source in the VHE regime, the latter is known since long but has hardly been studied due to its rather low luminosity. For neither of them, simultaneous MW observations were available.

In the following Section 2, the blazar phenomenon will be introduced, giving an overview of the current state of knowledge and open questions with a focus on MW aspects. The instruments participating in the observation campaigns will be shortly introduced in Section 3, whereas the MAGIC telescope and the corresponding data analysis will be described in greater detail in Section 4. Sections 5 and 6 will be devoted to 1ES 1011+496 and 1ES 2344+514, respectively. After a short historical overview on the objects, the corresponding MW observations will be presented, followed by the data analysis and results description. Special emphasis will be given to the MAGIC data. The results will be discussed individually as well as in the MW and a historical context, applying theoretical models to the obtained simultaneous SEDs. Section 7 will interpret the results in the light of a potential quiescent state of blazars and the current paradigms of blazars. A short summary and concluding remarks are given in Section 8.

2 Blazars

The term "blazar" originates from a banquet speech given by Edward Spiegel in 1978[1], merging "BL Lacertae objects"[2] and "optically violent variable quasars" into one word to underline their similarity (Angel & Stockman 1980). They belong to the class of active galactic nuclei (AGN), galaxies harbouring a bright nucleus exhibiting strong variability and non-thermal radiation. According to the commonly accepted paradigm, the broad-band emission of blazars is dominated by Doppler-boosted emission from a relativistic jet which is viewed at small angles to the line of sight. Despite constituting only a minority of extragalactic objects[3], the boosted emission makes these objects the dominant source class in the radio, microwave, high energy (HE, $\gtrsim 100\,\mathrm{MeV}$) and, especially, very high energy (VHE, $\gtrsim 100\,\mathrm{GeV}$) regime (see e.g. Abdo *et al.* 2010b; Giommi *et al.* 2012a,b, and references therein). They belong to the most luminous ($L \approx 10^{47-49}\,\mathrm{erg\,s^{-1}}$; e.g. Foschini 2010) and most variable objects in the Universe.

Blazars are particularly interesting due to giving the possibility of investigating black hole (BH), accretion and jet physics as well as being a laboratory to study relativistic beaming. They enable indirect measurements of the extragalactic background light (EBL) (e.g. Aharonian *et al.* 2006a; Albert *et al.* 2008d; Raue & Mazin 2011; Ackermann *et al.* 2012) and by that infer conclusions about cosmological galaxy evolution and structure formation. AGN, and to some extent also blazars, are prime candidates for the production of the omnipresent Cosmic Rays (CRs) at the highest energies (e.g. Inoue 2008; Blümer *et al.* 2009; Dermer & Razzaque 2010; Letessier-Selvon & Stanev 2011; Murase *et al.* 2012). They may also shed light on galaxy evolution and our own galaxy (e.g. Zubovas & Nayakshin 2012).

Despite their number dominance at several energy ranges, detailed investigations of blazars are quite rare. That is due to their broad-band spectral energy distribution (SED), spanning from the radio up to the TeV range about 18 order of magnitude, as well as their strong variability, showing time lags, correlations as well as anti-correlations with varying amplitude in different energy regimes (see Section 2.3). The variability time scales are reaching from years (e.g. Aller *et al.* 2006; Nieppola *et al.* 2007) down to minutes (Aharonian *et al.* 2007c; Albert *et al.* 2007e; Arlen *et al.* 2012). Due to that, simultaneous multi-wavelength (MW) campaigns and densely sampled monitoring projects are required to meaningfully investigate the origin of their emission. Due to the scarcity of these, our understanding of blazars is still rather limited, leaving many questions unanswered.

In the following, AGNs will be described shortly (Section 2.1), followed by an overview of the jets of blazars, governing their broad-band appearance, in Section 2.2). The most

[1] during the Pittsburgh conference on BL Lac Objects

[2] Named after the first such object detected.

[3] $\sim 10\,\%$ of AGN, which in turn account for only $\sim 1\,\%$ of known galaxies (e.g. Silverman *et al.* 2005).

important characteristics of blazars in the different energy regimes will be addressed in Section 2.3. These are used to distinguish different subclasses of blazars, as will be summarised in Section 2.4. In the model of Fossati *et al.* (1998), the different classes are thought to arise from a sequence in bolometric luminosity, the so called "blazar sequence", presented in Section 2.5. An overview of theoretical models to describe the SED of blazars will be given in Section 2.6. In Section 2.7, the most important results of former efforts to measure the blazar SED will be recapitulated. Most of these concentrated on high activity states of blazars, and measurements of the underlying steady emission state of blazars, discussed in Section 2.8, is hardly available.

2.1 Blazars in Active Galactic Nuclei Unification Models

The innermost regions of AGN are brighter than the rest of the galaxy in the optical light. Due to their quasi-stellar appearance (see e.g. Schmidt 1963), these objects were called "quasars". They are rather rare, constituting only $\sim 1\,\%$ of all known galaxies (Silverman *et al.* 2005).

Classification AGN are classified according to their radio-to-optical flux ratio and optical line properties. Sources with a flux ratio between the 5 GHz and B-band $F_{5\,\mathrm{GHz}}/F_{\mathrm{B}} \geq 10$ are called radio-loud, the remaining ones radio-quiet, where the former ones make up $15-20\,\%$ of all AGN (Kellermann *et al.* 1989). The radio-loudness is observationally given by the appearance of a radio jet. The emission line width is another classification criterion (following Urry & Padovani 1995): so-called type 2 AGN are characterised by narrow emission lines produced within regions moving with less than $10^3\,\mathrm{km/s}$ (radio-quiet Seyfert 2 and narrow-emission line X-ray galaxies as well as radio-loud narrow-line radio galaxies, which are subdivided into Fanaroff-Riley type I and II galaxies (FR-I and FR-II; Fanaroff & Riley 1974)), whereas type 1 AGN exhibit broad emission lines from regions with speeds up to $10^4\,\mathrm{km/s}$ (Antonucci 1993). The latter comprise Seyfert 1 galaxies and quasars (radio-quiet), as well as broad-line radio galaxies, steep and flat spectrum radio quasars (FSRQs) (radio-loud). A third type is defined by having weak or no emission lines at all. These are blazars, comprising the radio-loud BL Lacertae objects (BL Lacs) and FSRQs. The fact that the latter are observed with broad as well as no lines may be explained by the rather arbitrary subclass definition, see below.

The Unified Scheme Urry & Padovani (1995) suggested that all these different characteristics of AGN would be just an effect of the anisotropic structure of these objects, causing different appearances depending on the observation angle. In fact, all AGN classes mentioned above could be ascribed to only one source layout. According to this empirical "unified scheme" for radio-loud AGN (for radio-quiet AGN, see Antonucci 1993), the center of these objects hosts a super-massive BH ($M_{\mathrm{BH}} \approx 10^{6-9}\,M_\odot$) surrounded by a hot accretion disc (for a BH of mass $10^8\,M_\odot$, radius $R \approx 1 - 30 \cdot 10^{14}\,\mathrm{cm}$) and an obscuring torus (inner radius $\sim 10^{17}\,\mathrm{cm}$ Urry & Padovani 1995), see Figure 2.1. Bipolar relativistic outflows are emanating from that system, up to a distance of several

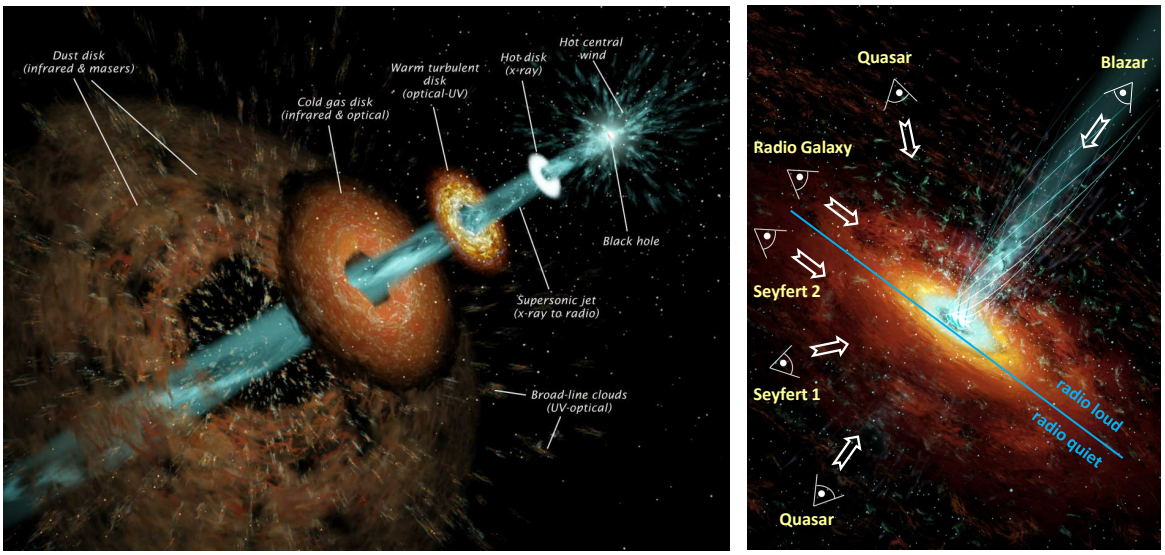

Figure 2.1: The unified scheme of AGN. *Left side:* An AGN is supposed to consist of a central black hole, an accretion disc (shown here subdivided into an infrared – optical, optical – UV and X-ray emitting disc), a broad and narrow line region as well as a relativistic plasma jet (also emitting in the gamma-ray regime). *Right side:* Depending on the viewing angle indicated by the arrows, the observer recognises different classes of AGN (see text for details). Images adapted from http://www.iaa.es/ jlgomez/Jose_L._Gomez/Animations.html (see also Gómez & Steffen 2009).

10^{24} cm (Urry & Padovani 1995). Clouds of material are situated nearby the central engine. These absorb and re-emit photons emitted from the disc. Due to their large velocity, the corresponding emission lines are broadened, giving these regions the name broad-line region (BLR). Further out, the slower moving narrow-line region (NLR) is located.

The obscuring torus, the BLR and NLR as well as the bipolar jets give rise to a non-spherical geometry, resulting in various observable forms of the same object depending on the part of the AGN visible to the observer. If observing the system edge-on, the central object will be masked by the torus and the jets may be clearly apparent. Therefore, emission from the BLR cannot be observed (Seyfert 2 and radio galaxies). With decreasing angle between the line-of-sight and the jet, the BLR becomes visible (Seyfert 1, quasars). At very small angles, or in the extreme case of looking directly into the jet which consists of relativistically moving plasma, the radiation will be strongly Doppler-boosted into the direction of the observer, dominating the overall emission of the object. Due to boosting away from the observer, the counter-jet is normally not detectable (blazars). Following this scheme, BL Lacs would be beamed FR-I galaxies (low luminosity) without extended radio structures (Browne 1983; Padovani 1992), whereas FSRQs are the beamed counterparts of the high luminosity FR-II galaxies (Barthel 1989), showing strong radio lobes or hot spots.

This unified scheme is still viable after more than 15 years, despite the original definition was created containing already some inconsistencies Urry & Padovani (1995). Particularly the analogy of BL Lacs and FR-I galaxies was insecure. On the one hand, narrow emission lines are missing for BL Lacs, whereas broad Mg II lines are present for

some high-redshift BL Lacs but not for FR-I galaxies. However, these problems may be attributed to the low instrument sensitivity and small source statistics available at that time. On the other hand, some BL Lacs with high luminosity and extended radio structure have been observed, resembling FR-II rather than FR-I galaxies (Urry & Padovani 1995). Finally, all studies relating FR-II and radio-loud quasars neglected the existence of low-excitation[4] radio galaxies (LERG) (of FR-II type) for simplicity, having a lower luminosity and more complex radio structure than their high-excitation radio galaxy (HERG) FR-II counterparts. These LERGs may in fact rather be BL Lac objects than quasars (Urry & Padovani 1995, and references therein). As the authors note: "It may well be that the parent population of BL Lac objects includes at least some FR II radio galaxies, presumably those with low-excitation optical spectra" (Urry & Padovani 1995).

From a study of quasi-simultaneous SEDs of 48 blazars [5], Abdo *et al.* (2010b) suggested a physical classification based on the unifying scheme, consisting only of thermal (accretion disc) and non-thermal (jet) dominated AGNs. The former encompasses radio-quiet quasars and Seyfert galaxies, the latter radio-loud AGN, i.e. blazars and misaligned blazars (radio galaxies and steep spectrum radio quasars).

Recently, Giommi *et al.* (2012a) noted that the unified scheme cannot account for transition objects between BL Lacs and FSRQs, i.e. objects changing their classification with their activity state due to appearance or vanishing of emission lines, and the different redshift distribution of the two classes. They suggested that this may be a consequence of different contributions in the optical regime, which is critical for the classification, and propose a modified scheme for blazars. In their model, blazars are divided into only two physical classes, which are LERGs and HERGs. Almost all FR-I sources belong to LERGs, whereas FR-II sources are both LERGs and (mostly) HERGs, hence taking into account the neglected FR-II LERGs mentioned by Urry & Padovani (1995). FSRQs can be identified with HERGs, BL Lacs are LERGs as well as (beamed) HERGs. For the latter, the non-thermal Doppler-boosted emission from the jet dilutes the emission lines, leading to the BL Lac classification. Hence, some objects regarded today as high power BL Lacs (i.e. FR-II HERGs) are in fact beamed HERGs and hence should be classified as FSRQs (see also Section 2.4). During high states, the non-thermal emission may disguise the lines of FSRQs, leading to a wrong classification if the observations are high-state biased.

[4] In terms of optical emission lines.

[5] We note however that the observations were not organised a priori and hence did make use of archival data. Gamma-ray data integrated over three months (regardless of potential variability) was combined with comparably short and few (for each individual source) UV/optical and X-ray data (amongst others) if the latter have been taken with less than three months time difference to the gamma-ray observations, in some cases even longer. With variability time scales in the optical, X-ray and gamma-ray bands of days and even below, we cannot support the "quasi-simultaneity" of these data sets claimed by the authors (see also Section 5).

2.2 Jets of Blazars

The first jet has been discovered nearly 100 years ago by H. Curtis in 1918. He observed in the optical band a "curious protuberance" emanating from the central region of the nearby radio galaxy M 87 (e.g. Foschini 2010). Today, jets are common phenomena in astrophysics, but still not well understood. Their appearance seems to be closely correlated with accretion discs, since jets have been reported for AGN, binary systems, protostars and even accreting brown dwarfs (Mirabel 2003; Foschini 2010; Coffey 2011). However, they are also supposed to be present in the extremely luminous gamma-ray bursts (since their observed energy budget can only be explained by ultra-relativistic motion) and have been successfully generated in the laboratory (see Huarte-Espinosa *et al.* 2011, and references therein). Their bulk speed may be related to the mass of the central object (e.g. Foschini 2010).

Jets produce the dominating, non-thermal part of the broad-band SED of blazars (see also Section 2.4). The jets of blazars are collimated, relativistic plasma streams extending from the central object up to ~ 1 Mpc into intergalactic space (e.g. Urry & Padovani 1995). They constitute one of the key ingredients of the unifying scheme of AGN (see Section 2.1), the different sources being characterised by their jet morphology. FR-II sources show powerful, highly collimated and long jets ending in radio lobes or so-called radio hot spots when interacting with the intergalactic medium, whereas for FR-I galaxies, the jets are less powerful, less collimated and of smaller extend. Examples are shown in Figure 2.2. Note that FR-II and FR-I galaxies are supposed to be the beamed counterparts of FSRQs and BL Lacs, respectively (see Section 2.1).

The mechanisms launching and forming jets are still not revealed, but in general the model of Blandford & Znajek (1977) is considered, described in the following. A spinning black hole accretes matter, which forms a rotating, hot accretion disc in the equatorial plane of the system. Due to the high temperatures (up to $\sim 10^5$ K), the matter becomes ionised. Differential rotation of the disc twists the magnetic field lines, increasing the strength of the field. Open field lines will be aligned in a cone perpendicular to the equatorial plane of the accretion disc. Along these lines, charged particles can be accelerated, extracting by that energy and angular momentum from the disc. The resulting Poynting-flux dominated anti-parallel jets may be further collimated by disc winds produced by the Blandford & Payne (1982) process. In the case of the FR-I radio galaxy M 87, the jet seems not to have had enough time to collimate in the direct vicinity (5.5 ± 0.4 Schwarzschild radii, R_S) of the radio core, hence collimation seems to occur at least for this source further downstream (Doeleman *et al.* 2012). VLBI observations of the FR-I radio galaxy Centaurus A and the LINER[6] galaxy NGC 1052 set the currently most stringent upper limits on the distance of the collimation region to the core, since the jet is already collimated on scales of hundreds of R_S (Müller *et al.* 2011; Baczko 2012). On larger scales, the jets become matter dominated. The process transforming the Poynting-dominated jet into a matter-dominated one are still a matter of debate (e.g. Sikora *et al.* 2005; Komissarov 2011; Ghisellini 2012).

High-resolution VLBI radio observations reveal several distinct, bright components in these jets, thought to be responsible for the strong variability observed from blazars at

[6] **L**ow **I**onisation **N**uclear **E**mission line **R**egion, which are objects very similar to Seyfert 2 galaxies.

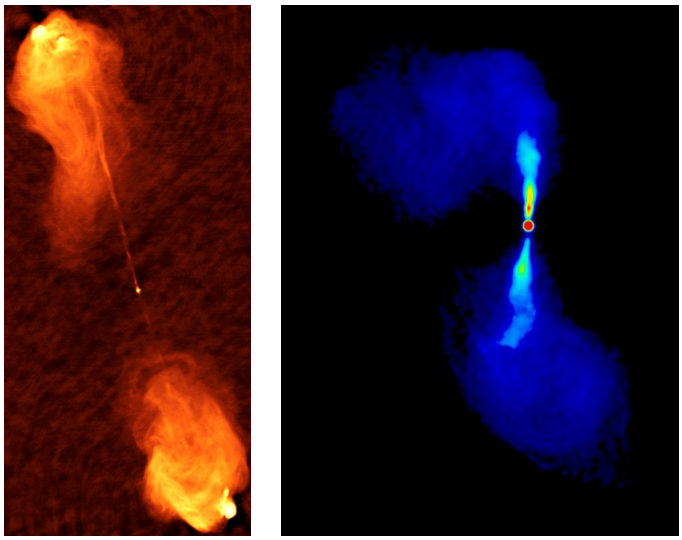

Figure 2.2: *Left side:* 5 GHz radio image of the FR-II radio galaxy Cygnus A, observed with the VLA. Clearly two highly collimated jets emanating from the central galaxy can be seen, which end in giant radio lobes and hot spots. The image height corresponds to $\sim$150 kpc at the distance of the source. Image courtesy of NRAO/AUI. *Right side:* VLA image at $\sim$5 GHz of the FR-I radio galaxy M 84. The jets are much broader, less collimated and shorter compared to the image on the left side. The height of the image corresponds to $\sim$12 kpc at the distance of the source. Image taken from http://www.jb.man.ac.uk/atlas/other/3C272P1.html (see also Bridle & Perley 1984).

all energy bands. The origin of the jet, the so-called "nozzle", could not yet be observed. The apparent starting point of the jet is commonly defined as the "radio core", which is the most compact unresolved structure at the beginning of the jet (but which is not identical to the BH) and often one of the brightest radio components. Due to synchrotron self-absorption (Blandford & Königl 1979; Königl 1981), transient objects (like new jet components) cannot be observed from this region in the radio regime. Since in this case the optical depth depends on the photon energy, the size of the core decreases with increasing observation frequency (e.g. Unwin *et al.* 1994), and the core position depends on the frequency (e.g. Lobanov 1998; Sokolovsky *et al.* 2011). Alternative scenarios explain the core as a conical shock ending in a shock transverse to the jet, supported by the fact that jet components are observed upstream of the core (Marscher 2006, 2008). Further bright regions are visible downstream of the radio core. These may be a consequence of interactions with the ambient medium, like clouds of gas, resulting in spatially stable features within the jet and sometimes a bending of the jet (e.g. Piner *et al.* 2010). Alternatively, stationary features may be produced by standing shocks (like recollimation shocks). Moving components may be attributed to shocks travelling the jet (e.g. Spada *et al.* 2001). The luminosity of a distinct region of the jet may also be enhanced by Doppler boosting without the need for shock acceleration, occurring if the velocity vector is aligned with the line of sight. This scenario might apply in case of bends in the jet or for an underlying helical jet structure (see also below).

For most of the blazars, these jet components are moving with apparent superluminal speeds. This can be explained as a simple geometrical effect when the emission region

is moving with relativistic speeds at a small angle with the line of sight of the observer. Figure 2.3 shows a sketch of the presumed layout. The jet is represented by the stationary radio core and one jet feature (labelled "blob"). The jet is oriented at a small angle θ to the line of sight and the blob moves with a relativistic speed $v \approx$ c. The blob is observed at two different times t_1 and t_2, defined as the time that has passed since the emission of the photons at the first blob location t_0. Due to the large speed of the blob in the direction of the observer, photons detected during the second observation will arrive significantly earlier than expected if the blob would move perpendicular to the observer. Hence, the apparent speed of the blob $\beta_{\rm app}$, determined by the photon arrival time difference $\Delta t = t_2 - t_1$, amounts to:

$$t_1 = \frac{r}{c} \tag{2.1}$$

$$t_2 = \frac{r}{c} - \frac{v}{c} t \cos\theta + t \tag{2.2}$$

$$v_\perp = \frac{r_\perp}{\Delta t} = \frac{vt\sin\theta}{-\frac{v}{c}t\cos\theta + t} \tag{2.3}$$

$$= \frac{\beta\sin\theta}{1-\beta\cos\theta} = \beta_{\rm app} \tag{2.4}$$

where $\beta = v/\mathrm{c}$. Differentiating Eq. 2.4 yields a maximal $\beta_{\rm app,max}$ for an angle $\cos\theta_{\rm max} = \beta$, or equivalently

$$\sin\theta_{\rm max} \equiv \sqrt{1-\cos^2\theta_{\rm max}} = \sqrt{1-\beta^2} \equiv \Gamma^{-1} \tag{2.5}$$

where Γ is the Lorentz factor. The highest apparent speed is then given by

$$\beta_{\rm app,max} = \frac{\beta\sqrt{1-\beta^2}}{1-\beta^2} = \beta\Gamma \tag{2.6}$$

The apparent superluminal speed results in Doppler-boosting (or "beaming") of the observed radiation, increasing the intensity I of the observed emission, reducing the variability time scale t and leading to a blue shift. The amount of Doppler boosting the observer witnesses is given by (e.g. Urry & Padovani 1995)

$$t_{\rm obs} = \delta^{-1} t_{\rm intr} \tag{2.7}$$

$$\nu_{\rm obs} = \delta\nu_{\rm intr} \tag{2.8}$$

$$I_{\rm obs}(\nu) = \delta^3 I_{{\rm intr},\nu_{\rm intr}}(\nu_{\rm intr}) \tag{2.9}$$

where the Doppler factor δ

$$\delta \equiv \frac{1}{\Gamma\left(1-\beta\cos\theta\right)} \tag{2.10}$$

relates intrinsic (intr) and observed (obs) quantities of a relativistically moving source. Since the counter-jet is boosted away from the observer ("de-boosting"), it can normally not be detected.

The jet speeds derived from radio observations are in general lower than what is being estimated by modelling of the SED. Piner *et al.* (2010) report an average Lorentz factor

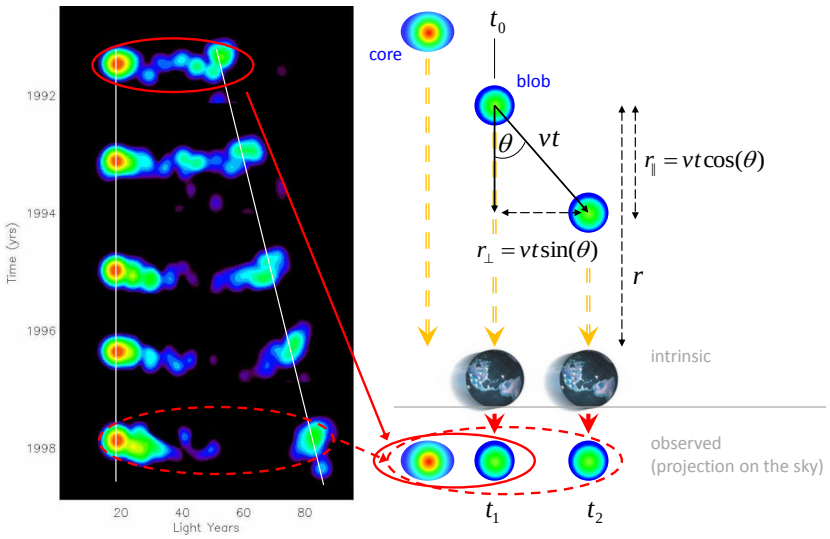

Figure 2.3: Illustration of the superluminal motion effect. *Left side:* VLBA radio image at 22 GHz showing the jet of the FSRQ 3C 279 at several epochs. One feature moving away from the core on the left side can be clearly identified. Image courtesy of NRAO/AUI. *Right side:* sketch of the radio core and the feature ("blob") moving away from the core. Orange arrows visualise emitted photons. The earth with the depicted VLBA telescopes (image courtesy of NRAO/AUI) symbolises the observer.

for blazars small luminosity of $\Gamma_{\rm VLBI} \leq 5$, whereas $\Gamma_{\rm model} \approx 25$. Similarly, the Doppler factor is much larger as determined from SED models compared to radio measurements (e.g. Levinson 2007; Stern & Poutanen 2008). Note that current SED models are not suited to describe the (self-absorbed) radio emission (see Section 2.6), hence these jet speed measurements are independent from each other. This discrepancy can be solved assuming that the corresponding emission is produced in different regions of the jet. Several different SED models have been proposed following this assumption, reaching from a layered jet (Ghisellini *et al.* 2005) to multizone models (Marscher 2012) (see also Section 2.6). Alternative scenarios explain the observations by decelerating jets (e.g. Levinson 2007; Stern & Poutanen 2008).

However, superluminal motion is not present for every blazar, despite being able to identify individual jet components. Recent studies report for TeV-detected BL Lacs subluminal speeds on mas scales (e.g. Piner *et al.* 2008; Britzen *et al.* 2009; Piner *et al.* 2010). Accounting for the rapid variability observed from these objects, the slow motion is rather representative for individual emission components than for all of them (Britzen *et al.* 2009). The apparently slower jets in TeV BL Lacs may be a consequence of their lower power compared to other blazars (Piner *et al.* 2008). There are also indications of a systematic difference in jet speeds for the different subclasses of blazars, that is, the jets of BL Lacs may be slower compared to FSRQs (e.g. Karouzos *et al.* 2012) and in turn HBLs may be slower than LBLs (Kharb *et al.* 2008) (see also Section 2.4). Karouzos *et al.* (2012) suggests that this is an effect of a helical jet structure viewed at smaller angles for blazars.

Multi-wavelength observations of a flare of BL Lac led Marscher *et al.* (2008) to conclude on a helical jet structure, which is also an appropriate description for a recent outburst from the same source (Arlen *et al.* 2012) and observations of a flare from the

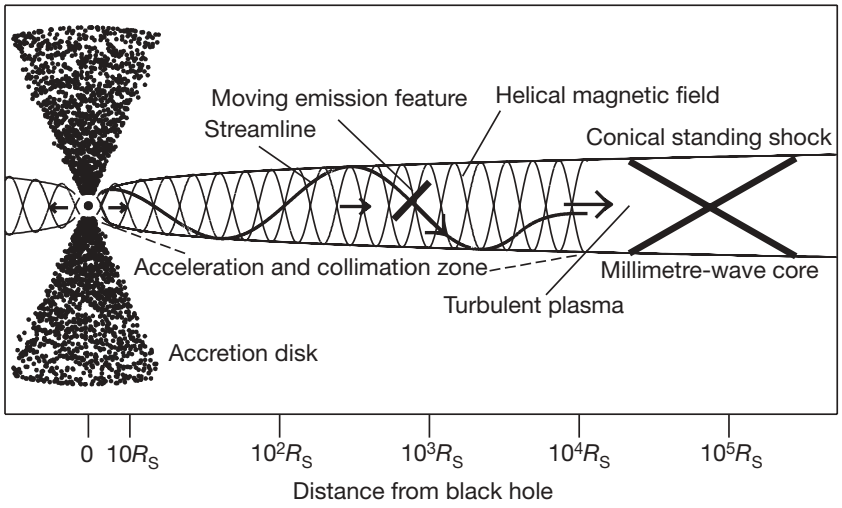

Figure 2.4: Helical jet model as proposed by Marscher *et al.* (2008). On the left side, the BH and the surrounding accretion disc is depicted, from which the jet is emanating. See text for details. Figure taken from Marscher *et al.* (2008).

FSRQ PKS 1510−089 (Marscher *et al.* 2010). In this model, a region containing energetic charged particles is moving through the collimation and acceleration zone on a spiral streamline due to a helical magnetic field, see Figure 2.4. A first flare is detected shortly before the region leaves the acceleration zone, when the Lorentz factor is maximal and the region direction of movement is aligned with the line of sight (Doppler boosting). A second flare occurs when the region hits the turbulent plasma in a standing shock, which in this case is interpreted as the radio core. By combination of the X-ray and gamma-ray light curves with high resolution VLBI observations, the authors were able to estimate the distance of the different putative jet constituents to the central BH (see Figure 2.4). However, a helical jet structure seems not to be a common feature of blazars, as long-term VLBA measurements of Faraday rotation in 149 sources revealed. Only for individual objects, strong rotations seems to be present (Hovatta *et al.* 2012).

2.3 Spectral Characteristics

Blazars are detected at all wavelength regimes, from radio up to TeV energies. They are the most numerous extragalactic source species in the radio, microwave, HE and VHE gamma-ray regime (see e.g. Abdo *et al.* 2010b; Giommi *et al.* 2012a,b, and references therein). Their spectral energy distribution (SED) in a spectral energy flux density (νF_ν) vs. frequency (ν) representation is characterised by two broad peaks, situated at variable frequencies (for different objects as well as for the same object in different activity states). Their location represents one important criterion of blazar classification (see Section 2.4). The *left side* of Figure 2.5 shows an idealised sketch of the SEDs of blazars, which should serve to illustrate the discussion in the following sections.

One of the most intriguing characteristics of blazars is their strong and manifold variability, thought to arise within the jet components mentioned in the previous section. Basically all currently testable variability time scales are verified for blazars, from min-

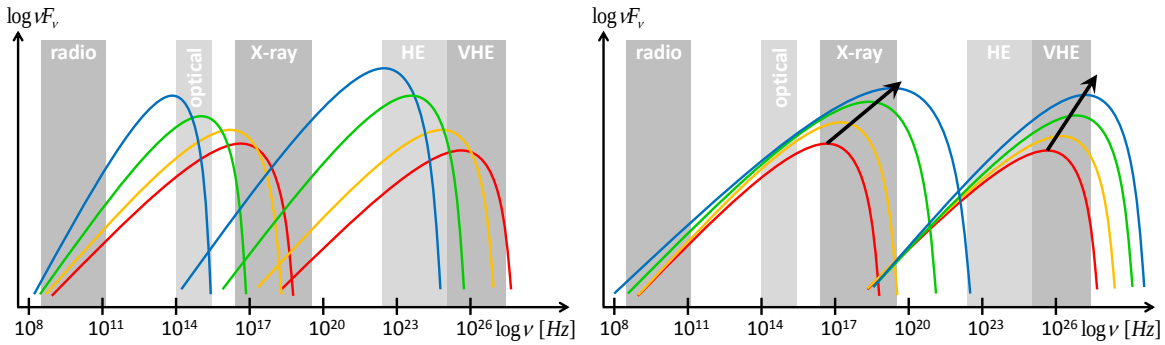

Figure 2.5: *Left side:* idealised SED sketches for different blazars. The frequency of the first SED peak varies between $\sim 10^{13}$ and $\sim 10^{17}$ Hz, hence their characteristics in different energy regimes depends strongly on that parameter. Blue indicates FSRQs, green LBLs, orange IBLs and red HBLs. *Right side:* concept thought to be responsible for the "harder when brighter" SED variability e.g. in SSC models, shown for an HBL. From red to blue, the strength of the flare increases. The frequencies of the peaks move with increasing flux. The dependency may indeed be different for the two peaks, e.g. because of Klein-Nishina effects, as indicated by the different slope of the arrows. Note that the slope and flux in the radio, optical and HE range is hardly changing.

utes up to years. Fast variability sets strong constraints on the size of the emission region from causality arguments:

$$R \leq c t_{\mathrm{var}} \frac{\delta}{1+z} \tag{2.11}$$

with R being the radius of the emission region, t_{var} the variability time scale and z the redshift of the source.

Apart from flux variability, also the spectral shape is changing during increased activity. This change is mostly associated with a shift of the two SED peaks to higher frequencies (see below), leading to a so-called "harder when brighter" behaviour above each of the two peaks, whereas below the spectra are hardly changing (see *right side* of Figure 2.5). In the following, the spectral characteristics of blazars in the different energy bands will be summarised. Correlations between different energy regimes during flux changes will be discussed subsequently in a separate section. The last section will describe the special case of blazars exhibiting particularly large shifts of their synchrotron peak frequency during outbursts, so-called "extreme blazars".

2.3.1 Individual Energy Bands

Radio The commonly cited flat radio spectrum of blazars is not measured in a spectral energy density distribution, where the spectral shape is in fact very hard (see Figure 2.5), but in a spectral flux density diagram (Jy vs. ν). In this representation, the spectrum is following basically a simple power law

$$S_\nu = S_0 \cdot (\nu/\nu_0)^{-\alpha} \tag{2.12}$$

where S is the flux density, ν is the frequency, S_0 the flux density normalisation and α the spectral index. The spectral index is typically close to zero between $\sim$1 and $\sim$70 GHz.

In the range 70 – 1000 GHz, the index steepens to ~ 0.5 for sources with a rather high synchrotron peak frequency, and to ~ 0.7 if the peak location is rather low (e.g. Giommi *et al.* 2012b).

In general, variability in the radio regime is slower and of smaller amplitude compared to the other energy regimes, having a typical flux density amplitude of about four (e.g. Giommi *et al.* 2012b). Flares occur on time scales of months to years; Nieppola *et al.* (2007) determined a mean flare duration of 17.6 months for 5 objects with well-sampled flares, out of their investigated 136 BL Lacs. Aller *et al.* (2006) found typical variability time scales of blazars of two years, with a large scatter around that value though, also reaching to more than a decade. These results are confirmed by Hovatta *et al.* (2007) on the basis of 80 BL Lacs, Hovatta *et al.* (2008) for 55 BL Lacs and Nieppola *et al.* (2009) for 24 BL Lacs. The authors find agreement of the flare origin with shocks travelling the jet. For some sources, very short flares were detected, with time scales of hours or days (Nieppola *et al.* 2007; Lichti *et al.* 2008; Liu *et al.* 2012a). These are very rare though. Particularly S5 0716+714 may be strongly variable (Nieppola *et al.* 2007), however the intra-day variability detected from the object may be an effect of interstellar scintillation rather than an intrinsic feature (Liu *et al.* 2012b). If the shocks in the jets supposed to be responsible for flares are moving downstream, the signature of the outburst should become visible first at high frequencies (high angular resolution) and progress then to lower frequencies (low angular resolution). This self-evidently causes also spectral variability over time during flares.

Interferometric radio observations yield the highest angular resolution images of sources. These provide information about the structure of the jet and location of emission regions, especially when combined with light curves at higher frequencies (e.g. Marscher *et al.* 2008). Apart from pure kinematic information like the apparent jet speed, jet opening angle and alignment direction, they can also be used to derive or constrain physical parameters of the plasma, like the Lorentz factor, the size of the radio core and the magnetic field (e.g. Sokolovsky *et al.* 2010b; Piner *et al.* 2010).

Optical In this work, we coin the "optical" properties of blazars as these determined by the continuum spectrum between the near infrared up to the UV regime. For some blazars, the synchrotron peak is located in or close to the optical regime, resulting in hard, flat as well as soft simple power law spectra or curved spectra.

In contrast to the remaining energy regimes, the optical may be dominated by thermal radiation rather than by non-thermal jet emission. Contributions from the host galaxy and the accretion disc (the so-called "big blue bump") are present for blazars and may be observable depending on the type of blazar (see also Section 2.4). Via spectroscopy of the emission and absorption lines, the distance of the blazar can be determined. Also the reservoir of thermal photons can be estimated in case the accretion disc emission is clearly observable. These are important for a certain kind of SED models (see Section 2.6).

In the optical, intra-day variability has been frequently reported for TeV-detected BL Lacs down to time scales of one hour, but not below (Gopal-Krishna *et al.* 2011, and references therein). The variability seems to be stronger for BL Lacs with lower synchrotron peak frequencies (Gopal-Krishna *et al.* 2011; Gaur *et al.* 2012b, and references

therein). Long-term monitoring, e.g. by the Tuorla Blazar Monitoring Program[7], reveals flux density changes by roughly one order of magnitude. A "bluer when brighter" trend of the peak frequency is observed in many synchrotron-dominated BL Lacs (e.g. Böttcher *et al.* 2010; Rani *et al.* 2010; Gaur *et al.* 2012a), analogous to the "harder when brighter" trend observed at X-rays and gamma rays (see *right side* of Figure 2.5 and paragraphs below). An opposite "redder when brighter" trend may be present for sources with a strong contribution by the accretion disc (e.g. Raiteri *et al.* 2008; Rani *et al.* 2010; Gaur *et al.* 2012a).

For some sources, optical measurements were recorded since many decades. Particularly the BL Lac object OJ 287 has been observed for nearly 100 years. From the data, a 12-year periodicity was derived, interpreted as arising from a binary BH system (Sillanpää *et al.* 1988). Subsequent dense observations during the outburst predicted from that model confirmed the periodicity and were taken as evidence of emission of gravitational waves (Valtonen *et al.* 2008). For the archetype of blazars, BL Lacertae, optical data are available for a time span of ~ 40 years (Villata *et al.* 2009). Combining long-term optical and radio data, the authors interpreted the quasi-periodicity in terms of the emission region following a rotating helical path within a curved jet.

X-Rays The soft X-ray regime contains crucial information for blazars with high synchrotron peak frequencies. For these, the spectral index is soft in low activity states, but may also become flat or even hard. Deviations from a simple power law behaviour are found frequently. The spectra can be well described in most of the cases by log-parabolic or broken power laws (see also Donato *et al.* 2005):

$$\frac{\mathrm{d}N}{\mathrm{d}E} = f_0 \cdot (E/E_0)^{-(\alpha+\beta\log_{10}(E/E_0))} \cdot \mathrm{e}^{-\tau} \tag{2.13}$$

$$\frac{\mathrm{d}N}{\mathrm{d}E} = \begin{cases} f_0 \cdot (E/E_0)^{-\alpha_1} & E < E_{\mathrm{break}} \\ f_0 \cdot (E_{\mathrm{break}}/E_0)^{\alpha_2-\alpha_1} \cdot (E/E_0)^{-\alpha_2} & E \geq E_{\mathrm{break}} \end{cases} \tag{2.14}$$

where f_0 is the flux normalisation, E the energy normalised at E_0, E_{break} the break energy and α, β, α_1 and α_2 are spectral indices. τ in X-ray astronomy is generally a measure for absorption and calculated from the product of the hydrogen-equivalent number density ($\mathrm{N_H}$) and the specific energy-dependent photoelectric cross section $\sigma(E)$. The spectral curvature is a result of the transition from the Thomson to the Klein-Nishina scattering regime for highly energetic photons ($E \approx m_\mathrm{e}c^2$), or simply arising from the underlying electron distribution.

For the remaining objects, the spectrum is either very soft, or already showing the onset of the second peak, producing also a hard spectrum. Note though that the hard spectrum in the latter case is most probably produced by different physical mechanisms than in the case of blazars with high peak frequencies (see also Section 2.6). If the non-thermal X-ray flux is sub-dominant, the accretion disc may also be visible in this regime (e.g. Giommi *et al.* 2012b; Nalewajko *et al.* 2012).

Also at X-rays, blazars are rapidly variable with typical variation time scales of one day (e.g. Gopal-Krishna *et al.* 2011, and references therein), though flares may also last for

[7] http://users.utu.fi/kani/1m/

some hours only (e.g. Giommi *et al.* 1990; Gaur *et al.* 2010; Gopal-Krishna *et al.* 2011). Over long time scales, flux changes by nearly two orders of magnitude are detected, e.g. for Mrk 421, Mrk 501 and PKS 2005−489 (Giommi *et al.* 2012b; Acero *et al.* 2010). Blazars with synchrotron peaks located at higher frequencies show in general stronger amplitude and faster variations than those with low peak frequencies (e.g. Pian 2002; D'Ammando *et al.* 2009), probably a result of the dominance of the non-thermal emission component. Most of the blazars show a trend of steepening spectral index at phases of higher luminosity ("harder when brighter" trend; e.g. Giommi *et al.* 1990; Sambruna *et al.* 1994; Pian *et al.* 1998; Gliozzi *et al.* 2006; Acciari *et al.* 2011a,b), which may be a sign of synchrotron emission by continuously re-accelerated particles (Sambruna *et al.* 1994), but also the opposite has been reported (e.g. Aharonian *et al.* 2009b).

High Energy Gamma Rays Analogous to the optical regime, the spectra of blazars in the HE gamma ray regime may be hard, flat, soft or even show a distinct peak. Due to the limited sensitivity of past and present observatories, soft spectra are rarely observed (e.g. Ackermann *et al.* 2011b). For most of the sources, the second SED peak is located above the HE range; only for 69 blazars out of 705, significant curvature is detected by *Fermi*-LAT (Ackermann *et al.* 2011b). With increasing observation time, more sources with soft spectra should be detected.

The sensitivity also limits variability studies. Significant flux variability has been reported for about half of the blazars detected by LAT, where the objects with high synchrotron peak frequencies seem to be less variable (Ackermann *et al.* 2011b). As in the optical regime, this can be understood assuming that these sources are characterised by larger frequencies of the second SED peak, hence, under the premise of the harder when brighter trend, the HE observations probe an SED range hardly variable during flares (see *right side* of Figure 2.5). Considering observations averaged over one month, most of the sources already detected by LAT show a significant signal for less than half of these time bins (Ackermann *et al.* 2011b), indicating that short term variability on time scales of days or even below can only be investigated for the most extreme flares. Such strong and short variability has been detected e.g. for PKS 1222+216 (Tanaka *et al.* 2011, and references therein), 3C 279 (Abdo *et al.* 2010c), PKS 1510−089 (Abdo *et al.* 2010a) and 3C 454.3 (Abdo *et al.* 2011a, and references therein), with short-term flux changes by one order of magnitude and more.

Above a few tens of GeV, photons are increasingly absorbed by pair production with the diffuse extragalactic background light (EBL) (e.g. Gould & Schréder 1967). This photon field in the infrared to ultraviolet regime is dominantly produced directly by stars and indirectly (through scattering) by interstellar dust (e.g. Kneiske & Dole 2010). Due to the zodiacal light, a direct measurement of the EBL in the infrared regime is difficult (e.g. Domínguez *et al.* 2011; Orr *et al.* 2011). With typical energies between $\sim 0.01\,\mathrm{eV}$ and $\sim 10\,\mathrm{eV}$, the EBL photons achieve a total energy larger than the threshold for pair production of 1022 keV for gamma photons with an energy above $\sim 50\,\mathrm{GeV}$:

$$\gamma_{\mathrm{gamma}} + \gamma_{\mathrm{opt/IR}} \quad \rightarrow \quad \mathrm{e}^+ + \mathrm{e}^- \tag{2.15}$$

if (for head-on collisions)

$$E_{\mathrm{gamma}} \cdot E_{\mathrm{opt/IR}} \geq 2 \cdot \left(m_{\mathrm{e}} c^2\right)^2 \tag{2.16}$$

where m_e is the electron rest mass. Due to the increasing integrated density of the target photons, the number of gamma photons lost by pair production is dependent on the distance to the source, leading to a cut-off of the spectrum in the gamma-ray regime where the optical depth $\tau = 1$ (the so-called "cosmic gamma-ray horizon" or Fazio-Stecker relation (Fazio & Stecker 1970; Kneiske *et al.* 2004)). In a recent publication, the HE data of 150 BL Lacs have been used to determine the opacity caused by the EBL (Ackermann *et al.* 2012). According to their results, only models assuming a minimal amount of EBL are still viable, like the ones of Franceschini *et al.* (2008); Kneiske & Dole (2010); Domínguez *et al.* (2011). In this work, we adopted the model of Kneiske & Dole (2010), since it gives a strict lower limit on the EBL density. Moreover, the differences between current models still consistent with the measurements from Ackermann *et al.* (2012) are very small (Domínguez *et al.* 2011), especially for the redshift range probed here ($z = 0.212$ for 1ES 1011+496).

Very High Energy Gamma Rays Until today (December 2012), 55 extragalactic objects have been detected at VHE[8], a small number compared to the remaining frequency regimes. 47 of these belong to the class of blazars (also called "TeV blazars"), among which the objects with high synchrotron peak frequencies dominate (see also Table A.1 and Figure 2.7). This is naturally explained by the fact that their SED peak is assumed to be located between the HE and VHE regime in low flux states, whereas for the remaining sources, the highest gamma-ray flux is expected at much lower frequencies. Therefore, similarly to the X-ray regime, at VHE gamma rays the blazar spectra are dominantly soft, but may become flat or even hard during high activity states. Some sources may even have hard spectra in low flux states (see e.g. Tavecchio *et al.* 2010).

Spectral downward curvature has been observed for very luminous sources (e.g. Mrk 421, Mrk 501 and PKS 2155−304; Aleksić *et al.* 2010a; Aharonian *et al.* 1999, 2009b). However, in most cases the spectra are compatible with a simple power law, also during high activity states (e.g. Donnarumma *et al.* 2009; Abdo *et al.* 2011d; Acciari *et al.* 2011a; Arlen *et al.* 2012):

$$\frac{\mathrm{d}N}{\mathrm{d}E} = f_0 \cdot (E/E_0)^{-\alpha} \tag{2.17}$$

The curvature is attributed to the transition from the Thomson to the Klein-Nishina scattering regime (e.g. Aharonian *et al.* 1999) as well as the intrinsic electron distribution and should be present in all blazars. Probably low statistics around TeV energies and large systematic errors hinder the detection of curved spectra for the weaker objects. Nevertheless, their absence for many sources also during high states is puzzling. Apart from the log-parabolic power law (see Eq. 2.13), a power law with exponential cut-off at E_{cut} is often used to describe curved spectra:

$$\frac{\mathrm{d}N}{\mathrm{d}E} = f_0 \cdot (E/E_0)^{-\alpha} \cdot \mathrm{e}^{-E/E_{\mathrm{cut}}} \tag{2.18}$$

Spectral curvature at VHE may also result from pair production with the EBL. However, even for the most distant sources, attenuation by the EBL could not be proven

[8] see e.g. http://tevcat.uchicago.edu/

to be the reason for such features. Assuming a minimal intrinsic photon index of 1.5 in the VHE regime (valid in the case of diffusive shock acceleration; Malkov & O'C Drury 2001; Aharonian *et al.* 2006a), upper limits on the EBL density were derived from these measurements (e.g. Aharonian *et al.* 2006a, 2007b; Albert *et al.* 2008d). This assumption may not always hold though, since diffusive shock acceleration may not be the only parameter influencing the gamma-ray spectral shape. Relativistic shock acceleration, adiabatic losses, stochastic acceleration processes, or blazar-internal absorption (e.g. Stecker *et al.* 2007; Krennrich *et al.* 2008; Lefa *et al.* 2011; Zacharopoulou *et al.* 2011), amongst others, could explain spectral indices below 1.5. New approaches to determine indirectly the EBL take advantage of the broad energy coverage provided by current gamma-ray satellites and ground-based Cherenkov telescopes (see also Chapter 3). With the underlying assumption that the VHE spectral index is softer than the (intrinsic) one measured at HE, upper limits on the EBL density may be derived (e.g. Georganopoulos *et al.* 2010; Orr *et al.* 2011; Aleksić *et al.* 2011a; Meyer *et al.* 2012). Costamante (2012) argues however that the VHE spectrum may be harder than the HE one, for example due to multiple emission components. The upper limits on the EBL density resulting from the different estimation methods are close to the lower limits derived from simple galaxy counts and in agreement with current low density EBL models like Franceschini *et al.* (2008); Kneiske & Dole (2010); Domínguez *et al.* (2011). For more information on the field of EBL research, we refer to current reviews like the one of Dwek & Krennrich (2012).

The blazar spectra in the VHE regime are also characterised by pronounced variability. Intense flaring has been observed e.g. for PKS 2155−304, Mrk 501, PKS 1222+216 and BL Lac with flux doubling time scales down to a few minutes (Aharonian *et al.* 2007c; Albert *et al.* 2007e; Aleksić *et al.* 2011a; Arlen *et al.* 2012). Snapshot observations reveal flux differences on time scales of months and years for several sources of one order of magnitude and more (see e.g. Aharonian *et al.* 2009b; Anderhub *et al.* 2009b; Tavecchio *et al.* 2010). The "harder when brighter" trend during high states has also been reported in the VHE regime (e.g. Krennrich *et al.* 2002; Albert *et al.* 2007e; Aharonian *et al.* 2009b; Aleksić *et al.* 2010a; Acciari *et al.* 2011b,a). Detailed variability studies, especially on the flaring duty cycle, are strongly limited though since only a handful of sources are detected regularly. For many blazars, only one spectrum is available from the initial VHE discovery. Systematic monitoring observations over long time scales have been conducted, to our knowledge, only by Whipple for five blazars (Horan *et al.* 2009; Pichel 2009) and, to a much smaller extend in coverage, by MAGIC for three blazars (Wagner 2011) out of the Whipple list. Dense monitoring campaigns with FACT (**F**irst G-**A**PD **C**herenkov **T**elescope; Anderhub *et al.* 2011, and references therein) are planned, eventually encompassing a network of small telescopes which may provide 24 hrs coverage of bright TeV blazars.

2.3.2 Correlations

If quasi-simultaneous multi-band observations are available during flares, correlations between the different energy regimes are frequently reported. Especially the X-ray and VHE flares of blazars with high synchrotron peak frequencies seem to obey a tight

correlation (e.g. Gliozzi *et al.* 2006; Fossati *et al.* 2008; Aharonian *et al.* 2009b; Acciari *et al.* 2011a,b). This indicates that the same particle population is responsible for the emission in the two energy regimes, in accordance with the framework of one-zone models where synchrotron and inverse-Compton radiation are responsible for the two SED peaks (see Section 2.6). For sources with lower peak frequencies, such a behaviour is hardly reported. That may on the one hand be attributed to the small number of such sources studied simultaneously, especially including VHE coverage; on the other hand, their X-ray emission may be dominated by thermal radiation, destroying a potential correlation. Nevertheless, correlated variability has been reported for example between the X-ray and HE (Wehrle *et al.* 1998) as well as between the radio, optical and HE regimes (Agudo *et al.* 2011; Gopal-Krishna *et al.* 2011). Moreover, there are indications that the optical and VHE regime may be correlated (e.g. Aharonian *et al.* 2009c; Reinthal *et al.* 2012).

With the continuous observations at HE by the current satellite experiments (see Chapter 3) and the corresponding extended monitoring programs at radio frequencies, a large data basis is available which can be probed for correlations without the need of significant variability. On that basis, significant correlations between the radio (single-dish as well as interferometric) and HE fluxes and luminosity were revealed (e.g. Nieppola *et al.* 2011; Ghirlanda *et al.* 2011; Ackermann *et al.* 2011a; Arshakian *et al.* 2012). Giommi *et al.* (2012b) caution though that these made use of non-simultaneous data. Searching instead for correlations on basis of contemporaneous SEDs of 105 blazars, the authors found that the radio and X-ray regime were clearly correlated. Such a dependence could not be significantly established for the radio and HE data though.

Correlations may also be notably absent, as has been reported for example for simultaneous X-ray – VHE (e.g. Gliozzi *et al.* 2006; Aharonian *et al.* 2009c; Acciari *et al.* 2009e) as well as radio/optical – VHE observations (e.g. Horan *et al.* 2009; Aharonian *et al.* 2009b; Acciari *et al.* 2009e, 2011b). One of the most discussed cases is the so-called "orphan" TeV flare of 1ES 1959+650 (Krawczynski *et al.* 2004), which had no counterpart at X-rays, requiring SED models different from the ones mentioned above. Also Mrk 421 may have shown such a behaviour (Błażejowski *et al.* 2005; Acciari *et al.* 2011b). Certainly, these are also present for other blazars, but hardly firmly established since (i) a strong flare and (ii) dense coverage of the other energy regime are mandatory to establish the orphan nature, a combination which is still rare for most of the sources.

Since the emission region is not transparent in the radio regime due to synchrotron self-absorption, time lags are expected between the radio and remaining energy regimes (e.g. Acciari *et al.* 2009b, see also Section 2.2). The existence of a general time lag of 1 – 8 months of the radio behind the gamma-ray regime was reported (Arlen *et al.* 2012, and references therein). Studies of delays between the other energy bands are rare. Analysing a series of correlated X-ray and VHE flares of Mrk 421, Fossati *et al.* (2008) found only one flare with a lag of the VHE flare of (2.1 ± 0.7) ks, the remaining ones were consistent with a lag $\lesssim 3$ ks. A significant time delay of ~ 4 days between the optical and HE flare emission, where the latter was leading, was reported for the source 3C 454.3 (Gaur *et al.* 2012c).

Time lags within the same energy band may also be present. For example, Sato *et al.* (2008) reported a lag of hard X-ray photons behind the soft X-ray photons by up to $2.3 \cdot 10^4$ s for the blazar 1ES 1218+304. However, soft lags have also been discovered (e.g.

Takahashi *et al.* 1996; Kataoka *et al.* 2000), and for the same source, both hard and soft lags have been found (Ravasio *et al.* 2004; Brinkmann *et al.* 2005). Soft lags may be explained by the emission processes being dominated by radiative cooling, whereas hard lags may be caused by loss of particles during acceleration (Chen *et al.* 2011), but may also be attributed to multiple emission regions within the jet (Brinkmann *et al.* 2005). Also at VHE, a hard lag has been detected (Albert *et al.* 2007e) and discussed in the context of potential Lorentz invariance effects (Albert *et al.* 2008b).

2.3.3 Extreme Blazars

Particularly interesting is the case of so-called "extreme blazars". According to the original definition by Costamante *et al.* (2001), these are blazars with observed first SED peak energies $> 1\,\mathrm{keV}$ during high activity states. They exhibit the lowest overall luminosity among blazars, but probably dissipate the jet power most efficiently, maybe close to the limit of acceleration mechanisms (Ghisellini 1999). We note that the term "extreme blazar" is also used sporadically for blazars with different extreme characteristics, like very hard spectra in the TeV band, high power, or very high redshift, which do not necessarily exhibit the spectral characteristics we imply here.

Only few objects have been claimed to belong to this kind of sources. Besides the prime examples Mrk 501 (Pian *et al.* 1998), 1ES 2344+514 (Giommi *et al.* 2000) and 1ES 1426+428 (Costamante *et al.* 2001; Wolter *et al.* 2008) with peak energies around 100 keV, these are (listed chronologically) 1ES 0033+595, PKS 0548−322, H 2356−309 (Costamante *et al.* 2001)[9], HESS J1943+213 (Abramowski *et al.* 2011a)[10], Mrk 180 (Rügamer *et al.* 2011), 1ES 0229+200 (Kaufmann *et al.* 2011) and 1ES 0414+009 (Abramowski *et al.* 2012b, and references therein). Further investigation reveal the regular occurrence of peak energies around 1 keV and occasionally above also for Mrk 421 and 1ES 1959+650 (see e.g. historical data presented in Abdo *et al.* 2010b; Giommi *et al.* 2012b). All these objects have also been detected by imaging air Cherenkov telescopes in the VHE regime (see also Section 4 and Table A.1). Note that the peak estimates given in Nieppola *et al.* (2006), who found ~ 80 objects with such high peak frequencies, are not based on X-ray spectra but solely on isolated, historical X-ray points, if any, and hence not reliable for estimating the X-ray spectral shape.

Why Only High-Peaked Objects? All extreme blazars mentioned above are characterised by high synchrotron peak energies, also in comparably low activity states, and hence belong to the blazar subclass of HBLs (see Section 2.4). However, there is no obvious reason why the extreme shift of the peak frequency should only be restricted to this subclass. Also the blazars with lower synchrotron peak frequencies might exhibit a pronounced spectral change of that form during outbursts. The fact that this has not been reported, to our knowledge, in literature until today may be explained

[9] Despite Costamante *et al.* (2001) listing the source as an extreme blazar, we did not consider the observations of 1ES 0120+340 indicative of that since the soft X-ray spectral index is not below unity and the hard X-ray data may be contaminated by other sources (Costamante *et al.* 2001).

[10] Note that the identification of this object is not yet secured. However, indications for a blazar nature are accumulating (Abramowski *et al.* 2011a; Leahy & Tian 2012).

by the comparably small number of X-ray spectra for many objects and potential confusion of intrinsically low-frequency peaked objects during outburst with high-peaked ones. The latter problem may even introduce a bias in object classification if based on few observational data.

2.4 Classification

Blazars constitute only a small percentage of radio-loud AGNs, which in turn are only $\sim 10\,\%$ of radio-quiet ones and Seyferts (e.g. Abdo *et al.* 2010b).

As described in the previous chapter, blazars exhibit a broad range of spectral characteristics, by which several subclasses were defined. The width of emission lines has been used historically to differentiate (rather arbitrarily) between FSRQs with strong, broad lines (equivalent width W_λ of the strongest line $> 5\,\mathring{A}$) and BL Lacs showing only weak or no lines ($W_\lambda < 5\,\mathring{A}$) (Stocke *et al.* 1991). For most of the FSRQs and BL Lacs, the radio morphology is also different, which can be understood in the context of the unified scheme of AGN. FSRQs are supposed to be beamed analogues of FR-II radio galaxies, producing most of their radio luminosity within extended radio lobes, whereas the BL Lacs would be beamed FR-I radio galaxies, not exhibiting strong radio features and their radio intensity falling with increasing distance from the nucleus (e.g. Urry & Padovani 1995). Note, however, that this does not hold for all these objects (Kollgaard *et al.* 1992; Rector & Stocke 2001; Landt & Bignall 2008; Kharb *et al.* 2010, see also Section 2.1). Moreover, FSRQs are detected at much higher redshifts than BL Lac objects. This may be a consequence of the absence of emission lines in BL Lacs though, preventing to derive a firm redshift estimate even with the most sensitive optical instruments (Giommi *et al.* 2012a; Padovani *et al.* 2012).

Synchrotron Peak Frequency BL Lacs are further subdivided according to their spectral shape. Padovani & Giommi (1995) used the ratio of the X-ray flux between 0.3 and 3.5 keV and the radio flux at 5 GHz to divide between "high"- and "low-energy cut-off BL Lacs" at $f_X/f_r \approx 10^{-11}\,\mathrm{erg\,cm^{-2}\,s^{-1}/Jy}$. In a subsequent work (Padovani & Giommi 1996), they refined their separation criterion on a sample of 85 BL Lacs using the frequency of the first peak[11] $\nu^{\mathrm{S}}_{\mathrm{peak}}$ in a νF_ν vs. ν representation. The border between these later called "low-frequency peaked BL Lacs" (LBL) and "high-frequency peaked BL Lacs" (HBL) (e.g. Sambruna *et al.* 1996) was defined at $\nu^{\mathrm{S}}_{\mathrm{peak}} \approx 10^{15}\,\mathrm{Hz}$. However, objects were found that did not support a dichotomy, but had peak frequencies intermediate to this definition (e.g. Sambruna *et al.* 1996), called "intermediate-peaked BL Lacs" (IBL). Laurent-Muehleisen *et al.* (1998, 1999) concluded on a basis of 127 BL Lacs that these objects are rather abundant, indicating a fluent transition between the LBL and HBL subclass. That is in agreement with the unified scheme, which does not foresee a process introducing a dichotomy between BL Lacs.

This classification scheme was always rather arbitrary and not motivated by physical differences, which is also obvious from the rather fluent transition between the classes and different boundary peak frequencies adopted in the literature. For example, Nieppola

[11] which is commonly attributed to synchrotron radiation, see Section 2.6

et al. (2006) defines LBLs to have a peak frequency of $\sim 10^{13-14}$ Hz, IBLs $\sim 10^{15-16}$ Hz and HBLs $\sim 10^{17-18}$ Hz for their study of more than 300 BL Lacs. Abdo *et al.* (2010b) incorporate FSRQs to this peak frequency classification scheme, defining for all blazars low ($\nu^{\mathrm{S}}_{\mathrm{peak}} \lesssim 10^{14}$ Hz), intermediate ($10^{14} \lesssim \nu^{\mathrm{S}}_{\mathrm{peak}} \lesssim 10^{15}$ Hz) and high ($\nu^{\mathrm{S}}_{\mathrm{peak}} \gtrsim 10^{15}$ Hz) synchrotron peaked blazars.

New studies on large samples of blazars seem to confirm a class separation depending on the peak frequency between FSRQs and high- and intermediate-peaked BL Lacs. While the peak frequency for BL Lacs is spanning $\sim 10^{13} - 10^{18}$ Hz (Abdo *et al.* 2010b; Giommi *et al.* 2012b), FSRQs do not show such a broad range. Instead, their corresponding distribution is rather narrow and peaked around 10^{13} Hz, lacking especially the highest frequencies (e.g. Abdo *et al.* 2010b; Giommi *et al.* 2012a,b).

New Approaches Recently, blazars have been found that are not in agreement with these classification criteria. That include e.g. FSRQs with high peak frequencies and without strong lines (e.g. Padovani *et al.* 2012) and BL Lacs with strong lines (e.g. Ghisellini *et al.* 2011)[12]. These findings corroborate the need for a clear and physically defined classification scheme. Especially in the light of the growing statistical data basis, unambiguous classifications are needed to enable systematic population studies on large data sets.

Ghisellini *et al.* (2011) suggest to distinguish between the blazar subclasses depending on the luminosity of the BLR in Eddington units, which should be related to the accretion efficiency of the central BH. At a dividing line of $L_{\mathrm{BLR}}/L_{\mathrm{Eddington}} \approx 5 \cdot 10^{-4}$, the accretion changes from the radiatively efficient (standard accretion disc Shakura & Sunyaev 1973) to the inefficient (advection dominated accretion flow) regime[13] (Ghisellini *et al.* 2011). This divide does not imply a sudden change in the properties of the source. A gradual transition is also possible considering distinct regions of the disc changing their radiative efficiency (Ghisellini *et al.* 2011). FSRQs and the different subclasses of BL Lacs would then be distinguished by the strength of their broad lines, with HBLs having the weakest ones.

Giommi *et al.* (2012a) disentangled the different emission components in the optical regime, which is crucial also for the currently applied classification criteria. They concluded that blazars are characterised by a different relative strength of three optical components: (i) light from the host galaxy, (ii) thermal radiation from the accretion disc and BLR and (iii) non-thermal radiation from the jet. Depending on the dominating component, emission lines from thermal processes may be apparent or swamped by the non-thermal featureless continuum (see also Figure 2.6). This interpretation also explains the (dis-)appearance of emission features connected to different activity states of the source (Ghisellini *et al.* 2011; Giommi *et al.* 2012a) and resolves some of the problems mentioned above. It also explains why the range of $\nu^{\mathrm{S}}_{\mathrm{peak}}$ is narrow for FSRQs, since for a larger contribution of the non-thermal emission component, the lines would become diluted and the object classified as a BL Lac. The authors propose that only two intrinsic blazar sources exist, which are high-excitation radio galaxies or HERGs (high

[12]The misidentification of these objects was decided by their luminosity and spectral index in the gamma-ray regime, their luminous but rather narrow lines or their intrinsic power, see references.

[13]That is the so-called "Fermi blazars' divide", see also Ghisellini *et al.* (2009).

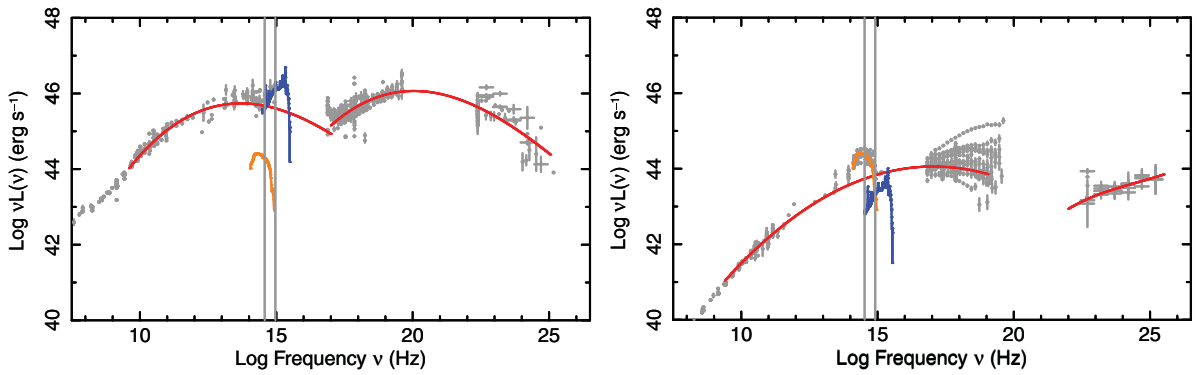

Figure 2.6: Spectral energy distributions of the FSRQ 3C 273 (*left*) and the HBL Mrk 501 (*right*). The grey data points show archival data. The red lines describe the non-thermal contribution from the jet, the orange ones a giant elliptical host galaxy, and the blue curves represent the thermal contribution from the accretion disc and BLR. The vertical grey lines denote the range of optical observations (380 – 800 nm). The optical range of the FSRQ is clearly dominated by the thermal component, whereas for the HBL, the non-thermal radiation swamps the thermal spectrum. For details see Giommi *et al.* (2012b). Figures taken from Giommi *et al.* (2012a).

radio luminosity, with a clear contribution by an accretion disc and broad lines) and low-excitation radio galaxies or LERGs (low luminosity, missing or less efficient accretion disc, weak or absent lines). The non-thermal engine in these is probably the same, whereas they differ by their thermal component. FR-I galaxies are basically all LERGs, whereas FR-II galaxies are mostly HERGs with some LERG contribution, in accordance with the (apparently forgotten) remark by Urry & Padovani (1995) (see also Section 2.1). Nearly all sources classified today as FSRQs are HERGs, whereas objects classified as BL Lacs are in fact LERGs as well as beamed (diluted emission line) HERGs, explaining the appearance of "BL Lacs" of FR-II nature. The authors suggest that high-power HERG FR-II sources, classified as BL Lacs because of their weak emission lines, are in fact FSRQs according to the hitherto used definition, which could be tested by infrared spectroscopy of the Hα line.

In fact, both new classification scenarios summarised here are in mutual agreement, as Giommi *et al.* (2012a) note, since HERGs are characterised by a standard accretion disc, whereas for LERGs the accretion is less efficient.

The TeV Regime Note that a dominant part of the TeV detected extragalactic sources belong to the blazar class, with objects from all the different subclasses detected (see also TableA.1). Among them, the HBLs are the most numerous ones (see Figure 2.7), though their relative abundance has been decreasing the last years with increasing sensitivity of the instruments. The HBL dominance may therefore be solely a selection effect caused by the flux limitation of the TeV instruments (see also Sect. 2.5) as well as the comparably strong EBL absorption at these energies for the more distant FSRQs. This is indicating that the physical mechanisms and conditions responsible for the emission may be similar or even identical for the different blazar classes, underlining that the current class divisions may not be physically motivated.

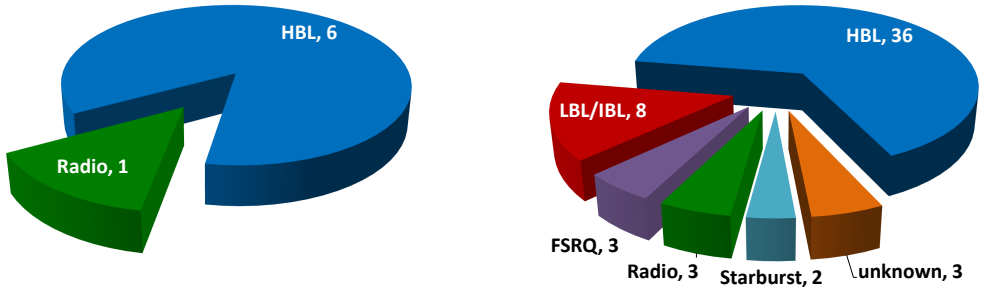

Figure 2.7: Census of extragalactic TeV sources before the new generation of TeV instruments (*left*) and today (*right*). The number behind the class name gives the number of corresponding objects. Classification according to Table A.1.

2.5 The Blazar Sequence

Studying the average broad-band properties of a sample of radio- and X-ray-selected blazars irrespective of their classification, Fossati *et al.* (1998) found a continuity in radio luminosity among them. The most luminous objects had their first SED peak located at the lowest frequencies. With decreasing luminosity, the peak is moving towards higher energies, from FSRQ over LBL to HBL objects. The different subclasses of blazars would therefore be only an effect of different source luminosity. The second SED peak is following that trend. Moreover, the luminosity ratio of the second and first peak increases with overall luminosity of the source (see Figure 2.8), which in the SSC scenario (see Sect. 2.6) corresponds to an increase of the IC dominance. The latter may be explained with an increasing importance of external photons in the SSC process with increasing luminosity, an interpretation supported by the increased emission line strength in these objects (Fossati *et al.* 1998). The blazar sequence scenario was supported by fitting the broad-band SED of gamma-ray bright blazars with an SSC and an EC model. In this framework, the lower synchrotron peak frequencies for higher luminosity sources may be explained by stronger cooling of the radiating electrons due to the denser photon field (Ghisellini *et al.* 1998).

The concept of the blazar sequence was confirmed or at least not contradicted by several authors (e.g. Donato *et al.* 2001; Sambruna *et al.* 2010; Abdo *et al.* 2010e; Ghisellini *et al.* 2010a; Chen & Bai 2011). The sequence cannot account for low power low-peaked and high power high-peaked sources, which consequently were sought intensively. Several authors claimed to have detected such objects (e.g. Padovani *et al.* 2002, 2003; Caccianiga & Marchã 2004; Antón & Browne 2005; Giommi *et al.* 2007; Bassani *et al.* 2007; Padovani *et al.* 2012). However, more detailed investigations showed that most, but not all, of the corresponding high frequency peaks were attributed rather to IC emission or the accretion disc, that the sources were wrongly classified or were not sufficiently luminous to contradict the sequence (Maraschi *et al.* 2008a; Padovani *et al.* 2012; Ghisellini *et al.* 2012). Also extended searches did not reveal clear evidence of such sources (Landt *et al.* 2008; Meyer *et al.* 2011). Nevertheless, indications speaking against the sequence in its simplest form were growing (Padovani 2007; Maraschi *et al.* 2008b; Chen & Bai

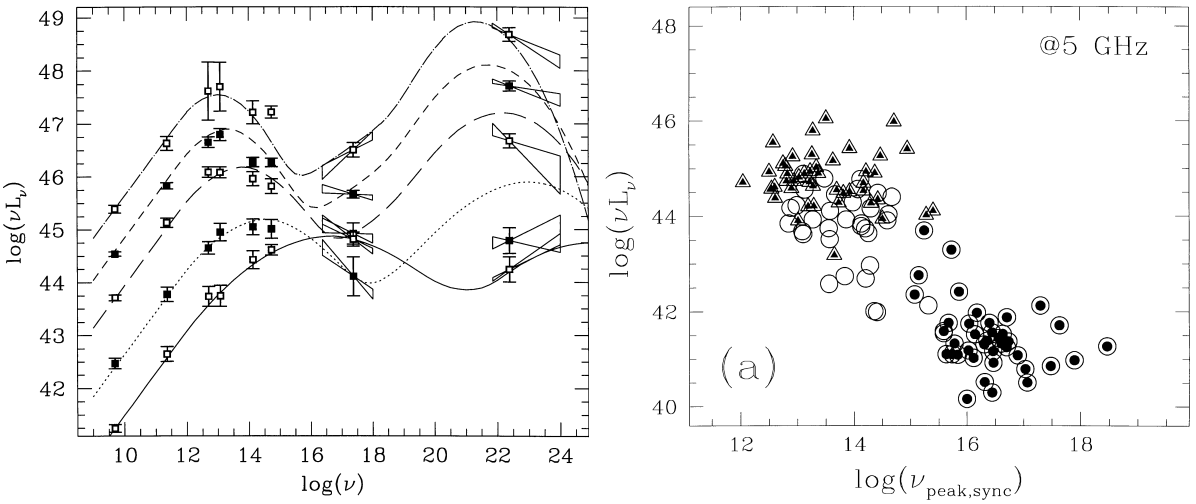

Figure 2.8: The blazar sequence as proposed by Fossati *et al.* (1998). *Left side:* the data points represent average fluxes for sources with similar radio luminosity, regardless of their classification. The shown curves are analytic approximations. With decreasing spectral luminosity, the synchrotron peak frequency increases. *Right side:* radio luminosity at 5 GHz vs. the synchrotron peak frequency. Triangles represent FSRQs, open circles radio-selected and open circles with a point X-ray-selected BL Lacs. Figures taken from Fossati *et al.* (1998).

2011).

Further arguments against the sequence were published. For example, Nieppola *et al.* (2006) studied the relation between peak frequency and luminosity for ∼380 radio-selected BL Lac objects and found that the blazar sequence would not be valid. However, the sample investigated by the authors was biased towards high radio flux densities and consisted of archival, largely non-contemporaneous data. From a study of 135 radio-loud AGN, Nieppola *et al.* (2008) concluded that the sequence proposed by Fossati *et al.* (1998) is an observational phenomenon, caused by not having corrected the peak frequencies for Doppler boosting. Instead, including such a correction, the negative correlation between luminosity and peak frequency would become positive. Ghisellini & Tavecchio (2008b) developed an extension of the sequence based on two physical parameters related to the accretion process, viz. the mass of the black hole and its accretion rate, instead of the luminosity only. In that model, high power sources with moderately high peak frequencies and low power sources with rather low peak frequencies may exist. Besides blazars, Meyer *et al.* (2011) also included radio-loud galaxies in their study of ∼440 objects and suggested to enlarge the "blazar sequence" to a "blazar envelope". A detailed discussion of these new models is beyond the scope of this work.

It has been argued in the past that the blazar sequence may just be a selection effect (e.g. Caccianiga & Marchã 2004; Antón & Browne 2005). Recent works strengthened this interpretation. (Giommi *et al.* 2012b) investigated simultaneous SEDs of 105 blazars selected according to their radio, soft and hard X-ray as well as their gamma-ray flux. The authors report the detection of low luminosity low-peaked objects not predicted by the blazar sequence. Moreover, the missing high luminosity high-peaked sources would be a result of not being able to determine their redshift and hence their luminosity

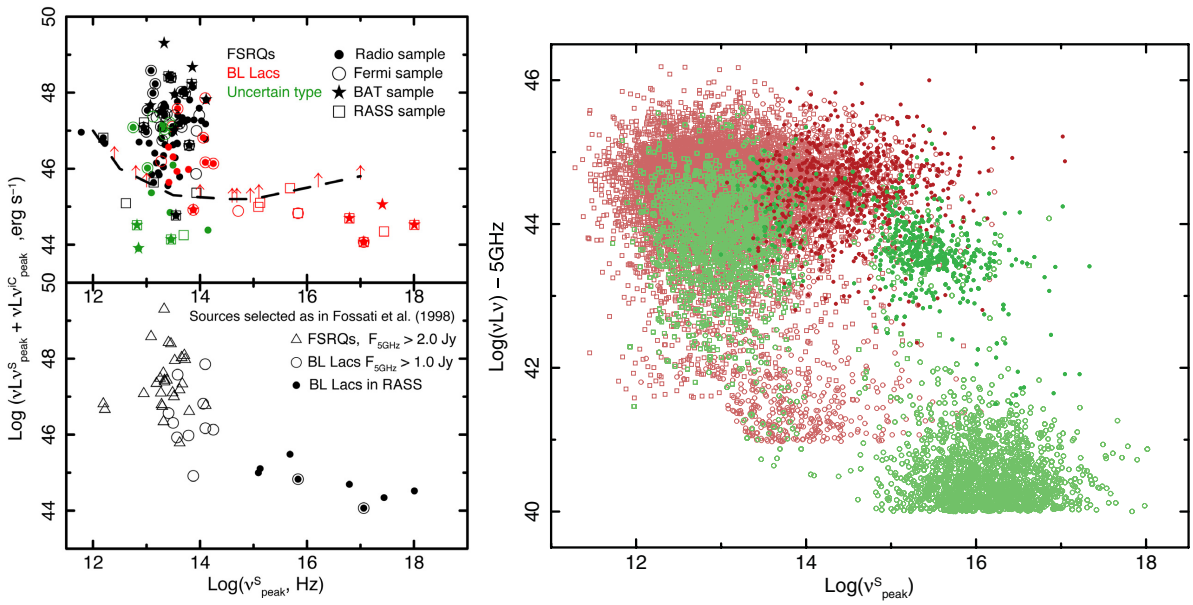

Figure 2.9: *Left side:* sum of the peak synchrotron and inverse-Compton luminosity as a function of the synchrotron peak energy for a flux limited sample of blazars. *Top panel:* all analysed blazars with a peak estimate, *bottom panel:* only blazars following the selection criteria of Fossati *et al.* (1998). For sources above the dashed line in the top panel, optical lines can hardly be detected, complicating a redshift estimate. Note the low luminosity low-peaked sources, not predicted by the blazar sequence. The bottom panel resembles the blazar sequence (see right side of Figure 2.8), emphasising its selection effect origin. Figure taken from Giommi *et al.* (2012b). *Right side:* radio luminosity as a function of the synchrotron peak frequency for a simulated sample of blazars with similar selection criteria as applied by Fossati *et al.* (1998). Open circles represent BL Lac objects, squares FSRQs. Red and green symbols refer to a radio flux density limited and an X-ray flux limited sample, respectively. Filled circles are BL Lacs that would proabably have no redshift measurement and hence luminosity estimate, i.e. these would be missing in case of real measurements. Neglecting these, the original blazar sequence is apparent, explaining this paradigm by the inability to measure the redshift of weak-lined sources. Figure taken from Giommi *et al.* (2012a).

(see *left side* of Figure 2.9). A correlation between the luminosity and peak frequency could only be found after applying the same selection criteria as Fossati *et al.* (1998), indicating that the sequence is not an intrinsic property of the sources but rather due to a selection bias. A similar conclusion is found by Giommi *et al.* (2012a) from a large simulation of blazar SEDs. Applying similar flux limit conditions as Fossati *et al.* (1998), the simulations can reproduce a blazar sequence-like distribution in luminosity vs. synchrotron peak frequency. However, adding BL Lac objects with faint or missing emission lines (i.e. in a real measurement, the redshift would be indeterminable and the source be missing in the study[14]), the sequence is no longer apparent (see Figure 2.9 *right side*). According to the authors, also the blazar envelope introduced by Meyer *et al.* (2011) is not real but rather an effect of not considering correctly the redshift for blazars without a distance estimate.

[14]Note that from the current Multifrequency Catalogue of Blazars (the *Roma*-BZCAT) http://www.asdc.asi.it/bzcat/, over 40 % of the more than 1200 BL Lac (candidate) objects have no redshift estimate (e.g. Massaro *et al.* 2009).

2.6 Spectral Models

From simultaneously measured broad-band SEDs of blazars, physical parameters of the emission region can be derived by applying theoretical models to the data. These mostly assume a compact spherical region moving relativistically along the jet, filled with an electron population following a broken power law distribution and a homogeneous magnetic field. The first peak of the blazar SED is generally described by synchrotron radiation of the accelerated electrons, whereas the second component is a matter of debate.

Model Overview The synchrotron photons can be inverse-Compton up-scattered in energy to the gamma-ray regime by the same electrons they originated from, producing the second SED peak (synchrotron self-Compton models, SSC; e.g. Jones *et al.* 1974; Marscher & Gear 1985; Maraschi *et al.* 1992; Bloom & Marscher 1996). These models are particularly successful explaining the SED of HBLs and partly IBLs and are predicting a strong correlation between X-rays and gamma rays as often observed for these sources, but mostly cannot describe the observational results of LBLs and FSRQs. Considering the discussions above, the latter objects are characterised by a non-negligible radiation component external to the jet, which serves as an additional photon reservoir for inverse-Compton scattering. Accordingly, models taking this component into account are called "external Compton" (EC) models. The photons may emanate from the accretion disc (e.g. Dermer *et al.* 1992; Dermer & Schlickeiser 1993), the BLR (e.g. Sikora *et al.* 1994; Ghisellini & Madau 1996) or the obscuring torus (Błażejowski *et al.* 2000), or several of these regions (e.g. Böttcher & Reimer 2004; Dermer *et al.* 2009)

Missing correlation between flares (e.g. Krawczynski *et al.* 2004) and extremely fast flares indicate that the emission of some blazars may not be restricted to purely leptonic emission processes. If electrons are accelerated within the jets, its natural to assume that also protons become co-accelerated. Since energy losses for protons are much lower than for electrons, these can reach energies up to 10^{19} eV. According to Mannheim & Biermann (1992); Mannheim (1993), these protons can induce pion cascades when interacting with synchrotron photons emitted by the accelerated electrons. Neutral pions give rise to gamma radiation ($p+\gamma \rightarrow \pi^0+p \rightarrow \gamma+\gamma+p$), whereas charged pions decay to neutrinos and electrons/positrons ($p+\gamma \rightarrow \pi^{\pm}+p \rightarrow e^{\pm}+3\nu+p$). Due to the high Lorentz factors of the resulting particles, Compton scattering occurs dominantly in the Klein-Nishina regime, leading to synchrotron radiation as the main mechanism for energy losses. These photons are down-cascaded in energy by the processes mentioned above until the emission region becomes transparent, leading to a considerable radiation contribution in the TeV and GeV range. Note that in this model a significant neutrino flux is produced, which may be detectable by current neutrino telescopes. Alternative models postulate that the synchrotron radiation of protons (in which case no accompanying neutrinos are expected; e.g. Aharonian 2000; Mücke & Protheroe 2000) or both, cascade emission and proton-synchrotron radiation (e.g. Mücke *et al.* 2003), may account for the detected gamma-ray emission. The largest difference between leptonic and hadronic models (apart from the contribution by hadrons) is a higher magnetic field (factor 10 – 100 larger) to be able to contain the protons within the emission region.

Apart from either a dominant leptonic or hadronic origin for the second SED peak,

both processes may contribute significantly to the observed emission, leading to the recent development of hybrid lepto-hadronic models (e.g. Weidinger & Spanier 2011; Aliu *et al.* 2012b; Cerruti *et al.* 2012). These include SSC as well as proton-synchrotron and proton-initiated cascade emission, successfully reproducing the SEDs of HBLs as well as FSRQs.

The inconsistency of jet speeds derived from direct interferometric radio observations and from SED modelling (see Section 2.2) as well as different types of time lags and correlations observed during flares (see previous section) indicated that the commonly applied assumption of one homogeneous emission zone may be oversimplified. Several models assuming different jet geometries have been proposed, like decelerating jets (Georganopoulos & Kazanas 2003; Levinson 2007), spine/sheath or needle/jet (Ghisellini *et al.* 2005; Ghisellini & Tavecchio 2008a), jet-in-jet or minijets (Giannios *et al.* 2009; Nalewajko *et al.* 2011), multiple emission zone jets (Weidinger & Spanier 2010; Marscher 2012), or multi-shock jets (Richter & Spanier 2012), which may serve to solve these problems.

In the following, we will give a few more details on the one-zone leptonic SSC model of Maraschi & Tavecchio (2003) and the leptonic two-zone model of Weidinger & Spanier (2010), which have been applied to the data presented in this work. Further discussion of SED models is out of the scope of this work, for which we refer to the given literature.

One-Zone SSC Model In the model of Maraschi & Tavecchio (2003) (see also Tavecchio *et al.* 1998), a spherical emission region is moving relativistically (Doppler factor δ, see Eq. 2.10) within the jet. The region of radius R is filled with a tangled magnetic field of strength B. Electrons are filling the emission region isotropically, following a phenomenological double-power law energy distribution given in the co-moving frame by:

$$N(\gamma) = K\gamma^{-e_1}\left(1 + \frac{\gamma^{e_1-e_2}}{\gamma_{\mathrm{break}}}\right) \quad \text{for} \quad \gamma_{\mathrm{min}} < \gamma < \gamma_{\mathrm{max}} \tag{2.19}$$

where γ is the Lorentz factor, K is the electron density at $\gamma_{\mathrm{min}} = 1$ and e_1 and e_2 are the spectral indices below and above the break γ_{break}, respectively. See also *top panel* of Figure 2.10. The nine parameters are defined a priori and adapted in an iterative process manually to the data points.

The resulting synchrotron spectrum is defined by the emissivity $j_{\mathrm{S}}(\nu_{\mathrm{S}})$ at a given frequency ν_{S}

$$j_{\mathrm{S}}(\nu_{\mathrm{S}}) = \frac{1}{4\pi}\int_{\gamma_{\mathrm{min}}}^{\gamma_{\mathrm{max}}} N(\gamma)\, P(\nu_{\mathrm{S}}, \gamma)\, \mathrm{d}\gamma \tag{2.20}$$

with $P(\nu_{\mathrm{S}}, \gamma)$ being the standard specific power emitted by a single electron. The spectrum is calculated between the self-absorption frequency $\nu_{\mathrm{S},1}$ and the maximum frequency $\nu_{\mathrm{S},2} \approx 2.8 \cdot 10^6 B\gamma_{\mathrm{max}}^2$. The IC emissivity is given by

$$j_{\mathrm{C}}(\nu_{\mathrm{C}}) = \int_{\gamma_{\mathrm{min}}}^{\gamma_{\mathrm{max}}} N(\gamma) \int_{\nu_{\mathrm{t,min}}}^{\nu_{\mathrm{t,max}}} n_{\mathrm{t}}(\nu_{\mathrm{t}})\, j_{\mathrm{C}}(\nu_{\mathrm{C}}; \gamma, \nu_{\mathrm{t}})\, \mathrm{d}\nu_{\mathrm{t}}\mathrm{d}\gamma \tag{2.21}$$

where $j_{\mathrm{C}}(\nu_{\mathrm{C}}; \gamma, \nu_{\mathrm{t}})$ represents the single electron emissivity dependent on the target photon frequency ν_{t} and $n_{\mathrm{t}}(\nu_{\mathrm{t}})$ is the numerical density of the target photons. Klein-Nishina effects are taken into account.

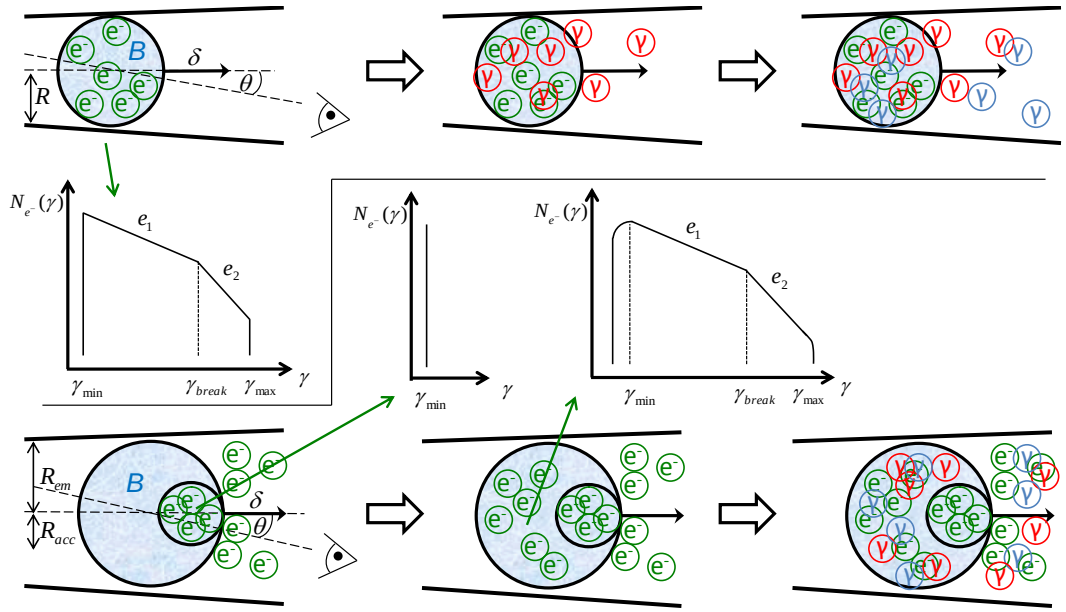

Figure 2.10: *Top panel:* sketch of the model geometry used by Maraschi & Tavecchio (2003). A spherical region filled with a tangled magnetic field B and electrons e^-, following a number distribution $N_{e^-}(\gamma)$, is moving with a small angle to the line of sight θ towards the observer. The electrons emit synchrotron radiation (red γ's), which are inverse-Compton upscattered to higher energies (blue γ's). *Bottom panel:* layout of the self-consistent two-zone model of Weidinger & Spanier (2010). Electrons with a monoenergetic number distribution are constantly entering the acceleration zone with radius $R_{\rm acc}$. They gain energy through acceleration and lose energy by cooling, self-consistently leading to an approximately broken power law distribution. Leaving this region, they emit synchrotron photons, which are inverse-Compton upscattered to higher energies. The text for details.

Though Maraschi & Tavecchio (2003) also describes a modified version of this model including an EC component, this approach has not been applied to the data presented here. For HBLs, the contribution by the jet-external photons should be minor.

Self-Consistent Two-Zone Model A spherical region ("blob") moving relativistically through the jet will accumulate and accelerate electrons from the jet plasma. The acceleration will be most efficient at the boundary between the sphere and the jet, having the largest density gradient and most turbulent plasma. Therefore, the assumption of a single homogeneous region is probably not correct.

Correspondingly, Weidinger & Spanier (2010) assumed a smaller (radius $R_{\rm acc}$), spherical acceleration region within the larger blob (the emission region with radius $R_{\rm em}$), see *bottom panel* of Figure 2.10. Both regions are characterised by the same constant, randomly oriented magnetic field B and the same Doppler factor δ. The electron are assumed to be isotropically and homogeneously distributed throughout the acceleration as well as the emission region, though the corresponding distributions are different.

Electrons are injected into the acceleration zone, described by the injection function $Q_{\rm inj}(\gamma, t) = Q_0 \delta(\gamma - \gamma_0)\,\vartheta(t - t_0)$, with $t_0 = 0$. The injection is assumed to be time independent, and the electron energy at injection γ_0 to be constant (see also Figure 2.10). The electrons gain energy via diffuse shock acceleration (Fermi-I and Fermi-II) and cool

by synchrotron and inverse-Compton emission, resulting in an electron distribution that can be approximated by a broken power-law shape (in case Fermi-II acceleration is subdominant to Fermi-I. The distribution is then characterised by K, $\gamma_{\rm min}, \gamma_{\rm break}, \gamma_{\rm max}, e_1$ and e_2, see above; however, K is defined at $\gamma_{\rm min}$ instead of at γ_0). The exact Klein-Nishina cross section is properly taken into account. The electrons are injected according to this distribution into the emission region, where no further acceleration takes place. Note that opposite to many other models assuming such a distribution ad hoc, here it is derived self-consistently from $Q_{\rm inj}$. In the emission region, the electrons lose their energy by synchrotron and corresponding inverse-Compton radiation. Since the volume of the emission region is much larger compared to the acceleration region, the observed SED is dominated by radiation emanating from the former. Apart from the parameters mentioned above, further variables relevant for the shape of the SED are the relative importance of acceleration and escape (from the emission region) time scales $t_{\rm acc}/t_{\rm esc}$ as well as the relation of shock acceleration and diffuse acceleration a.

This leptonic SSC approach can also be modified to accelerate protons as well, adding radiation from proton-synchrotron processes and proton-initiated cascades (Weidinger & Spanier 2011). The corresponding lepto-hadronic model has only two more free parameters, which are the injection function of the protons $Q_{\rm inj,p}\,(\gamma, t)$ and their energy at injection $\gamma_{0,\rm p}$.

Outlook The input parameters of many models mentioned above are set by hand a priori, rather defined by experience and expectation than physically motivated, which induces a human bias to the results of the modelling. Though the parameters are constrained by physical limits (see e.g. Tramacere *et al.* 2009), their viable range of results is quite broad. Self-consistent approaches employed by e.g. Acciari *et al.* (2009d); Weidinger & Spanier (2010) are an important step towards unbiased results. Recently, model fits were determined by minimising the χ^2 of the model in comparison to the SED data (Mankuzhiyil *et al.* 2011; Zhang *et al.* 2012). The resulting parameter values are partly deviating strongly from previous results of manual fitting (see also Section 6.4.6).

It should be noted that current SED models can not describe the self-absorbed radio data and generally have to ignore them, although they contain much information on the emission processes. Results of a broad-band model being able to self-consistently assess also the radiation in the radio regime have been presented (e.g. Richter & Spanier 2012).

The variety of models listed above is due to the lack of data of sufficient time resolution and energy coverage, generally obtained from simultaneous multi-wavelength campaigns, which both are crucial to constrain and finally reject or verify different model approaches. Only for some sources, such observations are available with reasonable statistics, however mostly concentrated on high activity states. Features observable during flares like correlated or missing variability in different energy bands, time lags, peak shifts and the variability time scales may shed more light on the physical mechanisms at work, rendering such observations very important. Another reason for such campaigns being conducted during high states is the higher detection probability. However, the baseline emission of the sources is one crucial ingredient to our understanding of the energetics and emission of these sources. The following two sections will concentrate on the currently available multi-wavelength data and the so-called "quiescent state" of blazars.

2.7 Multi-Wavelength Observations

The SED of blazars ranges from the radio up to the VHE gamma-ray regime, covering more than 18 orders of magnitude in energy. For BL Lacs, the X-ray and VHE components are particularly important, since they can constrain the electron number distribution and identify the processes leading to the higher frequency peak. Radio observations are crucial to determine the physical location of the emitting zone, and optical and HE data can be used to determine the frequencies of the two SED peaks. Due to the strong and frequent variability of blazars, observations in these different energy bands have to be conducted at the same time (on time scales smaller than the typical variability time scale in the corresponding energy regime, which is about one day; see Section 2.3) or quasi-simultaneously (which we define in this work as no variability being present on the considered time scales). In the following, only SEDs resulting from (quasi-)simultaneous multi-wavelength (MW) campaigns including at least optical, X-ray and VHE detections are discussed[15], which is not required though for light curve variability studies (where coverage of two energy regimes is sufficient). Such SEDs have sufficient coverage to yield a good estimate of the two SED peaks. The same criteria have been applied for indicating available MW data in Table A.1.

Until the advent of the new generation of imaging air Cherenkov telescopes ($\sim$ 2003, 2004), only the strongest sources were detected at VHE. For four of these seven known sources (Mrk 421, Mrk 501, PKS 2155−304, 1ES 1959+650; see also Table A.1) simultaneous campaigns including VHE detection were published. At the time the campaigns presented in this work were organised, the number of objects studied during such campaigns had increased only marginally to 7 out of 17, adding the sources M 87, PG 1553+113 and 1ES 1101−232.

Today, the number of objects observed in the context of simultaneous MW observations amounts to 23, out of 55 sources detected by imaging air Cherenkov telescopes (see also Table A.1). We emphasise that only for 14 of these objects, MW campaigns have been organised a priori. The bulk of such campaigns (note that for some objects, several MW observations are available) was conducted after a high state trigger by one of the participating instruments (see also Abdo *et al.* 2010b; Giommi *et al.* 2012b), leaving the low state basically unexplored. Only for PKS 2155−304, Mrk 501, PKS 2005−489 and Mrk 421, such low state observations have been reported (e.g. Aharonian *et al.* 2005b; Anderhub *et al.* 2009b; Acero *et al.* 2010; Abdo *et al.* 2011b). That may, however, also be due to the sparseness of MW campaigns for the remaining objects, which prevents to identify a low activity state.

In the following, we give a short and by no means complete list of the most important results derived from simultaneous MW campaigns.

- HBLs are mostly well fit by simple one-zone SSC models (e.g. Krawczynski *et al.*

[15] Authors sometimes call their MW SEDs "contemporaneous" or "simultaneous" if VHE observations averaged over years' time scale are accompanied by one day of observation in optical and/or X-rays during that time span, without further monitoring data available. Though some simultaneity is indeed given, in that case no information on potential variability in the latter bands is available. Consequently it is not known if these data are representative of the flux state during the integrated VHE data, and the SED is not reliable. We do not consider such observations as simultaneous here.

2004; Anderhub *et al.* 2009b; Abdo *et al.* 2011d; Acciari *et al.* 2011c; Abdo *et al.* 2011b; Acciari *et al.* 2011b,a; Aleksić *et al.* 2012b; Abramowski *et al.* 2012a) whereas IBLs, LBLs and FSRQs need an increasing contribution from external photons (EC) or require multi-zone models (e.g. Acciari *et al.* 2008; Abdo *et al.* 2011e; Aleksić *et al.* 2011b). This can be understood in the framework of the unified scheme due to the growing importance of the emission from the BLR and accretion disc.

- In most of the campaigns where significant variability was detected, a correlation between the X-ray and VHE flux is reported (e.g. Fossati *et al.* 2008; Acciari *et al.* 2011a; Abramowski *et al.* 2012a), in accordance with expectations from SSC models. There are indications from the source PKS 2155−304 that this only holds for high states, whereas no correlation may be present during low states (Aharonian *et al.* 2005b, 2009c; Abramowski *et al.* 2012a).

- Detailed campaigns on HBLs suggest that although individual SEDs may be well fit with one-zone SSC models, these cannot reproduce the observed variability (Abramowski *et al.* 2011b; Aleksić *et al.* 2012d). That conclusion is supported by the discovery of "orphan flares" (e.g. Krawczynski *et al.* 2004; Błażejowski *et al.* 2005), requiring different model approaches (see Section 2.6).

- The correlation between the X-ray and VHE regime may be disguised by the transition to the Klein-Nishina regime during strong flares, lowering the variability amplitude at VHE compared to X-rays (Acciari *et al.* 2011c; Abramowski *et al.* 2011b).

- Gamma-ray outbursts seem to be accompanied by changes in the optical polarisation vector (e.g. Marscher *et al.* 2008; Aleksić *et al.* 2011b; Arlen *et al.* 2012).

- For FSRQs, the gamma-ray emission region is probably situated outside of the BLR (due to transparency conditions for the VHE photons), whereas the synchrotron emission may come from regions further upstream. That requires multi-zone emission models (e.g. Aleksić *et al.* 2011b, and references therein).

- The jet may contain a helical magnetic field, where flares occur when an emission feature of freshly injected particles is moving along the streamlines within the acceleration and collimation zone. If passing the radio core downstream of this region, another flare occurs (Marscher *et al.* 2008; Arlen *et al.* 2012)[16].

- The VHE emission of the radio galaxy M 87 may originate from the core (Acciari *et al.* 2009b; Abramowski *et al.* 2012c), speaking against the possibility of the knot HST-1 being the production site of emission (e.g. Stawarz *et al.* 2006). If true, the radiation is produced within $\sim 50\,\mathrm{pc}$ from the central BH (Abramowski *et al.* 2012c), or possibly within some hundreds of Schwarzschild radii ($200\,R_\mathrm{S} \approx 0.11\,\mathrm{pc}$

[16]Note that Marscher *et al.* (2008) have erroneously defined the time of VHE detection to be restricted to end of September 2005, whereas the observations in fact spanned from August to December 2005, without a sign of significant flux variability (see Albert *et al.* 2007a).

for M 87) (Acciari *et al.* 2009b). The latter would be in contrast to claims that the VHE emission region has to be located outside of the BLR (see above).

These results illustrate the importance of such observations, but also emphasise the need for more of such campaigns. The statistics of simultaneous SEDs has to be enlarged not only for the TeV blazars as a class, but also for individual objects, as the partly contradicting results above suggest. Moreover, this is the only meaningful way to investigate the low state of the sources.

2.8 Steady Emission States

Apart from the high activity states and flares, a rather steady and constant, underlying emission is thought to exist, which should give direct information on the basic physical mechanisms driving the broad-band radiation. This "quiescent" emission has to be produced by a feature stable on long time scales, like the jet launching site (so-called "nozzle", see e.g. Donea & Biermann 2002), a reconfinement shock (Sikora *et al.* 2008, and references therein), or the radio core, which is supposed to contain a high number of weak, individual emission components the superposition of which would appear to be stable (e.g. jet model of Blandford & Königl 1979). On top of that baseline emission, flares may occur through injection of fresh particles into the jet or shocks travelling the jet. Consequently, the understanding of the quiescent state would also establish a firm basis to investigate the origin of flares.

With the knowledge of the quiescent state, the complete evolution of the SED during a flare may be described applying time-dependent SED models (like the one of Weidinger & Spanier 2011). Moreover, the knowledge of the lowest flux state in combination with an estimate of the duty cycle of the sources allows for a more precise determination of the contribution of unresolved blazars to the CR and diffuse gamma-ray background, setting more stringent limits on theories of CR production. Recent studies propose that under the assumption of a Blandford & Königl (1979)-type jet within the Blandford & Znajek (1977) framework, the quiescent state synchrotron spectrum can be used to derive the Kerr parameter of the central BH (Steinbring 2012).

Due to the increased probability of detection, higher statistics and potentially stronger and faster variability, previous MW campaigns were focusing mostly on high states of blazars. In particular the limited sensitivity of the HE and VHE instruments before about 2004 allowed to study only the strongest sources, still preferentially in high states. Therefore, simultaneous MW observations during low emission states are hardly available (see previous section). Still today, detections during a low state can only be achieved by observations spread over several days or weeks, especially in the HE regime. This renders simultaneous MW observations during low activity states even more challenging. However, the data basis on the dominating (in time) low state is improving and increasing thanks to the all-sky survey mode of *Fermi*-LAT, averaging all activity states of the sources.

3 Multi-Wavelength Instrumentation

This section will give a short overview of the instruments that participated in the multi-wavelength campaigns on 1ES 1011+496 and 1ES 2344+514, or contributed monitoring data. The MAGIC telescope will be described in greater detail in Chapter 4. The exact layout of the observations will be presented in Sections 5.2 and 6.2. Table 3.1 summarises the most important instrument parameters. Errors of data points shown in the following chapters are always given with statistical errors only, unless stated here otherwise.

3.1 Radio Regime

Effelsberg The Effelsberg radio telescope (e.g. Wielebinski *et al.* 2011) is the second-largest movable telescope in the world, with a mirror diameter of 100 m, operated by the Max-Planck-Institut for radio astronomy in Bonn. It is situated near Effelsberg in the Eifel mountains, Germany, at an altitude of ~ 320 m. First data was taken in 1972. The accessible frequency range spans from 0.3 to 86 GHz (90 – 0.35 cm), achieving an angular resolution of $\sim 35''$ at 22.2 GHz. Through the F-GAMMA program[1], it is participating in a monitoring campaign for ~ 60 *Fermi*-LAT detected AGNs.
Homepage: http://www.mpifr-bonn.mpg.de/8964/effelsberg

The data obtained from Effelsberg by the author are fully reduced. Note that the given error bars contain already systematic uncertainties and are applied as such throughout this work unless stated otherwise.

IRAM Apart from the Plateau de Bure interferometer, the **I**nstitut de **R**adioastronomie **M**illimétrique operates a 30-m telescope on Pico Veleta (2850 m above sea level) near Granada in the Spanish Sierra Nevada. Single pixel observations with the latter can be conducted at frequencies of ~ 86, 140, 230 and 345 GHz (3 – 0.8 mm). For good observation conditions, the detection limit ($4\,\sigma$) amounts to ~ 0.2 Jy for one pointing of 1200 – 1400 s. This telescope is also taking part in the F-GAMMA program.
Homepage: http://www.iram-institute.org/

Also the received IRAM data products are final and contain already systematic errors.

Metsähovi The Metsähovi radio telescope is equipped with a 13.7-m dish, observing at 36.8 GHz (e.g. Aleksić *et al.* 2012f). Located at Metsähovi, Kylmälä, Finland, it is

[1] ***F****ermi*-**G**amma-ray space telescope **A**GN **M**ulti-frequency **M**onitoring **A**lliance (Fuhrmann *et al.* 2007)

Instrument	**Range**$^{(a)}$	$\Delta E/E^{(b)}$	**FOV**	$\Delta\theta/\theta^{(c)}$	**Sensitivity**$^{(d)}$
Effelsberg	0.3 – 86 GHz	...	...	$35''$	...
IRAM	86 – 345 GHz	...	...	...	...
Metsähovi	36.8 GHz	...	...	...	~ 0.2 Jy/~ 1300 s
OVRO	15.0 GHz	...	...	...	...
RATAN-600	0.6 – 30 GHz	...	...	...	...
VLBA	0.3 – 96 GHz	...	...	...	...
Bell	600 nm	...	$10'$	...	...
CrAO	586 nm	...	...	...	...
KVA	640, 550, 440 nm	...	...	...	...
Swift UVOT	600 – 170 nm	~ 0.5 %	$17' \times 17'$	$0.9''$	24 mag/10^3 s
INTEGRAL ISGRI	15 keV – 1 MeV	8 %	$9^\circ \times 9^\circ$	$12'$	1 mCrab/10^6 s
MAXI GSC	2 – 30 keV	18 %	$1.5^\circ \times 160^\circ$	1.5°	4.5 mCrab/day
RXTE ASM	2 – 10 keV	...	$6^\circ \times 90^\circ$	$3' \times 15'$	10 mCrab/day
Swift BAT	15 – 150 keV	~ 5 %	$100^\circ \times 60^\circ$	$20'$	$\sim$ 1 mCrab/2 yrs
Swift XRT	0.2 – 10 keV	~ 2 %	$23.6' \times 23.6'$	$18''$	1 mCrab/10^4 s
AGILE GRID	0.03 – 50 GeV	1	2.5 sr	$1.2^\circ - 3.5^\circ$	$1 - 2 \cdot 10^{-7}$/yr
Fermi-LAT	0.02 – > 300 GeV	$< 6 - 15$ %	2.4 sr	$< 0.15^\circ - 3.5^\circ$	$3 \cdot 10^{-9}$/yr
MAGIC-I	0.05 – > 10 TeV	~ 20 %	$3.5^\circ \times 3.8^\circ$	0.1°	1.6 % Crab/50 hrs

Notes. $^{(a)}$ Observable energy, frequency or wavelength range. $^{(b)}$ Energy resolution. $^{(c)}$ Angular resolution. $^{(d)}$ Instrument sensitivity within the given time frame. Note that some experiments define their sensitivity at a different significance σ, see text. In case of AGILE and *Fermi*, the units are ph cm^{-2} s^{-1}.

Table 3.1: Summary of the most important characteristics of the instruments participating in the MW campaigns. "..." indicates that no information could be found. References are given in the paragraphs below.

operated by the Metsähovi Radio Observatory.
Homepage: http://metsahovi.aalto.fi/en/

OVRO 40-m The **O**wens **V**alley **R**adio **O**bservatory of the California Institute of Technology operates, amongst several interferometers, a 40-m radio telescope observing at 15.0 GHz (Richards *et al.* 2011). The instrument is located in California, USA, at an altitude of 1222 m above sea level, and observing since 1968. Having established since 2008 an own blazar monitoring program of 1500 sources (Richards *et al.* 2011), it is also participating in the F-GAMMA program.
Homepage: http://www.ovro.caltech.edu/, http://www.astro.caltech.edu/ovroblazars/

OVRO data are given with statistical errors only. Systematic uncertainties are estimated to amount to $\sim 5\%$ (Richards *et al.* 2011).

RATAN-600 **R**adio **A**stronomical **T**elescope **A**cademy **N**auk (science) is observing since 1974 and is operated by the Russian Academy of Sciences. The antenna consists of a circle of mirror elements with an overall radius of 576 m, separated into four reflectors (North, South, West and East). It is located at Zelenchukskaia in the northern Caucasus, Russia, at an altitude of 970 m above sea level. Observations are performed between 0.6

and 30 GHz (1 – 31 cm).
Homepage: http://www.sao.ru/Doc-en/index.html, http://www.sao.ru/ratan/

VLBA The **V**ery **L**ong **B**aseline **A**rray (Napier 1995) conducts interferometric radio observations since 1993, operated by the National Radio Astronomy Observatory (NRAO). It consists of ten telescopes, each equipped with a 25-m dish and reaching a maximum baseline of ∼ 8600 km (from Hawaii to the Virgin Islands). The accessible frequency range spans 1.2 – 96 GHz (28 – 0.3 cm). Using VLBA, monitoring observations at 15.4 GHz of nearly 300 AGNs are conducted within the MOJAVE program (**M**onitoring **O**f **J**ets in **A**GN with **V**LBA **E**xperiments[2].
Homepage: https://science.nrao.edu/facilities/vlba

The final data products obtained by the author and presented in this work include also systematic uncertainties.

3.2 Optical Regime

All optical data obtained in this work were originally given as flux in units of magnitudes, which had to be converted, host-galaxy corrected and de-reddened by the author.

Bell The Bell observatory, situated near Bowling Green, Kentucky, USA, is operated by the Western Kentucky University (Carini *et al.* 2004). The telescope is equipped with a 0.6 m mirror, observing in the R-band at 600 nm. More than 50 blazars are monitored on an irregular basis.
Homepage: http://astro.wku.edu/observatory/

CrAO The **Cr**imean **A**strophysical **O**bservatory operates several telescopes near Nauchny, Ukraine. Observations in the context of this work were conducted with the 1.25 m AZT-11 telescope, built in 1981, at a central wavelength of 586 nm.
Homepage: http://www.crao.crimea.ua/

KVA The **K**ungliga **V**etenskaps**A**kademien system consists of two telescopes with 0.35 and 0.6 m, where data of the former have been used in this work. It is situated on the Canary island of La Palma, Spain, at an altitude of ∼ 2350 m and operated by the Tuorla observatory. Observations can be conducted in differential photometry mode in the R-band (640 nm), B-band (550 nm) and V-band (440 nm). The telescope is observing in the R-band simultaneously with MAGIC. In cooperation with the Tuorla 1.0 m telescope at the Tuorla Observatory (near Turku, Finland, at an altitude of ∼ 50 m), the Tuorla Blazar Monitoring Program[3] is maintained, observing on a regular basis more than 50 blazars in the R-band.
Homepage: http://www.astro.utu.fi/research/telescopes/

[2] http://www.physics.purdue.edu/MOJAVE/
[3] http://users.utu.fi/kani/1m/

***Swift* UVOT** Apart from its X-ray instruments, the *Swift* satellite (see below) is equipped with the 30 cm **U**ltra**V**iolet/**O**ptical **T**elescope to perform optical observations simultaneous to the X-ray measurements. The telescope can observe at white light and additional six different filters: V, B, U, UVW1, UVM2 and UVW2 (547, 439, 347, 260, 225, 193 nm), achieving a $5\,\sigma$ sensitivity of 24 magnitudes within 10^3 s for white light (Gehrels *et al.* 2004). The energy resolution amounts to $\sim$0.5 % at 400 nm.
Homepage: http://swift.gsfc.nasa.gov/

3.3 X-Rays

Since the atmosphere is not transparent for X-ray radiation, corresponding measurements have to be conducted by satellite-borne telescopes.

INTEGRAL The ESA satellite **INTE**rnational **G**amma-**R**ay **A**strophysics **L**aboratory was launched in 2002. It observes with four different instruments: the imaging instrument IBIS (**I**mager on-**B**oard the *INTEGRAL* **S**atellite), the **SP**ectromenter on *INTEGRAL* (SPI), the X-ray monitor JEM-X and the **O**ptical **M**onitoring **C**amera OMC (Winkler *et al.* 2003). Data used in this work were obtained with ISGRI (*INTEGRAL* **S**oft **G**amma-**R**ay **I**mager), which is one of the two IBIS detectors. The ISGRI camera consists of 128×128 CdTe detectors shadowed by a coded mask, achieving a nominal energy range of 15 keV – 1 MeV and energy resolution of ~ 8 % at 60 keV (Lebrun *et al.* 2003) with a $3\,\sigma$ sensitivity of 1 mCrab in 10^6 s at ~ 60 keV.
Homepage: http://sci.esa.int/science-e/www/area/index.cfm?fareaid=21

MAXI The Japanese **M**onitor of **A**ll-sky **X**-ray **I**mage instrument (Matsuoka *et al.* 2009) is attached to the International Space Station ISS since 2009, with a planned life time of more than two years. Equipped with a **G**as **S**lit **C**amera (GSC) and a **S**olid-state **S**lid **C**amera (SSC), MAXI is performing all-sky monitoring between 2 and 30 keV (energy resolution: 18 % at 5.6 keV) and producing all-sky X-ray maps between 0.5 and 12 keV, respectively. Publicly available GSC monitoring data have been used in this work. The estimated sensitivity of the GSC all-sky monitoring amounts to ~ 4.5 mCrab or $1.6 \cdot 10^{-10}\,\mathrm{erg\,cm^{-2}\,s^{-1}}$ per day ($5\,\sigma$), and 0.2 mCrab after 2 years of observations.
Homepage: http://maxi.riken.jp/top/

RXTE Between 1996 and 2012, NASAs **R**ossi **X**-ray **T**iming **E**xplorer was observing with the pointed **P**roportional **C**ounter **A**rray (PCA, 2 – 60 keV) and the **H**igh **E**nergy **X**-ray **T**iming **E**xperiment (HEXTE, 15 – 250 keV) as well as with the **A**ll-**S**ky **M**onitor (ASM, 2 – 10 keV Levine *et al.* 1996). The latter consists of three proportional counters with coded apertures, each observing a field of view of $6° \times 90°$, achieving a sensitivity of 10 mCrab ($2\,\sigma$) for one-day averages.
Homepage: http://xte.gsfc.nasa.gov/

Swift The NASA *Swift* mission (Gehrels *et al.* 2004) was launched in 2004 to study gamma-ray bursts. For this purpose, the satellite is equipped with the **B**urst **A**lert

Telescope (BAT) to monitor the X-ray range between 15 and 150 keV for such events. The pointed **X**-**R**ay **T**elescope (XRT, 0.2 – 10 keV) as well as the UVOT (see above) are intended for follow-up observations of BAT-triggered outbursts. Short notice target-of-opportunity proposals are often successful for applying for observation time as long as no competing gamma-ray bursts observations are imminent.

The BAT consists of > 32000 CdZnTe elements shadowed by a coded mask of 54000 tiles. After the guaranteed life time of two years, the $5\,\sigma$ sensitivity of the BAT all-sky monitoring amounts to ~ 1 mCrab or $\sim 2 \cdot 10^{-11}\,\mathrm{erg\,cm^{-2}\,s^{-1}}$ between 15 and 150 keV. The XRT focuses X-rays by a grazing incidence Wolter telescope onto a CCD, achieving a $5\,\sigma$ sensitivity of $2 \cdot 10^{-14}\,\mathrm{erg\,cm^{-2}\,s^{-1}}$ or 1 mCrab within 10^4 s and an angular resolution of $18''$. The energy initial resolution amounted to $\sim 2\,\%$ at 6 keV, not expected to fall below 5 % on mission lifetime scales.
Homepage: http://swift.gsfc.nasa.gov/

The XRT data used in this work contain only statistical errors, same as the BAT monitoring data. The total uncertainty (including systematics) of the latter is estimated to be 110 % of the systematic one (W. Baumgartner, 2012, private communication).

3.4 Gamma Rays

Also gamma rays cannot penetrate the atmosphere of the earth. Therefore, direct measurements in this regime are conducted by satellite-based instruments. However, due to the low photon flux declining further with increasing energy, the accessible frequency range is limited by the detector area. Therefore, the gamma-ray regime has been divided historically into the High Energy (HE, $0.1 \lesssim E \lesssim 100$ GeV) and Very High Energy (VHE, $0.1 \lesssim E \lesssim 100$ TeV) range. Though *Fermi*-LAT (see below) can measure photons up to VHE directly, this regime is originally attributed to indirect observation techniques, based on air showers produced by the incoming photons within the atmosphere. This method is limited though to lower energies by the size and light content of the showers. Both, the indirect and indirect method, are needed to cover the whole gamma-ray regime.

AGILE The HE **A**stro-rivelatore **G**amma a **I**mmagini **LE**ggero satellite, observing since 2007, is operated by the Italian Space Agency. The satellite has two main instruments: the X-ray instrument Super-AGILE (18 – 60 keV) and the **G**amma-**R**ay **I**maging **D**etector (GRID) (Tavani *et al.* 2009), sensitive between ~ 30 MeV and 50 GeV. Data of the former are not available for guest observers. The latter consists of a tracker made of silicon-tungsten and a caesium-iodide calorimeter surrounded by an anti-coincidence shield, achieving a $5\,\sigma$ sensitivity > 100 MeV of $3 \cdot 10^{-7}\,\mathrm{ph\,cm^{-2}\,s^{-1}}$ within 10^6 s. The effective area is comparable to the one of its predecessor EGRET. The energy resolution amounts to 100 % at 400 MeV. It is primarily designed for monitoring taking advantage of its large field of view (2.5 sr).
Homepage: http://agile.asdc.asi.it/

Fermi The NASA *Fermi* **G**amma-ray **S**pace **T**elescope (GST) (Atwood *et al.* 2009), formerly known as GLAST (**G**amma-ray **L**arge **A**rea **S**pace **T**elescope), started science data taking at HE end of 2008. Apart from the main instrument LAT (**L**arge **A**rea **T**elescope), sensitive between 20 MeV and > 300 GeV, the **G**amma-ray **B**urst **M**onitor (GBM) searches a large part of the sky between 8 keV and 40 MeV for strong, transient events. The LAT is a pair conversion instrument composed of a tracker made of silicon strips with interleaved tungsten converters and a caesium-iodide calorimeter, surrounded by an anti-coincidence detector. The detector layout allows for a large field of view (2.4 sr) and a good angular and energy resolution at 1 GeV of 0.6° and ∼9 %, respectively. Its peak effective area of $\sim 8000\,\mathrm{cm}^2$ surpasses the one of EGRET by a factor of six (Nolan *et al.* 2012). For a steady source at high galactic latitudes, the LAT is assumed to achieve a $5\,\sigma$ sensitivity > 100 MeV of $3 \cdot 10^{-9}\,\mathrm{ph\,cm^{-2}\,s^{-1}/yr}$.
Homepage: http://fermi.gsfc.nasa.gov/

MAGIC The two 17 m **M**ajor **A**tmospheric **G**amma-ray **I**maging **C**herenkov telescopes are performing stereoscopic observations at VHE since mid of 2009. The accessible energy range spans from ∼ 50 GeV to > 10 TeV, with an angular resolution of $\sim 0.07°$ at 300 GeV, an integral sensitivity of 0.76 % Crab ($5\,\sigma$) within 50 hrs of observations above 290 GeV and an energy resolution at medium energies of ∼ 16 % (Aleksić *et al.* 2012e).
Homepage: http://wwwmagic.mppmu.mpg.de/

The observations presented in this work were conducted before 2009, i.e. in mono mode with MAGIC-I only. This telescope and its characteristics will be presented in the following section, together with an overview of the Cherenkov observation technique.

4 The MAGIC-I Telescope

Since 2004, the **M**ajor **A**tmospheric **G**amma-ray **I**maging **C**herenkov (MAGIC) collaboration[1] operates the MAGIC-I telescope on the Canary Island of La Palma, Spain, at an altitude of 2200 m above sea level. The construction of a MAGIC-I clone, MAGIC-II, was completed mid of 2009, albeit incorporating a new data acquisition system and a camera with more pixels. The two telescopes are observing in stereoscopic mode, increasing the sensitivity, angular and energy resolution as well as lowering the energy threshold. Since the observations presented in this work were conducted with MAGIC-I only, details of the stereo system will not be given here. These can be found in e.g. Aleksić *et al.* (2012e).

4.1 Working Principle

MAGIC-I is an **I**maging **A**ir **C**herenkov **T**elescope (IACT). These instruments observe photons in the VHE domain indirectly through detection of Cherenkov light, emitted in particle cascades which are triggered by interaction of highly energetic particles with atmospheric atoms. The next sections will describe the origin and nature of the cascades, followed by an explanation of the Cherenkov effect and of the method making use of this effect to facilitate ground-based VHE astronomy.

4.1.1 Particle-Induced Extensive Air Showers

The atmosphere opens only two observations windows for direct ground-based astronomy, which is at radio and optical wavelengths, and is opaque otherwise. Photons of the VHE regime ($\gtrsim 100\,\mathrm{GeV}$) bear sufficient energy E_0 to pair-produce in the presence of the electric field of an atmospheric atom, being absorbed for direct detection. The secondary electron and positron will propagate further down the atmosphere, due to their relativistic speeds at small angles from the original trajectory, and produce more photons via Bremsstrahlung (see Figure 4.1 *left side*). After one radiation length X_0, their energy has dropped by a factor of e, where for air $X_0 \approx 37\,\mathrm{g\,cm^{-2}}$. This electromagnetic air shower cascade will continue until the mean energy of the cascade particles reaches the critical energy $E_\mathrm{c} \approx 85\,\mathrm{MeV}$ (e.g. Engel *et al.* 2011), below which ionisation becomes the dominant energy loss mechanism for $e^\pm$.

Estimations of the height of the shower maximum and the number of produced generations can be made in the framework of the Heitler model (see e.g. Engel *et al.* 2011, and references therein). It is assumed that the radiation length for pair production and Bremsstrahlung are the same, which is approximately justified for the ultrarelativistic particles under study. The probability for each of these processes is then one half at a

[1] representing more than 150 scientists from 27 institutes in 9 countries.

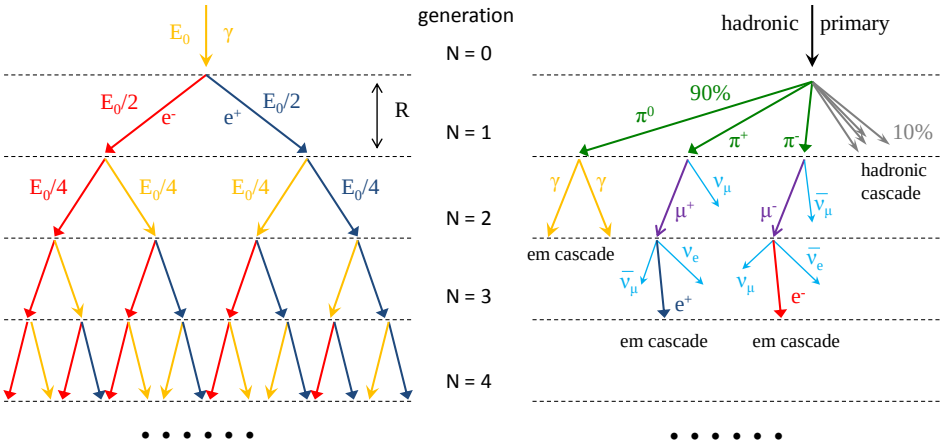

Figure 4.1: Sketch of the air shower cascades produced by a photon (*left side*) and hadronic primary particle (*right side*). The photon cascade is depicted in the framework of the Heitler model, where the radiation lengths are the same for photons and $e^{\pm}$ and the energy is shared equally between the secondaries at each interaction. See text for details.

distance $R = X_0 \ln(2)$. Each interaction, the energy is equally distributed among the secondary products; i.e. the first $e^{\pm}$ produced after one R each have $E_0/2$, and these radiate photons each with $E_0/4$ after another R. In this model, 2^N particles (photons and $e^{\pm}$) of energy $E_0/2^N$ will have been produced after N generations (see Figure 4.1). The shower maximum is reached when $E_0/2^{N_{\max}} = E_c$, and the maximum number of generations $N_{\max} = \frac{\ln(E_0/E_c)}{\ln(2)}$. The shower reaches an atmospheric depth of

$$X_{\max} = N_{\max} R = X_0 \ln(E_0/E_c) \tag{4.1}$$

depending logarithmically on the primary photon energy E_0. The number of photons and $e^{\pm}$ is approximately E_0/E_c, hence scales linearly with the primary energy.

For energies accessible to MAGIC-I, i.e. $\sim 50\,\text{GeV} - 10\,\text{TeV}$, the shower maximum is located well above the altitude of the telescope (2200 m above sea level). The instrument achieves its highest sensitivity around $200 - 300\,\text{GeV}$. Showers of that energy have their maximum around 10 km altitude (see Figure 4.2).

Extensive air showers are also produced when charged particles, like protons or ionised atoms, of very high energies are entering the atmosphere. These scatter inelastically at atmospheric nuclei, transferring about half of their energy into a hadronic shower consisting at the beginning mainly of pions π^0, π^+, π^- (90 %) and kaons (10 %) (e.g. Grupen 2000). Pions with all charges are produced at approximately equal abundance. Charged pions will decay with a mean life time of $\tau = 2.6 \cdot 10^{-8}\,\text{s}$ into charged muons and neutrinos: $\pi^+ \rightarrow \mu^+ + \nu_\mu$, $\pi^- \rightarrow \mu^- + \bar{\nu}_\mu$. The rather long mean lifetime of muons ($\tau = 2.2 \cdot 10^{-6}\,\text{s}$) will allow most of them to reach the ground, but some also decay during the shower development and produce additional neutrinos as well as electrons and positrons: $\mu^+ \rightarrow e^+ + \nu_e + \bar{\nu}_\mu$, $\mu^- \rightarrow e^- + \bar{\nu}_e + \nu_\mu$. Neutral pions will decay into two photons after $\tau = 8.4 \cdot 10^{-17}\,\text{s}$: $\pi^0 \rightarrow \gamma + \gamma$. All pion decay channels will therefore produce an electromagnetic subshower, whereas the kaon component can develop further hadronic subshowers (see Figure 4.1 *right side*). Since most of the energy of the primary particle

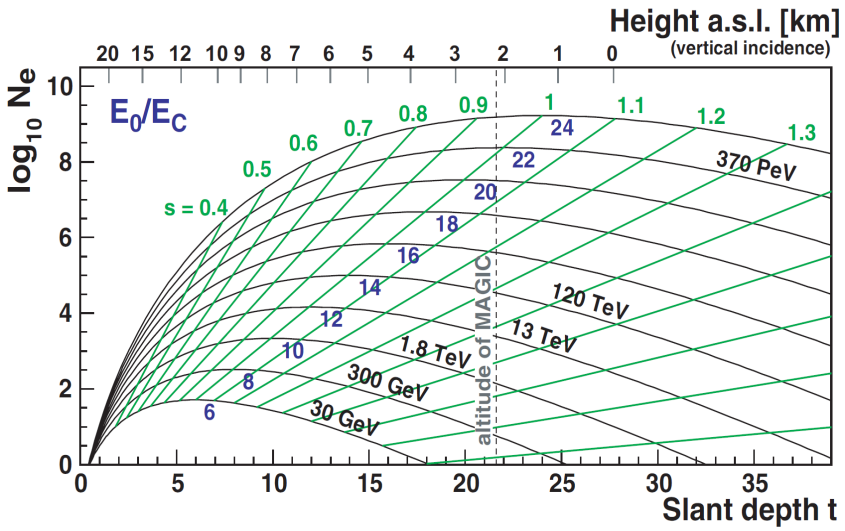

Figure 4.2: The number of secondary electrons produced in a photon-induced air shower as a function of the slant depth t, corresponding to R as defined here. The green lines give the shower age. At unity, the shower maximum is reached. The blue numbers give E_0/E_c, corresponding to a primary shower energy as noted in black at the different lines. The height of the MAGIC-I telescope is indicated by the vertical dashed line. Figure taken from Wagner (2006).

is conveyed to the pion channels, hadronic showers are dominated by the electromagnetic component, same as photon-induced ones. The shower dies out if the mean energy falls below the threshold for multiple pion production ($\sim 1\,\mathrm{GeV}$). Due to the large energy of the primary particle, the secondary products can gain considerable transverse momenta, leading to a larger lateral spread of the cascade. The maximum number of generations $N_{\max} \approx 27$ for hadronic cascades, hence only particle showers produced by primaries with energy $\gtrsim 100\,\mathrm{TeV}$ can be detected directly on the ground (Grupen 2000). Also for hadronic showers, the number of secondaries and atmospheric depth of the shower maximum scales approximately linearly and logarithmically, respectively, with the energy of the primary particle (e.g. Grupen 2000).

Since both photon- and hadron-induced showers are dominated by the electromagnetic component, their morphology is very similar. Basic differences can be predicted from the above described evolution though. Hadronic showers should exhibit larger lateral distributions, due to the transverse momentum transferred on secondary hadrons (e.g. Engel *et al.* 2011), and subshowers may be identifiable (see also Figure 4.3). Also muons might be used to distinguish between them, since these are not produced in photon-induced showers.

Direct detection of leptonic or hadronic showers is not feasible in the VHE domain, since the showers die out before reaching the ground. However, the secondaries are moving with relativistic speeds, faster than speed of light in the atmosphere. If these are charged, they will stimulate emission of Cherenkov radiation, described in the following section.

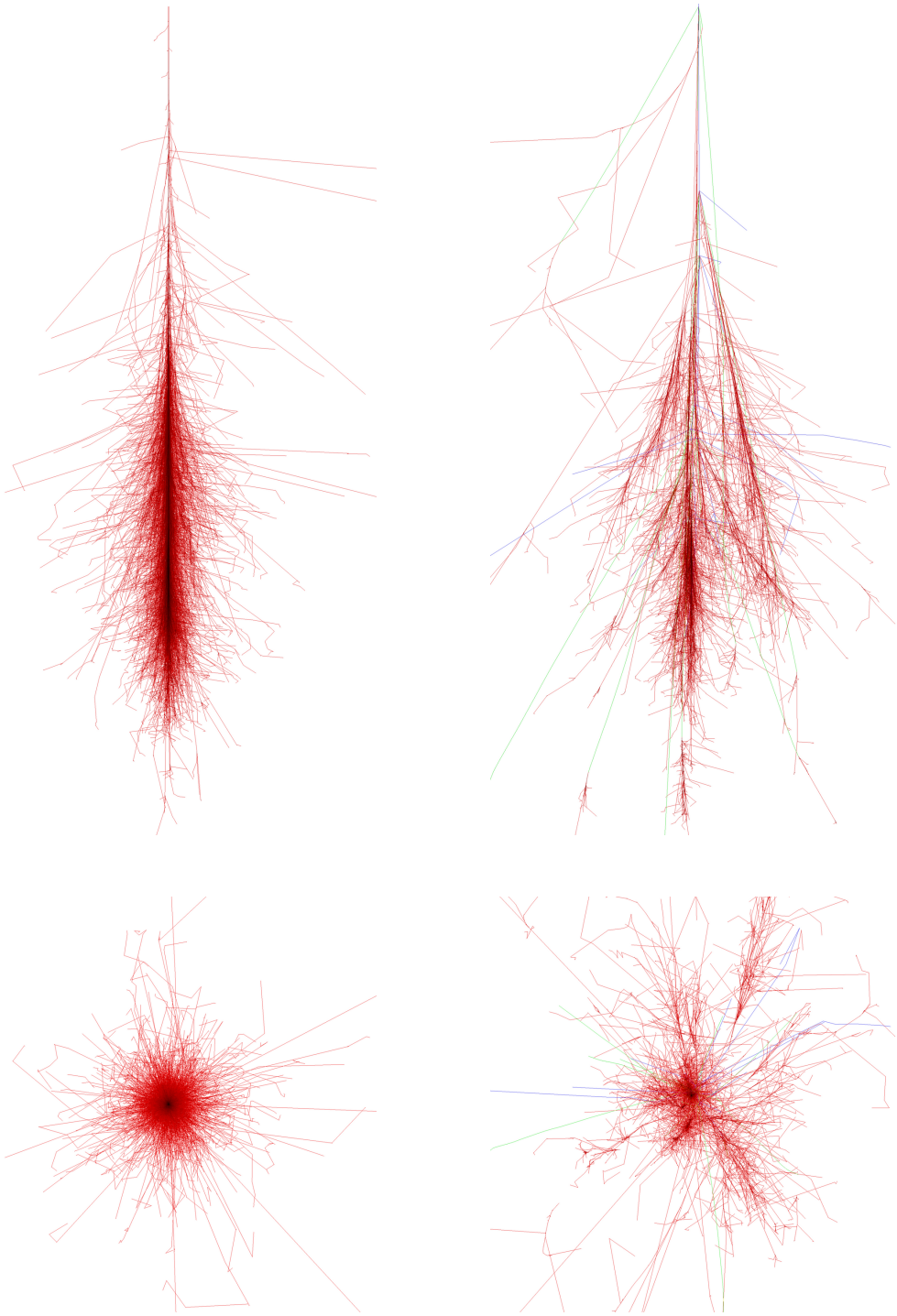

Figure 4.3: Simulations of air showers. Red lines indicate photons, electrons and positrons with $E > 0.1\,\mathrm{MeV}$, green lines muons and blue lines hadrons (for each with $E > 0.1\,\mathrm{GeV}$). *Left side:* images of a photon with primary energy of 100 GeV, *top* lateral distribution and *bottom* shower projection on the ground. On the *right side*, the same distributions for a proton of energy 100 GeV are shown. Images acknowledgement: F. Schmidt, 2005, "CORSIKA Shower Images", taken from http://www.ast.leeds.ac.uk/ fs/showerimages.html.

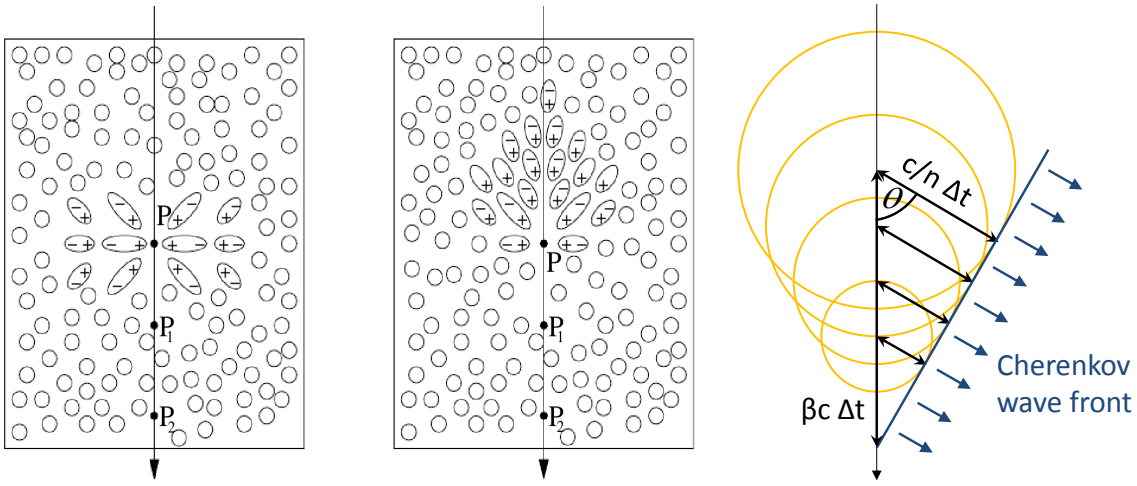

Figure 4.4: *Left panel:* a charged particle is moving through a dielectric medium, polarising the atoms in its direct environment at point "P". At sub-relativistic speeds, the polarisation will be symmetric around the particle trajectory, and no Cherenkov light will be visible. If, however, the particles moves at relativistic speeds, the asymmetry in polarisation will lead to emission of Cherenkov light in forward direction (*middle*). *Right side:* Cherenkov light will interfere constructively for relativistic particle speeds, leading to the formation of a Cherenkov wave front, observable as a Cherenkov light flash. Figures taken from Weekes (2003), partly adapted.

4.1.2 The Cherenkov Effect

The electric field of a charge particle moving through a dielectric medium will polarise the ambient atoms. Upon relaxation of those, light will be emitted, interfering destructively as long as the particle is not moving at a relativistic speed (see Figure 4.4 *left panel*). Since secondaries of air showers travel faster (with $v = \beta c$) than the speed of light in the medium $v_\mathrm{m} = c/n$, with $n > 1$ being the refraction index of the medium and c the vacuum speed of light, the emitted photons will lead to a constructive interference in propagation direction (see Figure 4.4 *middle*) analogous to the supersonic interference. This results in visible radiation, which is called "Cherenkov radiation" (Čerenkov 1937, and references therein).

Cherenkov radiation is emitted under a certain angle θ that is given as (see also Figure 4.4 *right panel*)

$$\cos\theta = 1/(\beta n) \tag{4.2}$$

Since particle speed cannot exceed the vacuum speed of light, given for $\beta_\mathrm{max} = 1$, a maximum Cherenkov emission angle $\theta_\mathrm{max} = arccos\,(1/n)$ is existing. We can also derive the energy threshold for production of Cherenkov light. Assuming emission in forward direction, $\theta = 0$, it follows that $\beta_\mathrm{min} = 1/n$. The particle energy is given by

$$E_\mathrm{min} = \frac{m_0 c^2}{\sqrt{1-\beta_\mathrm{min}^2}} = \frac{m_0 c^2}{\sqrt{1-n^{-2}}}, \tag{4.3}$$

amounting to $\sim 21\,\mathrm{MeV}$ for an electron, $\sim 39\,\mathrm{GeV}$ for a proton and $\sim 4.4\,\mathrm{GeV}$ for a muon (assuming $n = 1.000292$, see below), and the minimum required speed is $v_\mathrm{min} = c/n$.

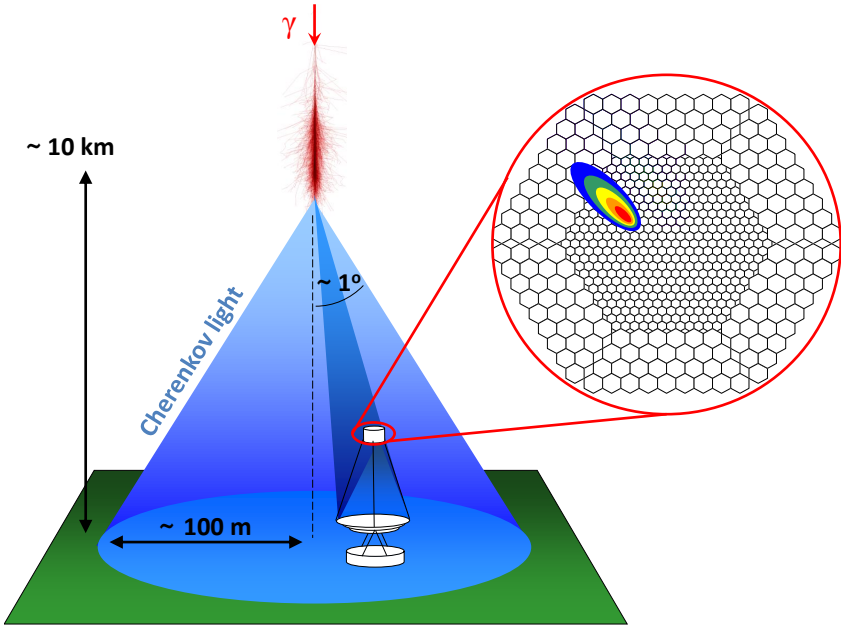

Figure 4.5: Principle of VHE observations with IACTs. If a telescope is located somewhere within the light cylinder produced by the photon-induced particle cascade, a conic section of this cylinder in form of a shower ellipse can be measured in the camera plane. The camera layout depicted here represents the MAGIC-I camera at the time of the observations presented in this work. The colours of the shower ellipse correspond to different light intensities. For reference of the particle cascade image, see caption of Figure 4.3.

Since the refraction index n is dependent on the height h,

$$n(h) = 1 + \eta_0 \mathrm{e}^{-h/h_0} \tag{4.4}$$

where $\eta_0 = 2.92 \cdot 10^{-4}$ and $h_0 = 8400\,\mathrm{m}$, the maximum Cherenkov angle and the threshold energy depend on the height of the shower in the atmosphere. Assuming a height of the shower maximum of 10 km, the critical angle will be $\theta_{\max} \approx 0.76°$, yielding a Cherenkov light cone with a radius of $\sim 100\,\mathrm{m}$ at the height of the MAGIC telescope.

4.1.3 The Imaging Air Cherenkov Technique

As has been seen in the previous section, the particle cascade caused by photons of very high energies cannot be observed directly from the ground at VHE. However, the Cherenkov light produced by charged particles within the shower will produce a light cylinder, geometrically defined by the maximum Cherenkov angle, that can be detected by a telescope located somewhere within the cylinder basis (see Figure 4.5). Instruments applying this detection technique are called **I**maging **A**ir (or **A**tmospheric) **C**herenkov **T**elescopes, IACTs. They have the advantage of using a huge calorimeter, viz. the atmosphere, and by that achieving collection areas of the order of several $10^4\,\mathrm{m}^2$ (compared to $\lesssim 1\,\mathrm{m}^2$ of HE satellite instruments). The disadvantage is the large background from charged Cosmic Rays, being ~ 1000 times more abundant than photon-induced showers.

Requirements to such telescope are sensitivity in the optical to UV regime and fast light detectors with corresponding trigger and data acquisition units, since the time duration

of such light flashes is of the order of some ns. The detectability of shower Cherenkov light and thus the primary particles is limited to lower energies by photon statistics, hence larger mirror collection areas decrease the energy threshold of the instruments. In contrast to standard optical telescopes, the mirror does not have to be of high surface accuracy though, see below. MAGIC-I is focussed on $\sim 10\,\mathrm{km}$ distance, since at this height the shower maxima for gamma-ray photons with energy around $200-300\,\mathrm{GeV}$ can be observed.

IACTs are observing a conic section of the light cylinder, dominantly at an angle larger than zero to the primary particle propagation direction, causing the measured images to appear in elliptical form (see Figure 4.5). From the first, second and third moments of the light distribution as well as the time structure of the ellipse, the nature, energy and direction of the primary particle can be reconstructed. This procedure will be described for the MAGIC-I telescope in Section 4.3.

4.2 Characteristics

Until the first light of the 28-m H.E.S.S.-II telescope on 26th of July 2012, MAGIC-I (see Figure 4.6) was the largest single-dish Cherenkov telescope worldwide, being equipped with a 17-m diameter $f/D = 1$ mirror covering $239\,\mathrm{m}^2$. In combination with the parabolic mirror shape, preserving the arrival time of air showers, and the fast 2 GHz MUX-**D**ata **A**c**Q**uisition system (DAQ[2]), allowing for a time resolution of down to 0.2 ns (Bartko *et al.* 2005), MAGIC-I achieved the lowest energy threshold of all IACTs at that time. Taking advantage of a special trigger logic, this threshold amounted to $\sim 25\,\mathrm{GeV}$ (Aliu *et al.* 2008), mainly used for pulsar observations though. For standard observations, the lowest threshold achievable at small zenith distances was $\sim 50\,\mathrm{GeV}$ (Albert *et al.* 2008e). With the upgrade of the old DAQ to the faster 2 GHz system, the time information of showers could be fully exploited to enhance the analysis chain. The sensitivity of MAGIC-I increased correspondingly from 2.2 % ($\gtrsim 250\,\mathrm{GeV}$) to $\sim 1.6\,\%$ ($\gtrsim 280\,\mathrm{GeV}$) of the Crab Nebula flux in 50 hrs, and the energy resolution from $25-40\,\%$ to $20-<40\,\%$ (Albert *et al.* 2008e; Aliu *et al.* 2009b).

One of the prime objectives of MAGIC is the observation of gamma-ray bursts, which last no longer than some hundreds of seconds (Albert *et al.* 2007c, and references therein). Therefore, the camera, telescope frame, the (aluminium) mirrors and the mirror support structures were built in a special lightweight layout, amounting to a weight of only $\sim 70\,\mathrm{t}$ for the whole movable system. Three 11 kW servo motors are able to position the telescope within $< 45\,\mathrm{s}$ to every reachable sky direction (Bretz *et al.* 2009), faster than any other IACT. The nominal pointing precision of the drive system is $< 1.3'$ (Bretz *et al.* 2009). The achieved angular resolution amounts in practice to $\sim 0.1^\circ$ (Albert *et al.* 2008e) though, limited by the shower direction reconstruction.

The reduced weight of the telescope goes along with a somewhat smaller stiffness of the structure compared to a steel frame. Therefore, an **A**ctive **M**irror **C**ontrol (AMC)

[2]The first MAGIC DAQ operated at 300 MHz (Albert *et al.* 2008a) and was substituted in February 2007. Note that as of now, the camera and the DAQ of MAGIC-I have been upgraded; the system used to obtain the data described here is no longer existent.

Figure 4.6: MAGIC-I in July 2007. Each the mirror diameter as well as the distance between the camera and the mirror centre amount to 17 m. The tesselated structure of the mirror as well as the hole at the centre housing several sub systems is clearly visible.

is implemented compensating for deformations of the mirror dish caused by the sagging of the structure at different zenith distances (Garczarczyk *et al.* 2003). The mirror positions are determined by lasers located in the centre of each mirror panel, where each panel contains four mirrors with a size of 0.5 m × 0.5 m, and corrected according to the deviation of the laser position measured with respect to the camera centre. The positions are saved in look-up tables for several different zenith distance pointings of the telescope, which are used to align the mirrors before each observation. With fully aligned mirrors, more than 85 % of the reflected light is concentrated on a spot of 3.5 cm diameter (Biland *et al.* 2008), roughly corresponding to one pixel of the inner camera (see below), and thus proving that the light focussing performance of the tessellated main mirror is more than sufficient. The centre of the main dish is not covered with mirrors, as visible in Figure 4.6, for housing several subsystems needed for calibration and to determine the pointing accuracy of the telescope, amongst others. One of the latter is the starguider camera, detecting stars in the region around the pointing position of the telescope. By comparing these star positions with a reference catalogue, the pointing direction of MAGIC-I can be determined to better than 15″ (Bretz *et al.* 2003).

The MAGIC-I camera contained 577 **P**hoto**M**ultiplier **T**ubes (PMTs, also called "pixels") with a hemispherical entrance window, coated with a wavelength shifter to increase the quantum efficiency to ∼ 30 % (Paneque *et al.* 2004) and equipped with light collectors (Winston cones) to maximise the effective detection area. The hexagonal camera was made up of pixels of two different sizes. The inner camera consisted of 397 pixels with

a diameter of 3 cm or 0.1° field of view (FOV), the outer camera of 180 pixels with 6 cm diameter or 0.2°, covering in combination a FOV of 3.5° × 3.8°. The small pixels were not needed at larger distances from the camera center due to the reduced light focussing efficiency caused by coma aberration of the parabolic mirror. The comparably small FOV causes large showers, normally having the largest energies, to be truncated at the camera edges, limiting the acceptance and hence decreasing the sensitivity of the telescope towards higher energies. The accessible energy range spanned 50 GeV – > 10 TeV (Albert *et al.* 2008e).

To reduce the weight of the camera, the DAQ is out-sourced to the operations building. The PMTs are connected with the DAQ via 162 m long optical fibres, which additionally reduces the weight of the camera compared to standard cables, renders the signal transmission less prone to electromagnetic cross talk between different lines and minimises the time spread of the signals. The PMTs were constructed to be operable also under mild moonlight or twilight conditions, increasing the MAGIC-I duty cycle by $\sim 25-30\,\%$ (Albert *et al.* 2007f; Britzger *et al.* 2009).

PMT signals were saved in a ring buffer and fed into the two stage trigger logic. Only 325 pixels of the inner camera, subdivided into 19 overlapping, hexagonal regions, were contained in the trigger region. In standard trigger mode, the event was recorded if a tight time coincidence (~ 6 ns) between the signals of four neighbouring pixels exceeded the so-called **D**iscriminator **T**hreshold (DT) (~ 7 photo-electrons in dark night conditions) and these pixels were located within one trigger region (Albert *et al.* 2008e). The second stage of the trigger could be used to perform a rough analysis (Bastieri *et al.* 2001). A normal trigger rate for extragalactic objects in dark nights amounted to ~ 250 Hz.

4.3 The Standard Data Analysis

The following sections will describe how observational data of MAGIC-I were obtained and reduced. Two main software packages are available for the latter task. From a common basis, one package was further developed basically within the Barcelona group of the MAGIC collaboration, whereas the other package was programmed and maintained by the Würzburg group. The most prominent difference between these is the different approach to remove background events from the data. Where the former is applying a random forest method based on Monte-Carlo simulations to calculate the probability for an event to be of background origin (so-called "hadroness"), the latter is applying a parabolic cut in the shower area vs. shower size plane (so-called "area cut"; Riegel *et al.* 2005), optimised on real data.

The area cut approach turned out to be that robust and efficient that a "standard analysis" could be set up in the data center in Würzburg, automatically performing all analysis steps from the raw data up to the energy estimation level with a minimum of manual interference. This pipeline is steered by a data base, which is also used to store the automatic analysis results and query them from a web front end, allowing for a sophisticated data quality check up to time scales of years. The author of this work helped to implement, update and maintain this automatic pipeline as well as the data center for many years. The pipeline is based on a standard calibration and image cleaning

procedure, which have been made use of in this work[3] and will be described below. The standard area cut applied in the pipeline was optimised to maintain a comparably high sensitivity, also able to cope with non-optimal observation parameters and conditions. By definition, such a cut is often not the most sensitive one, because of which in this work a new set of parameters has been determined for both sources.

4.3.1 Data Taking Procedure and Data Structure

As mentioned above, IACT data are background dominated. On the one hand, air showers of produced by hadronic primaries as well as electrons and positrons dominate over the photon-induced ones. On the other hand, also a diffuse background of gamma rays is present, which has to be subtracted from the data. Moreover, since an IACT is sensitive in the optical regime, noise produced by star light, zodiacal light, moon light and light of man-made origin is has to be filtered out of the data.

The data taking procedure of the MAGIC telescopes has been structured to account for these different influences. The data taking is based on so-called "runs". A first run is taken to calibrate the detector and the electronic chain by means of an artificial light source situated in the centre of the MAGIC-I mirror dish. A second run is dedicated to record the ambient night sky brightness in the FOV of the source and noise of the detector and electronic chain, used as a pedestal to calculate the true individual pixels signals. Finally, data runs are taken from the source. A calibration run is defined to contain 4096 camera images, triggered by the calibration system with 512 Hz. The pedestal run contains 1000 random shower events with a fixed rate of 500 Hz, which are only recorded if none of the standard trigger conditions is fulfilled. The duration of data runs is restricted by a fixed file size. Under normal conditions and a data rate of ~ 250 Hz, a MAGIC-I run in the above described hardware configuration lasted for ~ 2 min, containing ~ 32000 shower events[4] (in the following abbreviated as "events"). To be able to compensate short-term changes of the detector or electronic chain, also during normal data taking calibration and pedestal events are recorded, with a frequency of 25 Hz each (so-called "interleaved" events).

These calibration, pedestal and data runs are grouped into a "sequence", which normally spans all the data runs until a subsequent calibration run. These sequences are calibrated and processed individually and grouped into "data sets" of a duration chosen by the analyser. Depending on the purpose this may be one day for producing standard light curves, some minutes to investigate short-term variability, or also the whole observation campaign for determining the overall signal significance.

To estimate and subtract the diffuse gamma-ray background, data from the source ("On" data) is compared to data from a nearby sky region not containing any known gamma-ray emitter ("Off" data). Two observations modes are available to record that Off data. In the so-called "wobble" mode, the telescope is pointing 0.4° away from the source, taking Off data simultaneously at the other side of the camera centre (see Figure 4.7).

[3] unless removal of data due to data quality reasons was necessary, which affords a manual analysis from the raw data stage on if quality parameters ought to be derived.

[4] This corresponds to a raw file size of 2 GB. Before 4th of June 2008, the size limit was set to 1 GB, halving the duration as well as the number of showers.

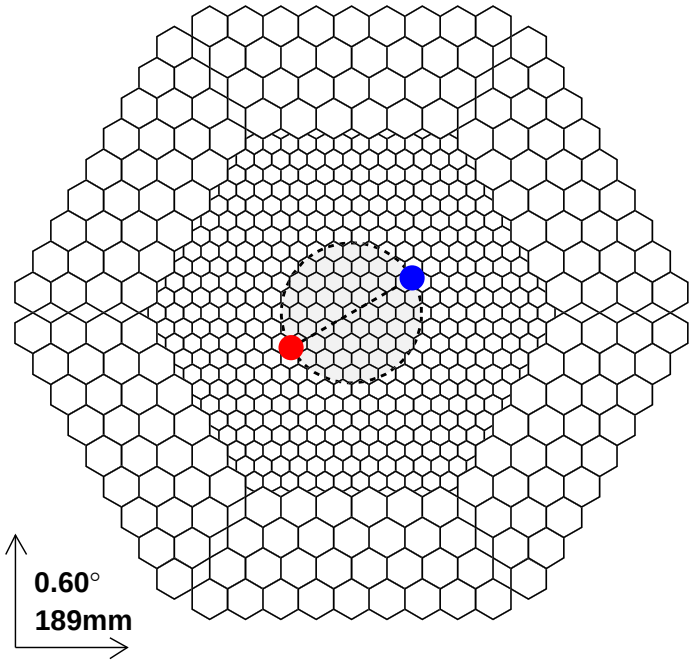

Figure 4.7: Sketch of wobble mode observations. Instead of pointing to the source, the telescope is observing a region 0.4° away from that position (blue point). This allows for taking simultaneously Off data (red point) on the opposite side of the camera centre, also 0.4° away. Like that, the two regions will not overlap. As a default, every 20 min the two positions are swapped. Note though that the effective trigger region (basically the inner camera) is smaller compared to normal On observations. Figure taken from Bretz (2006).

To compensate for potential detector inhomogeneities, the On and Off source position are changed after a certain observation time (typically 20 min), the telescope "wobbles" around the source. Due to the smaller effective trigger area, these off-axis observations are conducted with $\sim 25\,\%$ reduced sensitivity.

In the second observation mode, dedicated On and Off data are taken by observing either the On or the Off region. Though for an On – Off ratio of 1 : 1 the second mode requires double as much observation time, this is compensated by the increased sensitivity of these observations compared to the off-axis measurements. However, a ratio of 1 : 3 is normally aspired to minimise background fluctuations. Since from wobble data background events can also be extracted from three (and sometimes more) different Off regions at a time, this can be easily achieved without the need for additional observations. Moreover, the importance of simultaneous On and Off observations can hardly be overestimated considering e.g. changes in the atmosphere on hour scales, compared to time differences between On and Off data in the second observation mode of occasionally days and weeks. Therefore, the observations presented in this work have been conducted in wobble mode.

4.3.2 Data Quality Parameters

The data quality was judged in this work on basis of many observational parameters for each sequence, compared among the observations themselves, but also in the context of

the long-term trends available through the Würzburg data base. The most important parameters shall be introduced here in short.

- **Event Rate after Image Cleaning**: A rate after image cleaning (see below) off from expectations (roughly $\sim R_0 \cdot (\cos(\text{zenith distance}))^{0.5}$ Hz) may indicate problems with the instrument, adverse atmospheric conditions or application of wrong observation settings. All these cases influence the data in a way that can often not be estimated and even more not corrected, hence such data is mostly not considered for further analysis. However, increasing zenith distance or stronger night sky background conditions will also decrease the rates, which normally poses no problem to the data quality. Hence deviations of the rate have to be investigated carefully for reliability. Apart from the mean rate on sequence basis, also the rate on run basis is inspected.

- **Cloudiness**: The "cloudiness" is a measure of the clearness of the sky in the pointing direction of the telescope. The parameter is calculated from the sky temperature (T_{sky} measured by a pyrometer), zenith distance zd, humidity h and air temperature T_{air} as $a \cdot (T_{\text{sky}} - p \cdot zd - 0.1 \cdot h - 0.31 \cdot T_{\text{air}})$, where a is a normalisation constant and p a 6th order polynomial (P. Temnikov, 2010, private communication). Consequently, if e.g. the MAGIC weather station is malfunctioning, also the cloudiness values (which is despite that calculated and partly even at reasonable values) cannot be trusted any more, speaking against a fixed cut in this parameter. A high value indicates absorbing layers in the atmosphere, mostly associated with cloud coverage. These may absorb the Cherenkov light or even whole showers of small energy, depending on their height, thickness and nature. Consequently, the photon flux and energy estimation will be affected by high cloudiness values. Note, however, that the strength of influence on the data is not linearly correlated with the cloudiness value, i.e. high values do not necessarily render the data useless, whereas data with a low value may sometimes not be analysable, which has to be judged in conjunction with other quality parameters. That is probably related to the changing nature and height of the clouds, which can not be evaluated for the present data[5]. Therefore, no fixed cut in cloudiness is applied in this work. Instead, the cut in cloudiness is evaluated anew for each sequence. In general, data with cloudiness $\lesssim 20$ should be fine though.

- **Atmospheric Extinction**: Another measure for the sky quality, determined at 625 nm from photometric observations of the **C**arlsberg **M**eridian **T**elescope (CMT), also located on La Palma. This parameter is often used as an indicator of Calima, Saharan dust transported by strong winds to the Canary Islands (see e.g. Dorner *et al.* 2009), which has a similar influence as cloud coverage on the observations. Good quality nights have an atmospheric absorption below $\sim 10\,\%$ (D. Dorner, 2011, private communication). Note, however, that only one value is given per night, averaged over a variable number of individual measurements. Hence, the value is not necessarily representative of the MAGIC observations.

[5]Since recently, a LIDAR is operated at the MAGIC site, which will serve to investigate the cloud nature and possibly correct for their influence.

- **Number of Stars**: The number of stars detected by the starguider is an additional measure of the sky quality. Moreover, if the number of such stars identified by comparison with a star catalogue is below eight, a reliable offline correction of the pointing position of the telescope can not be performed any more.

- **PMT Currents, PedRMSIn, DTs**: These parameters (PedRMSIn denotes the RMS of the pedestal measured for the inner camera pixels) give an estimate on the brightness of the night sky background, which influences the noise of the signal. It should be noted that the light condition flag (with the possible values "No_Moon", "Moon" and "Twilight") introduced for MAGIC data is not well suited to judge on that. On the one hand, a sequence is rated as "Moon" or "Twilight" if at least one of its runs fulfils that condition, i.e. the remaining runs may be not be influenced by a higher night sky background. Moreover, "Moon" means that the moon is above the horizon, which gives no information on the strength of moon light though. Its effect may even be negligible if the moon rises behind the shadowing mountains on La Palma.

- **Malfunctioning Pixels**: Dead or unreliable camera pixels may pose problems if they are clustered or their number becomes too large. These will not only complicate or bias the reconstruction of showers, but if located in the inner camera may also inhibit triggers of showers, biasing the flux measurement from the source.

- **Camera Inhomogeneity**: If events get lost due to an inhomogeneous acceptance of the camera to events, the flux estimation will be biased. Moreover, the signal measured from the source might be wrong due to an incorrect determination of the background from the Off data, potentially faking a signal.

- **Signal Timing**: The DAQ digitises PMT signals in units of time slices. The measured signal is determined from a predefined time window of these slices. If the trigger timing is not correct, the signals may shift partly or completely out of the extraction window, which leads to a wrong or impossible signal extraction. Hence, the arrival time of calibration and data signals have to be checked.

- **Muon Parameters**: Completely recorded muon ring images are used for an absolute calibration of the DAQ counts – to – photo-electron conversion factors and for calculation of the instrument PSF. If their number in a sequence is $\lesssim 300$ (Meyer 2008), the muon parameters are no not reliable. The PSF is a measure of the optical quality of the main reflector. The muon ratio is a measure of a successful light calibration. If below or above 100 %, the calibration factors should be adapted. The deviations should be $\lesssim 4\,\%$. Finally, the rate of completely recorded muon rings should not vary strongly with time. Since such muon showers are produced within ~ 500 m above the telescope (Rügamer 2006), they reflect the atmospheric conditions directly above the instrument.

- **Relative On-Time**: If the ratio of effective on-time and total on-time is above 100 % or much below that, problems in calculating these quantities are present.

Especially a correct effective on-time is essential to determine a reliable flux of the source.

- **Runbooks**: Observing conditions and possible problems during observations have to be noted down by the observation crew in so-called "runbooks". These reports contain information that cannot be easily extracted from the data themselves and may yield clues on the reason for a deviation of certain quality parameters.

4.3.3 Analysis Software: MARS Cheobs Ed.

The MAGIC-I analyses presented in this work have been conducted with MARS CHEOBS ED. (**M**odular **A**nalysis and **R**econstruction **S**oftware - **Che**renkov **Obs**ervatory **E**dition, short version used throughout the document: MARS; Bretz & Dorner 2008), developed in Würzburg. The software has been programmed in C++ within the ROOT framework. The results presented here have been obtained with MARS version 2.4 and ROOT version 5.12.00f. The following sections will describe the different steps of the standard analysis, reaching from data calibration over noise reduction, shower extraction and image parameter calculation to the background suppression method and eventually the flux and spectrum calculation.

4.3.3.1 Calibration

Since every PMT and the corresponding electronic chain has its own response to incoming signals, they have to be calibrated individually. The calibration is performed by means of the calibration runs. These contain the signals measured for each PMT produced by a constant light source with known intensity. After the pedestal (see above) has been subtracted from the signals, the arrival time of the signal pulses as well as the amplitude of the signal is determined for each PMT by means of a spline interpolation. Having extracted the pulses, a factor for the conversion of measured counts to photo-electrons (phe) can be calculated, which is used to calibrate the data signals.

4.3.3.2 Image Cleaning

In the next analysis step, the shower images are analysed. To do so, pixels that contain solely night sky background light have to be separated from the shower pixels. This so-called "image cleaning" is performed in two steps. First, all pixels above a certain phe value (standard: 6), called cleaning level, are considered as "core pixels". Neighbouring pixels to these core pixels with a signal above a second cleaning level (standard: 3 phe) are also flagged as shower pixels (see Figure 4.8). For the larger outer camera pixels, the phe limits are scaled accordingly. Second, only pixels having at least two neighbours with a small arrival time difference are kept (time image cleaning; standard time difference: 1.75 ns). This stage is removing e.g. single core pixels. In a last stage, the second step is repeated, however requiring only one neighbour pixel within the allowed time window. The last stage removes the central pixel of a former isolated row of three pixel, which has been reduced in the second step to one pixel only and are rather numerous (T. Bretz, 2009, private communication). Note that the time image cleaning applied here is not

identical to the one of Aliu *et al.* (2009b), since these authors were using the MARS version of the Barcelona group (see above).

After the cleaning, the showers are characterised by different parameters. The most used parameter set are the so-called "Hillas parameters" (Hillas 1985), defined by the first, second and third moments of the light distribution, and others. The wealth of different parameters shall not be described here. An explanation for most of them is given e.g. in Bretz (2006). We give a short definition only of the parameters used in the following, which are calculated having in mind the ellipsoidal representation of the first moment of the light distribution (see Figure 4.8 (e) and (f)).

- *size*: sum of the light content of the shower in phe.

- *area*: a representative value for the area of the shower, given by $\pi \cdot length \cdot width$, where *length* and *width* are the second moments of the light distribution along the major and minor axis, respectively, of the shower ellipse.

- α: angle between the major axis of the shower and the line connecting the center of gravity (CoG) of the light distribution with the source position in the camera. The length of the latter is called *dist*.

- *slope*: gradient of the arrival time along the major shower axis.

- *m3long*: third moment of the light distribution along the major shower axis.

- *leakage*: sum of the light content of shower pixels in the outermost camera ring divided by *size*. This parameter gives an estimate on the truncation of the shower at the camera edge.

- *disp*: used to reconstruct the source position. The parameter gives the distance of this position from the CoG. Since the source position has to be located on the major axis of the ellipse, two possible locations exist. The correct position, i.e. the sign of *disp*, is determined by *m3long* and *slope* (see Figure 4.8).

$$disp = c_0 + c_1 \cdot slope + c_2 \cdot leakage + k \cdot c_3 \left(\log_{10}(size) - c_4\right)^2 \cdot \left(1 - \frac{width}{length}\right) \quad (4.5)$$

$$m3long > c_5, \qquad slope < c_6 \cdot (dist - c_7) \quad (4.6)$$

  where $k = 0$ for $\log_{10} size < c_4$ and $k = 1$ in case $\log_{10} size \geq c_4$. The constants c_x are given in Table 4.1.

- ϑ^2: squared angular distance between the source position in the camera and the source position reconstructed from the shower ellipse, defined as:

$$\vartheta^2 = dist^2 + disp^2 - 2 \cdot dist \cdot disp \cdot \cos(\alpha) \quad (4.7)$$

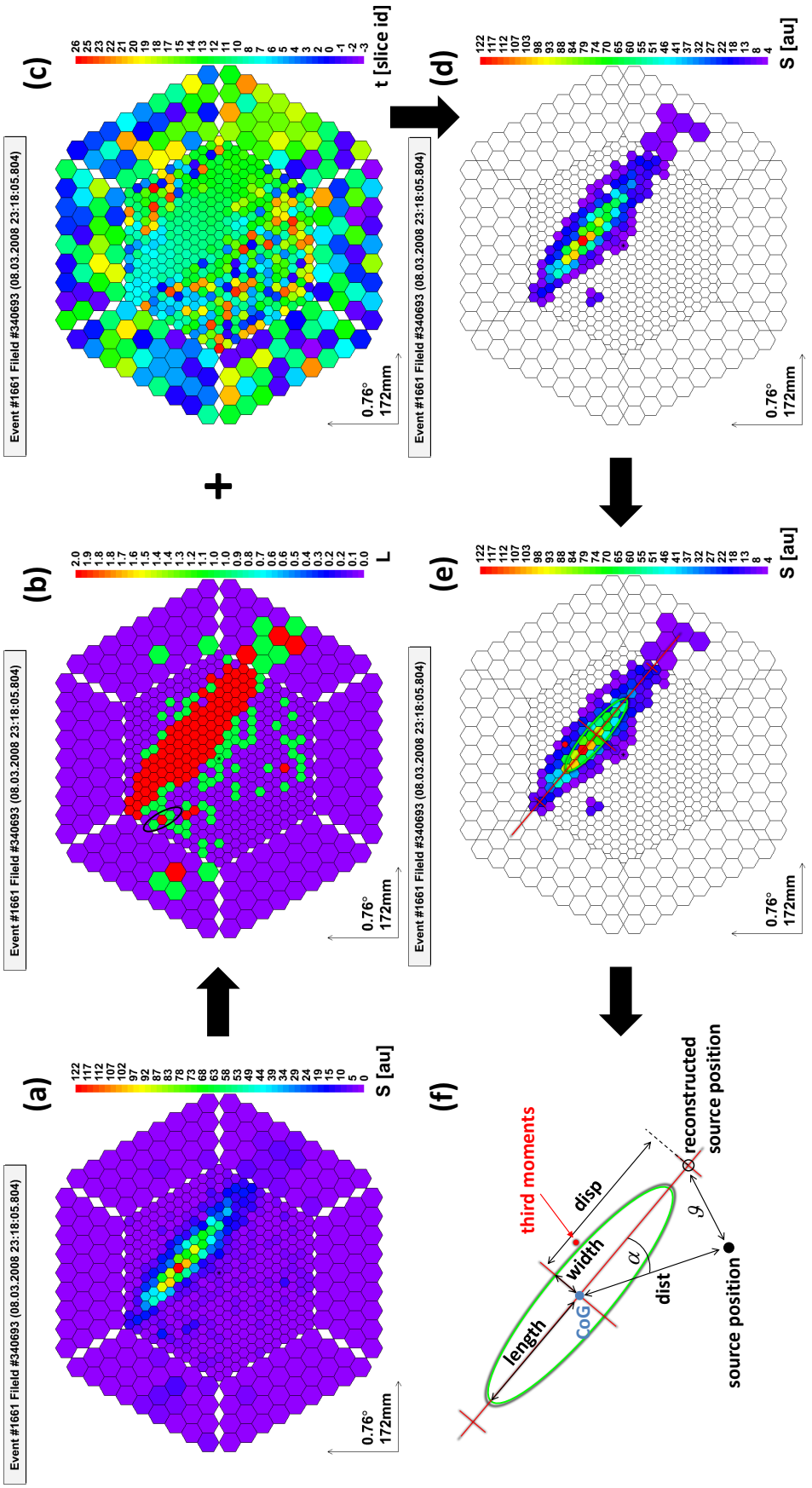

Figure 4.8: Shower image measured by MAGIC-I (after calibration). (a): before cleaning, colour scale represents light content. (b): Pixels with a light content above the first and second cleaning level are marked red and green, respectively. However, only green pixels being neighbour of a red pixel will not be removed. The signal of purple pixels is below both levels. Note the row of three pixels marked with a black circle. The central red pixel would survive the second cleaning stage, but is removed in the third stage (c): Arrival time distribution of the PMT signals. Note the random arrival time of the background, in contrast to the smooth structure of the shower pixels. (d): Cleaned shower image. (e): Calculated image parameters. (f): Definition of some image parameters. Note that the third moment point has been shifted compared to (e) for simplicity. See text for details.

4.3.3.3 Gamma – Background Separation

In the first two analysis steps, the instrumental and night sky noise has been removed from the data, and the shower images have been identified and characterised by image parameters. With this information, an attempt to separate gamma-induced from background showers can be made by applying separation cuts in different parameter spaces. Showers produced by the diffuse gamma rays will be removed by subtracting On from the Off data.

Some events can be removed from further analysis due to not being real showers or not having sufficient information for characterisation. These are identified by the so-called "quality cuts". Events not fulfilling the following conditions will not be considered further:

$$\#islands < 3 \tag{4.8}$$

$$\#usedpixels > 5 \tag{4.9}$$

$$leakage < 0.3 \tag{4.10}$$

$$\log_{10}(concCOG) < -0.45 + 0.08 \cdot k_1 \cdot (\log_{10}(size) - 3.9)^2 \tag{4.11}$$

$$\log_{10}(conc) < -0.75 + 0.10 \cdot k_2 \cdot (\log_{10}(size) - 3.8)^2 \tag{4.12}$$

$$length > -3.6 \cdot (\log_{10}(size) - 6.0)^2 + 70 \tag{4.13}$$

$\#islands$ denotes the number of individual showers in one camera image. A value > 2 indicates a hadronic origin of the shower as well as does not allow to characterise the shower correctly with the image parameters. The number of used pixels is the number of pixels a shower is consisting of. If too low, image parameters cannot be reliably calculated, same as in the case the *leakage* is too large. The last three cut conditions, where *conc* and *concCOG* are the ratio of light content of the brightest pixel and the three pixels next to the *CoG* with respect to the *size* of the shower, respectively, will remove small but bright events (so-called "sparks"), presumably caused by discharges between two pixels in the camera. $k_1 = 1$ for $\log_{10}(size) < 3.9$ and 0 otherwise, $k_2 = 1$ for $\log_{10}(size) < 3.8$ and 0 otherwise.

The separation between the background and photon-induced showers is accomplished by basically two cuts only. The first one is applied in the *area* vs. *size* plane (so-called "area cut") by means of a parabolic function:

$$area(size) < c_8 \cdot \left(1 - c_9 \cdot (\log_{10}(size) - c_{10})^2\right) \tag{4.14}$$

This cut is removing most of the background showers, however at the expense of also losing quite some photon showers, as can be seen in Figure 4.9.

The second cut is performed in ϑ^2. Showers coming from the targeted source should have a reconstructed source position close to the observed source position, hence a rather tight cut in this parameter is feasible:

$$\vartheta < c_{11} \tag{4.15}$$

This cut defines the signal region. Using the On and Off events in that region, the significance of the signal is calculated according to Eq. 17 of Li & Ma (1983). The

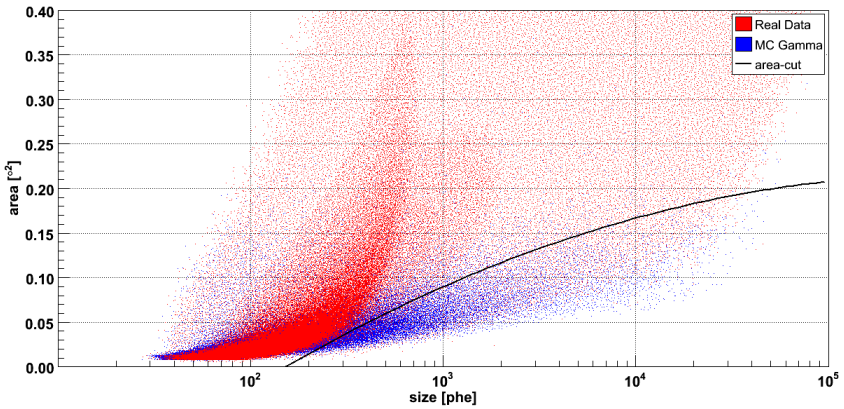

Figure 4.9: Distribution of shower *area* as a function of the *size* of the shower for measured events (i.e. dominantly hadronic background showers, red points) and simulated photon events (blue points). Only quality cuts have been applied at this stage. The *area* cut following the standard parametrisation is shown as the black line.

Constant	Value		Constant	Value		Constant	Value
c_0	1.15136		c_5	-0.07		c_8	0.215468
c_1	0.0681437		c_6	7.2		c_9	0.0836169
c_2	2.62932		c_7	0.5		c_{10}	5.63973
c_3	1.51279					c_{11}	0.215
c_4	0.0507821						

Table 4.1: Constants needed to define *disp* (left columns), the sign of *disp* (middle columns) and the *area* and ϑ^2 separation cuts (right columns).

number of events detected from the source (so-called *excess* events) is determined by subtracting the Off events in the signal region (supposedly all coming from the diffuse gamma-ray background) from the On events.

The cut constants c_{0-11} have been optimised on $\sim$9 hrs of wobble data of the Crab Nebula taken after the DAQ upgrade, under dark night, twilight as well as moon light conditions and at zenith distances ranging from 6° to 28°. The time span of the data amounted to $\sim$1 month. These different conditions render the cuts robust against changes in the observation parameters, yielding cuts well suited for most of the data taken by MAGIC-I. These constants are therefore used in the standard analysis, with values as given in Table 4.1.

As mentioned above, these cuts do not yield the highest significance though, and moreover depend on the spectral shape of the source, because of which a new optimisation might be reasonable in some cases. The largest improvement in sensitivity can be accomplished by changing the constants for the area cut and ϑ^2 cut. The remaining constants have proven to change only marginally after optimisation. Therefore, for a given source to be analysed, data with similar quality parameters, observation conditions, expected spectrum and a significant signal are searched. The constants of the *area* and ϑ^2 cut are then optimised on this data set and applied to the source data of interest.

For finding the best cut parameters, different optimisation strategies are implemented in MARS. The standard cuts have been determined applying the kSignificanceLogEx-

cess strategy, yielding the parameters giving the highest value of signal significance $\times \log_{10}(excess)$. Alternatively, kSignificance (yielding the highest significance), kSignificanceSqrtExcess (highest signal significance $\times\sqrt{excess}$), kSignificanceExcess (highest signal significance $\times excess$), kExcess (highest $excess$), kWeakSource (highest value of $excess/\sqrt{background}$) and kWeakSourceLogExcess (highest value of $excess/\sqrt{background}$ $\times \log_{10}(excess)$) can be employed. The latter two are thought to be especially well suited for sources with a weak signal, but systematic tests on that have not been conducted, yet.

4.3.3.4 Spectrum Derivation

Basic Concept Having identified photon shower candidates (the *excess* events), their energy has to be determined. However, laboratory experiments, which would yield the shower image for a given energy of the incident particle, are not possible in this energy regime and for this detection technique, using the atmosphere as part of the detector. Therefore, air shower simulations are used, conducted by means of a Monte-Carlo (MC) method within the CORSIKA framework (version 6.019; Heck *et al.* 1998). The simulated showers are reflected at a model of the MAGIC-I mirror and fed into simulations of the detector as well of the electronic chain (Majumdar *et al.* 2005). These are analysed with the same pipeline and parameters as the real data, hence the image parameters of the simulated showers can be directly compared with the ones of measured showers from the source. Since for simulated showers the energy of the primary particle is known, the energy of real showers can be estimated.

The MC simulations are conducted for photon showers with energy between 10 GeV and 30 TeV, following a simple power law of spectral index 2.6 (see Eq. 2.17). Since the mirror PSF has a considerable influence on the shower images, sets of MC events with different PSF values have been generated, to resemble the PSF of the real data as good as possible. Events of different zenith distances are grouped into bins of equal width in cosine of zenith distance range, so-called "zbins".

The energy estimation for the measured events is conducted by a random forest regression method in two steps. First, the random forest determines a function consisting of a set of image parameters to yield the known energy of the showers as good as possible. This function is optimised on an MC data set (so-called "train" sample) within 100 steps. The most important image parameters for energy estimation have turned out to be *size*, *dist*, zenith distance and *slope*. In a second step, the determined function is verified on an independent MC data set ("test" sample). For a correct energy estimation, the MC distribution has to be weighted to the spectral shape expected from the source to be analysed. Since in turn the resulting source spectrum depends on the energy estimation, this step has to be iterated several times until the spectral shape converged.

The MCs are also used to calculate the effective area A_{eff} per energy bin, which is given as the number of MC events after analysis $N(E)$ divided by the number of simulated events $N_0(E)$ per energy bin:

$$A_{\text{eff}}(E) = A_0 \cdot \frac{N(E)}{N_0(E)} \tag{4.16}$$

where A_0 is the initial area MC events have been simulated with (normally $\pi \cdot (300\,\mathrm{m})^2$).

With this information, the differential flux of the source per energy bin i can be determined as

$$\frac{\mathrm{d}N_i}{\mathrm{d}E} = \frac{N_{\mathrm{excess,i}} \cdot f_i}{A_{\mathrm{eff,i}} \cdot t_{\mathrm{eff}} \cdot \Delta E_i} \tag{4.17}$$

where $N_{\mathrm{excess,i}}$ is the number of excess events, $\mathrm{d}t_{\mathrm{eff}}$ the effective on-time, ΔE_i the width of the energy bin and f_i the so-called spill-over factor, given by the ratio of number of MC events before and after energy estimation per energy bin. The energy range a spectrum is spanning is limited roughly by the analysis threshold at low energies and by statistics at high energies. The analysis threshold energy is defined as the energy at which the differential energy distribution $\mathrm{d}N/\mathrm{d}E$ of MCs is maximal. For more details on the spectrum determination, see Bretz (2006).

Specific Methods Applied in this Work Within this work, some specific procedures for the spectrum determination have been applied. First, the background separation cuts have been loosened and adapted in order to lessen systematic biases during the energy estimation close to the analysis threshold. At the same time, these cuts increase event statistics and lower the analysis threshold. Specifically, the ϑ^2 cut is increased from the optimised (normally lower) value to the standard value. The *area* cut parabola (see Eq. 4.14) is no longer determined to result in the highest significance, but to yield a constant cut efficiency over *size*. This is the so-called "efficiency" or "eff" cut, with a slightly changed parametrisation with respect to the *area* cut:

$$area\,(size) = eff_1 + eff_2 \cdot \log_{10}(size) + eff_3 \cdot (\log_{10}(size))^2 \tag{4.18}$$

where eff_{1-3} are free parameters, optimised on MC events to yield a constant cut efficiency. An example of this cut in comparison to the *area* cut is shown in Figure 4.10. As for the energy estimation, the spectral shape of the MC distribution should resemble that of the source to be analysed, because of which also the efficiency cut optimisation has to be iterated until the resulting source spectrum is stable.

The second specific method used throughout this work is the determination of the lower energy limit ("threshold") and upper energy limit for the light curve, which generally are not strictly defined in this MARS version. Here, we define the light curve threshold as the energy above which the significance of the integral signal is maximal (see also Figure 5.17). The highest energies are given by the availability of events. The limit is set where neither signal nor excess events are present any more.

Third, the energy range and number of bins of the differential spectrum is determined here by a scan through different setups of these parameters, instead of set arbitrarily by hand. The lower limit is given by the energy at which statistical and systematic effects do not yet dominate, determined by eye from the fluctuation of the points and their error bars. The upper energy limit is given as the highest energy the upper error bar of a bin with sufficient statistics (≥ 10 excess events, $\geq 1.5\,\sigma$) is reaching for a given number of bins. By changing also the amount of bins during the scan, statistical effects can be rather well assessed, since for a low number of bins event statistics is normally subdominant, whereas for a large bin number, statistical fluctuation often become obvious. For each

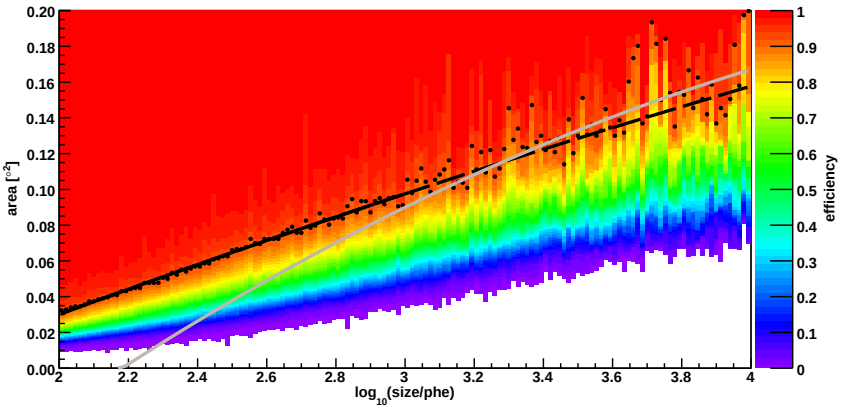

Figure 4.10: Cut efficiency in the *area* vs. *size* plane for MC events. An efficiency of 92 % is indicated by the black points. The grey line corresponds to the standard area cut, whereas the black line shows the efficiency cut, given by a fit to the black points. The solid line visualises the range the cut has been fit, whereas the dashed line is just an extrapolation of that fit, independent of the black points.

bin of the final binning not obeying the limits of ≥ 10 excess events, $\geq 1.5\,\sigma$, an upper limit (UL) at 95 % confidence level (c.l.) calculated using the ROOT implementation of Rolke *et al.* (2005) is given[6].

Finally, instead of using the linear or logarithmic bin centre for plotting and fitting the spectral data points, a centre calculated according to Lafferty & Wyatt (1995) has been adopted in this work. This bin centre is explicitly calculated to represent events following a power-law spectrum (which is the predominant case in VHE astronomy) selected by a bin of fixed width. The central energy E_{LW} of a bin reaching in energy from E_1 to E_2 is then given as:

$$E_{\mathrm{LW}} = \left(\frac{E_2^{-\alpha+1} - E_1^{-\alpha+1}}{(-\alpha+1)\cdot(E_2 - E_1)} \right)^{-\frac{1}{\alpha}} \tag{4.19}$$

where *alpha* is the power-law spectral index (see Eq. 2.17).

[6]Model ID 4, i.e. assuming a Poissionian distributed background and a known efficiency of unity.

5 1ES 1011+496 Multi-Wavelength Campaign

1ES 1011+496 is an HBL (Nieppola *et al.* 2006; Abdo *et al.* 2010b) at a comparably high redshift of $z = 0.212$ (Albert *et al.* 2007b). The mass of the central black hole has been estimated to be between $10^{8.3}$ and $10^{8.7}\,M_\odot$ (Ghisellini *et al.* 2010b, and references therein). The source was discovered at VHE by MAGIC in 2007 (Albert *et al.* 2007b). Until today, no confirmation of the MAGIC detection has been published, and no MW campaign has been conducted for that object. Giommi *et al.* (2012b) analysed the Planck observations of the source (resulting in ULs only) and presented them in combination with quasi-simultaneous archival *Swift* and *Fermi*-LAT data, which is until today the best simultaneous data basis for that object, albeit without TeV coverage. The authors did not try to model the such constructed SED, though. A few SED model fits were reported (e.g., Costamante & Ghisellini 2002; Albert *et al.* 2007b; Tavecchio *et al.* 2010; Abdo *et al.* 2010b; Zhang *et al.* 2012). However, neither of them is based on a reasonably simultaneous or even quasi-simultaneous data set with sufficient energy coverage, or they are affected by problems with the data (see below).

Based on the first VHE detection, (Albert *et al.* 2007b) applied a one-zone SSC model fit to the SED of 1ES 1011+496 (for details, see Sect. 5.4.6). They found the inverse-Compton component to be dominating over the synchrotron component, reaching in luminosity up to $L \approx 10^{46}\,\mathrm{erg\,s^{-1}}$. In combination with the rather low magnetic field value of $B = 0.15\,\mathrm{G}$, the emission region would be strongly electron dominated. These conclusions have been derived from a rather limited simultaneous data basis without sufficient coverage in the synchrotron regime. Hence they have to be confirmed by simultaneous observations of the two SED peaks, as the authors note.

In a more recent effort, Abdo *et al.* (2010b) collected quasi-simultaneous data of blazars bright in the *Fermi*-LAT band and investigated the such constructed SEDs. For 1ES 1011+496, the quasi-simultaneity of the data set is highly doubtful considering that each of the optical/UV/X-ray data sets from *Swift* were taken within a single day on 2 May and 8 May 2008, whereas the LAT HE data were averaged over three month of observations conducted between 4 August and 31 October 2008. Additional radio data was obtained from OVRO observations 8 August and 6 December. That time difference is much longer than the typical variability time scale at X-rays and gamma rays (days, see Section 2.3). Hence the truly quasi-simultaneous data set is restricted to the HE data (taking into account that no significant variability was present) and one OVRO measurement. The SED is shown in Figure 5.1.

Assuming that the non-simultaneous data is indeed representative of the broad-band flux state, the study by Abdo *et al.* (2010b) reveals that the Compton dominance for 1ES 1011+496 is in fact not that strong as estimated by Albert *et al.* (2007b).

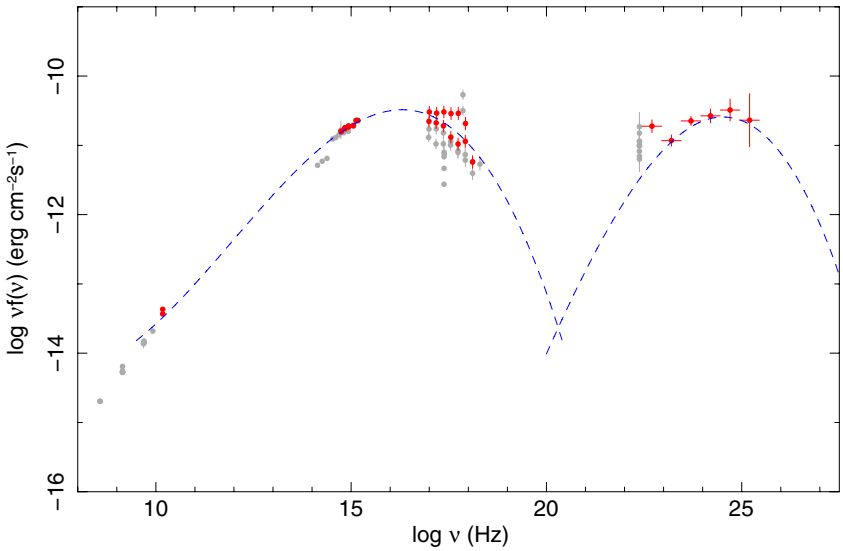

Figure 5.1: SED of 1ES 1011+496. "Quasi-simultaneous" data (according to the authors, but see text) is marked red, archival data is shown in grey. The blue dashed curve denotes an SSC fit using the model of Tramacere *et al.* (2009). Figure taken from Abdo *et al.* (2010b).

The ratio of inverse-Compton and synchrotron spectral flux density at the respective peaks $\nu F_{\nu\mathrm{peak,IC}}/\nu F_{\nu\mathrm{peak,S}}$ amounts to only 0.8 for the source, which is, however, still higher than the values found for the "classical" HBLs Mrk 501 (0.5), Mrk 421 (0.3), PKS 2155−304 (0.3) and 1ES 1959+650 (0.3).

Hence the putative Compton dominance of 1ES 1011+496 reported in Albert *et al.* (2007b) was not confirmed, nevertheless the contribution of the second SED component is stronger than for other HBLs.

5.1 Historical Overview

At VHE, 1ES 1011+496 was discovered by MAGIC in 2007 (Albert *et al.* 2007b). The observations followed a high state trigger by the optical KVA telescope. From ∼ 19 hrs of good quality data, a signal on a level of ∼ 8 % of the Crab Nebula flux was detected with a statistical significance of $6.2\,\sigma$. No statistically significant variability was detected on daily time scales. The differential spectrum of the source is well described by a simple power law (see Eq. 2.17) between 120 and 750 GeV with a steep index of 4.0±0.5 (3.3±0.7 after correcting for EBL effects). The extremely soft spectral index can not be explained by the high redshift of the source only, though at the time of discovery, 1ES 1011+496 constituted the farthest away source in the VHE sky with a reliable redshift estimate. The index and energy range of the spectrum was consistent with the tested EBL models. Until today, no confirmation of the VHE detection was reported. Previous MAGIC observations in 2006 did not result in a significant detection, indicating variability of the source flux at VHE. Since at that time the optical core flux density was ∼ 50 % lower than during the discovery, a correlation between these two energy bands may be present.

The third EGRET catalogue lists a source ∼ 1° away from the position of 1ES 1011+496, 3EG J1009+4855 (Hartman *et al.* 1999). Due to the weakness of the signal, which just

meets the statistical significance to be included in the catalogue, 1ES 1011+496 is just contained within the 99 % confidence contour of that source (Nakagawa *et al.* 2005). Considering the rather large distance of the two objects, the association with 1ES 1011+496 is nevertheless questionable. The authors note that the flux, significance and position of the source may be contaminated from extended or multiple objects. Searching for counterparts for such weakly identified EGRET sources through a multi-band approach, Sowards-Emmerd *et al.* (2003) could not identify a more plausible counterpart candidate, but classify 3EG J1009+4855 as a non-blazar object, disfavouring the association with 1ES 1011+496. On the other hand, *Fermi*-LAT did not report a detection at the position of the EGRET source. Either 3EG J1009+4855 is variable (however, non-blazar of nature as it was reported), or it is identical with 1ES 1011+496 and the confusion is solely due to the limited angular resolution of EGRET.

1ES 1011+496 itself is listed in the "*Fermi*-LAT Bright AGN Sample" (called "J1015.2+4927"), i.e. it exhibited a signal $\gtrsim 10\,\sigma$[1] after three months of LAT observations and belonged to the brightest 106 AGNs (and 10 HBLs) detected by the *Fermi* satellite at HE (Abdo *et al.* 2009a). Significant variability was not found after eleven months of data taking (1FGL catalogue; Abdo *et al.* 2010d), but is reported in the 2FGL catalogue, comprising 24 months of observations (Nolan *et al.* 2012, ; see also the *Fermi*-LAT light curve shown in Figure 5.28). Variability is also indicated when comparing the simple power law spectral indices and the integral photon fluxes of the two catalogues. Both decreased from 1FGL to 2FGL, the spectral index changing from $\alpha_{\mathrm{1FGL}} = 1.93 \pm 0.04$ to $\alpha_{\mathrm{2FGL}} = 1.72 \pm 0.04$ and the flux from $F_{1-100\,\mathrm{GeV,1FGL}} = (8.7 \pm 0.6) \cdot 10^{-9}\,\mathrm{photons\,cm^{-2}\,s^{-1}}$ to $F_{1-100\,\mathrm{GeV,2FGL}} = (7.8 \pm 0.3) \cdot 10^{-9}\,\mathrm{photons\,cm^{-2}\,s^{-1}}$. However, in 2FGL the best-fit model to describe the LAT spectrum is a log-parabolic power law (see Eq. 2.13) , indicating an SED peak at a few GeV (Ackermann *et al.* 2011b). Out of the 69 sources with significant spectral curvature in the HE regime, 1ES 1011+496 is the only HBL being described best by that model in the HE range. Taking into account the rather low redshift of the source (when compared to the remaining sources with significantly curved spectra), the EBL should be responsible for only a small portion of this curvature (Ackermann *et al.* 2011b).

The *HEAO 1* satellite discovered an X-ray signal in the region of 1H 1013+498 (Wood *et al.* 1984), which is within the comparably small angular distance of $\sim 20'$ likely identical to 1ES 1011+496. The latter was first identified at X-rays within the *Einstein* (*HEAO 2*) IPC Slew Survey (Elvis *et al.* 1992) and subsequently by *ROSAT* (Lamer *et al.* 1996; Voges *et al.* 1999). After a gap of nearly ten years, detections by *Swift* XRT were reported (Massaro *et al.* 2008; Tavecchio *et al.* 2010; Abdo *et al.* 2010b; Giommi *et al.* 2012b). The first power law spectral index observed by *ROSAT* between 0.1 and 2.4 keV was steep (1.49 ± 0.08), which was confirmed by all following XRT measurements but one (finding a flat spectrum). Massaro *et al.* (2008) and Abdo *et al.* (2010b) found a parabolic power law to be preferred over a simple power law fit to describe the X-ray spectrum of 1ES 1011+496, yielding synchrotron peaks between 0.04 and 0.74 keV[2]. The integral flux between 2 and 10 keV was reported to vary by a factor of nearly 20 ($0.36 \cdot 10^{-11}$ to $6.67 \cdot 10^{-11}\,\mathrm{erg\,cm^{-2}\,s^{-1}}$; Massaro *et al.* 2008; Giommi *et al.* 2012b).

[1] The signal in fact amounted to $23.8\,\sigma$.

[2] Calculated from the spectral indices given in the publications.

In the optical, 1ES 1011+496 shows strong and frequent variability, reaching up to a factor 2 or 3 in brightness between low and high activity states (as revealed by the Tuorla Blazar Monitoring Program[3]). The host galaxy is comparably weak for that source (R-band: (0.49 ± 0.02) mJy; Nilsson *et al.* 2007). Optical multi-band observations conducted with the Michigan-Dartmouth-MIT observatory between 2005 and 2010 detected significant though moderate variability without clear signs of time lags between the individual bands (Böttcher *et al.* 2010). A "bluer when brighter" trend was found (see also Section 2.3), indicating a shift of the synchrotron peak to higher frequencies with increasing source activity. The position of the peak itself was typically found between ~ 2 and ~ 3 eV for all flux states, consistent with the *Swift* observations during a very low flux state presented by Giommi *et al.* (2012b).

However, these results are hard to reconcile with the positions determined from the remaining *Swift* observations (see above). Also synchrotron peak estimates from the combination of archival optical and X-ray data suggest a peak around ~ 0.23 keV (Nieppola *et al.* 2006). Abdo *et al.* (2010b) determined from their (overall non-simultaneous, but indeed simultaneous in the optical – X-ray regime) data set a peak around 0.083 keV. The estimation based on the optical – X-ray and radio – optical index yielded a peak at ~ 0.013 keV, though (Abdo *et al.* 2010b). Since the multi-band optical data used by Böttcher *et al.* (2010) to determine the peak positions span a large time and variability range (and were possibly partly quasi-simultaneous to the *Swift* observations), they should be representative of the source behaviour and be consistent, at least in high flux states, with the measurement from *Swift*. However, Böttcher *et al.* (2010) note that 1ES 1011+496 was detected at moderately faint states in the optical throughout the monitoring. Considering the positive correlation of the synchrotron peak with the flux state of the source, the higher peak frequencies derived from the *Swift* observations can be explained by the higher X-ray flux during these observations.

In the radio regime, 1ES 1011+496 shows significant variability at 1.4 GHz, with reported flux densities of ~ 380 and ~ 470 mJy (Nakagawa *et al.* 2005, and references therein). Metsähovi detected the source on 1 December 2002 with a flux density of (0.56 ± 0.12) mJy, whereas from 11 of the 12 remaining observations between July 2002 and March 2005, ULs ($S/N > 4$) below the measured flux density level were derived (Nieppola *et al.* 2007). This may be due to varying observation conditions and consequently different detection limits of the instrument, but since the worst such limit is 0.5 mJy, this may also be a sign of variability. The radio morphology of 1ES 1011+496 is characterised by the typical core-jet structure of blazars (Augusto *et al.* 1998; Nakagawa *et al.* 2005). The pc- and kpc-scale jets are well aligned, having a position angle of $\sim -99°$ (Augusto *et al.* 1998) and $\sim -105°$ (Nakagawa *et al.* 2005), respectively (see also Figure 5.2). Analysing two VLBI observations spanning 2.2 years, Nakagawa *et al.* (2005) report a position of the dominating jet feature relative to the radio core consistent with no motion. A counter-jet has not been observed. The fractional polarisation detected from the core is rather high for an HBL object ($\geqq 4\,\%$ compared to $< 3\,\%$ for HBLs), better consistent with values found for LBLs (Kharb *et al.* 2008). Public data from the MOJAVE[4] archive confirm the comparably high degree of polarisation

[3] http://users.utu.fi/kani/1m/
[4] http://www.physics.purdue.edu/MOJAVE/

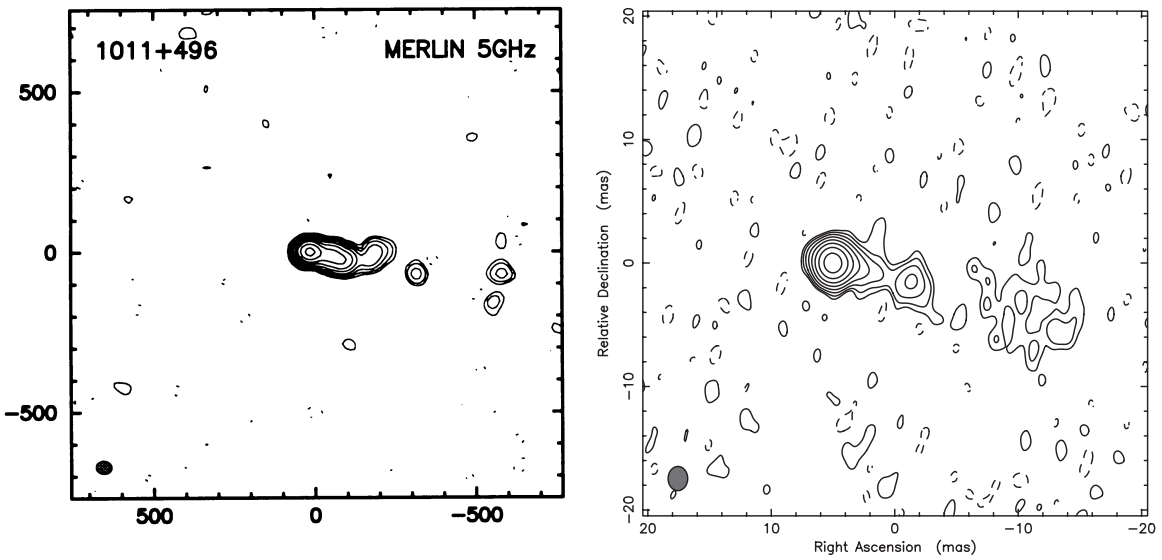

Figure 5.2: Archival radio maps of 1ES 1011+496 at 5 GHz. *Left side:* April – July 1995 measured by MERLIN. peak flux: 0.189 Jy/beam, logarithmic contours are drawn at $-6, -3, 3, 6, ...\sigma$, dashed lines denote negative flux densities. The beam size is (48×41) mas. Y axis: relative declination [mas], x axis: relative right ascenion [mas]. Image taken from Augusto *et al.* (1998). *Right side:* 20 January 1997, observed with the VLBA. peak flux: 0.112 Jy/beam, contour levels are drawn at $-0.5, 0.5, 1, 2, 4, 8, 16, 32, 64$ % of the peak flux density. The beam size is (2.0×1.6) mas at $-1°$. Image taken from (Nakagawa *et al.* 2005).

and reveal variability ranging from 2.9 to 8.1 %[5].

A Special Object? The historical overview revealed several properties of 1ES 1011+496 rather atypical for HBLs. Neither of these alone is well suited to require a new classification of the source but the low peak frequencies found by Böttcher *et al.* (2010), which however represent only a faint state excerpt of the behaviour of the source. Combining the characteristics displayed in all the individual energy regimes, a new picture of the source may be emerging. Specifically, we suggest to change the classification of 1ES 1011+496 from an HBL to an IBL exhibiting during high activity states HBL characteristics. Since the LBLs/IBLs/HBLs classification scheme is not uniquely and physically motivated defined and the limits are not hard but fluent (see Section 2.4), such objects are in fact expected to exist. The argumentation for our new classification is the following:

- At VHE, the source is characterised by a spectrum atypically soft for an HBL even after correcting for EBL absorption (index 3.3 ± 0.7; Albert *et al.* 2007b).
- The HE spectrum is the only HBL one in 2LAC being best described by a log-parabolic power law, requiring the second SED peak to be located in this energy

[5]Note that these values are given for the whole system of core+jet. Adding these up, a fractional polarisation of ~ 4 % is achieved for the measurements presented in Kharb *et al.* (2008), compared to 4.7 % for the radio core only.

regime. Apart from this source, such a behaviour is found only for IBLs, FSRQs and radio galaxies.

- The X-ray spectrum can be very soft, as has been measured by *ROSAT* (Lamer *et al.* 1996) and once by *Swift* XRT (Giommi *et al.* 2012b), requiring a peak around optical frequencies. However, most of the X-ray observations constrain the peak to be much higher in energy.
- Long-term optical monitoring find the peak within the optical regime (Böttcher *et al.* 2010), but individual observations by *Swift* sometimes constrain it to be located much higher in energy. An indication for a synchrotron peak moving to higher energies with increasing flux has been found (Böttcher *et al.* 2010).
- The fractional polarisation of the source in the radio regime is comparably high for HBLs, but is well consistent with an LBL nature.
- From SED modelling, a comparably high Compton dominance is found (Albert *et al.* 2007b; Abdo *et al.* 2010b) (however, the underlying data sets are mostly based on non-simultaneous data).
- The HBL classification from Nieppola *et al.* (2006) arose from a dividing line for the first SED peak between IBLs and HBLs of $\nu_{peak} = 10^{16.5}$ Hz. The reported value of $10^{16.74}$ Hz for 1ES 1011+496 is close to that (rather arbitrary) limit.
- Overall, the HE and optical monitoring as well as the radio observations (for which variability time scales are much longer) should represent the typical state of the source, i.e. an IBL. The X-ray measurements, on the other hand, constitute only snapshots of the source, apparently characteristic for high activity states. These are in agreement with the HBL nature of 1ES 1011+496. The transition between both can be explained by the shift of the peak energy during high activity.

The VHE discovery spectrum does not fit into that picture though, representing a snapshot of the source (since no variability has been detected) during a high flux state but exhibiting a soft spectral index characteristic for an LBL. That discrepancy may be resolved considering the large uncertainty of the index. Alternatively, the VHE observations may indeed have caught the source during a high flux state, but the second peak did not shift strong enough to cause a hard spectral index characteristic for an HBL. That would implicate that the source can hardly be detected during a low state by current VHE instruments.

Also it is unclear why most of the X-ray observations apparently have been conducted during a rather high activity of the source. Since these, to our best knowledge, were not triggered by flares, they should not be biased towards high flux states and hence should show IBL and HBL characteristic of the source at about an equal amount.

5.2 Observation Campaign Details

The MW campaign was organised to be conducted during simultaneous observation windows of MAGIC and AGILE. The observation proposal to AGILE was accepted, whereas

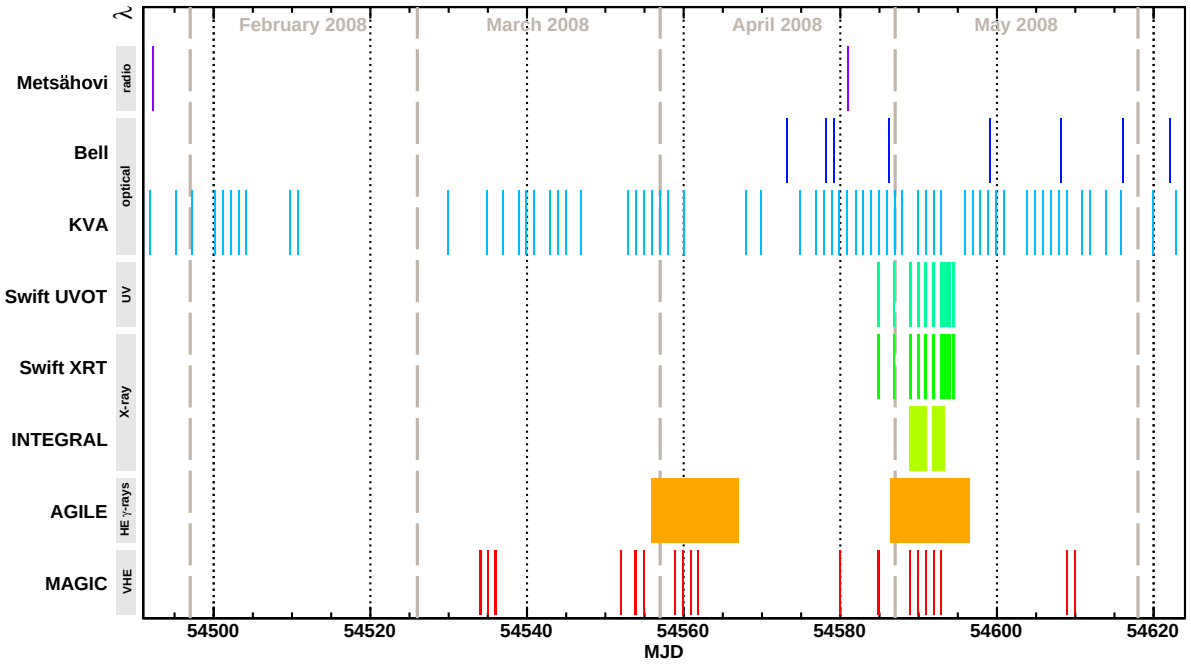

Figure 5.3: Observations of 1ES 1011+496 during the MW campaign in early 2008. The lines indicating the observation time and length have been smoothed for clarity by 0.2 days. The grey bars on the left hand side of the figure gives the energy regime of the instruments.

the proposals to *Suzaku* and VLBA were not successful. Additional simultaneous coverage was achieved in the radio band by cooperation with the Metsähovi telescope, in the optical by means of the KVA telescope, and in X-rays by short notice ToO proposals to *Swift* during the second AGILE window. The Metsähovi schedule was strongly influenced by bad weather, leading to very little observation time spent on weak radio sources like 1ES 1011+496. The conducted measurements are summarised in Figure 5.3, exact numbers are listed in the Appendix (Chapter E), and details on the instruments can be found in Chapter 3. *INTEGRAL* was observing the source also in the MW time slot in X-rays, and additional measurements by the Bell observatory were conducted in the optical R-band. The *Fermi* Gamma-ray Space Telescope was not yet launched at the time of observations.

5.3 MAGIC Data Analysis and Results

1ES 1011+496 was observed with MAGIC-I from beginning of March until end of May 2008 at zenith distances between 21° and 37° in wobble mode for a total of ∼28.2 hrs. The observations took place mainly in dark night, only ∼1 h of data was taken in mild moon or twilight conditions.

The data were analysed with MARS CheObs Ed. version 2.4 under ROOT 5.12.00f. The standard spline calibration was applied, followed by the standard time image cleaning with cleaning levels of 6 and 3 phe and a time coincidence window of 1.75 ns. More details on the analysis procedure can be found in Section 4.3.

5.3.1 Data Quality Evaluation

The observation conditions during the 1ES 1011+496 measurements were partly influenced by strong winds, causing the MAGIC-I camera to close for safety reasons, and high *cloudiness*. Also Calima was present for some nights, see Tables B.1 and 5.1. Additionally, the data of two nights were lost due to hardware or software failures (calibration and AMC).

After evaluating the data quality according to the criteria discussed in Section 4.3.2, ~ 19.9 hrs of data were selected for further processing. The reasons for excluding data are listed in Table B.1. Some relevant issues with the data quality have been found during the investigations, which will be discussed in the following.

- **Closing Camera** To save the MAGIC-I camera lids from damage due to strong wind gusts, the camera is being closed automatically if the weather station reports wind speeds in excess of 40 km/h. The camera is also closed in case the humidity rises above 90 %. The DAQ is not stopped automatically though, leading to data being taken during closing of the camera or even with closed camera. As a consequence, showers may become truncated and, if showers get lost, the effective on time calculation may become wrong.

  The MAGIC-I camera had been closed seven times during the MAGIC-I observations. It has been checked that the duration of these events is small (camera closing takes ~ 30 s and shifters stop DAQ normally before the camera is closed) so that the influence on the data should be negligible. Affected runs have been removed from the data analysis (see Table B.1) if not too much good quality data had to be excluded at the same time.

- **Cloudiness** Clouds in the MAGIC-I FOV can be identified not only through the pyrometer data, but also from the trigger rate and the number of stars identified by the starguider. Also the shift crew is inspecting the sky by eye, giving valuable information on the sky conditions in the runbooks.

  Clouds were present frequently during the 1ES 1011+496 observations. Their effect on the data has to be studied carefully though, being dependent on the nature and height of the clouds. Very high altitude clouds (above ~ 10 km), for example, might not influence the data at all, but would be visible in the pyrometer data and would reduce the number of stars. Therefore, a hard cut in the *cloudiness* parameter has not been applied. Instead, the rate has been chosen as one of the most important parameters to judge the effect on the data. The rate dependency on the zenith distance as well as on the DTs (which were basically constant throughout all observations, see Table B.2) has been taken into account. Indeed sequences have been found for which the rate was higher than expected from the *cloudiness* value and number of stars (e.g. mean rate of sequence 347959: ~ 199 Hz), whereas the rate of other sequences was strongly affected by a comparably high *cloudiness* (e.g. sequence 350632, mean rate: ~ 180 Hz).

  The effect of absorption by clouds on the data is twofold. On the one hand, a part of the Cherenkov light is being absorbed, leading to an overall reduction of

photon content in the MAGIC-I shower images and hence an underestimation of the original shower energy. On the other hand, low energy showers may become completely absorbed by the clouds, or may be reduced in size to a value indistinguishable from the background for MAGIC-I, and hence get lost. These effects will lead to a reduced flux and altered spectral index of the source spectrum. They also require a new optimisation of the *area* cut, as different shower events will be shifted in the *area* vs. *size* plane in a different manner (the shower *size* will decrease by a constant factor for all pixels and all showers, while the *area* of smaller showers will be reduced by a stronger factor compared to larger showers, the relative loss in area being, in approximation of a circular shower event with radius r, $(2\pi r) \,/\, (\pi r^2) = 2/r$). Muon events, on the other hand, will be rarely affected by the clouds, being only visible to Cherenkov telescopes if produced some hundred metres above the reflector.

A first try of correcting for the effects of clouds did not succeed (see Section 5.3.2), which would have enabled to retain a larger amount of the affected data. Therefore, the rate vs. zenith distance cut for good quality data had to be tightened and was finally set at 82 % (see Figure 5.7). Additionally, the higher mean *cloudiness* of the data has been taken into account for the determination of the new background separation cut.

- **Arrival Times** The arrival times of calibration pulses were not stable during the observations, see Figure 5.4. Late as well as early pulses in comparison to the long-term evolution are visible. It has been investigated if this behaviour caused problems for the data quality, but the arrival times of calibration event as well as shower event pulses could be calibrated successfully for all sequences, resulting in comparable arrival times. Only for sequence 1000131, which had a very early arrival time, negative effects were found, leading to a detailed investigation (see below).

- **Muon Ratio** Figure 5.5 is showing the evolution of the muon *ratio* around the 1ES 1011+496 observations. Clearly the *ratio* was not stable on long time scales. The corresponding muon calibration factors, though determined for every period individually, may have to be updated. But as the mean *ratio* of the 1ES 1011+496 periods was already around 100 %, adapting the factors for the periods unrelated to this analysis is beyond the scope of this work. Nevertheless also the data used in this analysis was characterised partly by high and low *ratio* values.

  Sequence 343689 was showing an especially low *ratio* value of 96.9 %. Due to the short duration of the sequence yielding only 222 muons suited for the calibration, this value was not statistically reliable. Since data taken the same night directly prior to sequence 343689 had an only slightly increased *ratio*, the sequence has not been removed from further analysis. Sequence 341446 exhibited a rather high *ratio* value of 104.4 %, which was still acceptable though considering an overall mean weighted muon *ratio* of 101.3 % for the 1ES 1011+496 data. The source of the high value could not be found, but as the surrounding sequences also showed a higher *ratio*, the reason is presumably not connected to the data itself but rather

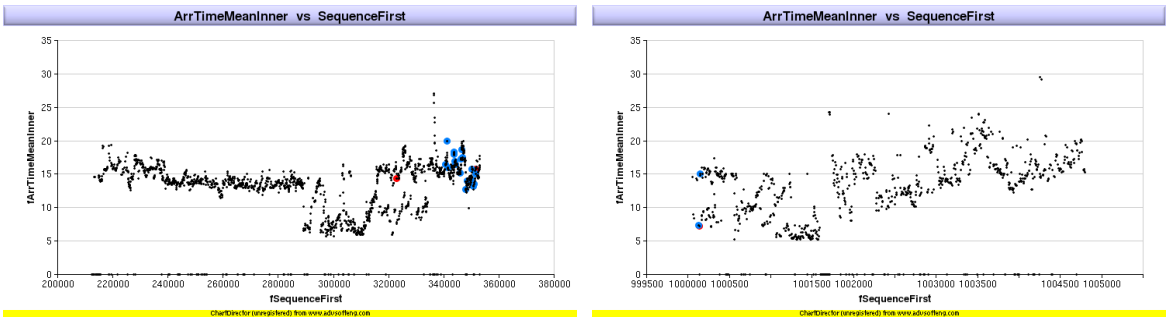

Figure 5.4: Arrival time of calibration pulses of automatically processed sequences. Blue points highlight 1ES 1011+496 data, while red points show Crab (sequence 322846) and Mrk 421 (sequences 351510 and 1000135) sequences. The x axis spans a time period of 9 February 2007 – 16 May 2008 (*left side*) and 21 May 2008 – 3 March 2009 (*right side*).

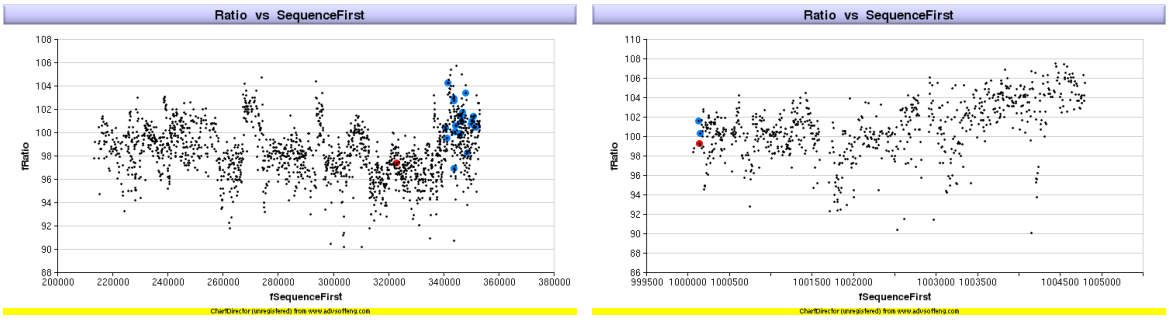

Figure 5.5: Same as Figure 5.4 but showing the muon *ratio*. Data points below a *ratio* of 90 are not given for clarity of the histograms.

an instrumental or seasonal effect.

- **Camera Inhomogeneity** The Center of Gravity (*CoG*) distribution of shower ellipses in the MAGIC-I camera plane revealed a non-uniform camera acceptance for the 1ES 1011+496 data. This inhomogeneity manifested itself in a series of holes forming a row through the upper half of the inner camera as well as a broad hole in the lower half before *area* cut (see Figure 5.6). After application of the *area* cut, a faint hole was still visible in the lower camera half at a slightly different position than before as well as one large hole upper right of the camera center, near one of the wobble positions. An inhomogeneous camera acceptance may fake a signal of the source due to a wrong background determination if the time spent in the two wobble positions is not comparable and the number of On and Off regions in the camera is not following a sixfold symmetry. Therefore, a detailed quality check has been performed, showing that the holes do not fake the signal detected from 1ES 1011+496 (see Section C.1.1 for details).

Apart from these general quality considerations, some problems of individual sequences should be discussed here in short:

- **Sequence 346267** This sequence is listed in the data base with a worrying number

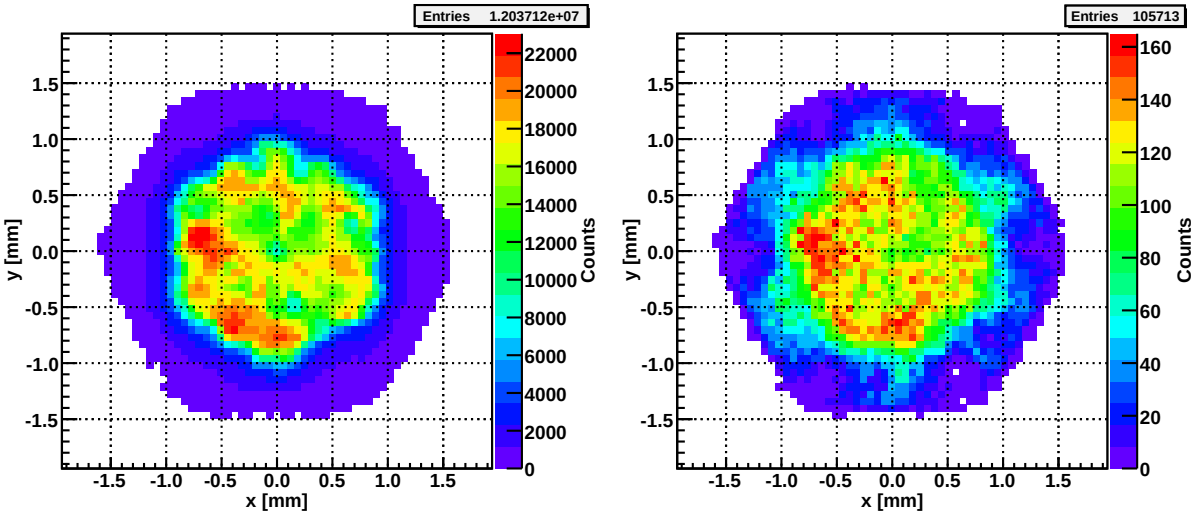

Figure 5.6: Center of Gravity distribution of shower events in the MAGIC-I camera for all good quality data. *Left side:* before *area* cut, *right side:* after *area* cut.

of 25 dead pixels. Having a closer look, these were only present for $\sim 30\,\mathrm{s}$ and were situated in the bottom outer camera. As at about the time of this event the camera was re-opened after having closed automatically due to a wind gust, the reason for the dead pixels is presumably that the data acquisition was started already before the camera was opened completely, and the true duration of that event was only some seconds. Additionally only a part of the outer camera was affected, so the effect on the data should be negligible.

- **Sequence 351058** The mean number of correlated stars was only 9.0 ± 3.5 for this sequence, 8 being the lower limit for the starguider to work. As this is a mean value, it may have happened that major parts of the sequence could not be corrected for mispointing. A closer inspection showed that $\sim 5\,\%$ of starguider measurements were not used for calculating a correction, which is above the normal values of $\sim 1\,\%$, but still sufficient for correcting for a potential mispointing for most of the duration of the sequence. The corresponding pointing plot shows that a correction has been applied for a dominant part of the data (see Figure C.6).

- **Sequence 1000131** As mentioned above, the arrival time of calibration pulses was very early for this sequence. This led to twelve pixels in the inner camera that could not be calibrated due to the arrival time falling out of the signal extraction window. These pixels were marked as unsuitable for further analysis automatically. As not more than two of them were direct neighbours, the automatic bad pixel treatment of the calibration could reconstruct the shower signal and arrival times of these pixels nevertheless. In principle a signal extraction algorithm specially adapted for early pulses may be used to compensate for that arrival time problem, which indeed could calibrate the unsuitable pixels mention above successfully. Taking into account though that the number of affected pixels was rather small, their shower signal could be reconstructed and that all data would have to be recalibrated using the new extractor, leading potentially to problems with data having a late arrival

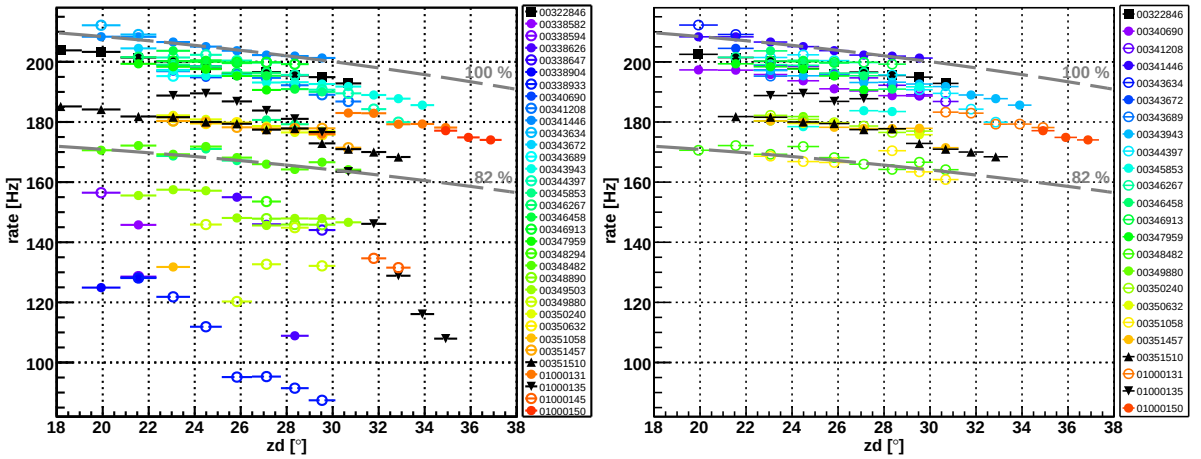

Figure 5.7: Rate after image cleaning as a function of zenith distance of the observations for the sequences of 1ES 1011+496 under study. Also shown are the sequences of Mrk 421 used for the optimisation of the separation cuts (351510 and 1000135, see below) as well as the Crab Nebula data used for verifying the analysis pipeline (sequence 322846). The legend entries correspond to the sequence numbers. *Left side:* automatically processed sequences without quality selection, *right side:* data after quality selection. The dashed lines indicate the reference rates which have been used as a quality criteria where 100 % means a rate of 215 Hz at zd = 0°.

time, the standard signal extraction was not changed.

The sequences and some of their most important quality parameters are listed in Table B.2. As can be seen, the quality parameters of data affected by a rather large *cloudiness* did not differ systematically from the ones of sequences not affected by clouds despite of a lower rate after image cleaning. This indicates that a special treatment of these data sets in the further analysis is not necessary. Figure 5.7 shows the rate after image cleaning of the sequences as a function of their zenith distance. As reference, a rate of 215 Hz at a zenith distance of 0° has been determined. 82 % of that reference line have been used as a lower limit, determined from the individual quality of the sequences. Note that the DTs of the individual sequences were well compatible apart from the Crab Nebula data. The Crab Nebula is located in the galactic plane, requiring as a standard a higher DT setting due to the brighter FOV. The distribution after quality selection (*right side* of the figure) does not show strong fluctuations and visualises the homogeneity of the data sample used for the analysis.

5.3.2 Gamma – Background Separation

Separation Cut Optimisation 1ES 1011+496 was observed dominantly below 35° in zenith distance and, from a first check, exhibits a clear signal. Hence a dedicated separation cut optimisation seemed not to be required. On the other hand, the spectrum of the source was very different from the one of the Crab Nebula, on which the standard separation cuts had been optimised. Additionally, about one third of the data was affected by absorption from clouds. Therefore a dedicated cut optimisation has been performed.

To analyse as much data of 1ES 1011+496 as possible without being affected by the high *cloudiness*, a new analysis strategy has been developed. This should have corrected

to a certain extend for the light absorption by clouds, rendering it possible to combine the results determined from the non-affected and cloud-affected data by stacking. The main steps of this strategy are:

- Separate the observational data into a non-affected and a medium affected sample.
- Determine dedicated separation cuts for both samples, using data of a comparable source for cut optimisation with a similar cloud characteristic as the corresponding sample.
- To determine the effect of clouds on the spectrum and light curve, find data of a source with constant flux and spectral index (Crab Nebula) affected in a similar way as the source data by clouds. For comparison, a sample of data unaffected by clouds is needed. Determine individual separation cuts also for these two data sets.
- From a comparison of the Crab Nebula spectrum and light curve derived from the cloud-affected and unaffected data set, calculate an energy-, zenith distance- and rate-dependent correction factor.
- Apply that correction factor to the cloud affected sample of the source, and stack the result with the one from the unaffected sample.

Surprisingly, there was not much data among the high *cloudiness* observations of Crab Nebula for which a significant effect on the rate was apparent, despite considering data in the time range of February 2007 (first MUX data) until April 2009 (two telescope system). This confirms the assumption that the effect of clouds has to be evaluated individually for every sequence instead of applying a hard cut in *cloudiness* as a quality criterion. Additionally requiring a similar zenith distance distribution as the 1ES 1011+496 observations and good data quality (except of the effect of clouds), the Crab Nebula spectrum resulting from the remaining data was significantly affected by statistical effects, making it impossible to determine a correction factor. Therefore, this analysis attempt had to be abandoned.

Instead of dividing the 1ES 1011+496 data into two samples of different quality, only one sample with a relaxed rate criterion was composed. Compared to the former approach, only $\sim 6\,\%$ of data had to be discarded. The now overall lower rate due to an increased mean *cloudiness* of the sample was accounted for by choosing data for the optimisation of the separation cuts that also showed a mild influence of clouds on the rates. This should yield on average a better result than a cut optimised on data with flawless quality.

From observations of sources detected significantly by MAGIC-I within the first half of 2008, Mrk 421 had the best suited data for that purpose. Sequence 351510 was taken the same night as 1ES 1011+496 data, offering a very good match of instrumental setup and observation conditions. To resemble the zenith distance distribution of 1ES 1011+496, obtain a wobble ratio close to unity and to compensate for potential systematic biases due to having data from only one night, sequence 1000135 was added, which was also recorded the same night as 1ES 1011+496 data. The most important quality parameters

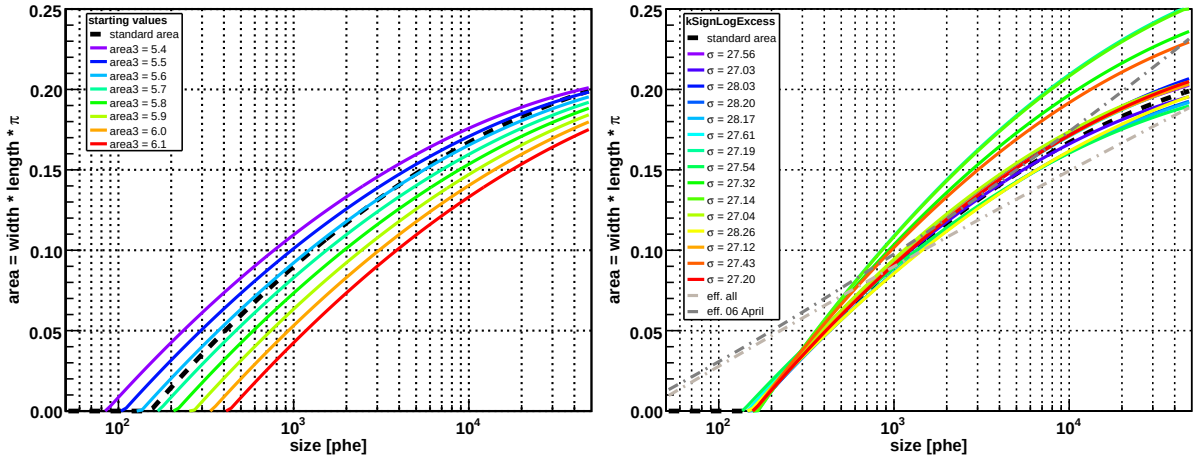

Figure 5.8: *Left side:* starting *area* cut parabolas for the optimisation of the 1ES 1011+496 separation cut. For each cut, ϑ values of 0.18, 0.20 and 0.22 were considered. *Right side: area* parabolas resulting from the optimisation procedure. For clarity, only the parabolas with a significance larger than 27 σ are shown. The significance of each parabola is given in the legend. Additionally the efficiency cuts (labeled "eff.") used for deriving the spectrum of the "all" and "6 April" data set are shown in grey.

of the two sequences are listed in Table B.2. They were well consistent with the ones of 1ES 1011+496 and were influenced by *cloudiness*, which is also visible from their lowered rate despite comparable DT values (see also Figure 5.7). It should be mentioned that sequence 1000135, same as sequence 1000131 of 1ES 1011+496 (see above), was suffering from a very early arrival time leading in this case to four pixels unsuitable for further analysis. The bad pixel treatment was able to compensate for this effect though. On the other hand, it could not correct for the effect of a 6.0 mag star in the FOV of Mrk 421, causing for a limited amount of time clusters of unsuitable pixels. The star did not have a measurable influence on the data after the high level analysis (see Section C.1.3).

The optimal cut has been determined on the Mrk 421 data set using the optimisation strategy kSignificanceLogExcess, being a standard tested on many different sources and yielding a high significance as well as number of excess events for sources with a sufficiently high signal. The optimisation was conducted several times, altering the starting values to cover a large part of the *area* vs. *size* plane (see left side of Figure 5.8). This has been achieved by changing the second parameter of the *area* parabola parametrisation from 5.4 to 6.1 in steps of 0.1. Each of this optimisation runs was conducted for an initial value of ϑ of 0.18, 0.20 and 0.22, yielding 24 parabolas optimised on Mrk 421. For clarity, only the parabolas with a significance above 27 σ are shown in the right panel of Figure 5.8 (the overall range of resulting significances was 26.22 – 28.26 σ).

Basically two regions where found into which most of the *area* parabolas were converging, one slightly above and one slightly below the standard *area* cut. The upper region contained a higher number of parabolas, whereas the significances of the lower region parabolas was higher. Considering that (1) absorption by clouds should result in a larger relative shift in *size* than in *area* for large showers, (2) this relative shift becomes smaller or inverted for small showers and (3) that the muons will hardly move in the *area* vs. *size* plane due to the clouds (see the discussion on *cloudiness* in the previous section), the upper convergence region is preferred. These cuts are more open at high *sizes* and

stricter at low *sizes* than the standard cut or the parabolas of the lower convergence region. The cut yielding the highest significance in that region resulted in a significance of $28.03\,\sigma$ for Mrk 421. Using a precision of three digits to overcome potential fluctuation effects, the cut was given by the following parameters (see Eq. 4.14):

$$\begin{aligned} \vartheta &= 0.181 \\ c_8 &= 0.226 \\ c_9 &= 0.0807 \\ c_{10} &= 5.72 \end{aligned}$$

With these reduced precision cuts, 591 excess events where detected with a significance of $27.85\,\sigma$ over a background of 133 events, compared to 620 excess and 195 background events ($26.33\,\sigma$) resulting from standard cuts.

Data Sets and Analysis Results These new optimised separation cuts where applied to all data of 1ES 1011+496 as well as the observations simultaneous to the AGILE pointings. For the latter, only the first observation window was considered, taking into account that the AGILE exposure during the second observation block was even too low to derive an UL. Additionally, the 1ES 1011+496 data were binned period-wise and on daily scales to search for potential variability. The such defined data sets and their corresponding results are listed in Table 5.1.

Figures 5.9 and 5.10 visualise the signal of the "all" data set in form of the ϑ^2 and sky plots. The sky plot showed a nicely centred and strong signal, though with some small outliers. Also from the ϑ^2 plot, indications of some excess outside of the signal region were apparent. Investigating further, mispointing could have been present for the data of 9 March, see left side of Figure 5.11. This hint was confirmed by analysing ten minutes of Crab Nebula data taken on the same night, as shown in the right side of Figure 5.11. A correction of that mispointing is not straightforward. Shifting the signal peak of 1ES 1011+496 to the expected source position would be an active bias of the results towards the expectation. An independent correction might be calculated in principle from the measured mispointing of the Crab Nebula data, but due to the largely different zenith distance of Crab Nebula and 1ES 1011+496 ($11° - 12°$ and $21° - 30°$, respectively) the resulting value may not be applicable to the source. As only a few events were concerned and the source wass significantly detected, no correction attempts have been undergone.

The ϑ^2 and sky plots for the different observation periods as well as 6 April are shown in Section D.1.1.

Sanity Checks A potential systematic effect of the new optimised separation cuts on the data has been tested by investigating the background rates of the daily data sets after separation cuts. Figure 5.12 is showing that the background rates were reasonably stable and the excess rate was not correlated with the background rate. No systematic trend of the background rate with *cloudiness* (see Figure 5.13) or zenith distance can be found, indicating that the separation cut was equally well suited for all data. All

Data Set[a]	**Sequences**	**Zenith Dist.**[b] [°]	**On-Time**[c] [h]	**Ext.**[d] [%]	**Sign.**[e] [σ]	**Exc.**[f]	**Bgd.**[g]	**Wobble Ratio**[h]
all	340690 – 1000150	21 – 37	19.92	...	7.6	421	2124	0.93
AGILE	345853 – 346913	22 – 30	2.61	...	3.3	65	263	0.62
period 64	340690 – 341446	21 – 30	7.16	...	5.3	181	811	1.02
period 65	343634 – 346913	21 – 34	6.10	...	4.0	118	620	0.58
period 66	347959 – 351457	21 – 31	5.99	...	3.4	101	618	1.33
period 67	1000131 – 1000150	30 – 37	0.69	...	2.1	22	73	0.73
09 March	340690	21 – 30	2.84	...[i]	3.5	73	303	1.14
10 March	341208	24 – 30	0.89	...[i]	2.5	28	84	0.57
11 March	341446	21 – 30	3.43	...[i]	3.1	76	424	1.09
27 March	343634 – 343689	21 – 23	0.89	...[i]	1.3	14	87	0.71
29 March	343943	23 – 34	1.34	...[i]	1.6	22	133	0.40
30 March	344397	23 – 32	1.27	0[j]	1.1	15	135	0.65
03 April	345853	25, 27 – 30	0.28	...[i]	1.0	5	24	2.48
04 April	346267	22 – 27	0.63	0.64	0.4	3	58	...[l]
05 April	346458	22 – 28	0.90	0[j]	0.7	8	91	0.58
06 April	346913	23 – 28	0.80	6.07	4.0	48	89	1.42
24 April	347959	21 – 27	1.08	0[j]	1.5	20	135	1.45
29 April	348482	21 – 30	1.61	4.59	2.2	32	159	1.45
03 May	349880	24	0.06	...[i]	2.9	9	4	...[l]
04 May	350240	23 – 30	0.92	3.44	1.6	19	93	1.82
05 May	350632	23 – 29	1.05	0.64	0.1[k]	0	110	0.66
06 May	351058	23 – 25, 29, 31	0.30	...[i]	1.8	9	18	1.46
07 May	351457	23 – 30	0.96	1.55	0.8	9	98	1.94
23 May	1000131	30 – 35	0.48	0.46	2.4	21	51	1.54
24 May	1000150	35 – 37	0.21	0[j]	0.2	1	22	...[l]
Mrk 421	351510 & 1000135	21 – 33	1.29	1.55 & 0.46	27.9	591	133	0.97
Crab	322846	21 – 30	0.72	...[i]	17.7	282	89	0.84

Notes. [a] The date corresponds to the day following the observation night. [b] Zenith distance range of the observations. [c] Effective observation time. [d] Atmospheric extinction measured by the CMT telescope on La Palma. [e] Significance of the signal calculated using Li & Ma (1983) Eq. 17 and optimised cuts. [f] Number of excess events. [g] Number of background events. [h] Ratio of time spent in each of the two wobble positions. [i] No CMT observations available. [j] Absorption below reference value for a clear night. [k] Note that for the calculation of the significance, the number of events is not an integer. After the calculation, the event numbers are rounded down. [l] Data taken during one wobble position only.

Table 5.1: Data set information and analysis results for 1ES 1011+496. The last last two data sets correspond to Mrk 421, observed 7 and 23 May 2008, and the Crab Nebula, taken 8 January 2008. All observations have been conducted in wobble mode with 3 Off regions (scale factor $f = 1/3$).

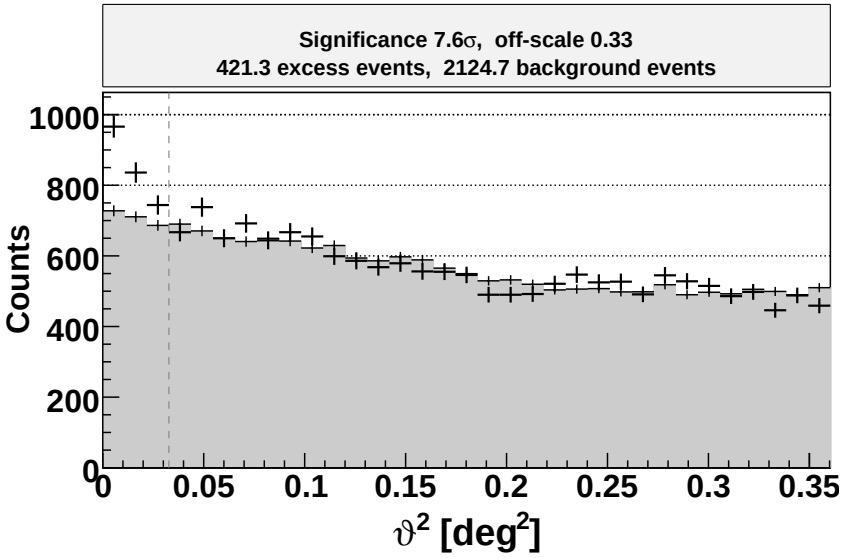

Figure 5.9: ϑ^2 plot for the "all" data set of 1ES 1011+496. The vertical dashed line shows the position of the ϑ^2 cut, defining the signal region. The grey-shaded area gives the background event distribution. The plot has been produced applying an anti-theta cut.

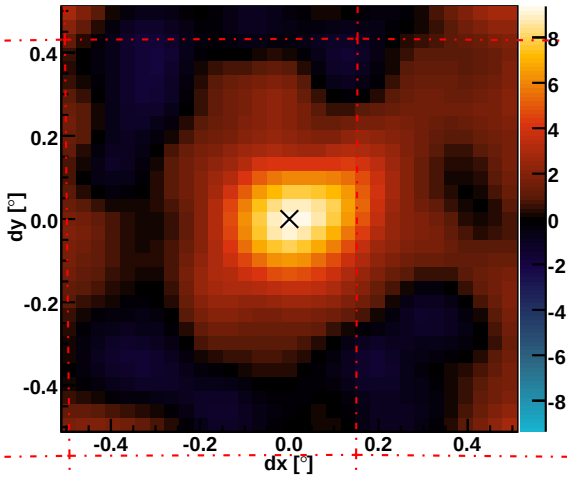

Figure 5.10: Background-subtracted distribution of reconstructed event directions on the sky smeared out with half of the MAGIC-I PSF for the "all" data set. The red dot-dashed lines give the sky coordinates.

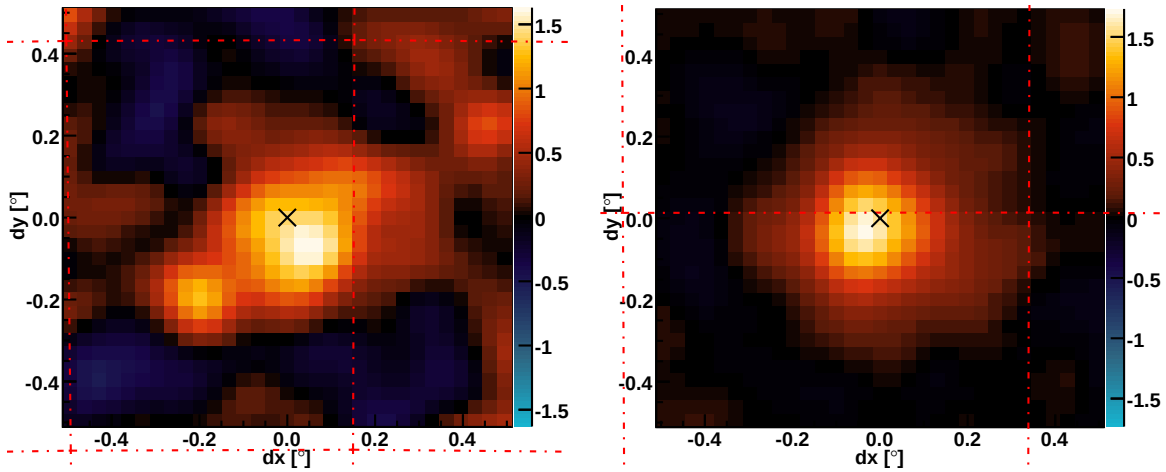

Figure 5.11: Same as Figure 5.10 but for the 6 April data set (*left side*) and a reference Crab Nebula sample (*right side*) from the same date. A mispointing is visible for both data sets.

background points were consistent with the fit line within $< 3\,\sigma$. This indicated also that the applied quality criteria yielded a stable and comparable data sample.

Considering the partly bad wobble ratio and camera inhomogeneity, the match between On and Off data in the ϑ^2 plots is of special importance. A wrong scaling may fake a signal and indicates severe problems in the analysis chain. For all data sets, the On and Off event distributions did not show signs of a mismatch (see also Section D.1.1).

5.3.3 Spectrum Derivation

Spectrum Cuts For deriving the spectrum, the separation cuts were opened to increase the event statistics and lower the energy threshold. This has been accomplished by means of the efficiency cut (see Section 4.3.3.4), which has been determined on the MC sequences listed in Table D.1. The ϑ cut has been opened to the default value. The final cut parametrisation (in the following called "spectrum cuts") for the "all" data set was given by (see Eq. 4.18):

$$\begin{aligned} \vartheta &= \quad 0.215 \\ eff1 &= -0.104 \\ eff2 &= \quad 0.0685 \\ eff3 &= -0.00129 \end{aligned}$$

The corresponding cut parabola is also shown in Figure 5.8.

Apart from the "all" data set, a spectrum was derived also for April 6. In principle, individual spectra could have been extracted also for the "AGILE" and most of the period-wise data sets, but as AGILE did not detect the source and could not set stringent ULs on the flux (see Section 5.4.1), and as from a quick check the MAGIC-I spectra did not differ significantly neither in flux nor in spectral index from the "all" results, no benefit would have been gained. For 6 April, on the other hand, the flux was clearly increased compared to the "all" result, as will be shown in the following. A dedicated efficiency cut

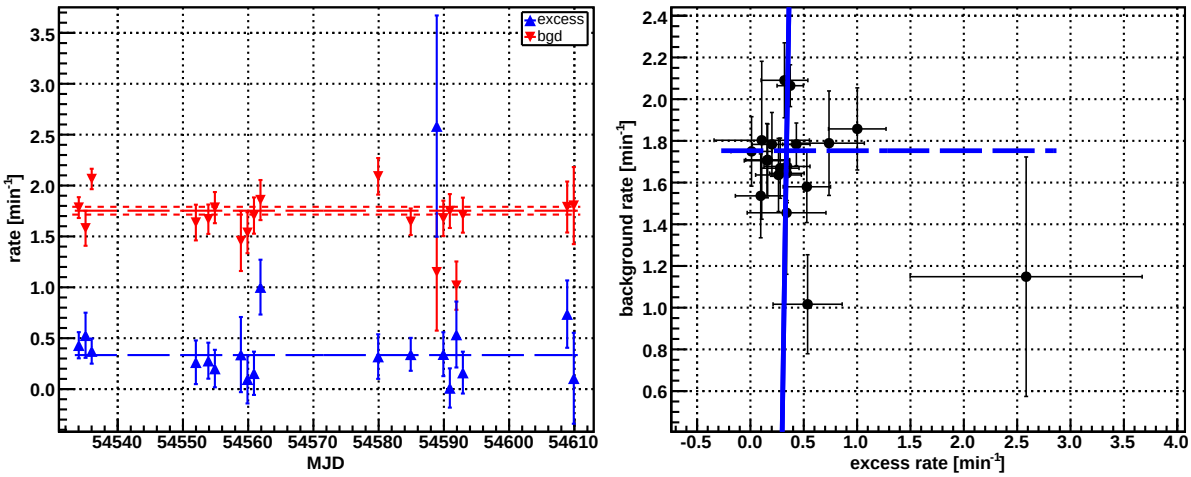

Figure 5.12: *Left side:* excess (blue upward triangles) and background (red downward triangles) rates after separation cuts for 1ES 1011+496 on a daily basis. The long-dashed lines are fits with a constant to the rates, the red short-dashed lines give the errors of the background rate fit. *Right side:* the dashed line shows a fit with a constant, the solid line a linear fit.

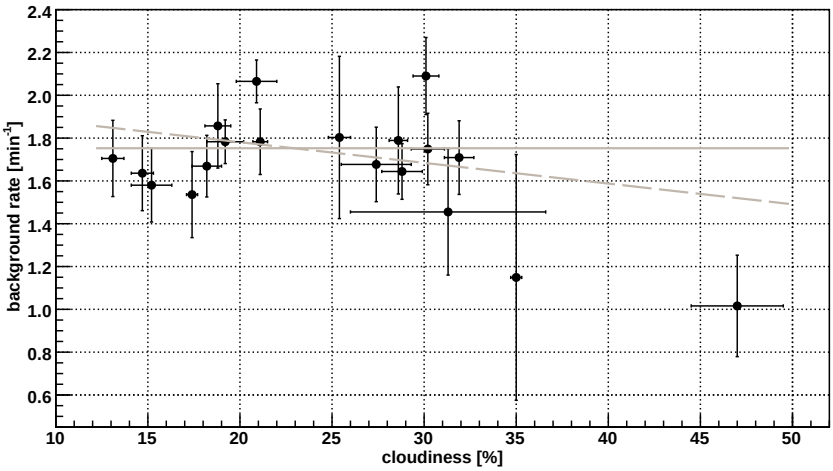

Figure 5.13: Background rate after separation cuts as a function of *cloudiness* for daily data sets of 1ES 1011+496. The x error bars are the RMS of the *cloudiness* value. A fit with a constant (solid line) has a χ^2/d.o.f. of 29.5/18 (4.3 % probability), for the linear fit (dashed line), χ^2/d.o.f. = 26.6/17 (6.5 % probability).

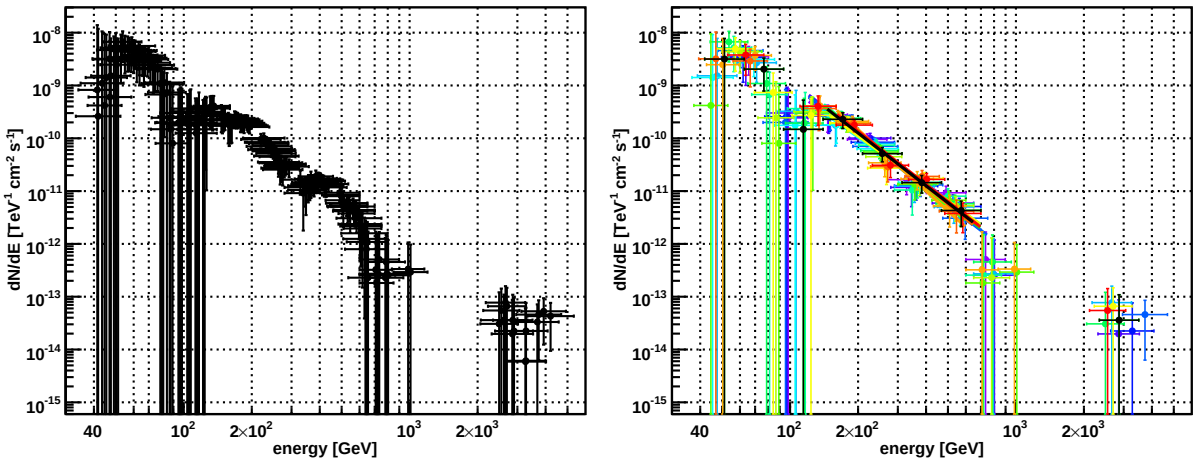

Figure 5.14: Spectra derived for the "all" data set of 1ES 1011+496 using the final spectral index and several different binning setups. *Left side:* spectra having 4 bins at varying energies. The spectra are basically stable between ∼130 GeV and ∼600 GeV. *Right side:* spectra having sufficient statistics in the relevant energy range. All bins are shown, though only the robust ones are fitted with a simple power law. In black the final spectrum is shown for comparison.

had to be determined for this data set. Figure 5.8 is showing the corresponding parabola which is defined by

$$\begin{aligned} \vartheta &= \quad 0.215 \\ eff1 &= -0.0750 \\ eff2 &= \quad 0.0435 \\ eff3 &= \quad 0.00468. \end{aligned}$$

Differential Spectra The spectral range and binning of the two spectra were determined as explained in Section 4.3.3.4. A scan over the spectral index was not necessary due to the rather good stability of the spectral fits, so only the binning had to be determined by a scan. Figure 5.14 left side reveals holes due to insufficient statistics around ∼100 GeV and ∼700 GeV for the "all" data set. At 3 – 4 TeV, still some events were located, which represented presumably statistical fluctuations. The right side of Figure 5.14 shows that all spectra with sufficiently significant points yield about the same spectral index.

The final spectral range of the "all" data set was chosen to be 140 – 700 GeV. The spectrum, shown in Figure 5.15, was well described by a simple power law of the form

$$\frac{\mathrm{d}N}{\mathrm{d}E} = (1.22 \pm 0.29) \cdot \left(\frac{E}{0.2\,\mathrm{TeV}}\right)^{-(3.32\pm0.50)} 10^{-10}\,\mathrm{ph\,TeV^{-1}\,cm^{-2}\,s^{-1}} \qquad (5.1)$$

yielding a $\chi^2/\mathrm{d.o.f.} = 0.18/2$. After correcting for the effects of EBL absorption using the model of (Kneiske & Dole 2010), the power law fit ($\chi^2/\mathrm{d.o.f.} = 0.58/2$) was given by

$$\frac{\mathrm{d}N}{\mathrm{d}E} = (1.57 \pm 0.40) \cdot \left(\frac{E}{0.2\,\mathrm{TeV}}\right)^{-(2.51\pm0.56)} 10^{-10}\,\mathrm{ph\,TeV^{-1}\,cm^{-2}\,s^{-1}}. \qquad (5.2)$$

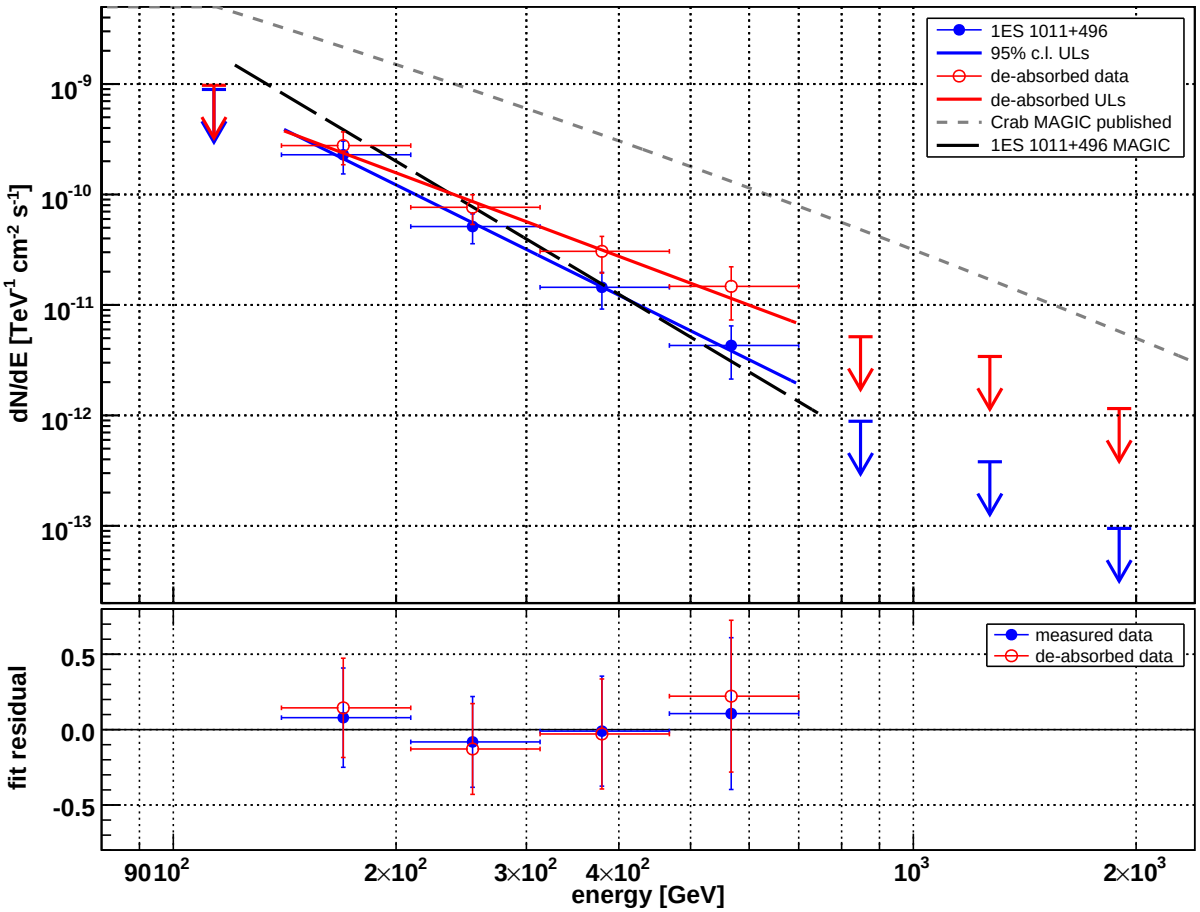

Figure 5.15: *Top panel:* measured differential spectrum of the "all" data set of 1ES 1011+496 fitted with a simple power law shown as the blue full circles. Red open circles give the spectrum corrected for EBL absorption using the model of (Kneiske & Dole 2010). For comparison, the MAGIC-I discovery spectrum (Albert *et al.* 2007b) is shown by the black long-dashed line, the MAGIC-I Crab Nebula spectrum (Albert *et al.* 2008e) by the grey short-dashed line. *Bottom panel:* fit residuals calculated as the difference between the flux point and the power law fit relative to the flux point for measured (blue, full circles) and EBL de-absorbed (red, open circles) data.

The spectrum of 6 April is shown in Figure 5.16. The flux was significantly higher than the overall flux during the campaign, whereas the spectral index stayed constant within the error bars. A power law fit (χ^2/d.o.f. $= 0.01/1$) from 150 GeV to 500 GeV yielded a flux normalisation at 200 GeV of $(5.42 \pm 1.68) \cdot 10^{-10}\,\mathrm{ph\,TeV^{-1}\,cm^{-2}\,s^{-1}}$ and a spectral index of $-(3.40 \pm 0.80)$. The EBL de-absorbed spectrum was given by a normalisation of $(7.08 \pm 2.29) \cdot 10^{-10}\,\mathrm{ph\,TeV^{-1}\,cm^{-2}\,s^{-1}}$ with a spectral index of $-(2.67 \pm 0.77)$. See Table D.2 for more information on the spectral points.

Light Curve For determining the threshold of the light curve, the energy dependence of the overall signal significance has been investigated, as described in Section 4.3.3.4. From Figure 5.17, a maximum has been found at 160 GeV, which was used as lower border for the light curve. The upper border was set at 8 TeV, above which no events were detected any more.

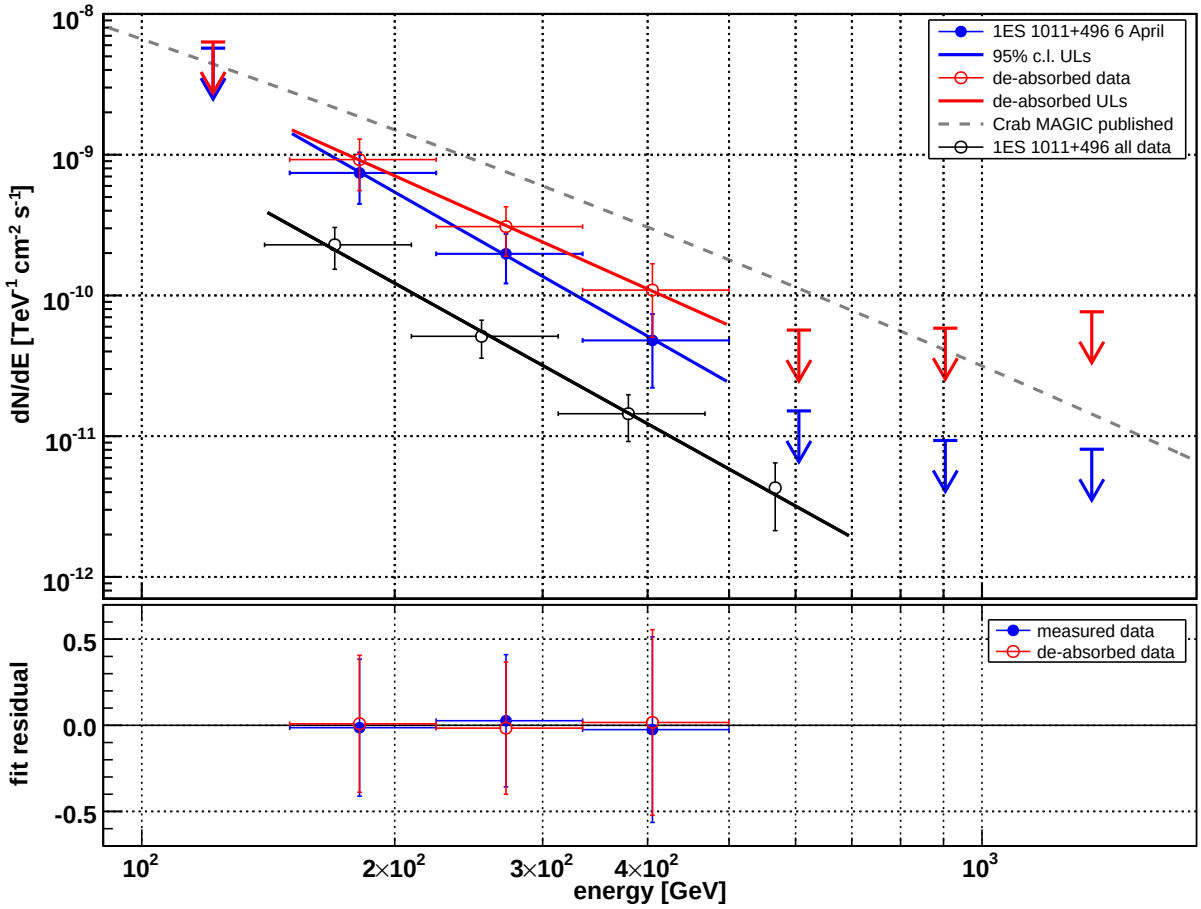

Figure 5.16: Same as Figure 5.15 but for 6 April. As a reference, the spectrum for the "all" data set is shown as the black points.

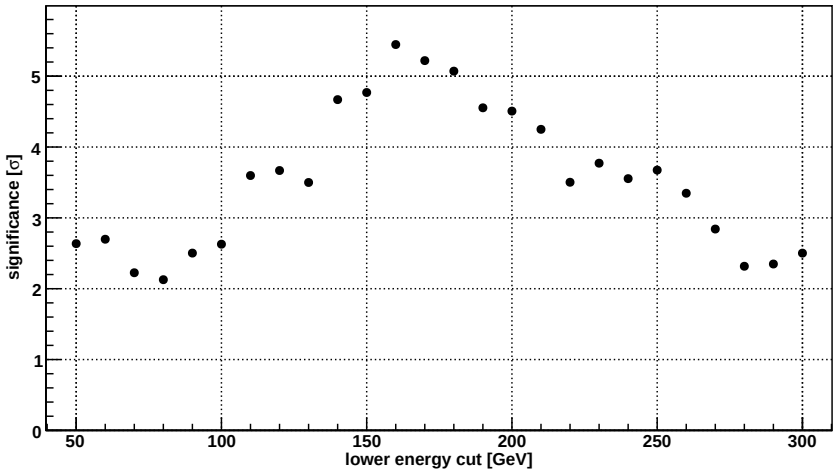

Figure 5.17: The significance of the signal for the "all" data set of 1ES 1011+496 as a function of a lower energy cut. The opened spectrum cuts have been used. The highest significance is reached at 160 GeV, which is consequently chosen as the light curve threshold.

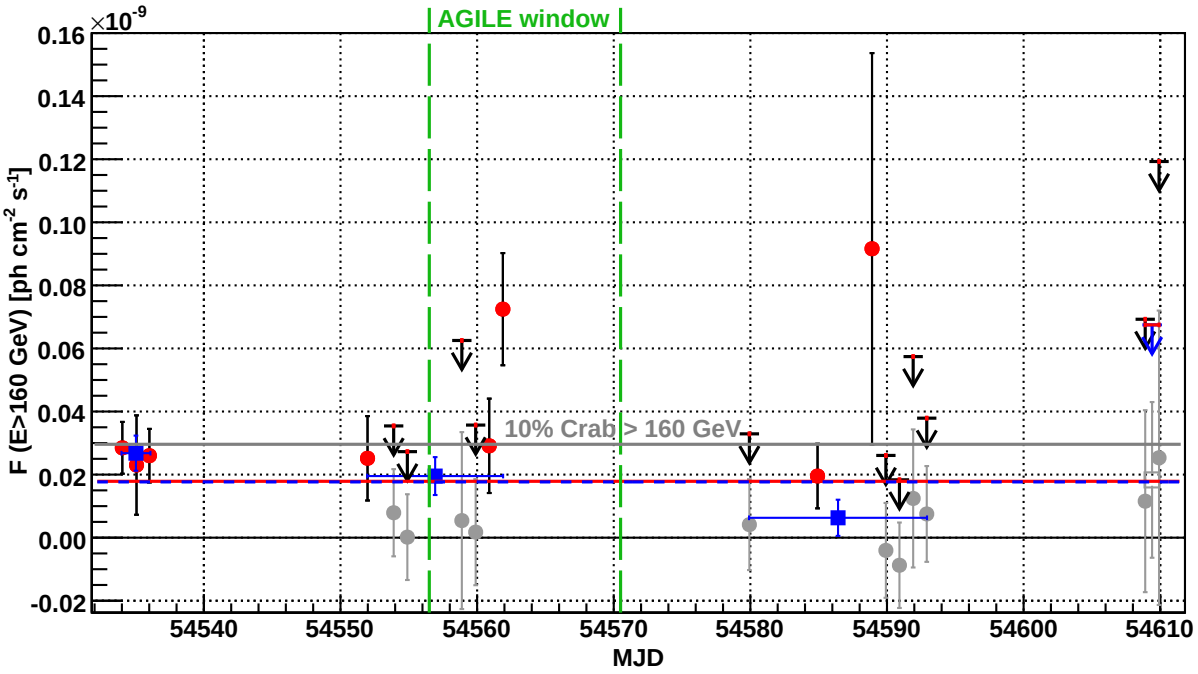

Figure 5.18: Evolution of the integral flux above 160 GeV of 1ES 1011+496 on daily (red full circles) and period-wise (blue open squares) time scales. Flux points consistent with or below zero are represented in grey and a 95 % c.l. UL is shown as a black arrow. The red bar on top of the arrow denotes the duration of the observation. A fit with a constant to the daily (period-wise) data points is shown as the red solid (blue dashed) line. In grey, 10 % of the Crab Nebula flux as measured by MAGIC-I is shown, calculated from the published MAGIC-I spectrum between above 160 GeV and 8 TeV (Albert *et al.* 2008e). The vertical green dashed lines visualise the observation window of AGILE.

The flux evolution of 1ES 1011+496 has been investigated on a daily as well as period-wise time scale as defined by the data sets given in Table 5.1. The average flux > 160 GeV throughout the observations amounted to $(1.80 \pm 0.33) \cdot 10^{-11}$ ph cm^{-2} s^{-1}, corresponding to ~ 6.1 % of the published MAGIC-I Crab Nebula flux above 160 GeV. The light curve is shown in Figure 5.18. The flux points were still consistent with a constant flux on daily as well as period-wise time scales, though with a rather low probability of 11.9 % (χ^2/d.o.f. = 25.2/18) and 8.2 % (χ^2/d.o.f. = 6.7/3), respectively. The most significant deviation from the flux fit was observed on 6 April, the flux point being nearly $3\,\sigma$ above the fit line. Not taking into account this point for the fit, the χ^2/d.o.f. = 15.5/17 corresponding to a probability of 56.0 % for a constant flux on daily scales. The the flux evolution results are summarised in Table 5.2.

Sanity Checks The applied analysis pipeline has been verified on Crab Nebula data. Observations with a zenith distance coverage comparable and close in time to the 1ES 1011+496 measurements have been searched. Additionally, the quality parameters should be similar to the ones of the source, which includes also a non-negligible influence of clouds. Crab Nebula data from the winter season 2007/2008 with these conditions were not available. Therefore, the zenith distance condition had to be relaxed, with the requirement of covering only the dominant part of 1ES 1011+496 observations. Details

Data Set[(a)]	**MJD**[(b)]	**Sign.**[(c)] [σ]	**Exc.**[(d)]	**Bgd.**[(e)]	$F_{>160\,\mathrm{GeV}}$ [$10^{-12}\,\mathrm{TeV}^{-1}\,\mathrm{cm}^{-2}\,\mathrm{s}^{-1}$]
all	54571.944	5.5	542	7211	18.0 ± 3.3
AGILE	54560.385	3.7	130	852	33.1 ± 9.1
period 64	54535.028	4.9	288	2470	26.8 ± 5.6
period 65	54556.929	3.3	180	2179	19.5 ± 6.0
period 66	54586.418	1.1	57	1977	6.3 ± 5.7
period 67	54609.404	0.8	21	585	< 67.5
09 March	54534.032	3.6	121	822	28.5 ± 8.2
10 March	54535.070	1.5	31	321	23.0 ± 15.8
11 March	54536.013	3.1	133	1327	26.0 ± 8.5
27 March	54551.979	1.9	33	206	25.2 ± 13.4
29 March	54553.893	0.6	16	599	< 35.4
30 March	54554.894	0.0	0	520	< 27.3
03 April	54558.882	0.2	2	107	< 62.5
04 April	54559.894	0.1	1	189	< 35.7
05 April	54560.886	2.0	39	276	29.1 ± 15.0
06 April	54561.885	4.3	87	278	72.5 ± 17.8
24 April	54579.928	0.3	6	399	< 32.9
29 April	54584.918	1.9	47	425	19.5 ± 10.2
03 May	54588.905	1.6	8	16	91.6 ± 62.0
04 May	54589.919	-0.3	-5	339	< 26.1
05 May	54590.912	-0.6	-14	363	< 18.4
06 May	54591.917	0.6	5	70	< 57.4
07 May	54592.911	0.5	11	362	< 37.9
23 May	54608.901	0.4	8	371	< 69.3
24 May	54609.913	0.6	9	214	< 119.3
Crab	54472.911	14.9	348	279	$(2.87 \pm 0.22) \cdot 10^2$

Notes. [(a)] The date corresponds to the day following the observation night. [(b)] Mid point of observation given in MJD. [(c)] Significance of the signal calculated using Li & Ma (1983) Eq. 17 and spectrum cuts. [(d)] Number of excess events. [(e)] Number of background events.

Table 5.2: Results for the individual data sets of 1ES 1011+496 and Crab Nebula using spectrum cuts. Flux ULs are given at a c.l. of 95 %.

on the chosen Crab Nebula data are listed in Tables B.1, B.2 and 5.1. The data quality matched the one 1ES 1011+496 quite well, the most important drawback being that the data has been taken already in January 2008.

Using the separation cuts optimised for 1ES 1011+496 on this Crab Nebula data, a signal of $17.7\,\sigma$ with 282 excess and 89 background events has been found from ~ 0.7 hrs of data (see Figure 5.19). This corresponds to a sensitivity of $20.9\,\sigma\sqrt{h}$. In terms of integral flux, the sensitivity above 160 GeV amounts to 2.04 % of the Crab Nebula flux to be detected with a significance of $5\,\sigma$ after 50 hrs of observations (assuming a 1ES 1011+496-like spectrum of the Crab Nebula).

To derive the differential spectrum of the Crab Nebula, the same efficiency cut parametrisation as determined for the "all" data set of 1ES 1011+496 has been used. The result is shown in Figure 5.20. The spectrum between ~ 150 GeV and ~ 2 TeV is well described ($\chi^2/\mathrm{d.o.f.} = 1.6/5$) by a simple power law with a flux normalisation at 200 GeV of $(5.65 \pm 0.45) \cdot 10^{-9}\,\mathrm{ph\,TeV^{-1}\,cm^{-2}\,s^{-1}}$ and a spectral index of $-(2.37 \pm 0.11)$ and

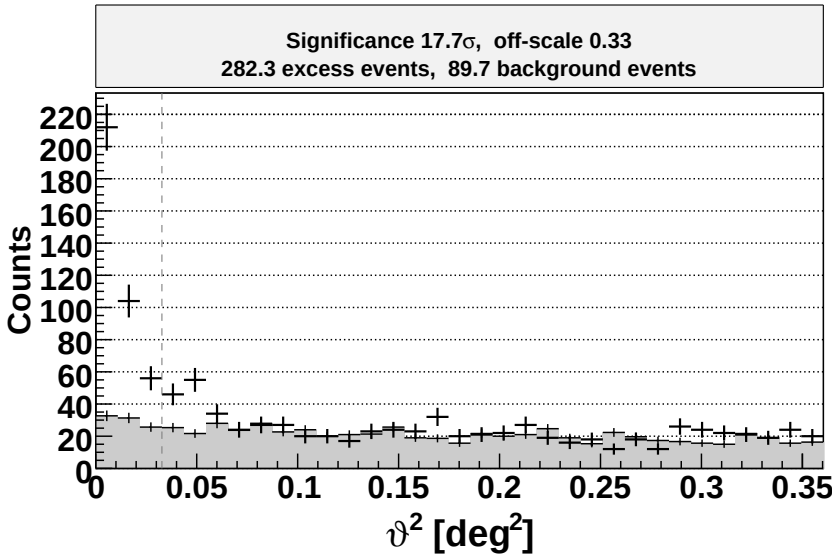

Figure 5.19: Same as Figure 5.9 but for the Crab Nebula data using the optimised 1ES 1011+496 separation cuts. Note that the higher second bin outside of the signal region is not due to the cuts but data intrinsic, as the comparison with standard cuts result is showing.

matches the published MAGIC-I Crab Nebula spectrum from Albert *et al.* (2008e) very well. The flux points above $\sim 2\,\mathrm{TeV}$ have not been considered for the fit because they do not contain a sufficient number of events and are just shown for illustrative purposes. The first bin has also not been used for the fit. A curved power law can also fit the spectral points well ($\chi^2/\mathrm{d.o.f.} = 1.6/4$), yielding:

$$\frac{\mathrm{d}N}{\mathrm{d}E} = (5.69 \pm 0.50)\cdot 10^{-10}\,\mathrm{ph\,TeV^{-1}\,cm^{-2}\,s^{-1}}\cdot\left(\frac{E}{0.3\,\mathrm{TeV}}\right)^{-\left((2.33\pm0.21)+(0.10\pm0.43)\log_{10}\left(\frac{E}{0.3\,\mathrm{TeV}}\right)\right)} \tag{5.3}$$

As can be seen, the curvature parameter is not significant though.

Due to the inhomogeneous camera acceptance, also a spectrum with only 1 Off region has been derived for the "all" data set. Additionally, a spectrum consisting of 3 and 5 bins is evaluated to test the stability of the final spectrum. These spectra are well compatible with the final spectrum in terms of flux as well as spectral index, see Figure 5.20. The spectrum derived using 1 Off regions shows a lower flux in the third spectral bin while the flux in the last bin is increased compared to the final spectrum, resulting in a slightly harder spectral index. The reason may be statistical fluctuations due to the reduced background statistics. Also a spill over of some single events between these two bins due to statistical fluctuations cannot be excluded. Despite these differences, all bins are compatible within their statistical error bars.

5.3.4 Discussion

Despite non-optimal observation conditions, the VHE discovery of 1ES 1011+496 (Albert *et al.* 2007b) was confirmed by this analysis with the highest significance until today. An independent MAGIC-internal analysis provided well-compatible results. The

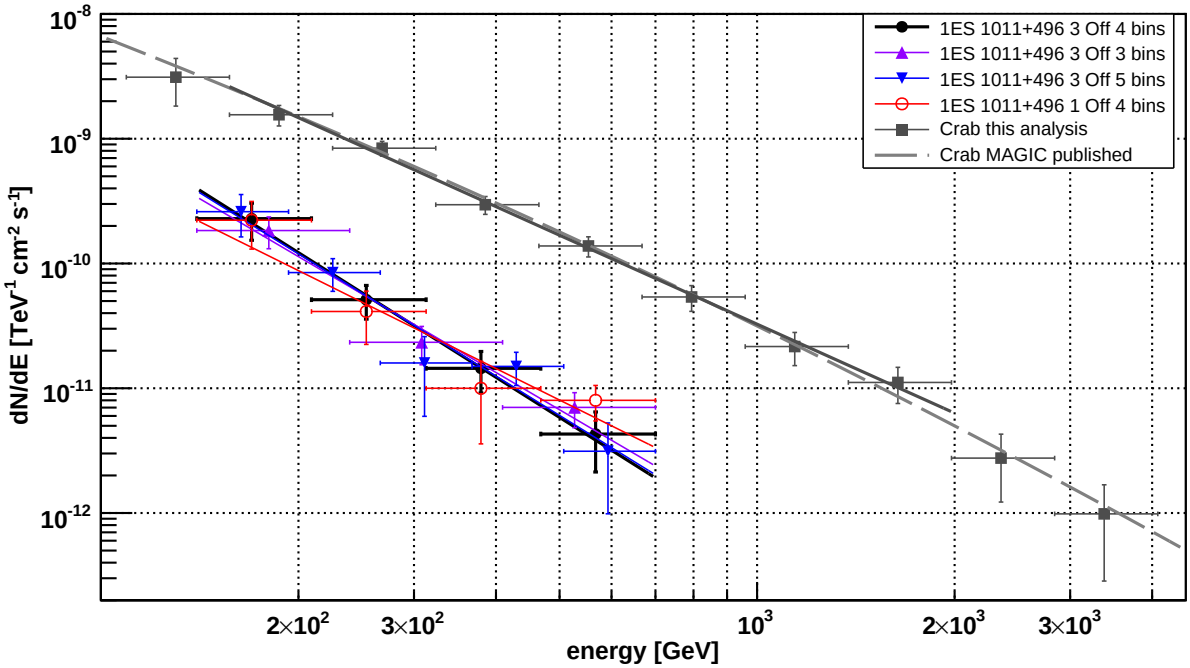

Figure 5.20: Measured differential spectrum of 1ES 1011+496 derived using different binnings as well as 1 Off region. Also shown is the differential Crab Nebula spectrum derived using the 1ES 1011+496 analysis pipeline and the published MAGIC-I Crab Nebula spectrum (Albert *et al.* 2008e) for reference.

derived measured spectral index was statistically well consistent with the discovery one though slightly harder ($-(3.32 \pm 0.50)$ compared to $-(4.0 \pm 0.5)$). Judging from the flux normalisation at 200 GeV, the source was more active during the discovery than during this campaign. This difference is statistically significant within the error bars, the value from the discovery being $(2.0 \pm 0.1) \cdot 10^{-10}\,\mathrm{ph\,TeV^{-1}\,cm^{-2}\,s^{-1}}$ compared to $(1.22 \pm 0.29) \cdot 10^{-10}\,\mathrm{ph\,TeV^{-1}\,cm^{-2}\,s^{-1}}$ derived from this campaign.

According to the lower limit EBL model of Kneiske & Dole (2010), the optical depth τ reaches unity at $\sim$470 GeV for 1ES 1011+496 ($z = 0.212$), which should result in a cut-off of the spectrum. Such a signature of the EBL was not apparent from neither the spectrum presented here nor the discovery spectrum despite a spectral range up to 700 GeV and 750 GeV, respectively. With deeper VHE observations of 1ES 1011+496, yielding a statistically more significant spectrum, current EBL models might be put to the test.

The light curve > 160 GeV derived in this work did not show statistically significant variability over the time scale of the campaign, a fit with a constant having a probability of $\sim$12 % and $\sim$8 % for the daily and period-wise flux points, respectively. One day with a flux nearly $3\,\sigma$ above the fit was found though, indicating that the source may be variable on short time scales.

The overall integral flux > 200 GeV amounted to $(9.01 \pm 2.03) \cdot 10^{-12}\,\mathrm{ph\,cm^{-2}\,s^{-1}}$, which is < 60 % of the integral flux reported from the discovery of 1ES 1011+496 in March – May 2007 (Albert *et al.* 2007b). Previous observations in March – April 2006, yielding a marginally significant signal of the source of $3.5\,\sigma$ (Albert *et al.* 2008c), resulted in a flux > 180 GeV of $(1.26 \pm 0.40) \cdot 10^{-11}\,\mathrm{ph\,cm^{-2}\,s^{-1}}$ (if being interpreted as a

detection), which is basically identical with the flux derived in this work above 180 GeV ($(1.26 \pm 0.25) \cdot 10^{-11}\,\mathrm{ph\,cm^{-2}\,s^{-1}}$). It should be noted that the results reported in Albert *et al.* (2008c) are not consistent with new results derived by the same author using an updated software version (Meyer 2008). According to the new analysis, the integral flux was a factor 3.4 lower than previously given. At TeV energies, Aharonian *et al.* (2004) reported a 99 % c.l. UL on the flux $> 1.02\,\mathrm{TeV}$ of $1.80 \cdot 10^{-12}\,\mathrm{ph\,cm^{-2}\,s^{-1}}$ from 2.0 hrs of HEGRA observations in March 1999. The MAGIC-I result from this campaign amounts to $F(> 1.02\,\mathrm{TeV}) < 3.59 \cdot 10^{-13}\,\mathrm{ph\,cm^{-2}\,s^{-1}}$ (c.l. 99 %), being a factor 5 below the archival HEGRA value.

We recall that the VHE discovery of 1ES 1011+496 in 2007 was triggered by high activity in the optical regime. Also the observations presented here were conducted during a high (albeit slightly lower than in 2007) flux density in the R-band. Considering the comparably low optical state at the time of the VHE observations in 2006, yielding no significant detection of the source, a correlation between these two energy bands seems to be present. A quantitative comparison is hard to accomplish since the source was always strongly variable in the R-band during the VHE observations. Ongoing observations will be able to test the putative correlation.

In Figure 5.21 the archival integral flux values are compared to the flux derived in this work. The value given in Albert *et al.* (2008c) is shown but not taken into account for the fit. Instead, its flux has been divided by 3.4, assuming that the reduction factor on the flux above 180 GeV applies also to the flux above 200 GeV. As the lowered flux was a consequence of a smaller number of excess events, it seems inappropriate to scale the flux error by the same factor, as lower statistics will result in turn in a larger error. Therefore, as a rough approximation, the flux error of the scaled point has not been changed. A fit with a constant to this data points has a $\chi^2/\mathrm{d.o.f.} = 9.1/2$, corresponding to a probability of 1.1 %. Increasing conservatively the flux error of the first point by a factor of 2, the probability for a constant flux would be 8.2 %. Thus, significant flux variability of 1ES 1011+496 on time scales of years is strongly favoured by the data points, but cannot be established yet with high confidence.

5.4 Multi-Wavelength Results

The following section will summarise the observations and results of the remaining instruments participating in the 1ES 1011+496 MW campaign, ordered by their energy band. The light curves will be investigated individually as well as in an inter-band context, searching for potential correlations, also beyond the time scale of this campaign. The spectral energy distribution, also incorporating archival data, will be presented and the results from applying state-of-the art SED models to the simultaneous data will be discussed.

The data organisation and collection as well as the evaluation of the light curves was performed by the author. Also the combined view on the MW data set in terms of the MW light curve and simultaneous SED has been conducted in this work. However, the raw data and low level analysis of the individual instruments have been carried out by the instrument experts unless stated otherwise, and hence will not be presented in

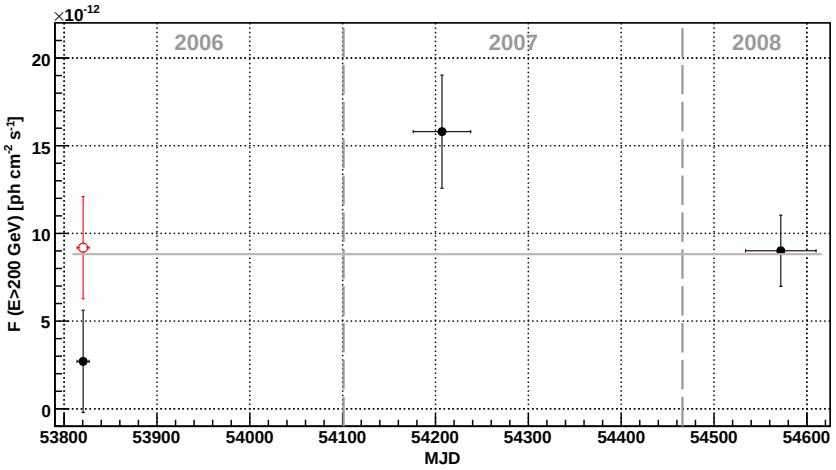

Figure 5.21: Integral fluxes of 1ES 1011+496 above 200 GeV from 2006, 2007 (Albert *et al.* 2007b) and 2008 (this work). The red open flux point has been falsified in Meyer (2008), where a flux a factor 3.4 below the actual value is being given (shown as the black point below). The flux error of the recalculated point is kept constant. A fit with a constant is shown as the solid grey line.

detail here. These are given in Aleksić *et al.* (2013). For details on the instruments, see Chapter 3.

5.4.1 High Energy Gamma-Rays

The AGILE observations of 1ES 1011+496 did not result in a significant detection over the course of the MW campaign. From the measurements between 30 March 2008 12:00 UTC and 10 April 2008 12:00 UTC with an effective exposure of $2.3{\cdot}10^7$ cm^2 s, only a 95 % c.l. UL on the flux above 100 MeV of $2.1 \cdot 10^{-7}$ ph cm^{-2} s^{-1} was derived. The exposure during the second observation window (30 April 2008 12:00 UTC – 10 May 2008 12:00 UTC) was too low to calculate an UL. The data has also been searched for a signal on shorter time scales of two days as well as one week, without finding a significant signal above $4\,\sigma$. This is still true when investigating all AGILE data taken on the source until January 2011 (C. Pittori, 2012, private communication).

5.4.2 X-Rays

***Swift* XRT** observations were conducted from 28 April 2008 until 8 May 2008 (observation IDs 35012008 – 35012017). 1ES 1011+496 was significantly detected for each ID apart from 35012010, having an exposure of only 1 s. Results were extracted applying a simple absorbed power law fit to the data (see Eq. 2.17). The data were also fitted using a log-parabolic power law, these were however not preferred by a likelihood ratio test. The analysis procedure is described in Aleksić *et al.* (2013). For details on the observations and results see Tables E.1 and E.2, respectively. The obtained light curve between 2 and 10 keV is shown in Figure 5.26.

XRT detected a flare-like structure during the MW campaign. The flux increased from the first observation by nearly 90 % within tow days to a peak value of $3.68 \cdot$

$10^{-11}\,\mathrm{erg\,cm^{-2}\,s^{-1}}$. In the following eight days, the flux level dropped to $\sim 35\,\%$ of that peak flux. The baseline of the flare was not observed, hence the total flare amplitude can not be determined. Additionally, the date of the highest flux during the flare is rather uncertain, since due to its large error ($\sim 35\,\%$) the peak flux measurement is consistent with the following flux point. Considering the low amplitude variability and rather steady flux evolution, no short-scale variability is expected, because of which no intra-night analysis has been performed. Quick-look analysis results and intra-night light curves, provided for many sources by the *Swift* XRT monitoring list[6], are not available for 1ES 1011+496.

The spectral index showed hints for variability, which was statistically not significant though (see Figure 5.26). A fit with a constant yielded a χ^2/d.o.f. of 11.7/8 (probability of 16.4 %).

***INTEGRAL* ISGRI** observed serendipitously during the second AGILE window at the time of the *Swift* observations. The orbital light curve was dominated by fluctuations and did not show a significant detection, because of which the data has been re-binned to daily time scales. This has been accomplished using the REBINGAUSSLC tool (see also Section E.2.2.2). The resulting light curve is shown in Figure 5.26. Still, no detection is obvious, the mean rate being even negative ($-\,(0.40 \pm 0.35)\,\mathrm{counts\,s^{-1}}$).

Monitoring Instruments The X-ray all sky monitoring instruments *RXTE* ASM and *Swift* BAT are providing public quick-look light curves[7] which have been investigated for potential detections within the MW time slot. Also in this case, the light curves have been re-binned to different time scales (one day as well as one week) using REBINGAUSSLC. Significant variability or detections were not apparent though. Therefore, no effort has been made to analyse the high level data. Note that, since the source is not included in the BAT 58-Month Catalog[8], BAT did not yet detect 1ES 1011+496.

Discussion The X-ray coverage during the MW campaign was rather sparse. Nevertheless, significant variability has been detected by *Swift* XRT. The overall flux level between 2 and 10 keV during the campaign was rather high with respect to archival data. The flux was varying between $1.33 \cdot 10^{-11}$ and $3.68 \cdot 10^{-11}\,\mathrm{erg\,cm^{-2}\,s^{-1}}$, whereas the highest flux in that energy range reported in literature amounted to $6.67 \cdot 10^{-11}\,\mathrm{erg\,cm^{-2}\,s^{-1}}$ (Massaro *et al.* 2008). This is the first time that a (partly) time-resolved X-ray flare is reported for 1ES 1011+496 in literature. However, this does not imply that flares are rare for that source. These have just not been reported until today because no observations over several consecutive days have been conducted for that object at X-rays, yet. From the evolution in time shown in Figure 5.26, the flux and spectral index seem to be anti-correlated, which is confirmed (on a small statistical basis though) by Figure 5.22. A logarithmic likelihood ratio test prefers the linear fit with 98.8 %.

[6] http://www.swift.psu.edu/monitoring/

[7] see http://xte.mit.edu/ASM_lc.html and http://swift.gsfc.nasa.gov/docs/swift/results/transients/, respectively.

[8] http://swift.gsfc.nasa.gov/docs/swift/results/bs58mon/

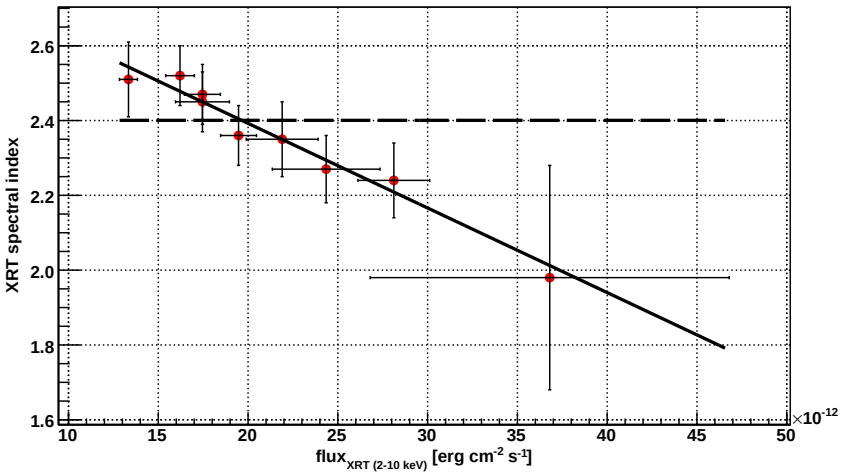

Figure 5.22: *Swift* XRT spectral index of 1ES 1011+496 during the MW campaign as a function of the integral flux between 2 and 10 keV, both determined by a simple absorbed power law fit between 0.5 and 10 keV. The dashed line corresponds to a fit with a constant (χ^2/d.o.f. = 11.7/8), a linear fit is shown by the solid line (χ^2/d.o.f. = 0.9/7). The latter is characterised by a slope of $-(2.26 \pm 0.76) \cdot 10^{-2}$ per 10^{-12} erg cm^{-2} s^{-1}.

This anti-correlation is typical for blazars (see Section 2.3), but is reported here for the first time for 1ES 1011+496.

5.4.3 Optical Regime

KVA KVA observations have been conducted in the R-band as part of the Tuorla Blazar Monitoring Program[9]. During the MW campaign, also measurements in the V- and B-band were scheduled, but erroneously taken for a rather short time period only. The observation method and analysis pipeline is described in Aleksić *et al.* (2012f). The individual results are given in Table E.3.

The R-band light curve, shown in Figure 5.23, is characterised by significant variability. Several small flares as well as a general rising trend of the flux density is visible. Overall, the flux density varied by $\sim 50\,\%$ between 2.79 and 4.30 mJy during the MW campaign. For the SED, the flux densities had to be converted to spectral energy density, which has been performed by the author and is described in detail in Section E.1.2.

Also the V- and B-band light curves showed significant variability, a fit with a constant having a χ^2/d.o.f. of 25.7/10 (probability of 0.4 %) and 36.4/10 (probability of $7 \cdot 10^{-3}$ %), respectively. The flux density evolution in the three bands followed in general the same trends. For some days, however, differences are apparent, like the second (drop in R- and V-band, rise in B-band), fourth (drop in R-band, rise in V- and B-band) and last day (constant in R-band, rise in V- and B-band) of the multi-band observations.

Bell Observatory 1ES 1011+496 was targeted on eight days during the MW campaign by the Bell observatory. The data calibration and reduction is the same as described in Aleksić *et al.* (2012f) for CrAO. The initial analysis results are shown in Figure 5.23.

[9] http://users.utu.fi/kani/1m/

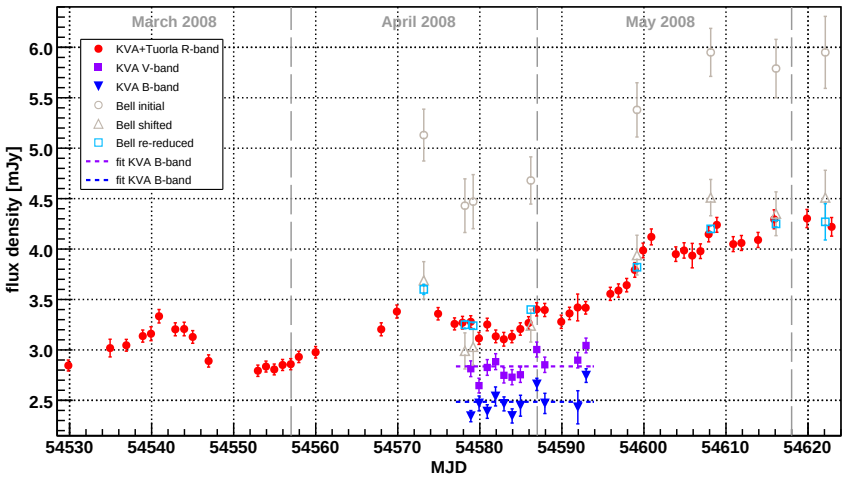

Figure 5.23: Daily optical R-band, V-band and B-band light curve of 1ES 1011+496 measured by KVA (+Tuorla in R-band). Also shown are the R-band results provided by the Bell observatory before and after an absoulte shift by 1.44 mJy as well as after a re-reduction (see text). The purple and blue dashed horizontal lines denote a fit with a constant to the V- and B-band, respectively.

Despite both instruments using differential photometry and the same reference stars, the flux densities measured by Bell were initially systematically larger compared to KVA. Detailed investigations revealed a systematically larger brightness of the Bell comparison stars, which amounted up to a difference of $\sim 50\,\%$ in flux density. Such a systematic offset between the two analysis pipelines can be corrected without introducing an artificial bias by shifting the Bell light curve by a fixed value. The shift has been calculated from the average difference in flux density between Bell and KVA measurements having a time difference < 0.3 days (~ 7 hrs, value chosen arbitrarily from a reasonable quasi-simultaneous upper limit of 0.5 days). Six out of the eight Bell observations fulfilled this criterion, resulting in a shift of -1.44 mJy. The Bell R-band light curve after the correction is also shown in Figure 5.23. After correction, the match between the Bell and KVA light curves improved significantly and the Bell light curve shows the same rising flux density trend in time that is obvious for KVA.

However, to ensure comparability between the two R-band light curves, the Bell data have been re-reduced using the same, fixed aperture as KVA and adopting the KVA comparison star magnitude. Additionally, a minor mistake in the error calculation has been corrected (M. Carini, 2012, private communication). The newly reduced data match very well the KVA ones without a need for a shift, as can be seen in Figure 5.23. The detailed results are given in Table E.3.

***Swift* UVOT** 1ES 1011+496 was detected significantly in each of the six UVOT bands but on MJD 54586, for which the observation time amounted to 143 s only. For a description of the analysis, see Aleksić *et al.* (2012f). The light curves are shown in Figure 5.24, judging from which no significant variability was apparent during the measurements. Detailed results are given in Tables E.5 and E.6. The obtained V- and B-band flux densities match well the quasi-simultaneous ones of KVA, though they do not hint on the variability detected by the latter. Such small amplitude changes would not be significant

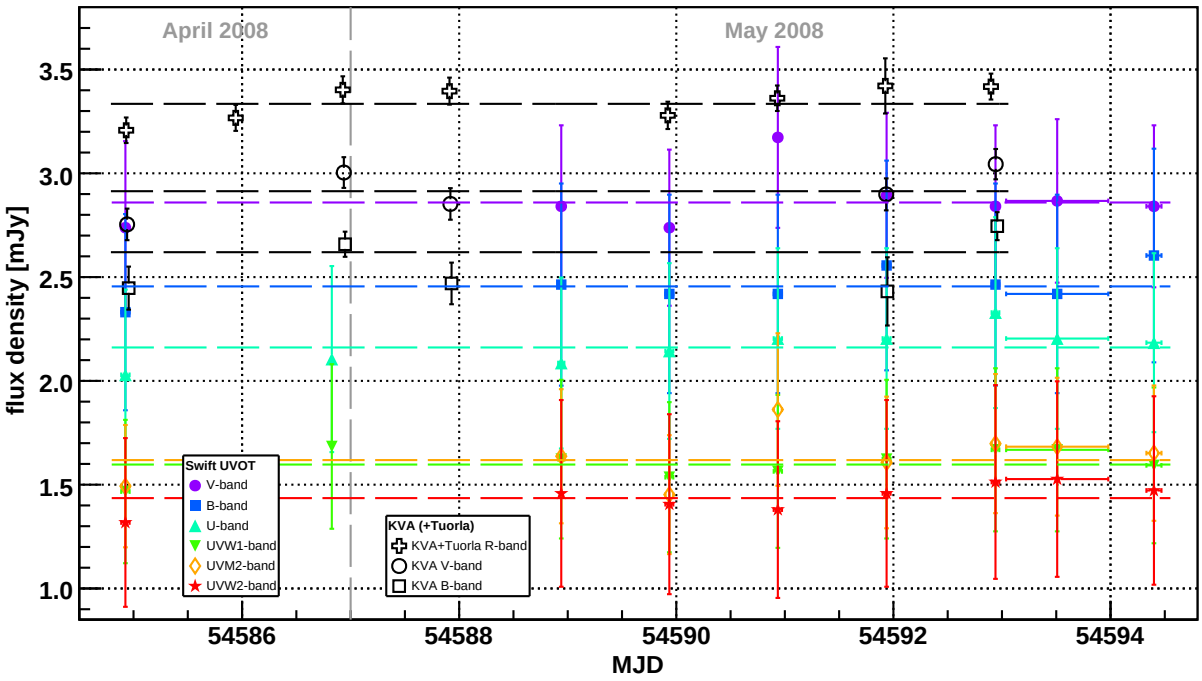

Figure 5.24: *Swift* UVOT light curve of 1ES 1011+496 in all six observations bands during the MW campaign. The observation time during the second measurement was too short to derive a flux density for all bands. Also shown are the (quasi-)simultaneous KVA (+Tuorla) observations (black symbols). Note that the KVA V- and B-band filter wavelengths differ only slightly from the corresponding effective UVOT ones (550 vs. 540 nm and 440 vs. 433 nm, respectively). The horizontal dashed lines denote fits with a constant, yielding the following χ^2/d.o.f. values (goodness of fits): UVOT V-band: 0.7/7 (99.8 %); UVOT B-band: 0.2/7 (100.0 %); U-band: 0.3/8 (100.0 %); UVW1-band: 0.3/8 (100.0 %); UVM2-band: 1.1/7 (99.4 %); UVW2-band: 0.2/7 (100.0 %); KVA+Tuorla R-band: 10.5/7 (16.1 %); KVA V-band: 9.8/4 (4.4 %); KVA B-band: 10.2/4 (3.7 %).

within the UVOT error bars, though.

For the SED, the UVOT results had to be corrected for the host galaxy and dereddened, as described in Section E.1.2.

Discussion Compared to its long-term behaviour, 1ES 1011+496 was found in the R-band on a high flux density level. Within the nearly ten years of KVA monitoring, the source displayed flux densities ranging from 1.85 to 4.63 mJy with a mean value of (2.792 ± 0.003) mJy (as determined from a fit with a constant). An underlying flaring periodicity of ~ 8 years peaking around December 2007 is suggestive from the long-term light curve (see Figure 5.25), though has to be confirmed with continuous monitoring. The amplitude of the individual short-term flares seems to correlate with the long-term variability, becoming larger towards the long-term maximum. On top of the putative 8-year cycle, several strong and rather slow flares are found. These have not been sampled completely, but the data available their rise or fall times range from 5 – 10 weeks. During these slow flares, faster ones with a smaller amplitude are found, having a total duration of ~ 2 weeks. Unfortunately, the gaps in the light curve due to moon, bad weather and zenith angle constraints do not allow to derive exact numbers for these potentially three-fold variability in the R-band. According to Figure E.1, a simple sinusoidal periodicity

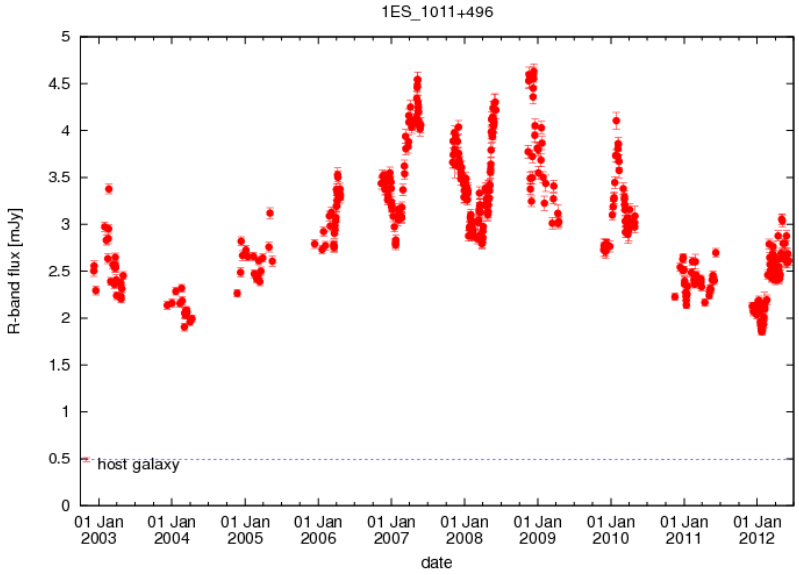

Figure 5.25: Tuorla Blazar Monitoring Program R-band light curve (red full circles) of 1ES 1011+496. The red point denotes the host galaxy contribution to the measured flux, also visualised as the grey dashed line. Figure taken from http://users.utu.fi/kani/1m/.

is not an adequate description of the medium-term variability, though.

Judging from the Tuorla monitoring light curves, the overall long-term amplitude and abundance of R-band variability is high, but not exceptional for TeV blazars. In this regard, 1ES 1011+496 is comparable to Mrk 421 and much stronger than e.g. Mrk 180, Mrk 501, 1ES 2344+514 or 1ES 1426+428, all of which are HBLs. More extreme characteristics than for Mrk 421 are only present for the HBL 1ES 1959+650 (arising from one strong flare though) and non-HBL objects like BL Lac, S5 0716+714 or 3C 279. This may be regarded as another tentative sign for 1ES 1011+496 not fitting to the HBL class, which needs however a confirmation based on a larger sample of sources and by detailed variability analyses.

Unfortunately, the Bell observations are basically simultaneous to the KVA ones but one measurement. Hence, these cannot provide coverage at times when KVA data are not available. On the other hand, the nearby Bell data represent an independent confirmation of the KVA results.

5.4.4 Radio Regime

Due to bad weather during the MW campaign, 1ES 1011+496 was observed only two times (MJDs 54492.2, 54581.0) at 37 GHz by the Metsähovi radio telescope (see also Figure 5.3). For details on the data analysis see Aleksić *et al.* (2012f). The source was not detected at these two instances. For the second observation conducted close to the core of this MW campaign, an UL ($S/N > 4$) of 0.62 Jy was determined.

This UL is consistent with three detections of the source by Metsähovi end of 2008 achieved within five days (flux density $\sim (0.45 \pm 0.10)$ Jy) (A. Lähteenmäki, 2012, private communication). In 2009 and 2010, the source was detected at a considerably higher

flux density level of nearly 0.60 Jy, see also Figure 5.28. Significant variability was found in April 2012, the flux density increasing from (0.28 ± 0.06) Jy to (0.53 ± 0.10) Jy within four days (Aleksić *et al.* 2012f). Such rapid activity changes in the radio regime are very rare for BL Lac objects. The flare of 1ES 1011+496 reported here confirms the indications for fast variability for this source found by Nieppola *et al.* (2007).

5.4.5 Multi-Wavelength Light Curve and Correlations

5.4.5.1 MW Campaign

The MW light curve constructed from the individual instruments participating in the campaign is shown in Figure 5.26. The simultaneous sampling was obviously rather sparse. Especially X-ray observations are available for only a small time span, due to the *Swift* ToO requests that had to substitute the planned Suzaku observations. Additionally, radio coverage by Metsähovi is missing due to bad weather.

Therefore, the data basis for investigating correlations between the different instruments is very limited. The best simultaneous coverage was achieved between KVA and *Swift* XRT. Figure 5.27 shows the R-band flux density as a function of the integral X-ray flux between 2 and 10 keV for data with a time difference < 0.9 days. A direct correlation is not clearly apparent, as also indicated by the MW light curve, since the linear fit is not preferred over the constant fit. Note though that there are too few data points to establish or reject a potential correlation between the two energy bands.

5.4.5.2 Long-Term

Since no firm conclusions on potential cross-band correlations can be drawn from the available MW campaign data, the archives have been searched for public observation results of 1ES 1011+496 from various instruments. Until mid of 2008, the data lack significant X-ray detections. *Swift* was targeting the source between June 2005 and March 2012 only 22 times, of which 10 observations are presented in this work. The remaining data are spread too much in time[10] to promise any impact on the flux evolution of the source. Hence, no dedicated analysis has been performed of the XRT data. From *INTEGRAL* ISGRI and the quick-look data of *RXTE* ASM and *Swift* BAT, no regular detections are achieved, if any at all. Also coverage at radio wavelengths is very limited. Only optical R-band data are available thanks to the Tuorla Monitoring Program. These have already been discussed above.

However, since some years additional X-ray monitoring observations are conducted by MAXI, and OVRO as well as *Fermi*-LAT are providing dense monitoring coverage in the radio and HE gamma-ray regime, respectively, from mid of 2008 on. The corresponding long-term MW light curve from is shown in Figure 5.28.

The MAXI data products are publicly available from the MAXI team web page[11]. The applied analysis software is still in a pre-release state, hence the results may contain bad quality points as well as artificial flare- and dip-like features. Therefore, any conclusions

[10] 3 observations from June – December 2005; 3 in September – October 2007; 2 in April 2010; 4 in March 2012 (http://www.swift.psu.edu/operations/obsSchedule.php)

[11] http://maxi.riken.jp/top/

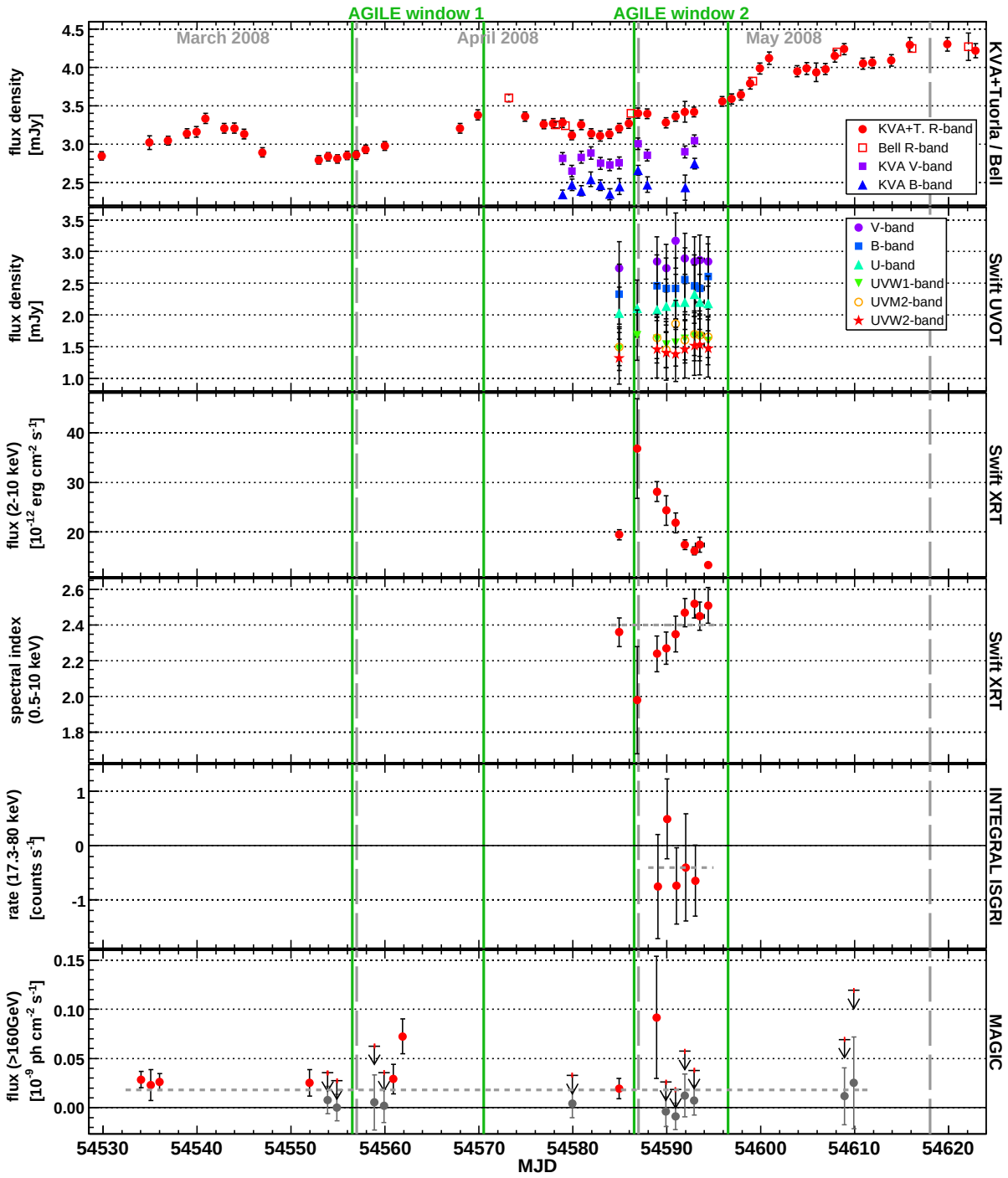

Figure 5.26: Multi-wavelength light curve for 1ES 1011+496 derived from this campaign. Grey horizontal dashed lines show fits with a constant to the data. The ISGRI light curve has been rebinned to daily time scales, see text. For an explanation of the MAGIC-I light curve, see caption of Figure 5.18. Green vertical solid lines visualise the two AGILE observation windows.

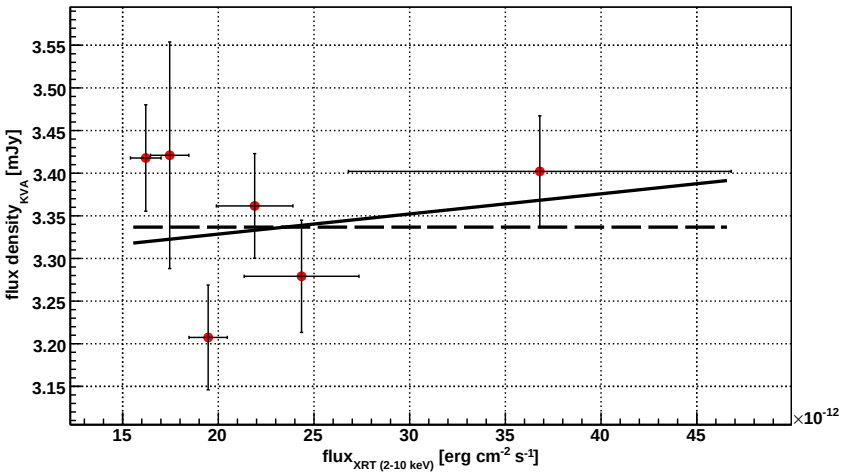

Figure 5.27: R-band flux density of 1ES 1011+496 measured by KVA in dependence of the *Swift* XRT integral flux between 2 and 10 keV. Only data pairs with a time difference < 0.9 days are shown. The dashed line represents a fit with a constant (χ^2/d.o.f. = 8.5/5, probability of 13.3 %), the solid line shows a linear fit (χ^2/d.o.f. = 8.1/4, probability of 8.8 %; slope: $(2 \pm 21) \cdot 10^{-2}$ mJy per 10^{-11} erg cm^{-2} s^{-1}).

derived from these results in the following remain speculative until confirmed by a final analysis pipeline.

All light curves but the Metsähovi one shown in Figure 5.28 are significantly variable. A fit with a constant yields χ^2/d.o.f. = 1918.8/222 for OVRO, χ^2/d.o.f. = 12.4/6 for Metsähovi, χ^2/d.o.f. = 20378.9/176 for KVA, χ^2/d.o.f. = 959.0/523 for MAXI, χ^2/d.o.f. = 24.3/10 for *INTEGRAL* ISGRI and χ^2/d.o.f. = 46.2/23 for *Fermi*-LAT. For Metsähovi, the goodness of the constant fit amounts to 5.4 %, giving a good hint for variability.

Individual Light Curve Features The individual light curves partly exhibit prominent features. Metsähovi detected nearly a flux density doubling from MJD 56026.0 to MJD 56029.7, representing remarkably fast variability at 37 GHz. In the R-band, KVA observed several strong flares, the most prominent ones having occurred around MJDs 54788, 54810 and 55224. Also MAXI significantly detected the source at some occasions. Figure 5.29 shows the distribution of rate/error for the MAXI observations displayed in Figure 5.28. The data can be reasonably described by a Gaussian (χ^2/d.o.f. = 28.7/31, mean of 0.26 ± 0.05) with an extension to positive values. Due to the preliminary nature of the MAXI data, single outliers are not necessarily reliable. Some of these are clustered though, especially around MJD 55148 and 55217, giving growing confidence in a potential detection of 1ES 1011+496 (see e.g. right side of Figure 5.28). In the HE regime, the first four and last two flux bins give evidence for increased activity of 1ES 1011+496 compared to most of the remaining measurements.

In the OVRO light curve, prominent features are hardly apparent. Overall, the flux density increased between MJD 54713 and 54762 by roughly 10 %. From $\sim$MJD 55650 on, the long-term average flux density declined again to a values slightly below the ones at the beginning of the monitoring. Potential outliers are present, like a single high flux density point at MJD 54812 or a strong dip at MJD 54854. A strong activity increase

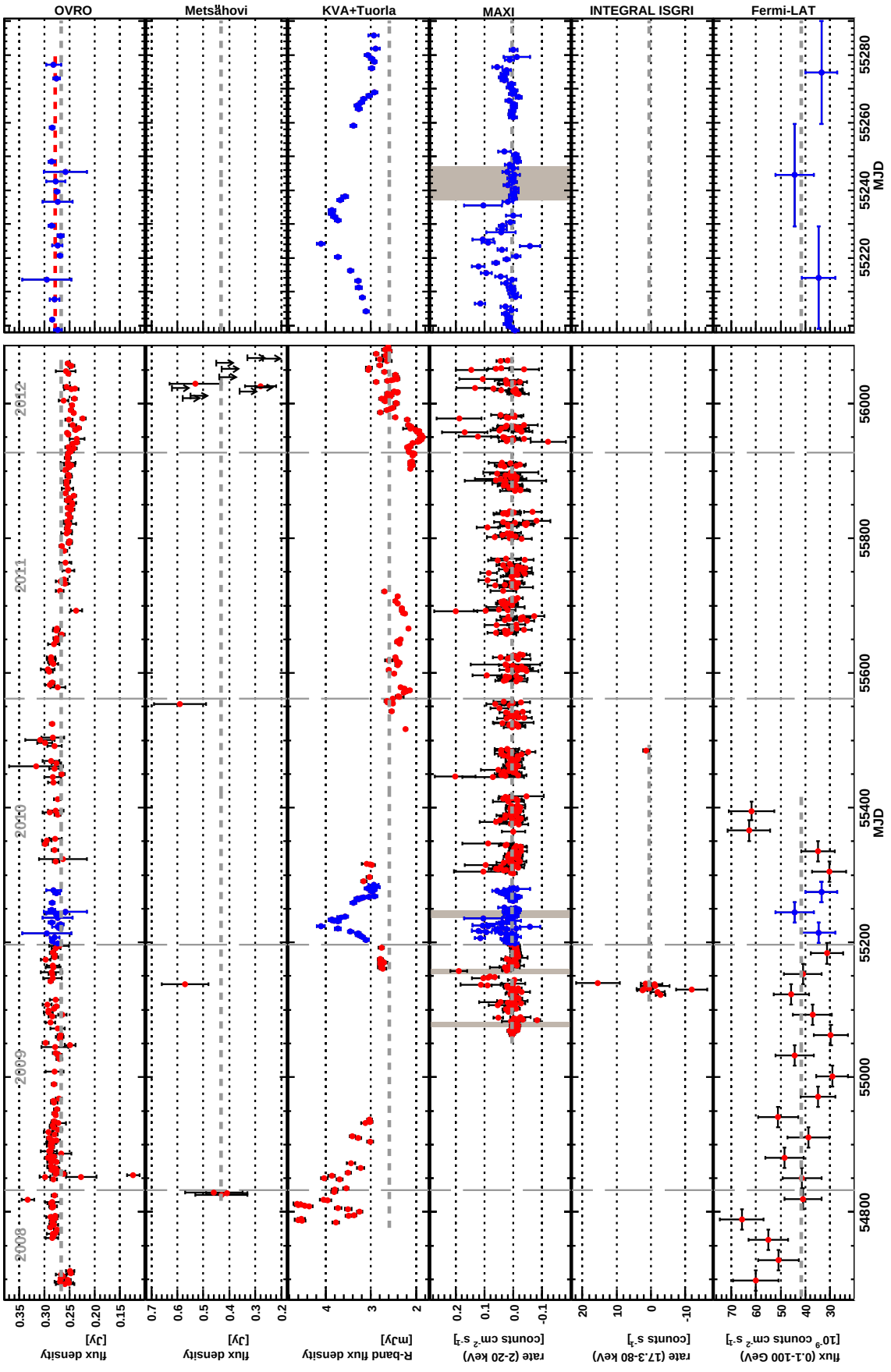

Figure 5.28: *Left side:* Long-term multi-wavelength light curve of 1ES 1011+496 since the start of OVRO and *Fermi*-LAT observations. Metsähovi ULs (S/N > 4) are available only for 2012, further non-detections are not indicated. MAXI and *INTEGRAL* ISGRI points are binned on daily scales, the *Fermi* points on monthly scales. The grey bars shown in the MAXI panel denote time periods when the space shuttle was obstructing the FOV. The blue points mark data which are shown enlarged on the *right side* of the figure. Grey dashed horizontal lines give fits with a constant, where the *right side* ones are the same as shown on the *left side*. The red horizontal dashed line is a fit with a constant only to the OVRO points shown in the right-hand side. *Fermi*-LAT data has been taken from the 2FGL.

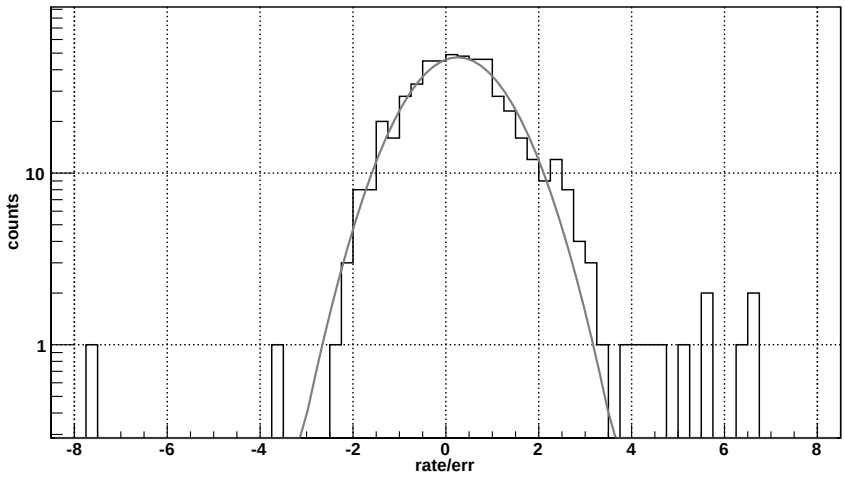

Figure 5.29: Distribution of rate/error for the MAXI observations shown in Figure 5.28. The grey line denotes a fit with a Gaussian.

from MJD 55048 to 55050 by $\sim 20\,\%$ was observed, but was no longer apparent for the following measurement (MJD 55057) and hence the probability for being real is rather low. *INTEGRAL* ISGRI did not detect the source significantly on daily time scales.

In general, the individual features detected by Metsähovi, KVA and MAXI are not present in the OVRO light curve, indicating that either there was no correlation between the radio and optical as well as radio and X-ray regime, respectively, or the flares have been missed due to potential time delays and unfortunate sampling. The latter is rather unlikely for the three prominent KVA flares, since the OVRO coverage was rather dense at these times and especially the duration of the third feature was quite long (about two months). During the Metsähovi flare, on the other hand, OVRO observations were sparse (three measurements from $\sim$ two weeks before to $\sim$ two weeks after the flare), hence the presence of a flare at the OVRO observation frequency can not be excluded.

Unfortunately, also KVA coverage is missing during the Metsähovi flare. From 12 days before until 2 days after the high flux state, no R-band observations were conducted. The measurements after the flare indicate the falling edge of a flare though, decreasing in flux density by $\sim 15\,\%$ within five days to an activity level also present before the Metsähovi flare. MAXI data do not show a hint for an increased flux from one day before until five days after the flare, which may however be due to the limited sensitivity of the instrument. Note that the KVA flux density was at that time much lower than during the flare around MJD 55224 possibly also present in the MAXI data. Consequently, the rare feature observed by Metsähovi can not be confirmed nor ruled out by the multi-wavelength data.

Also the considerably higher flux in the HE regime at the beginning and end of the 2FGL light curve is not significantly reflected in the radio regime. Indeed the first data in the OVRO light curve show an (timely unresolved) increase in flux density, but that is not apparent in the *Fermi*-LAT data. This can in principle be explained by potential time lags between the two energy regimes and the fact that earlier data have not been recorded. During the last two high flux bins in the HE regime, the OVRO sampling is rather sparse. Nevertheless a two month high state as seen by LAT should have

been apparent in the OVRO light curve in case the two energy regimes are directly correlated. Directly correlated flares with comparable time scales are therefore rather unlikely between the 15 GHz and HE regime at that time. LAT-simultaneous KVA data is only available for the fourth high flux bin, at the time of which indeed a strong flare was present in the R-band. However, a direct correlation is missing during the KVA flare around MJD 55224.

Early 2010 The KVA flare around MJD 55224 is especially interesting and well covered by OVRO, MAXI and LAT. In contrast to the first two KVA flares at MJDs 54788 and 54810, this high state was extended in time (about two months) and characterised by a well-shaped rising flank. The peak of the flare was not covered, but must have occurred between MJDs 55224 and 55231. The flux density decline was not sampled well enough to judge on that. A closer look (see right side of Figure 5.28) reveals that apart from the peak at MJD 55224, another one was present at MJD 55233. The rather high flux density after the observation gap between MJDs 55238 and 55259 indicates that during the not covered time period, the flux was not declining steadily and hence may have contained another peak.

At the time of increasing R-band flux density, the MAXI light curve revealed one high rate point at MJD 55206 (which is not reliable though considering the preliminary nature of the analysis products) and two well-shaped and rather symmetrical flares with peak rates occurring around MJDs 55217 and 55226. The latter is coinciding in time with the first maximum in the KVA light curve (the position of which is not precisely constrained though).

The rather sparsely sampled OVRO data do not indicate the trend observed by KVA. A significantly higher flux density (compared to the previous measurement) was recorded only at MJD 55230, but compared to the average flux during that time period, no significant deviation is present (fit with a constant: $\chi^2/\text{d.o.f.} = 15.6/15$).

Fermi-LAT did not detect a significant increase in flux during that event. However, this may be attributed to the rather long integration time of one month, which would dilute potential day-scale flares. In fact, the second light curve bin is slightly higher in flux, which may indicate the presence of a short flaring component. This would be then delayed with respect to both MAXI and the first KVA flare. A light curve with smaller binning is needed to test a potential correlation.

Long-Term Cross-Band Correlations Only one of the individual features presented above is most likely present at other wavelengths, which may also be due to bad sampling on the short time scales. For investigating dependencies between the different light curves on long time scales, a simple C++ ROOT macro has been written which compares the light curve points of two experiments and selects only data pairs with a time difference smaller than a predefined value. No data point may be selected twice, and if multiple data points fulfil the time difference condition to one point of the other instrument, only the data pair closest in time is being used. The flux densities/fluxes/rates of the resulting data selection are then searched for dependencies by a fit with a constant and a linear function. In this case, the time difference has been set to 0.9 days, considering

the sampling of KVA and MAXI as well as the typically variability time scales of blazars at these energies.

The comparison between OVRO and KVA reveals ambiguous results. The missing correlation during individual features reported above is confirmed by the fits shown in Figure E.2 considering that neither of them can describe the data well $\chi^2/\text{d.o.f.}_{\text{const}} = 469.9/42$, $\chi^2/\text{d.o.f.}_{\text{lin}} = 252.9/41$). Mathematically, a likelihood ratio test prefers the linear fit with a probability of 98.9 % though, which is highly significant. Also from an inspection by eye, a dependency between the two instruments is suggestive. In conclusion, a correlation on long time scales between the two instruments cannot be excluded. The ever growing data basis will probe this on a high statistical basis in the future.

The OVRO and MAXI and KVA and MAXI data are clearly not correlated (see Figure E.3). Also between KVA and MAXI, such a correlation is not present from Figure E.4. This may be attributed to the limited number of useful data pairs and the low signal significance of MAXI, but also the common time delay between the radio and other energy regimes as well as the above described potential time delay between KVA and MAXI may be the reason.

Correlations including Metsähovi, *INTEGRAL* ISGRI and *Fermi*-LAT have not been investigated due to the small amount of available simultaneous points, missing significant detections and incompatible time basis, respectively.

Discussion 1ES 1011+496 was rather sparsely covered during the MW campaign. In combination with the faintness at gamma-ray energies, correlated variability at different wavelengths cannot be meaningfully investigated.

Observations on longer time scales have therefore been considered, revealing significant variability at all energy regimes. A rare flare was observed by Metsähovi mid of 2012 (MJD 56029.7) having a flux doubling time close to four days. The multi-wavelengths observations are not suited to investigate that event. OVRO can not confirm a higher flux density, which may be due to sparse sampling. KVA did not observe at that time, but saw a hint for a decaying flare two days afterwards. The MAXI data did not reveal an increased rate, which may be due to sensitivity constraints though.

The R-band light curve reveals strong variability with flux density increases of up to $\sim 40\,\%$ within ten days, but also a flare with remarkably slow an steady increase of activity beginning of 2010 ($\sim$ MJD 55224). The decaying part of the latter was not covered, but the total duration of the high activity state may have been up to ~ 80 days. During that, two or probably even three flux density peaks occurred, where the time difference between the first and second one amounted to $\lesssim 9$ days. At the same time, MAXI detected the source significantly at two or three occasions, resolving two distinct flares separated by ~ 9 days. The probability for that correlation between optical and X-ray energies being by chance is rather low. However, the two optical flares were delayed by ~ 7 days with respect to the two X-ray ones. Such time lags may be realised though assuming a low value of the magnetic field (around 0.05 G) in combination with large emission region radii (order of 10^{17} cm; F. Spanier, 2012, private communication), and by that increasing the cooling time scales.

Also the monthly HE light curve showed indications for an increased flux, a distinct flare was not resolved though which can be explained by the broad time binning. If

the slightly increased flux was indeed due to a short-lived flare at HE, the gamma-rays would lag behind the X-rays and optical regime. At 15.0 GHz, no significantly increased activity is present during the high optical activity state despite suitable coverage. That can be explained either be a missing correlation or time lags, the latter being rather unlikely though considering the long activity phase in the optical.

The remaining R-band flares were also not clearly present in the radio light curve, which is hard to explain by missing coverage or time lags due to the good overall sampling. The search for a correlation on long time scales did not reveal a clear result. The higher flux states at HE were not apparent in radio, too. A missing correlation between the 15 GHz evolution and the remaining energy bands seems therefore likely for 1ES 1011+496.

No correlation was obvious between OVRO and MAXI as well as KVA and MAXI, which however may be a result of small statistics or time lags between the energy regimes.

With the strong and frequent variability present for 1ES 1011+496, more data, especially in the future at VHE by CTA, would easily shed light on inter-band correlations and potential time lags. These will help to reveal the location of the emission region as well as the mechanisms responsible for the observed radiation. The comparably large redshift of the source enables studies of the EBL, making this object an extremely interesting target for CTA.

5.4.6 Spectral Energy Distribution

From the MW light curve, days with a considerable flux difference characterised by good simultaneous coverage have been selected for constructing simultaneous SEDs. MAGIC-I did not detect the source with sufficient significance to derive a spectrum neither on day-wise nor on period-wise time scale around the time of the *Swift* observations. Therefore, the average VHE spectrum from the complete MW campaign will be used for SED modelling (which is justified since no significant variability was present in the MAGIC-I light curve), and the SEDs are chosen according to the X-ray flux state. Instead of the highest X-ray flux measurement, the second-highest flux has been used due to its considerably smaller uncertainty and higher statistics. However, optical data by KVA is not available for that day. For the low flux data set, the second-lowest X-ray flux day has been chosen (differing by only 9 % from the lowest measured flux) in order to have simultaneous multi-band data by KVA. The observation times of the corresponding "high" and "low" data sets are listed in Table 5.3.

The *Fermi* satellite was not launched yet at the time of the MW campaign, hence (quasi-)simultaneous detections at HE are not available. Since the LAT light curve showed significant variability after 24 months of observations (< 1 % probability for a constant flux), neither the 1FGL nor the 2FGL spectrum can be considered quasi-simultaneous. Thus these points represent a very rough estimate of the flux state and are not considered for SED modelling. Apart from the 1FGL and 2FGL data, also the results from the first three month of data are shown. As discussed in Section 5.4.5.2, the first four month of LAT observations have caught the source in a higher flux state, which is clearly visible in the three months LAT spectrum. The flux of the EGRET association 3EG J1009+4855 matches well the ones of 1FGL and 2FGL for 1ES 1011+496, indicating

Data Set	Instrument	Observation Time
"low"	KVA	54592.899
	Swift	54592.905 – 54592.976
	INTEGRAL	54592.560 – 54593.278$^{(a)}$
	AGILE	54561.000 – 54572.000$^{(a)}$
	MAGIC-I	54533.970 – 54609.918
"high"	Metsähovi	54580.992$^{(a)}$
	Swift	54588.912 – 54588.969
	INTEGRAL	54588.890 – 54589.548$^{(a)}$
	AGILE	54561.000 – 54572.000$^{(a)}$
	MAGIC-I	54533.970 – 54609.918

Notes. $^{(a)}$ No detection.

Table 5.3: Definition of the "low" and "high" data set used for SED modelling of 1ES 1011+496.

that the two sources may in principle be the same object at HE.

Additional archival data have been added to the SED, visualising the range of variability of 1ES 1011+496. The comparison shows that the source has been observed within this campaign in a rather high flux state at optical and X-ray wavelengths. The quasi-simultaneous ULs in the radio and HE range are consistent with archival observations. At VHE, the spectrum derived here is basically consistent with the archival MAGIC-I discovery (Albert *et al.* 2007b). Only the lowest energy point is not consistent within the error bars. The flux seemed to have been higher at these energies during the discovery. However, the 1FGL and 2FGL data indicate that such a high flux at these energies is rather exceptional than normal, and also the high state observed within the first three month indicates a lower flux at these energies. No other VHE detections have been reported from the source to date (see also Section 5.3.4). In general, the high and low state SED are very similar in flux. However, the spectral index at X-rays differs considerably, justifying the application of two different SED fits.

SED Modelling The low and high state SEDs were modelled with a simple one-zone as well as a self-consistent two-zone SSC model ((Maraschi & Tavecchio 2003) and (Weidinger & Spanier 2010), respectively). The former was applied by hand as well as by a χ^2 minimisation technique (Mankuzhiyil *et al.* 2011), where for the minimisation also the 1FGL data were taken into account. For details on the models on the models, see Section 2.6. The modelling results are summarised in Table 5.4, the SEDs and the corresponding models are shown in Figure 5.30.

Also the model parameters reported in Albert *et al.* (2007b) are listed in Table 5.4. That model is based on the first VHE data published for 1ES 1011+496 and one quasi-simultaneous R-band point. The remaining data considered for the modelling were not contemporaneous. Two SEDs have been constructed, differing only in the value adopted for γ_{min} (1 and 3000). The archival data are not sufficiently constraining to differentiate between these two models but the archival EGRET point, which is overestimated adopting a the value of unity but well described by $\gamma_{min} = 3000$. Therefore, only that SED is shown in Figure 5.30. Note that some of the archival data and models in the literature

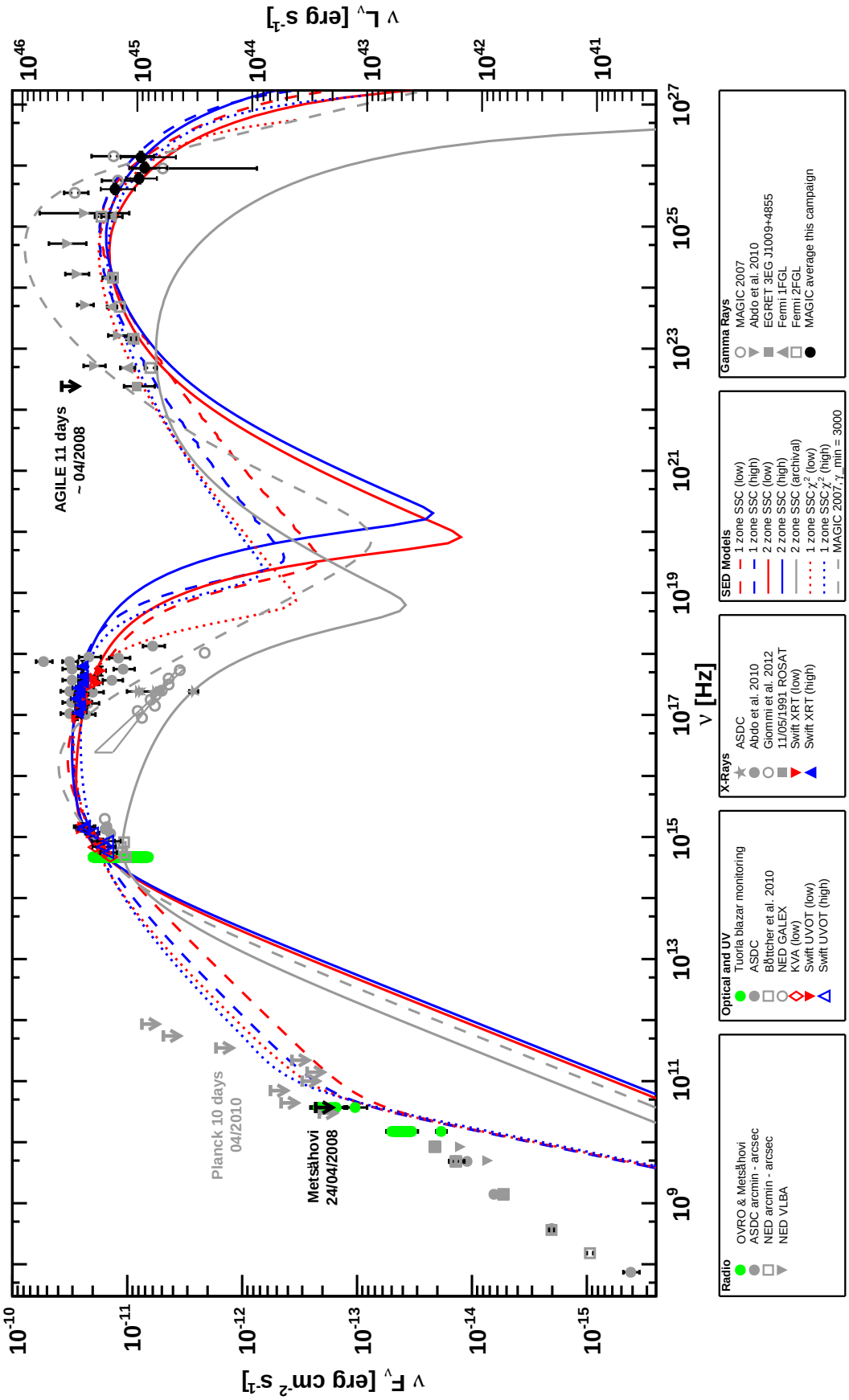

Figure 5.30: The quasi-simultaneous SED of 1ES 1011+496 based on this MW campaign. Blue and red data points correspond to the high and low activity state, respectively, of the source as found in this MW campaign. Black markers denote quasi-simultaneous data, whereas grey ones are representing archival data. Green points visualise the variability range as found by source monitoring. UV data have been de-reddened, optical data additionally host-galaxy corrected. XRT data have been corrected for galactic absorption. The VHE data have been EBL de-absorped using the model of Kneiske & Dole (2010). ULs are given at a c.l. of 2 σ for AGILE and Planck and at S/N > 4 for Metsähovi. Archival data has been obtained from the ASDC SED Builder (http://tools.asdc.asi.it), (Lamer *et al.* 1996), (Albert *et al.* 2007b), (Abdo *et al.* 2010b), (Böttcher *et al.* 2010) and (Giommi *et al.* 2012b). Archival optical data are not shown due to missing host-galaxy correction.

Campaign	(1)		(1)			(1)		(2)
Model	**MaTa03**		**WeSp10**			**MaTa03** χ^2		**Ta01**
Flux Level	low	high	low	high	archival	low	high	...
B [G]	0.05		0.18	0.13	0.59	0.08	0.07	0.15
δ	26		40	49	31	22	24	20
$R_{\rm em}$ [10^{15} cm]	32	33	10	9	3	29	29	10
$K^{(a)}$ [10^2 cm^{-3}]	5	8	150	85	4200	9	14	200
e_1	1.9		... [b]	2.5	... [b]	1.9	1.9	2
e_2	3.7	3.2	3.1	3.5	3.8	3.1	3.1	5
$\gamma_{\rm min}$ [c]	1		5100	4300	1900	1		1 or 3000
$\gamma_{\rm break}$ [10^4]	5	2	... [b]	~ 1	... [b]	1	0.1	5
$\gamma_{\rm max}$ [10^6]	1		~ 6	~ 3	1	0.4	0.7	20
$\chi^2_{\rm red}$	...	...	...	...	...	0.21	0.20	...

Notes. [a] For the one-zone model, K is defined in the emission region at $\gamma_{min} = 1$, whereas in the two-zone case, K is given for the acceleration region at γ_{min}. Hence these values are not directly comparable between the two different models. [b] e_1 and $\gamma_{\rm break}$ not existent since $\gamma_{\rm break} < \gamma_{\rm min}$. [c] γ_{min} was fixed a priori for the one-zone model.
Campaign References. (1) This Campaign. (2) MAGIC 2007 and archival data (Albert *et al.* 2007b).
Model References. MaTa03: Maraschi & Tavecchio (2003). WeSp10: Weidinger & Spanier (2010). MaTa03 χ^2: Mankuzhiyil *et al.* (2011). Ta01: Tavecchio *et al.* (2001).

Table 5.4: Parameters defining the SED models of 1ES 1011+496 shown in Figure 5.30. For a description of the models and parameters, see Section 2.6. Note that the model of (Tavecchio *et al.* 2001) is for HBLs basically identical to the one of (Maraschi & Tavecchio 2003) (F. Tavecchio, 2012, private communication).

have been found not to be suited for this work and hence are not listed here (for details, see Section E.1.4).

To get an estimate of a low state SED and to test our interpretation of the source being an IBL during low activity states, we considered the lowest flux archival data as representative of a low state of the source. The case of the MDM data is particularly interesting, showing a synchrotron peak around $5 \cdot 10^{14}$ Hz in the lowest flux state (Böttcher *et al.* 2010). The authors did not take into account the host galaxy contribution though. We estimated a correction factor from the KVA multi-band data and applied it to the data (see also Section E.1.2), resulting in shift of $\sim 30\,\%$ of the peak location towards higher frequencies. An estimation of the host galaxy flux in the I- and U-band were not available. For the latter, this contribution is negligible, having already decreased to $\sim 3\,\%$ in the B-band. However, since the influence in the I-band is much stronger, we removed that point from the SED. A fit with the two-zone model has been applied to the optical data and the lowest X-ray flux point (assuming a spectral shape as given by *ROSAT* and Giommi *et al.* (2012b) in a slightly higher flux state) and the 2FGL data. The results are given in Table 5.4 and shown in Figure 5.30.

The different models can describe the data well. However, the narrow synchrotron peak in the low state is broadened by all models assuming a softer spectrum than given by the optical data. These seem to be rather challenging for leptonic SSC models, because of which Weidinger (2011) applied a lepto-hadronic fit to the data, yielding a

better description of the SEDs.

The model parameters reveal a rather large emission region in case of the manual one-zone SSC model (see e.g. Tavecchio *et al.* 2010), combined with a low electron density. The parameters do not match well the ones presented in Albert *et al.* (2007b), where the emission region and Doppler factor was much lower, whereas the magnetic field, electron number density, electron spectral index after the break and maximum electron energy were considerably larger. This may be explained by the sparseness of simultaneous data for the latter fit.

The transition from the high to the low state is described in the one-zone model basically by a lower electron density, softer spectral index after the break and a shift of the break to higher energies. The remaining parameters stay constant. Consequently, the changes leading from the high to the low flux state affected dominantly the high energy electrons. The parameters obtained with the same model but taking advantage of a χ^2 minimisation routine to determine the fit are mostly consistent with the manually derived ones. However, the spectral index is hardly changing between the two flux states, the number density of electrons is larger and $\gamma_{\rm break}$ lower. The transition from the high to the low state is explained by a reduced electron density and maximum electron energy as well as a larger electron break energy. Hence, also in this case, the difference between the two models can be ascribed mainly to the high energy electrons in combination with an overall loss of electrons., Both effect indicate that electrons cooled down to lower energies, partly low enough to no longer contribute to the SSC process.

In the two-zone SSC case, the Doppler factors are required to be very high, same as the minimum electron energy. In the low state, $\gamma_{\rm break}$ is below $\gamma_{\rm min}$, meaning that the electron number distribution is not characterised by a broken power law but a simple power law. Since the break is indicative of equality between the electron escape and cooling time scales, the former has to be much larger than the latter in the low state. Opposite to the one-zone SSC model, nearly all parameters are changing considerably between the high and low state in the two-zone case. Especially the electron distribution is evolving strongly, which may be due to the missing shock acceleration. The lower and upper energy limit is increasing for the low state, and the spectral index becomes harder. Since K is defined at $\gamma_{\rm min}$, a change in the electron number density can not be assessed from these parameters. Overall, the high Doppler factor and peculiar change in electron distribution indicate that a pure leptonic model may not be adequate to describe the first simultaneous SED of 1ES 1011+496.

Comparing the one- and two-zone model in terms of their parameter values, the differences are rather large, especially for the Doppler factor, size of the emission region and transition between the high and low state, rendering the two hardly being compatible.

The two-zone fit to the archival low state data reveals a very low second peak component, much below the *Fermi* data at higher energies suggest. Since the data are simultaneous it cannot be excluded that the HE component was indeed much lower during the optical and X-ray observations. On the other hand, the HE data represent an average over two years, the flux of which should be rather close to a quiescent state, if not dominated by flares (which normally seems not to be the case). Moreover, the second peak has to shift by about two order of magnitude to be compatible with the peak determined from the simultaneous SEDs. Statistics for spectral changes at VHE are rather

low, but from observations of Mrk 421 and PKS 2155−304, peak shifts of only about one order of magnitude have been found (see references given in Section 2.7). It should be noted that the narrow synchrotron peak suggests high magnetic fields in the emission region, indicating that hadronic processes may not be negligible. The high value of B is particularly apparent when comparing the results with the ones of the simultaneous SEDs. A smaller Doppler factor, missing break in the electron spectrum and the low values of γ_{min} and γ_{max} reflect the smaller activity of the source, whereas the smaller radius of the emission region would rather be expected for a compact region travelling the jet, normally associated with outbursts. However, these conclusions are indications only, which have to be verified on simultaneous data.

Regarding the classification of 1ES 1011+496, the low IC dominance found for the simultaneous SEDs indicates an HBL object. Note that these SEDs were conducted in a rather high activity state of the source. Conclusions from the archival low state on the classification are hard to draw. Taking the two-zone fit with its low flux IC component for real, this would speak against an IBL nature of the source. As discussed above, the fit may not be appropriate though, possibly requiring hadronic components to be considered for the emission. If instead the peak flux in the optical regime measured by Böttcher *et al.* (2010) is compared with the 2FGL data, potentially representative of the quiescent state, the IC component would dominate over the synchrotron component. Such a behaviour is often observed for blazars with lower peak frequencies, like IBLs, and would support the new classification proposed in this work. However, the high Compton dominance suggested by Albert *et al.* (2007b) to be present during rather high activity states can not be confirmed here. Instead, a behaviour as reported by Abdo *et al.* (2010b) is supported.

6 1ES 2344+514 Multi-Wavelength Campaign

The rather nearby source 1ES 2344+514 at a redshift $z = 0.044$ (Perlman *et al.* 1996) has been classified as an HBL object (Perlman *et al.* 1996; Scarpa *et al.* 2000). It is one of the few blazars showing extreme synchrotron peak frequencies (Giommi *et al.* 2000). The mass of its central black hole has been estimated to be between $10^{8.80\pm0.16}\,M_\odot$ (Barth *et al.* 2003) and $10^{9.52}\,M_\odot$ (Wu *et al.* 2002). Despite being one of the first extragalactic VHE sources, 1ES 2344+514 has been observed only occasionally at most frequencies due to its overall faintness. No simultaneous MW campaign had been reported at the time of organising the observations described below.

6.1 Historical Overview

1ES 2344+514 was the third extragalactic source discovered at VHE (Catanese *et al.* 1998), after Mrk 421 (Punch *et al.* 1992) and Mrk 501 (Quinn *et al.* 1996). The Whipple telescope detected a signal $> 350\,\mathrm{GeV}$ on the $6\,\sigma$ level from 1.85 hrs of observations performed on 1995 December 20, corresponding to a flux of $\sim 63\,\%$ of the Crab Nebula flux. The remaining measurements in the winter seasons 1995/6 and 1996/7 with ~ 19 and ~ 25 hrs of observation, respectively, did not result in a significant detection. The derived flux ULs were significantly below the flux level from the flare, giving evidence for variability of the source at VHE. The spectrum of this flare was presented in 2005, being compatible with a power law between 0.8 and 12.6 TeV of the form $\mathrm{d}N/\mathrm{d}E = (5.1 \pm 1.0_{\mathrm{stat}} \pm 1.2_{\mathrm{sys}}) \cdot 10^{-11}\,(E/\mathrm{TeV})^{-2.54\pm0.17_{\mathrm{stat}}\pm0.07_{\mathrm{sys}}}\ \mathrm{TeV\,cm^{-2}\,s^{-1}}$ (Schroedter *et al.* 2005). The discovery was confirmed several years later by HEGRA on a $4\,\sigma$ level (Tluczykont *et al.* 2003; Aharonian *et al.* 2004). The first high significance detection ($11.5\,\sigma$) was reported by MAGIC, finding the source after 23.1 hrs of observation at a flux level $\sim$ a factor six lower than the Whipple flare, representing the lowest VHE flux state up to now[1] (Albert *et al.* 2007d). The spectrum could be described by a simple power law between 140 GeV and 5 TeV of the form $\mathrm{d}N/\mathrm{d}E = (1.2 \pm 0.1_{\mathrm{stat}} \pm 0.2_{\mathrm{sys}}) \cdot 10^{-12}\,(E/0.5\,\mathrm{TeV})^{-2.95\pm0.12_{\mathrm{stat}}\pm0.20_{\mathrm{sys}}}\ \mathrm{TeV\,cm^{-2}\,s^{-1}}$. Though the source was found to be constant throughout the observations, a comparison with the Whipple spectrum proofs flux as well as spectral variability of 1ES 2344+514. Recently, the source was also detected by VERITAS (Acciari *et al.* 2011a) which reported for the first time significant variability of 1ES 2344+514 during one observation campaign. A 1-day flare with a flux doubling time of ~ 1 day was found.

[1] VERITAS claims to have seen the source at an even lower flux level, but without giving absolute flux values or analysis details (Benbow & for the VERITAS Collaboration 2011)

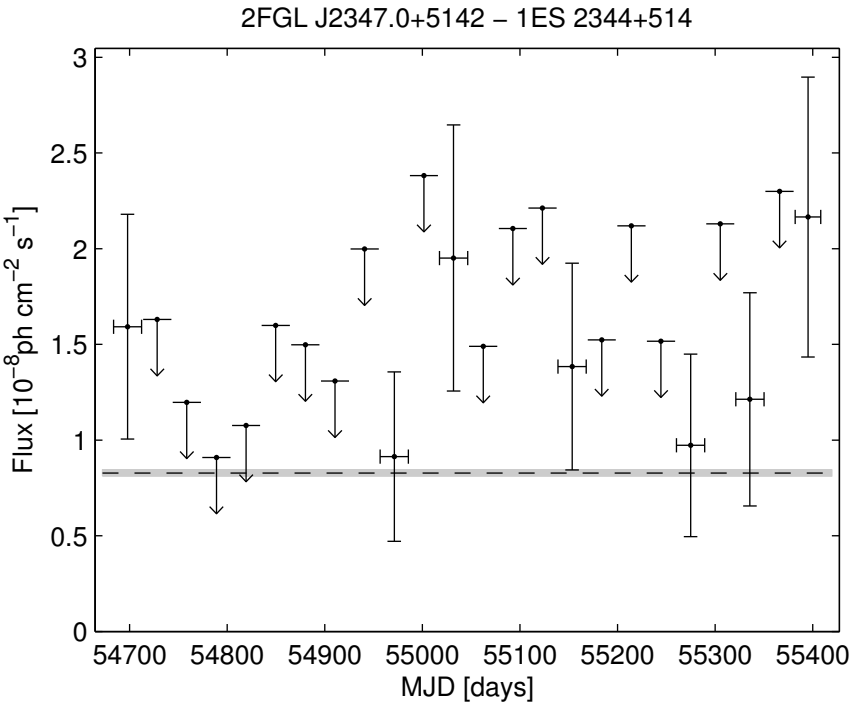

Figure 6.1: 2FGL monthly light curve of 1ES 2344+514 between 0.1 and 100 GeV, taken from the 2FGL Catalog[3].

At HE, no detection of the source was reported in the 3rd EGRET catalogue (Hartman *et al.* 1999). A 95 % c.l. UL > 100 MeV of $\sim 1.5 \cdot 10^{-7}$ ph cm^{-2} s^{-1} can be derived from Figure 3 in Hartman *et al.* (1999). Also AGILE was not able to detect the source, giving a 95 % c.l. UL on the flux > 100 MeV of $2.7 \cdot 10^{-8}$ ph cm^{-2} s^{-1} for the observation period 2007 July – 2011 January (F. Longo, L. Lucarelli, C. Pittori & S. Vercellone, 2012, private communication). The first detection of 1ES 2344+514 at HE was reported by *Fermi*-LAT after eleven months of data taking (*Fermi* Large Area Telescope First Source Catalog (1FGL); Abdo *et al.* 2010d). The flux between 1 and 100 GeV of $(1.40 \pm 0.30) \cdot 10^{-9}$ ph cm^{-2} s^{-1} did not change significantly compared to the value found after 24 months ($(1.55 \pm 0.18) \cdot 10^{-9}$ ph cm^{-2} s^{-1}; Nolan *et al.* 2012), same as the spectral index (1.57 ± 0.12 and 1.72 ± 0.08 for 1FGL and 2FGL, respectively). Note that 1ES 2344+514 is not listed as a "clean" source in the currently available two *Fermi*-LAT AGN Catalogs (1LAC/2LAC) due to its low galactic latitude. The publicly available 2FGL monthly light curve (see Figure 6.1) does not show significant variability over the 2 years time span, same as the daily or weekly results[2]. The variability index from 2FGL is 28.1, where a value $\gtrsim 42$ indicates less than 1 % chance for a steady source. Hence 1ES 2344+514 is within the limits of the *Fermi*-LAT sensitivity a stable and rather faint source.

Strong X-ray variability of 1ES 2344+514 was reported by Giommi *et al.* (2000) from *BeppoSAX* observations in 1996 and 1998. From 1996 to 1998, the flux changed by

[2]http://fermi.gsfc.nasa.gov/ssc/data/access/lat/msl_lc/
[3]http://heasarc.gsfc.nasa.gov/W3Browse/fermi/fermilpsc.html

a factor of ∼eight. Comparing the results from all six observations days, a "harder spectrum when brighter" trend was visible. In fact, the synchrotron peak shifted from $\sim 10^{17}$ Hz to $\geq 3 \cdot 10^{18}$ Hz which corresponds to ∼10 keV, making 1ES 2344+514 the second "extreme blazar" after Mrk 501 (Pian *et al.* 1998). The authors interpreted the change in peak position as a sign of a second synchrotron emission component on top of a steady emission one, though they annotate that the lag of the hard X-rays behind the soft ones argues against this explanation. Evidence for very fast flux variability with a flux increase of ∼40 % within ∼5000 s was found. Further X-ray observations by ASCA, *Swift* and *RXTE* (Donato *et al.* 2001; Tramacere *et al.* 2007; Acciari *et al.* 2011a) prove the variable nature of 1ES 2344+514 at soft X-rays, though not at such extreme levels. At hard X-rays, *Swift* BAT detected the source after 58 month of data taking[4]. The fact that the source was not included in the 22 month catalogue (Tueller *et al.* 2010) as well as the absence of major flares in the monthly light curve of the 58 month catalogue indicates that 1ES 2344+514 belongs to the faint and rather stable sources also at hard X-rays. The spatial structure of the source was investigated at X-rays by *Chandra* (Donato *et al.* 2003), finding a weak evidence for faint diffuse X-ray emission on the scale of the galaxy's halo.

In the optical regime, 1ES 2344+514 is dominated by a bright and large elliptical host galaxy which contributes ∼90 % to the flux in the R-, V- and B-bands (Nilsson *et al.* 1999; Tramacere *et al.* 2007). Due to that, only moderate variability of the order of 0.1 magnitude has been detected in these bands[5]. At UV energies, the host galaxy contribution becomes much lower (Tramacere *et al.* 2007). Due to its low galactic latitude, the galactic extinction is rather high ($E\,(B-V) = 0.191$)[6].

1ES 2344+514 is rather faint at radio frequencies, having a core flux density measured by VLA of $S_{\mathrm{core,5GHz}} = 211.6$ mJy and $S_{\mathrm{ext,5GHz}} = 3.6$ mJy for the extended source components (Perlman *et al.* 1996). VLBI measurements determined the flux densities as $S_{core,\mathrm{5GHz}} = 70.0$ mJy and $S_{ext,\mathrm{5GHz}} = 46.7$ mJy (Giroletti *et al.* 2004). The structure of the source seems rather complicated. At 1.4 GHz two bright components besides a core-halo morphology are apparent on kpc scales. The eastern structure, at a position angle of ∼105°, is related to the core, in contrast to the isolated northwestern component. 5 GHz VLBA observations on pc scales, on the other hand, reveal a well collimated jet structure at a position angle of ∼145° which is bending by ∼25° and broadening after about 10 pc (Rector *et al.* 2003; Giroletti *et al.* 2004) (see Figure 6.2). Piner & Edwards (2004) performed 15 GHz VLBA observations of 1ES 2344+514 between 1999 October and 2000 March, confirming this result. No author finds signs of a counter-jet. Despite the smoothness of the jet, Piner & Edwards (2004) identified three individual jet components. Whereas the two components with the smallest separation from the core were consistent with being stationary, for the third an apparent jet speed of $(1.15 \pm 0.46)\ c$ was determined. Combining these measurements with new data at 43 GHz from 2008 – 2009 (Piner *et al.* 2010), all jet components showed a rather slow though significant motion, where the most robust and highest value was determined for the most distant component as $(0.62 \pm 0.05)\ c$. The authors note however that a frequency-dependent separation

[4]http://swift.gsfc.nasa.gov/docs/swift/results/bs58mon/
[5]see e.g. the http://users.utu.fi/kani/1m/
[6]from http://ned.ipac.caltech.edu/

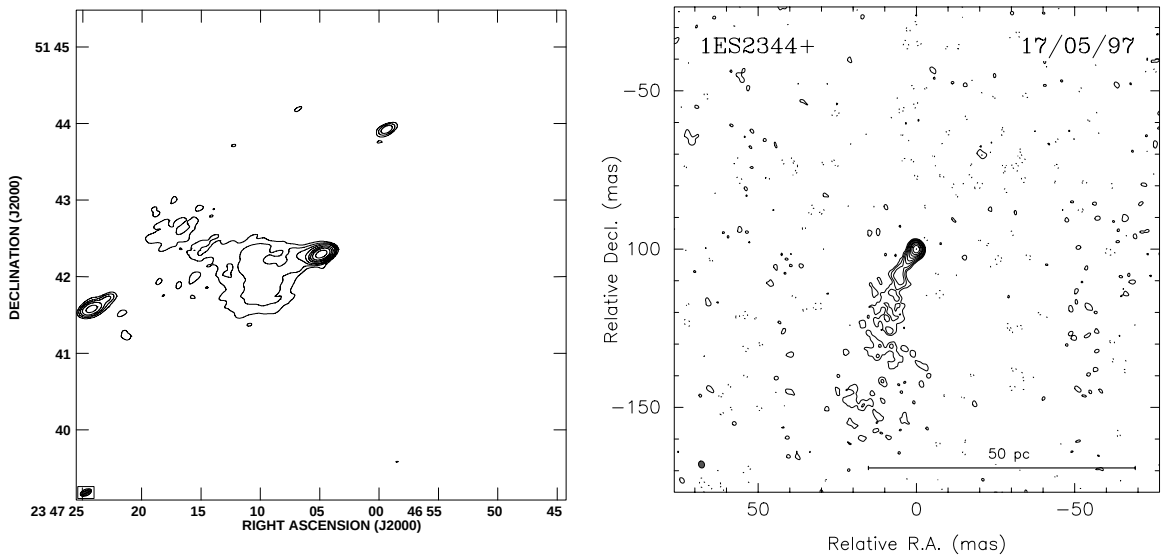

Figure 6.2: Archival radio maps of 1ES 2344+514 taken from Rector *et al.* (2003). *Left side:* map retrieved from VLA observations at 1.4 GHz on 10 October 1998, *right side:* from 5 GHz VLBA observations from 17 May 1997. For further details see Rector *et al.* (2003).

from the core has not been taken into account, which may lead to an overestimation of the apparent jet speeds. Additional measurements at 22 GHz in 2006 reveal a core region with a polarisation of $\sim 1\%$ at an angle nearly orthogonal to the jet (Piner *et al.* 2010). As a member of the extended MOJAVE-II sample, 1ES 2344+514 is monitored by VLBA since spring of 2008.

Despite being one of the first extragalactic VHE sources, previous broad MW campaigns are sparse for 1ES 2344+514. That led Albert *et al.* (2007d) to perform the first broad SED modelling for the source on non-simultaneous data. Hence the corresponding results are rather speculative, as the authors note. VERITAS organised the first simultaneous MW campaign from the optical to the VHE band on the source in the winter season of 2007/8 (Acciari *et al.* 2011a). Apart from VERITAS, observations were conducted with *Swift* and *RXTE*. Strong variability was reported in the X-ray and VHE bands which enabled to construct a low and high state data set for SED modelling. The resulting SEDs are shown in Figure 6.3 and will be discussed in Section 6.5.7. More recently, Giommi *et al.* (2012b) took advantage of the *Planck* and *Fermi* all sky observations and combined them with dedicated *Swift* pointings to construct quasi-simultaneous SEDs from radio to the HE regime. As 1ES 2344+514 was only detected at UV and soft X-ray energies, no meaningful constraints could be attained on the broadband SED.

6.2 Observation Campaign Details

The core observations were centred on simultaneous observations of MAGIC-I, AGILE, KVA and Metsähovi. Observation proposals to Swift, Suzaku and VLBA were not successful, the latter one because 1ES 2344+514 was already on the MOJAVE list of monitored sources. Through a direct cooperation with people from MPIfR in Bonn, VLBA,

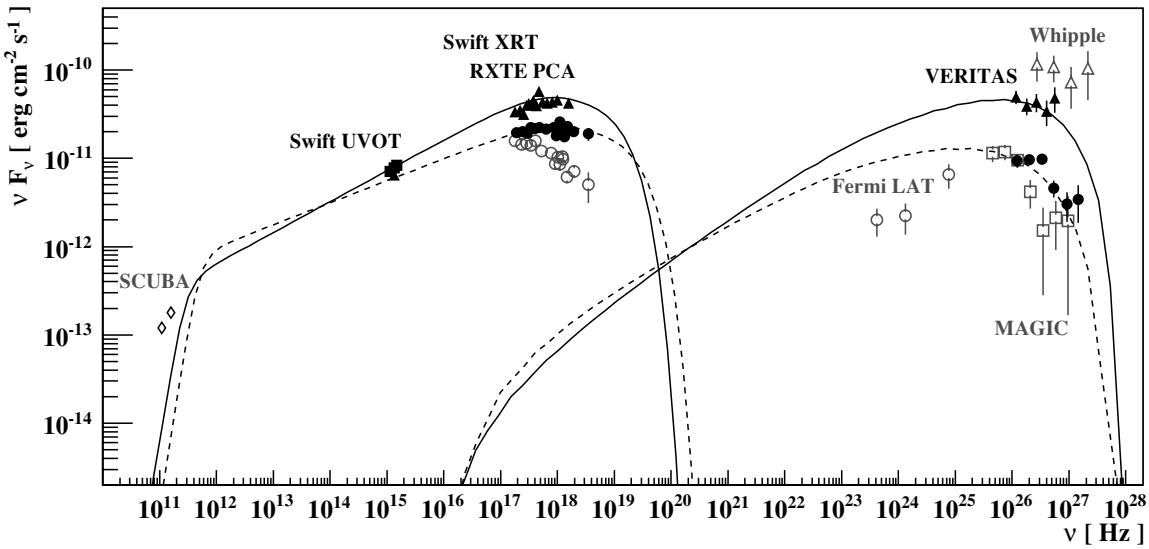

Figure 6.3: SED of 1ES 2344+514 as measured by VERITAS in 2007/8 (Acciari *et al.* 2011a). Full and open symbols represent quasi-simultaneous and historical data, respectively. The VHE data have been corrected for EBL absorption (Franceschini *et al.* 2008). The solid and dashed lines give one-zone SSC model fits to the data (Krawczynski *et al.* 2004). More details can be found in Section 6.5.7 and Acciari *et al.* (2011a).

RATAN-600 and Effelsberg coverage could be achieved. X-ray observations were provided by means of ToO observations by *Swift*. Finally, monitoring data by *Fermi*-LAT, CrAO, OVRO, Effelsberg and IRAM (the latter two through the F-GAMMA program) complemented the MW campaign. Details on the instruments and their observing ranges can be found in Section 3. The observation times are visualised in Figure 6.4. Exact numbers are given in Section E of the Appendix.

6.3 MAGIC-I Data Analysis and Results

MAGIC-I observed 1ES 2344+514 end of 2008 for in total 26.4 hrs in wobble mode at zenith distances of $23^\circ - 31^\circ$ mostly in moonless nights. The observations have been conducted after a quite long (40 days) shutdown of the telescope after which in the past often hardware failures had to be repaired and adjustments of the telescope subsystems had to be performed. During that time, no pointing calibration data (so-called "tpoints") could be taken. Therefore, to correct for a potential mispointing, a new starguider pointing model (i.e. calibration) not yet included in the used MARS version has been calculated from starguider tpoints taken November and December 2008. The pointing accuracy of the new starguider model is $\sim 0.7'$, the normal tpoints give a pointing accuracy of the telescope structure of $< 0.5'$ (T. Bretz, 2010, private communication).

The analysis has been conducted with the newest MARS CheObs Ed. version 2.4 and ROOT 5.12.00f, being the latest ROOT version tested for this MARS release. The data have been calibrated using the standard spline extractor for MUX data and were further processed with the standard time image cleaning with cleaning levels of 6 and 3 phe and a time coincidence window of 1.75 ns. For further details on the analysis

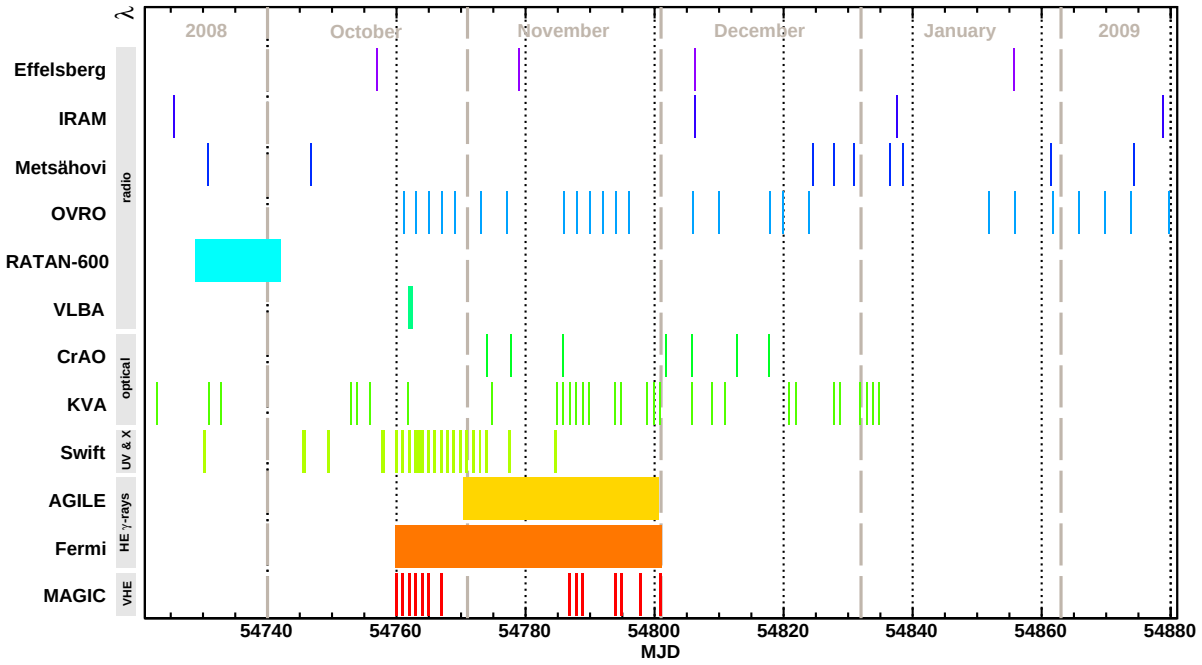

Figure 6.4: Observations of 1ES 2344+514 conducted in the course of this MW campaign. The grey bar right hand side of the instrument names indicates the observation band. RATAN-600 and *Fermi* observations were not performed continuously during the indicated time windows. Note that only *Fermi* data within the MAGIC-I time window were included in the MW campaign. The lines indicating the observation windows have been smoothed for clarity by 0.3 days.

procedure see Section 4.3.

6.3.1 Data Quality Evaluation

The quality of the data has been judged by the parameters discussed in Section 4.3.2. $\sim$20.8 hrs of data fulfilled the applied quality criteria. The reasons for excluding data are listed for all sequences in Table B.3. In general, the data quality turned out to be rather good, despite the following problems that have been found, evaluated and, if possible, corrected:

- **Cloudiness** For some data, the *cloudiness* information were missing or wrong but could be judged from the runbooks and different quality parameters like number of stars identified by the starguider or data rate (if not influenced by other observation parameters). One of the affected sequences (1002971) has been discarded due to potential high *cloudiness*.

- **Arrival Times** The arrival times of calibration pulses were not stable during the observations (see Figure 6.5), which may cause a wrong or failing calibration if the pixel arrival time falls outside of the trigger window. This problem is probably also a consequence of the long shutdown. A careful quality inspection at the calibration, image cleaning and background separation stages showed that the unstable arrival times did not have a significant effect on the data. Most importantly, the

extracted arrival times of shower events were comparable for all sequences. As another check, sequences 1002707 and 1002713, having the earliest average arrival times, were calibrated with a special signal extractor, determining the signal at the pulse maximum instead of at half of the rising flank, which makes the procedure more robust against early pulses. There were no significant differences between the standard and the specially calibrated data apart from the expected increased arrival time for calibration and shower events, confirming that the standard extractor works well also for the data with the earliest arrival times.

- **Inhomogeneity** The camera acceptance was not homogeneous in this time period, as shown by the distribution of the *CoGs* of the showers in Figure 6.6. Surprisingly, the inhomogeneity quality parameter values, being well below the acceptable limit of ~ 13, indicate a quite homogeneous camera (see Table B.4). The reason for this problem could not be determined. Obviously it was not due to bad pixels or stars in the field of view, which normally are causing these features. After applying the *area* cut, the effect was less pronounced, but still a deficiency of showers especially at one of the wobble positions (at $\mathrm{y} = 0\,\mathrm{mm}, \mathrm{x} = +0.4\,\mathrm{mm}$) was apparent. This could in principle induce fake signals in the ϑ^2 plot by lowering systematically the background counts towards smaller ϑ^2 values. Therefore a detailed quality check has been performed (see Section C.2.1), showing that the deficit of events is not exhibiting a significant effect on the results.

- **Muon Ratio** The *ratio* for period 72 turned out to be too high (mean of $\sim 105.8\,\%$) for the automatically processed data due to having used a standard, not tested value for the spline calibration factors in MARS. This would lead to an overestimation of the shower size and hence a wrong energy estimation. The shutdown of the telescope may be a reason for the considerably altered values. After determining the calibration factors anew[7] (the mean value for the period changed by $> 5\,\%$ from 0.9751 to 0.9218, where $\pm\,4\,\%$ is still acceptable) and reprocessing the data, the ratio was still above 100 %, but within the quality limits (see Figure 6.7). Though the *ratio* values for the 1ES 2344+514 data of period 73 were showing a large scatter in Figure 6.7, the mean ratio throughout the period ($\sim 100.4\,\%$) did not require the determination of new calibration factors. After quality selection, the observation time-weighted mean *ratio* for the period 73 1ES 2344+514 data reached an acceptable value of $\sim 101.6\,\%$ (see also Table B.4).

- **Missing Starguider Information** For some sequences, pointing information from the starguider was not available. For sequence 1002943 this was due to starguider LEDs accidentally not switched on for the first ~ 30 minutes, for sequences 1003142 and 1003260 clouds seem to be the reason though the *cloudiness* was only at medium values. For these sequences, the starguider correction could partly not be applied. As the wind speed was low or only moderate ($\lesssim 16$ km/h) and rather constant (change over sequence observation time $< 6\,\mathrm{km/h}$) and the zenith distance

[7] The new factor has been determined by dividing the old calibration factor by the average of all ratio values for that period for sequences having more than 300 identified muon events (Meyer 2008). All sequences used were processed with the newest MARS release.

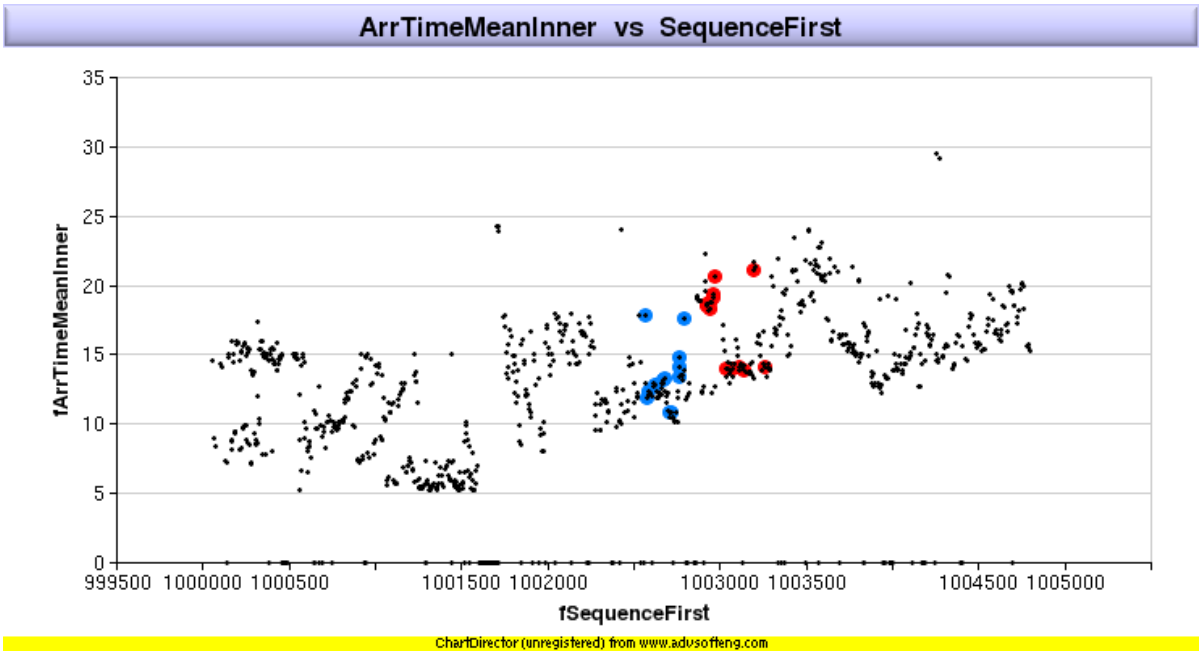

Figure 6.5: Mean arrival times for inner pixels for automatically processed sequences in the sequence range 1000000 to 1004800 (∼ early August 2008 until ∼ early February 2009). The arrival times of outer pixels show a similar distribution. The data of 1ES 2344+514 are marked by blue (period 72) and red (period 73) dots. Note that the values may have changed for the actually analysed sequences due to removal of data runs. The plot has been made with the tool ChartDirector.

did not change much during the observations (at maximum by 3.5°) as well as the pointing of the telescope was rather good at the time of observations (T. Bretz & M. Garczarczyk, 2008, private communication), no significant mispointing is expected. A potential influence cannot be evaluated from the corresponding quality plots as the individual signals were too low. But comparing the results from the "all" data set with and without starguider correction, only marginal differences are found between the sky map as well as ϑ^2 plots. This indicates that the amount of correction calculated from the starguider data was very small and consequently, taking into account the stable observation conditions, partly missing starguider information should generate a marginal mispointing only. This interpretation could be confirmed on Crab Nebula data taken at the same night as sequence 1003142, showing (1) a well-centred signal when using the most recent starguider model and (2) only a small offset when switching off the starguider correction (see Figure C.17).

Figure 6.8 proves the good data quality by means of the data rate vs. zenith distance before (left side) and after (right side) quality selection. The reference lines have been calculated according to the expected rate decrease with zenith distance, i.e.

$$\text{rate} = R_0 \cdot (\cos(\text{zd}))^{0.5} \tag{6.1}$$

where R_0 is the reference rate at zd = 0. In this case, R_0 is chosen as = 220 Hz. The lower value of 87 % of the reference line has been chosen arbitrarily. Obviously sequence

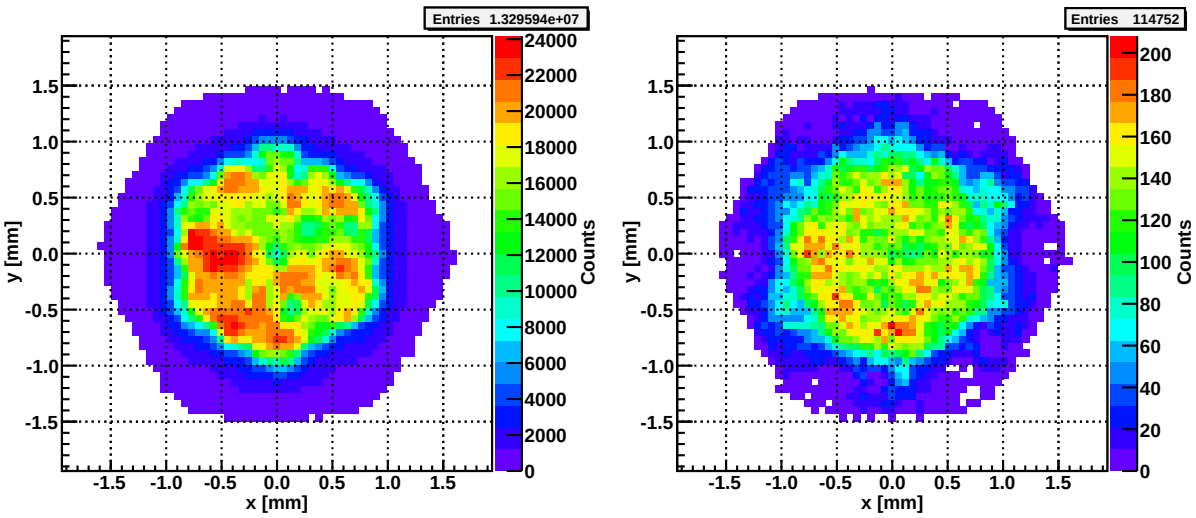

Figure 6.6: Center of gravity distributions of shower events in the MAGIC-I camera plane before (*left*) and after (*right*) applying the *area* cut (but without ϑ^2 cut) for the "all" data set. A deficit of events is clearly visible at some camera locations before cuts. After cuts, the camera is much more homogeneous, but still two small holes remain, one of which is located near one of the wobble positions.

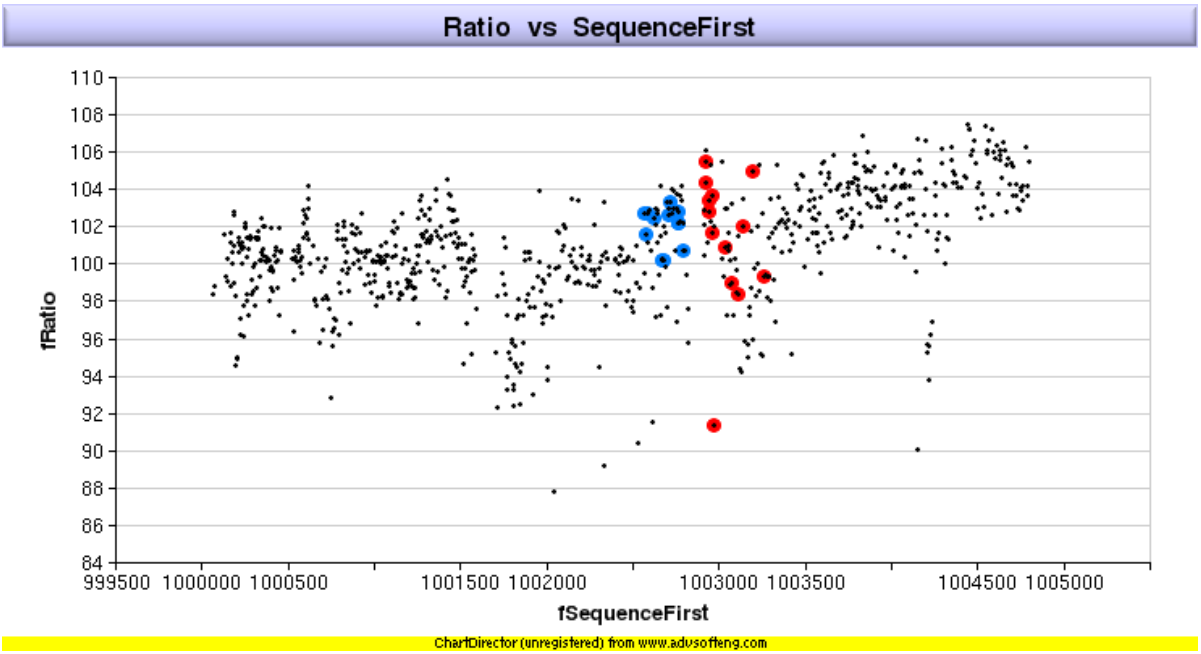

Figure 6.7: Same as Figure 6.5, but showing the evolution of the muon *ratio*. Data points below a *ratio* of 90 are not shown for clarity.

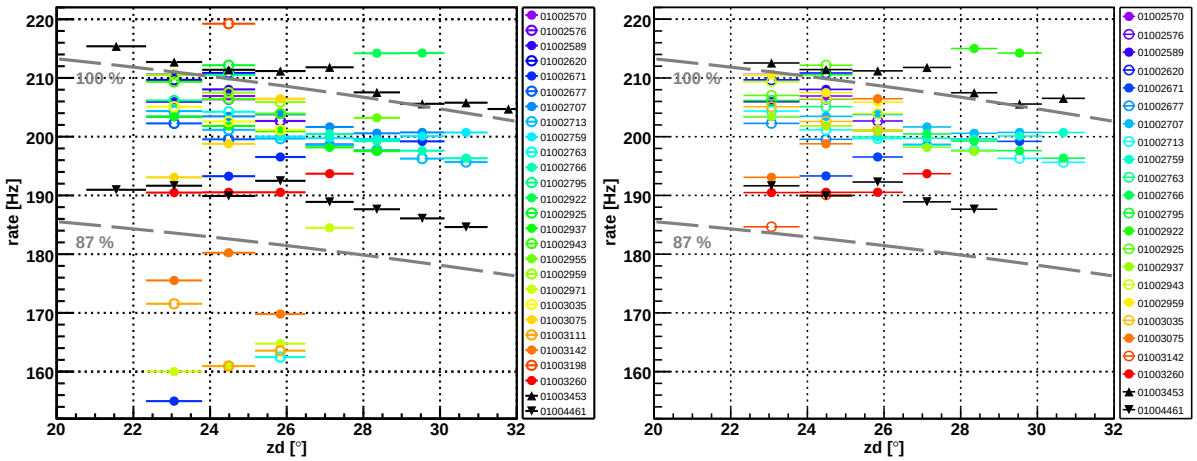

Figure 6.8: Data rate after cleaning for all sequences of 1ES 2344+514, one sequence of Crab Nebula (1004461) and one sequence of Mrk 421 (1003453) vs. zenith distance. The legend entries correspond to the sequence numbers. The dashed lines indicate the reference rates which have been used as a quality criteria where 100 % means a rate of 220 Hz at zd = 0. *Left side:* automatically built sequences from the Würzburg data center, *right side:* sequences edited manually according to quality criteria.

1002922 is significantly above the 100 % reference line, despite being taken shortly after sunset (which demands higher DT values, causing a lower rate). After some investigations this seems to be due to a higher PMT current level (increased by ∼10 %, although surprisingly the PedRMSIn value is normal), presumably due to the small duration of the sequence (∼8 min) in combination with a too low initial DT value ("dark time" instead of "twilight" setting) which did not allow the individual pixel rate control, adapting the DTs, to stabilise the rates for these twilight observations. Being this the correct interpretation, the additional events will be triggered by noise of low *size*, which is being removed in the further analysis steps anyway and hence should not influence the final result. Figure 6.9 is confirming this interpretation, showing that sequence 1002922 has more low *size* events than most of the other sequences.

6.3.2 Gamma – Background Separation

Separation Cut Optimisation In principle, the good data quality and standard observation conditions do not require the utilisation of dedicated separation cuts; the standard cuts give robust results for various time periods and source spectra. However, these have been optimised for rather strong signals and do not represent the most sensitive separation cuts. Taking into account that the standard cuts yield a significance of only 2.9 σ for 1ES 2344+514, a dedicated cut optimisation was performed.

The optimisation has been conducted on data of Mrk 421 from 5 December 2008 (see Table 6.1) for which also the new pointing model was used. Apart from these data, close-by observations[8] with similar zenith distances were only available for the Crab Nebula. Mrk 421 is favoured over the Crab Nebula for optimisation, being a nearby AGNs same as 1ES 2344+514. To average out potential biases in individual data sets, optimisations

[8]Time period searched: October 2008 (data after the shutdown) until February 2009 (thunderstorm damaging parts of the telescope)

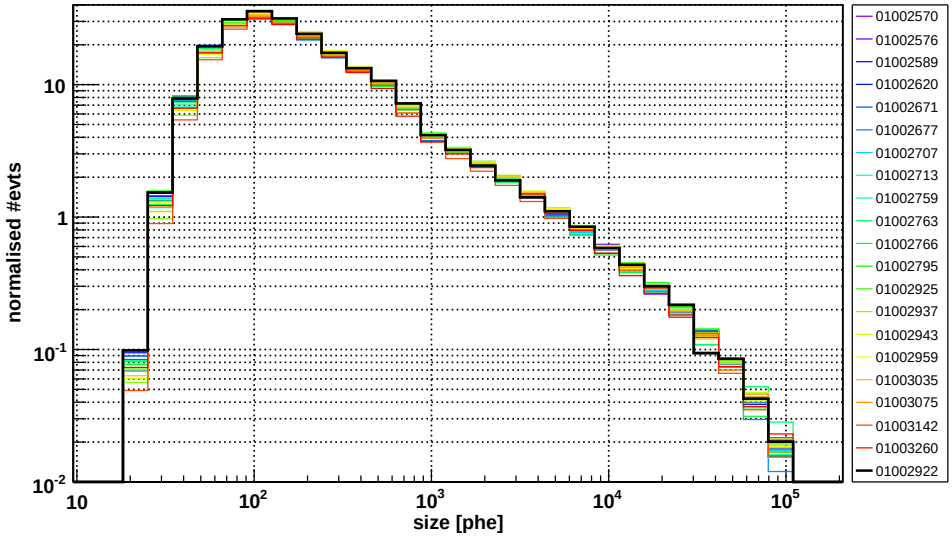

Figure 6.9: *size* distribution normalised to the effective on-time for the good quality sequences of 1ES 2344+514. Compared to the other sequences, sequence 1002922 has the highest event statistics at *sizes* $\lesssim$ 170 phe.

should be performed on sufficiently large data sets. The Mrk 421 observations were rather short, but exhibit on the one hand a strong signal, on the other hand the observation conditions and quality parameters match well the ones of 1ES 2344+514 and do not show hints of problems. The rate was higher than for most of the 1ES 2344+514 data, which is due to a lower DT setting and therefore caused dominantly by low energy triggers which will be removed in the subsequent analysis chain anyway. Also the calibrated pulse position of calibration and shower events was comparably high, but from the performed checks it is obvious that the arrival times could be extracted correctly. The extinction measurements performed by the CMT telescope indicate a minor presence of absorbing particles in the air.

To find the best suited cuts for 1ES 2344+514, not only the standard optimisation strategy kSignificanceLogExcess has been used on Mrk 421, but also kWeakSource, kWeakSourceLogExcess and kSignificance. The range of starting *area* parabolas for the optimisation has been systematically covered as shown in the top left panel of Figure 6.10 by changing the second *area* parameter from 5.4 to 6.1 in steps of 0.1. For each of these parabolas, ϑ starting values of 0.18 (rather low) and 0.22 (rather high) have been used. From all the parabolas resulting for each optimisation strategy, the ones with the highest significance have been investigated for regions in which several of them are converging, indicating convergence of the whole optimisation procedure. In each of these regions, one parabola yielding the highest significance as well as good excess and background event statistics has been chosen. For each kWeakSource and kWeakSourceLogExcess, one of these regions was found, whereas for the other two strategies, one region above ("high") and below ("low") the standard area cut has been determined. All the "best" convergence parabolas are shown in the bottom right plot of Figure 6.10. As 1ES 2344+514 was rather faint during the MW campaign, the harder cuts in the lower region were preferred in order to remove more of the highly dominating background compared to the softer cuts.

Therefore, "kSignificance high" and "kSignificanceLogExcess high" were excluded, and "kSignificanceLogExcess low" was chosen as the optimal separation parabola (yielding 284 excess events compared to 227 from "kSignificance low"), being given by the following parameters (see Eq. 4.14):

$$\begin{aligned} \vartheta &= 0.187 \\ c_8 &= 0.202 \\ c_9 &= 0.0813 \\ c_{10} &= 5.65 \end{aligned}$$

With these cuts, Mrk 421 was detected with a significance of $17.3\,\sigma$ and 283 excess and 100 background events, compared to $16.1\,\sigma$, 280 excess and 124 background events determined from the standard cuts analysis (note that during the optimisation, the full precision of the cut parameter values is applied, whereas for the source analysis, the precision is reduced to a more robust 3 digit value which may lead to a small difference between the optimisation and analysis results).

Data Sets and Results The data of 1ES 2344+514 were analysed on an overall as well as period-wise and daily time scale as shown in Table 6.1. Applying the optimised cuts to the "all" data set of 1ES 2344+514, a faint signal of $3.5\,\sigma$ with 217 excess and 2775 background events has been found (see Figure 6.11). The signal is well centred in the FS plot but smeared out, which is due to the low signal and low excess statistics (see Figure 6.12). To exclude the signal to be a result of the camera inhomogeneity, an analysis using only 1 Off region has also been performed (see Section C.2.1).

Sanity Checks Figure 6.13 shows the excess and background rates of 1ES 2344+514 after applying the optimised separation cuts. Deviations larger than $3\,\sigma$ from the mean background rate were not visible, and the excess and background rates seemed not to be dependent on each other, confirming that the new cuts did not introduce systematic biases.

A wrong background scaling may fake a signal in the ϑ^2 plot, because of which the On and Off distributions in the α and ϑ^2 plots have been checked for a mismatch for all data sets. Special care had to be used for data set 2016, having only 1 wobble position. No such significant mismatch has been found. For some data sets, statistics was not sufficient to assess a possible scaling problem, but for the overall ϑ^2 (Figure 6.11) and α plot, a good match between On and Off was found.

6.3.3 Spectrum Derivation

Spectrum Cuts The spectrum could not be derived by using efficiency cuts (see Section 4.3.3.4) as these result in a complete loss of the signal, presumably due to the large background. Also opening the area cut parabola in different configurations resulted in a strong signal reduction. Therefore, only the ϑ parameter has been opened slightly, from 0.187 to 0.215, where the latter is the standard cuts value.

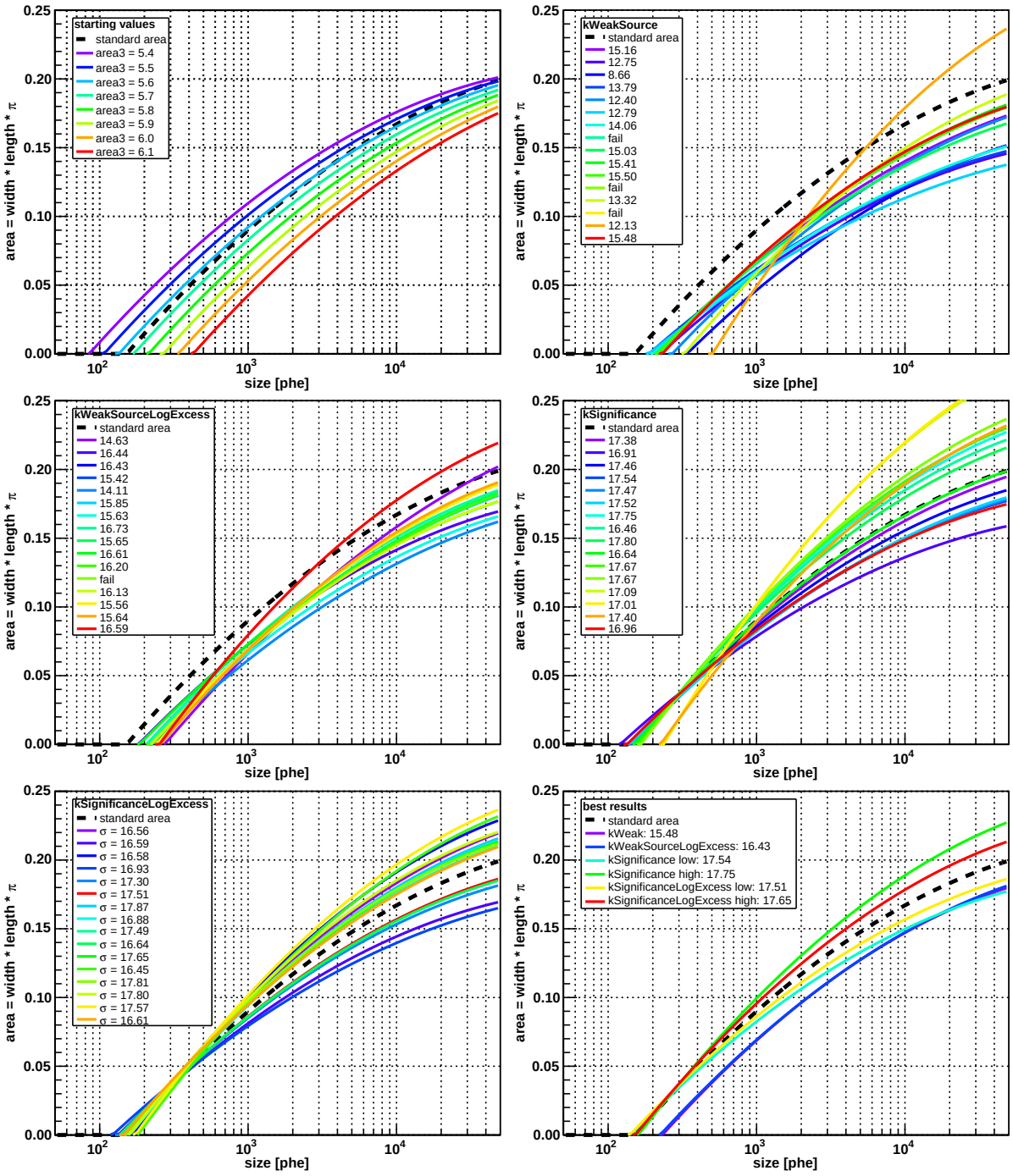

Figure 6.10: *Top left:* starting *area* parabolas for optimisation on Mrk 421 data. *Top right, middle panel and bottom left: area* parabolas after optimisation using the optimisation strategy as given in the legend caption, where for each starting parabola two ϑ starting values have been used, consequently yielding two times more resulting than starting parabolas. For each parabola, the resulting significance is given in the legend, where "fail" indicates that the optimisation procedure did not converge. For kSignificanceLogExcess, the red parabola is giving the cut chosen for the analysis of 1ES 2344+514. *Bottom right:* Best parabolas from the convergence regions of the different optimisation strategies.

Data Set[a]	**Sequences**	**Zenith Dist.**[b] [°]	**On-Time**[c] [h]	**Ext.**[d] [%]	**Sign.**[e] [σ]	**Exc.**[f]	**Bgd.**[g]	**Wobble Ratio**[h]
all	1002570 – 1003260	23 – 31	20.75	...	3.5	217	2775	1.06
AGILE	1002922 – 1003142	23 – 29	9.69	...	2.7	115	1312	1.05
period 72	1002570 – 1002795	23 – 31	10.26	...	1.9	80	1382	1.11
period 73	1002922 – 1003260	23 – 29	10.49	...	3.1	137	1393	1.02
21 October	1002570 & 1002576	23 – 26	1.42	0.46	1.3	22	192	1.04
22 October	1002589	23 – 25	1.41	0.55	0.6	8	182	0.88
23 October	1002620	23 – 24	1.35	0.46	1.1	17	172	1.06
24 October	1002671 & 1002677	23 – 30	1.42	...[i]	0.4	5	174	1.04
25 October	1002707 & 1002713	23 – 31	3.22	0.37	1.5	38	456	1.47
26 October	1002759 – 1002766	25 – 31	1.14	...[i]	0.0	0	165	1.38
28 October	1002795	23 – 24	0.30	0.18	−2.0	−13	40	...[j]
17 November	1002922 & 1002925	23 – 29	1.03	0.09	2.5	36	143	2.27
18 November	1002937 & 1002943	23 – 29	2.14	0.73	−0.1	−1	333	0.71
19 November	1002959	23 – 26	1.77	0.92	2.0	36	238	0.87
24 November	1003035	23 – 26	2.12	0.09	1.2	25	295	1.19
25 November	1003075	23 – 26	2.01	0.92	1.4	26	242	1.04
28 November	1003142	23 – 25	0.62	2.19	−1.2	−10	61	1.37
01 December	1003260	23 – 27	0.81	...[i]	2.0	21	81	0.68
Mrk 421	1003453	23 – 31	0.68	5.03	17.3	283	100	0.93
Crab	1004461	22 – 29	0.41	0.73	14.0	177	57	1.19

Notes. [a] The date corresponds to the day following the observation night. [b] Zenith distance range of the observations. [c] Effective observation time. [d] Atmospheric extinction measured by the CMT telescope on La Palma. [e] Significance of the signal calculated using Li & Ma (1983) Eq. 17 and optimised cuts. [f] Number of excess events. [g] Number of background events. [h] Ratio of time spent in each of the two wobble positions. [i] No CMT observations available. [j] Data taken during one wobble position only.

Table 6.1: Data set information and analysis results for 1ES 2344+514, besides the last two data sets, where the Mrk 421 have been taken 5 December 2008, the Crab Nebula data 24 January 2009. All observations have been conducted in wobble mode with 3 Off regions (scale factor $f = 1/3$).

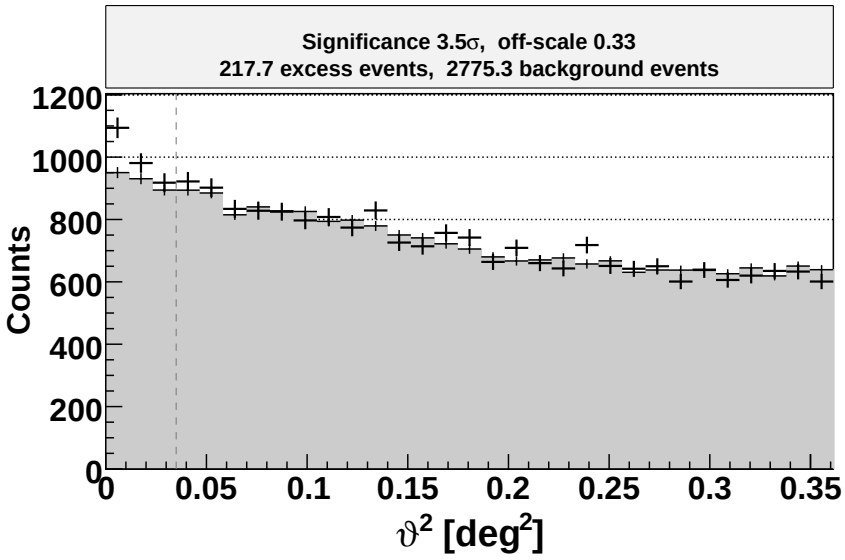

Figure 6.11: ϑ^2 plot for the "all" data set of 1ES 2344+514. The grey-shaded area shows the background event distribution. The vertical dashed line indicates the ϑ^2 cut. Note that the plot has been produced including the anti-theta cut.

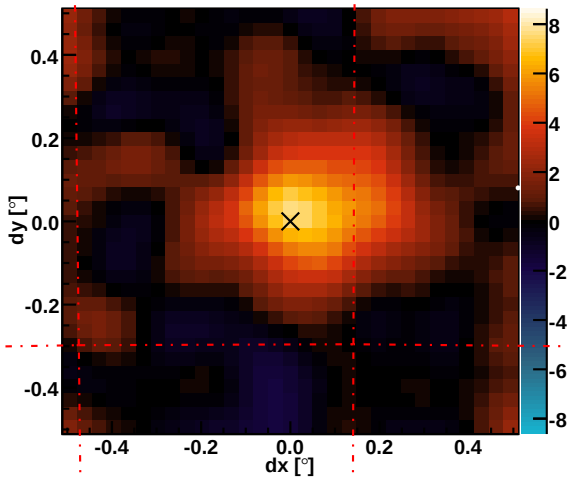

Figure 6.12: Background-subtracted distribution of reconstructed event directions on the sky smeared out with half of the MAGIC-I PSF (FS plot). The white spot on the left side marks a star.

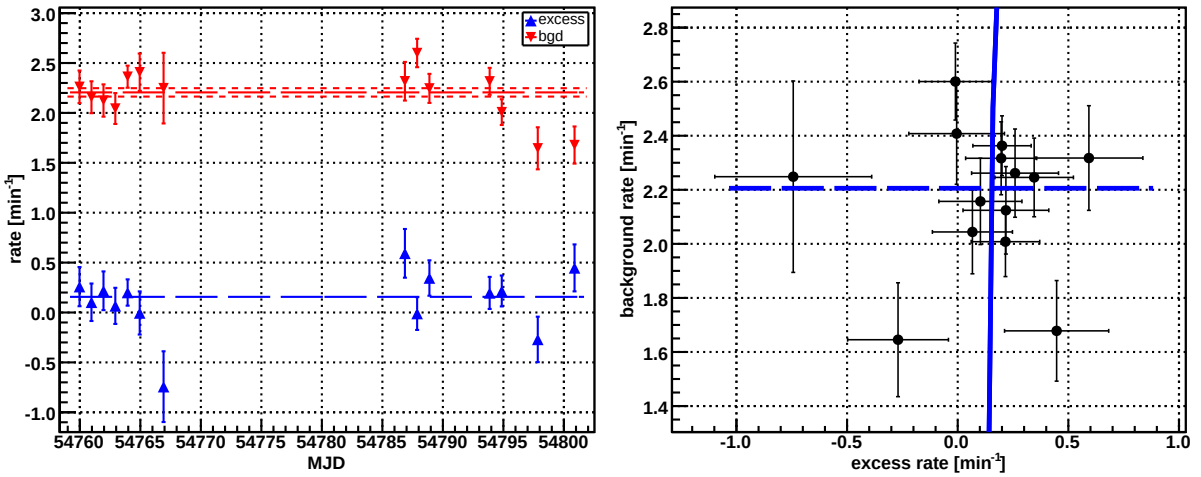

Figure 6.13: Excess and background rates of the daily data sets after separation cuts for 1ES 2344+514. *Left side:* The long-dashed lines denote a fit with a constant, the short-dashed lines visualise the errors of the fit to the background rate. *Right side:* The dashed line corresponds to a fit with a constant, whereas the solid line shows a linear fit.

Differential Spectrum For all data sets the feasibility of deriving a spectrum after opening the cuts has been tested. As expected, this was only possible for the "all", "AGILE" and "period 73" data sets. For the others, the signal and event statistics were too small. For the latter two no spectrum has been derived because (i) the light curve of 1ES 2344+514 was consistent with constant during the observations (see below) and the two data sets are part of the "all" data set, so no strong change in flux with respect to the "all" result is expected, (ii) establishing a significantly different spectral index than found for the "all" data set would hardly be possible due to the large error bars of the "all" spectrum (see below) and (iii) the AGILE and *Fermi*-LAT observations did not result in a detection of the source at the time of the MW campaign, leaving the second SED peak largely unconstrained even when having a VHE spectrum comparable to the "all" one. For some daily data sets where the MW coverage was promising (28/10, 17/11 and 01/12), the usefulness of upper limits (95 % c.l.) for SED modelling has been evaluated, but none of them could set significantly more stringent constraints on the SED than the "all" spectrum.

The MCs used for energy estimation are listed in Table D.3. They have been chosen according to the DAQ type, observation mode, zenith distance as well as PSF of the data. From the MCs, an analysis threshold for the "all" data set of ~ 190 GeV was determined.

The energy range and binning of the 1ES 2344+514 spectrum has been determined as discussed in Section 4.3.3.4. Figure 6.14 shows the distribution of simple power law spectral indices resulting from several input spectral indices and the distribution of resulting spectral indices. A fit with a Gaussian (χ^2/d.o.f. = 1.5/5) to the latter yields a mean of 2.38 ± 0.01, which has been chosen as the final spectral index. To determine the final binning, bin scans with 3, 4 and 5 bins in the aspired final energy range have been conducted. Note that using this technique the individual bin widths are changing, reducing the included signal and event statistics and potentially revealing holes in the spectrum. The holes especially at high energies can be explained with statistical

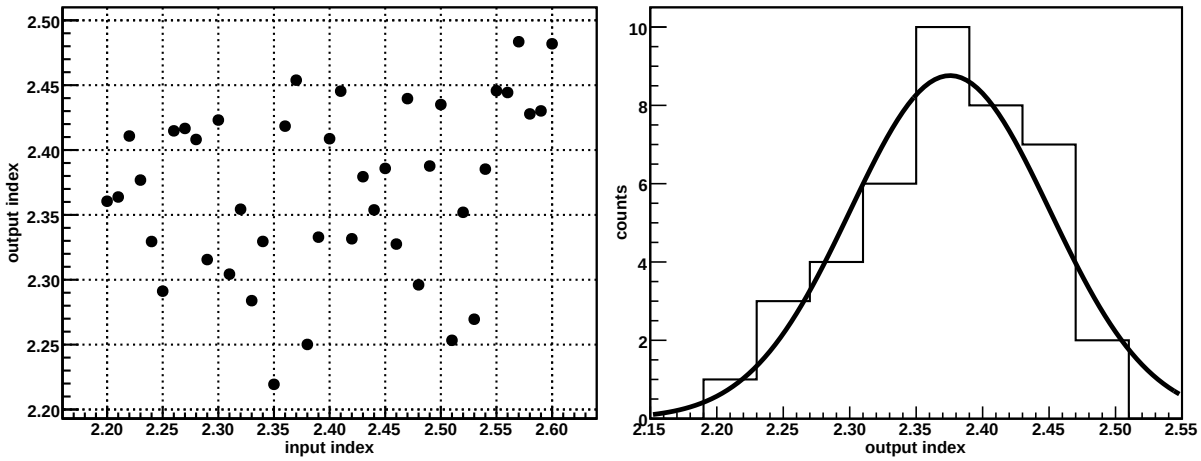

Figure 6.14: *Left side:* Simple power law spectral indices used as input for deriving the spectra versus the output spectral index. A significant clustering or trend cannot be seen over the investigated input parameter range. *Right side:* Distribution of simple power law output spectral indices fitted by a Gaussian function. The fit has a mean of 2.38 ± 0.01.

fluctuations, though. As an example, the results for 4 bins using different upper and lower energy bounds are shown in the left side of Figure 6.15. A hole is visible around 700 GeV, which is apparent only for small bin widths and hence presumably caused by statistical fluctuations. At ~ 2 TeV, event statistics are becoming crucial also for broader bins, but it is obvious that still events are above that limit. Using a binning of 3 bins, these events can be included in the spectrum, as the right side of Figure 6.15 is showing. The latter plot is proving that the spectral shape does not depend strongly on the binning, and that the final spectrum is close to the mean of all the spectral shapes.

The final spectrum of 1ES 2344+514 was described well (χ^2/d.o.f. = 0.36/1) from 160 to 3400 GeV by a simple power law:

$$\frac{\mathrm{d}N}{\mathrm{d}E} = (3.98 \pm 1.21) \cdot \left(\frac{E}{0.5\,\mathrm{TeV}}\right)^{-(2.38\pm0.43)} 10^{-12}\,\mathrm{ph\,TeV^{-1}\,cm^{-2}\,s^{-1}} \qquad (6.2)$$

After correcting for attenuation effects caused by the EBL using the model of Kneiske & Dole (2010), the spectrum could be well fit (χ^2/d.o.f. = 0.36/1) by

$$\frac{\mathrm{d}N}{\mathrm{d}E} = (4.83 \pm 1.47) \cdot \left(\frac{E}{0.5\,\mathrm{TeV}}\right)^{-(2.18\pm0.43)} 10^{-12}\,\mathrm{ph\,TeV^{-1}\,cm^{-2}\,s^{-1}} \qquad (6.3)$$

Both spectra and their fit residuals are shown in Figure 6.16. The individual spectral points are listed in Table D.4.

Light Curve The light curve threshold was determined as given in Section 4.3.3.4 using the "all" data set of 1ES 2344+514. No clear evolution or structure was visible from Figure 6.17, showing the energy dependency of the significance of the signal. A lower energy border of 170 GeV was yielding a high significance, was in accordance with the energy range of the derived spectrum and was only slightly below the analysis threshold. Though it may seem that the point was located at higher values due to a fluctuation,

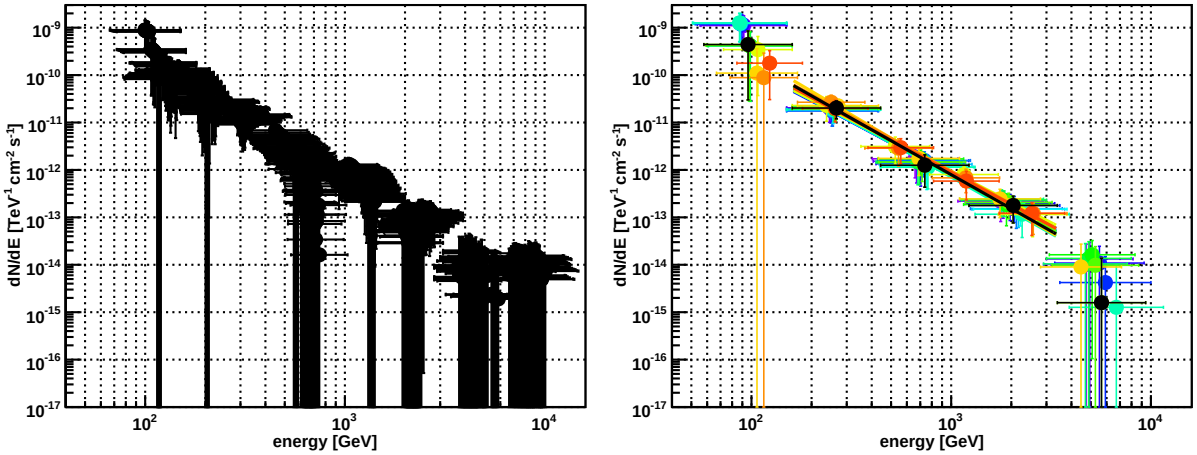

Figure 6.15: *Left side:* Spectra of the "all" data set of 1ES 2344+514 using the final spectral index and different binning setups. The number of bins in the aspired energy range is kept constant (here: 4) whereas the lower and upper energy border is changed continously. *Right side:* Spectra having significant ($\geq 1.5\,\sigma$) bins in the aspired energy range resulting from the bin scans with 3, 4 and 5 bins. Fits with a simple power law are also shown. The black points and curve represent the final spectrum of 1ES 2344+514. For both plots, the first bins are shown here for illustrative purposes only, they are not meaningful. The last bins are not considered relevant due to low event statistics and low significance.

even if true this would not be of major importance for the light curve as the "all" data set is not used for that plot. Hence the light curve threshold has been set to 170 GeV. Above 15 TeV, no more excess or background events were found, which was consequently chosen as the upper energy border for the light curve. The light curve of 1ES 2344+514 has been investigated on a daily and period-wise data basis, the results of which are shown in Figure 6.18. The mean flux determined from all data turned out to be $(7.37 \pm 2.06) \cdot 10^{-12}\,\mathrm{ph\,cm^{-2}\,s^{-1}}$ or $\sim 2.7\,\%$ of the published MAGIC-I Crab Nebula flux above 170 GeV. Significant variability was not found on daily or period-wise scales. A fit with a constant yielded a probability of only 12.3 % (χ^2/d.o.f. = 19.0/13) and 4.6 % (χ^2/d.o.f. = 4.0/1), respectively. The results are summarised in Table 6.2.

Sanity Checks To check the robustness of the derived spectrum, Figure 6.20 compares the final 3 bin spectrum of 1ES 2344+514 with a spectrum consisting of only 2 and of 4 bins as well as a 3 bin spectrum derived from an analysis using only 1 Off region. The spectra are well compatible with each other, showing that binning effects are negligible and that the spectrum is hardly influenced by the camera inhomogeneity (see Section 6.3.1).

The correctness of the applied analysis pipeline has been verified on data of the Crab Nebula (sequence 1004461, see Table 6.1) using the same detection and spectrum cuts as for 1ES 2344+514. The quality parameters of this sequence matched well the 1ES 2344+514 ones, though the PSF, muon *ratio* and DTs were higher, the latter one probably causing the rather low rate of the sequence. Nevertheless the rate was well within the quality limits, and the *ratio* was just compatible with the mean *ratio* of the 1ES 2344+514 data (102.0%). Due to the higher PSF, different MCs had to be used, as listed in Table D.3.

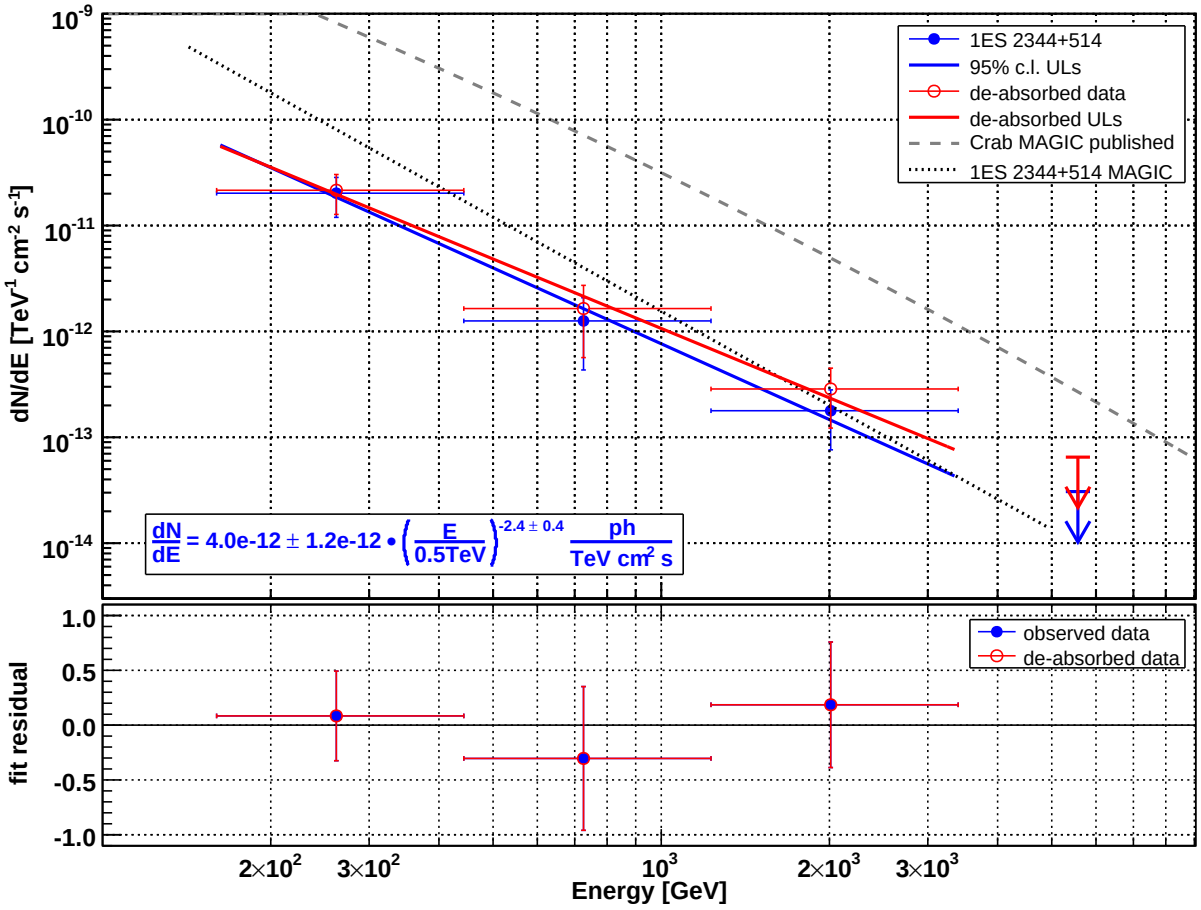

Figure 6.16: *Top panel:* measured (blue, full circles) and EBL de-absorbed (red, open circles) differential VHE spectrum for the "all" data set of 1ES 2344+514. For comparison, also the measured MAGIC-I spectrum from 2005/2006 (Albert *et al.* 2007d) and the MAGIC-I Crab Nebula spectrum is shown. *Bottom panel:* distribution of simple power law fit residuals for the measured (full blue circles) and EBL de-absorbed (open red circles) data.

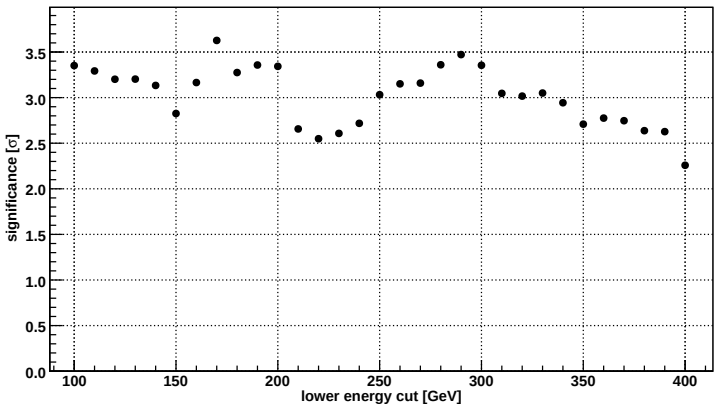

Figure 6.17: Dependence of the signal significance on a lower energy cut for the "all" data set of 1ES 2344+514 using spectrum cuts.

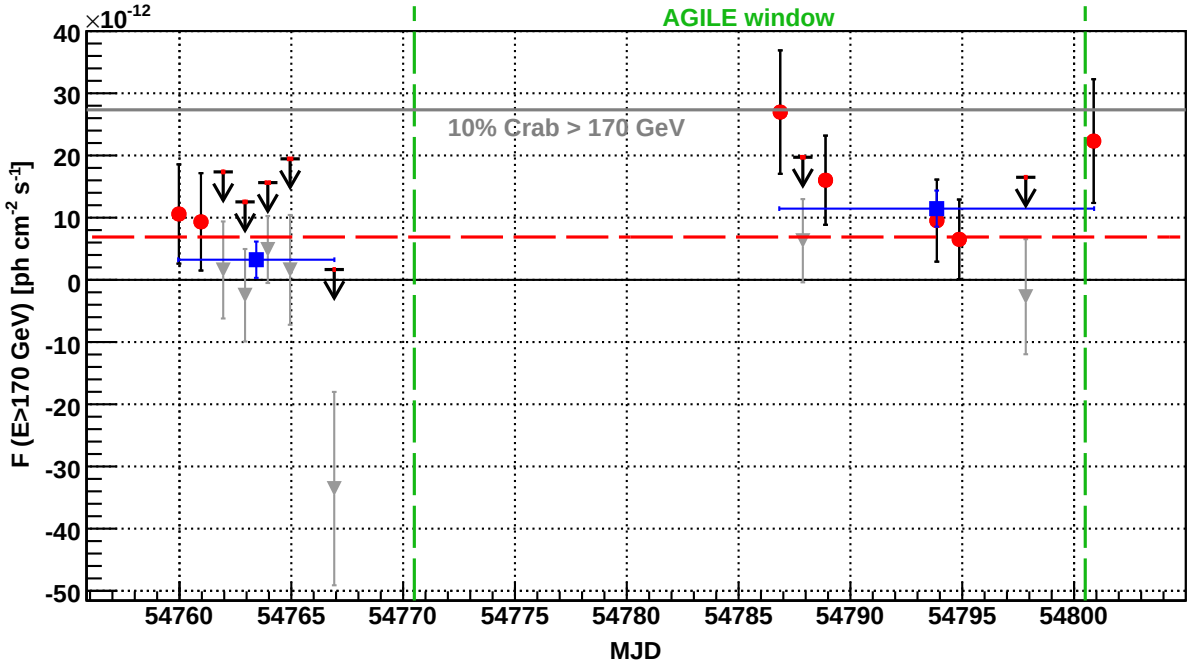

Figure 6.18: Light curve of 1ES 2344+514 during the MW campaign. Full circles represent the daily fluxes, where the flux of grey triangles is consistent with zero or negative. For the grey triangles, 95 % c.l. UL were calculated, and the observation length is indicated by the red bar on top of the UL arrow. Blue squares show the fluxes from period 72 and 73. The vertical dashed lines are visualising the observation window of AGILE. The red horizontal dashed line shows a fit with a constant to the daily data points. The horizontal solid line shows the integral flux between 170 GeV and 15 TeV calculated from the published MAGIC-I spectrum (Albert *et al.* 2008e).

The detection cuts yielded a signal of $14.0\,\sigma$ (see Figure 6.19), corresponding to $21.9\,\sigma/\sqrt{h}$. The reference sensitivity using standard cuts for the Crab Nebula amounts to $19.8\,\sigma/\sqrt{h}$ (T. Bretz, 2007, private communication). Note though that the data on which this reference value has been derived were taken partly at high PedRMSIn conditions. Nevertheless the comparison indicates a sensitivity of this analysis above the standard. Expressed in integral flux, the sensitivity amounts to 1.76 % of the Crab Nebula in 50 hrs with $5\,\sigma$ above 170 GeV assuming a 1ES 2344+514-like spectrum for the Crab Nebula.

The Crab Nebula spectrum derived with the 1ES 2344+514 cuts is shown in Figure 6.20, from which a good agreement with the published MAGIC-I Crab Nebula spectrum (Albert *et al.* 2008e) was evident. Both spectra could be described by a curved power law of the form

$$\frac{d\mathrm{N}}{d\mathrm{E}} = f_0 \cdot \left(\frac{E}{0.3\,\mathrm{TeV}}\right)^{-(a+b\log_{10}(E/0.3\,\mathrm{TeV}))} \tag{6.4}$$

with $f_0 = (6.0 \pm 0.2) \cdot 10^{-10}\,\mathrm{ph\,TeV^{-1}\,cm^{-2}\,s^{-1}}$, $a = 2.31 \pm 0.06$ and $b = 0.26 \pm 0.07$ for the published spectrum and $f_0 = (7.1 \pm 0.7) \cdot 10^{-10}\,\mathrm{ph\,TeV^{-1}\,cm^{-2}\,s^{-1}}$, $a = 2.27 \pm 0.24$ and $b = 0.24 \pm 0.43$ for the spectrum derived here. Errors are statistical only. The curvature parameter b is no longer significant for the latter spectrum, which may be due to the reduced energy range compared to the published Crab Nebula spectrum

Data Set[(a)]	**MJD**[(b)]	**Sign.**[(c)] $[\sigma]$	**Exc.**[(d)]	**Bgd.**[(e)]	$F_{>170\,\mathrm{GeV}}$ $[10^{-12}\,\mathrm{TeV}^{-1}\,\mathrm{cm}^{-2}\,\mathrm{s}^{-1}]$
all	54780.419	3.6	215	2554	7.4 ± 2.1
AGILE	54792.339	3.5	143	1168	10.6 ± 3.0
period 72	54763.433	1.1	46	1309	3.2 ± 2.9
period 73	54793.858	4.0	168	1245	11.5 ± 2.9
21 October	54759.973	1.4	21	172	10.6 ± 8.0
22 October	54760.960	1.2	18	163	9.3 ± 7.8
23 October	54761.954	0.2	3	160	< 17.4
24 October	54762.931	−0.3	−5	173	< 12.5
25 October	54763.949	0.9	22	438	< 15.6
26 October	54764.946	0.2	2	159	< 19.5
28 October	54766.919	−2.0	−14	42	$<\ 1.7$
17 November	54786.862	2.9	39	125	27.0 ± 9.9
18 November	54787.873	1.0	19	292	< 19.7
19 November	54788.888	2.3	39	206	16.0 ± 7.2
24 November	54793.866	1.5	28	267	9.5 ± 6.6
25 November	54794.866	1.0	18	229	6.5 ± 6.4
28 November	54797.841	−0.3	−2	49	< 16.5
01 December	54800.879	2.4	25	76	22.3 ± 10.0
Crab	54855.016	14.7	181	51	$(3.24 \pm 0.28) \cdot 10^2$

Notes. [(a)] The date corresponds to the day following the observation night. [(b)] Mid point of observation given in MJD. [(c)] Significance of the signal calculated using Li & Ma (1983) Eq. 17 and opened spectrum cuts. [(d)] Number of excess events. [(e)] Number of background events.

Table 6.2: Analysis results using open cuts for 1ES 2344+514 and the Crab Nebula (from 24 January 2009). ULs are calculated at a c.l. of 95 %.

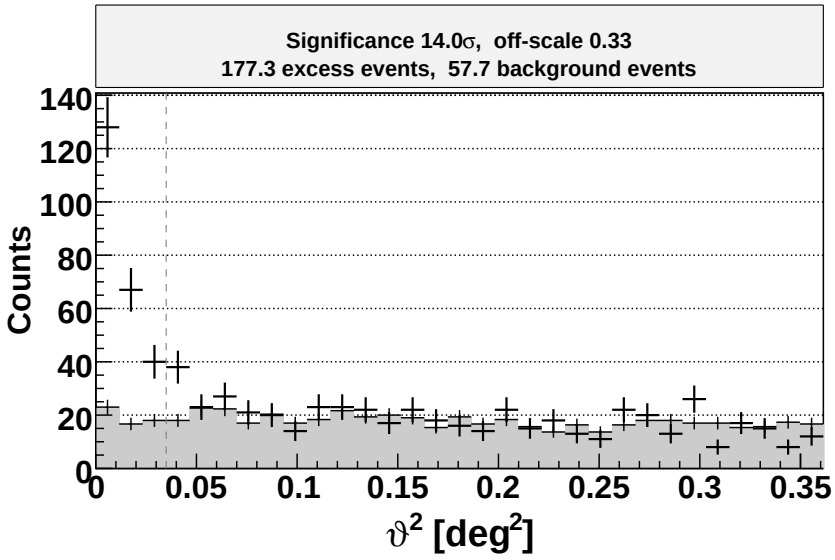

Figure 6.19: ϑ^2 plot for the Crab Nebula taken at similar observation conditions as 1ES 2344+514. For further explanations see Figure 6.11. The signal is clearly broader than the applied ϑ^2 cut. Note though that the cut has been optimised on Mrk 421 data, not for the Crab Nebula.

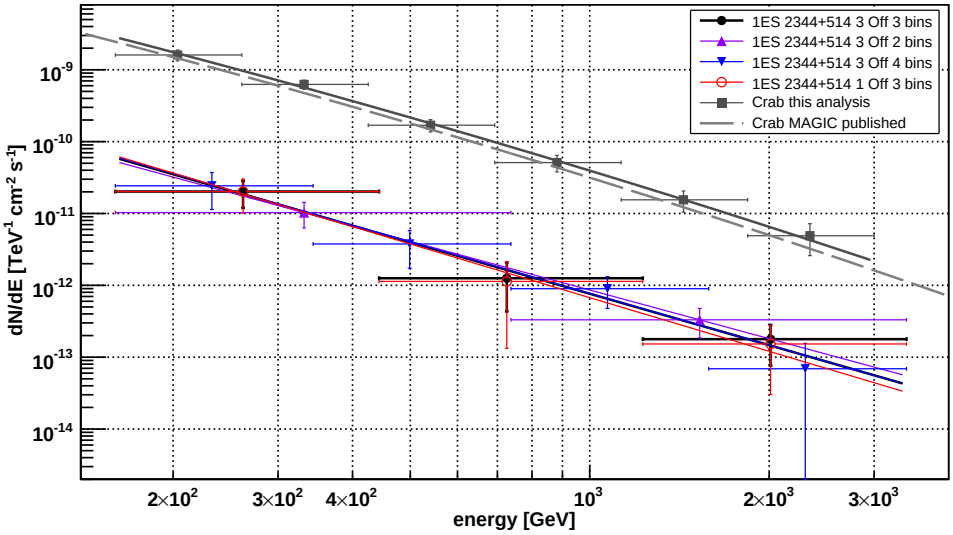

Figure 6.20: Comparison of spectra of 1ES 2344+514 derived by different analysis setups. Besides the final 3 bin spectrum derived with 3 Off regions, a spectrum using 2 and 4 bins is shown as well as a 3 bin spectrum where only 1 Off region has been used. Additionally, the Crab Nebula spectrum derived with the same analysis pipeline is compared to the published MAGIC-I Crab Nebula spectrum.

(maximum energy of 3 TeV and 9 TeV, respectively). Consequently, a simple power law is statistically the better description of the Crab Nebula spectrum ($\chi^2/\text{d.o.f.}_{\text{PL}} = 1.1/4$, $\chi^2/\text{d.o.f.}_{\text{curved}} = 0.8/3$), yielding (see Eq. 2.17) $f_0 = (2.1 \pm 0.2) \cdot 10^{-10}\,\text{ph}\,\text{TeV}^{-1}\,\text{cm}^{-2}\,\text{s}^{-1}$ and $alpha = 2.40 \pm 0.12$.

An indication for a systematically higher flux is apparent, though within the error bars of the individual points negligible. The integral flux from 170 GeV to 15 TeV (see Table 6.2) is $\sim 19\,\%$ above the integral flux calculated mathematically from the published MAGIC-I Crab Nebula spectrum. The source of this effect may on the one hand be the applied analysis pipeline, but on the other hand it cannot be excluded that the measured Crab Nebula spectrum changed slightly with the new MAGIC-I readout hardware installed in 2007. Also a source-intrinsic higher flux cannot be dismissed, taking into account that the Crab Nebula is known to show outbursts at HE (Tavani *et al.* 2011; Abdo *et al.* 2011c; Striani *et al.* 2011; Buehler *et al.* 2012), and also at VHE (insignificant) flux changes of $> 25\,\%$ for MAGIC-I (Strübig 2009) and $\sim 17\,\%$ for the MAGIC stereo system (Aleksić *et al.* 2012e) have been found.

6.3.4 Discussion

The signal found within this analysis of 1ES 2344+514 of $3.5\,\sigma$ is below the VHE standards to claim a source discovery. Considering that 1ES 2344+514 is a long-known source confirmed independently by several TeV facilities and the lack of potential VHE sources in the MAGIC-I field of view around the source (see also Section 6.5.6), a confusion of the signal with another source is highly unlikely. Additionally, the signal is not dominated by a transient event but growing rather constantly with time (see light curve in the previous section). Finally, the long observation time of ~ 21 hrs and fairly large events statistics of ~ 220 excess events makes us confident that the signal is real and com-

Data Set	Sign.[a]	$F_{>200\,\mathrm{GeV}}$[b]	$F_{>300\,\mathrm{GeV}}$[b]	$F_{>350\,\mathrm{GeV}}$[b]	$F_{>970\,\mathrm{GeV}}$[c]	Ref.[d]
Whipple avg	5.8	...	...	1.7 ± 0.5	...	(1)
Whipple flare	5.3	...	...	6.6 ± 1.9	...	(1)
HEGRA avg	4.4	...	...	...	6.0 ± 1.9	(2)
MAGIC-I 2005/6	11.0	2.38 ± 0.30	...	...	...	(3)
VERITAS avg	...	...	1.06 ± 0.09	...	...	(4)
VERITAS flare	20.2	...	6.76 ± 0.62	...	...	(4)
This campaign	3.5	0.55 ± 0.17	0.34 ± 0.10	0.23 ± 0.09	4.8 ± 3.1	...

Notes. [a] Significance of the signal. [b] Integral flux in units of $10^{-11}\,\mathrm{ph\,cm^{-2}\,s^{-1}}$. [c] Integral flux in units of $10^{-13}\,\mathrm{ph\,cm^{-2}\,s^{-1}}$. [d] References: (1) (Schroedter *et al.* 2005); (2) (Aharonian *et al.* 2004); (3) (Albert *et al.* 2007d); (4) (Acciari *et al.* 2011a)

Table 6.3: Integral fluxes reported in the literature for 1ES 2344+514. "avg" denotes average fluxes. Note that in the case of VERITAS, the flare reported in the following line is not included in the avg data set, whereas for Whipple the flare is included.

ing from 1ES 2344+514. A MAGIC-internal independent analysis confirmed the results presented here.

However, the faintness of the detection does not allow for individual spectra or dedicated short-term (sub-day) variability analyses. A comparison of the integral flux derived here with archival values (see Table 6.3) indicates that 1ES 2344+514 has been observed in one of the lowest VHE flux state reported up to now. Despite that, the spectral index is rather hard, in contrast to the "harder when brighter" trend commonly found for HBLs (see Section 2.3). Such a trend can not be confirmed for 1ES 2344+514 when plotting the spectral index versus the differential flux at 1 TeV, see Figure 6.21. The probability for no correlation amounts to 16.3 % (χ^2/d.o.f. = 7.9/5), whereas a simple power law fit with a probability of 41.5 % (χ^2/d.o.f. = 3.9/4) is not clearly preferred (logarithmic likelihood ratio probability 94.2 %, which is nearly identical to the value of 96.5 % determined before taking into account the results presented here). Due to the rather large uncertainty of the spectral parameters determined here, no firm conclusion can be drawn from these result, though.

Significant variability at VHE has already been reported for 1ES 2344+514 on short (day scale; Catanese *et al.* 1998; Acciari *et al.* 2011a) as well as long (several years; see e.g. Albert *et al.* 2007d) time scales. For the observations presented here, the strongest hint for potential variability on day scale is given by the result from 17 November, which is still compatible with the average flux with $> 2\,\sigma$. Comparing the two observation periods, the corresponding fluxes are also compatible within $> 2\,\sigma$. Overall, the daily light curve is consistent with a constant flux. Hence, no significant variability could be detected from 1ES 2344+514 throughout this campaign. The individual results exclude a flare of a factor > 9 above the mean flux to have happened during the observations, which rules out flux states as reported during the VERITAS flare (~ 20 times higher flux than the mean flux reported here; Acciari *et al.* 2011a).

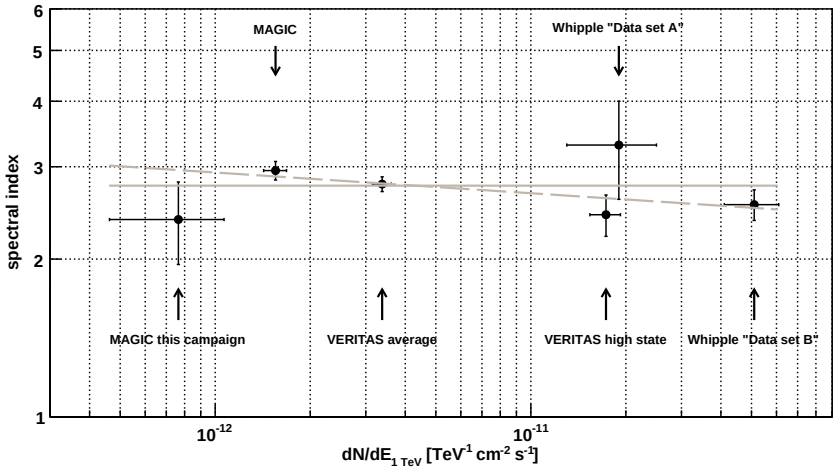

Figure 6.21: Differential flux at 1 TeV versus simple power law spectral indices for 1ES 2344+514 for archival spectra as well as this campaign. The Whipple data have been taken from Schroedter *et al.* (2005), the VERITAS data from Acciari *et al.* (2011a) and the MAGIC-I data from Albert *et al.* (2007d). As the "MAGIC" differential flux is given at 500 GeV, the corresponding value and error has been determined from the spectral fit given in the paper and the relative flux error at 500 GeV, respectively. The solid line is given by a fit with a constant, whereas the dashed line denotes a simple power law fit. Only statistical errors are shown.

6.4 Multi-Wavelength Results

The following sections will summarise the observations, data analysis and results of the instruments besides MAGIC-I that have contributed to the MW campaign. The data will be combined in a multi-wavelength view of the flux evolution of 1ES 2344+514 as well as a simultaneous spectral energy distribution. Though the individual raw data analyses have not been performed by the author, the coordination of the instrument teams, specification of the required analysis end products, assessment, collection and partly conversion and correction of the results as well as the combination of the individual findings in the MW context were part of the present work. Also the *Swift* BAT high level analysis has been carried out by the author, using as basis the published catalogue data.

6.4.1 High Energy Gamma Rays

AGILE The AGILE measurements have been conducted in pointing mode, observing for a large fraction of time the same sky position. 1ES 2344+514 was observed $\sim 40°$ off-axis while pointing to the "Cygnus Field" in the AGILE observation block 6400, lasting from 31 October 2008 to 30 November 2008 (each 12:00:00 UTC). The GRID data analysis is described in detail in Aleksić *et al.* (2012f).

1ES 2344+514 could not be detected by AGILE-GRID during the MW campaign. From an effective exposure of $\sim 2.8 \cdot 10^8\,\mathrm{cm^2\,s}$, a 95 % c.l. UL of $3.7 \cdot 10^{-8}\,\mathrm{ph\,cm^{-2}\,s^{-1}}$ above 100 MeV was derived. For the calculation, a standard spectral index of 2.1 was used, since AGILE did not have detected the source yet using data until January 2011 (F. Longo, L. Lucarelli, C. Pittori & S. Vercellone, 2012, private communication). The

data have also been investigated for potential short flares, searching for a significant signal on time scales of two as well as seven days, without yielding a detection.

Fermi is operating in all-sky mode, observing the whole sky every 3 hrs. For the present analysis, only the *Fermi*-LAT measurements taken in the time period of the MAGIC-I pointings have been investigated, i.e. 20 October 2008 22:35:00 UTC until 30 November 2008 21:31:00 UTC (see also Figure 6.4). Analysis details are given in Aleksić *et al.* (2012f).

Despite an only $\sim 30\,\%$ longer observation time, the effective exposure exceeds the one of AGILE by more than one order of magnitude ($3.7 \cdot 10^9\,\mathrm{cm}^2\,\mathrm{s}$) thanks to the larger effective area of LAT compared to GRID. Nevertheless the source was not detected within the MW time slot. An analysis on a daily and weekly time basis also did not reveal a significant signal from 1ES 2344+514. The sensitivity was high enough though to derive several ULs, as listed in Table E.7.

Interestingly, the overall AGILE UL $> 100\,\mathrm{MeV}$ is slightly below the *Fermi* UL between 100 and 300 MeV despite the higher effective exposure of LAT. This may be explained by the higher sensitivity of the GRID instrument compared to LAT.

6.4.2 X-Rays

***Swift* XRT** MW coverage by *Swift* was achieved by means of short-notice ToO proposals. The observations of 1ES 2344+514 analysed for this campaign spanned the observation IDs 35031019 – 35031040 (September to November 2008) with observation times ranging between $\sim 200\,\mathrm{s}$ and $\sim 5\,\mathrm{ks}$. Details of the individual observations are listed in Table E.8 and visualised in Figure 6.4. Two representative spectra were extracted for the IDs with a good coverage at other wavelengths and an especially low and high flux, respectively. The XRT data analysis has been carried out as described in Aleksić *et al.* (2012f). Potential intra-day flux variability was assessed by studying the publicly available automatically processed quick-look light curves from the *Swift* Monitoring Program[9]. As no conclusive hint of significant variability for the MW data was found, a dedicated intra-day analysis has not been conducted.

The XRT analysis results are listed in Table E.9 and shown in Figure 6.31. The integral flux between 2 and 10 keV was clearly variable during the MW campaign, a fit with a constant yielding a χ^2/d.o.f. of 131.8/18. After three measurements with about the same flux level, an asymmetric flare-type structure was visible with a flux increase by nearly 50 % within two days. From the peak value, the flux declined to the original value within about five days and decreased further for three days to $\sim 80\,\%$ of the flux prior to the flare. In the following, the flux showed an irregular but seemingly increasing behaviour, reaching the highest value during the MW campaign on the last day.

In contrast to the variable flux, the spectral index was consistent with being constant throughout the MW campaign (see Figure 6.31). The goodness of a fit with a constant amounts to 90.5 % (χ^2/d.o.f. = 10.8/18). The hardness ratio (HR) on the other hand, defined here as the excess event count rate ratio r between two energy bands

[9] http://www.swift.psu.edu/monitoring/

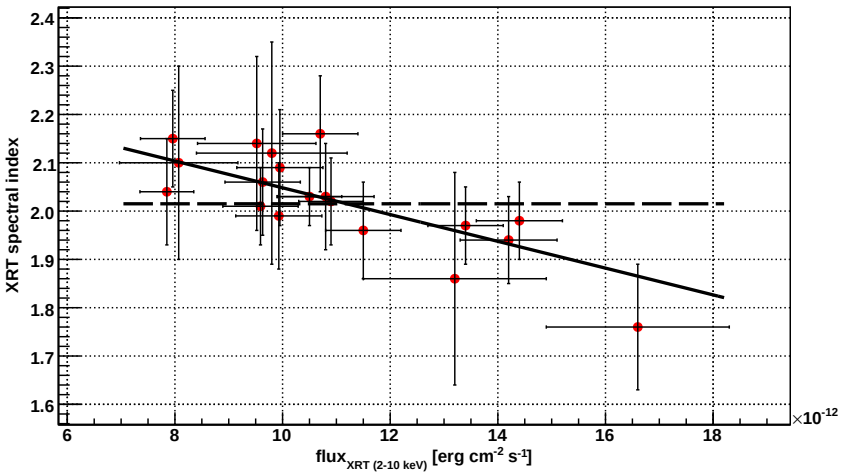

Figure 6.22: *Swift* XRT spectral index as a function of the integral flux, both determined by a simple absorbed power law fit between 2 and 10 keV. Only the data corresponding to the MW campaign is shown. The dashed line represents a fit with a constant, the solid line shows a linear fit.

($r_{2-10\,\mathrm{keV}}/r_{0.2-1\,\mathrm{keV}}$), showed signs of variability. The probability for a constant HR is 2.5 % (χ^2/d.o.f. = 31.6/18). From the timely evolution of the HR in Figure 6.31, indications for a higher value with increasing flux are visible. Both the spectral index and the HR are a measure of the spectral shape and should therefore show the same trend. That the spectral index is not significantly variable may be due to the simple power law not always being an optimal description of the XRT spectrum (see Table E.9). A curved power law can also describe individual spectra well, these fits are, however, not preferred significantly by a logarithmic likelihood ratio test.

Taking advantage of the significant flux variability, a correlation between the spectral index and the integral flux has been investigated, as shown in Figure 6.22. The data points can be described well both by a fit with a constant and a linear fit (χ^2/d.o.f.$_{\mathrm{const.}}$ = 10.8/18, χ^2/d.o.f.$_{\mathrm{lin.}}$ = 4.2/17). A likelihood ratio test favours the linear fit with 97.9 %, giving a good hint for a linear correlation between the two parameters. The slope of the linear fit amounts to $(-2.77 \pm 1.11) \cdot 10^{-2}$ per $10^{-12}\,\mathrm{erg\,cm^{-2}\,s^{-1}}$, indicating a harder spectrum with increasing flux. From the figure it is obvious though that the worse constant fit is mostly due to the highest flux point. Excluding that as a test, the linear fit is preferred with an insignificant 92.1 % by the likelihood ratio test (χ^2/d.o.f.$_{\mathrm{const.}}$ = 6.8/17, χ^2/d.o.f.$_{\mathrm{lin.}}$ = 3.4/16). The rather low reliability of the correlation may be due to the comparably small dynamical range of the spectral index.

An independent test on a potential correlation of the spectral shape with flux can be obtained by using the HR instead of the spectral index. The former has been determined by the photon counts without the need of assumptions on the spectral shape, whereas the latter is dependent on the spectral model adopted to described the data. Figure 6.23 is showing the HR as a function of integral flux. Again a linear fit is clearly preferred over a fit with a constant (χ^2/d.o.f.$_{\mathrm{const.}}$ = 31.6/18, χ^2/d.o.f.$_{\mathrm{lin.}}$ = 12.6/17, likelihood ratio probability of linear fit: 98.9 %). This still holds when not considering the highest flux point (χ^2/d.o.f.$_{\mathrm{const.}}$ = 26.6/17, χ^2/d.o.f.$_{\mathrm{lin.}}$ = 12.3/16, likelihood ratio probability of linear fit: 98.9 %). The positive slope ($(5.09 \pm 1.20) \cdot 10^{-2}$ per $10^{-12}\,\mathrm{erg\,cm^{-2}\,s^{-1}}$)

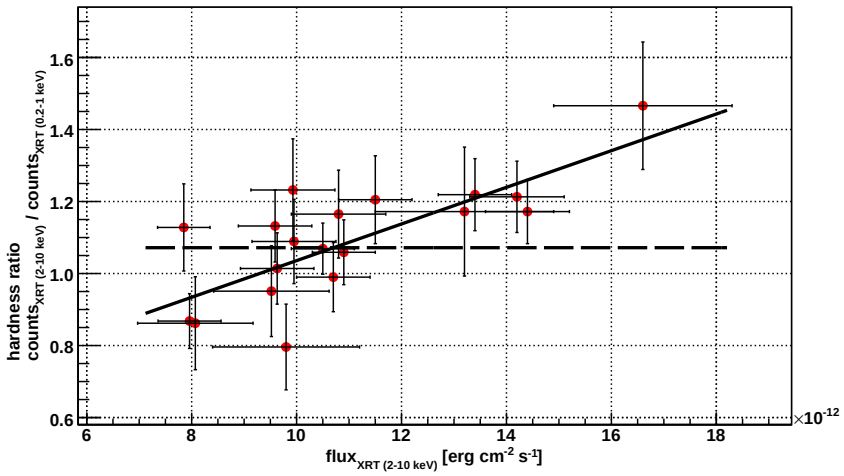

Figure 6.23: Same as Figure 6.22 but showing the hardness ratio (defined as the ratio of count rates between 2 – 10 keV and 0.2 – 1 keV) instead of the spectral index.

corroborates the finding from the potential correlation between spectral index and flux, i.e. a harder spectrum with increasing integral flux. This conclusions was also reported for 1ES 2344+514 by Giommi *et al.* (2000) and Acciari *et al.* (2011a).

More reasonable in terms of theoretical models would be to investigate a correlation between the integral flux and the peak energy. Depending on the underlying physical processes that produce the synchrotron radiation, the peak may shift to higher energies with increasing flux (e.g. when increasing $\gamma_{\rm max}$) or may not change its location (e.g. in case of changing the magnetic field) (Mastichiadis & Kirk 1997). But due to lack of significant curvature for most of the XRT spectra, the peak positions cannot be determined with sufficient accuracy.

***Swift* BAT** The rather hard spectrum observed by *Swift* XRT during the campaign (down to a spectral index of ~ 1.8) rendered a potential BAT detection feasible. To get a first impression, the BAT Transient Monitor quick-look results[10] have been inspected for the MW time period, indeed revealing a sign of a positive rate for several consecutive days around MJD 54765, though with insufficient statistics. Consequently, the data from the BAT 58-Month Catalog (containing after an update the results from the first 66 months of observations[11]) have been obtained and re-binned to different time intervals. Note that the units given for the rate in the data files were wrong at that time, instead of counts $\rm s^{-1}$ these should be counts $\rm s^{-1}$ detector^{-1} (W. Baumgartner, 2012, private communication). This analysis has been conducted by the author and is described in Section E.2.2.2.

From the weekly binned count rates, a rate point with a significance of 4.9 has been found at MJD 54772.5 (see also Figure 6.41). The rate, at a level of $(2.40 \pm 0.49) \cdot 10^{-4}$ counts $\rm s^{-1}$ detector^{-1}, was a factor ~ 8 higher than the mean rate during the MW campaign ($(2.99 \pm 0.96) \cdot 10^{-5}$ counts $\rm s^{-1}$ detector^{-1}). A fit with a constant over the weekly BAT data points yielded a χ^2/d.o.f. = 30.3/22, indicating a probability for a constant rate of only 11.1 %. Fitting the monthly binned rate points, the hint of

[10] available from http://swift.gsfc.nasa.gov/docs/swift/results/transients/
[11] see http://swift.gsfc.nasa.gov/docs/swift/results/bs58mon/

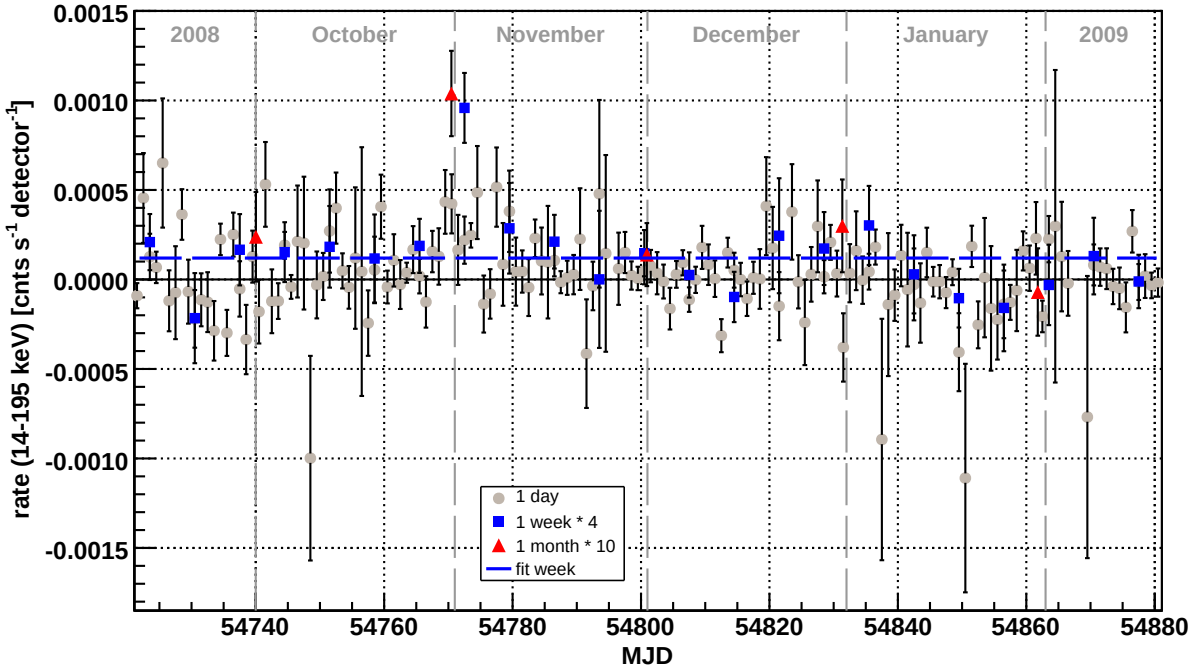

Figure 6.24: Light curve of 1ES 2344+514 measured by *Swift* BAT during the MW campaign. The data has been binned to a daily, weekly and monthly time basis. The weekly and monthly data points have been multiplied for clarity by a factor of 4 and 10, respectively. The weekly data have been fit with a constant, shown as the blue dashed line. Note that due to the scaling of the points, the fit value is artificially increased also by a factor of 4.

variability became more significant (χ^2/d.o.f. = 12.8/4, probability of 1.2 %). Also the daily points were not consistent with a constant rate (χ^2/d.o.f. = 220.8/156). The mean rates derived from the different fits were showing a significantly positive rate over the MW time period (in 10^{-5} counts s^{-1} detector^{-1}: $< r_{\rm day} >= 2.79 \pm 0.97$, $< r_{\rm week} >= 2.99 \pm 0.96$, $< r_{\rm month} >= 3.06 \pm 1.01$), which indicated that 1ES 2344+514 may be detectable by BAT over longer time scales. Indeed, BAT reported a detection of the source in the 58-Month Catalog. The BAT rate evolution with different binnings is shown in Figure 6.24. A spectrum has been derived for the weekly flare as well as the 58-Month Catalog detection (see Section E.2.2.2 for analysis details).

Discussion Compared to historical observations of 1ES 2344+514 between 2 and 10 keV, *Swift* XRT detected the source during the MW campaign in one of the lowest flux states until now. *BeppoSAX* observed in 1996 and 1998 a flux of $8 \cdot 10^{-12}$ erg cm^{-2} s^{-1} (Giommi *et al.* 2002) and $8.4 \cdot 10^{-12}$ erg cm^{-2} s^{-1} (Giommi *et al.* 2000), respectively, similar to the *Swift* XRT flux of $9 \cdot 10^{-12}$ erg cm^{-2} s^{-1} reported from measurements in 2005 (Tramacere *et al.* 2007). Acciari *et al.* (2011a) reported from the MW campaign in 2007/2008 a minimum flux measured by *RXTE* PCA of $(9.5 \pm 2.6) \cdot 10^{-12}$ erg cm^{-2} s^{-1} and of $(9.6 \pm 0.6) \cdot 10^{-12}$ erg cm^{-2} s^{-1} seen by *Swift* XRT. None of these values is below the lowest flux found within this campaign, which amounted to $(7.9 \pm 0.5) \cdot 10^{-12}$ erg cm^{-2} s^{-1} (see also Table E.9). It is probable though that the measurements of 1996, 1998 and 2005 were compatible within the (not given) errors with that flux.

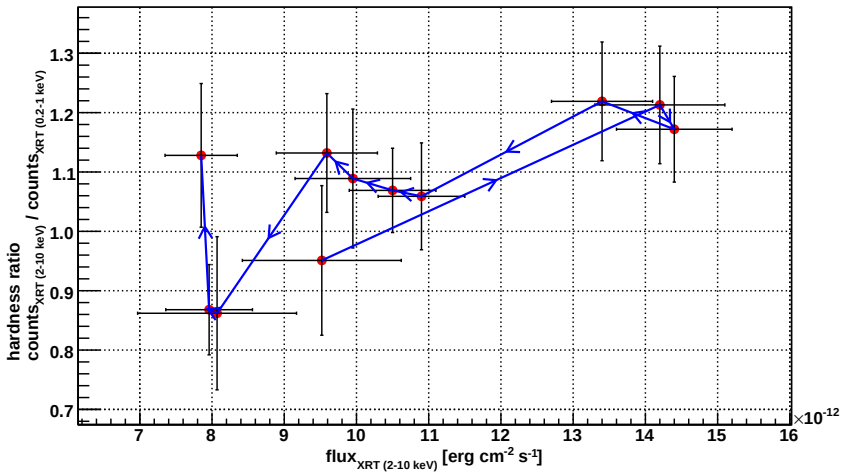

Figure 6.25: Same as Figure 6.23 but showing only the data during the XRT flare (MJD 54757 – 54769).

The flare found by XRT was only small in amplitude considering the extreme behaviour 1ES 2344+514 has shown in the past (see also Section 6.1). This may also be the reason for the relatively small dynamical range of spectral indices found in this work, which spanned the values of 1.76 ± 0.13 to 2.16 ± 0.12. The spectral indices listed in (Acciari *et al.* 2011a) were varying between 1.86 ± 0.04 and 2.72 ± 0.19, giving a more significant evidence for a correlation between flux and spectral index. On the other hand, as noted above, the HR was correlated significantly with the integral flux over the whole MW time period. Only investigating the flare (MJD 54757 – 54769), indications for a counter-clockwise evolution of the HR with the flux were apparent, see Figure 6.25. In the model of Kirk *et al.* (1998), such a behaviour is expected if electrons are accelerated at a shock front which is travelling within a relativistic jet. They emit synchrotron radiation in the post-shock region, which is assumed to contain a homogeneous magnetic field. Due to the constant magnetic field, spectral changes can be directly related to the energy of the electrons, which in turn is dependent on the relative time scale of the acceleration and cooling processes. Therefore, different frequency bands will show a different evolution in time during a flare depending on the relative importance of acceleration and cooling. A counter-clockwise behaviour in the spectral index – intensity plane, or analogous HR – integral flux plane, is expected if observing close to the maximum emission frequency, i.e. where acceleration and cooling time scales are comparable. The constant spectral index during the flare (χ^2/d.o.f. = 1.4/10) corroborates this finding. If this was indeed the case here, no accompanying high state in the inverse-Compton regime is expected, so there should be no flare at VHE energies. This will be discussed in Section 6.4.5.

The potential high state observed by BAT was hard to reconcile with the simultaneous XRT measurements. The energy to produce a flare at hard X-rays from an extragalactic object can not be produced thermally but has to arise from non-thermal processes. Therefore, the flare should have been also visible at lower X-ray energies, but the XRT light curve did not show indications of flux changes even close to a factor of 8, and neither the spectral index nor the HR changed significantly at that time. XRT did not observe continuously though, and measured only four times within this week, so may have missed

a potential short, large flare. This origin for the high BAT rate was excluded though by the BAT data on daily basis, as the high rate seemed to have accumulated over several days characterised by an increased rate. The latter data was obtained from continuous monitoring and hence cannot have missed such a short and strong flare. Also judging from the simultaneous SED (see Figure 6.33; the low state XRT SED has been obtained quasi-simultaneously from the last XRT day falling within the 1-week BAT window), the break between the soft and hard X-rays is unexpected. Consequently, the XRT data represented an independent argument speaking against the high state BAT point. It should be noted though that archival XRT measurements found the source at flux levels comparable to the ones derived for BAT (see Figure 6.33), hence a flare that strong in BAT is not excluded a priori.

A deep investigation of the BAT data revealed that the high state most probably was an artefact of the applied coded mask technique (H. Krimm, 2012, private communication) instead of a real increase of the flux. In short, bright sources in the fov of BAT may not always be completely cleaned away from the images due to the coded-mask imaging, causing systematic noise and point-like "ghosts" to appear. To overcome an accumulation of such an effect, *Swift* is normally changing its roll angle between two pointings ("roll angle dithering"). In the case of the observations in question, no roll angle dithering was applied and ghosts were present in the fov of 1ES 2344+514, leading to the observed high rate points. When removing the data apparently affected by ghosts, the putative signal is dropping below $1\,\sigma$ (H. Krimm, 2012, private communication).

6.4.3 Optical

KVA and Tuorla The optical coverage by KVA and Tuorla during the MW campaign is shown in Figure 6.4. Due to problems with the PC steering the CCD camera as well as with the protecting dome, KVA observations were not available end of October and early November, respectively. The loss of observations was partly (hindered by bad weather) covered by the Tuorla telescope. The measurements were conducted erroneously in the R-band only instead of in all three available filters. In the following, "KVA" is used as a synonym for both instruments.

The optical emission of 1ES 2344+514 is dominated by a strong host galaxy, contributing $\sim 90\,\%$ of the flux in the R-band (see also Section 6.1). Additionally, the source is located at low galactic latitudes, causing a considerable reddening of the optical light. The measured flux densities have to be corrected for these effects to obtain the flux density of the core, needed for the SED. To investigate the flux density evolution, on the other hand, these correction do not have to be applied. The low level data analysis has been described in Aleksić *et al.* (2012f), from which results the light curve can be constructed directly. The correction and conversion procedures needed to obtain the SED points have been accomplished as part of this work and are described in Section E.2.3. The results are listed in Table E.10, the light curve is shown in Figure 6.26.

A fit with a constant to the light curve of 1ES 2344+514 measured by KVA had a goodness of fit of $99.5\,\%$ ($\chi^2/\text{d.o.f.} = 13.1/29$), not giving a sign of variability during the MW campaign. The mean flux density as determined by the fit amounts to $(4.19 \pm 0.01)\,\text{mJy}$.

CrAO The CrAO monitoring was covering some days during the MW campaign. The received data products (see Aleksić *et al.* (2012f) for an analysis description) were also not corrected for host galaxy contribution nor galactic extinction, nevertheless the overall as well as individual flux density level did not match the one of KVA. A part of this difference may be attributed to different central wavelengths at which the R-band data were taken (586 nm for CrAO, 640 nm for KVA), but cannot account for the high level of discrepancy. Both analysis pipelines were based on differential photometry, using partly the same comparison stars. For one star used by both observatories, the measured magnitudes matched very well, hence the calibration could not be the source of the difference.

On the other hand, the CrAO data were taken with a variable aperture, which in turn leads to varying host galaxy contributions. In the case of 1ES 2344+514 where the flux density is dominated by the host galaxy, this causes rather large changes of the measured flux density. With fixed aperture, the data are affected by the seeing, which is much smaller though for AGN compared to the variations caused by adapting the aperture to seeing (Nilsson *et al.* 2007, K. Nilsson, 2012, private communication).

Therefore, the CrAO data were re-reduced using the same aperture as KVA, leading to a much lower systematic difference between the two light curves. Still the light curves were offset by $\sim 10\,\%$, which is about the difference expected from observing at different R-band wavelengths. To overcome this, the author was shifting the CrAO points by a constant factor, which had been determined by the average flux density difference of measurements by the two telescopes with a time delay < 0.3 days. For the present data, two such data pairs have been found, leading to a shift of $+0.49$ mJy. See Table E.10 for detailed results.

The CrAO light curves at different stages of correction are shown in Figure 6.26. A fit with a constant to the newly reduced and shifted CrAO data yielded a χ^2/d.o.f. of 22.2/6, corresponding to only 0.1 % probability for a constant flux density.

***Swift* UVOT** data were taken in all six filters at the dates listed in Table E.8. The analysis procedure is described in Aleksić *et al.* (2012f). The flux densities were obtained in units of mag and still had to be de-reddened and host galaxy corrected by the author. The different processing steps and results are given in Section E.2.3. In the UV filters, the host galaxy contribution is very small and hence does not have to be corrected (Tramacere *et al.* 2007). For the V-, B- and U-bands, a host galaxy value has not been reported in the literature yet, because of which the corresponding contribution has been extrapolated from the measured R-band value (see Aleksić *et al.* 2012f). As the host galaxy is dominant in these bands and the errors of the such determined values were large, these bands have not been considered for the SED modelling.

The light curve for all bands is shown in Figure 6.27. Variability is not obvious, 1ES 2344+514 was constant within the error bars in all UVOT filters.

Discussion Also after re-reducing and shifting the CrAO light curve, some incompatibility with the KVA points was present. Especially for the two days with nearly simultaneous measurements of CrAO and KVA (see also Table E.10), the measured CrAO flux densities were lower and higher than the KVA ones, respectively, though both were

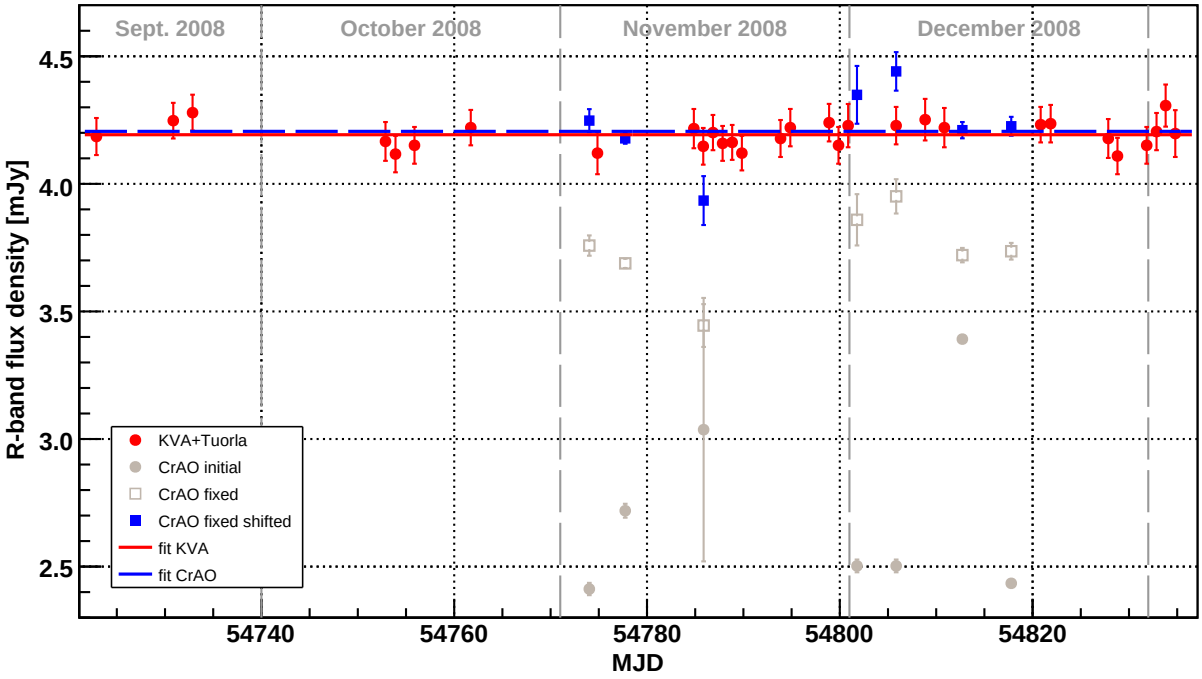

Figure 6.26: Optical light curves of 1ES 2344+514 obtained during the MW campaign. The CrAO data reduced with varying aperture ("CrAO initial") and with fixed aperture but without applying a shift ("CrAO fixed") are shown together with the final CrAO results ("CrAO fixed shifted") and the KVA+Tuorla data. The red (blue) dashed line shows a fit with a constant to the KVA+Tuorla (CrAO) data.

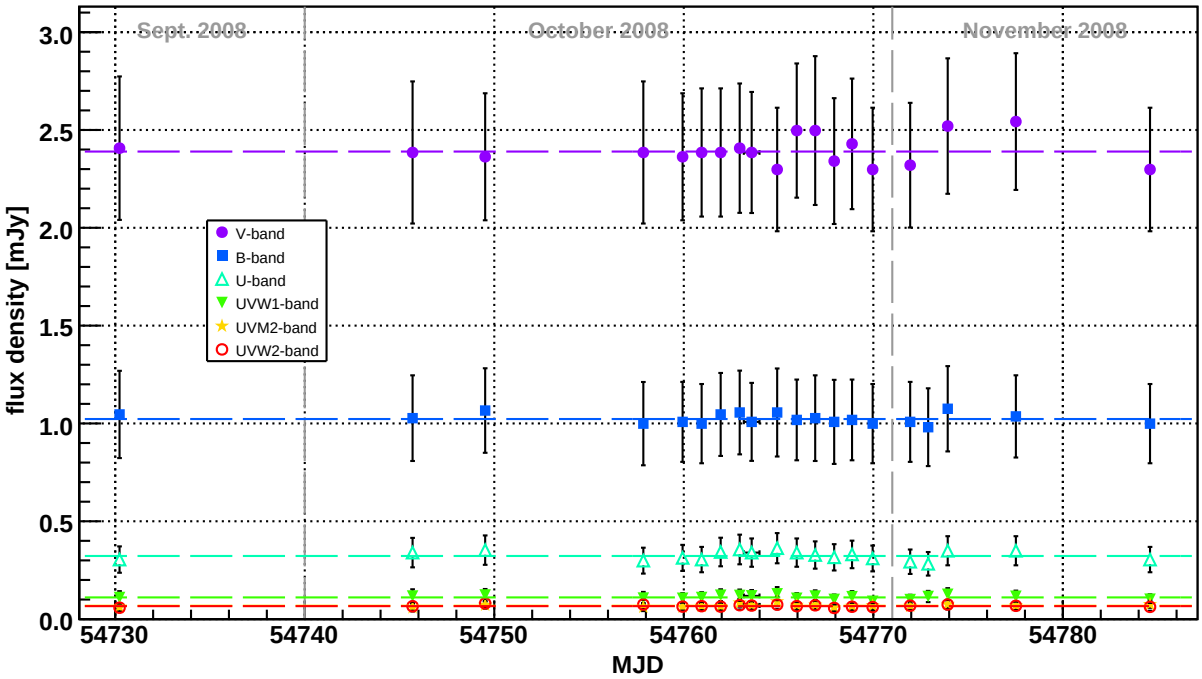

Figure 6.27: Light curves of 1ES 2344+514 measured by *Swift* UVOT during the MW campaign. The horizontal dashed lines denote fits with a constant to the data points, with the following χ^2/d.o.f. values (goodness of fits): V-band: 0.9/13 (100.0 %); B-band: 0.3/19 (100.0 %); U-band: 2.2/19 (100.0 %); UVW1-band: 2.6/19 (100,0 %); UVM2-band: 3.0/19 (100.0 %); UVW2-band: 1.6/19 (100.0 %).

consistent within $2\,\sigma$. The CrAO light curve showed significant variability, whereas the KVA and UVOT measurements were well consistent with being constant. This may be due to the different sampling, but the more likely explanation seems to be unknown systematics of CrAO. Combining the R-band measurements of KVA and CrAO, a fit with a constant had a χ^2/d.o.f. = 35.8/36, which is still compatible with a constant flux.

Judging from the KVA long-term monitoring, 1ES 2344+514 was in a modest flux density state during the MW campaign (see also Section6.5.6).

6.4.4 Radio

Single Dish Observations 1ES 2344+514 has been observed quasi-simultaneously by Effelsberg and IRAM within the F-GAMMA program (Fuhrmann *et al.* 2007; Angelakis *et al.* 2008). The source is also included in the OVRO monitoring program, where about 1500 gamma-ray blazars are observed twice per week (Richards *et al.* 2011). Additionally, dedicated observations in the radio band have been conducted with Metsähovi and RATAN-600. The observations are depicted in Figure 6.4, the data analysis is described in Aleksić *et al.* (2012f). The obtained results are summarised in Table E.14.

Due to the faintness of the source, the 37 GHz, observations by Metsähovi did not yield a detection of 1ES 2344+514 during the MW campaign. An UL (signal/noise ratio > 4) on the flux density was calculated for the measurement closest in time to the MAGIC-I observations, i.e. 07/10/2008, amounting to 0.33 Jy. Metsähovi detected the source prior to the MW campaign though with a flux density of (0.38 ± 0.09) Jy, consistent with the derived UL.

RATAN-600 performed observations from 20/09/2008 to 03/10/2008. The results presented here have been averaged over this period of time and hence cannot be studied for variability. The flux densities are shown in Figure 6.31. They are basically consistent within the errors with the measurements from Effelsberg about three weeks later.

The Effelsberg monitoring revealed a slightly higher flux density (increase of $\sim 6\,\%$ at 4.85 GHz, 8.35 GHz and 10.45 GHz) around MJD 54779 compared to its first observations during this campaign. Thanks to the high precision measurements of Effelsberg, these small changes have nevertheless been detected significantly. During the following two pointings, the flux densities were decreasing again.

Significant variability was not detected by OVRO at 15 GHz over the complete MW campaign, as the light curve in Figure 6.31 is showing. A fit with a constant to the flux density yielded a χ^2/d.o.f. of 33.9/24, corresponding to a probability for a constant flux of 8.7 %. Excluding the potential outlier around MJD 54870, the probability rises to 13.6 % (χ^2/d.o.f. = 30.5/23). This rather low goodness-of-fit is mostly due to the first point of the light curve, having a comparably low flux density and small uncertainty. Not considering this point for the fit, the χ^2/d.o.f. amounts to 15.3/22, giving high confidence for a constant flux density.

The IRAM high frequency observations did not result in the detection of a significant signal from 1ES 2344+514. ULs with a c.l. of $3\,\sigma$ have been calculated. Due to the weakness of the source at the IRAM frequencies, it has finally been removed from the initial monitoring sample (L. Fuhrmann, 2012, private communication).

Figure 6.28 shows the quasi-simultaneous (separated by ~ 5 days) radio spectra of

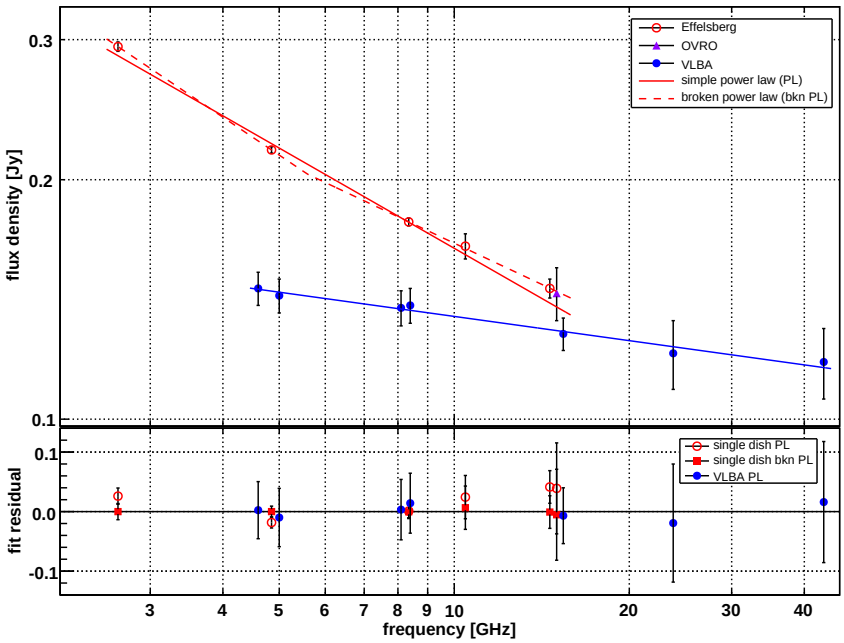

Figure 6.28: *Top panel:* spectra of 1ES 2344+514 measured quasi-simultaneously by the single-dish instruments Effelsberg (MJD 54756.96 – 54756.97) and OVRO (MJD 54761.10) as well as by VLBA (MJD 54762.19). Note that the error bars include the systematic contribution. Simple power law fits are shown by the solid lines, the dashed line is given by a broken power law. *Bottom panel:* residuals of a simple power law fit to both spectra as well as a broken power law fit to the single-dish spectrum. The residuals are calculated as the difference between the point and the fit relative to the point value.

1ES 2344+514. The Effelsberg spectrum has been combined with an OVRO measurement. Compared to the VLBA spectrum, the latter is much flatter and lower in flux. A fit with a simple power law (Eq. 2.12, $\alpha = 0.10 \pm 0.04$) is matching well[12] the VLBA points but not the Effelsberg+OVRO spectrum (fit given by $\alpha = 0.42 \pm 0.01$). A broken power law fit seems to be a better description of the latter, which is confirmed by the residuals shown in Figure 6.28. The broken power law is given by:

$$\begin{aligned} S(E) &= S_0 \cdot (E/E_0)^{-\alpha_1} && E < E_{break} \\ S(E) &= S_0 \cdot (E_{break}/E_0)^{\alpha_2-\alpha_1} \, (E/E_0)^{-\alpha_2} && E \geq E_{break} \end{aligned} \tag{6.5}$$

with $S(E)$ being the flux density, $E_0 = 10\,\mathrm{GHz}$, a normalisation S_0 of $(0.153 \pm 0.004)\,\mathrm{Jy}$ at E_0, a break energy E_{break} of $(5.6 \pm 1.0)\,\mathrm{GHz}$ and spectral indices $\alpha_1 = 0.49 \pm 0.03$ and $\alpha_2 = 0.34 \pm 0.05$.

Interferometric Observations of 1ES 2344+514 were conducted on 23 September 2008 by the VLBA at several frequencies. The exact mode of observation and details of the data analysis are given in Aleksić *et al.* (2012f). The cosmological model adopted for

[12]Note that for VLBA, the error bars include already the systematic contribution since these are dominating and statistical errors are hard to estimate. To maintain comparability, also the Effelsberg and OVRO data are shown including systematic errors. χ^2 tests are not applicable in this case, therefore fit probabilities cannot be given. See the residuals in Figure 6.28 for an estimate of the goodness of the fit.

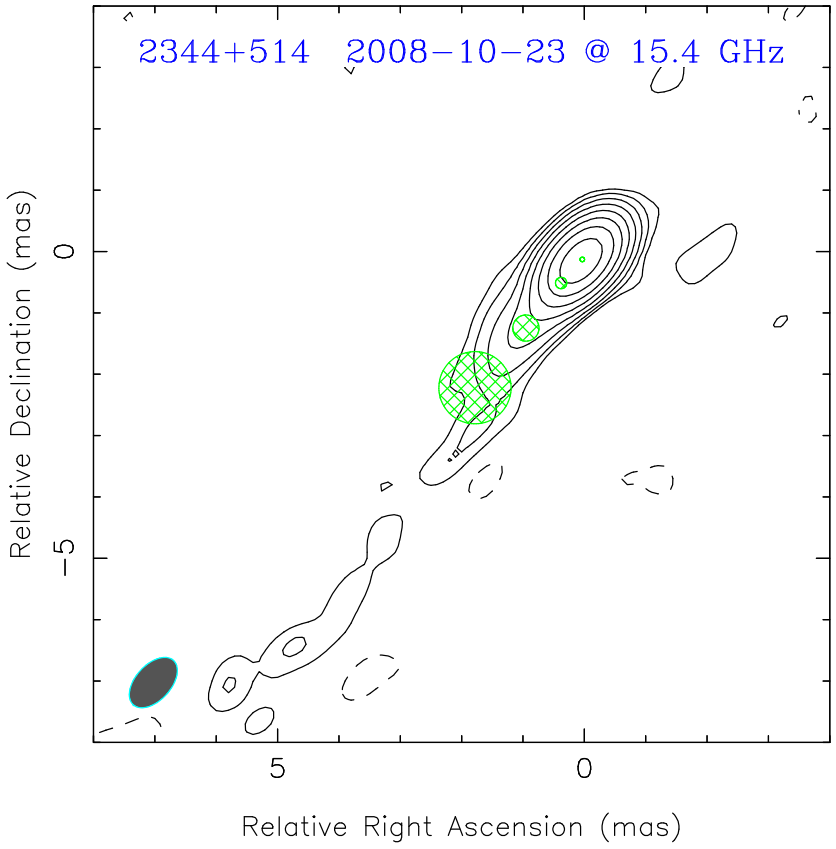

Figure 6.29: Naturally weighted CLEAN (Högbom 1974) VLBA image of 1ES 2344+514 taken at 15.4 GHz on 23 October 2008. Position and sizes of individual model components are visualised by the green circles. From North-West (top right) to South-East (bottom left): the core, C 3, C 2 and C 1. The first contour corresponds to 0.50 mJy/beam, subsequent contours mark an increase by a factor of 2. The peak has 0.11 Jy/beam. The beam is 0.98×0.58 mas at a PA of $-42.2°$, as indicated by the filled ellipse bottom left. For $z = 0.044$, the linear scale is 0.9 pc/mas. Image taken from Aleksić *et al.* (2012f).

determining the absolute length scales is given by $\Omega_m = 0.27, \Omega_\Lambda = 0.73$ and $H_0 = 71\,\mathrm{km\,s^{-1}\,Mpc^{-1}}$.

The VLBA map at 15.4 GHz is shown in Figure 6.29. The radio emission of 1ES 2344+514 is dominated by the core and exhibits a rather featureless and smooth jet. Three components could be identified within the jet, being located on a straight line as seen from the radio core (i.e. the unresolved feature at the North-Western end of the jet in Figure 6.29). Table 6.4 is listing the core size at each observation frequency determined by modelling it with a circular Gaussian emission component (Aleksić *et al.* 2012f). At low frequencies, the core could be resolved, while at higher frequencies, ULs on its size were determined.

Discussion The difference between the Effelsberg+OVRO and VLBA spectra obvious in Figure 6.29 is due to the different nature of observations. The single-dish observatories integrate over all the emission from the radio core, the small and steep spectrum of the large scale jet. Interferometric measurements, on the other hand, resolve the parsec-scale

ν	Size		Resolution Limit
[GHz]	[mas]	[10^{17} cm]	[mas]
43.2	< 0.06	< 1.7	0.06
23.8	< 0.04	< 1.1	0.04
15.4	0.07 ± 0.04	1.9 ± 1.1	0.04
8.4	0.14 ± 0.05	3.9 ± 1.4	0.05
8.1	0.09 ± 0.05	2.5 ± 1.4	0.06
5.0	0.16 ± 0.07	4.4 ± 1.9	0.08
4.6	< 0.11	< 3.1	0.11

Table 6.4: Core size of 1ES 2344+514 determined at different frequencies ν.

structures of the source and have a limited capability to detect low surface brightness extended emission, hence are sensitive dominantly to the flat spectrum of the central structure. With increasing frequency, the resolution of the single-dish instruments becomes better and the brightness of the extended structures decreases. Therefore, the contribution from the large scale jet is diminished, which causes the spectrum to flatten. The spectral indices confirm this explanation. For an optically thin kpc-scale jet, an index of 0.5 is expected, which agrees very well with the value found at small frequencies ($\alpha_1 = 0.49 \pm 0.03$) by the single-dish observatories.

The OVRO light curve was not significantly variable during the MW campaign, though also not highly significant constant. Apart from an outlier, the very first point in the light curve (MJD 54761.1) was reducing the compatibility with a constant flux density strongly. From the first to the second point, a significant flux density increase by $\sim 16\,\%$ within two days was found. In the following the light curve stayed constant (χ^2/d.o.f. = 4.0/16) until a monitoring gap of 29 days at MJD 54823.9, after which the flux density had dropped by $\sim 10\,\%$ to a mean level again consistent with the first OVRO point. Also the Effelsberg measurement after the gap at MJD 54855.7 showed a flux density level consistent with the simultaneous OVRO data and the Effelsberg observation before the high state. Under the assumption that the Effelsberg flux density increase detected at MJD 54779.0 from 4.85 to 10.45 GHz was present also at 14.60 GHz (such observations had not been conducted that day), this increase represented rather a broad high state lasting for $\gtrsim 60$ days than a short-lived peak.

From the variability time scale, the variability Doppler factor $D_{\rm var}$ of the emission region may be obtained. We follow here the method described by Lähteenmäki & Valtaoja (1999) and Teräsranta & Valtaoja (1994). They assume that during a flare, the flare-intrinsic brightness temperature $T_{\rm b,int}$ equals the equipartition brightness temperature $T_{\rm eq} = 5 \cdot 10^{10}$ K independent of the Doppler boosting. Using Eq. (1) given in Lähteenmäki & Valtaoja (1999)

$$T_{\rm b,var} = 5.87 \cdot 10^{21} h^{-2} \lambda^2 S_{\rm max} \tau_{\rm obs}^{-2} \left(\sqrt{1+z} - 1 \right)^2 , \tag{6.6}$$

$D_{\rm var}$ is given by (Eq. (2) of the same paper):

$$D_{var} = (T_{\rm b,var}/T_{\rm b,int})^{1/3} \tag{6.7}$$

(where $T_{\rm b,var}$ is the variability brightness temperature in K, λ is the observation wavelength in m, $S_{\rm max}$ is the maximum flux density during the flare in Jy, $\tau_{\rm obs}$ is the variability

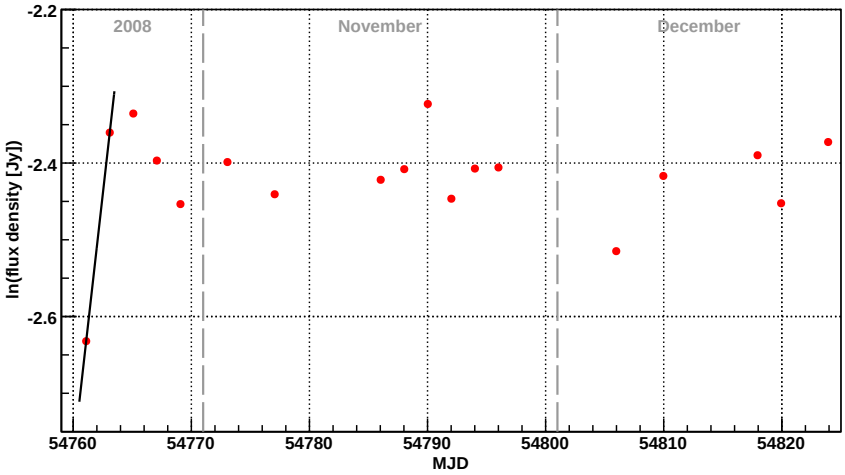

Figure 6.30: Flux density of 1ES 2344+514 as measured by OVRO at 15.0 GHz for estimating the variability time scale. From every single point, half of the baseline flux has been subtracted (Teräsranta & Valtaoja 1994). The black solid line denotes a linear fit to the first two points with a slope of ln(0.14 Jy) per day. Due to fitting only two points and the extremly small error bars in natural logarithmic scale, the error of the slope is not meaningful and hence not given.

time scale and z is the redshift of the source. The Planck constant h is set to unity here.). S_{max} is derived here as $S_{\rm peak} - S_{\rm base}/2$ (Teräsranta & Valtaoja 1994, A. Lähteenmäki, 2012, private communication), with the peak flux density $S_{\rm peak} = 0.166$ and the baseline flux density $S_{\rm base} = 0.144$. The latter is assumed to be on the level of the OVRO measurement at MJD 54761.1. This seems justified taking into account that the observations after the 60 day long high state showed a flux density level comparable with this point[13], see Figure 6.31. $\tau_{var} = {\rm d}t/{\rm d}(ln\, S)$ is given by the inverse of the slope determined from Figure 6.30 (Teräsranta & Valtaoja 1994). Since the rising flank of the flare was not resolved, the variability time scale may have been even smaller (if our choice of baseline flux is correct), hence we can only calculate a lower limit on the Doppler factor. Inserting these values in Eq. 6.7 yields $D_{\rm var} \geq 3.4$.

This estimate has rather speculative, considering that it is based solely on two data points and that the flare has not been resolved in time. Also, this method has not been tested yet for radio-faint TeV blazar objects (A. Lähteenmäki, 2012, private communication). Nevertheless, the value is not in disagreement with Doppler factor results obtained from SSC model fitting of TeV blazars in general and specifically for this simultaneous data set of 1ES 2344+514 (see also Section 6.4.6).

The VLBA data reveal a flat integrated pc-scale spectrum, as typically found for blazars. Such a shape can be caused by synchrotron emission from electrons following a hard power law energy spectrum (e.g. Sokolovsky *et al.* 2010a). The latter is hard to reconcile with first order Fermi acceleration, but feasible in the context of second order Fermi acceleration. Alternatively, a flat radio core spectrum can be understood in the framework of Blandford & Königl (1979) (see Section 2.2). The unresolved, inhomogeneous core is believed to contain several emission components (in the form of distinct

[13]This flux density level seems to be representative for the baseline flux of the source also on years' time scale, as the long-term OVRO light curve shown in Section 6.5.6 proves.

blobs, a homogeneous jet or a combination of these) characterised by different peak frequencies, whose spectra superpose to a flat overall spectrum. The angular separation increase between the core and the closest jet component C 3[14] (Piner *et al.* 2010) as well as the core size decrease (see Table 6.4) with increasing observation frequency give additional evidence for the applicability of this model. Therefore, the observational data are in accord with the core being defined as a surface with optical depth $\tau \simeq 1$ due to synchrotron self-absorption in a conical jet (Blandford & Königl 1979), arguing against the alternative scenario of interpreting the core as a standing shock further downstream of the jet (e.g. Marscher 2008).

Despite the potential 2-day flare observed by OVRO within this campaign, variability time scales in the radio regime are typically of the order of a few weeks, and flux changes are rather modest (see also Section 2.7). Therefore, sources have to be studied over longer time scales than just this MW campaign, which will be done in Section 6.5.

6.4.5 Multi-Wavelength Light Curve

The individual instrument results discussed above are combined in a multi-wavelength light curve in Figure 6.31 to search for features common to all energy regimes. Correlations or time lags between different wavelength regimes during flux changes are important tools to investigate the physical mechanisms responsible for the change in emission. In this MW campaign, a flare was clearly measured by XRT. Also the OVRO light curve showed one short flux density increase, which is confirmed independently by the Effelsberg observations. The other instruments (AGILE, *Fermi*-LAT, IRAM, MAGIC-I, Metsähovi and *Swift* BAT) did not find a significantly variable flux over time, partly due to the faintness of the source.

Potential correlations between the different instruments have been investigated with the macro described in Section 5.4.5.2, also requiring a time difference of < 0.9 days.

Since during the short-time OVRO flux density increase the XRT flux was decreasing from its maximum to about 75 % of that value, an anti-correlation may be present between 15.0 GHz and the integral flux between 2 and 10 keV. The corresponding distribution is presented in Figure 6.32. A likelihood ratio test prefers the linear fit with 98.9 %. However, the data basis is small, and the correlation is dominated by the highest XRT flux point. Not considering the latter, no correlation would be present, and hence the putative correlation is not representative of all the data.

The comparison of OVRO – KVA, OVRO – BAT (daily), KVA – XRT, KVA – BAT (daily) and XRT – BAT (daily) also does not give a clear hint for correlations between the different instruments. The corresponding figures and fit results are shown in Section E.2.5. One reason for this is the small amount of significant variability. On the other hand, the small statistical basis does often not allow for a meaningful investigation of correlations. UVOT data have not been considered due to their constancy and relatively large errors, and CrAO data were not investigated because of their potentially dominating systematics.

[14] Long-term MOJAVE monitoring shows that the jet components C 3, C 2 and C 1 are basically stationary, see Section 6.5.5.

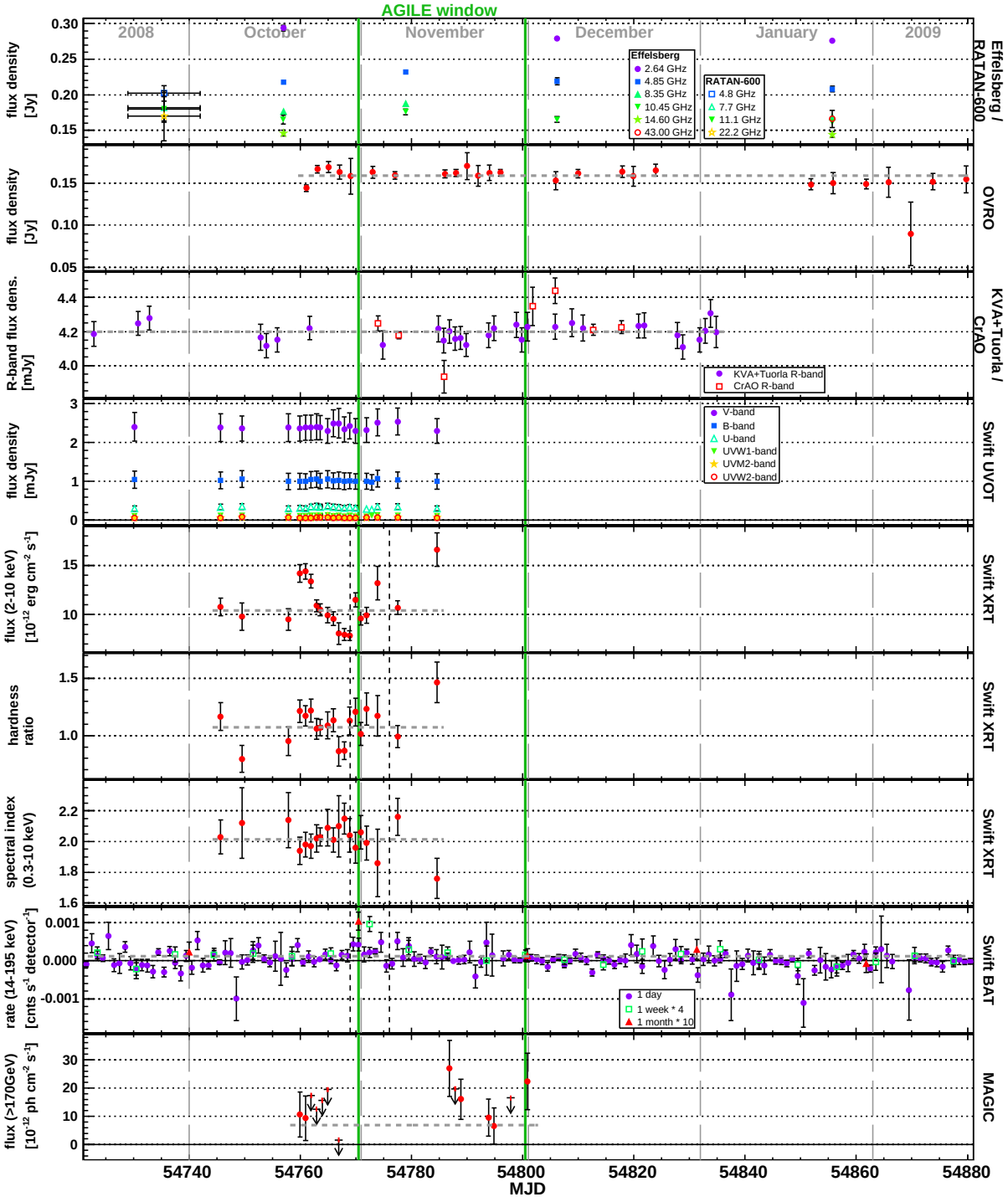

Figure 6.31: Multi-wavelength light curve of 1ES 2344+514 obtained in this campaign. One point (MJD 54867.5) of the daily *Swift* BAT light curve has been omitted for clarity, having a rate of $(-6.08 \pm 3.49) \cdot 10^{-3}$ cnts s^{-1} detector^{-1}. Note that the rates of the weekly and monthly BAT points have been increased by a factor as indicated in the legend for clarity. Dashed grey horizontal lines represent fits with a constant to the data points, in the case of the R-band observations for the combined KVA+Tuorla and CrAO points, in case of the BAT data to the weekly binned points only. Solid green vertical lines show the AGILE observation window. The dashed black vertical lines visualise the bin width of the probably artificial 1-week flare of BAT (see Section 6.4.2). For an explanation of the MAGIC light curve see the caption of Figure 6.18; note though that the grey points are not shown here for clarity. Details of the individual light curves are given in the corresponding paragraphs of Section 6.4.

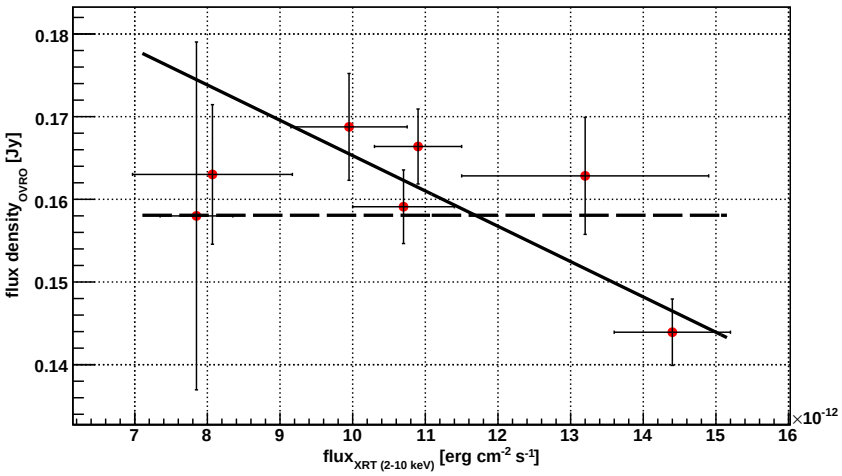

Figure 6.32: The flux density at 15.0 GHz measured by OVRO from 1ES 2344+514 during the MW campaign as a function of the *Swift* XRT integral flux between 0.3 and 10 keV for data pairs with a time difference < 0.9 days. The dashed line represents a fit with a constant (χ^2/d.o.f. = 19.4/6 (probability of 0.4 %)), the solid line gives a linear fit (χ^2/d.o.f. = 4.7/5 (probability of 45.2 %) with a slope of $-(4.3 \pm 1.2) \cdot 10^9$ Jy per erg cm^{-2} s^{-1}).

A correlation with the MAGIC-I data is not tested due to their low significance. However, the highest flux point of the VHE light curve is rather significant (see also Table 6.2) and coincides with the highest flux reported by *Swift* XRT during the campaign within less than 2.5 days. Since there was no *Swift* coverage ~ 7 days around that high state and also nearby MAGIC observations prior to the measurement have not been conducted, it cannot be excluded that both points belong to a flare present in X-rays and VHE gamma rays with a duration of a few days (or less in case of frequency-dependent time lags). This rather speculative interpretation gets strengthened by the corresponding very hard XRT spectral index and high HR during the high state, indicating a change which affects the underlying electron population. Either fresh electrons following a different distribution were injected into the emission region, or the existing electrons were accelerated, e.g. by a shock front entering the region. In the SSC framework, these electrons would also induce an increase in flux at VHE gamma rays (e.g. Mastichiadis & Kirk 1997).

6.4.6 Spectral Energy Distribution

Data Sets and Applied Models From the multi-wavelength light curve presented in the previous chapter, data sets with a good simultaneous coverage have been defined as a basis for SED modelling. Additionally, the data sets should represent different flux states to investigate a potential evolution of the source. Since the gamma-ray observations did not yield significant results, the data sets have been selected according to the X-ray flux state. For all bands but the radio one only data with a time difference less than 1 day should be considered. However, the gamma-ray results had to be averaged over rather long time scales, and in the radio regime, the typical variability time scale is ~ 14 days. Hence this condition can only be applied to the X-ray and optical data. In the case of the lower flux data set, KVA observations were only available with ~ 1 week time difference due to hardware problems. Though the KVA light curve was significantly constant for the

Data Set	Instrument	Observation Time
"low"	Effelsberg	54778.947 – 54778.950
	OVRO	54769.077
	Swift	54768.806 – 54768.948
	AGILE	54770.500 – 54800.500$^{(a)}$
	Fermi-LAT	54759.941 – 54800.897$^{(a)}$
	MAGIC-I	54759.941 – 54800.897
"high"	Effelsberg	54756.960 – 54756.970
	OVRO	54761.095
	VLBA	54761.96 – 54762.42
	KVA	54761.718
	Swift	54760.899 – 54760.983
	AGILE	54770.500 – 54800.500$^{(a)}$
	Fermi-LAT	54759.941 – 54800.897$^{(a)}$
	MAGIC-I	54759.941 – 54800.897

Notes. $^{(a)}$ No detection; 95 % c.l. ULs have been calculated.

Table 6.5: Definition of the "low" and "high" data set used for SED modelling of 1ES 2344+514.

duration of the MW campaign, a potential change in flux during the *Swift* observations cannot be excluded, preventing the use of the R-band data for the SED. Note that the use of the averaged HE and VHE gamma-ray results on a quasi-simultaneous basis is reasonable, since no significant variability has been detected over the MW time scale.

The exact observation times of the instruments contained in the such defined "low" and "high" data set are shown in Table 6.5. The two data sets correspond to the lowest and highest X-ray flux measured during the MW campaign and describe the evolution from the flare peak down to a flux level even lower than prior to the flare. Due to the rather long duration of this decay (~ 8 days), the variability time scale cannot be used to obtain a meaningful constraint on the size of the flaring region.

Since the *Fermi*-LAT data did not show an indication for a variable flux up to the currently published 24 month time scale, the 1FGL data have been included on a quasi-simultaneous basis. Also the *Swift* BAT monitoring light curve did not show significant variability after 66 months of observation (see Section 6.5), which indicates that the signal detected from 1ES 2344+514 is not dominated by high or flaring states and hence is representative of the long-term flux level of the source. Therefore, the BAT spectrum was also considered for the SED modelling.

The low and high data sets have been fit using a single one-zone (Maraschi & Tavecchio 2003) and a self-consistent two-zone SSC model (Weidinger & Spanier 2010). For the one-zone model, the model parameters have been determined both by a manual fitting procedure and a χ^2 minimisation technique (Mankuzhiyil *et al.* 2011). The minimum Lorentz factor $\gamma_{\rm min}$ has been set a priori to the minimum value 1 and a rather high value of 4000 and 1000 in the case of the manual and χ^2one-zone fitting, respectively, covering a large fraction of the reasonable parameter range. For a detailed description of the models see Section 2.6.

The SEDs and the resulting model fits are shown in Figure 6.33. For the modelling,

the 60 GeV point (reaching from 10 to 100 GeV) from 1FGL has not been considered, as it is dominated by low statistics(< 10 events; D. Bastieri, 2012, private communication) and hence potentially biased by flaring states as well as subject to rather large systematic uncertainties. Additionally, the 6 GeV point does not connect smoothly to the 60 GeV point, which may be a source intrinsic effect, but more likely is caused by the aforementioned bias by high flux states. The *Swift* BAT 66 months spectrum has been taken into account for the high data set only. The upturn from soft to hard X-rays in the low state cannot be explained by the applied SSC models nor is expected from other up-to-date theoretical models. Since the data has not been taken simultaneously, the incompatibility with current models does not justify the application of completely new models.

It should be noted that in SSC models, the emission in $\sim$the sub-millimetre regime is synchrotron self-absorbed by the emitting electrons. The flux observed by the radio instruments is coming from cooled electrons, potentially from regions located further downstream in the optically thin part of the jet (see e.g. Maraschi & Tavecchio 2003; Rüger *et al.* 2010). Therefore, SSC models naturally cannot describe the SED in the radio regime.

Results and Discussion In Figure 6.33 also the probably artificial *Swift* BAT flare is shown. As noted in Section 6.4.2, the spectrum cannot be reconciled with the quasi-simultaneously measured *Swift* XRT low spectrum. On the other hand, it connects rather smoothly with the XRT spectrum from 8 December 2007 with the highest X-ray flux published until today from 1ES 2344+514 (Acciari *et al.* 2011a). Hence a spectrum as derived for the 1-week high state measured by BAT could in principle be realised in this source. Nevertheless it is not considered for the SSC model fits.

The 1FGL data constrain the SED models rather well in the HE regime. Especially the "manual" one-zone model fits assuming a $\gamma_{\mathrm{min}} = 1$ are basically excluded. The remaining models can describe the data quite well, though the compatibility between the manual one-zone fits with $\gamma_{\mathrm{min}} = 4000$ and the LAT data would be better assuming a softer spectrum at HEs. The manual one-zone model also requires slightly higher X-ray fluxes in the high state. Using the χ^2 minimisation technique, the 1FGL data could be reproduced well, but small discrepancies become apparent at soft X-rays where the model assumes lower fluxes than the data suggest. γ_{min} could not be constrained by the data sufficiently in this case. A notable difference between using $\gamma_{\mathrm{min}} = 1$ or 1000 was only apparent in the energy regimes not probed by the data points (which is not surprising considering that both fits are optimised to match the same data). Therefore only the results of $\gamma_{\mathrm{min}} = 1000$ are shown in Figure 6.33 for clarity, a value which is in better agreement with results from particle acceleration simulations.

The resulting model parameters are listed in Table 6.6. We note that a spectral break larger than unity, as given by the one-zone model, is hard to reconcile in the present case of pure synchrotron cooling. In general, the parameter values of the manual one-zone fit and the two-zone model match quite well, whereas the χ^2 minimisation results are partly not complying with these. Particularly the magnetic field B, electron density K and first electron spectral index e_1 are very low, whereas the emission region is determined to be rather large. In contrast to the other modelling results, these values have

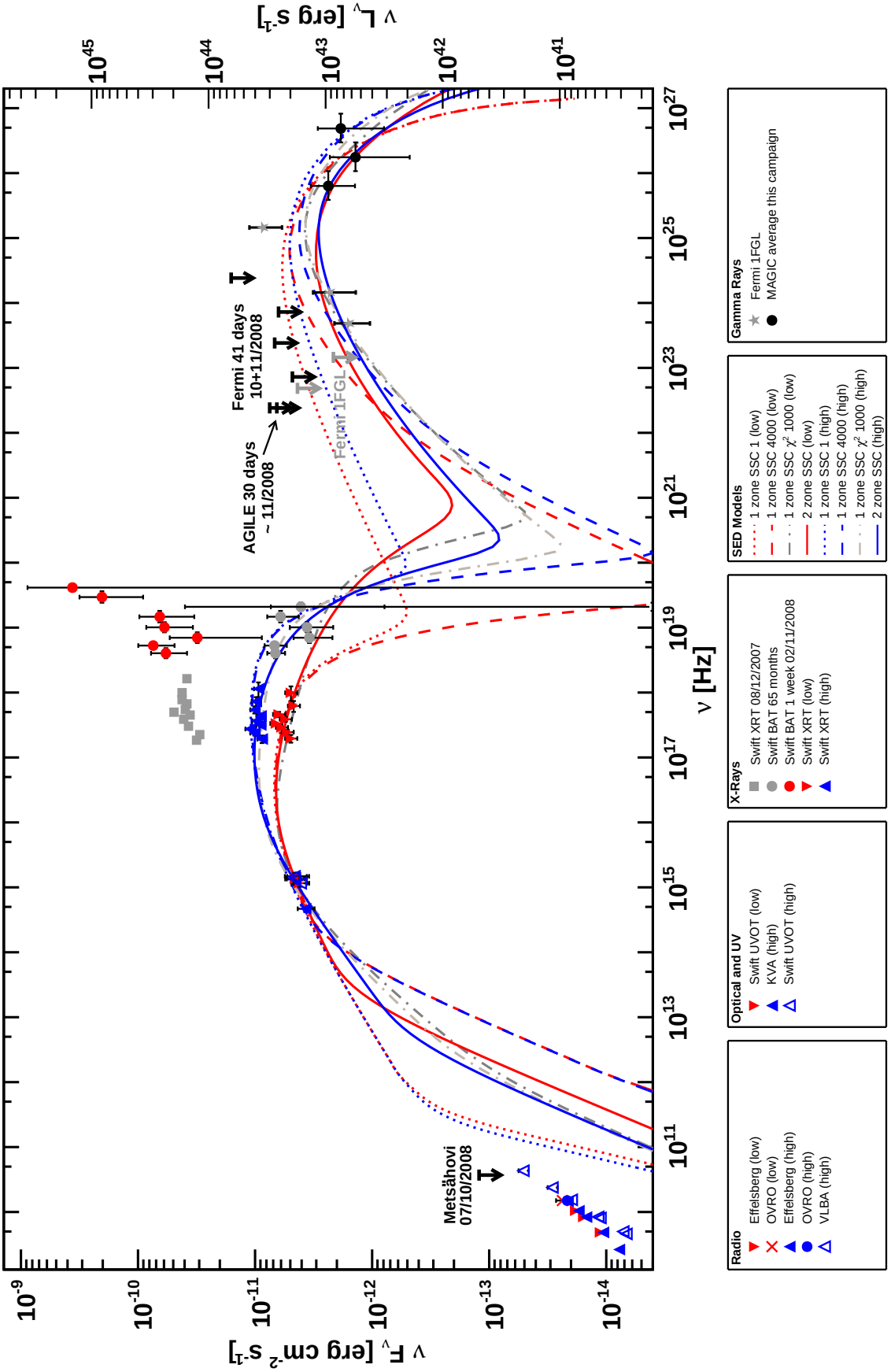

Figure 6.33: (Quasi-)Simultaneous SEDs of 1ES 2344+514 as measured within this MW campaign. Optical data have been corrected for the host galaxy contribution as well as de-reddened, UV data have only been de-reddened. The V-, B- and U-band fluxes are not shown due to their large uncertainty (see Section 6.4.3). The XRT measurements were corrected for galactic absorption. The AGILE UL has been calculated for energies $> 100\,\mathrm{MeV}$. The VHE flux densities were corrected for absorption be the EBL applying the model by (Kneiske & Dole 2010). The numbers appended to the model legend entries represent their corresponding γ_{min}. The SEDs are shown in a historical context in Figure 6.45. 1FGL data are taken from the ASDC SED builder (http://tools.asdc.asi.it/), *Swift* XRT data are taken from (Acciari *et al.* 2011a).

Model	**One-Zone**		**Two-Zone**		**One-Zone using χ^2 minimisation**			
Flux Level	low	high	low	high	low	high	low	high
B [G]	0.07		0.05	0.09	0.02	0.03	0.02	0.02
δ	20		26	29	16	15	15	16
R_{em} [10^{15} cm]	3	4	9	5	21	19	23	19
$K^{(a)}$ [10^5 cm^{-3}]	4.5	1.9	0.2	0.1	$5.6 \cdot 10^{-4}$	$6.3 \cdot 10^{-4}$	$2.7 \cdot 10^{-4}$	$1.1 \cdot 10^{-3}$
e_1	2.3		2.5	2.3	1.7	1.7	1.6	1.8
e_2	3.4	3.2	3.5	3.3	3.3	3.3	3.3	3.2
$\gamma_{\rm min}$ $^{(b)}$	1 or 4000		1800	550	1		1000	
$\gamma_{\rm break}$ [10^4]	5	8	10	3	5	6	5	5
$\gamma_{\rm max}$ [10^6]	0.7	1.5	6.3	1.5	3.6	4.1	8.2	3.5
χ^2_{red} $^{(c)}$	...	...	...	...	0.92	0.67	0.91	0.67

Notes. $^{(a)}$ For the one-zone model, K is defined in the emission region at $\gamma_{\rm min} = 1$, whereas in the two-zone case, K is given for the acceleration region at $\gamma_{\rm min}$. Hence these values are not directly comparable between the two different models. $^{(b)}$ $\gamma_{\rm min}$ was fixed a priori for the one-zone model. In case of the manual modelling, the other parameter values do not depend on $\gamma_{\rm min}$. $^{(c)}$ d.o.f. in low state: 9; d.o.f. in high state: 18.

Table 6.6: Parameters defining the SED models of 1ES 2344+514 shown in Figure 6.33. For a description of the models and parameters, see Section 2.6

been determined basically bias-free (though they are restricted to a physically motivated range according to N. Mankuzhiyil, 2012, private communication). Nevertheless from the theoretical point of view, an electron index e_1 below 2 is hard to reconcile with standard theory and observed cosmic ray spectra. This would require extremely efficient accelerators, which is not the case for BL Lacs. The cooling time scale for electrons producing 1 keV X-ray photons is > 16 days, which is not in agreement with the observed X-ray variability time scales. Finally, the position of the spectral break is not consistent with synchrotron cooling. As determined from B and R_{em}, it should be located around $\gamma = 3 \cdot 10^6$ (F. Spanier, 2012, private communication). Because of these inconsistencies, we refrain from a deeper investigation and discussion of the χ^2 minimisation results and concentrate on the manual one-zone and two-zone models. Their results are compared to archival values in Section 6.5.7.

Due to the comparably large variability time scale at X-rays, the two flux states were modelled independently of each other in case of both models. Nevertheless a comparison might help to understand the physical conditions within the source. The transition from the high to the low SED is explained in the one-zone model mainly by an electron distribution characterised by a decreased $\gamma_{\rm break}$ and $\gamma_{\rm max}$ as well as a harder spectral index in that range, whereas in the two-zone model, $\gamma_{\rm min}$, $\gamma_{\rm break}$, $\gamma_{\rm max}$ and the corresponding spectral indices increased. In the latter case, this is accompanied by a self-consistently decreased magnetic field strength in a larger emission region, whereas the acceleration region shrank and lost electrons.

The change of the acceleration region and electron reservoir in the two-zone model can be understood in terms of a standing shock in the jet (see e.g. Marscher *et al.* 2008), the passage of which caused the flux increase. When leaving this shock region again, the volume in which electrons are being accelerated will become smaller and the magnetic

field will decrease (which is supposed to be larger at the shock front), as observed. Once accelerated electrons entering the emission region are "lost" for acceleration processes, leading to a reduced electron density K. The altered electron energy distribution for both models may be a consequence of changing acceleration mechanism, caused e.g. by different efficiencies of the underlying Fermi processes. It is interesting that the electron energy distribution changed in opposite directions for the two models. We recall that in the two-zone case, the γ_x parameters are derived self-consistently, whereas in the one-zone model the values are set a priori. Additionally, in terms of synchrotron cooling, the γ_{break} depends on the magnetic field, hence constancy of the latter in the one-zone model is inconsistent with the decrease in γ_{break}. In summary, the parameter changes are not in all cases physically consistent, so that the most likely explanation is the observation of two independent emission regions responsible for the low and high SED.

For all model fits presented here, the inverse-Compton component of the low state SED is above the corresponding high state one, which is not necessarily expected. In fact, the bolometric luminosities in case of the one-zone model fits yield practically identical values (considering the rather large uncertainties involved) for the low and high SED ($10^{44.7}$ and $10^{44.8}\,\mathrm{erg\,s^{-1}}$ ($10^{44.6}$ and $10^{44.7}\,\mathrm{erg\,s^{-1}}$) in case of $\gamma_{\mathrm{min}} = 1$ ($= 4000$), respectively). If this coincidence is not by chance, this implies that flares can also be produced without changes in the total luminosity of the emission region. Such a behaviour has been reported e.g. for the FSRQ 3C 454.3, though the flux changes amounted for this source to ~ 2 and ~ 1 orders of magnitude in the optical and X-ray regime, respectively (Pian *et al.* 2006; Ghisellini *et al.* 2007).

It is interesting to note that the radius of the emission region determined from theoretical model fits is ~ 1 order of magnitude lower than obtained from direct VLBI imaging (see Section 6.4.4). If the SSC models applied here are the correct description of the emission region, it is very unlikely that the VLBI radio emission and the radiation at higher frequencies share the same production site.

Figure 6.33 reveals significant differences between the models in the radio – optical and hard X-ray – soft gamma-ray regime. These are covered partly by *Planck* (see also Section 6.5.7), *Swift* BAT and *INTEGRAL* IBIS, though with a sensitivity insufficient for simultaneous MW campaigns. Future, more sensitive experiments measuring in these energy bands might be able to probe the validity of the applied models.

A small shift of the synchrotron peak between the two SEDs is visible. The peak location can be determined from a log-parabolic power-law fit in apex form to the optical and X-ray data (Tramacere *et al.* 2007):

$$\nu F_\nu = f_0 \cdot 10^{-b\left(log_{10}\left(\nu/\nu_{\mathrm{peak}}\right)\right)^2}\,\mathrm{erg\,cm^{-2}\,s^{-1}} \tag{6.8}$$

with the normalisation f_0, the curvature parameter b and the peak frequency ν_{peak}. Applying the formula to the low and high data set and converting to energy scale yields $E_{\mathrm{peak,low}} = (0.27 \pm 0.24)\,\mathrm{keV}$ ($\chi^2/\mathrm{d.o.f.} = 6.5/8$) and $E_{\mathrm{peak,high}} = (2.8 \pm 4.5)\,\mathrm{keV}$ ($\chi^2/\mathrm{d.o.f.} = 5.6/10$), see Figure 6.34. Apart from the hardly significant peak energies, the fits are not significantly preferred by a likelihood ratio test over a simple power law (79.5 % and 95.7 % in case of the low and high data, respectively). Hence this procedure cannot constrain the peaks sufficiently.

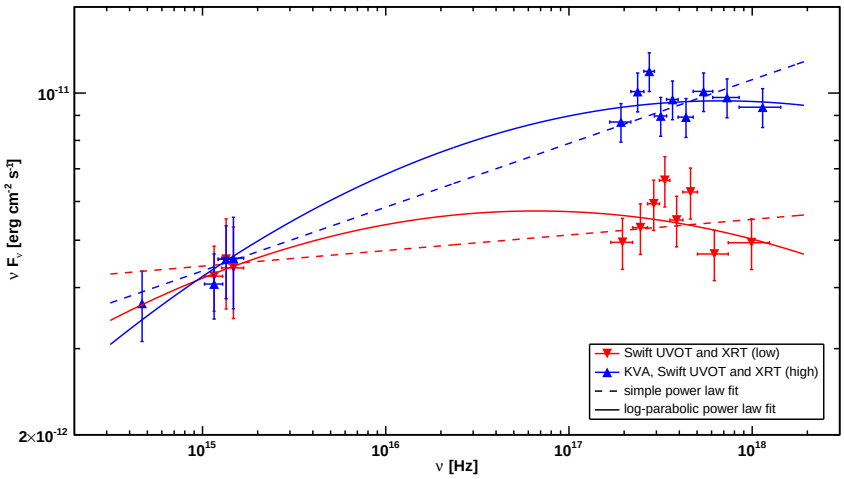

Figure 6.34: Simultaneous optical, UV and X-ray data of 1ES 2344+514 measured by KVA, *Swift* UVOT and *Swift* XRT, respectively. The KVA and UVOT data have been de-reddened, the former additionally host-galaxy corrected. X-ray data have been corrected for galactic absorption. The "low" (red downward triangles) and "high" (blue upward triangles) data points have been fit with a simple power law (dashed lines) as well as a log-parabolic power law (Eq. 6.8) shown as the solid lines.

Determining the peak position instead from the one-zone $\gamma_{\mathrm{min}} = 4000$ (two-zone) modelling results in a shift from $\sim 0.15\,\mathrm{keV}$ ($\sim 0.13\,\mathrm{keV}$) in the low state to $\sim 1.7\,\mathrm{keV}$ ($\sim 0.46\,\mathrm{keV}$) in the high state, corresponding to ~ 1.1 (~ 0.35) orders of magnitude. These numbers are quite different and were derived without an estimation of the error due to the unknown uncertainty introduced by a potential mismatch between the data and the model. Also in the case of the χ^2 minimisation, were a quantitative goodness of the fit is available, the X-ray data are not well described (as stated above) and hence will not result in a more reliable estimation. Consequently a significant shift of the peak position cannot be proven with the present data. In any case the peak position change is much smaller than reported in the literature for the "extreme blazar" 1ES 2344+514 (Giommi *et al.* 2000), which is expected due to the rather small flux change found in this MW campaign.

6.5 Long-Term Characteristics

The advent of *Fermi*-LAT triggered several monitoring programs at different wavelengths concentrating on blazars (e.g. F-GAMMA, OVRO). From these and the Tuorla Blazar Monitoring Program[15] as well as all-sky instruments (*Fermi*-LAT itself, *RXTE* ASM and *Swift* BAT), long-term observations are available for 1ES 2344+514 which will be investigated in the following. Long-term studies are especially interesting in the radio regime, where typical variability time scales are much larger compared to higher frequencies. The source has also been targeted several times by *Swift* XRT.

Since *RXTE* ASM, *Swift* BAT and *INTEGRAL* ISGRI turned out to be hardly sensitive enough to detect the source on small time scales ($\sim 1\,\mathrm{day}$), the corresponding light

[15] http://users.utu.fi/kani/1m/

MJD	Energy [GeV]	R.A.[a] [°]	Dec.[b] [°]	Sep.[c] [arcmin]
54879.961	221	356.59	51.80	9
54992.961	174	356.79	51.61	6
55041.439	283	356.73	51.75	3
55358.826	495	356.86	51.63	6
55553.247	201	357.01	51.60	10
55896.009	114	356.79	51.68	2
55702.733	207	356.97	51.63	9
55936.262	107	356.79	51.91	11
55948.736	231	356.74	51.73	2

Notes. [a] Right ascension (J2000) and [b] declination (J2000). [c] Angular Separation between the event direction and 1ES 2344+514.

Table 6.7: *Fermi*-LAT detected events with an energy > 100 GeV from the direction of 1ES 2344+514 (R.A. 356.77°, Dec. 51.71°).

curves have been re-binned to bin widths of 1 week, 1 month, 1 quarter and 1 year as described in Section E.2.2.2.

6.5.1 High Energy Gamma Rays

1ES 2344+514 was not detected at HE gamma rays during the MW campaign. Also considering longer time scales (July 2007 – January 2011), AGILE did not detect a significant signal from the source. The derived UL on the integral flux > 100 MeV of $2.7 \cdot 10^{-8}\,\mathrm{ph\,cm^{-2}\,s^{-1}}$ was still consistent with the 2FGL average flux above 100 MeV ($\sim 0.9 \cdot 10^{-8}\,\mathrm{ph\,cm^{-2}\,s^{-1}}$).

As reported in Section 6.1, *Fermi*-LAT was able to detect the source on longer time scales, but also did not find significant variability, neither from the 24 month light curve nor from a comparison between the 1FGL and 2FGL spectra.

A dedicated high energy analysis revealed nine events with energies in excess of 100 GeV detected by LAT within the first 44 months (4 August 2008 – 18 April 2012) from the direction of 1ES 2344+514 (see Table 6.7 and Figure 6.41). The highest energy event reached nearly 500 GeV.

Until today, no LAT catalogue of sources with events above 100 GeV over this large time scale is available with which these results could be compared. Therefore, the TeV HBLs with a comparable redshift Mrk 421, Mrk 501, Mrk 180 and 1ES 1959+650 have been analysed with the same pipeline. Due to the irregular observation sampling in combination with strong variability at VHE, a representative luminosity at these energies cannot be determined from the published results. However, *Fermi* is operating in all-sky mode, making its measurements basically not biased by observation sampling. Additionally, the mean flux from 2FGL should not be dominated by flares of the source due to its rather large observation time basis of 24 months (note though that Mrk 421, Mrk 501 and 1ES 1959+650 are significantly variable in the HE band).

Therefore, to a first approximation, the fluxes in the highest LAT energy bin (10 – 100 GeV) from 2FGL have been used to derive the source luminosity at 60 GeV. Since

Source	$z^{(a)}$	$D_L{}^{(b)}$ [Mpc]	**Index**$^{(c)}$	$F_{60\,\mathrm{GeV}}{}^{(d)}$ [erg cm^{-2} s^{-1}]	$L_{60\,\mathrm{GeV}}{}^{(e)}$ [erg s^{-1}]	$N^{(f)}$	$N_\mathrm{n}{}^{(g)}$
Mrk 421	0.030	130	1.77 ± 0.01	$(9.48 \pm 0.55) \cdot 10^{-11}$	$(1.92 \pm 0.11) \cdot 10^{44}$	35	18
Mrk 501	0.034	142	1.74 ± 0.03	$(2.88 \pm 0.31) \cdot 10^{-11}$	$(6.95 \pm 0.75) \cdot 10^{43}$	16	10
1ES 2344+514	0.044	183	1.72 ± 0.08	$(5.75 \pm 1.39) \cdot 10^{-12}$	$(2.30 \pm 0.56) \cdot 10^{43}$	9	9
Mrk 180	0.046	194	1.74 ± 0.08	$(4.47 \pm 1.13) \cdot 10^{-12}$	$(2.01 \pm 0.51) \cdot 10^{43}$	1	1
1ES 1959+650	0.048	198	1.94 ± 0.03	$(1.28 \pm 0.17) \cdot 10^{-11}$	$(6.00 \pm 0.80) \cdot 10^{43}$	3	4

Notes. $^{(a)}$ Redshift of the source. $^{(b)}$ Luminosity distance taken from NED (2012). $^{(c)}$ *Fermi*-LAT 2FGL simple power law spectral index (Nolan *et al.* 2012). $^{(d)}$ *Fermi*-LAT flux at 60 GeV (integrated between 10 and 100 GeV), photon counts taken from Nolan *et al.* (2012). $^{(e)}$ Calculated luminosity of the source at 60 GeV. $^{(f)}$ Number of events with an energy > 100 GeV detected from the source. $^{(g)}$ N normalised to the distance of 1ES 2344+514.

Table 6.8: HE properties of TeV HBLs located at a distance comparable to the one of 1ES 2344+514.

the energy range to be probed lies above 100 GeV, the spectral shape of the sources is important to get an estimate if relative changes in VHE luminosity need to be considered. For all sources, simple power laws are strongly preferred over curved power law shapes, and the spectral indices are matching very well for four of the sources. Therefore their luminosities can be compared directly. Only for 1ES 1959+650 the index is slightly flatter than for the others (Nolan *et al.* 2012). In Table 6.8, the source parameters are summarised and the number of events > 100 GeV are given.

The event energies of the five sources are compared in Figure 6.35. The distribution of 1ES 2344+514 seems to be shifted slightly to higher energies, peaking around 200 GeV. In contrast, most of the events from Mrk 421 are located at low energies, whereas the distribution of Mrk 501 shows a peak around 150 GeV. However, the individual event statistics but for Mrk 421 are too small to allow for a detailed investigation and discussion. In principle, differences in the distribution and number of such events could arise from different flaring duty cycles of the sources. If the high energy component is dominated by large flares, the event distribution may be shifted to higher energies, as seems to be the case for 1ES 2344+514 and Mrk 501. If on the other hand the event origin lies in a higher baseline flux of the source, most of the events should be located around low energies, just like for Mrk 421. Longer observations are needed to investigate the duty cycle of the sources and the occurrence of the highest energy photons.

The number of events should be directly correlated with the luminosity of the source. Since the luminosity is an intrinsic source property, the intrinsic event counts have to be used for a comparison. The counts depend on the distances to the source ($\propto$ distance squared) and thus have been normalised to the distance of 1ES 2344+514. Note that absorption effects caused by the EBL are negligible at the distance and energy ranges under investigation.

Figure 6.36 shows that a clear positive correlation between the normalised number of events > 100 GeV and the source luminosity exists. The slope of the linear fit ((0.99 ± 0.24) counts per 10^{43} erg s^{-1}) is very well compatible with the expected dependence of unity, despite the different time basis for the event counts (44 months) and luminosities (24 months). This indicates that the 2FGL fluxes are a suitable representation

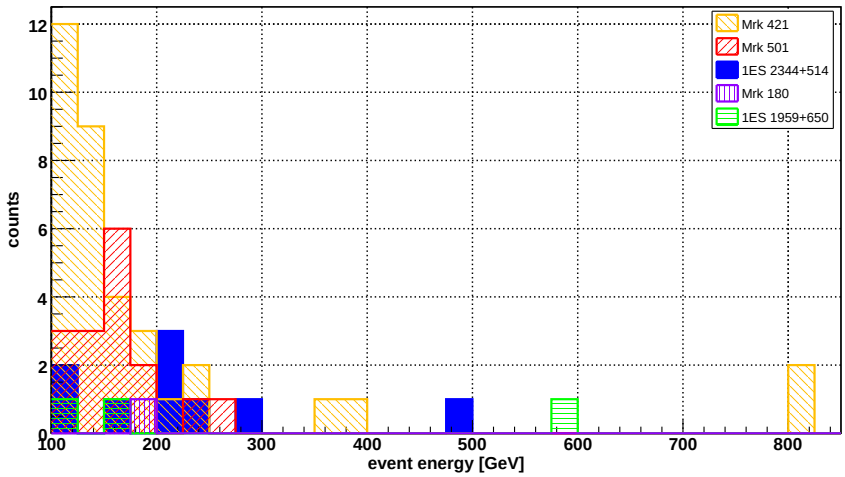

Figure 6.35: Distribution of events with an energy $> 100\,\mathrm{GeV}$ detected by *Fermi*-LAT from five HBLs.

of the long-term flux averages of the sources. It should be noted that this interpretation is rather speculative considering that there are only five data points available.

As expected from the flatter spectral index and hence lower flux at VHE compared to the HE luminosity, 1ES 1959+650 is slightly below the fit line. The event counts of 1ES 2344+514 on the other hand are larger than supposed (2 – 3 photons would be expected from the fit), as the corresponding point is above the fit by more than $2\,\sigma$. A higher number of events $> 100\,\mathrm{GeV}$ despite a comparably low luminosity may be explained by a few strong flaring events or in general higher duty cycle of the source. As Table 6.7 is showing, the events detected from 1ES 2344+514 are not strongly clustered in time and hence favour a higher duty cycle above a rather low number of strong flares. This interpretation would be in line with the findings from the event energy distributions, also indicating a higher duty cycle of 1ES 2344+514 compared to the one of the other four sources. An alternative explanation involves a misidentification of diffuse galactic foreground events, which would artificially increase the event counts of the low galactic latitude source 1ES 2344+514. To estimate the number of such events, two region at the same galactic latitude but offset by 2.5° in galactic longitude have been analysed with the same pipeline. These regions are not known to contain a HE source and are are therefore representative of the diffuse galactic emission. No event $> 100\,\mathrm{GeV}$ was detected from these two regions, hence the contaminating fluxes are negligible (Aleksić *et al.* 2012f).

6.5.2 X-Rays

***Swift* XRT** Apart from the simultaneous multi-wavelength data, the long-term X-ray flux has also been studied analysing all 67 XRT observations of the source publicly available. The analysis procedure is described in Aleksić *et al.* (2012f). The resulting light curve between 2 and 10 keV is shown in Figure 6.41, which proves strong variability of the source. A fit with a constant yields an unacceptable χ^2/d.o.f. of 491.8/66 with a significantly positive mean integral flux $F_{2-10\,\mathrm{keV}}$ of $(8.99 \pm 0.18) \cdot 10^{-12}\,\mathrm{erg\,cm^{-2}\,s^{-1}}$.

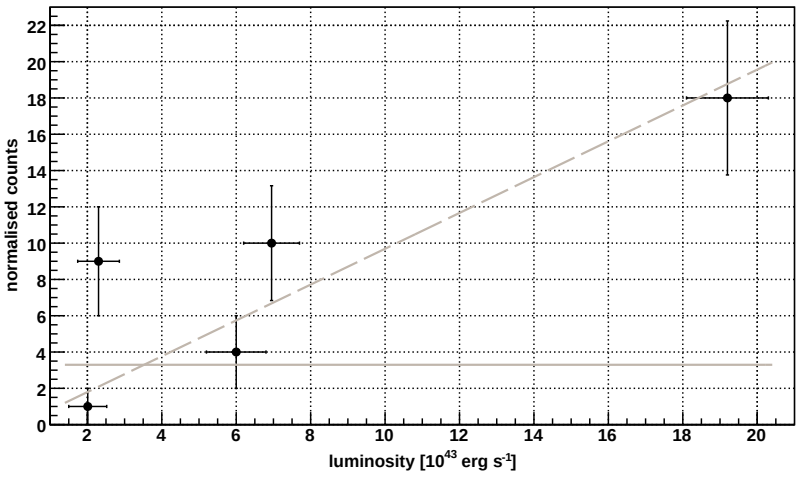

Figure 6.36: Number of events $> 100\,\mathrm{GeV}$ compared to the HE luminosity of the source (see also Table 6.8). For the counts, Poissonian errors have been assumed. The goodness of the constant fit (solid line) amounts to $4.0 \cdot 10^{-3}\,\%$ (χ^2/d.o.f. = 25.5/4), whereas for the linear fit χ^2/d.o.f. = 7.4/3 (6.1 %). The slope of the linear fit is 0.99 ± 0.24 counts per $10^{43}\,\mathrm{erg\,s^{-1}}$. A logarithmic likelihood ratio test prefers the linear fit with 98.9 %.

Also the distribution of flux over error shows a clear deviation from zero. The source has always been detected significantly by XRT.

The flux evolution shows several strong flares. The time period of comparably high activity between MJD 54370 and 54467, showing the highest flare of all the XRT measurements of 1ES 2344+514, was part of the VERITAS MW campaign Acciari *et al.* (2011a), the main results of which are summarised in short in Section 6.5.7. The highest flux observed during the MW campaign presented here was a factor 3.5 lower than this long-term high.

***RXTE* ASM** ASM is offering the longest time coverage of 1ES 2344+514. However, the data later than 1 January 2011 have not been considered for this study due to a considerable loss of instrument sensitivity caused by degradation of the detectors (J. Wilms, 2012, private communication). Analysis details are given in Aleksić *et al.* (2012f), the light curve with weekly binning is shown in Figure 6.41. Further binnings are presented in Section E.3.

The ASM light curve is showing several peak-like features on different binning time scales from day to month-wise binnings. These features can be related to solar influence on ASM due to a small angle of the instrument to the sun, and hence cannot be attributed to 1ES 2344+514.

On daily time scales, ASM indeed saw one high state of the source at MJD 54468.0 (see Figure 6.43). With a signal/error fraction of ~ 5 this measurement is significant and off from the expectations of a Gaussian distribution (see Figure E.11). It will be discussed in a multi-wavelength context in Section 6.5.6. Note though that due to the coded mask observation technique, the ASM data points are not supposed to follow a Gaussian behaviour. No significant detection by ASM has been found on other time scales. The source seems in general to be too faint for ASM to be detected. This is further sup-

Instrument	Binning	χ^2_c/d.o.f.$^{(a)}$	Mean$_c$$^{(b)}$	χ^2_G/d.o.f.$^{(c)}$	Mean$_G$$^{(d)}$
RXTE ASM	day	4215.6/3007	$-(2.86 \pm 0.67) \cdot 10^{-2}$	41.4/51	$-(0.072 \pm 0.022)$
	week	685.3/436	$-(2.87 \pm 0.67) \cdot 10^{-2}$	23.3/26	$-(0.179 \pm 0.062)$
	month	166.1/99	$-(2.83 \pm 0.68) \cdot 10^{-2}$	22.7/19	$-(0.52 \pm 0.20)$
	quarter	48.7/32	$-(2.85 \pm 0.67) \cdot 10^{-2}$	...	...
	year	14.9/7	$-(2.69 \pm 0.70) \cdot 10^{-2}$	...	...
Swift BAT	day	2364.1/1733	$(2.14 \pm 0.28) \cdot 10^{-5}$	58.9/49	0.175 ± 0.029
	week	440.3/280	$(2.14 \pm 0.28) \cdot 10^{-5}$	17.8/24	0.327 ± 0.079
	month	118.8/65	$(2.14 \pm 0.28) \cdot 10^{-5}$	8.5/16	1.11 ± 0.22
	quarter	30.9/21	$(2.14 \pm 0.28) \cdot 10^{-5}$	...	...
	year	5.1/5	$(2.14 \pm 0.28) \cdot 10^{-5}$	...	...
INTEGRAL ISGRI	day	228.8/214	$(4.5 \pm 3.1) \cdot 10^{-2}$	10.2/15	0.111 ± 0.074
	week	105.2/94	$(4.5 \pm 3.1) \cdot 10^{-2}$	4.3/9	0.11 ± 0.12
	month	54.7/46	$(4.5 \pm 3.1) \cdot 10^{-2}$	2.6/8	$-(0.01 \pm 0.20)$
	quarter	25.7/20	$(4.5 \pm 3.1) \cdot 10^{-2}$	...	...
	year	8.2/5	$(4.5 \pm 3.1) \cdot 10^{-2}$	...	...

Notes. $^{(a)}$ χ^2/d.o.f. of a fit with a constant to the light curve. $^{(b)}$ Mean value of the fit with a constant. Units are counts s^{-1} for ASM and ISGRI and counts s^{-1} detector^{-1} for BAT. $^{(c)}$*and*$^{(d)}$ Same as $^{(a)}$ and $^{(b)}$, respectively, but for a fit with a Gaussian to the rate/error distribution.

Table 6.9: Results of a fit with a constant to the differently binned light curves of *RXTE* ASM, *Swift* BAT (14 – 195 keV) and *INTEGRAL* ISGRI as well as of a fit with a Gaussian to the corresponding signal/error distributions. The latter has not been performed for the quarterly and yearly binning due to low statistics.

ported by the fact that the mean rate observed by ASM of 1ES 2344+514, determined by a fit with a constant, is negative on all binning time scales (see Table 6.9). A possible explanation are systematics in the background determination, which may become apparent for faint sources (J. Wilms, 2012, private communication). The corresponding fit probabilities are very low, but do not give evidence for variability due to Gaussian statistics not being appropriate to describe the ASM data.

***Swift* BAT** The BAT long-term data have been analysed as described in Section E.2.2.2. In Figure 6.41, the light curve (14 – 195 keV) with weekly binning is displayed. Further binnings are shown in Section E.3.

Apart from the probably artificial high state on weekly time scales (see Section 6.4.2), no significant detection of 1ES 2344+514 was apparent in any of the light curves with different binning. Also the signal/error distribution histograms did not show points significantly offset from a Gaussian distribution. Though BAT is performing coded-mask observations like *RXTE* ASM, Gaussian statistics is still applicable due to the high number of mask elements (J. Wilms, 2012, private communication). Therefore, the low probabilities given by a fit with a constant to the light curves (see Table 6.9) is suggesting variability of the source on long time scales. The significantly positive mean fit values indicate that 1ES 2344+514 is seen marginally by BAT on rather small time scales, which was proven by the significant detection first reported in the BAT 58-Month Catalog.

***INTEGRAL* ISGRI** The data have been obtained from HEAVENS[16]. No significant detection was present in the differently binned light curves, which are all consistent with a constant rate, or in the signal/error distribution on any of the probed time scales. A positive trend of the fit mean value is obvious though from Table 6.9, indicating that ISGRI may detect a cumulative signal from 1ES 2344+514 after subsequent observations.

6.5.3 KVA and Tuorla

Significant variability is obvious from the R-band light curve of 1ES 2344+514 obtained within the Tuorla Blazar Monitoring Program, see Figure 6.41. Over the more than nine years of observations, the flux density was varying between 3.97 and 4.94 mJy. A fit with a constant yields a mean flux density of (4.342 ± 0.004) mJy, but cannot describe the evolution of the data (χ^2/d.o.f. = 2058.3/437). Compared to the long-term trend, the MW campaign has been conducted in a time of exceptional steady and rather low flux density (see Section 6.4.3). The light curve shows several distinct flares, which will be discussed in a MW context in Section 6.5.6.

6.5.4 Single-Dish Radio Observations

F-GAMMA 1ES 2344+514 has been observed in the framework of the F-GAMMA program since the beginning of 2007 by Effelsberg and IRAM. The data reduction is described in Aleksić *et al.* (2012f). The light curves measured by both instruments are shown in Figure 6.37. IRAM did not detect the source significantly also on longer time scales than the MW campaign.

The Effelsberg data on the other hand show significant variability with diverse and complex characteristics. Some features are present at all (observed) frequencies, like the flares at MJD 54547 and 54779, others are visible at certain bands only. The latter is apparent at MJDs 54239 and 54486, where dips occurred at 2.64 and 4.85 GHz while the higher frequencies show a rise in flux. At MJD 54275, the 14.6 GHz flux density shows an increase compared to the constancy (with respect to the measurement at MJD 54184) at the other frequencies, similar to the behaviour at MJD 54935, where the 14.6 GHz flux density is decreasing in contrast to the flare observed at the other frequencies. It is also obvious from the light curves that the strength of distinct features may decrease with increasing frequency and finally the trend may even flip its direction, which is apparent at MJDs 54239, 54486 and 54935. The flares at MJD 54547 and 54779, on the other hand, are about constant in amplitude at all frequency bands, i.e. showing a flux increase of 8 – 9 % and 6 – 7 %, respectively (for the former, the 4.85 GHz band is not following this trend, though). Angelakis *et al.* (2012) have studied and interpreted the flaring characteristics of blazars, see below.

These different characteristics may be generated on the one hand by re-acceleration of particles within the jet or changes in the ambient medium. On the other hand, the comparably sparse sampling in combination with frequency-dependent time lags (see below) may also account for such a behaviour.

[16] http://www.isdc.unige.ch/heavens/

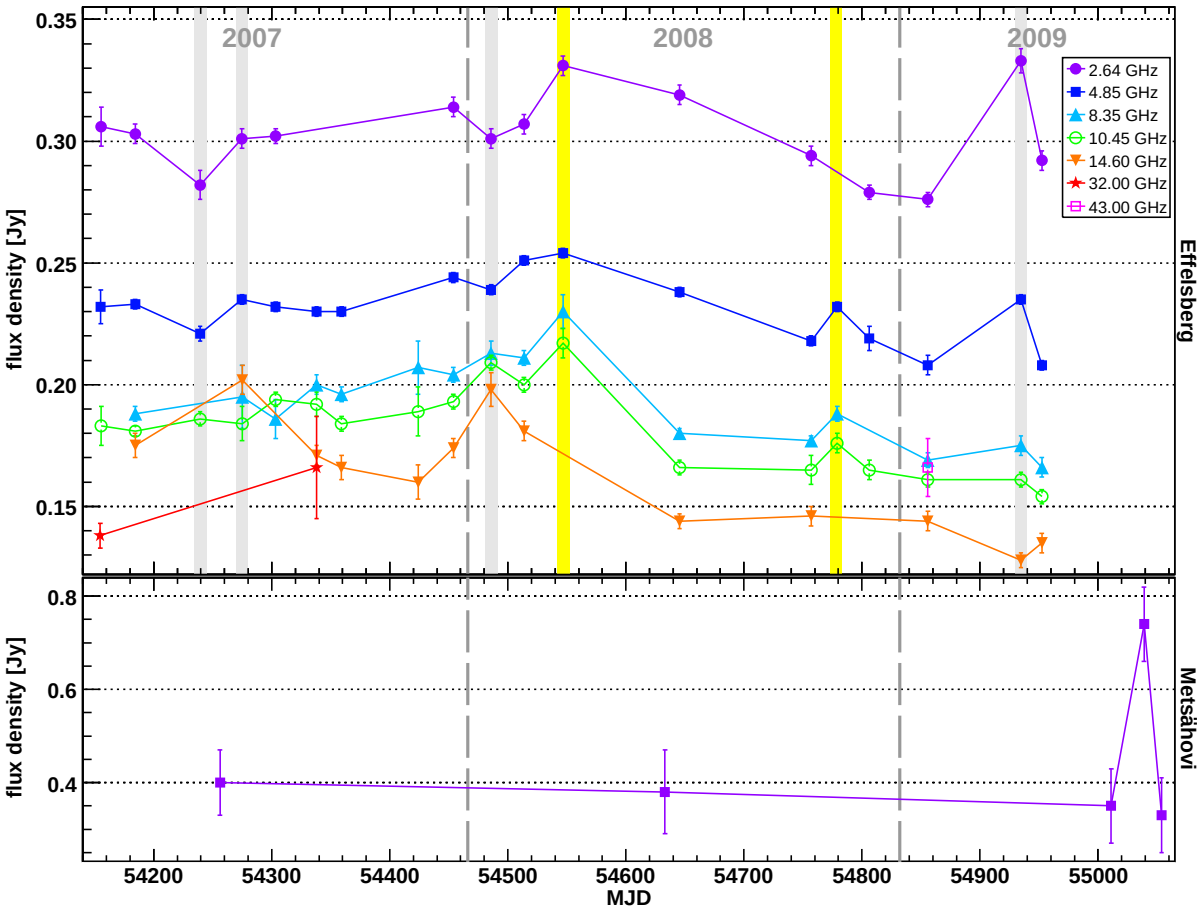

Figure 6.37: *Top panel:* light curve of 1ES 2344+514 measured by Effelsberg within the F-GAMMA program. Yellow and grey thick vertical lines denote the occurence of flares at all Effelsberg observations frequencies and at particular frequencies only, respectively. *Bottom panel:* Metsähovi detections, revealing a strong and short flare. The thin solid lines connecting the points are shown for illustrative purposes only.

OVRO The long-term light curve measured by OVRO is shown in Figure 6.41. Details of the data analysis can be found in Aleksić *et al.* (2012f). The light curve reveals significant variability. A fit with a constant is basically excluded (χ^2/d.o.f. = 3929.6/317) and yields an average flux density from beginning of 2008 until 2012 of (0.1776 ± 0.0004) Jy. During the MW campaign, the flux density was considerably lower (mean of (0.159 ± 0.001) Jy) than this average.

Metsähovi 1ES 2344+514 is at the edge of detectability for Metsähovi. From 47 observations between January 2007 and November 2009, the source was significantly detected Aleksić *et al.* (S/N $>$ 4, for analysis details see 2012f) five times only. Three of them have been obtained in direct sequence and reveal a more than doubling of the flux density at 37 GHz at the second measurement compared to the remaining two. They are included in the F-GAMMA light curve plot (Figure 6.37) for comparison. Due to the sparse sampling (the observations have been made at MJDs 55011, 55039 and 55054), the rise and fall times of this flare cannot be determined. They are restricted though

from the observations to $\lesssim 28$ and $\lesssim 15$ days, respectively. This feature will be further discussed in the following paragraph.

The Combined View The spectra of the Effelsberg and RATAN-600 have been combined with each other and with further measurements by Metsähovi and OVRO if the time difference between the observations was less than 14 days. ULs by IRAM are not shown since the lowest one is at 0.96 Jy, which is compared to the other measurements too high to constrain the behaviour of the source. Figure 6.38 is showing all the spectra from 2007 through 2009 fulfilling this condition. The individual spectra are shown in Figure E.10. Note that the sensitivity of Metsähovi may not be sufficient to detect the source in a low state of activity, hence the points at 37 GHz may be biased by high states and do not necessarily represent the typical flux density of the source. The lower flux density detected by Effelsberg at 32.00 and 43.00 GHz confirm this interpretation.

Below ~ 20 GHz, the radio spectra of 1ES 2344+514 are flat and show little variability, whereas they become flatter or are bending upwards above that frequency. The latter is most probably a result of selection effects due to low sampling at higher frequencies and a variable emission component emanating from a more compact region than the one dominating the cm-band radiation. Angelakis *et al.* (2012) explain this variability characteristics as combined emission from a two-component system. It consists of radiation (i) from an optically thin large-scale jet, relic flaring event or both (producing a steep power-law spectrum with index ~ -0.5, see also Section 6.4.4), and (ii) from a highly variable synchrotron self-absorbed component, possibly from a recent shock travelling through the jet (following the model of Marscher & Gear 1985). In this model, different source characteristics are a result of observing different evolutionary stages of the system. According to the phenomenological classification presented in Angelakis *et al.* (2012), 1ES 2344+514 represents a "type 4b" object, which is dominated by the steep quiescent spectrum and exhibits the largest such contribution among the five defined blazar types.

The strong flare observed by Metsähovi should also be visible at other radio frequencies. If such outbursts are caused by shocks or blobs travelling the jet downstream, they should be moving from higher to lower observation frequencies in the radio regime due to frequency-dependent opacity effects. Therefore, the flare may be detected with a time lag at other frequencies.

IRAM was observing two days after the highest flux observed by Metsähovi (MJD 55041), but no significant signal was detected, yielding ULs of 1.74 and 1.95 Jy at 86.24 and 142.33 GHz, respectively. Judging from the nine OVRO measurements within two weeks prior and posterior to the flare, the flux density did not vary significantly. A fit with a constant yields a probability of 77.3 % (χ^2/d.o.f. = 4.9/8). Particularly the observation 0.5 days before the Metsähovi flare did not reveal any increased activity; only from the measurement 3.5 days after the flare a small and insignificant flux density increase (by ~ 3 % compared to the mean OVRO flux density during this four weeks time span) was visible. Consequently, neither the IRAM nor the OVRO observations do confirm the Metsähovi flare, which may also be due to the comparably sparse sampling and low sensitivity.

Taking the flare for real, the non-detection by OVRO 0.5 days before and 3.5 days

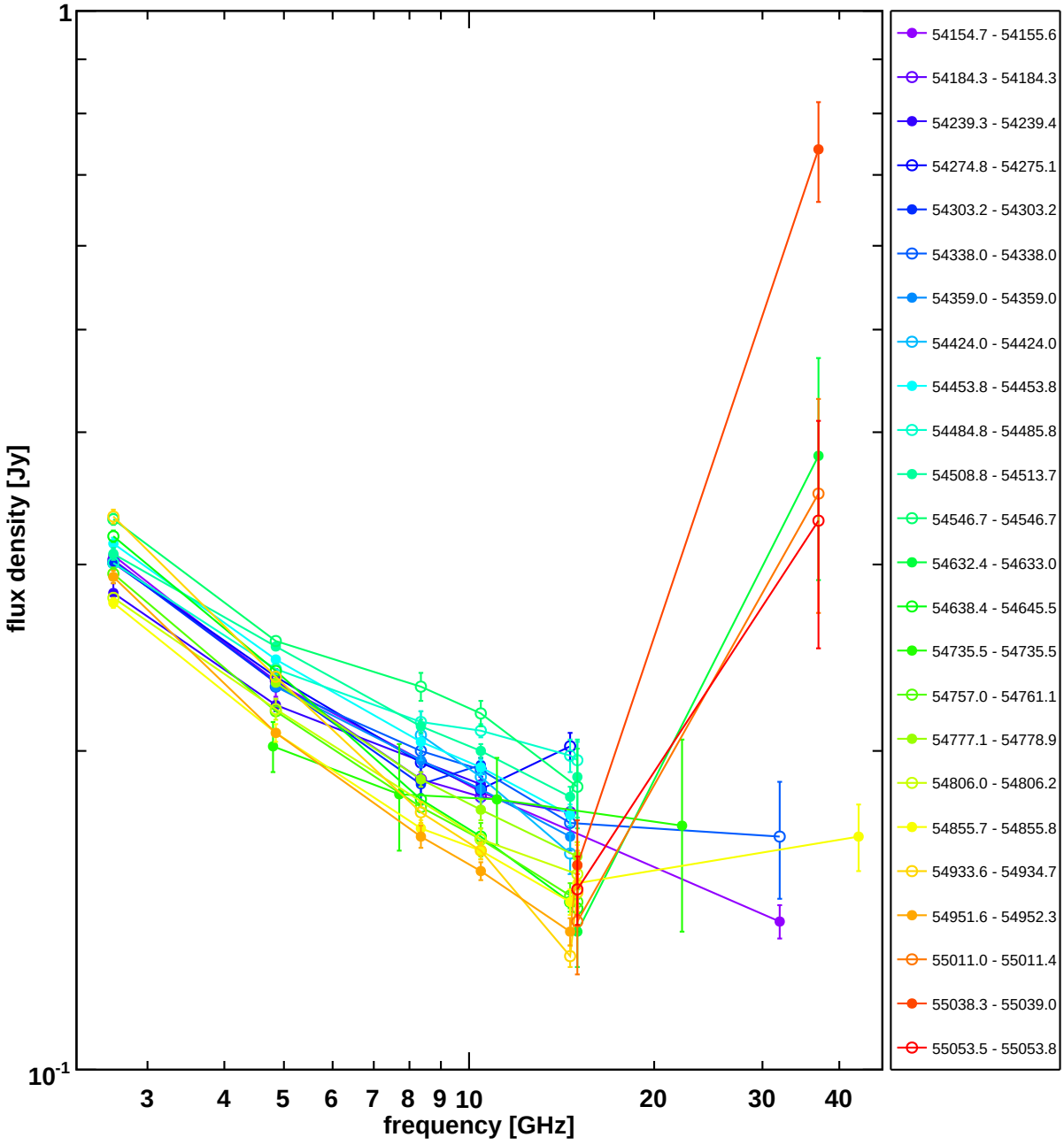

Figure 6.38: Combined radio spectra obtained from Effelsberg, Metsähovi, OVRO and RATAN-600 from 2007 through 2009. Spectra from different instruments have been combined if the time difference was less than 14 days. Legend entries correspond to the MJD range of the spectra. The solid lines simply connect the points to visualise general trends. *Note that the figure shall illustrate the long-term behaviour of the source and is not intended to identify every single spectrum. These are shown in Figure E.10.*

after the event require a comparably fast flare to have happened. Such strong, short-lived outbursts are rarely seen for HBLs at 37 GHz, but have been reported for e.g. Mrk 421 (Lichti *et al.* 2008). This may be due to the limited sensitivity of Metsähovi and consequently small statistical basis for this comparably faint objects. However, strong flares have also been detected during periods of non-detections, giving an indication for such fast flares (Nieppola *et al.* 2007).

OVRO and Effelsberg observe at similar frequencies (15.0 and 14.60 GHz, respectively), giving in principle the possibility of an independent cross check as well as a compensation for measurements not conducted. A reasonable match between the data points is present in Figure E.10. Also a correlation between the two frequency bands is found. However, a linear fit is not highly significant (see Figure E.16), which on the other hand may be due to the small statistical basis. Also the slope of the linear fit ((1.39 ± 0.25) Jy per Jy) is slightly off from the expected value of unity, which is still the case when the fit is forced to go through the origin of ordinates ((0.951 ± 0.017) Jy per Jy). Consequently, the quasi-simultaneous Effelsberg and OVRO data seems to match, the significance of which is not very high though. More observations are needed to determine a potentially offset between the instruments.

As mentioned above, the Effelsberg light curve exhibits different features, one of which being flares present at all frequency bands. No observations at 14.60 GHz had been conducted for the two such cases found, hence the OVRO data may be used to confirm the flare presence at this frequency. The OVRO observations (quasi-)simultaneously taken to the Effelsberg ones (time difference < 8 days) are shown together with the Effelsberg light curve in Figure 6.39. In case of the Effelsberg flare at MJD 54547, OVRO was observing the source with ~ 30 minutes time difference at a flux density marginally higher than the previous Effelsberg measurement. The uncertainty of the point is large enough though to still be consistent with the potential Effelsberg flux density increase of $\sim 10\,\%$. For the second flare at MJD 54779, an OVRO measurement ~ 2 days earlier is available (see also Figure 6.31). The corresponding flux density is $\sim 10\,\%$ higher than the Effelsberg measurements before and after that flare, significantly confirming the flux increase at the remaining frequencies.

In general, the OVRO observations are in agreement with the two flares at MJD 54547 and 54779 having been present at 14.60 GHz with about the same amplitude as at the other frequencies. This may represent an independent confirmation of different feature characteristics in the low frequency radio regime. It should be noted though that despite most of the quasi-simultaneous OVRO measurements match the Effelsberg points quite well, for the last two observations the OVRO flux density was considerably higher (which also decrease considerably the probability of a correlation in Figure E.16). This can hardly be explained by source intrinsic changes, since OVRO observed only ~ 1.1[17] and ~ 0.7 days before Effelsberg. Instrumental or observational effects have been excluded to be the reason (J. L. Richards & E. Angelakis, 2012, private communication), hence the discrepancy can not be resolved, yet.

[17]The OVRO measurement ~ 0.05 days apart has not been considered due to its large error of $\sim 25\,\%$, within which it would be compatible with the Effelsberg point though.

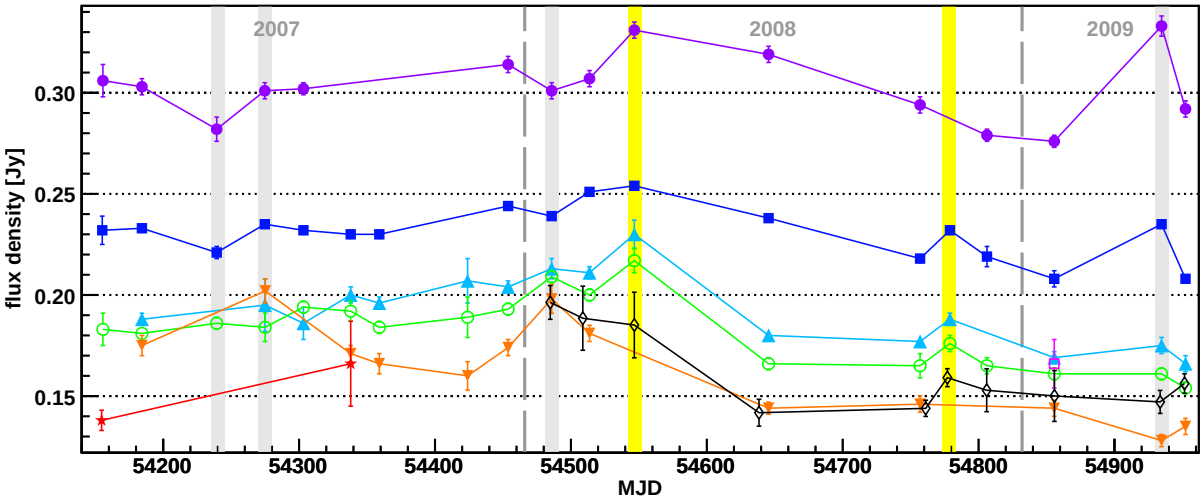

Figure 6.39: Same as the upper panel of Figure 6.37 but presenting additionally (quasi-)simultaneous OVRO measurements (black open diamonds). For an explanation of the figure please refer to Figure 6.37.

6.5.5 MOJAVE

Long-term VLBA coverage of 1ES 2344+514 at 15.4 GHz is provided by the MOJAVE monitoring program since 1999. The analysis details and results are described in Aleksić *et al.* (2012f). In most of the MOJAVE maps, three components can be identified within the jet. Investigating their motion relative to the core position over time reveals that these components do not showing any superluminal motion. In fact, they are basically stationary, see also Figure 6.40. The difference in position before and after the large monitoring gap from early 2000 until mid of 2008 is even lower than the spread measured after 2008, indicating that these features are really stable and not a potential artefact of discrete Gaussian components within the smooth jet. The apparent speed estimations yield $v_{\mathrm{app}} = -\,(0.01 \pm 0.02)\ c$ for component C 3, $(0.02 \pm 0.02)\ c$ for C 2 and $-\,(0.06 \pm 0.07)\ c$ for C 1 (Aleksić *et al.* 2012f).

As mentioned in the historical overview (Section 6.1), Piner & Edwards (2004) report significant motion ($(1.2 \pm 0.5)\ c$) for component C 1 from the observations conducted 1999 – 2000, whereas the other two jet components were found to have been stationary. In Piner *et al.* (2010), these results were combined with new measurements, resulting in significant motion for all three components. The most significant speed was measured for C 1, yielding $v_{\mathrm{app}} = (0.62 \pm 0.05)\ c$. However, the authors note that their results could be subject to a bias by frequency-dependent core – component separation, having combined measurements at different frequencies. For Mrk 421 and 1ES 1959+650, such effects had been found to be small, as the authors say.

The results obtained here are not consistent with the estimations of v_{app} for C 1 in Piner & Edwards (2004) and for all three components in Piner *et al.* (2010). This may be explained with the smaller statistical basis available at that time and the above mentioned core shift effect which has not been taken into account by the authors. The absent superluminal motion in the inner jet of 1ES 2344+514 is also in agreement with values reported from VLBI observations for high-frequency peaked blazars (see Section 2.2). However, this is in contrast to the requirements of current one-zone SED modelling.

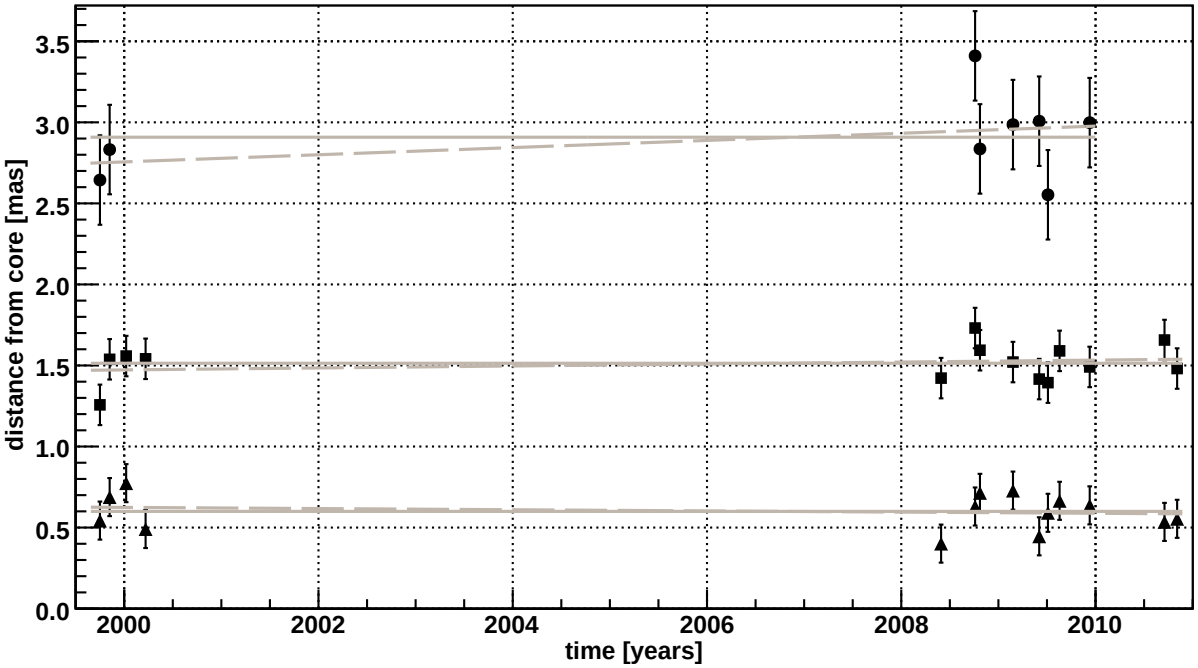

Figure 6.40: Distance with respect to the radio core over time of the three components identified within the jet of 1ES 2344+514. From top to bottom: component C 1, C 2 and C 3 (compare also with Figure 6.29). Grey solid lines represent fits with a constant, dashed lines give linear fits. The fits are shown for illustrative purposes only. The plot has been produced with the data given in Table A.4 of Aleksić *et al.* (2012f). Errors have been calculated from the scatter of the position of the Gaussian fits, which give values comparable to the standard conservative approach of adopting 1/5 of the beam size (Lister *et al.* 2009b, M. L. Lister, 2012, private communication).

Multi-zone approaches (see Section 2.6) are a viable solution of this ambiguity. Alternatively, the discrepancy may be explained if the derived jet component speed is not indicative of the actual jet speed. This interpretation is disfavoured by the rather low core brightness temperatures of $\sim 8 \cdot 10^{10}$ K derived from the observations (see Table A.4 in Aleksić *et al.* 2012f), which is well below the inverse Compton limit and thus indicates only moderate relativistic beaming (Aleksić *et al.* 2012f).

6.5.6 Long-term Light Curve and Correlations

The light curves obtained from Effelsberg, OVRO, KVA, *Swift* XRT, *RXTE* ASM, *Swift* BAT and *INTEGRAL* ISGRI have been combined in Figure 6.41 (for the last three with a weekly binning; for further binnings, see Section E.3.2). The individual light curves have been discussed in the previous sections. The focus of this part will be to investigate correlations between the different light curves.

Long-term Inter-Band Correlations ASM, BAT and ISGRI did not find a significant signal of the source on any of the binning time scales apart from the one day high rate of ASM and the potentially artificial one week high state observed by BAT already discussed in Section 6.5.2. Therefore, we concentrate on a comparison of the well-sampled OVRO and KVA light curves as well as the XRT measurements.

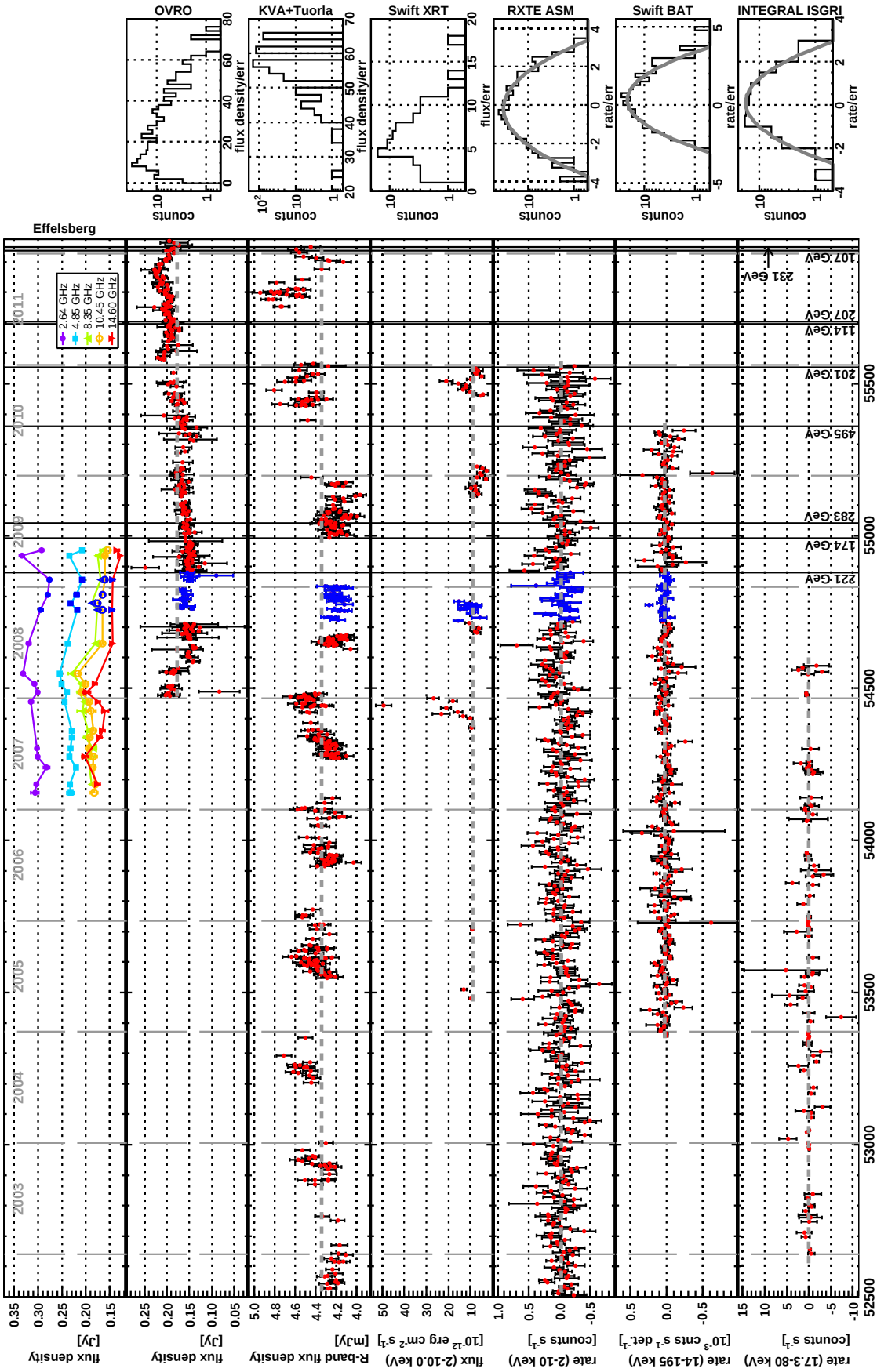

Figure 6.41: *Left side:* long-term light curves of 1ES 2344+514. Blue points denote the MW campaign time period. The first four light curves are binned on observation-wise (sub-day) scale, whereas the points of the last three panels have been re-binned to weekly scales. For the latter, light curves with different time binnings can be found in Section E.3.2. No ASM data after 01 January 2011 are shown, see text. Two points measured by BAT are not shown for clearness (MJD 54177.5, rate $(2.26 \pm 0.91) \cdot 10^{-3}$ cnts s^{-1} per detector; MJD 54541.5, rate $(3.16 \pm 1.82) \cdot 10^{-3}$ cnts s^{-1} per detector) and the (linear) error bar of one point (MJD 53729.5) has been cut at the plot edge. The black vertical lines indicate the arrival time of *Fermi*-LAT detected events with an energy > 100 GeV. Fits with a constant are visualised by grey horizontal dashed lines. *Right side:* event distribution corresponding to the light curves shown on the right side, for the last three including a fit with a Gaussian shown as the grey solid line.

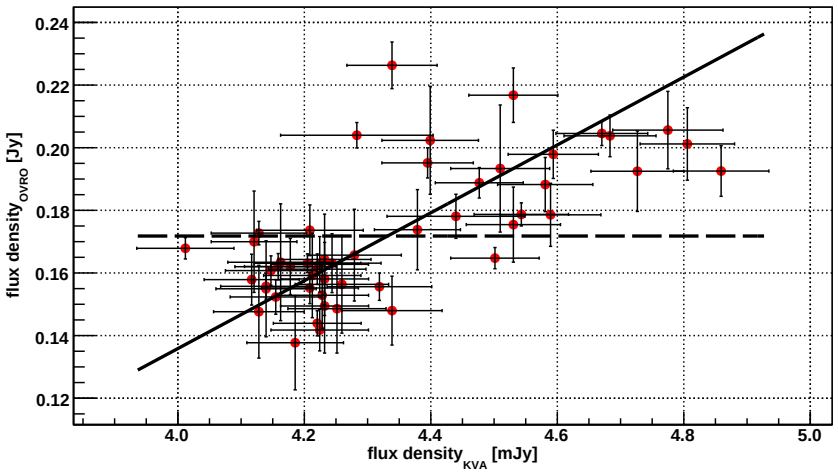

Figure 6.42: The flux density at 15.0 GHz measured by OVRO from 1ES 2344+514 as a function of the KVA R-band flux density. Only data pairs with a time difference < 0.9 days have been considered. OVRO data with an error $\gtrsim 0.02$ Jy have not been used. The dashed line represents a fit with a constant (χ^2/d.o.f. = 505.0/51), the solid line gives a linear fit (χ^2/d.o.f. = 115.1/50 with a slope of (0.108 ± 0.009) Jy per mJy).

An elementary check of a correlation between OVRO and KVA is performed in Figure 6.42. A linear fit is clearly preferred over a constant fit (likelihood ratio probability of 98.9 %), but both fits do not describe the data well. Additionally, such an investigation can not account for potential time lags (which are in fact expected due to radio emission arising from an optically thick region), though, and is subject to biases by the sampling. The long observation time scales available here allow for a detailed correlation analysis between the two instruments using the discrete correlation function (Edelson & Krolik 1988). The analysis has been conducted on all data as well as on a reduced data set from which OVRO outliers (point uncertainty > 0.02 Jy; E. Lindfors, 2012, private communication) were excluded (amounting to ~ 15 % of the data). Time lags up to ± 100 days have been investigated. Details are described in Aleksić *et al.* (2012f). The analysis found a hint for correlated variability, but did not reveal a significant correlation between the two instruments. With more data, a correlation is likely to be found in the future.

Also the investigation of OVRO and XRT as well as KVA and XRT for a potential dependency did not yield a significant correlation (see Figs. E.17 and E.18). However, the statistical basis for these is rather small (17 and 15 data pairs with a time difference < 0.9 days, respectively), since *Swift* is not conducting regular monitoring of the source. Due to that, no dedicated correlation analysis has been performed in these two cases.

Individual Light Curve Features Correlations between different energy bands may also be investigated on basis of single flares. The most prominent flare was observed by XRT around MJD 54442 with a flux increase by a factor > 5 over the average flux. Figure 6.43 shows the light curves of the different instruments during this period of time. No simultaneous activity increase is present for the remaining instruments. The KVA flux density was even declining slightly, and neither ASM nor BAT saw a sign of

increased rate. On the other hand, flares are expected to lag behind in the radio regime. The peaks in the Effelsberg light curve detected at MJD 54486 and 54547 may therefore be related to the XRT flare. Such a large time lag has already been reported for e.g. M 87 (Acciari *et al.* 2009b), supposed to be a "misaligned blazar". Also in the optical, the flux density was slightly increased about six days later (around MJD 54448), though this is a quite long time difference for these two energy regimes. Consequently, the X-ray flare might have been present in the optical R-band and radio bands with a time lag. Unfortunately, the incomplete sampling does not allow for definitive conclusions.

Another, yet smaller, flux increase was detected by XRT at MJD 54467, also shown in Figure 6.43. Again, KVA observed a slightly higher flux density ~ 5 days later, around MJD 54472. At MJD 54468, ASM was also observing a higher rate – the only significant detection by ASM during the whole time period investigated here. If the XRT and ASM flares are correlated, the XRT flux may just have started to rise and should have surpassed even the flare around MJD 54442 in flux. The two Effelsberg flares may also be related to this XRT flare, as a potential time lag can hardly be constrained. BAT did not see a sign of increased activity of the source. Hence, indications for correlated variability in the X-ray, optical and radio regime are present, but can not be significantly confirmed nor rules out due to the comparably sparse sampling.

An unusually fast flare occurred in the radio regime, observed by Metsähovi at MJD 55039. This flare could not be confirmed by IRAM and OVRO, which may however be due to the sensitivity and sampling constraints. Thanks to the monitoring observations, KVA data are available between MJD 55032 and 55042 on a daily basis. No significant flux density increase was observed (χ^2/d.o.f. = 9.2/10 for a fit with a constant), only an indication for increased activity was present at MJDs 55040 and 55041. 1ES 2344+514 was covered rather densely by KVA from MJD 55002 – 55048, still not finding evidence for significant variability (χ^2/d.o.f. = 19.2/28 for a fit with a constant). Though the Metsähovi flare might have been missed due to sampling and unknown time lag by the KVA monitoring, the available optical data disfavours a correlation between the 37 GHz and R-band. This would be in agreement with the missing correlation on long time scales between OVRO and KVA (see above). If this trend is confirmed, it would require the radio and optical emission either to be produced by different flaring mechanisms, or to originate from different regions of the jet.

It is noteworthy that two of the nine *Fermi*-LAT events > 100 GeV were detected at MJD ~ 54993 and ~ 55041, which may be related to the (comparably violent) Metsähovi flare. At the time of arrival of the remaining seven LAT events, no peculiar behaviour is found for any of the instruments under investigation. The multi-wavelength coverage was comparably bad at these times though (see also Figure 6.41). In case the LAT events are not accompanied by higher activity at other wavelengths, the interpretation of them being a sign for an increased duty cycle presented above would be rejected.

Multi-Wavelength Sky Map The radio structure of 1ES 2344+514 is rather complicated, as described in Section 6.1. The 1.4 GHz VLA map shown in Figure 6.2, produced from observations October 1998, has been confirmed October 2002 (Giroletti *et al.* 2004). These maps show a second radio feature separated from the AGN by ~ 180" (~ 160 kpc) which seems to be connected with the central structure (Giroletti *et al.* 2004). However,

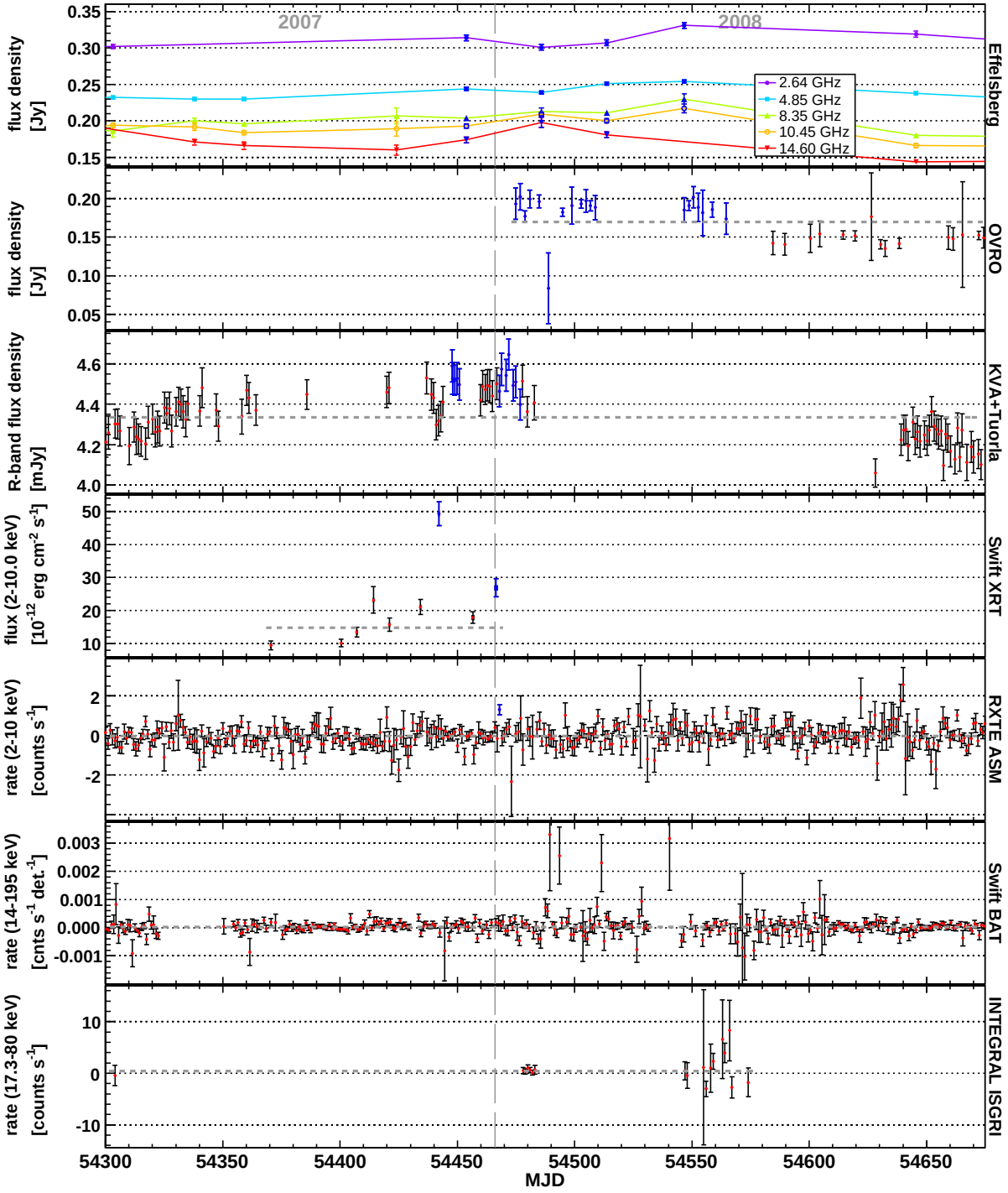

Figure 6.43: Long-term light curve with day-wise binning for the time period MJD 54300 – 54675. One point of the BAT lightcurve has been omitted for clarity, and the linear error bars of three points have been cut at the plot edge. Grey horizontal dashed lines represent fits with a constant to the data. The blue markers highlight potentially correlated flares in the radio, optical and X-ray regime (see Section 6.5.6). Signal/error histograms are displayed in Figure E.11 (for all daily binned data).

its position angle with respect to the pc scale jet is $\sim 45°$. No further interpretation on the nature of this object is given in the literature.

Comparing the publicly available[18] NVSS 1.4 GHz maps with the seven additional X-ray sources detected by *Chandra* in the field of 1ES 2344+514 (Donato *et al.* 2003), this feature is the only one with an X-ray counterpart and coincides very well with the weak component "E" (see Figure 6.44). However, it is not detected in the 2MASS All-Sky Catalog of Point Sources (Cutri *et al.* 2003) (having a limiting J magnitude of ~ 17 in this fov). Judging from the DSS2 IR-, R- and B-band maps, it is also not present in the optical, which disfavours the classification as a foreground/background star, supernova remnant or galaxy unless being obscured. An obscuration is rather unlikely though considering that stars are identified nearby.

Pulsars, which are hardly visible in the optical, are still viable candidates. The proximity of the feature to 1ES 2344+514 is rendering that possibility rather unlikely, strongly indicating a connection between these two. Alternatively, the pc-scale jet may bend on kpc scales and interact with the ambient intergalactic medium, which may explain the difference in position angle. On the other hand, such a radio hot spot should be visible in the NIR, which is not the case here, and is additionally disfavoured by the wide opening angle and low surface brightness of the jet, indicating a small amount of collimation at the putative hot spot position. Moreover, the existence of radio hot spots of BL Lac objects is not in agreement with the blazar unification scenario, where a FR-I structure would be expected. Note, however, that such hot spots have already been detected for BL Lac objects (e.g. Landt & Bignall 2008; Kharb *et al.* 2010). Future observations studying the variability and spectral shape of the object may reveal its true nature, especially a determination of its radio spectrum by VLBI measurements.

In principle, the above interpretation is vague considering that the MW sky map is not simultaneous. DSS2 data have been taken between 1984 and 1999, the NVSS data are from 12/03/1995, the *Chandra* observations were made 08/02/2000 and the (northern) 2MASS Catalog of Point Sources contains measurements between 06/1997 and 12/2000. During the time difference of five years between the *Chandra* and NVSS observations, the radio structure may have changed. However, the pc scale jet of 1ES 2344+514 is stationary on time scales of several years (see Section 6.5.5), which seems to be the case also for the 1.4 GHz feature, not having changed its relative location during the detections in 1995, 1998 and 2002. This is in fact another indication that the pc scale jet and kpc scale radio structure may be related. In conclusion, the spatial coincidence of the 1.4 GHz feature and the *Chandra* component "E" may in principle be by chance, which is highly unlikely though considering the stability of the radio feature as well as the very good positional agreement.

6.5.7 Spectral Energy Distribution

The spectral information of 1ES 2344+514 obtained in this MW campaign is combined with archival results in Figure 6.45. The source was in one of the lowest flux states at X-ray and VHE gamma-ray energies yet reported. The measured UVOT fluxes are

[18] Provided by NED (2012).

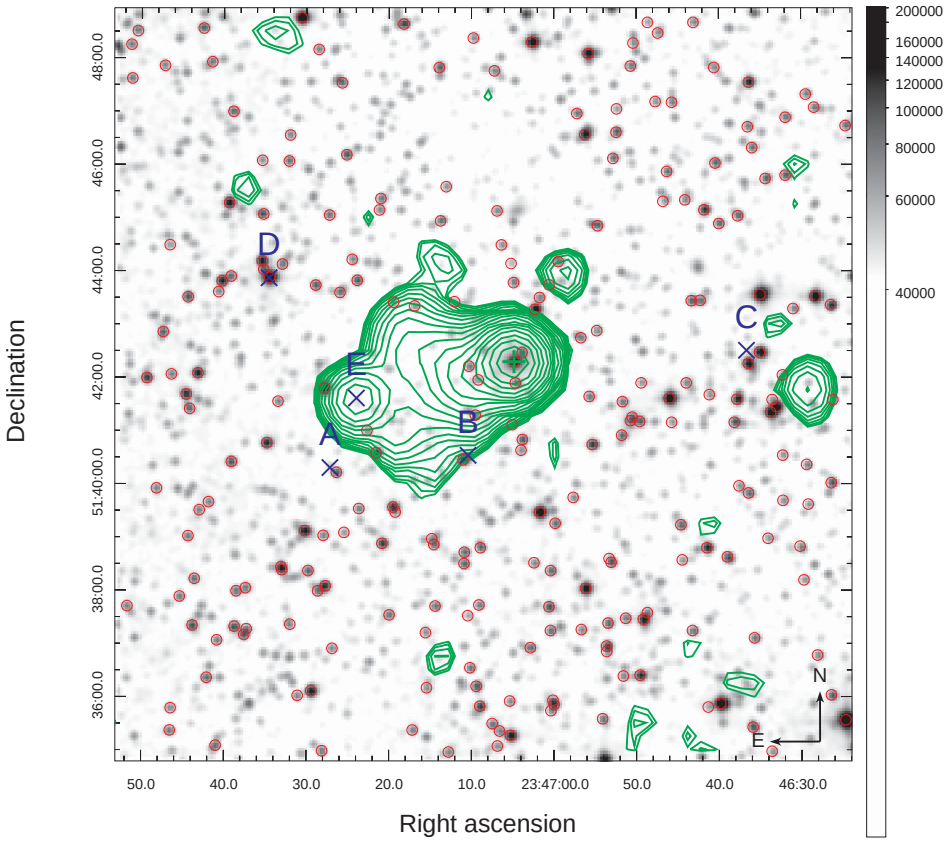

Figure 6.44: Map of the sky region in the R-band around 1ES 2344+514, with green radio contours at 1.4 GHz overlayed. The X-ray components identified by *Chandra* are shown as blue "X"s, labelled according to Donato *et al.* (2003). NIR point sources from the 2MASS catalogue are displayed as red circles. The green cross marks the position of 1ES 2344+514. The logarithmic grey scale is showing scaled densities. Radio contours are given from 0.001 Jy/beam until 0.241 Jy/beam in 20 logarithmically scaled steps. Only NIR sources with a J magnitude < 15 are shown. References: X-rays: Donato *et al.* (2003); optical: DSS2Red: obtained from http://heasarc.gsfc.nasa.gov/cgi-bin/vo/datascope/init.pl; 2MASS positions obtained through DS9 plugin; radio: NVSS, obtained from NED (2012).

among the lowest ones ever published, though the KVA data (with a considerably larger data basis and time coverage) prove that this is just a sampling effect, detecting the source frequently at lower fluxes levels. In the R-band and the radio regime, the (quasi-) simultaneous data are not particularly low in flux but only mildly below the average of the archival measurements.

The *Fermi*-LAT bow-tie derived from 5.5 months of observations showed a flux extrapolation to VHE inconsistent with the (non-simultaneous) MAGIC-I low state spectrum from 2005/6 (Abdo *et al.* 2009b). Also the extrapolation from 2FGL does not match the data well. Considering instead the MAGIC-I spectrum from this campaign and taking into account that the 60 GeV LAT flux point is subject to a rather large uncertainty due to low statistics (< 20 events; D. Bastieri, 2012, private communication), the discrepancy with the 5.5 month as well as the 2FGL spectra is resolved. Since the published *Fermi*-LAT results are averaged over rather long time scales and 1ES 2344+514 was not significantly variable at HE, they should constitute a measurement of the average flux

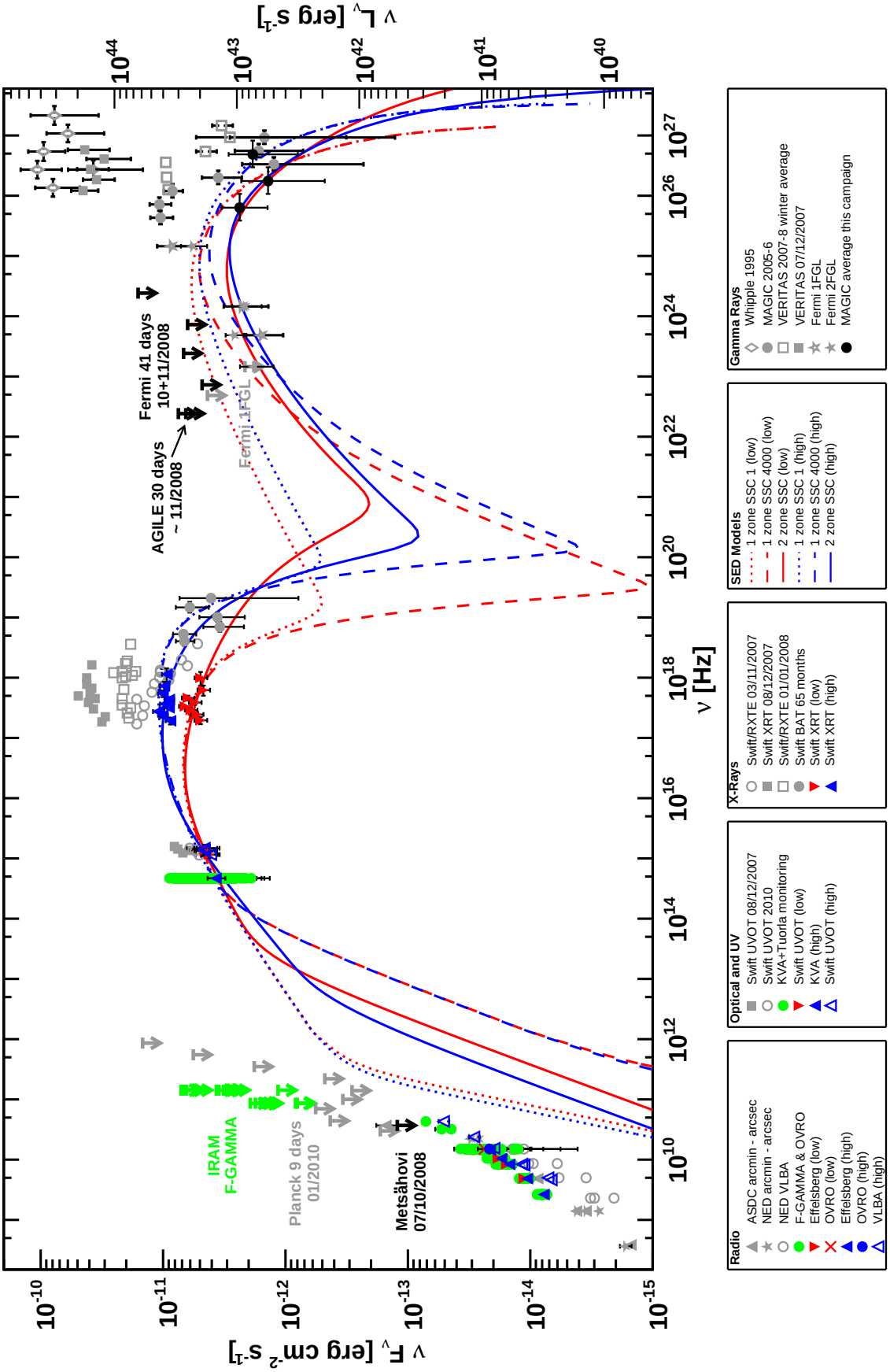

Figure 6.45: Same as Figure 6.33 but including archival measurements (in grey) for comparison. Green points represent measurements from OVRO, the F-GAMMA and Tuorla Blazar Monitoring Program. The BAT high state data, being most probably an artifact from the analysis, were removed. Archival data have been taken from the ASDC SED Builder (http://tools.asdc.asi.it), Acciari *et al.* (2011a), Schroedter *et al.* (2005) (Whipple) and Albert *et al.* (2007d) (MAGIC). Since the optical data given at ASDC are not host-galaxy corrected, they have been omitted. Note that the Metsähovi UL has a c.l. of 4 σ, the IRAM ones 3 σ. The *Planck* 2 σ ULs were taken from Giommi *et al.* (2012b). Archival VHE data from Whipple and MAGIC have been EBL-de-absorbed using Kneiske & Dole (2010), the VERITAS data by Franceschini *et al.* (2008).

state of the source. Hence the MAGIC-I spectrum from this work seems representative of the long-term average activity of 1ES 2344+514.

Archival SED Modelling The first attempt to model the spectral energy distribution of 1ES 2344+514 was conducted in Albert *et al.* (2007d) using a highly significant, low flux level VHE detection accomplished by MAGIC in 2005/6. The VHE data were combined with simultaneous R-band measurements by KVA, a simultaneous *RXTE* ASM UL and archival *BeppoSAX* X-ray observations from 1998, representing a low flux state of the source. A template high state SED was modelled using data from Whipple (1995) and *BeppoSAX* (1996). The authors adopted the one-zone SSC model of Krawczynski *et al.* (2004). Since the data was only partly taken simultaneously, the modelling results are rather speculative, as the authors note. Additionally, as has been found out in this work, the Whipple high state fluxes and EGRET UL were adopted wrongly by the paper authors, leading to an erroneous data basis for the high state SED.

Taking advantage of availability of the *Fermi* satellite, Tavecchio *et al.* (2010) constructed an SED consisting of a three months LAT UL and archival measurements, notably also the VHE results from Albert *et al.* (2007d). The one-zone SSC model of Maraschi & Tavecchio (2003), used also in the present work, was applied to the non-contemporaneous SED. Note that the optical point used for the SED modelling was not host-galaxy corrected, as the authors confirmed, introducing an error for the SED model results[19]. Changing $\gamma_{\rm min}$ to ~ 8000 can account for that mistake (F. Tavecchio, 2012, private communication).

The first simultaneous SED was built from a MW campaign organised by the VERITAS collaboration end of 2007/beginning of 2008 (Acciari *et al.* 2011a). A VHE spectrum obtained during a flare of 1ES 2344+514 was combined with a quasi-simultaneous X-ray flare spectrum measured by *Swift* XRT as well as UVOT data. The X-ray during the flare is the highest reported until today from 1ES 2344+514. It should be noted that the time difference between the VHE and X-ray spectrum was > 24 hrs, which was at that time also the value of the flux doubling time. Hence the quasi-simultaneous VHE and X-ray fluxes could in reality be off by a factor of ~ 2. For the low state SED of the source, the average VERITAS spectrum (excluding the aforementioned flare) and a representative 1-day low flux X-ray spectrum measured by *Swift* XRT and *RXTE* PCA were used, similar to the procedure applied in the present work. Note, though, that the VERITAS light curve was showing significant variability even when excluding the large flare (variability amplitude (Vaughan *et al.* 2003) $F_{var} = (34 \pm 16)\,\%$). Consequently, the averaged VHE spectrum is not representative of the low flux state of the source. The low and high state SED was modelled with the one-zone SSC code of Krawczynski *et al.* (2004). Non-contemporaneous HE data from 1FGL are highly overestimated by the model curves, indicating that the SEDs are not representative of the long-term behaviour of 1ES 2344+514. An indeed higher flux at HE during the MW campaign cannot be excluded though (despite the rather constant emission of the source for two years), since *Fermi* was not yet in operation at that time.

Recently, archival data of 1ES 2344+514 were modelled using the χ^2 minimisation

[19] We recall that the host galaxy of 1ES 2344+514 is rather strong in the optical.

approach by Zhang *et al.* (2012). The authors applied a one-zone SSC code to a low and high state SED, the first one consisting of the MAGIC-I and KVA data of Albert *et al.* (2007d) and archival *Swift* data, the second one of the high state data from the VERITAS MW campaign (Acciari *et al.* 2011a). The authors derive a variability time scale Δt of 12 hrs from few-hours VHE variability of the source reported allegedly in Albert *et al.* (2007d), which we cannot confirm as the latter paper clearly states constancy of the VHE flux. Since Acciari *et al.* (2011a) have observed significant variability on 1-day time scale, this assumptions is generally speaking nevertheless reasonable. The electron spectral indices below and above the spectral break (e_1, e_2) were determined a priori by (independent) power-law fits to the data, the radius of the emission region was calculated as $R_{em} = c\delta\Delta t/(1+z)$. $\gamma_{\rm min}$ and $\gamma_{\rm max}$ were also constrained by the available data or set to 2 and $100 \cdot \gamma_{\rm break}$, respectively. Since $\gamma_{\rm break}$ and the electron density K can be expressed in terms of the Doppler factor δ and the magnetic field B, only the latter two parameters had to be minimised with the χ^2 method.

Model Parameter Comparison and Discussion For the models without χ^2 minimisation, the parameters derived in this campaign match rather well the archival ones. All of the results cover ranges typical for HBLs (see e.g. Tavecchio *et al.* 2010). Only $\gamma_{\rm min}$ is rather high for the one-zone model, and $\gamma_{\rm max}$ is high for the two-zone low state fit. In general, $\gamma_{\rm min}$ shows a broad range of possible values. This is partly due to the incomplete data the model fits are based on. As has been shown in Section 6.4.6, only the quasi-simultaneous *Fermi*-LAT data could constrain the parameter within this campaign. For previous modelling attempts, no LAT data was available though. It should also be noted that the spectral breaks > 1 obtained from the one-zone models are hard to explain within the established theoretical framework (see also Section 6.4.6). The reason for that is the non-dependency of the two parameters in contrast to the two-zone model, where the parameters are derived self-consistently.

In general, resulting individual parameters are hard to compare due to their interdependencies and the parameter degeneracy of the manual fitting. Only in the case of the two zone model, a part of the results have been derived self-consistently and could be compared to other studies, which are however not yet available.

As noted in Section 6.4.6, the results from this campaign derived with the χ^2 minimisation method are partly considerably different. However, they are coinciding well with the trend found for Mrk 501 derived by the same technique (Mankuzhiyil *et al.* 2012), which is again not the case for Mrk 421 (Mankuzhiyil *et al.* 2011). In comparison, Zhang *et al.* (2012) found for a low state of 1ES 2344+514 similarly low values for K (at least in the low state case), e_1 and an emission region of comparable size (assuming a variability time scale of 12 hrs), but considerably larger magnetic field strengths (~ 0.1 G). Hence most of the parameter values that are off from the standard ranges are confirmed independently. This indicates that the χ^2 minimisation technique may yield in general considerably different physical parameter values than the biased, manual fitting procedures. The new technique for SED fitting is a promising approach to reduce the parameter degeneracy, shedding a new light on the model parameter values which still has to be investigated thoroughly. However, a detailed evaluation and discussion of the differences is beyond the scope of this work.

Campaign	(1)		(1)		(2)		(3)	(4)		(1)		(5)	
Model	(MaTa03)		(WeSp10)		(Kr04)		(MaTa03)	(Kr04)		(MaTa03) $\chi^{2\,(a)}$		(Zh12)	
Flux Level	low	high	low	high	low	high	...	low	high	low	high	low	high
B [G]	0.07		0.05	0.09	0.10	0.08	0.1	0.09	0.03	0.02	0.02	$0.12^{0.42}_{0.05}$	< 0.11
δ	20		26	29	8	15	25	13	20	15	16	13^{22}_{7}	> 10
R_{em} [10^{15} cm]	3	4	9	5	10		4	10		23	19	$16^{(b)}$	$> 12^{(b)}$
$K^{(c)}$ [10^5 cm^{-3}]	4.5	1.9	0.2	0.1	~ 0.5	~ 0.4	0.3	~ 0.4		$2.7 \cdot 10^{-4}$	$1.1 \cdot 10^{-3}$	$7.0 \cdot 10^{-4\,(e)}$	$0.3^{(e)}$
e_1	2.3		2.5	2.3	2.2		2	2.5	2.3	1.6	1.8	1.8	2.2
e_2	3.4	3.2	3.5	3.3	3.2		3.2	3.2		3.3	3.2	3.8	3.4
$\gamma_{\rm min}$ $^{(d)}$	1 or 4000		1800	550	~ 2500	~ 1500	1 (8000)$^{(f)}$	~ 200		1000		2	2
$\gamma_{\rm break}$ [10^4]	5	8	10	3	~ 15		1	~ 40	~ 50	5	5	$6^{(e)}$	$36^{(e)}$
$\gamma_{\rm max}$ [10^6]	0.7	1.5	6.3	1.5	~ 0.8	~ 1.6	0.7	~ 2.0		8.2	3.5	$0.5^{(e)}$	$6.1^{(e)}$
χ^2_{red} $^{(g)}$	...	...	...	...	...	...	...	...	...	0.91	0.67	1.8	2.8

Notes. $^{(a)}$ Tavecchio using χ^2 minimisation. Only the results for $\gamma_{\rm min} = 1000$ are shown for clarity of the table, for the values corresponding to $\gamma_{\rm min} = 1$ see Table 6.6. $^{(b)}$ Calculated using $R_{em} = c\delta\Delta t/\,(1+z)$ with $\Delta t = 12\,\mathrm{hrs} = 43200\,\mathrm{s}$ (Zhang *et al.* 2012). $^{(c)}$ For the one-zone models, K is defined in the emission region at $\gamma_{\rm min} = 1$, whereas in the two-zone case, K is given for the acceleration region at $\gamma_{\rm min}$. Hence these values are not directly comparable between those models. $^{(d)}$ $\gamma_{\rm min}$ was fixed a priori for (MaTa03). In case of the manual modelling, the other parameter values do not depend on $\gamma_{\rm min}$. $^{(e)}$ J. Zhang, 2012, private communication. $^{(f)}$ The missing host-galaxy correction can be accounted for by increasing the factor to 8000 (see text). $^{(g)}$ d.o.f. for model (MaTa03) in low state: 9; d.o.f. in high state: 18.
Campaign References. (1) This Campaign. (2) MAGIC 2005/6 and archival data (Albert *et al.* 2007d). (3) *Fermi*-LAT and archival data (Tavecchio *et al.* 2010). (4) VERITAS MW campaign (Acciari *et al.* 2011a). (5) Archival data consisting of the low state of Albert *et al.* (2007d) plus *Swift* data and the high state SED of Acciari *et al.* (2011a) (see Zhang *et al.* 2012).
Model References. (MaTa03) Maraschi & Tavecchio (2003). (WeSp10) Weidinger & Spanier (2010). (Kr04) Krawczynski *et al.* (2004). (Zh12) Zhang *et al.* (2012).

Table 6.10: Parameters from archival SED models fits. A part of the models and parameters are described in Section 2.6; for the remaining ones, see the references given.

A transition from the low to the high state in the models or vice versa can not be investigated thoroughly because these are not connected causally but artificially constructed. For Albert *et al.* (2007d), the two (anyway non-contemporaneous) SEDs are separated by about 10 years. Several years are also separating the models calculated by Zhang *et al.* (2012) in time. In the case of Acciari *et al.* (2011a), the low and high X-ray state were $\sim$1 month apart, and at least two further flares destroying a potential correlation were present between these two states. Even in the case of the present campaign, the variability time scale in X-rays was too large for the two flux states to be connected, since a blob travelling an expanding, relativistic jet downstream would also expand by several orders of magnitude within $\sim$1 week. Only if the emission region is confined externally, e.g. by magnetic fields, a connection may be existing. Alternatively, the variability may be caused by two different emission regions, or by a standing shock within the jet. In the latter case, variability would be explained by changes in the jet composition (Tagliaferri *et al.* 2008).

Nevertheless, a general trend of the low state models having systematically smaller values of δ compared to the high state ones seems apparent. This is expected considering that the boosting is the most efficient way to increase the flux from the source ($F \propto \delta^4$). Also the radius of the emission region is mostly hardly changing or constant between the low and high state models, which would disfavour the blob-in-jet model if the two states were causally connected.

7 A Quiescent Flux State?

The motivation behind this work was to investigate hardly studied, modestly variable blazars in a pre-organised (unbiased by high state triggers) multi-wavelength (MW) campaign taking advantage of the newest generation of instruments. By that, the number of sources with (quasi-)simultaneously measured SEDs should be increased and light should be shed on the quiescent state of blazars. This state is characterised by small overall activity and a low flux state. It is representative of the baseline emission of the source, and can therefore be used to investigate the underlying physical processes at work in the emission region. Despite the low flux, the quiescent state is dominating the blazar energy budget due to their comparably low duty cycle.

1ES 1011+496 was observed in a comparably high activity state, which was rather fortunate considering the potential IBL nature and consequent VHE-faintness of the object. This enabled us to investigate here the first quasi-simultaneous SED of that blazar. The goal of revealing the quiescent state of the source could naturally not be achieved in that case. However, a combined multi-band archival data study yielded for the first time strong indications in every single band for an IBL nature of the source during low activity, which may constitute the quiescent state of 1ES 1011+496. Characterising this state by SED modelling indicated a Compton dominance expected for IBLs, confirming the new classification proposed here.

Considering that the obtained low state SED of 1ES 2344+514 constitutes one of the lowest ever published for a BL Lac object, the good compatibility of the archival parameter results with the ones derived from this MW campaign were not necessarily expected. Significant variability was not present in the optical, HE and VHE regime, and the increased activity at radio and X-rays was of small amplitude only. Low flux and little, if at all, variability are expected for the quiescent state of the source. If this state would indeed have been observed here, it is not described by significantly different SED parameters than during higher flux states and even flares. The rather broad allowed range for the parameters and their degeneracy might prevent an identification of a certain set of quiescent parameters, though. The self-consistent two-zone model or the χ^2 minimisation technique applied on the data obtained from this work are a step towards breaking this degeneracy, but comparison results with these methods are hardly available. Of course, it is also possible that the quiescent state has not been observed in this campaign, or possibly a distinct quiescent state is not existing at all. Alternatively, the problem would be solved assuming that the one-zone models, which have also been adopted to derive the archival data used for the parameter comparison, would not be an adequate description of the source.

In line with that possibility are several, partly independent, indications that the emission is not produced solely by one component in the case of 1ES 2344+514. Particularly, these are:

- The size of the emission region determined from VLBI observations is ~ 1 order of magnitude larger than the size obtained from SED models, indicating a different origin of the two components. This interpretation is strengthened by the fact that in general the Lorentz factors of VLBI jets are much smaller than estimated from SED modelling (see, e.g. Piner *et al.* 2010, and references therein).

- A correlation between the long-term radio and optical light curves (and in general between the radio and other frequency ranges investigated here) is missing, indicating different origins of the emission. Note though that studies on a large sample of sources shows that correlations are existing (see Section 2.3). Also during the Metsähovi flare, no correlation with the KVA light curve was apparent.

- The parameters of the one-zone models are partly not compliant with standard theory, whereas the two-zone model, matching the data as well, yields values physically well motivated (which is expected from the self-consistency of the two-zone model).

- Comparing the parameters of the high and low state SED models, they are hardly compatible with emanating from the same emission region if the region is not externally confined or the emission is generated by a standing shock within the jet. Remember that the low state SED found here is a potential candidate for representing the quiescent state of the source.

- Combining the long-term radio spectra, their characteristics can be described according to Angelakis *et al.* (2012) as consisting of an emission component produced within the optically thin large-scale jet and a transient component on top of that, generated potentially by a shock travelling the jet.

Together, these disfavour a one-zone origin of the total blazar emission and suggest a system of (at least) two independent components. This may consist of a rather faint and steady component with one or more bright, rapid burst components overlaid. A one-zone model may still be applicable though in describing single flares. The identification of the steady emission component as the lowest possible, quiescent flux state is straightforward.

Nevertheless it has to be acknowledged that the questions about the existence and characteristics of the quiescent state can still not be answered with the data from the present MW campaigns. That is due to the limited instrument sensitivity, the partly degenerate SED models as well as the small statistics in number of sources with truly simultaneous data, the latter of which has been enlarged clearly by the campaigns presented here. However, the growing monitoring data basis, MW campaign efforts and increased instrument sensitivity are very promising of reaching that goal in the near future.

From the cumulative VHE signal of a stacked source analysis of several undetected blazars (mostly HBLs) as well as archival radio, optical and X-ray data, Höhne-Mönch (2010) constructed a "representative steady-state SED". The author found a flux dominance of the first peak over the second in that low state.The quasi-simultaneous low state SED of 1ES 2344+514 (see Figure 6.45) is consistent with that result. In fact, this may be characteristic of a quiescent state, since during the high flux state observed by

VERITAS, the luminosity at the second peak matches or even exceeds the one of the first peak. Also for the simultaneous SED of 1ES 1011+496, the synchrotron luminosity at the peak exceeds the one at the peak of the second component. Note, however, that this source has been observed in a rather high flux state and that the second peak is hardly constrained. Archival data in the TeV range is not available to judge on the variability amplitude (apart from the original MAGIC discovery, which is however consistent with the activity state found here), and *Fermi* is not yet observing long enough to obtain a representative high state spectrum of the source.

It is noteworthy that Mrk 180, the third source incorporated in the AGILE MW campaigns organised by the author, may in fact be another extreme blazar (Rügamer *et al.* 2011, publication in preparation). Consequently, all three sources studied here for the first time in a simultaneous MW campaign from radio to TeV are characterised by significant spectral evolution during high flux states, exhibiting shifts of their synchrotron peak by ~ 2 orders of magnitude and even more. The chance coincidence for selecting only such variable TeV sources among less variable ones is quite low, indicating that other objects may show similar characteristics if studied in-depth. This may be interpreted as a common physical origin for the emission and variability, at least for the three sources under study, despite 1ES 1011+496 having a much higher luminosity than the two remaining objects and probably belonging to a different blazar sub-class. Hence the differences between the sources should come from observational or alignment effects rather than source intrinsic ones, in accordance with the principles of the blazar paradigm.

These conclusions are debatable considering that they are based on three sources only. But if future studies can confirm this trend, the blazar sequence in its classical, luminosity-dependent form as well as the current blazar classification scheme[1] may have to be revised. Especially for the classification, a system should be found that also takes into account the variability of the sources, instead of forcing them into an inflexible and artificial, physically not motivated framework. With a sharpened and physical class definition, large source statistics studies like conducted by Abdo *et al.* (2010b) and Giommi *et al.* (2012b) may firmly shed a new light on blazars. Since the blazar paradigm may still hold, the morphology of the objects may be a powerful discriminator between the sources, like the overall structure of the source, the jet angle, speed or length. The corresponding data basis is increasing steadily through the ongoing MOJAVE and TANAMI (Ojha *et al.* 2010) projects.

Note though that also the blazar paradigm is in question considering that BL Lacs with radio hot spots have been found (e.g. Landt & Bignall 2008; Kharb *et al.* 2010), which may also be the case from the studies on 1ES 2344+514 presented here (see Figure 6.44 and corresponding discussion).

[1]The current blazar classification is based on the synchrotron peak in the quiescent state, but since for a large part of the sources the peak location is constrained by only a few observations, it is not clear if the determined position is representative for the source and hence the classification itself is rather arbitrary. See also Section 2.4.

8 Conclusions and Outlook

This work presented the first simultaneous multi-wavelength (MW) campaigns from the radio to the VHE regime for the two objects 1ES 1011+496 and 1ES 2344+514. The MW observations, analyses and results were described and correlations among the light curves of the different instruments were investigated, also on a multi-year long-term basis. Quasi-simultaneous SEDs were confronted with state-of-the-art models and the resulting model parameters were discussed in comparison to archival findings.

1ES 1011+496

The investigation of archival publications addressing 1ES 1011+496 revealed indications at all energy regimes for a behaviour atypical of its current HBL classification. Combining these for the first time in a multi-band approach to classify an object, we are confident that this source is better described as an IBL in the quiescent and low state that exhibits HBL characteristics during higher activity. To our knowledge, no such object has yet been described in literature, though they are supposed to exist due to the rather arbitrary definition of the different BL Lac subclasses. They may be regarded as the high-luminosity analogues of HBLs becoming "extreme blazars" in high states. The quasi-simultaneous SEDs obtained within this MW campaign were in line with this interpretation.

The long-term optical light curve is suggestive of an 8-year periodicity directly correlated with flaring behaviour on medium time scales ($\sim 10-20$ weeks). On top of these, a third flaring component may be present, causing short-term variability with a flare duration of ~ 2 weeks. This interpretation can be tested with continued monitoring observations and a denser sampling.

We presented the first confirmation of the VHE nature of this source as well as the first dense X-ray light curve, revealing a flare that followed the common "harder when brighter" trend frequently observed in blazars. Multi-band observations reveal spectral variability in the optical regime despite an overall low flux amplitude. Correlations between the different energy bands during the MW campaign could not be studied meaningfully due to unfortunate sampling. However, on long time scales the VHE and optical regime may be correlated, and a double flare seems to have been present in the optical as well as in the X-ray regime with a time lag of ~ 7 days, but not in the radio band. Such a large time lag is feasible considering low magnetic fields in combination with large emission region radii. Further strong optical flares could also not be identified in the comparably well sampled radio light curve, which may be evidence for a missing direct correlation between these two energy bands.

The observed SEDs reveal that the source has been observed in an overall rather high

flux state. SED modelling with two different leptonic models could describe the data well, but partly required extreme physical parameters, indicating that a pure leptonic description may not be adequate for this source. During the MW observations, a notable Compton dominance during the high activity state, as reported in literature, was not found. However, archival data indicate that this may be the case in low flux states, which is in line with the suggested new classification of 1ES 1011+496.

1ES 2344+514

Radio maps of the source show a feature at a distance of ~ 160 kpc from the central object, which may be connected with the AGN but has a difference in position angle with respect to the pc-scale jet of 45°. In this work we tried for the first time to characterise this object. From a data set consisting of radio, IR, optical and X-ray measurements, most of the potential source candidates could be ruled out. Pulsars are still a viable explanation, but rather unlikely considering the observed connection at radio frequencies and the proximity of the objects. The identification with a radio hot spot would be suggestive, but is not supported by the wide opening angle and low surface brightness of the jet. If the latter turned out to be true, 1ES 2344+514 would be one of the few blazars characterised by an FR-II structure, in contrast to the blazar paradigm.

The MW campaign revealed one of the lowest, if not the lowest, flux state of 1ES 2344+514 reported at X-rays and VHE until today. In the radio and optical regime, a modest flux was observed. The overall activity of the source was rather low, being constant in the optical and VHEs. Mild variability was present at radio and X-ray frequencies, where for the latter a small flare was detected. A correlation between the spectral shape and the integral flux was found at X-rays, which displayed hints of a counter-clockwise evolution during the flare. In the model of Kirk *et al.* (1998), such a feature would be explained by a shock front travelling through the jet, where the observations would have been conducted at a frequency characterised by comparable acceleration and cooling time scales.

Due to the overall low variability of the source as well as partly unfortunate sampling, correlations between different energy bands could not be established during the MW campaign. A correlation analysis between the radio and R-band on a multi-year time basis, also taking into account potential time lags, did not yield a significant dependency. The long-term data in various energy regimes revealed several individual flares, some of which may have been present contemporaneously also at other bands. However, incomplete sampling prevented a firm multi-wavelength identification.

Multi-year interferometric kinematic studies revealed the jet of 1ES 2344+514 to be stationary, contrary to previous publications for this object but in line with recent findings of slower jets of HBL objects compared to other blazars. The measurements were in concordance with a Blandford & Königl (1979)-type jet, arguing against alternative scenarios of (e.g. Marscher *et al.* 2008). From HE observations, a higher number of events with energies above 100 GeV than expected from a simple extrapolation have been detected. That may be interpreted as a higher flaring duty cycle of the source in comparison to other nearby TeV HBLs, but may also arise from the small statistical

basis available for this study.

The obtained MW data have been used to construct one of the few quasi-simultaneous blazar SEDs during a low state, which may have been close to the quiescent state of the source. However, SED modelling did not reveal parameters characteristic of a quiescent state. These were in fact consistent with the rather broad range of values reported in literature, probably a consequence of the degeneracy of the different parameters in simple one-zone SSC models. In combination with quasi-simultaneous HE data, the MW campaign results favour γ_{min} values considerably larger than unity for one-zone SSC models. Several indications were found that the broad-band emission of the source is not produced within a single emission region.

On the Quiescent State

The quiescent state of blazars could not be identified or characterised in this work. This may simply be a consequence of not having observed during the quiescent state of the source, though the low state SED detected from 1ES 2344+514 may be close to that baseline. Alternatively, a unique set of quiescent SED parameters may not have been found due to the degeneracy and interdependencies of the different parameter of the one-zone SSC models, allowing a broad range for each parameter value. Additionally, the one-zone models themselves may not be adequate to describe the BL Lac SEDs, since several indications for more than one zone being responsible for the emission have been found within this campaign. The self-consistent two-zone and χ^2 minimisation approach applied in this work are promising methods to overcome these problems in the near future, even more so when being combined. The latter, however, still has to resolve in its current form considerable inconsistencies with observations, implied cooling time scales and variability time scales. For both, more results from different flux states of several sources are needed to identify the quiescent state.

The combined results of the three MW campaigns organised by the author may be interpreted in a way disfavouring the blazar sequence and sub-classification of blazars. With the upcoming broad – in time as well as in energy coverage – monitoring data basis and increased efforts to organise MW campaigns, refined SED models will be needed to describe the data adequately and physically motivated. These will also put the more and more weakened blazar sequence and current classification scheme to the test, enabling large statistical studies and potentially revolutionising the current view on blazars in the near future.

Outlook

Still today, and even more so at the start of the observations back in 2008, there are too few simultaneous broad-band MW campaigns concentrating on too few sources to constrain current SED models and by that uncover the physical mechanisms at work. Though a handful of sources is carefully studied by now in extended campaigns up to the TeV range (especially Mrk 421, Mrk 501 and PKS 2155−304; Abdo *et al.* 2011b,d; Abramowski *et al.* 2012a), these concentrate mostly on the bright objects; a meaningful

SED in a low state is still today a very ambitious and hardly accomplished project. Mutually, no major efforts are required from the theoreticians' side to adapt their models. To put these to the test, (i) simultaneous SEDs (ii) for many different blazars (iii) in different activity states, especially in the underlying quiescent state (iv) with a broad energy coverage are needed. The work presented here was a first step towards that direction, emphasising the need for more refined models and model approaches.

The monitoring campaigns available since some years by e.g. F-GAMMA, OVRO, Tuorla and *Fermi*-LAT are a major and promising effort to reach that goal, enabling systematic studies on a large set of sources. From the work presented here it became clear though that still a better observation sampling is needed, which could be achieved by additional instruments joining these campaigns. Promising in this sense are the planned or already started programs to cover regularly critical energy regimes like the sub-mm band (APEX; Larsson *et al.* 2012), the hard X-rays (GRIPS; Greiner *et al.* 2012) and VHEs (FACT and to some extent CTA; Anderhub *et al.* 2011; Actis *et al.* 2011). However, a major obstacle will be the soft X-ray regime in the near future, since follow-up missions for *Swift* XRT or *XMM-Newton* are not scheduled yet. As a final word of caution, inspired by the revealed inaccuracy of some archival data, even a good data basis is worthless if not handled deliberate and with care.

A Extragalactic Objects Detected at TeV

#[a]	Source	Dist.[b]	Type[c]	Date[d]	Telescope	Ref.[e]	M[f]
1	Mrk 421	0.031	HBL	03 – 06/1992	Whipple	Pu92	Y
2	Mrk 501	0.034	HBL	03 – 07/1995	Whipple	Qu96	Y
3	1ES 2344+514	0.044	HBL	12/1995	Whipple	Ca98	Y
4	PKS 2155−304	0.117	HBL	09/1996	Durham	Ch99	Y
5	1ES 1959+650	0.047	HBL	05/1998	Utah	Ni99	Y
6	1H 1426+428	0.129	HBL	1999 – 2001	Whipple	Ho01	...
7	M 87	0.004	FR-I	1998 – 1999	HEGRA	Ah03	Y
8	PKS 2005−489	0.071	HBL	06 – 10/2004	H.E.S.S.	Ah05	Y
9	PG 1553+113	>0.40	HBL	05&08/2005	H.E.S.S.	Ah06a	Y
10	H 2356−309	0.165	HBL	04 – 12/2004	H.E.S.S.	Ah06b	...
11	1ES 1101−232	0.186	HBL	03/2005	H.E.S.S.	Ah06b	Y
12	1ES 1218+304	0.182	HBL	01/2006	MAGIC	Al06a	...
13	Mrk 180	0.046	HBL	03/2006	MAGIC	Al06b	...
14	PKS 0548−322	0.069	HBL	2004 – 2006	H.E.S.S.	Su08	...
15	BL Lacertae	0.069	LBL	08 – 09/2005	MAGIC	Al07a	Y
16	1ES 1011+496	0.212	HBL	03 – 05/2007	MAGIC	Al07b	Y
17	1ES 0347−121	0.188	HBL	08 – 12/2006	H.E.S.S.	Ah07a	...
18	1ES 0229+200	0.140	HBL	2005 – 2006	H.E.S.S.	Ah07b	...
19	1ES 0806+524	0.138	HBL	2006 – 2008	VERITAS	Sw08a,Ac09a	...
20	W Comae	0.102	IBL	01 – 04/2008	VERITAS	Sw08b,Ac08	Y
21	RGB J0152+017	0.080	HBL	10 – 11/2007	H.E.S.S.	Ah08	Y
22	S5 0716+714	0.31	LBL/IBL	04/2008	MAGIC	Te08,An09	...
23	3C 279	0.536	FSRQ	01 – 04/2006	MAGIC	Al08	Y
24	3C 66A	>0.096	IBL	2007 – 2008	VERITAS	Sw08c,Ac09b	Y
25	MAGIC J0223+403	...	UNID	08,09&12/2007	MAGIC	Al09	...
26	RGB J0710+591	0.125	HBL	01 – 03/2009	VERITAS	On09a,Ac10b	Y
27	Centaurus A	0.002	FR-I	2004 – 2008	H.E.S.S.	Ah09	...
28	PKS 1424+240	<0.66	IBL	02 – 06/2009	VERITAS	On09b,Ac10a	Y
29	VER J0521+211	...	HBL	10/2009	VERITAS	On09c	...
30	RBS 0413	0.190	HBL	2008 – 2009	VERITAS	On09d,Al12c	...
31	1ES 0414+009	0.287	HBL	2005 – 2009	H.E.S.S.	Ho09	Y
32	1ES 0502+675	...	HBL	09 – 11/2009	VERITAS	On09e	...
33	NGC 253	<3.9 Mpc	Starburst	2005,2006,2008	H.E.S.S.	Ac09c	...
34	PKS 0447−439	>0.107	HBL	11 – 12/2009	H.E.S.S.	Ra09	Y
35	M 82	3.4 Mpc	Starburst	2007 – 2009	VERITAS	Ka09	...
36	PKS 1510−089	0.361	FSRQ	...	H.E.S.S.	Wa10	...
37	VER J0648+152	0.179	HBL	03/2010	VERITAS	On10a,Al11b	Y
38	IC 310	0.019	UNID	10/2009 – 02/2010	MAGIC	Ma10a,Al10	...

continued on the following page

Table A.1: continued.

#[a]	Source	Dist.[b]	Type[c]	Date[d]	Telescope	Ref.[e]	M[f]
39	PKS 1222+216	0.432	FSRQ	06/2010	MAGIC	Ma10b,Al11a	...
40	AP Lib	0.049	LBL	06 – 07/2010	H.E.S.S.	Ho10a	Y
41	MAGIC J2001+4351	<0.2	UNID	07/2010	MAGIC	Ma10c	...
42	1ES 1440+122	0.162	IBL	2008 – 2010	VERITAS	On10b	...
43	B3 2247+381	0.119	HBL	09 – 10/2010	MAGIC	Ma10d,Al12b	Y
44	NGC 1275	0.018	FR-I	08/2010	MAGIC	Ma10e,Al12a	...
45	SHBL J001355.9−185406	0.095	HBL	07 – 08/2010	H.E.S.S.	Ho10b	...
46	1ES 1215+303	>0.130	IBL	01/2011	MAGIC	Ma11a,Al12d	Y
47	HESS 1943+213	>0.14	HBL	2005 – 2009	H.E.S.S.	Ab11	...
48	1RXS J101015.9−311909	0.143	HBL	2006 – 2010	H.E.S.S.	Be11a	...
49	1ES 1312−423	0.105	HBL	2004 – 2010	H.E.S.S.	Be11a	...
50	1ES 1741+196	0.083	HBL	2010 – 2011	MAGIC	Be11b	...
51	1ES 0647+250	∼0.4	HBL	2010 – 2011	MAGIC	Lo11	...
52	1ES 0033+595	>0.086	HBL	08 – 10/2009	MAGIC	Ma11b	...
53	1ES 1727+502	0.055	HBL	05 – 06/2011	MAGIC	Ma11c	...
54	KUV 00311−1938	>0.506	HBL	2009 – 2011	H.E.S.S.	Be12	...
55	RGB J0136+391	>0.4	HBL	11/2009	MAGIC	Ma12	...

Table A.1: Extragalactic objects detected by IACTs. The first horizontal line marks the advent of the new generation of IACTs, the second the date of organisation of the campaigns discussed in this work, and the third the start of MAGIC Phase-II observations.

Notes. [a] Ordered by publication date of VHE discovery (see references). Detection announcements given at conferences have only been been taken into account for the ordering if proceedings are not available. [b] Source distance. If no unit is given, the value corresponds to the redshift. In case of no reliable distance estimate, no value is given. [c] Classification as given in the VHE discovery publication and subsequent papers. Ambiguous classifications or sources without counterpart at other wavelengths are labelled as "UNID". [d] Period of observation leading to the VHE discovery. [e] Reference for VHE discovery. [f] (Quasi-)Simultaneous multi-wavelength SED including IACT detection published (Y ≡ Yes)? See Section 2.7 for the definition of such observations adopted in this work.

References. Pu92: Punch *et al.* (1992); Qu96: Quinn *et al.* (1996); Ca98: Catanese *et al.* (1998); Ch99: Chadwick *et al.* (1999); Ni99: Nishiyama (1999); Ho01: Horan & VERITAS Collaboration (2001); Ah03: Aharonian *et al.* (2003); Ah05: Aharonian *et al.* (2005a); Ah06a: Aharonian *et al.* (2006b); Ah06b: Aharonian *et al.* (2006a); Al06a: Albert *et al.* (2006a); Al06b: Albert *et al.* (2006b); Su08: Superina *et al.* (2008); Al07a: Albert *et al.* (2007a); Al07b: Albert *et al.* (2007b); Ah07a: Aharonian *et al.* (2007a); Ah07b: Aharonian *et al.* (2007b); Sw08a: Swordy (2008c), Ac09a: Acciari *et al.* (2009a); Sw08b: Swordy (2008b), Ac08: Acciari *et al.* (2008); Ah08: Aharonian *et al.* (2008); Te08: Teshima & MAGIC Collaboration (2008), An09: Anderhub *et al.* (2009a); Al08: Albert *et al.* (2008d); Sw08c: Swordy (2008a), Ac09b: Acciari *et al.* (2009c); Al09: Aliu *et al.* (2009a); On09a: Ong (2009a), Ac10b Acciari *et al.* (2010b); Ah09 Aharonian *et al.* (2009a); On09b: Ong (2009c), Ac10a Acciari *et al.* (2010a); On09c: Ong (2009d); On09d: Ong & Fortin (2009), Al12c: Aliu *et al.* (2012a); Ho09: Hofmann & Fegan (2009); On09e: Ong (2009b); Ac09c Acero *et al.* (2009); Ra09: Raue *et al.* (2009); Ka09 Karlsson & for the VERITAS collaboration (2009); Wa10 Wagner (2010); On10a Ong *et al.* (2010), Al11b Aliu *et al.* (2011); Ma10a: Mariotti (2010c), Al10: Aleksić *et al.* (2010b); Ma10b: Mariotti (2010b), Al11a: Aleksić *et al.* (2011a); Ho10a: Hofmann (2010a); Ma10c: Mariotti (2010a); On10b: Ong (2010); Ma10d Mariotti & MAGIC Collaboration (2010a), Al12b: Aleksić *et al.* (2012b); Ma10e Mariotti & MAGIC Collaboration (2010b), Al12a: Aleksić *et al.* (2012a); Ho10b: Hofmann (2010b); Ma11a: Mariotti (2011a), Al12d: Aleksić *et al.* (2012c); Ab11: Abramowski *et al.* (2011a); Be11a: Becherini *et al.* (2011); Be11b: Berger (2011); Lo11: De Lotto (2011); Ma11b: Mariotti (2011c); Ma11c: Mariotti (2011b); Be12: Becherini *et al.* (2012); Ma12: Mazin (2012)

B Analysed MAGIC Data

B.1 1ES 1011+496

Sequence	Comment
338582	
338594	
338626	excluded due to a dead cluster of pixels and low and partly strongly fluctuating
338647	rate potentially due to clouds
338904	
338933	
340690	added runs 340702 – 340856 which were not sequences due to altered HV of one pixel
341446	removed run 341545 due to a rate of > 65 kHz with unknown reason
343634	removed run 343651 which included fluctuating rates up to 800 Hz, reason unknown
345853	removed runs 345860, 345861, 345866 – 345869, 345873 – 345884 and 345889 – 345904 because of significant drops in the rate due to passing clouds
346267	removed run 346282 due to low rate (closing camera)
346458	removed run 346482 due to a rate of > 65 kHz with unknown reason
348113	excluded due to missing calibration events
348294	added runs 348300 – 348314 which were not sequenced automatically due to a missing P run; excluded the sequence due to low rate presumably due to *cloudiness* $\sim 40\%$ and Calima (atmospheric absorption of 13.1 %)
348890	excluded due to low rate (clouds and Calima, atmospheric absorption of 8.8 %)
349503	excluded due to low rate, presumably due to high *cloudiness* ($40 - 60$ %) and AMC problems
349880	removed runs $>$ 349885 due to low rate (caused by high *cloudiness* up to 98%)
351058	added runs 351065 – 351119 which were not sequenced due to changed DTs; removed runs 351060 – 351065 due to low rate because of twilight DTs; removed runs 351070, 351075 – 351079, 351085 – 351107, 351110 – 351117 and 351119 due to low and fluctuating rate presumably caused by high and *cloudiness* (up to 66 %)
1000131	removed run 1000133.1 due to low rate (first run)
1000141	data could not be calibrated due to trigger failure
1000145	excluded due to low rate, presumably due to twilight DTs and clouds
322846	removed runs $>$ 322888 due to zenith distances not matching with 1ES 1011+496
351510	removed runs $<$ 351529 due to zenith distances not matching with 1ES 1011+496
1000135	removed runs $>$ 1000137 : 17 due to zenith distances not matching with 1ES 1011+496

Table B.1: 1ES 1011+496, Mrk 421 (351510 & 1000135) and Crab Nebula (322846) sequences that have been changed compared to the standard setup or excluded from the analysis.

Sequence	**Observation Start** [UTC]	**Light Cond.**[a]	**On Time**[b] [h]	**Zenith Dist.**[c] [°]	**Mean Rate**[d] [Hz]	**Ped. RMS**[e] [phe]	**Inh.**[f]	**PSF** [mm]	**Muon** *Ratio* [%]	**Cloud.**[g] [%]	**Mean DT**[h]
340690	08/03/2008 23:17	Dark	2.84	21 – 30	195.1	0.95	5.0	13.8	100.1	19.2 ± 1.0	14.33
341208	10/03/2008 01:13	Dark	0.89	24 – 30	196.8	0.92	5.8	13.3	99.5	15.2 ± 1.1	14.29
341446	10/03/2008 22:31	Dark	3.43	21 – 30	206.0	0.94	6.0	13.8	104.4	20.9 ± 1.1	14.29
343634	26/03/2008 22:55	Dark	0.55	21	214.1	0.88	7.7	14.2	102.5	16.0 ± 0.5	14.97
343672	26/03/2008 23:37	Dark	0.25	21 – 22	206.5	0.91	7.8	15.3	102.9	13.4 ± 0.8	14.92
343689	26/03/2008 23:59	Moon	0.09	23	198.8	0.96	7.1	11.3	96.9	9.8 ± 0.4	15.08
343943	28/03/2008 20:43	Twilight	1.34	23 – 34	195.1	0.94	7.9	13.6	100.1	18.2 ± 0.8	14.86
344397	29/03/2008 20:47	Dark	1.27	23 – 32	198.2	0.94	7.7	14.0	100.6	21.1 ± 0.4	14.85
345853	02/04/2008 20:50	Dark	0.28	25, 27 – 30	184.7	0.95	7.0	12.4	99.7	31.3 ± 5.3	14.93
346267	03/04/2008 21:03	Dark	0.63	22 – 27	198.1	0.92	7.9	14.4	101.8	17.4 ± 0.3	14.80
346458	04/04/2008 20:48	Twilight	0.90	22 – 28	201.0	0.92	7.7	13.7	101.1	13.1 ± 0.6	14.94
346913	05/04/2008 20:49	Twilight	0.80	23 – 28	200.7	0.94	7.8	13.5	101.7	18.8 ± 0.7	14.90
347959	23/04/2008 21:43	Moon	1.08	21 – 27	198.5	0.97	7.3	14.0	103.4	30.1 ± 0.7	14.91
348482	28/04/2008 21:11	Dark	1.61	21 – 30	169.7	0.96	7.9	13.2	98.3	28.8 ± 1.1	14.84
349880	02/05/2008 21:41	Dark	0.06	24	178.9	0.96	7.6	12.4	99.7	35.0 ± 0.3	14.80
350240	03/05/2008 21:35	Dark	0.92	23 – 30	180.4	0.96	7.0	13.6	101.0	27.4 ± 1.9	14.78
350632	04/05/2008 21:20	Dark	1.05	23 – 29	179.9	0.95	7.4	12.9	101.4	30.2 ± 0.9	14.77
351058	05/05/2008 21:27	Dark	0.30	23 – 25, 29, 31	167.8	0.97	7.9	13.3	99.8	47.0 ± 2.5	14.79
351457	06/05/2008 21:21	Dark	0.96	23 – 30	179.1	0.95	7.9	13.7	100.5	31.9 ± 0.8	14.75
1000131	22/05/2008 21:23	Twilight	0.48	30 – 35	183.0	0.99	7.0	12.8	100.9	28.6 ± 0.5	14.97
1000150	23/05/2008 21:49	Dark	0.21	35 – 37	176.1	0.94	7.8	13.9	100.3	25.4 ± 0.6	14.68
322846	07/01/2008 21:29	Dark	0.72	21 – 30	199.1	1.00	6.2	13.1	97.8	19.2 ± 1.2	16.11
351510	06/05/2008 22:45	Dark	0.98	21 – 33	177.8	0.95	8.0	14.0	100.2	37.6 ± 2.9	14.99
1000135	22/05/2008 21:56	Dark	0.30	23 – 27	190.0	0.97	7.9	13.0	102.2	31.4 ± 0.1	15.14

Notes. [a] Light conditions during the observations. For an explanation see Section 4.3.2. [b] Effective observation time of the measurements. [c] Zenith distance range covered by the observations. [d] Event rate after image cleaning. [e] Mean inner pedestal RMS value. [f] Inhomogeneity. [g] Mean *cloudiness* during the observations and its corresponding RMS. [h] Mean DT value during the observations.

Table B.2: Sequences of 1ES 1011+496 and their most important quality parameters after quality selection used for the data analysis. Also shown are the Mrk 421 sequences (351510 and 1000135) used for cut optimisation and the Crab Nebula sequence (322846) on which the analysis pipeline has been tested.

B.2 1ES 2344+514

Sequence	Comment
1002585	added 1ES 2344+514 runs with wrong source name "intensitycalib"; excluded sequence due to low mean rate, high PedRMSIn, low PSF
1002671	removed run 1002676:3 due to closing camera (because of high humidity)
1002763	removed run 1002765:3 due to closing camera (because of high humidity)
1002922	removed run 1002924:5 due to closing camera (communication problem)
1002925	added runs 1002929:1 – 1002932:5; removed run 1002931:5 due to closing camera (communication problem)
1002955	excluded sequence because drive system stopped tracking
1002971	excluded sequence due to high ArrTimeIn, low *ratio*, low muon rate and low rate (presumably because of clouds)
1003111	removed run 1003113:3 due to control software problems; removed runs 1003113:2 and > 1003114:4 due to low rate (because of high *cloudiness*); still, background rate after cleaning is too low, excluding sequence
1003142	removed runs 1003145.1 and > 1003146:7 (but 1003147.6:7) due to low rate (because of high *cloudiness*)
1003198	excluded due to low RelOnTime, high ArrTimeIn, high MeanCalibrPulsePos, high PSF, high muon rate and Calima
1003453	removed runs 1003455:1 – 1003457:3 and > 1003459:4 due to not matching zenith distance
1004461	removed run 1004466.7 due to high rate (presumably because of inconsistent DAQ state); removed runs < 1004466:1 and > 1004467:7 due to not matching zenith distance

Table B.3: 1ES 2344+514, Mrk 421 (1003453) and Crab Nebula (1004461) sequences that have been changed compared to the standard setup or excluded from the analysis.

Sequence	**Observation Start** [UTC]	**Light Cond.**[a]	**On Time**[b] [h]	**Zenith Dist.**[c] [°]	**Mean Rate**[d] [Hz]	**Ped. RMS**[e] [phe]	**Inh.**[f]	**PSF** [mm]	**Muon** *Ratio* [%]	**Cloud.**[g] [%]	**Mean DT**[h]
1002570	20/10/2008 22:36	Dark	1.02	23 – 24	213.0	1.06	7.4	14.2	102.7	10.6 ± 1.0	37.41
1002576	20/10/2008 23:42	Moon	0.40	24 – 26	210.8	1.13	7.5	13.5	101.6	12.9 ± 0.2	37.65
1002589	21/10/2008 22:18	Dark	1.41	23 – 25	208.6	1.10	7.3	14.1	102.7	13.6 ± 0.6[i]	37.81
1002620	22/10/2008 22:12	Dark	1.35	23 – 24	212.6	1.03	7.4	14.3	102.4	7.9 ± 3.1[i]	37.60
1002671	23/10/2008 21:08	Dark	1.03	24 – 30	198.7	1.11	6.7	13.9	100.1	...[j]	37.61
1002677	23/10/2008 23:08	Dark	0.39	23 – 24	204.1	1.11	8.0	13.3	100.2	9.3 ± 0.8	37.32
1002707	24/10/2008 21:00	Dark	1.29	24 – 30	203.9	1.13	7.9	13.7	102.8	...[j]	37.60
1002713	24/10/2008 22:30	Dark	1.93	23 – 31	204.2	1.14	7.8	13.2	103.3	24.0 ± 0.8[i]	37.58
1002759	25/10/2008 20:56	Dark	0.59	26 – 30	204.8	1.12	7.4	13.6	102.4	...[j]	37.67
1002763	25/10/2008 23:33	Dark	0.07	25	203.0	1.12	6.7	14.4	102.9	10.1 ± 0.9	37.09
1002766	25/10/2008 23:59	Dark	0.49	27 – 31	200.0	1.13	8.4	13.0	102.8	11.5 ± 2.1	37.52
1002795	27/10/2008 21:54	Dark	0.30	23 – 24	210.1	1.10	7.7	14.7	100.7	...[j]	37.28
1002922	16/11/2008 19:40	Dark	0.12	28 – 29	217.0	1.10	6.6	13.9	105.3	3.7 ± 0.1	38.86
1002925	16/11/2008 20:22	Dark	0.91	23 – 25	211.4	1.11	7.8	13.5	104.5	4.5 ± 0.5	37.50
1002937	17/11/2008 19:34	Twilight	1.18	23 – 29	203.1	1.16	6.7	13.5	103.4	7.0 ± 0.5	37.99
1002943	17/11/2008 21:18	Dark	0.96	23 – 26	209.9	1.13	7.0	13.2	102.8	9.2 ± 1.5	37.60
1002959	18/11/2008 20:22	Dark	1.77	23 – 26	213.4	1.10	7.1	13.3	101.7	1.8 ± 1.4[i]	37.65
1003035	23/11/2008 19:39	Dark	2.12	23 – 26	207.3	1.13	6.7	13.8	100.9	2.3 ± 0.9	38.16
1003075	24/11/2008 19:43	Dark	2.01	23 – 26	199.9	1.10	6.6	13.8	99.0	6.4 ± 3.3	37.39
1003142	27/11/2008 19:41	Dark	0.62	23 – 25	190.9	1.12	8.1	13.9	104.8	34.6 ± 5.2	39.47
1003260	30/11/2008 20:40	Dark	0.81	23 – 27	193.1	1.06	8.0	13.6	99.3	19.7 ± 3.5	36.83
1003453	05/12/2008 04:13	Dark	0.68	23 – 31	214.0	0.99	7.6	14.3	104.3	4.3 ± 0.2	36.53
1004461	23/01/2009 23:03	Dark	0.41	22 – 29	191.6	1.12	8.2	14.9	105.5	0.0 ± 0.0	39.76

Notes. [a] Light conditions during the observations. For an explanation see Section 4.3.2. [b] Effective observation time of the measurements. [c] Zenith distance range covered by the observations. [d] Event rate after image cleaning. [e] Mean inner pedestal RMS value. [f] Inhomogeneity. [g] Mean *cloudiness* during the observations and its corresponding RMS. [h] Mean DT value during the observations. [i] The value is not indicative for the whole sequence, as *cloudiness* information is partly missing. [j] No *cloudiness* information available.

Table B.4: Sequences used for the analysis of 1ES 2344+514 and their parameters, after removing bad quality data. 1003453 belongs to Mrk 421 and has been used for cut optimisation, 1004461 is a Crab Nebula sequence on which the analysis pipeline has been verified.

C MAGIC Data Quality

C.1 1ES 1011+496

C.1.1 Inhomogeneity Problem

From the *CoG* distribution, an inhomogeneous camera acceptance for showers became obvious. After *area* cut, the event deficit for the hole right of the camera center amounted to $\sim 20\,\%$, for the hole below and left of the center to $15\,\%$. The radial profile confirms a hole in a circular region between 0.2 and 0.6 mm from the camera center, see Figure C.1. From the azimuthal profile, no conclusive picture can be drawn.

These holes may lead to a wrong background determination and hence wrong signal calculation, potentially faking a signal. Especially when using On and Off regions not following the sixfold camera symmetry, i.e. not 1, 2 or 5 Off regions, and when the effective observation time spent in each of the two wobble positions (wobble ratio) is not comparable. From Table 5.1 it is obvious that several data sets had a wobble ratio not compatible with unity. As this analysis has been performed using 3 Off regions, a detailed investigation of the problem was necessary.

From the FS plot it can be judged if a wobble ratio not around unity in connection with camera inhomogeneity has an effect on the data. An asymmetry of reconstructed event directions should be visible, as more excess events should be coming from one of the wobble positions. The data sets having a potentially problematic wobble ratio were searched for signs of such an asymmetry. For three data sets, such a sign was visible, i.e. 27 March, 3 April and 5 May. Their corresponding excess event counts amounted to only 14, 5 and 0, respectively, which is too small to provide statistically significant evidence for asymmetry. It should be noted also that not all days with a problematic wobble ratio showed signs of an asymmetry. Figure C.2 shows the FS plots for 27 of March (wobble ratio 0.71) and 29 April (wobble ratio 1.45). The latter shows no obvious asymmetry despite the high wobble ratio value.

The characteristics of this inhomogeneity changed when applying the *area* cut, indicating that the problem was *size* and energy dependent. Therefore the *CoG* distribution has been investigated after different energy cuts. The lower hole is basically unidentifiable after a lower energy cut of $\sim 300\,\mathrm{GeV}$, whereas the upper hole persists until $\sim 500\,\mathrm{GeV}$ (see Figs. C.3 and C.4). Circumventing the problem by applying such a high energy cut on the data would render the analysis of 1ES 1011+496 infeasible, as the far-away source has been discovered with a steep spectrum (spectral index of -4.0 (Albert *et al.* 2007b)) reaching only until 750 GeV.

Consequently, the inhomogeneity may have a biasing effect on the results. To get an estimate of this bias, the data were also analysed using only 1 Off region, so establishing symmetry between the On and Off regions in terms of the camera layout. The results

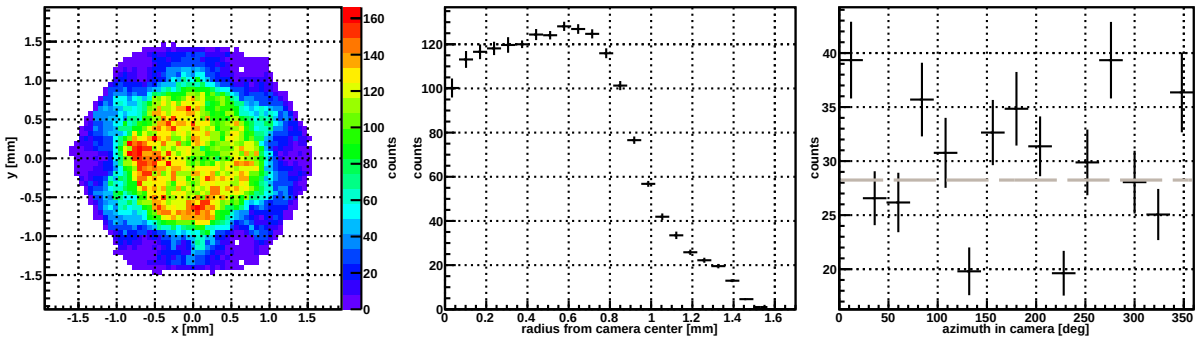

Figure C.1: *Left side: CoG* distribution after *area* cut for the "all" data set of 1ES 1011+496 as well as its radial (*middle*) and azimuthal (*right side*) profile. The horizontal dashed line shown in the azimuthal histogram represents a fit to the data points (χ^2/d.o.f. = 72.0/14).

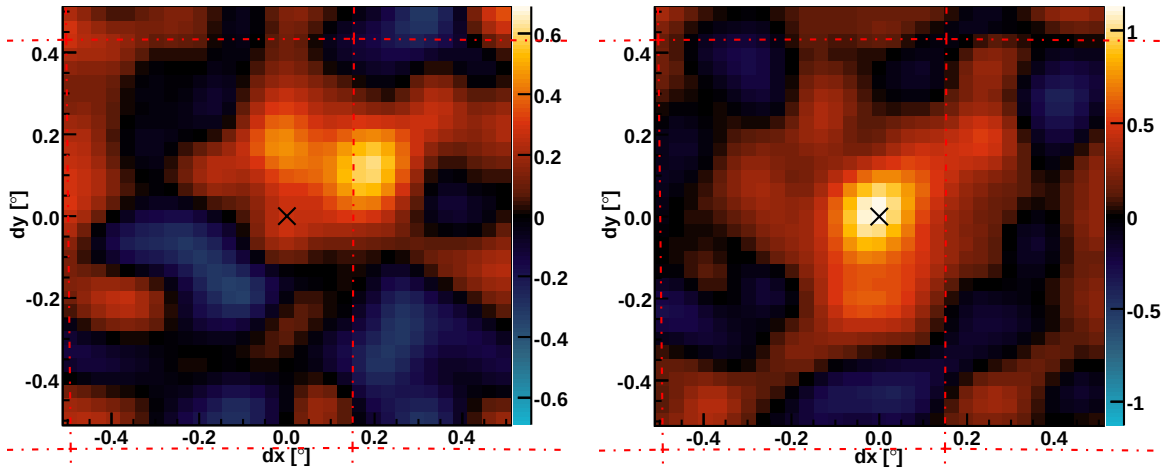

Figure C.2: FS plots for 1ES 1011+496 observations conducted on 27 March and 29 April 2008. The first one is showing a considerable asymmetry, whereas the latter is rather well centred.

are listed in Table C.1 and the ϑ^2 plot for the "all" data set is shown in Figure C.5. The latter was still showing a clear signal above $5\,\sigma$. The decrease in significance was predominantly due to a larger scaling factor because of using only 1 Off region. The excess event numbers changed by only 6 %. The results for the other data sets showed that the event statistics and significances did not increase or diminish systematically but rather arbitrarily. There was no connection between the increase or decrease of excess event statistics and a wobble ratio far away from unity. These results can be understood as the expected statistical background fluctuations due to reducing the event statistics by 1/3 using 1 Off region instead of 3, indicating that the determined signal is not affected by a systematic bias due to camera inhomogeneity.

Summarising, holes were present in the *CoG* distribution of events in the camera. These holes persisted until rather high energies, but did not produce a fake signal of the source.

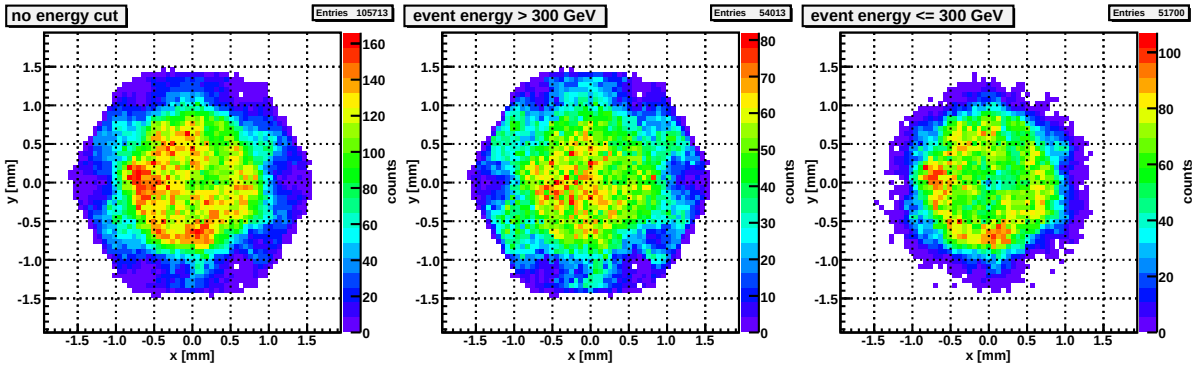

Figure C.3: *CoG* distribution for the "all" data set of 1ES 1011+496 without an energy cut (*left side*) and with a lower (*middle*) and upper (*right side*) energy cut of 300 GeV.

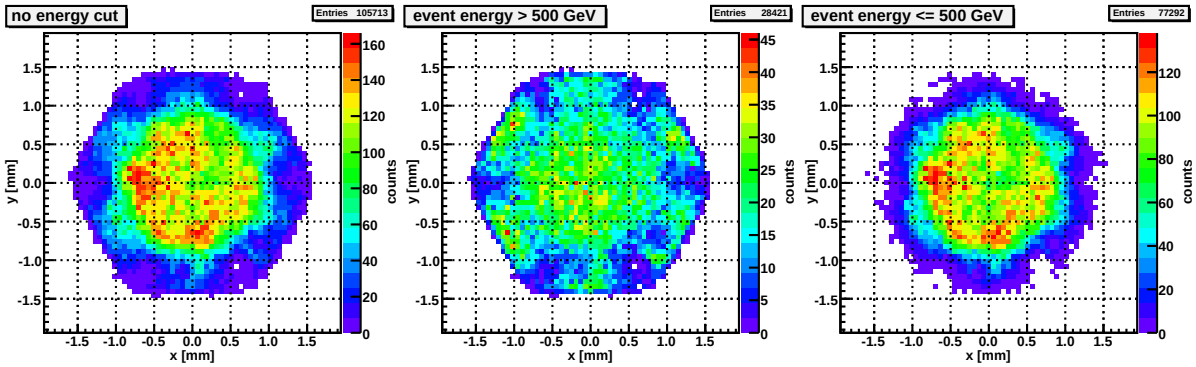

Figure C.4: Same as Figure C.3 but setting the energy cut at 500 GeV.

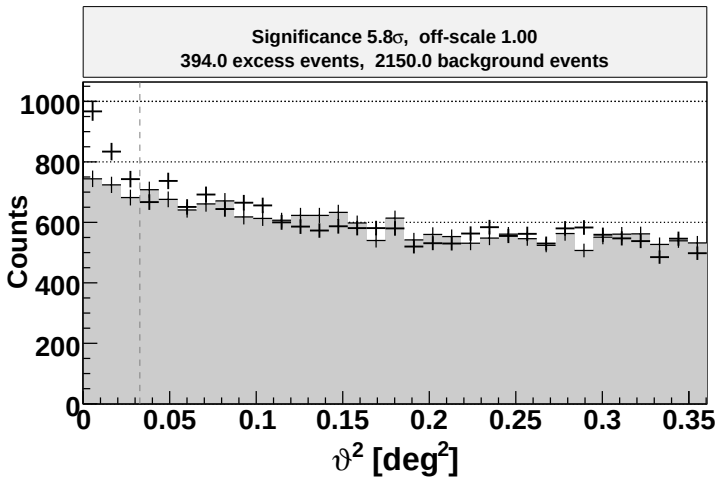

Figure C.5: ϑ^2 plot for 1ES 1011+496 using only 1 Off region. The grey-shaded area shows the background event distribution. The vertical dashed line indicates the ϑ^2 cut. Note that the plot has been produced including the anti-theta cut.

Data Set[a]	**Sign.**[b] $[\sigma]$	**Exc.**[c]	**Bgd.**[d]	**Wobble Ratio**[e]
all	5.8	394	2150	0.93
AGILE	3.4	81	248	0.62
period 64	3.5	150	842	1.02
period 65	2.8	105	632	0.58
period 66	3.1	113	607	1.33
period 67	2.2	28	68	0.73
09 March	2.0	53	325	1.14
10 March	1.9	27	85	0.57
11 March	2.3	69	433	1.09
27 March	−0.3	−4	105	0.71
29 March	0.5	9	146	0.40
30 March	1.1	19	133	0.65
03 April	0.8	6	24	2.48
04 April	−0.4	−4	66	...[f]
05 April	2.0	26	74	0.58
06 April	3.6	53	84	1.42
24 April	1.5	25	131	1.45
29 April	1.5	29	163	1.45
03 May	1.4	6	7	...[f]
04 May	2.2	30	82	1.82
05 May	−0.1	−1	112	0.66
06 May	2.6	16	12	1.46
07 May	0.6	9	99	1.94
23 May	1.9	21	51	1.54
24 May	1.1	7	17	...[f]

Notes. [a] The date corresponds to the day following the observation night. [b] Significance of the signal calculated using Li & Ma (1983) Eq. 17 and optimised cuts. [c] Number of excess events. [d] Number of background events. [e] Ratio of time spent in each of the two wobble positions. [f] Data taken during one wobble position only.

Table C.1: Analysis results of the individual data sets using only 1 Off region. Also compare with the values given in Table 5.1.

C.1.2 Starguider Correction

For the data of 6 May 2008 (sequence 351058), the number of correlated stars was close to the lower limit for the starguider to calculate a correction. Figure C.6 shows that a correction has indeed been applied for a dominant part of the data.

C.1.3 Influence of a Star on the Optimisation Data

The data of Mrk 421 used for the separation cut optimisation of 1ES 1011+496 were influenced by stars in the FOV of MAGIC. An example of their position in the camera is shown in Figure C.7. In this case, the stars caused pixels to be unsuitable for further processing. This can be seen from Figure C.8, showing for sequence 351510 a small three pixel cluster unsuitable for $\sim 30\,\%$ of the time above the camera center and a five pixel cluster unsuitable for $\sim 20-70\,\%$ of the time below the center. Both are due to

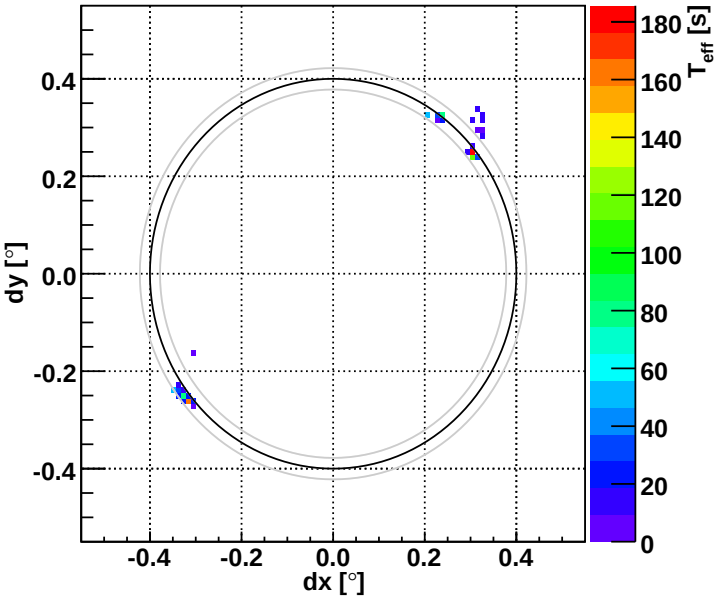

Figure C.6: Reconstructed pointing positions during the 1ES 1011+496 observations on 6 May 2008. The black ring shows the track a source is following on the sky if observed in wobble mode (0.4° offset from the camera center), the grey circles correspond to the black circle shifted by ± one shaft encoder step. A point offset from this circle is showing how much the pointing position has been corrected due to the starguider measurements. In case no starguider correction would have been applied, all points would lie exactly on the circle. The colour code denotes the effective observation time spent at each of the pointing positions.

the same star (6.0 mag), which was changing its position in the camera after changing the wobble position. As the ratio of wobble positions was roughly 2/3, the star was wandering a larger distance in the lower camera, affecting more pixels. Additionally, two larger clusters of pixels for a larger time span are visible in the outer camera, which are due to a second star (5.1 mag) comparably off from the optical axis and hence with a broader and fainter light distribution (coma), causing a larger area to be influenced. Comparing with other sequences it is obvious that the other unsuitable pixels are either due to fluctuations (most of the purple ones) or unsuitable also for other sequences (red). For sequence 1000135, three pixels at the same position as for 351510 just above the camera center were unsuitable for 100 % of the time. As this sequence consisted only of one wobble position, no pixels below the camera center were affected and the star did hardly change its position in the camera. For this sequence, outer pixels seem not to be affected by the second star, which is presumably due to most of the starlight falling in the empty section between two outer camera sectors and the star being further away from the optical axis, smearing out its intensity profile even more.

The inner camera pixels unsuitable due to the star light can no longer trigger showers and may cause holes in the *CoG* distribution. Indeed, before separation cuts an additional deficit of showers is visible, which is not apparent any more after separation cuts (though low statistics do not allow to exclude the presence of the hole with high confidence). This is due to the fact that only a small number of pixels is affected at the same time by the star, hence only very small showers will not be triggered. But as showers of

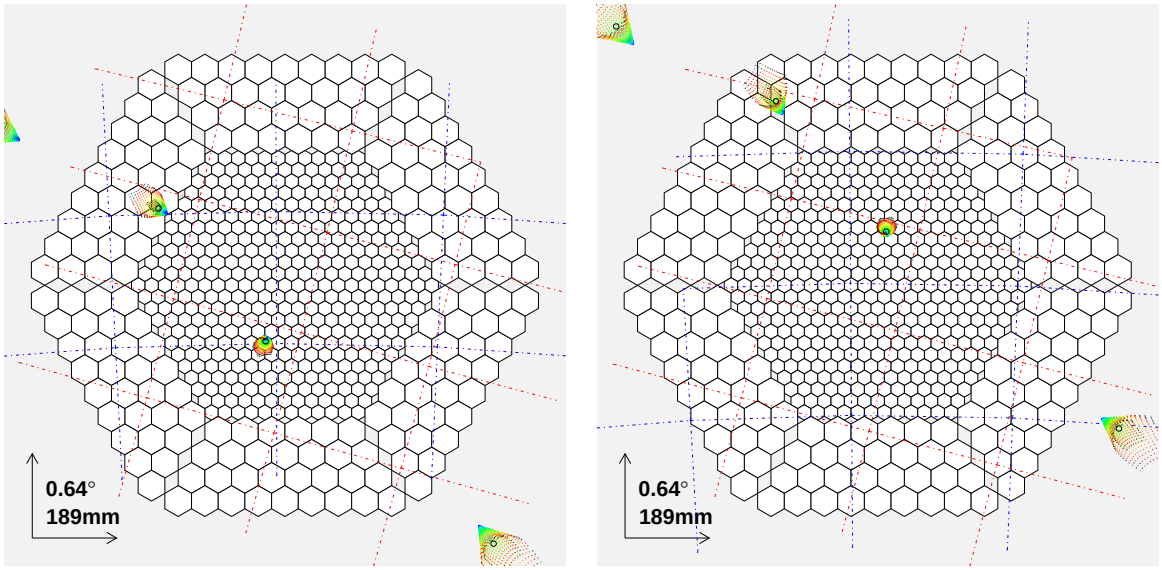

Figure C.7: Stars in the FOV of the Mrk 421 sequences used for optimisation of the 1ES 1011+496 separation cut. The plots show only a snapshot of the stars normally moving in the camera center over time. The blue dashed lines give the local coordinates, while the red lines show the sky coordinates. The cones surrounding the stars visualise their PSF, which becomes larger with increasing distance to the optical axis (coma effect). *Left side:* sequence 351510 wobble position 1, *right side:* sequence 1000135 wobble position 2.

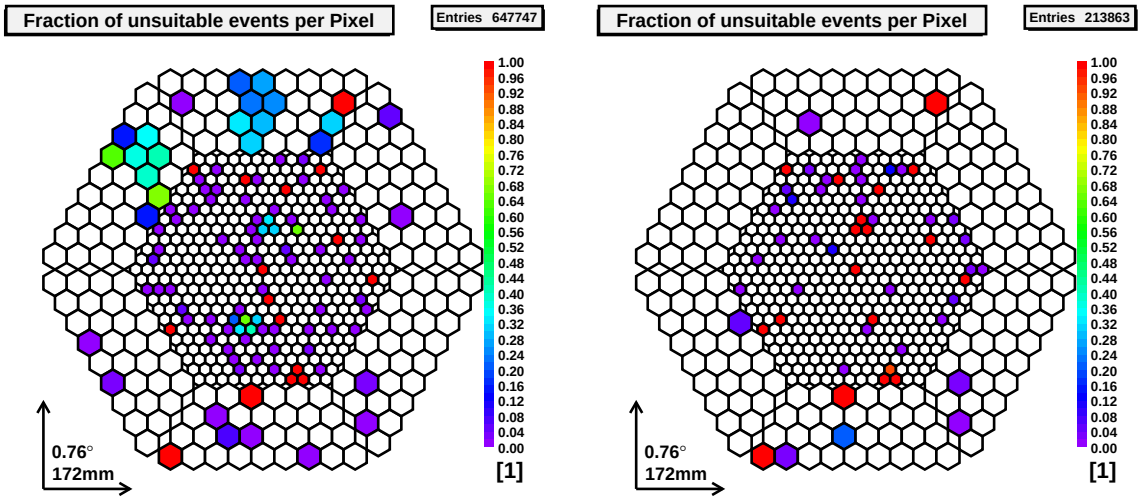

Figure C.8: Fraction of unsuitable pixels of sequences 351510 (*left side*) and 1000135 (*right side*). Pixels marked purple are presumably due to fluctuations, red pixels (unsuitable for 100 % of the time) are potentially defect. In the case of sequence 1000135, the cluster of three red pixels above the camera center is due to a star though.

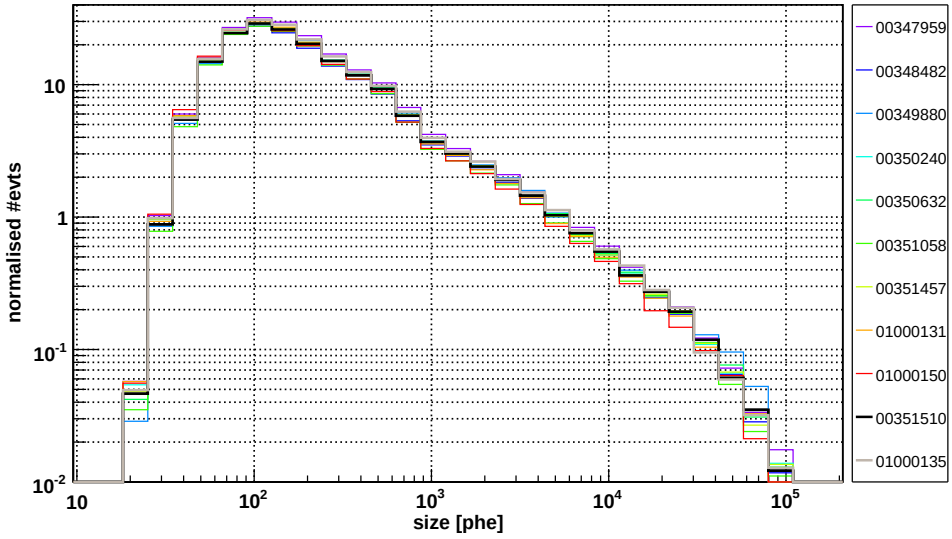

Figure C.9: *size* distribution normalised to the effective on-time for the Mrk 421 sequences 351510 (thick black line) and 1000135 (thick grey line). For comparison, 1ES 1011+496 sequences from the corresponding time periods 66 and 67 are also shown.

such low *size* will be removed by the separation cut anyway, and are not important for the cut optimisation, this is not causing a problem for further analysis.

Apart from preventing showers to get triggered, star light may in this case also decrease the *size* of showers through the unsuitable pixels. Figure C.9 is showing the *size* distribution normalised to the effective observation time for the Mrk 421 sequences (thick black and grey lines) and 1ES 1011+496 sequences from period 66 and 67 (coloured thin lines). For both of the Mrk 421 sequences, the bin contents over *size* were rather stable compared to the other sequences. Sequence 351510 was for all *size* bins at average values, whereas sequence 1000135 had amongst the highest number of normalised counts, a difference which can simply be explained by the higher event rate of this sequence. No systematic bias is visible for the Mrk 421 sequences, so the stars do not seem to have had a significant effect on the *size* distributions.

In conclusion, effects of two stars on the Mrk 421 data used for optimisation of the separation cuts of 1ES 1011+496 were visible. Their impact on the high level analysis and optimisation procedure was not significant though.

C.2 1ES 2344+514

C.2.1 Inhomogeneity Problem

The Center of Gravity (CoG) distribution showed a deficit of events at several positions in the camera. After *area* cut, these holes vanished or became less pronounced, but a deficit at one of the wobble positions became apparent. If the effective observation time spent in each of the two wobble positions (w1/w2 ratio) is comparable and if the On and Off regions are symmetrically aligned in the hexagonal MAGIC camera, i.e. if their sum is 2, 3 or 6, this would not cause any problem. For this analysis, 1 On and 3 Off regions have been used, hence not following a sixfold symmetry. Additionally, the w1/w2 ratio was not ~ 1 for some data sets (see Table 6.1). This could induce a systematic bias in background determination and hence produce fake signals in the ϑ^2 plot. To assess the existence and strength of such a bias, several checks have been performed:

- **Radial and Azimuthal CoG Distributions** From directly reading the bin contents of the CoG plot after *area* cut, the deficit of events could be quantified to be $\sim 25\,\%$ for the lower and $\sim 30\,\%$ for the upper hole. The radial CoG distribution (Figure C.10) was confirming this finding, revealing a loss of $\sim 7\,\%$ of events between $\sim 0.12°$ and $\sim 0.6°$. The azimuthal profile plot also shown in Figure C.10 was not showing clear trends, presumably due to combined influences by the camera geometry, low statistics and the inhomogeneity.

- **w1/w2 Ratio** The FS plot is projecting the reconstructed excess event directions on the sky. If a different amount of observation time in each of the wobble positions had a significant effect on the data, this effect would also be direction dependent and hence visible in the FS plot manifesting itself in an asymmetry. Note that the FS plot shows in any case an asymmetry at two times the wobble distance from the camera center if the w1/w2 ratio is not around unity. For assessing an effect on the signal, only the region $\sim \pm 0.4°$ in x and y is important though. The feasibility of this study is limited strongly by the small number of excess events of the individual data sets. Taking this into account, all data sets but the one from 17 November did not show clear signs of such an asymmetry. For the latter, an asymmetry may have been present, see Figure C.11. The data have been used nevertheless considering that (1) the signal amplitudes shown in the FS plot were all consistent with statistical fluctuations (note the colour scale with a maximum of ~ 1), hence an asymmetry could not be established on a significant basis and (2) using only 1 Off region, the hint for a signal was still apparent.

- **Analysis with 1 Off Region** Using only 1 Off region for the analysis, the statistical errors of the determined background will be larger compared to using 3 Off regions, but the systematic errors will be reduced. The On and Off regions will follow a sixfold symmetry, so camera inhomogeneities will cancel out to a certain extend if the w1/w2 ratio is comparable. The resulting ϑ^2 plot for the "all" data set is shown in Figure C.12. The signal was still present, though the significance decreased from $3.5\,\sigma$ to $3.1\,\sigma$. This decrease is due to the higher background scaling

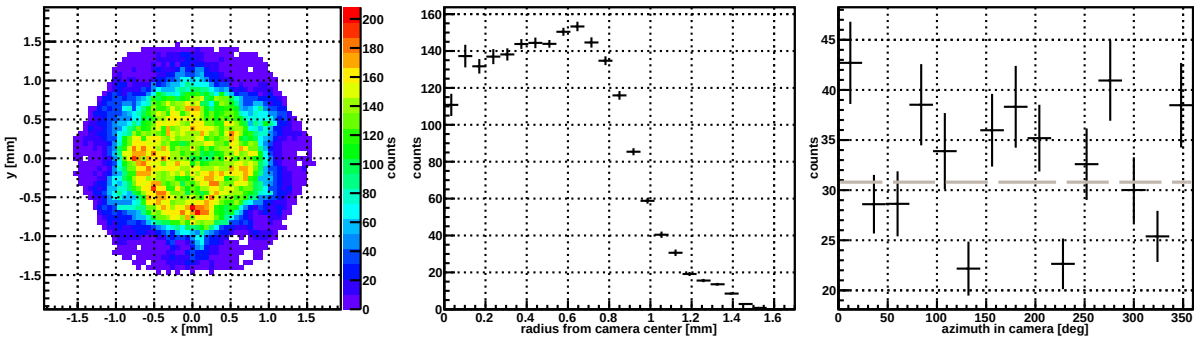

Figure C.10: *Left side: CoG* distribution after *area* cut for the "all" data set of 1ES 2344+514 as well as its radial (*middle*) and azimuthal (*right side*) profile. The horizontal dashed line shown in the azimuthal histogram represents a fit to the data points (χ^2/d.o.f. = 56.1/14).

factor; the number of excess events is even larger and the number of background events lower than in the 3 Off regions case. The spectrum derived from this result was very well compatible with the one determined from 3 Off regions, see Figure 6.20.

- **Energy Dependency of the Deficit** As the comparison between the *CoG* distributions before and after *area* cut have shown, the problem became less pronounced applying the cut. This indicated that mostly showers of low *size* were affected by this deficit. Therefore, the *CoG* distributions after *area* and a variable energy cut have been investigated. A ϑ^2 cut could not be added due to the low statistics obtained already after *area* cut. Figs. C.13, C.14 and C.15 show that the hole at $y \approx 0.4\,\mathrm{mm}$ was much less pronounced at a lower energy cut of 160 GeV, whereas the hole at $y \approx 0\,\mathrm{mm}$ was still visible at an energy cut of 260 GeV and also above (as far as statistics are sufficient to judge). If the signal from 1ES 2344+514 would be due to the holes in the *CoG* plot, the signal strength should decrease strongly with decreasing effect strength, i.e. increasing energy cut. Figure C.16 is showing that there is no strong correlation between these two parameters. Especially the signal is not vanishing at high energy cut values, proving that the signal is not due to the holes in the *CoG* distribution.

In conclusion, the deficit of events is clearly visible in the *CoG* plot also above low energies. The deficit does not fake the signal though, and does not exert a significant effect on the detection significance, overall spectrum or FS plot, which partly may be due to the w1/w2 ratio being close to 1. Note also that these studies had to be performed without applying the ϑ^2 cut due to limited statistics. The cut itself may additionally reduce the inhomogeneity.

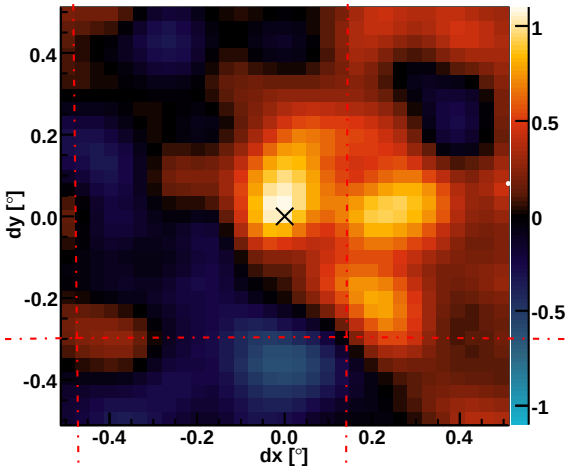

Figure C.11: FS plot for the data of 1ES 2344+514 taken November 17. An asymmetry may be present. Note though that the signal amplitudes are all consistent with statistical fluctuations.

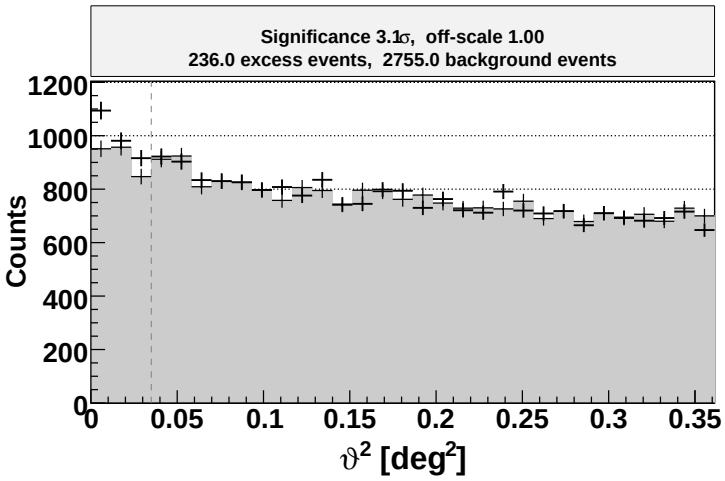

Figure C.12: ϑ^2 plot for 1ES 2344+514 using only 1 Off region. The grey-shaded area shows the background event distribution. The vertical dashed line indicates the ϑ^2 cut. Note that the plot has been produced including the anti-theta cut.

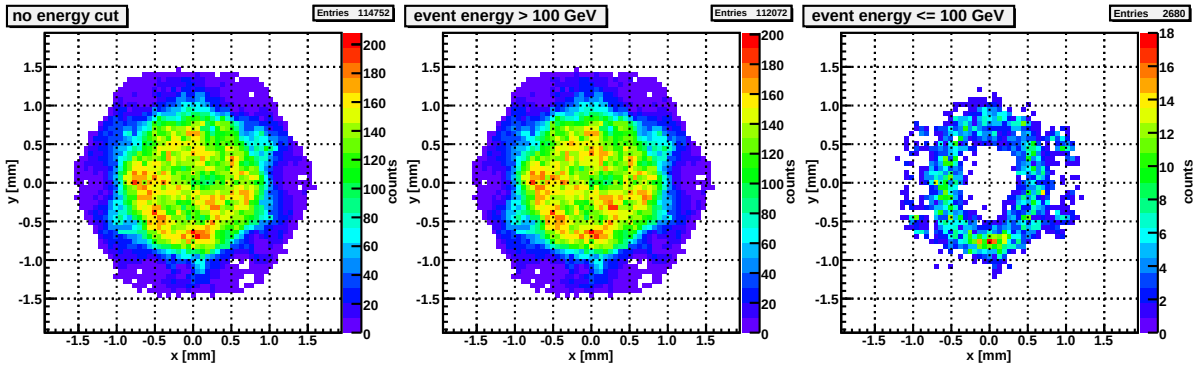

Figure C.13: *CoG* distribution for the "all" data set of 1ES 2344+514 without an energy cut (*left side*) and with a lower (*middle*) and upper (*right side*) energy cut of 100 GeV, respectively.

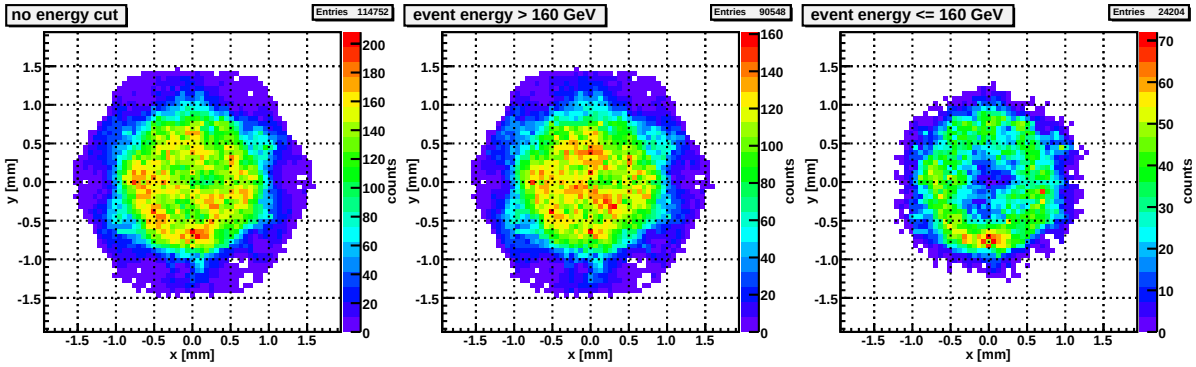

Figure C.14: Same as Figure C.13 but using an energy cut of 160 GeV.

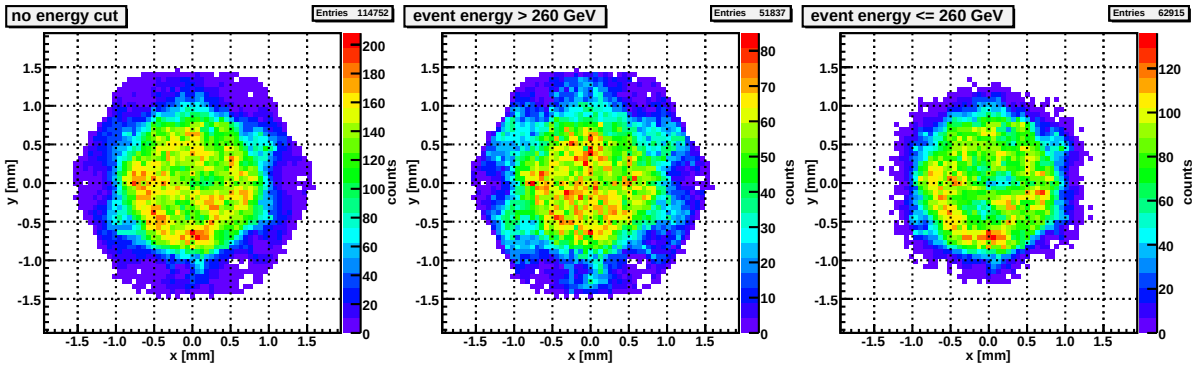

Figure C.15: Same as Figure C.13 but using an energy cut of 260 GeV.

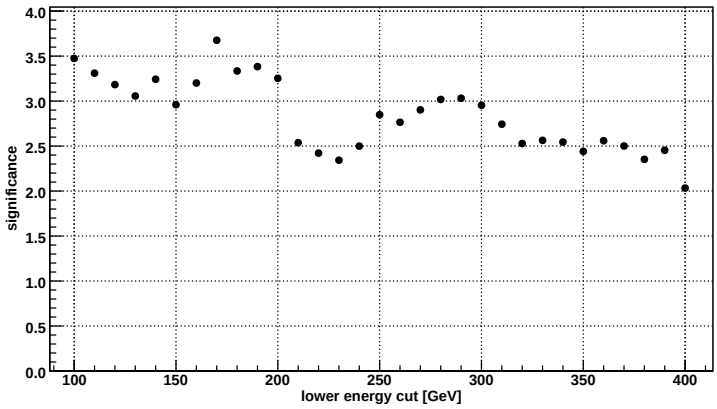

Figure C.16: Significance of the "all" data set of 1ES 2344+514 after separation cuts as a function of a lower energy cut.

C.2.2 Pointing Check

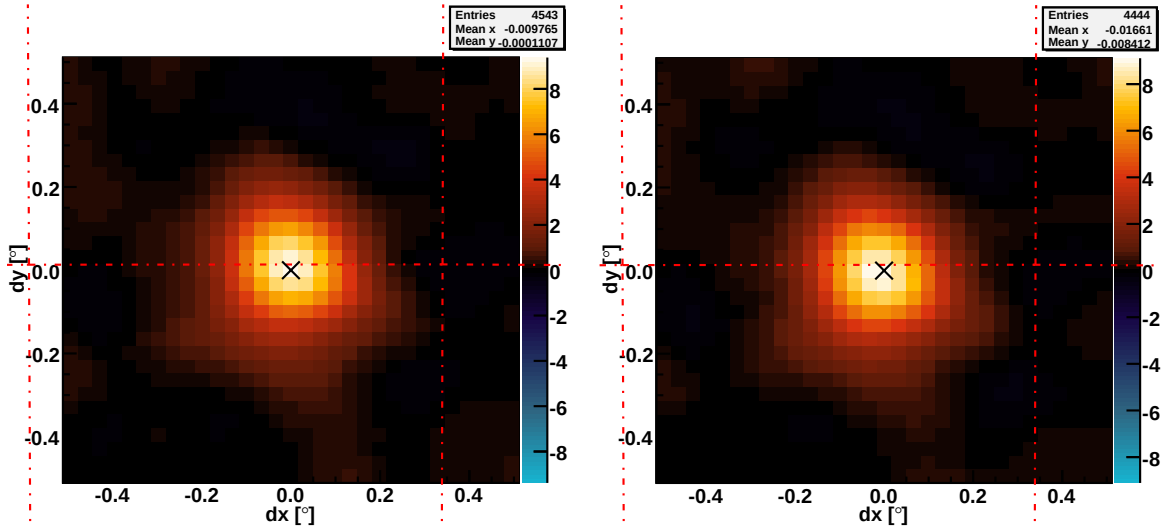

Figure C.17: FS plots for Crab Nebula data taken 28 October 2008 analysed with the optimised separation cuts of 1ES 2344+514. The *left side* shows the plot applying a starguider correction, whereas for the *right side* the correction was switched off. A difference is hardly visible, indicating that also observations without starguider correction measurements should be centred well on the source.

D Additional MAGIC Analysis Details

D.1 Background Separation

D.1.1 1ES 1011+496

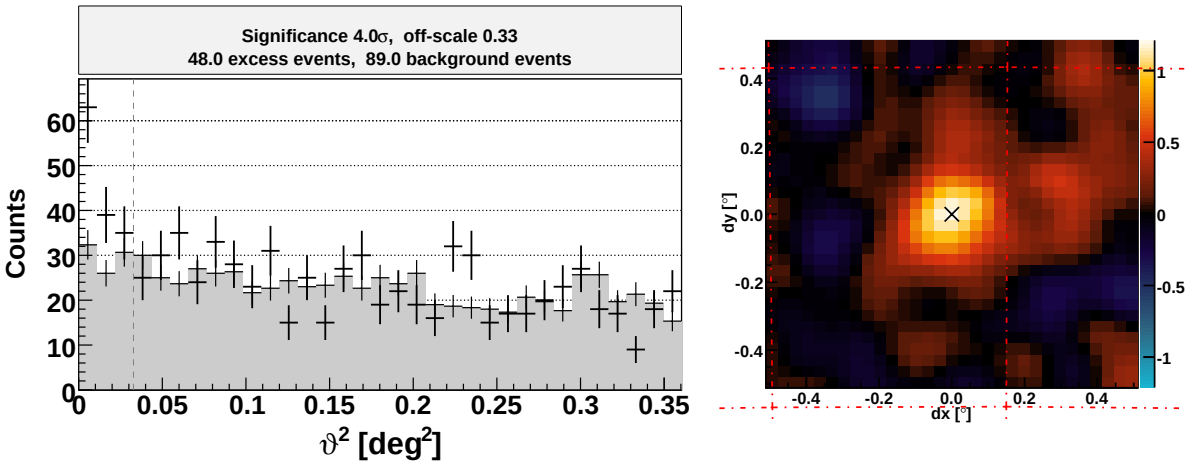

Figure D.1: ϑ^2 plot (*left side*) and FS plot (*right side*) for 1ES 1011+496 data of 6 April 2008.

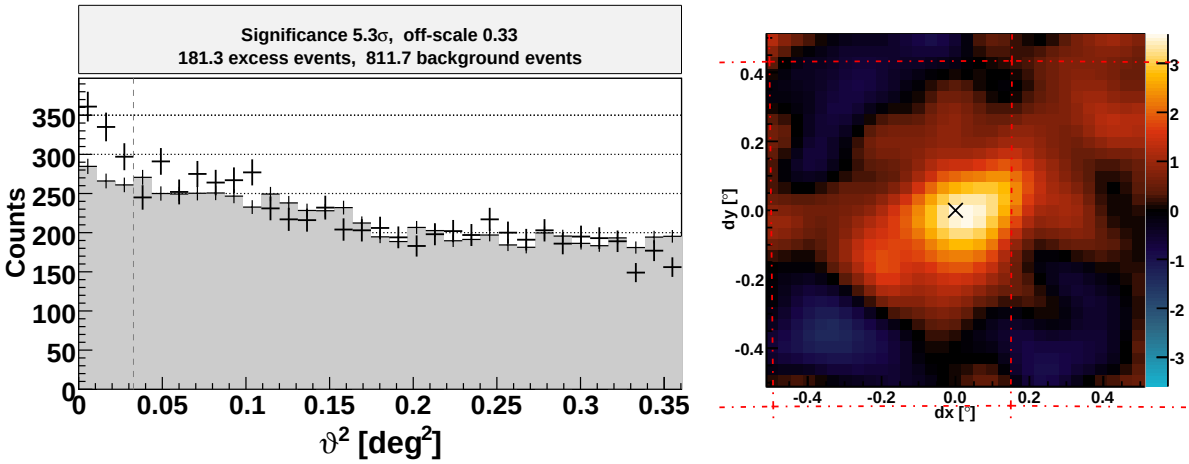

Figure D.2: ϑ^2 plot (*left side*) and FS plot (*right side*) for 1ES 1011+496 data of MAGIC observation period 64.

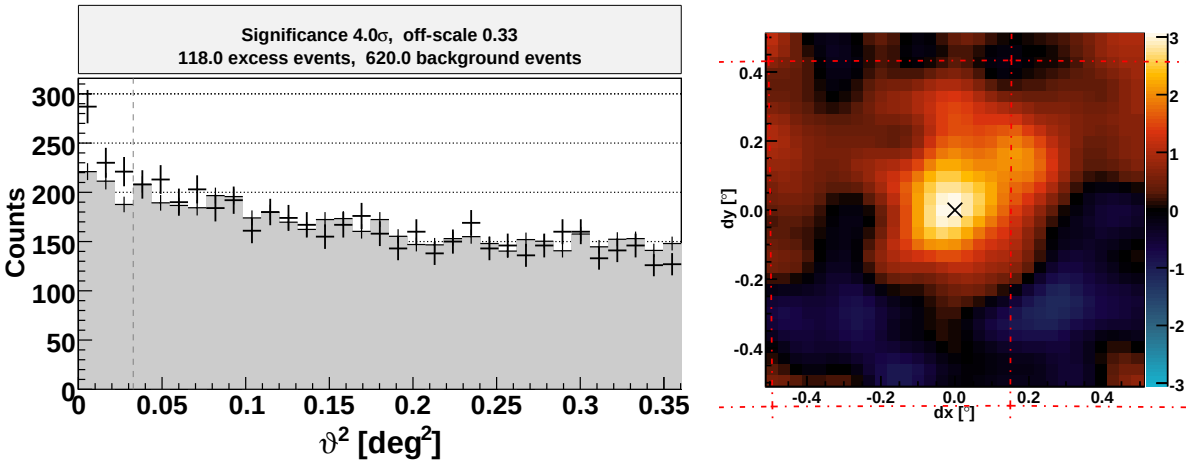

Figure D.3: ϑ^2 plot (*left side*) and FS plot (*right side*) for 1ES 1011+496 data of MAGIC observation period 65.

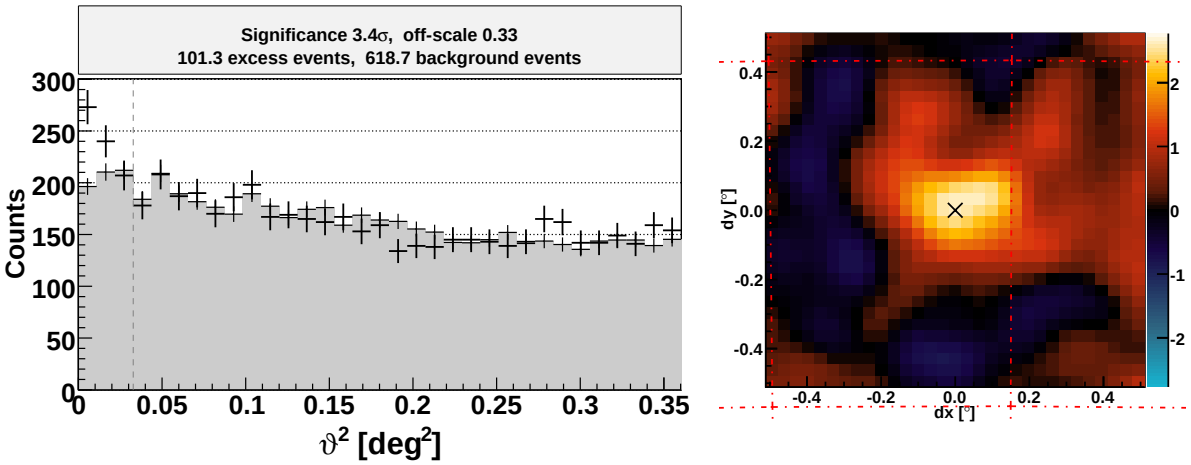

Figure D.4: ϑ^2 plot (*left side*) and FS plot (*right side*) for 1ES 1011+496 data of MAGIC observation period 66.

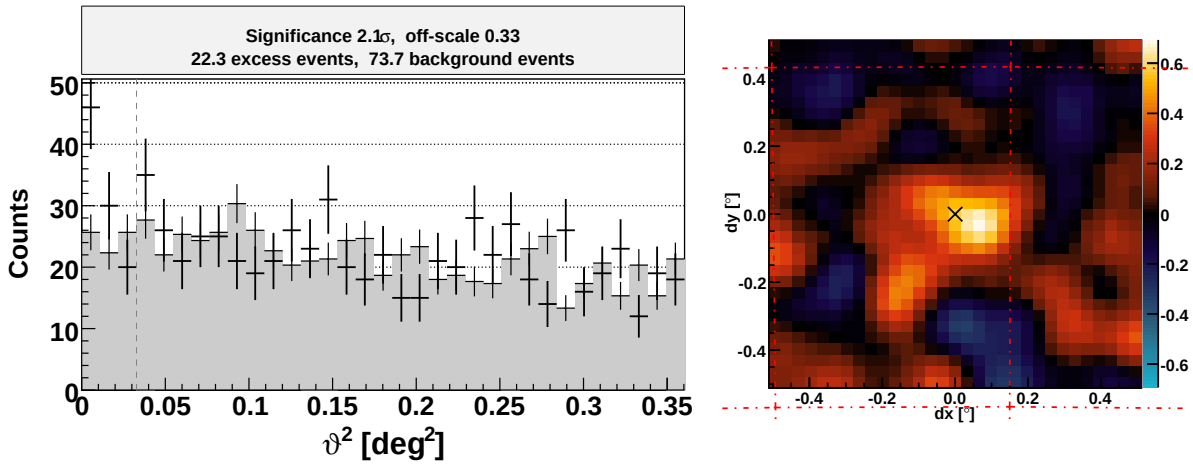

Figure D.5: ϑ^2 plot (*left side*) and FS plot (*right side*) for 1ES 1011+496 data of MAGIC observation period 67.

D.2 Spectrum Derivation

D.2.1 1ES 1011+496

zbin[(a)]	**Sequence**	**Assignment**[(b)]	**#Events$_{sim}$**[(c)]	**#Events$_{trig}$**[(d)]
6	7012		300000	7870
7	7030		400000	10290
8	7050		400000	10334
9	7070		400000	10252
10	6842		400000	10130
11	6877		400000	10021
12	6897		400000	9959
13	7935	train	400000	9892
14	7955		400000	9874
15	7975		400000	9788
16	7995		400000	9759
17	8015		400000	9467
18	8035		400000	9610
19	8055		400000	9395
20	8075		400000	9157
6	7015		1464844	34673
7	7034		1600000	36915
8	7054		1600000	36439
9	7074		1600000	35460
10	6846		1600000	34769
11	6881		1600000	34080
12	6901		1600000	33625
13	7939	test	1599809	33056
14	7959		1600000	32687
15	7979		1600000	32233
16	7999		1600000	31633
17	8019		1600000	30876
18	8039		1600000	30487
19	8059		1600000	29779
20	8079		1600000	29393

Notes. [(a)] Zenith distance bin, see Section 4.3.3.4. [(b)] Denotes if sequence was used for testing or training (see Sext. 4.3.3.4). [(c)] Number of simulated MC events. [(d)] Number of MC events that have fulfilled the MAGIC trigger conditions (see Section 4).

Table D.1: MC sequences used for the analysis of 1ES 1011+496 as well as the Crab Nebula (with a reduced zbin range). All MCs have been produced for MUX FADCs in wobble observation mode with a spectral slope of -2.6 and a PSF of 13.1 mm.

Data Set	Energy[a] [GeV]	F[b] [$\mathrm{TeV}^{-1}\,\mathrm{cm}^{-2}\,\mathrm{s}^{-1}$]	F_{cor}[c] [$\mathrm{TeV}^{-1}\,\mathrm{cm}^{-2}\,\mathrm{s}^{-1}$]	Sign.[d] [σ]	Exc.[e]	Bgd.[f]
all	114	$< 8.93 \cdot 10^{-10}$	$< 9.74 \cdot 10^{-10}$	0.4	109	59749
	170	$(2.29 \pm 0.75) \cdot 10^{-10}$	$(2.77 \pm 0.91) \cdot 10^{-10}$	3.1	373	11076
	254	$(5.13 \pm 1.54) \cdot 10^{-11}$	$(7.65 \pm 2.31) \cdot 10^{-11}$	3.4	165	1733
	380	$(1.44 \pm 0.53) \cdot 10^{-11}$	$(3.06 \pm 1.12) \cdot 10^{-11}$	2.8	86	684
	567	$(4.30 \pm 2.16) \cdot 10^{-12}$	$(1.47 \pm 0.74) \cdot 10^{-11}$	2.0	41	293
	849	$< 8.85 \cdot 10^{-13}$	$< 5.15 \cdot 10^{-12}$	-0.9	-12	134
	1269	$< 3.80 \cdot 10^{-13}$	$< 3.42 \cdot 10^{-12}$	-1.0	-8	58
	1897	$< 9.48 \cdot 10^{-14}$	$< 1.15 \cdot 10^{-12}$	-1.4	-7	25
06 April	122	$< 5.72 \cdot 10^{-9}$	$< 6.32 \cdot 10^{-9}$	1.8[g]	97	2138
	182	$(7.42 \pm 2.95) \cdot 10^{-10}$	$(9.23 \pm 3.67) \cdot 10^{-10}$	2.6	56	333
	271	$(1.98 \pm 0.76) \cdot 10^{-10}$	$(3.09 \pm 1.18) \cdot 10^{-10}$	2.8	29	71
	405	$(4.79 \pm 2.58) \cdot 10^{-11}$	$(1.09 \pm 0.59) \cdot 10^{-10}$	2.0	13	28
	605	$< 1.51 \cdot 10^{-11}$	$< 5.67 \cdot 10^{-11}$	-0.7	-3	17
	904	$< 9.32 \cdot 10^{-12}$	$< 5.85 \cdot 10^{-11}$	-0.1[h]	0	8
	1351	$< 8.08 \cdot 10^{-12}$	$< 7.65 \cdot 10^{-11}$	1.5	3	2

Notes. [a] Bin central energy at the Lafferty-Wyatt position. [b] Measured differential flux. [c] Differential flux corrected for absorption by the EBL using Kneiske & Dole (2010). [d] Signal significance according to Li & Ma (1983) Eq. 17. [e] Number of excess events. [f] Number of background events. [g] From a detailed investigation a not negligible amount of the excess seems to be a fluctuation, therefore an UL has been calculated despite a significance $> 1.5\,\sigma$. [h] The non-zero significance despite zero excess events is due to using full precision (non-integer) event counts for the significance calculation in the software, whereas the event counts value itself is rounded down.

Table D.2: Differential spectral points of 1ES 1011+496 for the "all" at "06 April" data set.

D.2.2 1ES 2344+514

zbin[(a)]	**Sequence**	**Assignment**[(b)]	**#Events$_{sim}$**[(c)]	**#Events$_{trig}$**[(d)]
8	7050	train	400000	10334
9	7070		400000	10252
10	6842		400000	10130
11	6877		400000	10021
12	6897		400000	9959
13	7935		400000	9892
14	7955		400000	9874
8	7054	test	1600000	36439
9	7074		1600000	35460
10	6846		1600000	34769
11	6881		1600000	34080
12	6901		1600000	33625
13	7939		1599809	33056
14	7959		1600000	32687
7	12661	train	400000	10049
8	12681		400000	9899
9	12701		400000	9878
10	12473		400000	9830
11	12508		400000	9740
12	12528		400000	9626
7	12665	test	1600000	35970
8	12685		1600000	35646
9	12705		1600000	34738
10	12477		1600000	34008
11	12512		1600000	33324
12	12532		1600000	32848

Notes. [(a)] Zenith distance bin, see Section 4.3.3.4. [(b)] Denotes if sequence was used for testing or training (see Sext. 4.3.3.4). [(c)] Number of simulated MC events. [(d)] Number of MC events that have fulfilled the MAGIC trigger conditions (see Section 4).

Table D.3: MC sequences used for the analysis of 1ES 2344+514 (upper sample) and the Crab Nebula (lower sample). All MCs have been simulated in wobble mode with a PSF of 13.1 mm (14.8 mm for the Crab Nebula) for MUX data with a spectral slope of −2.6.

Energy[(a)] [GeV]	$\boldsymbol{F}^{(b)}$ [$\mathrm{TeV}^{-1}\,\mathrm{cm}^{-2}\,\mathrm{s}^{-1}$]	$\boldsymbol{F_{cor}}^{(c)}$ [$\mathrm{TeV}^{-1}\,\mathrm{cm}^{-2}\,\mathrm{s}^{-1}$]	**Sign.**[(d)] [σ]	**Exc.**[(e)]	**Bgd.**[(f)]
262	$(2.02 \pm 0.83) \cdot 10^{-11}$	$(2.15 \pm 0.88) \cdot 10^{-11}$	2.5	134	2159
726	$(1.26 \pm 0.82) \cdot 10^{-12}$	$(1.64 \pm 1.08) \cdot 10^{-12}$	1.5	40	511
2011	$(1.78 \pm 1.02) \cdot 10^{-13}$	$(2.86 \pm 1.64) \cdot 10^{-13}$	1.8	18	71
5569	$< 3.07 \cdot 10^{-14}$	$< 6.50 \cdot 10^{-14}$	0.1[(g)]	0	4

Notes. [(a)] Bin central energy at the Lafferty-Wyatt position. [(b)] Measured differential flux. [(c)] Differential flux corrected for absorption by the EBL using Kneiske & Dole (2010). [(d)] Signal significance according to Li & Ma (1983) Eq. 17. [(e)] Number of excess events. [(f)] Number of background events. [(g)] The non-zero significance despite zero excess events is due to using full precision (non-integer) event counts for the significance calculation in the software, whereas the event counts value itself is rounded down.

Table D.4: Differential spectral points derived for the "all" data set of 1ES 2344+514.

E Detailed Multi-Wavelength Observations and Results

E.1 1ES 1011+496

E.1.1 Swift

E.1.1.1 Swift Observations and XRT Results during the MW Campaign

Obs. ID[a]	**Obs. Start**[b]	**Obs. End**[c]	**MJD$_{mean}$**[d]	t_{XRT}[e] [ks]	t_{UVOT}[f] [ks]	t_{BAT}[g] [ks]
35012008	28/04/2008 21:17:02	23:08:56	54584.925	2.00	1.95	2.04
35012009	30/04/2008 19:48:02	19:53:11	54586.827	0.19	0.14	0.00
35012010	01/05/2008 22:53:02	22:56:32	54587.955	0.00	0.00	0.01
35012011	02/05/2008 21:53:54	23:15:57	54588.940	0.86	0.80	0.88
35012012	03/05/2008 21:35:02	23:20:57	54589.936	1.51	1.39	1.54
35012014[h]	04/05/2008 21:32:02	23:22:57	54590.935	1.67	1.54	1.70
35012013[h]	05/05/2008 21:37:02	23:22:57	54591.937	1.37	1.25	1.41
35012015	06/05/2008 21:43:02	23:25:57	54592.940	1.79	1.74	1.82
35012016	07/05/2008 00:55:02	23:30:57	54593.509	1.87	1.80	1.92
35012017	08/05/2008 07:56:02	11:16:59	54594.400	1.77	1.70	1.82

Notes. [a] *Swift* observation ID. [b] Start time of observation in UTC. [c] End time of observation in UTC. The observations ended the same day they began. [d] Mean MJD of the observation. [e] Exposure of XRT. [f] Total exposure of all UVOT filters. [g] Exposure of BAT. [h] The reason for the not chronologically ID numbering is not known, but possibly just a mistake caused by manual insertion (A. Stamerra, 2012, private communication).

Table E.1: *Swift* observations of 1ES 1011+496 during the MW campaign. Note that *Swift* is performing several pointings per observation ID, the given start and end times of the observations are the total ones for the whole ID though. For a more detailed list, see http://www.swift.psu.edu/operations/obsSchedule.php.

Obs. ID[(a)]	Simple Power Law Fit			Log-Parabolic Power Law Fit				
	$F\,(2-10\,\mathrm{keV})$[(b)] $[10^{-11}\,\mathrm{erg\,cm^{-2}\,s^{-1}}]$	a[(c)]	χ^2_{red}/d.o.f.	$F\,(2-10\,\mathrm{keV})$[(d)] $[10^{-11}\,\mathrm{erg\,cm^{-2}\,s^{-1}}]$	a[(e)]	b[(e)]	χ^2_{red}/d.o.f.	L[(f)] [%]
35012008	1.95 ± 0.10	2.36 ± 0.08	1.02/45	1.70 ± 0.12	2.28 ± 0.06	0.30 ± 0.20	0.92/56	0.0
35012009	3.68 ± 1.00	1.98 ± 0.30	1.16/3	2.32 ± 1.10	1.93 ± 0.40	$0.60^{+1.9}_{-0.60}$	1.52/2	48.2
35012010	...[(g)]	...[(g)]	...[(g)]	...[(g)]	...[(g)]	...[(g)]	...[(g)]	...[(g)]
35012011	2.81 ± 0.20	2.24 ± 0.10	0.96/26	2.41 ± 0.30	2.12 ± 0.09	0.39 ± 0.23	0.74/31	83.4
35012012	2.44 ± 0.30	2.27 ± 0.09	1.09/37	2.17 ± 0.18	2.24 ± 0.08	0.19 ± 0.20	0.91/45	0.0
35012014	2.19 ± 0.20	2.35 ± 0.10	0.71/34	1.98 ± 0.20	2.30 ± 0.07	0.20 ± 0.20	0.76/43	0.0
35012013	1.75 ± 0.10	2.47 ± 0.08	1.70/40	1.36 ± 0.12	2.28 ± 0.07	0.67 ± 0.21	1.48/48	0.0
35012015	1.62 ± 0.08	2.52 ± 0.08	1.37/41	1.36 ± 0.12	2.42 ± 0.07	0.42 ± 0.20	1.08/52	6.9
35012016	1.75 ± 0.15	2.45 ± 0.08	1.31/44	1.46 ± 0.15	2.40 ± 0.07	0.34 ± 0.20	1.05/55	0.0
35012017	1.33 ± 0.05	2.51 ± 0.10	1.21/34	1.24 ± 0.15	2.42 ± 0.07	0.24 ± 0.23	1.17/43	0.0

Notes. [(a)] *Swift* observation ID (see also Note (*h*) of Table E.1). [(b)] Integral flux from 2 to 10 keV determined by a simple power law fit from 0.5 – 10 keV. [(c)] Spectral index determined by a simple power law fit from 0.5 – 10 keV. [(d)] Integral flux from 2 to 10 keV determined by a log parabolic power law fit from 0.3 – 10 keV. [(e)] Spectral indices determined from a log parabola fit from 0.3 – 10 keV. [(f)] Probability that the log parabolic power law fit is preferred over the simple power law fit by means of a likelihood ratio test. [(g)] Observation time too short for extracting results.

Table E.2: Analysis results for the *Swift* XRT observations listed in Table E.1. The data have been analysed applying an absorbed simple power law as well as am absorbed log-parabolic power law. For all IDs, the simple power law fit is clearly preferred.

E.1.2 Corrections, Conversions and Results for the Optical Regime

E.1.2.1 KVA

The KVA data had to be corrected for the influence of the host galaxy and interstellar absorption to obtain the SED points. This has been accomplished by using

$$F_{hcor}(\lambda) = -2.5 \log_{10}\left(\frac{F_m(\lambda) - F_h(\lambda)}{F_0(\lambda)}\right) \tag{E.1}$$

$$F_{core}(\lambda) = F_0(\lambda) \ 10^{-0.4(F_{hcor}(\lambda) - A(\lambda))} \tag{E.2}$$

with F_{hcor} being the host galaxy corrected flux density of the source in units of mag, F_m and F_h being the measured and host galaxy flux density in Jy, respectively, and F_0 being the photometric zero point in Jy. F_{core} denotes the host galaxy corrected and de-reddened core flux density in Jy, where $A(\lambda)$ is the galactic absorption in mag. Combining Eqs. E.1 and E.2 yields:

$$F_{core}(\lambda) = 10^{0.4\ A(\lambda)} \ (F_m(\lambda) - F_h(\lambda)). \tag{E.3}$$

The galactic absorption at a given wavelength can be calculated from the selective extinction in the V band $E(B-V)$ multiplied by a wavelength-dependent extinction coefficient $R(\lambda)$ determined by reddening laws. In this case, the model of Fitzpatrick (1999) has been adopted using $R_V = 3.07$ (McCall & Armour 2000), which yields $R = 2.392$[1] for the KVA R-band (640 nm), 2.972 for the B-band (550 nm) and 3.998 in case of the V-band (440 nm). For 1ES 1011+496, $E(B-V) = 0.011$ (Schlafly & Finkbeiner 2011). According to Nilsson *et al.* (2007), the host galaxy flux density in the R-band amounts to (0.49 ± 0.02) mJy. Values in the V- and B-band have been determined to be (0.27 ± 0.04) mJy and (0.075 ± 0.054), respectively, using the same procedure as outlined in (Aleksić *et al.* 2012f).

Instrument	**Date**	**MJD**	$\boldsymbol{F_m}^{(a)}$ [mJy]	$\boldsymbol{F_{core}}^{(b)}$ [10^{-11} erg cm^{-2} s^{-1}]
KVA R-band	04/03/2008 20:23	54529.849	2.845 ± 0.055	1.130 ± 0.028
	09/03/2008 22:33	54534.939	3.018 ± 0.088	1.213 ± 0.043
	11/03/2008 21:56	54536.914	3.046 ± 0.058	1.227 ± 0.030
	13/03/2008 22:01	54538.917	3.137 ± 0.060	1.271 ± 0.030
	14/03/2008 22:09	54539.923	3.161 ± 0.069	1.282 ± 0.035
	15/03/2008 21:39	54540.902	3.334 ± 0.067	1.365 ± 0.034
	17/03/2008 21:13	54542.884	3.204 ± 0.064	1.303 ± 0.032
	18/03/2008 23:12	54543.967	3.207 ± 0.067	1.304 ± 0.034
	20/03/2008 00:09	54545.006	3.129 ± 0.063	1.266 ± 0.032
	21/03/2008 22:40	54546.945	2.890 ± 0.061	1.152 ± 0.031
	27/03/2008 22:48	54552.950	2.794 ± 0.056	1.106 ± 0.029
	28/03/2008 22:33	54553.940	2.835 ± 0.054	1.125 ± 0.028

continued on the following page

[1]Determined using the York Extinction Solver from the Canadian Astronomy Data Centre http://www3.cadc-ccda.hia-iha.nrc-cnrc.gc.ca/community/.

Table E.3: continued.

Instrument	**Date**	**MJD**	$\boldsymbol{F_m}^{(a)}$ [mJy]	$\boldsymbol{F_{core}}^{(b)}$ [10^{-11} erg cm^{-2} s^{-1}]
KVA R-band	29/03/2008 22:40	54554.945	2.806 ± 0.054	1.112 ± 0.028
	30/03/2008 23:00	54555.959	2.851 ± 0.055	1.133 ± 0.028
	31/03/2008 22:53	54556.954	2.859 ± 0.055	1.137 ± 0.028
	01/04/2008 22:34	54557.940	2.931 ± 0.056	1.171 ± 0.029
	03/04/2008 23:40	54559.986	2.977 ± 0.057	1.193 ± 0.029
	11/04/2008 23:32	54567.981	3.204 ± 0.064	1.303 ± 0.032
	13/04/2008 21:20	54569.889	3.380 ± 0.065	1.387 ± 0.033
	18/04/2008 21:57	54574.914	3.359 ± 0.061	1.377 ± 0.031
	20/04/2008 22:00	54576.917	3.258 ± 0.060	1.328 ± 0.030
	21/04/2008 21:22	54577.890	3.270 ± 0.063	1.334 ± 0.032
	22/04/2008 21:28	54578.895	3.279 ± 0.060	1.339 ± 0.030
	23/04/2008 21:28	54579.894	3.114 ± 0.060	1.259 ± 0.030
	24/04/2008 21:38	54580.902	3.252 ± 0.062	1.326 ± 0.031
	25/04/2008 22:35	54581.941	3.134 ± 0.063	1.269 ± 0.032
	26/04/2008 22:06	54582.921	3.106 ± 0.068	1.255 ± 0.034
	27/04/2008 21:52	54583.911	3.132 ± 0.060	1.268 ± 0.030
	28/04/2008 22:23	54584.933	3.207 ± 0.061	1.304 ± 0.031
	29/04/2008 22:36	54585.942	3.267 ± 0.063	1.333 ± 0.032
	30/04/2008 22:16	54586.928	3.402 ± 0.065	1.398 ± 0.033
	01/05/2008 21:51	54587.911	3.396 ± 0.065	1.395 ± 0.033
	03/05/2008 22:07	54589.922	3.279 ± 0.066	1.339 ± 0.033
	04/05/2008 22:20	54590.930	3.362 ± 0.061	1.378 ± 0.031
	05/05/2008 22:13	54591.926	3.421 ± 0.133	1.407 ± 0.065
	06/05/2008 21:34	54592.899	3.418 ± 0.062	1.405 ± 0.031
	09/05/2008 21:45	54595.906	3.556 ± 0.065	1.471 ± 0.033
	10/05/2008 21:28	54596.894	3.589 ± 0.066	1.487 ± 0.033
	11/05/2008 21:31	54597.896	3.642 ± 0.067	1.513 ± 0.033
	12/05/2008 21:16	54598.886	3.793 ± 0.073	1.585 ± 0.036
	13/05/2008 21:35	54599.899	3.986 ± 0.073	1.678 ± 0.036
	14/05/2008 21:39	54600.902	4.121 ± 0.079	1.742 ± 0.039
	17/05/2008 21:13	54603.884	3.950 ± 0.072	1.660 ± 0.036
	18/05/2008 21:25	54604.892	3.986 ± 0.076	1.678 ± 0.038
	19/05/2008 21:20	54605.889	3.935 ± 0.121	1.653 ± 0.059
	20/05/2008 21:17	54606.887	3.979 ± 0.073	1.674 ± 0.036
	21/05/2008 21:21	54607.889	4.147 ± 0.076	1.755 ± 0.038
	22/05/2008 21:18	54608.887	4.240 ± 0.074	1.800 ± 0.037
	24/05/2008 21:10	54610.882	4.049 ± 0.074	1.708 ± 0.037
	25/05/2008 21:08	54611.881	4.060 ± 0.074	1.713 ± 0.037
	27/05/2008 21:51	54613.910	4.090 ± 0.075	1.728 ± 0.037
	29/05/2008 21:03	54615.877	4.295 ± 0.094	1.826 ± 0.046
	02/06/2008 20:58	54619.874	4.303 ± 0.090	1.830 ± 0.044
	05/06/2008 20:59	54622.874	4.220 ± 0.092	1.790 ± 0.045
KVA V-band	22/04/2008 21:32	54578.897	2.813 ± 0.078	1.429 ± 0.048
	23/04/2008 21:31	54579.897	2.646 ± 0.073	1.335 ± 0.046
	24/04/2008 21:42	54580.904	2.826 ± 0.078	1.436 ± 0.048
	25/04/2008 22:16	54581.928	2.884 ± 0.079	1.468 ± 0.049
	26/04/2008 22:25	54582.934	2.748 ± 0.076	1.392 ± 0.047
	27/04/2008 22:11	54583.924	2.730 ± 0.075	1.382 ± 0.047
	28/04/2008 22:35	54584.941	2.754 ± 0.076	1.395 ± 0.047
	30/04/2008 22:30	54586.938	3.004 ± 0.074	1.536 ± 0.046
	01/05/2008 22:03	54587.919	2.853 ± 0.076	1.451 ± 0.047
	05/05/2008 22:25	54591.934	2.899 ± 0.077	1.477 ± 0.048

continued on the following page

Table E.3: continued.

Instrument	**Date**	**MJD**	$\boldsymbol{F_m}^{(a)}$ [mJy]	$\boldsymbol{F_{core}}^{(b)}$ [10^{-11} erg cm^{-2} s^{-1}]
KVA V-band	06/05/2008 22:37	54592.942	3.044 ± 0.073	1.558 ± 0.046
KVA B-band	22/04/2008 21:42	54578.904	2.343 ± 0.056	1.609 ± 0.055
	23/04/2008 21:45	54579.906	2.470 ± 0.074	1.699 ± 0.065
	24/04/2008 21:45	54580.907	2.389 ± 0.067	1.642 ± 0.061
	25/04/2008 21:56	54581.914	2.539 ± 0.094	1.748 ± 0.077
	26/04/2008 22:43	54582.946	2.465 ± 0.069	1.696 ± 0.062
	27/04/2008 22:29	54583.937	2.345 ± 0.070	1.611 ± 0.063
	28/04/2008 22:56	54584.956	2.447 ± 0.104	1.683 ± 0.083
	30/04/2008 22:46	54586.949	2.658 ± 0.061	1.833 ± 0.058
	01/05/2008 22:19	54587.930	2.470 ± 0.100	1.699 ± 0.081
	05/05/2008 22:40	54591.945	2.431 ± 0.164	1.672 ± 0.123
	06/05/2008 22:58	54592.957	2.745 ± 0.067	1.895 ± 0.061
Bell R-band	17/04/2008 04:00	54573.167	3.60 ± 0.05	...
	22/04/2008 04:22	54578.182	3.25 ± 0.04	...
	23/04/2008 04:32	54579.189	3.24 ± 0.03	...
	30/04/2008 05:04	54586.211	3.40 ± 0.02	...
	13/05/2008 03:39	54599.152	3.82 ± 0.03	...
	22/05/2008 03:17	54608.137	4.20 ± 0.03	...
	30/05/2008 02:21	54616.098	4.25 ± 0.03	...
	05/06/2008 02:30	54622.104	4.27 ± 0.18	...

Table E.3: Optical multi-band observations of 1ES 1011+496 during the MW campaign. Times are given in UTC.

Notes. $^{(a)}$ Measured flux density. $^{(b)}$ KVA-measured core flux density derived by subtracting the host galaxy, correcting for interstellar absorption and converting to the desired units.

E.1.2.2 Swift UVOT

Also the *Swift* UVOT data had to be converted to mJy as well as corrected for galactic absorption and host galaxy contribution. The standard formula for the conversion from mag to mJy for studying the flux density evolution is:

$$F(\lambda) = F_0(\lambda) \cdot 10^{-0.4\ F_m(\lambda)} \tag{E.4}$$

where $F(\lambda)$ is the flux density in mJy, λ the effective wavelength of the instrument, $F_0(\lambda)$ the photometric zero point of the instrument in mJy and $F_m(\lambda)$ the measured flux density in mag. $F_0(\lambda)$ was only available in mag, obtained for each UVOT band from Breeveld *et al.* (2011). Therefore, a different conversion formula had to be used, taking advantage of the count-rate-to-flux ratios (CRFs) included in the UVOT CALDB document 02[2]. The analysis has been conducted using version R03 (30 November 2010). These ratios have only been calculated for representative star and GRB spectra. Additionally, their validity is restricted to a certain B − V range which is smaller than determined from the observations of 1ES 1011+496 (see also Table E.5. Therefore, the applicability of these values for the current analysis is a priori questionable.

Considering these problems, (Raiteri *et al.* 2010) derived their own UVOT effective wavelengths and CRFs for their analysis of BL Lacertae (BL Lac), an LBL at a redshift $z = 0.069$. They reported differences to the GRB values of Poole *et al.* (2008) of $\lesssim 1\,\%$ for the V, B and U filters. For the UVW1, UVM2 and UVW2 filters, on the other hand, the effective wavelengths (CRFs) were larger by $\sim 5.4\,\%$ ($\sim 7.8\,\%$), $\sim 2.9\,\%$ ($\sim 0.5\,\%$) and $\sim 9.6\,\%$ ($\sim 8.4\,\%$), respectively. However, the present analysis makes use of more recent UVOT calibration values (see above). Comparing the results found by Raiteri *et al.* (2010) with these, the corresponding differences amount to $\sim 7.1\,\%$ ($\sim 2.4\,\%$), $\sim 3.0\,\%$ ($\sim 1.1\,\%$) and $\sim 9.4\,\%$ ($\sim 12.5\,\%$). Obviously, the updated UVOT CALDB CRF for the UVW1 filter is matching the value for BL Lac much better, whereas the difference in the UVW2 filter is increasing to nearly 13 %.

All of the intrinsic errors of the effective wavelengths (see also Table E.4) are larger than the differences resulting from the new calibration on BL Lac. Concerning the CRFs, the change is considerable only for the UVW2 band. Therefore, the intrinsic error of the ratio of $\sim 2.2\,\%$ has been artificially increased to 13 %, which has already been applied for the values listed in Table E.6. A large fraction of the increase in CRFs is arising solely from the increase in effective wavelengths (causing in this case a decrease in effective area), which have not been changed for this analysis. The actual changes in CRF are hence much lower, and the procedure applied here represents a conservative estimate. Despite the rather large increase of the CRF error for the UVW2 filter, the relative error of the de-reddened fluxes increases from $\sim 15\,\%$ to $\sim 20\,\%$ only. Considering that, no changes seem necessary for the other filters, so the values from the UVOT CALDB have been adopted unchanged.

With these ratios, the conversion formula becomes:

$$F(\lambda) = 10^{0.4(F_0(\lambda) - F_m(\lambda))} \cdot ratio \cdot \lambda \cdot \frac{10^{26}\ \lambda\ 10^{10}}{c} \tag{E.5}$$

[2]http://swift.gsfc.nasa.gov/docs/heasarc/caldb/swift/docs/uvot/

UVOT Filter	$\boldsymbol{\lambda}^{(a)}$ [Å]	$\boldsymbol{F_0}^{(b)}$ [mag]	$\boldsymbol{F_h}^{(c)}$ [mJy]	$\boldsymbol{ratio}^{(d)}$ [$10^{-16}\,\mathrm{erg\,cm^{-2}\,s^{-1}\,Å^{-1}}$]	$\boldsymbol{A}^{(e)}$ [mag]
V	5402 ± 327	17.89	0.27 ± 0.04	2.613 ± 0.009	0.034
B	4329 ± 414	19.11	0.075 ± 0.054	1.471 ± 0.006	0.045
U	3501 ± 333	18.34	0.02 ± 0.12	1.628 ± 0.025	0.053
UVW1	2591 ± 294	17.44	...	4.21 ± 0.13	0.073
UVM2	2229 ± 211	16.85	...	8.446 ± 0.053	0.102
UVW2	2033 ± 279	17.38	...	5.98 ± 0.78	0.097

Notes. [(a)] Effective wavelength, taken from the UVOT CALDB 02 version R03. The errors have been calculated from the FWHM of the corresponding filter as given in Poole *et al.* (2008). [(b)] Photometric zero points from Breeveld *et al.* (2011). [(c)] Host galaxy flux density of 1ES 1011+496, see (Aleksić *et al.* 2012f). [(d)] count-rate-to-flux ratios for GRBs, taken from the UVOT CALDB 02 version R03. [(e)] Galactic absorption for 1ES 1011+96, calculated as described above for KVA.

Table E.4: Parameters used for the *Swift* UVOT analysis of 1ES 1011+496. For the UV filters, no host galaxy contribution was assumed, see text. The error of the count-rate-to-flux ratio of the UVW2 filter has been increased artificially from $0.13 \cdot 10^{-16}\,\mathrm{erg\,cm^{-2}\,s^{-1}\,Å^{-1}}$ ($\sim 2.2\,\%$) to 13 %, see text for details.

with *ratio* given in units of $\mathrm{erg\,cm^{-2}\,s^{-1}\,Å^{-1}}$ because of which the last factor as a conversion to mJy has to be added.

Using the same procedure to convert the measured magnitudes for the SED and adding the host galaxy correction and de-reddening, the formula is given as:

$$F_{core}\,(\lambda) = 10^{0.4(F_0(\lambda) - F_{hcor}(\lambda) - A(\lambda))} \cdot ratio \cdot \lambda, \tag{E.6}$$

where $F_{core}\,(\lambda)$ is in units of $\mathrm{erg\,cm^{-2}\,s^{-1}}$, $F_{hcor}\,(\lambda)$ is obtained by Eq. E.1 and the galactic absorption $A\,(\lambda)$ is calculated as described above for KVA. The host galaxy contribution in the U-band, amounting to 0.02 ± 0.12 mJy, is already very small and insignificant. For the three UV filters, the value would be even smaller and less reliable, making a host galaxy correction in these bands hardly feasible and unessential (E. Lindfors, 2012, private communication). Therefore, no correction has been performed for the UV bands. The values used for the flux density calculation and conversions are summarised in Table E.4, the results for the different UVOT filters are given in Tables E.5 and E.6.

E.1.2.3 Archival MDM Data

From monitoring 1ES 1011+496 over several years with the Michigan-Dartmouth-MIT (MDM) observatory, Böttcher *et al.* (2010) derived several simultaneous multi-band spectra in the optical regime. The authors corrected for the effect of dust absorption, but did not correct their data for the host galaxy flux. Photometric zero points for the MDM observatory could be found in literature, hence an exact calculation of the corrected flux was not possible. Instead, the amount of necessary correction was estimated from KVA multi-band data with a similarly low flux density (MJD 54583.9). The MDM fluxes were multiplied by the ratio of host-corrected+de-reddened KVA flux and the de-reddened KVA flux in νF_ν, yielding for the MDM R-, V- and B-band a factor of 0.84, 0.90 and 0.97, respectively. Note that the central frequencies of KVA and MDM match very well. The error bars have not been changed, considering that the uncertainty in host galaxy

Obs. ID[(a)]	$F_{\mathbf{V}}$		$F_{\mathbf{B}}$		$F_{\mathbf{U}}$	
	[mag]	$[10^{-11}\,\mathrm{erg\,cm^{-2}\,s^{-1}}]$	[mag]	$[10^{-11}\,\mathrm{erg\,cm^{-2}\,s^{-1}}]$	[mag]	$[10^{-11}\,\mathrm{erg\,cm^{-2}\,s^{-1}}]$
35012008	15.31 ± 0.10	1.41 ± 0.26	15.60 ± 0.07	1.55 ± 0.36	14.63 ± 0.07	1.44 ± 0.34
35012009	...[(b)]	...[(b)]	...[(b)]	...[(b)]	14.59 ± 0.10	1.50 ± 0.36
35012010	...[(b)]	...[(b)]	...[(b)]	...[(b)]	...[(b)]	...[(b)]
35012011	15.27 ± 0.07	1.47 ± 0.24	15.54 ± 0.05	1.64 ± 0.37	14.60 ± 0.05	1.48 ± 0.34
35012012	15.31 ± 0.07	1.41 ± 0.23	15.56 ± 0.05	1.61 ± 0.37	14.57 ± 0.05	1.52 ± 0.35
35012014	15.15 ± 0.07	1.66 ± 0.27	15.56 ± 0.05	1.61 ± 0.37	14.54 ± 0.05	1.57 ± 0.36
35012013	15.25 ± 0.07	1.50 ± 0.25	15.50 ± 0.05	1.70 ± 0.39	14.54 ± 0.05	1.57 ± 0.36
35012015	15.27 ± 0.07	1.47 ± 0.24	15.54 ± 0.05	1.64 ± 0.37	14.48 ± 0.05	1.66 ± 0.38
35012016	15.26 ± 0.07	1.49 ± 0.24	15.56 ± 0.05	1.61 ± 0.37	14.54 ± 0.05	1.57 ± 0.36
35012017	15.27 ± 0.07	1.47 ± 0.24	15.48 ± 0.05	1.74 ± 0.39	14.55 ± 0.05	1.55 ± 0.36

Notes. [(a)] *Swift* observation ID (see also Note (*h*) of Table E.1). [(b)] Observation time too short for deriving results.

Table E.5: Results of the *Swift* UVOT observations of 1ES 1011+496 in the V-, B- and U-band during the MW campaign. The values in [mag] are in contrast to the ones in $[10^{-11}\,\mathrm{erg\,cm^{-2}\,s^{-1}}]$ not host-galaxy corrected or de-reddened.

Obs. ID[a]	F_{UVW1}		F_{UVM2}		F_{UVW2}	
	[mag]	[10^{-11} erg cm^{-2} s^{-1}]	[mag]	[10^{-11} erg cm^{-2} s^{-1}]	[mag]	[10^{-11} erg cm^{-2} s^{-1}]
35012008	14.46 ± 0.05	1.81 ± 0.24	14.28 ± 0.05	2.21 ± 0.24	14.37 ± 0.05	2.13 ± 0.42
35012009	14.31 ± 0.05	2.08 ± 0.27	...[b]	...[b]	...[b]	...[b]
35012010	...[b]	...[b]	...[b]	...[b]	...[b]	...[b]
35012011	14.35 ± 0.05	2.01 ± 0.26	14.18 ± 0.05	2.42 ± 0.26	14.26 ± 0.05	2.35 ± 0.46
35012012	14.41 ± 0.05	1.90 ± 0.25	14.31 ± 0.05	2.15 ± 0.23	14.30 ± 0.05	2.27 ± 0.45
35012014	14.39 ± 0.05	1.94 ± 0.25	14.04 ± 0.05	2.75 ± 0.30	14.32 ± 0.05	2.23 ± 0.44
35012013	14.35 ± 0.05	2.01 ± 0.26	14.20 ± 0.05	2.38 ± 0.26	14.26 ± 0.05	2.35 ± 0.46
35012015	14.32 ± 0.05	2.06 ± 0.27	14.14 ± 0.05	2.51 ± 0.27	14.22 ± 0.05	2.44 ± 0.48
35012016	14.32 ± 0.05	2.06 ± 0.27	14.15 ± 0.05	2.49 ± 0.27	14.21 ± 0.05	2.46 ± 0.48
35012017	14.37 ± 0.05	1.97 ± 0.26	14.17 ± 0.05	2.44 ± 0.27	14.25 ± 0.05	2.37 ± 0.47

Notes. [a] *Swift* observation ID (see also Note (*h*) of Table E.1). [b] Observation time too short for deriving results.

Table E.6: Results of the *Swift* UVOT observations of 1ES 1011+496 in the UV filters during the MW campaign. The values in [mag] are in contrast to the values in [10^{-11} erg cm^{-2} s^{-1}] not de-reddened. Note that the errors of the UVW2 data have been increased artificially (see text).

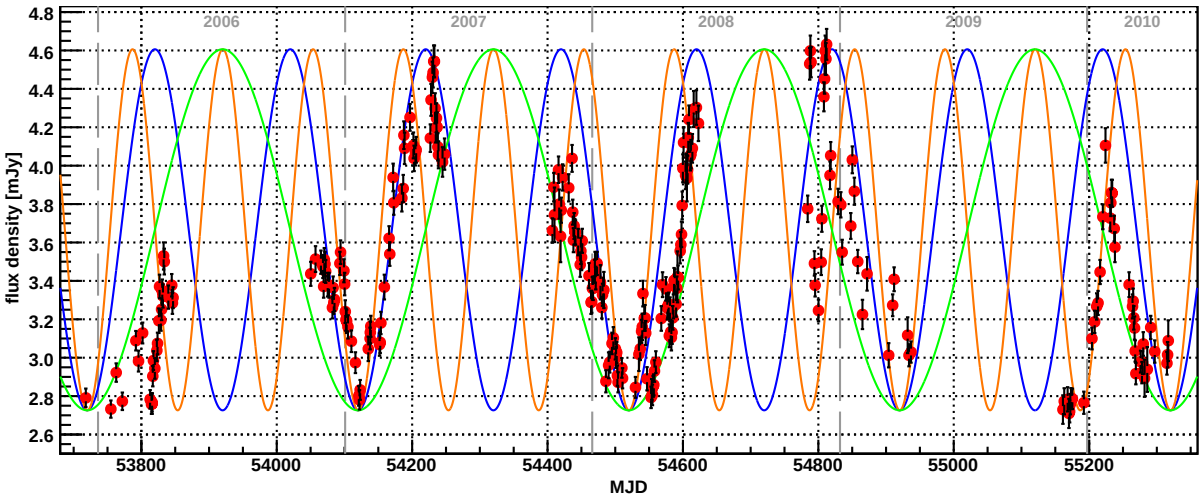

Figure E.1: Long-term high state excerpt of Figure 5.25. Sinusoidal functions are shown in green, blue and orange. They have been manually adapted to match the low flux densities around MJD 54120 and MJD 54520 within 1, 2 or 3 periods. Neither of them can describe the data sufficiently.

flux introduces an additional error, which is partly compensating the smaller absolute error caused by the reduced flux after correction.

The data is used to estimate a low state broad-band SED from strictly archival data, hence the accuracy of this estimation is more than sufficient compared to the error introduced by the assumption that the lowest X-ray flux point and spectral shape during a higher flux state is representative for a low state.

E.1.3 Correlations between Different Instruments

E.1.4 Literature Data not Considered

The data and SED model results for 1ES 1011+496 is rather sparse in literature. Nevertheless the following results have not been adopted in this work.

- Archival data given in Fossati *et al.* (1998) are not included in the SED of 1ES 1011+496 (Figure 5.30). The authors averaged for each chosen frequency from the radio to the optical regime the data available in literature at that time, hence the corresponding data points would not represent real measurements of the source. The optical data have not been corrected for the host-galaxy flux. Additionally, it is not clear from the paper which and how many data sets have been averaged, and from where the data has been obtained. For the purpose of Fossati *et al.* (1998) this procedure seems justified, but for reporting exact archival measurements such results are not suited.

- The data and SED models presented in Costamante & Ghisellini (2002) are not used because part of the data is based on Fossati *et al.* (1998). If archival data was found that is not given at the chosen monochromatic frequencies, these have been extrapolated, introducing an unknown uncertainty (errors are not given). Additionally, a host-galaxy correction in the optical has not been applied. Since

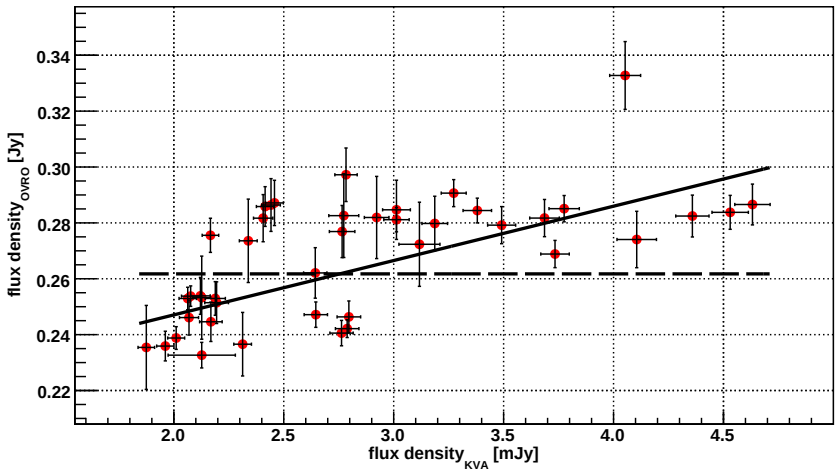

Figure E.2: The flux density at 15.0 GHz measured by OVRO from 1ES 1011+496 as a function of the KVA R-band flux density. Shown are data pairs from the time range displayed in Figure 5.28 with a time difference < 0.9 days. OVRO data with an error $\gtrsim 0.02$ Jy have not been used. The dashed line represents a fit with a constant (χ^2/d.o.f. = 469.9/42), the solid line gives a linear fit (χ^2/d.o.f. = 252.9/41 with a slope of $(1.95 \pm 0.13) \cdot 10^{-2}$ Jy per mJy).

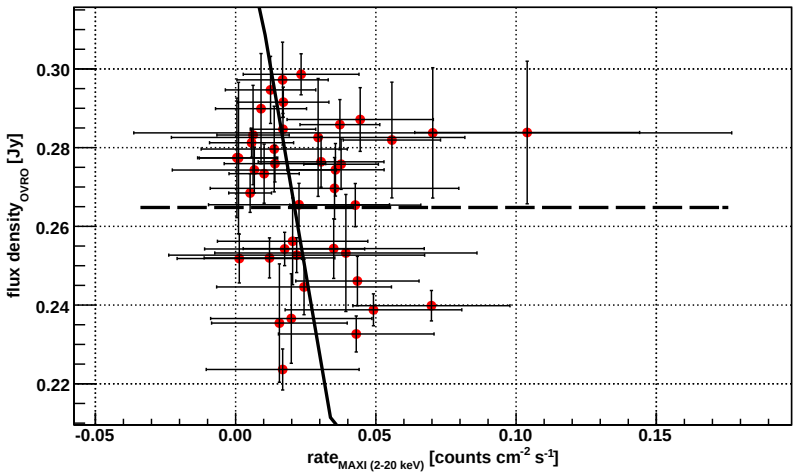

Figure E.3: The flux density at 15.0 GHz measured by OVRO from 1ES 1011+496 as a function of the MAXI count rate between 2 and 20 keV. Shown are data pairs from the time range displayed in Figure 5.28 with a time difference < 0.9 days. OVRO data with an error $\gtrsim 0.02$ Jy have not been used, same as MAXI data with a rate < 0. The dashed line represents a fit with a constant (χ^2/d.o.f. = 459.7/41), the solid line gives a linear fit (χ^2/d.o.f. = 32.4/40 with a slope of $-(4.2 \pm 3.9)$ Jy per counts cm^{-2} s^{-1}).

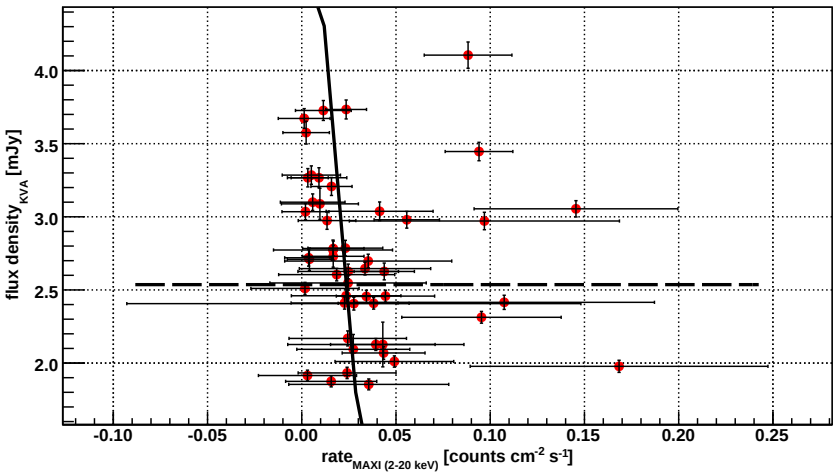

Figure E.4: The flux density in the R-band measured by KVA from 1ES 1011+496 as a function of the MAXI count rate between 2 and 20 keV. Shown are data pairs from the time range displayed in Figure 5.28 with a time difference < 0.9 days. MAXI data with a rate < 0 are not shown. The dashed line represents a fit with a constant (χ^2/d.o.f. = 4681.1/49), the solid line gives a linear fit (χ^2/d.o.f. = 68.8/48 with a slope of $-(1.5 \pm 1.2) \cdot 10^2$ mJy per counts cm^{-2} s^{-1}).

sufficient data at the considered frequencies is available today, these data have not been used in this work.

- The ROSAT data and bow tie are taken from the original publication (Lamer *et al.* 1996) instead of Fossati *et al.* (1998). Presumably due to the averaging of several measurements, Fossati *et al.* (1998) adopted a different flux at 1 keV than given in Lamer *et al.* (1996), which seemingly was subsequently used by Costamante & Ghisellini (2002), Albert *et al.* (2007b) and Tavecchio *et al.* (2010). However, the difference is marginal ($F_{1\mathrm{keV}_{\mathrm{orig}}} = 2.15\,\mu$Jy, $F_{1\mathrm{keV}_{\mathrm{Fosatti}}} = 2.351\,\mu$Jy).

- The VHE flux of 1ES 1011+496 estimated from a tentative MAGIC detection from observations in 2006 (Albert *et al.* 2008c) turned out to be much lower applying an updated analysis software (Meyer 2008), see also Section 5.3.4.

- Tavecchio *et al.* (2010) analysed the same *Swift* XRT data as presented in this work (8 May 2008), albeit reporting a ~ 20 times higher flux. Though this analysis differed in the investigated XRT energy range (0.3 – 10 keV vs. 0.5 – 10 keV in this work), applied power-law model (broken power law vs. simple power law) and did not consider galactic absorption, these points can not account for a difference that large. Note that Abdo *et al.* (2010b) also analysed that XRT data, the resulting X-ray flux being compatible with what is shown in the present work. Since the SED modelling in Tavecchio *et al.* (2010) relied also in this data, neither the corresponding X-ray spectrum nor the resulting SED parameters are considered for this work. Same applies to the results of 1ES 1011+496 presented in Zhang *et al.* (2012) which are based on the data shown in Tavecchio *et al.* (2010).

E.2 1ES 2344+514 (Campaign)

E.2.1 Fermi-LAT

Energy Range [MeV]	$\boldsymbol{F}$ [ph cm^{-2} s^{-1}]	$\boldsymbol{\nu F_\nu}$ [erg cm^{-2} s^{-1}]
100 – 300	$3.0 \cdot 10^{-8}$	$7.5 \cdot 10^{-12}$
300 – 1000	$6.7 \cdot 10^{-9}$	$4.8 \cdot 10^{-12}$
1000 – 3000	$2.7 \cdot 10^{-9}$	$6.8 \cdot 10^{-12}$
3000 – 10000	$8.8 \cdot 10^{-10}$	$6.3 \cdot 10^{-12}$
10000 – 100000	$8.6 \cdot 10^{-10}$	$1.6 \cdot 11^{-11}$

Table E.7: 95 % c.l. ULs derived from the *Fermi*-LAT observations of 1ES 2344+514. The ULs on the photon flux have been converted to spectral flux density values assuming a spectral index of 2.1. The latter are given at the lower energy border of the energy bin.

E.2.2 Swift

E.2.2.1 Swift Observations and XRT Results

Obs. ID[(a)]	**Obs. Start**[(b)]	**Obs. End**[(c)]	$\mathbf{MJD_{mean}}$[(d)]	$t_{\mathbf{XRT}}$[(e)] [ks]	$t_{\mathbf{UVOT}}$[(f)] [ks]	$t_{\mathbf{BAT}}$[(g)] [ks]
35031019	21/09/2008 03:48:02	07:08:59	54730.228	0.59	0.89	1.02
35031020	26/09/2008[(h)]	...	...	0	0	0
35031021	06/10/2008 13:17:02	19:49:56	54745.690	1.75	1.63	1.83
35031022	10/10/2008 12:19:02	12:37:58	54749.519	0.94	0.88	0.96
35031023	18/10/2008 18:17:02	23:14:56	54757.865	1.23	1.14	1.31
35031024	20/10/2008 21:29:02	23:29:01	54759.937	2.23	2.18	2.26
35031025	21/10/2008 21:34:02	23:35:00	54760.941	2.31	2.26	2.35
35031026	22/10/2008 21:41:02	23:41:00	54761.945	2.27	2.23	2.31
35031027	23/10/2008 21:48:28	23:46:59	54762.949	2.42	2.38	2.46
35031028	24/10/2008 04:00:02	23:52:59	54763.581	4.91	4.83	4.16
35031029	25/10/2008 20:34:07	23:54:58	54764.926	1.58	1.52	1.54
35031030	26/10/2008 22:00:01	00:01:58	54765.959	2.53	2.48	2.57
35031031	27/10/2008 20:46:00	00:00:05	54766.933	1.19	1.15	1.23
35031032	28/10/2008 20:51:02	00:00:01	54767.934	2.75	2.68	2.81
35031033	29/10/2008 19:21:02	22:45:00	54768.877	2.29	1.25	1.80
35031034	30/10/2008 22:22:02	23:59:59	54769.966	1.87	1.82	1.90
35031035	31/10/2008 21:09:02	22:54:59	54770.918	2.10	2.05	2.14
35031036	01/11/2008 22:24:02	22:54:00	54771.944	1.65	1.63	1.67
35031037	02/11/2008 21:25:53	21:29:57	54772.894	0.19	0.18	0.09
35031038	03/11/2008 21:25:02	22:59:59	54773.925	0.94	0.91	0.97
35031039	07/11/2008 11:36:02	13:26:59	54777.522	1.59	1.54	1.63
35031040	14/11/2008 14:13:02	14:32:00	54784.599	1.06	1.03	1.07

Notes. [(a)] *Swift* observation ID. [(b)] Start time of observation in UTC. [(c)] End time of observation in UTC. The observations ended the same day they began but for the IDs 35031030, 35031031 and 35031032, where the observations were stopped the following day. [(d)] Mean MJD of the observation. [(e)] Exposure of XRT. [(f)] Total exposure of all UVOT filters. [(g)] Exposure of BAT. [(h)] No observations conducted.

Table E.8: *Swift* observation log of 1ES 2344+514 during the MW campaign. Note that *Swift* is performing several pointings per observation ID, the given start and end times of the observations are the total ones for the whole ID though. For a more detailed list, see http://www.swift.psu.edu/operations/obsSchedule.php.

E.2.2.2 Re-Binning and Analysis of the BAT Data

Due to the small statistics of the orbital light curve from the BAT 58-Month Catalog, the data have been re-binned to various time scales to search for potential significant variability of 1ES 2344+514: one day, one week (= 7 days), one month (= 30.44 days), one quarter (= 91.31 days) and one year (= 365.24 days). This has been accomplished using the REBINGAUSSLC tool from the HEASOFT software package version 6.11.1 distributed by NASA's HEASARC[3]. The tool is recommended especially for irregularly sampled light curves like obtained from BAT or *RXTE* ASM. No change in the default settings

[3]http://heasarc.nasa.gov/lheasoft/

Obs. ID[a]	Simple Power Law Fit			Log-Parabolic Power Law Fit						Hardness Ratio[g]
	$F(2-10\,\mathrm{keV})$[b] [$10^{-12}\,\mathrm{erg\,cm^{-2}\,s^{-1}}$]	a[c]	χ^2_{red}/d.o.f.	$F(0.2-1\,\mathrm{keV})$[d] [$10^{-12}\,\mathrm{erg\,cm^{-2}\,s^{-1}}$]	$F(2-10\,\mathrm{keV})$[d] [$10^{-12}\,\mathrm{erg\,cm^{-2}\,s^{-1}}$]	a[e]	b[e]	χ^2_{red}/d.o.f.	L[f] [%]	
35031019	...[h]	...[h]	...[h]	...[h]	...[h]	...[h]	...[h]	...[h]	...[h]	...[h]
35031020	...[h]	...[h]	...[h]	...[h]	...[h]	...[h]	...[h]	...[h]	...[h]	...[h]
35031021	10.8 ± 0.9	2.03 ± 0.11	0.77/17	2.50 ± 0.30	9.2 ± 0.8	1.79 ± 0.25	0.51 ± 0.30	0.61/18	85.1	1.17 ± 0.12
35031022	9.8 ± 1.4	2.12 ± 0.23	0.79/7	3.05 ± 0.50	9.8 ± 1.5	2.12 ± 0.35	0.00 ± 0.00	0.93/6	0.0	0.80 ± 0.12
35031023	9.5 ± 1.1	2.14 ± 0.18	1.55/13	3.09 ± 0.50	9.5 ± 1.4	2.14 ± 0.30	0.00 ± 0.00	1.68/12	0.0	0.95 ± 0.13
35031024	14.2 ± 0.9	1.94 ± 0.09	1.10/30	2.90 ± 0.25	13.0 ± 0.8	1.80 ± 0.18	0.27 ± 0.25	1.07/29	82.9	1.21 ± 0.10
35031025	14.4 ± 0.8	1.98 ± 0.08	1.04/42	3.16 ± 0.22	13.0 ± 0.9	1.80 ± 0.16	0.36 ± 0.26	0.95/41	96.0	1.17 ± 0.09
35031026	13.4 ± 0.7	1.97 ± 0.08	1.32/32	2.91 ± 0.23	12.3 ± 0.9	1.84 ± 0.17	0.26 ± 0.25	1.29/31	85.6	1.22 ± 0.10
35031027	10.9 ± 0.6	2.02 ± 0.09	1.12/28	1.67 ± 0.22	10.3 ± 0.8	1.94 ± 0.16	0.17 ± 0.17	1.12/27	69.9	1.06 ± 0.09
35031028	10.5 ± 0.6	2.03 ± 0.06	1.20/48	2.61 ± 0.17	9.7 ± 0.6	1.92 ± 0.12	0.25 ± 0.21	1.15/47	93.0	1.07 ± 0.07
35031029	10.0 ± 0.8	2.09 ± 0.12	0.97/17	2.64 ± 0.30	9.0 ± 1.0	1.92 ± 0.27	0.35 ± 0.34	0.93/16	78.5	1.09 ± 0.12
35031030	9.6 ± 0.7	2.01 ± 0.08	1.36/26	2.11 ± 0.23	8.4 ± 0.8	1.75 ± 0.19	0.51 ± 0.30	1.07/25	98.6	1.13 ± 0.10
35031031	8.1 ± 1.1	2.10 ± 0.20	0.88/8	2.25 ± 0.50	7.2 ± 1.2	1.99 ± 0.40	0.26 ± 0.26	0.99/7	24.9	0.86 ± 0.13
35031032	8.0 ± 0.6	2.15 ± 0.10	0.76/26	2.58 ± 0.25	8.0 ± 0.9	2.14 ± 0.13	0.00 ± 0.00	0.79/25	6.9	0.87 ± 0.08
35031033	7.9 ± 0.5	2.04 ± 0.11	0.99/18	1.82 ± 0.20	6.9 ± 0.8	1.78 ± 0.26	0.51 ± 0.42	0.84/17	92.9	1.13 ± 0.12
35031034	11.5 ± 0.7	1.96 ± 0.10	1.09/20	2.44 ± 0.25	10.7 ± 0.9	1.83 ± 0.22	0.25 ± 0.25	1.07/19	76.4	1.21 ± 0.12
35031035	9.6 ± 0.7	2.06 ± 0.11	0.58/21	2.60 ± 0.25	9.3 ± 1.0	2.02 ± 0.20	0.00 ± 0.00	0.60/20	31.8	1.01 ± 0.10
35031036	9.9 ± 0.8	1.99 ± 0.11	1.36/15	1.93 ± 0.22	8.6 ± 0.9	1.58 ± 0.32	0.73 ± 0.50	1.01/14	97.7	1.23 ± 0.14
35031037	...[h]	...[h]	...[h]	...[h]	...[h]	...[h]	...[h]	...[h]	...[h]	...[h]
35031038	13.2 ± 1.7	1.86 ± 0.22	0.30/7	2.43 ± 0.50	12.4 ± 2.0	1.80 ± 0.50	0.14 ± 0.14	0.35/6	0.0	1.17 ± 0.18
35031039	10.7 ± 0.7	2.16 ± 0.12	1.36/22	3.55 ± 0.30	10.6 ± 1.2	2.15 ± 0.25	0.00 ± 0.00	1.43/19	89.2	0.99 ± 0.10
35031040	16.6 ± 1.7	1.76 ± 0.13	0.32/13	2.48 ± 0.30	15.9 ± 1.9	1.69 ± 0.30	0.13 ± 0.13	0.33/12	33.5	1.47 ± 0.18

Notes. [a] *Swift* observation ID. [b] Integral flux between 2 and 10 keV determined by a simple power law fit from 0.3 – 10 keV. [c] Spectral index determined by a simple power law fit from 0.3 – 10 keV. [d] Integral flux determined by a log parabolic power law fit from 0.3 – 10 keV. [e] Spectral indices determined from a log parabola fit from 0.3 – 10 keV. [f] Probability that the log parabolic power law fit is preferred over the simple power law fit by means of a likelihood ratio test. [g] Hardness ratio is defined here as $\mathrm{counts}_{(2-10\,\mathrm{keV})}/\mathrm{counts}_{(0.2-1\,\mathrm{keV})}$. [h] Observation time too short for extracting results.

Table E.9: Results of *Swift* XRT observations of 1ES 2344+514 during the MW campaign. Both the results from the simple absorbed power law fit as well as the absorbed log-parabolic fit are shown. The likelihood test prefers in most cases the simple power law.

of the tool have been made, i.e. no trials in the selection of the starting point of the bins have to be considered. This re-binning has been conducted for each of the eight BAT energy bands (14 – 20 keV, 20 – 24 keV, 24 – 35 keV, 35 – 50 keV, 50 – 75 keV, 75 – 100 keV, 100 – 150 keV and 150 – 195 keV) as well as the whole energy range (14 – 195 keV).

The such obtained light curves have been investigated for potential variability by eye as well as their rate/error distributions. One point with a high rate/error value of 4.9 was found in the weekly binned data from the whole energy range (around MJD 54772.5), which was statistically significantly off the Gaussian rate/error distribution (see Figure 6.41). To exclude systematic effects to be responsible for that signal, a cross check on data of the rather nearby and constant source Cas A has been performed. Comparing the weekly binned light curves of 1ES 2344+514 and Cas A, some outliers are apparent in both of them, indicating that these are due to systematic or instrumental effects. At the time of the putative BAT high state of 1ES 2344+514, the Cas A light curve was constant without a sign of systematic influences.

From that weekly high flux point as well as all data from the 58-Month Catalog, a spectral flux density spectrum has been obtained, following the procedure described in Tueller *et al.* (2010). As the systematic uncertainties in the BAT response matrix are larger than the ones of the Crab Nebula spectrum, spectra are derived on basis of the Crab Nebula spectrum. The Crab Nebula flux in each of the eight BAT energy bands is given as the integral over the Crab Nebula spectrum:

$$F_{Crab} = \int_a^b E\ F\,(E)\ \mathrm{d}E \tag{E.7}$$

with a and b being the lower and upper energy border of the bin. The Crab Nebula spectrum $F\,(E)$ is given as

$$F\,(E) = 10.17\ E^{-2.15}\,\mathrm{ph\,cm^{-2}\,s^{-1}\,keV^{-1}} \tag{E.8}$$

(see Tueller *et al.* 2010).

From the integration over the total bandwidth of 14 – 195 keV, a total Crab Nebula flux of $2.39{\cdot}10^{-8}\,\mathrm{erg\,cm^{-2}\,s^{-1}}$ has been obtained for the 22 month data, slightly lower than the value of $2.44{\cdot}10^{-8}\,\mathrm{erg\,cm^{-2}\,s^{-1}}$ given in Tueller *et al.* (2010). Though the difference is only $\sim 2\,\%$, a correct Crab Nebula flux, being the basis of the further analysis, is critical for deriving the spectrum of 1ES 2344+514. According to W. Baumgartner (2012, private communication), the reason for the difference is a wrong value given in Tueller *et al.* (2010) and the calculations presented here are correct.

The integral source flux in each of the eight BAT energy bands was then calculated as the such derived Crab Nebula flux weighted with the relative count rate of the source and the Crab Nebula. For the conversion to spectral energy density units at energy E, consider

$$EF_E = E^2 F\,(E) = E^2 f_0 \left(\frac{E}{E_0}\right)^{-\alpha} \tag{E.9}$$

where E_0 is the energy normalisation and α the spectral index. The flux normalisation

f_0 at E_0 can be obtained from the integral flux F_{int} as

$$\begin{aligned} F_{int} &= \int_a^b f_0 E \left(\frac{E}{E_0}\right)^{-\alpha} \mathrm{d}E \\ &= \frac{f_0}{E_0^{-\alpha}} \int_a^b E^{1-\alpha} \mathrm{d}E \\ &= \frac{f_0}{E_0^{-\alpha}} \left[\frac{E^{2-\alpha}}{2-\alpha}\right]_a^b \\ f_0 &= F_{int} \frac{E_0^{-\alpha}\,(2-\alpha)}{b^{2-\alpha} - a^{2-\alpha}} \end{aligned} \tag{E.10}$$

Inserting that in Eq. E.9 and using $E = E_0$:

$$E F_E = F_{int} \frac{E_0^{2-\alpha}\,(2-\alpha)}{b^{2-\alpha} - a^{2-\alpha}} \tag{E.11}$$

The value for the spectral index has been adopted from the BAT catalogue as $\alpha = 2.62$, and E_0 has been chosen to be at the Lafferty-Wyatt position of the corresponding BAT energy bin. The such obtained spectra are shown in Figs. 6.33 and 6.45.

E.2.3 Corrections, Conversions and Results for the Optical Regime

R-band The R-band data has been corrected and converted as described in Section E.1.2 using $E\,(B-V) = 0.191$ (Schlafly & Finkbeiner 2011) for 1ES 2344+514. The host galaxy flux density of (3.70 ± 0.05) mJy has been taken from Nilsson *et al.* (2007) as described in Aleksić *et al.* (2012f).

***Swift* UVOT** The UVOT data of 1ES 2344+514 are processed as described for 1ES 1011+496 (see Section E.1.2). Also for 1ES 2344+514, the B – V range is larger than the applicable range for the count-rate-to-flux ratios so that the relative error of the UVW2 filter has been increased to 13 %. A special treatment is not necessary though for 1ES 2344+514, considering that the relative error of the de-reddened fluxes increased in this band from $\sim 18\,\%$ to $\sim 22\,\%$. No changes have been applied to the remaining bands.

For the three UV filters, the host galaxy contribution is very small (Tramacere *et al.* 2007) and therefore no corresponding correction has been performed. The values used for the flux density calculation and conversions are summarised in Table E.11, the results for the different UVOT filters are given in Tables E.12 and E.13.

Instrument	Date	MJD	F_m [a] [mJy]	F_{core} [b] [10^{-12} erg cm^{-2} s^{-1}]	F_{scaled} [c] [mJy]
KVA	13/09/2008 21:13	54722.884	4.186 ± 0.073	3.46 ± 0.63	...
	21/09/2008 20:32	54730.856	4.248 ± 0.070	3.91 ± 0.61	...
	23/09/2008 20:35	54732.858	4.279 ± 0.070	4.13 ± 0.62	...
	13/10/2008 20:54	54752.871	4.166 ± 0.076	3.33 ± 0.65	...
	14/10/2008 21:49	54753.909	4.117 ± 0.071	2.97 ± 0.62	...
	16/10/2008 21:05	54755.879	4.151 ± 0.072	3.22 ± 0.63	...
	22/10/2008 17:14	54761.718	4.220 ± 0.069	3.71 ± 0.61	...
	04/11/2008 20:42	54774.863	4.121 ± 0.083	3.00 ± 0.69	...
	14/11/2008 20:37	54784.859	4.217 ± 0.077	3.69 ± 0.66	...
	15/11/2008 20:04	**54785.836**	4.147 ± 0.072	3.19 ± 0.63	...
	16/11/2008 20:12	54786.842	4.201 ± 0.069	3.58 ± 0.61	...
	17/11/2008 20:15	54787.844	4.159 ± 0.068	3.27 ± 0.61	...
	18/11/2008 20:06	54788.837	4.163 ± 0.068	3.30 ± 0.61	...
	19/11/2008 20:12	54789.842	4.121 ± 0.068	3.00 ± 0.60	...
	23/11/2008 20:27	54793.852	4.178 ± 0.073	3.41 ± 0.63	...
	24/11/2008 20:47	54794.866	4.220 ± 0.073	3.71 ± 0.63	...
	28/11/2008 21:22	54798.891	4.240 ± 0.074	3.85 ± 0.64	...
	29/11/2008 20:48	54799.866	4.151 ± 0.072	3.22 ± 0.63	...
	30/11/2008 20:45	54800.865	4.228 ± 0.085	3.77 ± 0.70	...
	05/12/2008 20:14	**54805.843**	4.228 ± 0.073	3.77 ± 0.63	...
	08/12/2008 20:29	54808.854	4.252 ± 0.081	3.94 ± 0.68	...
	10/12/2008 20:16	54810.844	4.220 ± 0.077	3.71 ± 0.66	...
	20/12/2008 20:06	54820.837	4.232 ± 0.070	3.80 ± 0.61	...
	21/12/2008 20:58	54821.874	4.236 ± 0.074	3.82 ± 0.63	...
	27/12/2008 20:24	54827.850	4.178 ± 0.076	3.41 ± 0.65	...
	28/12/2008 19:19	54828.805	4.109 ± 0.071	2.92 ± 0.62	...
	31/12/2008 20:04	54831.836	4.151 ± 0.072	3.22 ± 0.63	...
	01/01/2009 20:33	54832.856	4.205 ± 0.073	3.60 ± 0.63	...
	02/01/2009 19:14	54833.801	4.307 ± 0.083	4.33 ± 0.69	...
	03/01/2009 19:14	54834.802	4.197 ± 0.092	3.55 ± 0.75	...
CrAO	04/11/2008 00:22	54774.015	3.758 ± 0.040	...	4.248 ± 0.045
	07/11/2008 17:48	54777.742	3.689 ± 0.019	...	4.178 ± 0.021
	15/11/2008 20:57	**54785.873**	3.445 ± 0.084	...	3.935 ± 0.096
	01/12/2008 18:48	54801.783	3.859 ± 0.101	...	4.349 ± 0.113
	05/12/2008 20:21	**54805.848**	3.951 ± 0.067	...	4.441 ± 0.076
	12/12/2008 17:08	54812.714	3.721 ± 0.028	...	4.211 ± 0.032
	17/12/2008 18:50	54817.785	3.736 ± 0.033	...	4.226 ± 0.037

Notes. [a] Measured flux density in the R-band. [b] KVA-measured core flux density derived by subtracting the host galaxy, correcting for interstellar absorption and converting to the desired units. [c] CrAO-measured flux density scaled to the KVA results.

Table E.10: R-band observations and measured flux densities of 1ES 2344+514 during the MW campaign. Times are given in UTC. The measured values for the light curves as well as the corrected and converted values for KVA used for the SED are given. Note that KVA is observing in the Cousins R-band, whereas CrAO is using the Johnson R-band. Therefore, the CrAO points have been shifted by +0.49 mJy determined from the two CrAO – KVA data pairs with a time difference < 0.3 MJD, marked bold.

UVOT Filter	$\boldsymbol{\lambda}^{(a)}$ [$\mathring{A}$]	$\boldsymbol{F_0}^{(b)}$ [mag]	$\boldsymbol{F_h}^{(c)}$ [mJy]	$\boldsymbol{ratio}^{(d)}$ [$10^{-16}\,\mathrm{erg\,cm^{-2}\,s^{-1}}\,\mathring{A}^{-1}$]	$\boldsymbol{A}^{(e)}$ [mag]
V	5402 ± 327	17.89	1.96 ± 0.16	2.613 ± 0.009	0.583
B	4329 ± 414	19.11	0.95 ± 0.20	1.471 ± 0.006	0.776
U	3501 ± 333	18.34	0.22 ± 0.20	1.628 ± 0.025	0.927
UVW1	2591 ± 294	17.44	...	4.21 ± 0.13	1.26
UVM2	2229 ± 211	16.85	...	8.446 ± 0.053	1.77
UVW2	2033 ± 279	17.38	...	5.98 ± 0.78	1.68

Notes. [(a)] Effective wavelength, taken from the UVOT CALDB 02 version R03. The errors have been calculated from the FWHM of the corresponding filter as given in Poole *et al.* (2008). [(b)] Photometric zero points from Breeveld *et al.* (2011). [(c)] Host galaxy flux density for 1ES 2344+514, see (Aleksić *et al.* 2012f). [(d)] count-rate-to-flux ratios for GRBs, taken from the UVOT CALDB 02 version R03. [(e)] Galactic absorption for 1ES 2344+514, calculated as described above for KVA.

Table E.11: Parameters used for the *Swift* UVOT analysis of 1ES 2344+514. For the UV filters, no host galaxy contribution was assumed, see text. The error of the count-rate-to-flux ratio of the UVW2 filter has been increased artificially from $0.13 \cdot 10^{-16}\,\mathrm{erg\,cm^{-2}\,s^{-1}}\,\mathring{A}^{-1}$ ($\sim 2.2\,\%$) to 13 %, see text for details.

Obs. ID[(a)]	F_{V} [mag]	F_{V} [10^{-12} erg cm^{-2} s^{-1}]	F_{B} [mag]	F_{B} [10^{-12} erg cm^{-2} s^{-1}]	F_{U} [mag]	F_{U} [10^{-12} erg cm^{-2} s^{-1}]
35031019	15.45 ± 0.10	4.24 ± 3.81	16.47 ± 0.10	1.29 ± 4.03	16.69 ± 0.12	1.35 ± 3.39
35031020	...[(b)]	...[(b)]	...[(b)]	...[(b)]	...[(b)]	...[(b)]
35031021	15.46 ± 0.10	4.03 ± 3.78	16.49 ± 0.10	1.04 ± 3.99	16.57 ± 0.12	1.92 ± 3.43
35031022	15.47 ± 0.07	3.83 ± 3.45	16.45 ± 0.07	1.56 ± 3.96	16.53 ± 0.10	2.12 ± 3.43
35031023	15.46 ± 0.10	4.03 ± 3.78	16.52 ± 0.10	0.66 ± 3.93	16.71 ± 0.12	1.26 ± 3.38
35031024	15.47 ± 0.07	3.83 ± 3.45	16.51 ± 0.07	0.78 ± 3.85	16.66 ± 0.10	1.49 ± 3.38
35031025	15.46 ± 0.07	4.03 ± 3.47	16.52 ± 0.07	0.66 ± 3.83	16.69 ± 0.10	1.35 ± 3.37
35031026	15.46 ± 0.07	4.03 ± 3.47	16.47 ± 0.07	1.29 ± 3.93	16.56 ± 0.10	1.97 ± 3.42
35031027	15.45 ± 0.07	4.24 ± 3.50	16.46 ± 0.07	1.42 ± 3.94	16.52 ± 0.10	2.18 ± 3.43
35031028	15.46 ± 0.05	4.03 ± 3.32	16.51 ± 0.05	0.78 ± 3.80	16.57 ± 0.10	1.92 ± 3.41
35031029	15.50 ± 0.07	3.21 ± 3.37	16.46 ± 0.10	1.42 ± 4.05	16.50 ± 0.10	2.28 ± 3.44
35031030	15.41 ± 0.07	5.10 ± 3.61	16.50 ± 0.07	0.91 ± 3.87	16.57 ± 0.10	1.92 ± 3.41
35031031	15.41 ± 0.10	5.10 ± 3.93	16.49 ± 0.10	1.04 ± 3.99	16.61 ± 0.10	1.72 ± 3.40
35031032	15.48 ± 0.07	3.62 ± 3.42	16.51 ± 0.10	0.78 ± 3.95	16.65 ± 0.10	1.53 ± 3.38
35031033	15.44 ± 0.07	4.46 ± 3.53	16.50 ± 0.07	0.91 ± 3.87	16.60 ± 0.10	1.77 ± 3.40
35031034	15.50 ± 0.07	3.21 ± 3.37	16.52 ± 0.07	0.66 ± 3.83	16.67 ± 0.10	1.44 ± 3.38
35031035	...[(b)]	...[(b)]	...[(b)]	...[(b)]	...[(b)]	...[(b)]
35031036	15.49 ± 0.07	3.42 ± 3.39	16.51 ± 0.07	0.78 ± 3.85	16.73 ± 0.10	1.17 ± 3.36
35031037	...[(b)]	...[(b)]	16.54 ± 0.07	0.41 ± 3.80	16.77 ± 0.10	1.00 ± 3.35
35031038	15.40 ± 0.07	5.32 ± 3.64	16.44 ± 0.07	1.69 ± 3.99	16.54 ± 0.10	2.07 ± 3.43
35031039	15.39 ± 0.07	5.54 ± 3.67	16.48 ± 0.07	1.16 ± 3.91	16.54 ± 0.10	2.07 ± 3.43
35031040	15.50 ± 0.07	3.21 ± 3.37	16.52 ± 0.07	0.66 ± 3.83	16.69 ± 0.10	1.35 ± 3.37

Notes. [(a)] *Swift* observation ID. [(b)] Observation time too short for deriving results.

Table E.12: Results of the *Swift* UVOT observations of 1ES 2344+514 in the V-, B- and U-band during the MW campaign. The values in [mag] are in contrast to the ones in [10^{-12} erg cm^{-2} s^{-1}] not host-galaxy corrected or de-reddened.

Obs. ID[(a)]	$F_{\mathbf{UVW1}}$		$F_{\mathbf{UVM2}}$		$F_{\mathbf{UVW2}}$	
	[mag]	$[10^{-12}\,\mathrm{erg\,cm^{-2}\,s^{-1}}]$	[mag]	$[10^{-12}\,\mathrm{erg\,cm^{-2}\,s^{-1}}]$	[mag]	$[10^{-12}\,\mathrm{erg\,cm^{-2}\,s^{-1}}]$
35031019	17.27 ± 0.20	4.07 ± 0.90	17.76 ± 0.30	4.17 ± 1.22	17.76 ± 0.15	4.04 ± 0.95
35031020	...[(b)]	...[(b)]	...[(b)]	...[(b)]	...[(b)]	...[(b)]
35031021	17.20 ± 0.20	4.34 ± 0.96	17.79 ± 0.30	4.06 ± 1.19	17.63 ± 0.20	4.55 ± 1.21
35031022	17.15 ± 0.10	4.54 ± 0.69	17.57 ± 0.15	4.97 ± 0.84	17.41 ± 0.10	5.58 ± 1.18
35031023	17.30 ± 0.20	3.96 ± 0.87	17.74 ± 0.30	4.25 ± 1.25	17.49 ± 0.15	5.18 ± 1.22
35031024	17.31 ± 0.10	3.92 ± 0.60	17.73 ± 0.15	4.29 ± 0.73	17.66 ± 0.10	4.43 ± 0.94
35031025	17.27 ± 0.10	4.07 ± 0.62	17.66 ± 0.15	4.57 ± 0.78	17.62 ± 0.10	4.60 ± 0.98
35031026	17.16 ± 0.10	4.50 ± 0.68	17.68 ± 0.15	4.49 ± 0.76	17.66 ± 0.10	4.43 ± 0.94
35031027	17.17 ± 0.10	4.46 ± 0.68	17.41 ± 0.15	5.76 ± 0.98	17.54 ± 0.10	4.95 ± 1.05
35031028	17.19 ± 0.10	4.38 ± 0.67	17.59 ± 0.15	4.88 ± 0.83	17.57 ± 0.10	4.81 ± 1.02
35031029	17.10 ± 0.15	4.76 ± 0.87	17.33 ± 0.20	6.20 ± 1.30	17.50 ± 0.10	5.13 ± 1.09
35031030	17.31 ± 0.10	3.92 ± 0.60	17.58 ± 0.15	4.92 ± 0.84	17.62 ± 0.10	4.60 ± 0.98
35031031	17.20 ± 0.10	4.34 ± 0.66	17.56 ± 0.30	5.01 ± 1.47	17.55 ± 0.15	4.90 ± 1.16
35031032	17.37 ± 0.10	3.71 ± 0.56	17.80 ± 0.20	4.02 ± 0.84	17.78 ± 0.10	3.97 ± 0.84
35031033	17.23 ± 0.10	4.22 ± 0.64	17.66 ± 0.20	4.57 ± 0.96	17.67 ± 0.10	4.39 ± 0.93
35031034	17.48 ± 0.10	3.35 ± 0.51	17.62 ± 0.15	4.74 ± 0.81	17.70 ± 0.10	4.27 ± 0.91
35031035	...[(b)]	...[(b)]	...[(b)]	...[(b)]	...[(b)]	...[(b)]
35031036	17.38 ± 0.10	3.68 ± 0.56	17.66 ± 0.15	4.57 ± 0.78	17.58 ± 0.10	4.77 ± 1.01
35031037	17.22 ± 0.10	4.26 ± 0.65	...[(b)]	...[(b)]	...[(b)]	...[(b)]
35031038	17.12 ± 0.10	4.67 ± 0.71	17.51 ± 0.20	5.25 ± 1.10	17.49 ± 0.15	5.18 ± 1.22
35031039	17.21 ± 0.10	4.30 ± 0.65	17.62 ± 0.15	4.74 ± 0.81	17.59 ± 0.10	4.72 ± 1.00
35031040	17.36 ± 0.10	3.74 ± 0.57	17.52 ± 0.15	5.20 ± 0.88	17.68 ± 0.10	4.35 ± 0.92

Notes. [(a)] *Swift* observation ID. [(b)] Observation time too short for deriving results.

Table E.13: Results of the *Swift* UVOT observations of 1ES 2344+514 in the UV filters during the MW campaign. The values in [mag] are in contrast to the values in $[10^{-12}\,\mathrm{erg\,cm^{-2}\,s^{-1}}]$ not de-reddened. Note that the errors of the UVW2 data have been increased artificially (see text).

E.2.4 Radio Regime

Instrument	Date	MJD	ν [GHz]	S [Jy]	S [erg cm^{-2} s^{-1}]
Effelsberg	17/10/2008 23:12	54756.967	2.64	0.294 ± 0.004	$(7.76 \pm 0.11) \cdot 10^{-15}$
	17/10/2008 23:11	54756.966	4.85	0.218 ± 0.002	$(1.06 \pm 0.01) \cdot 10^{-14}$
	17/10/2008 23:07	54756.963	8.35	0.177 ± 0.002	$(1.48 \pm 0.02) \cdot 10^{-14}$
	17/10/2008 23:02	54756.960	10.45	0.165 ± 0.006	$(1.72 \pm 0.06) \cdot 10^{-14}$
	17/10/2008 23:17	54756.970	14.60	0.146 ± 0.004	$(2.13 \pm 0.06) \cdot 10^{-14}$
	08/11/2008 22:48	54778.950	4.85	0.232 ± 0.002	$(1.13 \pm 0.01) \cdot 10^{-14}$
	08/11/2008 22:47	54778.949	8.35	0.188 ± 0.003	$(1.57 \pm 0.03) \cdot 10^{-14}$
	08/11/2008 22:44	54778.947	10.45	0.176 ± 0.004	$(1.84 \pm 0.04) \cdot 10^{-14}$
	06/12/2008 04:44	54806.197	2.64	0.279 ± 0.003	$(7.37 \pm 0.08) \cdot 10^{-15}$
	06/12/2008 04:41	54806.195	4.85	0.219 ± 0.005	$(1.06 \pm 0.02) \cdot 10^{-14}$
	06/12/2008 04:31	54806.188	10.45	0.165 ± 0.004	$(1.72 \pm 0.04) \cdot 10^{-14}$
	24/01/2009 16:48	54855.700	2.64	0.276 ± 0.003	$(7.29 \pm 0.08) \cdot 10^{-15}$
	24/01/2009 16:44	54855.697	4.85	0.208 ± 0.004	$(1.01 \pm 0.02) \cdot 10^{-14}$
	24/01/2009 16:41	54855.695	8.35	0.169 ± 0.003	$(1.41 \pm 0.03) \cdot 10^{-14}$
	24/01/2009 16:36	54855.692	10.45	0.161 ± 0.003	$(1.68 \pm 0.03) \cdot 10^{-14}$
	24/01/2009 16:17	54855.679	14.60	0.144 ± 0.004	$(2.10 \pm 0.06) \cdot 10^{-14}$
	24/01/2009 16:32	54855.689	43.00	0.166 ± 0.012	$(7.14 \pm 0.52) \cdot 10^{-14}$
IRAM	16/09/2008 12:22	54725.515	86.24	< 0.96	$< 8.3 \cdot 10^{-13}$
			142.33	< 3.96	$< 5.64 \cdot 10^{-12}$
	06/12/2008 07:21	54806.306	86.24	< 1.86	$< 1.60 \cdot 10^{-12}$
	06/12/2008 07:18	54806.304	142.33	< 2.16	$< 3.07 \cdot 10^{-12}$
	06/01/2009 12:03	54837.502	86.24	< 1.83	$< 1.58 \cdot 10^{-13}$
			142.33	< 2.25	$< 3.20 \cdot 10^{-12}$
	16/02/2009 20:57	54878.873	86.24	< 1.86	$< 1.60 \cdot 10^{-13}$
			142.33	< 4.77	$< 6.79 \cdot 10^{-12}$
Metsähovi	21/09/2008 17:15	54730.719	36.8	...	...
	07/10/2008 17:21	54746.723	36.8	< 0.33	$< 1.2 \cdot 10^{-13}$
	24/12/2008 11:50	54824.493	36.8	...	...
	27/12/2008 20:42	54827.863	36.8	...	...
	30/12/2008 20:35	54830.858	36.8	...	...
	05/01/2009 10:26	54836.435	36.8	...	...
	07/01/2009 10:45	54838.448	36.8	...	...
	30/01/2009 08:56	54861.372	36.8	...	...
	12/02/2009 07:33	54874.315	36.8	...	...
OVRO	22/10/2008 02:16	54761.095	15.0	0.144 ± 0.004	$(2.16 \pm 0.06) \cdot 10^{-14}$
	24/10/2008 02:09	54763.089	15.0	0.166 ± 0.005	$(2.50 \pm 0.07) \cdot 10^{-14}$
	26/10/2008 02:01	54765.084	15.0	0.169 ± 0.007	$(2.53 \pm 0.10) \cdot 10^{-14}$
	28/10/2008 01:53	54767.078	15.0	0.163 ± 0.008	$(2.45 \pm 0.13) \cdot 10^{-14}$
	30/10/2008 01:51	54769.077	15.0	0.158 ± 0.021	$(2.37 \pm 0.32) \cdot 10^{-14}$
	03/11/2008 01:21	54773.056	15.0	0.163 ± 0.007	$(2.44 \pm 0.11) \cdot 10^{-14}$
	07/11/2008 01:20	54777.056	15.0	0.159 ± 0.005	$(2.39 \pm 0.07) \cdot 10^{-14}$
	16/11/2008 00:48	54786.033	15.0	0.161 ± 0.005	$(2.41 \pm 0.07) \cdot 10^{-14}$
	18/11/2008 00:40	54788.028	15.0	0.162 ± 0.004	$(2.43 \pm 0.06) \cdot 10^{-14}$
	20/11/2008 00:32	54790.022	15.0	0.170 ± 0.016	$(2.55 \pm 0.24) \cdot 10^{-14}$
	22/11/2008 00:24	54792.017	15.0	0.159 ± 0.012	$(2.38 \pm 0.18) \cdot 10^{-14}$
	24/11/2008 00:16	54794.011	15.0	0.162 ± 0.009	$(2.43 \pm 0.14) \cdot 10^{-14}$
	26/11/2008 00:08	54796.006	15.0	0.162 ± 0.004	$(2.43 \pm 0.06) \cdot 10^{-14}$
	05/12/2008 23:30	54805.979	15.0	0.153 ± 0.011	$(2.29 \pm 0.16) \cdot 10^{-14}$
	09/12/2008 23:14	54809.968	15.0	0.161 ± 0.005	$(2.42 \pm 0.07) \cdot 10^{-14}$
	17/12/2008 22:42	54817.946	15.0	0.164 ± 0.007	$(2.46 \pm 0.10) \cdot 10^{-14}$
OVRO	19/12/2008 22:34	54819.941	15.0	0.158 ± 0.012	$(2.37 \pm 0.18) \cdot 10^{-14}$

continued on the following page

Table E.14: continued.

Instrument	**Date**	**MJD**	$\boldsymbol{\nu}$	$\boldsymbol{S}$	
			[GHz]	[Jy]	[erg cm^{-2} s^{-1}]
	23/12/2008 22:10	54823.924	15.0	0.165 ± 0.007	$(2.48 \pm 0.10) \cdot 10^{-14}$
	20/01/2009 20:20	54851.847	15.0	0.148 ± 0.007	$(2.23 \pm 0.10) \cdot 10^{-14}$
	24/01/2009 20:12	54855.842	15.0	0.150 ± 0.013	$(2.25 \pm 0.19) \cdot 10^{-14}$
	30/01/2009 19:49	54861.826	15.0	0.149 ± 0.006	$(2.23 \pm 0.09) \cdot 10^{-14}$
	03/02/2009 19:33	54865.814	15.0	0.151 ± 0.018	$(2.26 \pm 0.27) \cdot 10^{-14}$
	07/02/2009 19:16	54869.803	15.0	0.090 ± 0.038	$(1.35 \pm 0.56) \cdot 10^{-14}$
	11/02/2009 19:01	54873.792	15.0	0.152 ± 0.010	$(2.27 \pm 0.14) \cdot 10^{-14}$
	17/02/2009 18:39	54879.777	15.0	0.155 ± 0.016	$(2.32 \pm 0.24) \cdot 10^{-14}$
RATAN-600	20/09/2008 – 03/10/2008	54729 – 54742	4.8	0.202 ± 0.011	$(9.70 \pm 0.53) \cdot 10^{-15}$
			7.7	0.182 ± 0.021	$(1.40 \pm 0.16) \cdot 10^{-14}$
			11.1	0.180 ± 0.017	$(2.00 \pm 0.19) \cdot 10^{-14}$
			22.2	0.170 ± 0.035	$(3.77 \pm 0.78) \cdot 10^{-14}$
VLBA	22/10/2008 23:02 – 23/10/2008 10:04	54761.96 – 54762.42	4.6	0.146 ± 0.007	$(6.72 \pm 0.34) \cdot 10^{-15}$
			5.0	0.143 ± 0.007	$(7.15 \pm 0.36) \cdot 10^{-15}$
			8.1	0.138 ± 0.007	$(1.12 \pm 0.06) \cdot 10^{-14}$
			8.4	0.139 ± 0.007	$(1.17 \pm 0.06) \cdot 10^{-14}$
			15.4	0.128 ± 0.006	$(1.97 \pm 0.10) \cdot 10^{-14}$
			23.8	0.121 ± 0.012	$(2.88 \pm 0.29) \cdot 10^{-14}$
			43.2	0.118 ± 0.012	$(5.10 \pm 0.51) \cdot 10^{-14}$

Table E.14: Radio observations and obtained flux densities S of 1ES 2344+514 during the MW campaign. Times are given in UTC. Note that the Effelsberg and VLBA errors contain systematic uncertainties. Metsähovi ULs are given for S/N > 4, IRAM ULs with a c.l. of $3\,\sigma$.

E.2.5 Correlations between Different Instruments

The following figures have been produced selecting data pairs of two instruments with a time difference < 0.9 days. No data point may be selected twice, and if multiple data points fulfil the time difference condition to one point of the other instrument, only the data pair closest in time is being used.

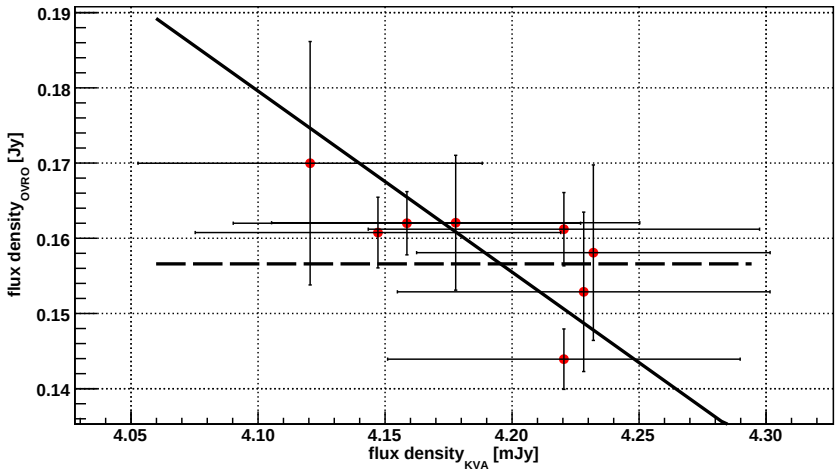

Figure E.5: The flux density at 15.0 GHz measured by OVRO from 1ES 2344+514 during the MW campaign as a function of the KVA R-band flux density. The dashed line represents a fit with a constant (χ^2/d.o.f. = 14.5/7), the solid line gives a linear fit (χ^2/d.o.f. = 1.0/6 with a slope of $-(2.41 \pm 2.42) \cdot 10^{-1}$ Jy per mJy).

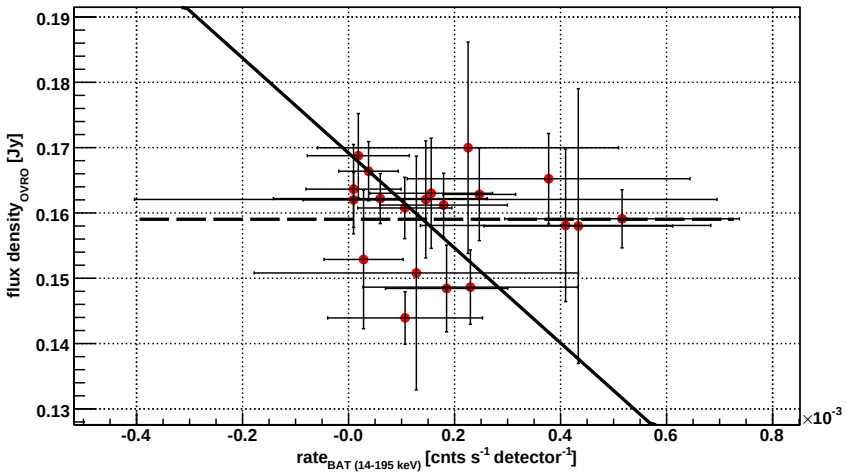

Figure E.6: The flux density at 15.0 GHz measured by OVRO from 1ES 2344+514 during the MW campaign as a function of the daily *Swift* BAT rate. The OVRO outlier at MJD 54869.8 has been omitted here. Only BAT points with rate > 0 are shown. The dashed line represents a fit with a constant (χ^2/d.o.f. = 29.3/19), the solid line gives a linear fit (χ^2/d.o.f. = 13.4/18 with a slope of $-(72.7 \pm 29.1)$ Jy per count s^{-1} detector^{-1}).

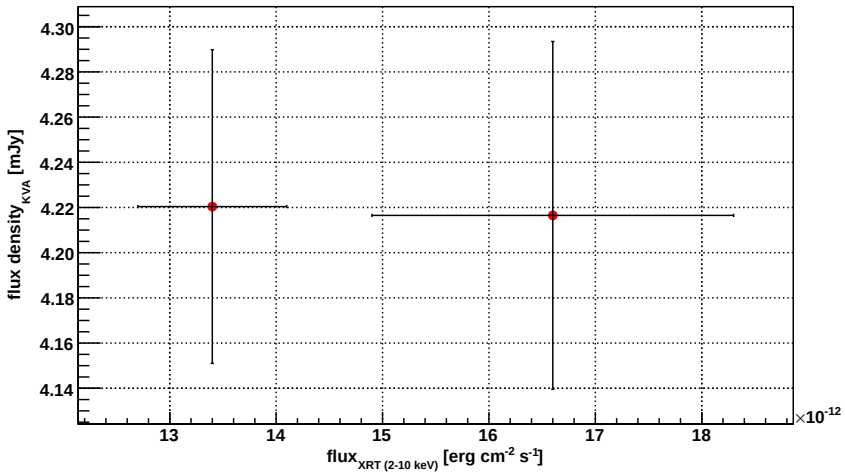

Figure E.7: The R-band flux density measured by KVA from 1ES 2344+514 during the MW campaign as a function of the *Swift* XRT integral flux between 2 and 10 keV. Due to having only two data points, no fits have been applied.

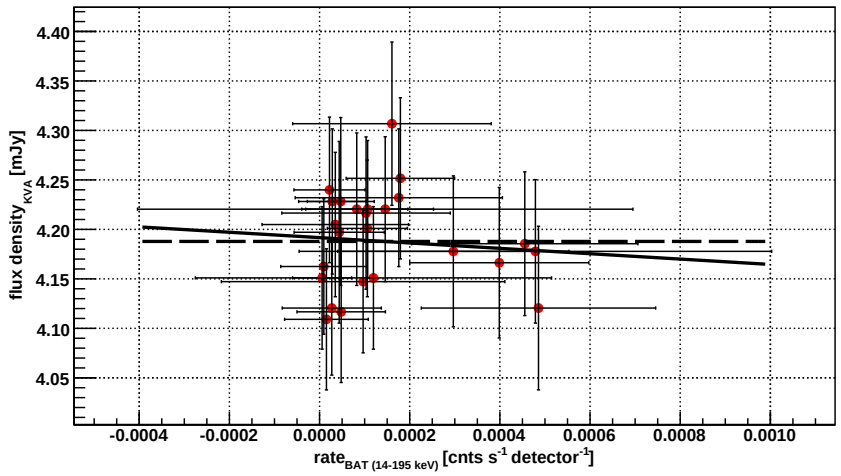

Figure E.8: The R-band flux density measured by KVA from 1ES 2344+514 during the MW campaign as a function of the daily *Swift* BAT rate. Only BAT points with rate > 0 are shown. The dashed line represents a fit with a constant (χ^2/d.o.f. $= 9.9/24$), the solid line gives a linear fit (χ^2/d.o.f. $= 9.9/23$ with a slope of $-(27 \pm 155)$ mJy per count s^{-1} detector^{-1}).

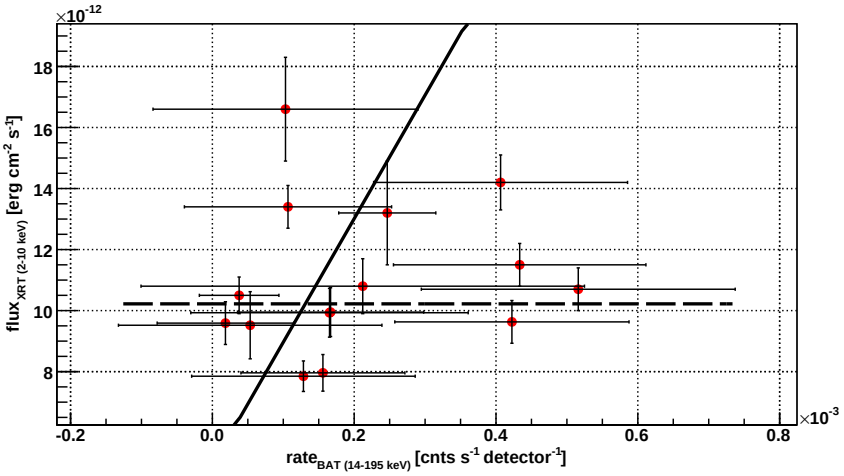

Figure E.9: The integral flux between 2 and 10 keV measured by *Swift* XRT from 1ES 2344+514 during the MW campaign as a function of the daily *Swift* BAT rate. Only BAT points with rate > 0 are shown. The dashed line represents a fit with a constant (χ^2/d.o.f. = 100.6/14), the solid line gives a linear fit (χ^2/d.o.f. = 16.0/13 with a slope of $(4.05 \pm 2.49) \cdot 10^{-8}\,\mathrm{erg\,cm^{-2}\,s^{-1}}$ per $\mathrm{counts\,s^{-1}\,detector^{-1}}$).

E.3 1ES 2344+514 (Long-Term)

E.3.1 Single-Dish Radio Spectra

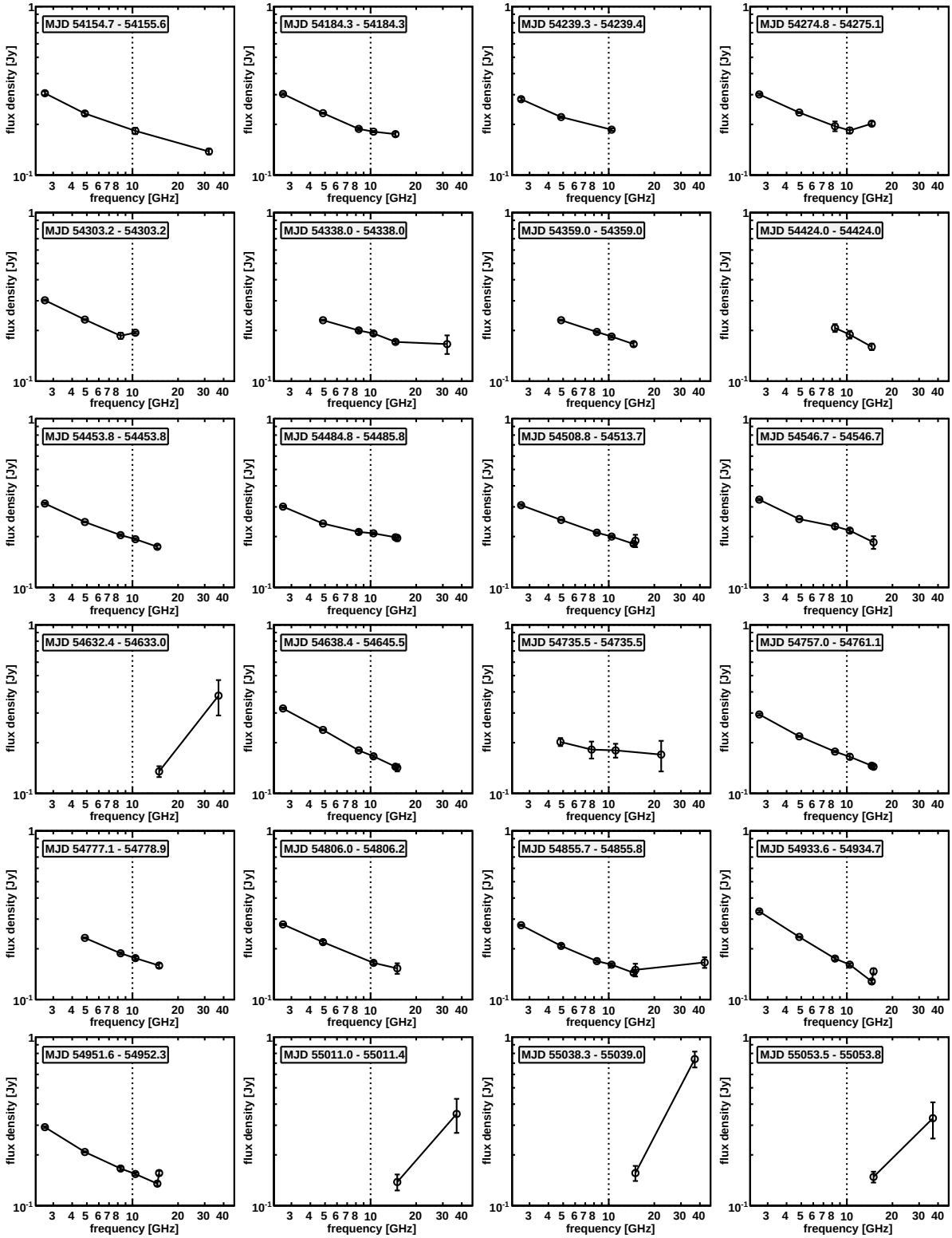

Figure E.10: Individual radio spectra from Figure 6.38.

E.3.2 Multi-Wavelength Light Curves

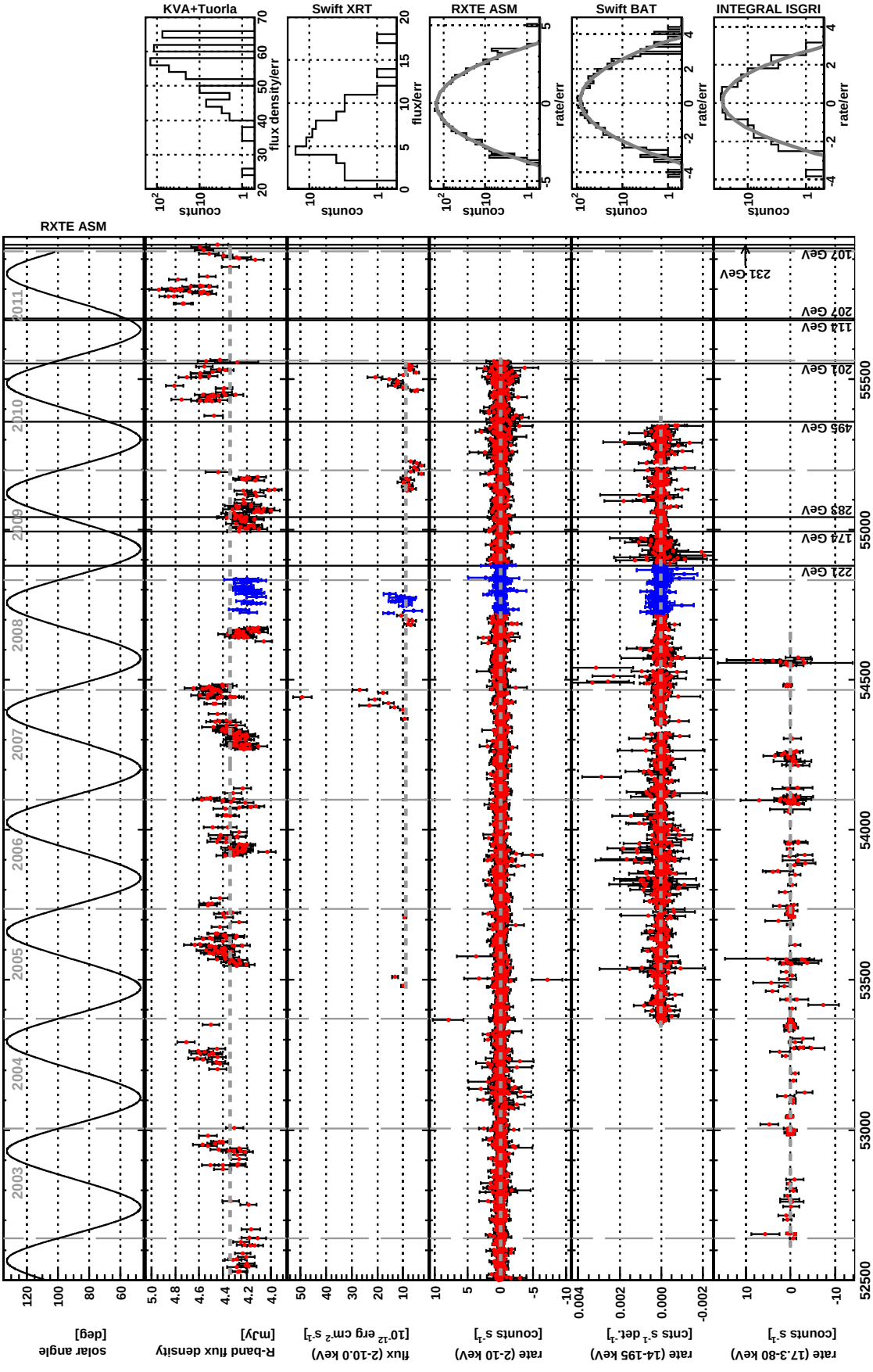

Figure E.11: Same as Figure 6.41 but with day-wise binning for *RXTE* ASM, *Swift* BAT and *INTEGRAL* ISGRI. Instead of the radio observations, the solar angle of *RXTE* ASM is shown. Seven outliers of the BAT light curve are not shown for clearness, for five points the linear error bars have been cut at the plot edge.

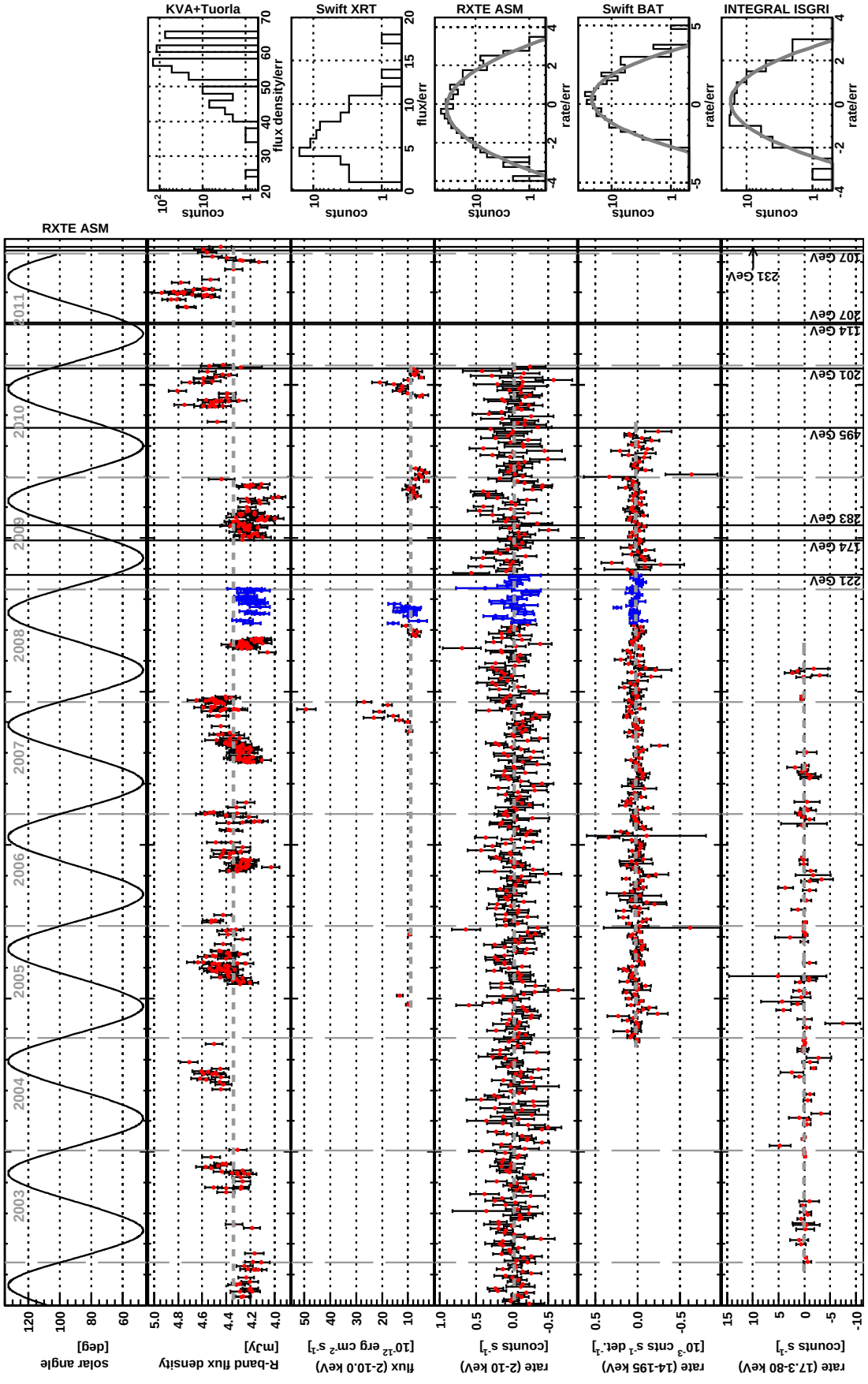

Figure E.12: Same as Figure 6.41 but with week-wise binning for *RXTE* ASM, *Swift* BAT and *INTEGRAL* ISGRI. Instead of the radio observations, the solar angle of *RXTE* ASM is shown.

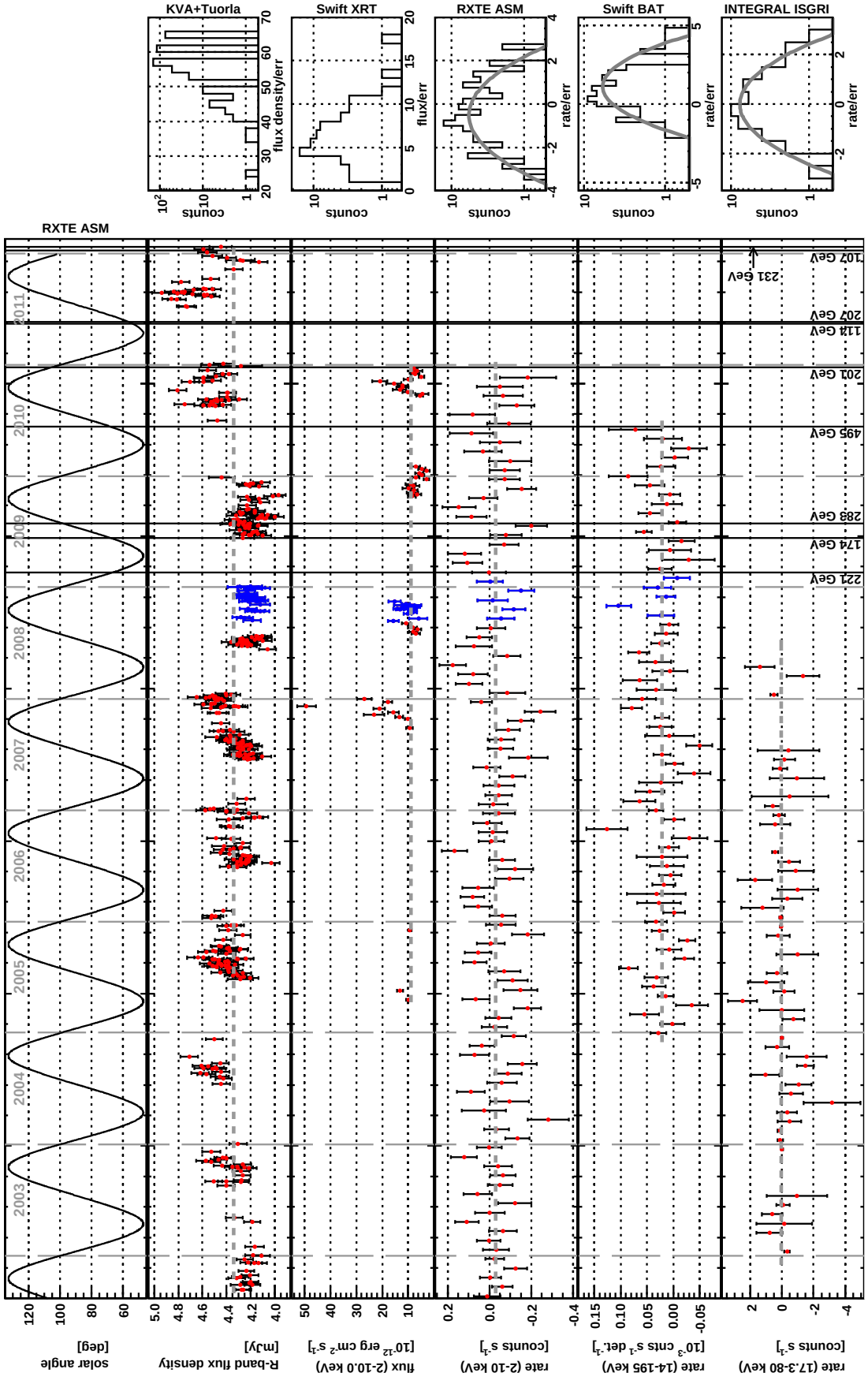

Figure E.13: Same as Figure 6.41 but with month-wise binning for *RXTE* ASM, *Swift* BAT and *INTEGRAL* ISGRI. Instead of the radio observations, the solar angle of *RXTE* ASM is shown.

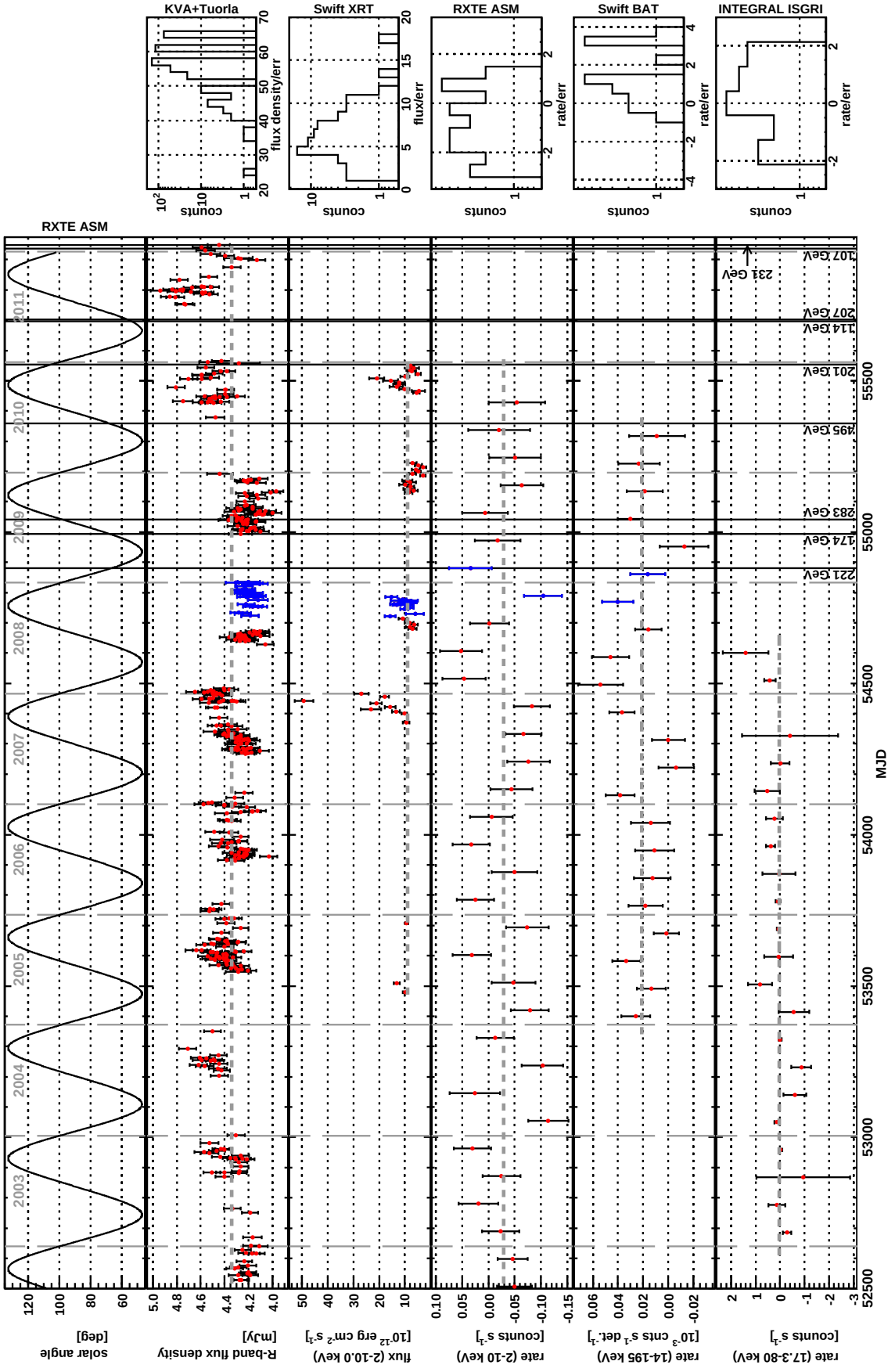

Figure E.14: Same as Figure 6.41 but with quarter-wise binning for *RXTE* ASM, *Swift* BAT and *INTEGRAL* ISGRI. Instead of the radio observations, the solar angle of *RXTE* ASM is shown.

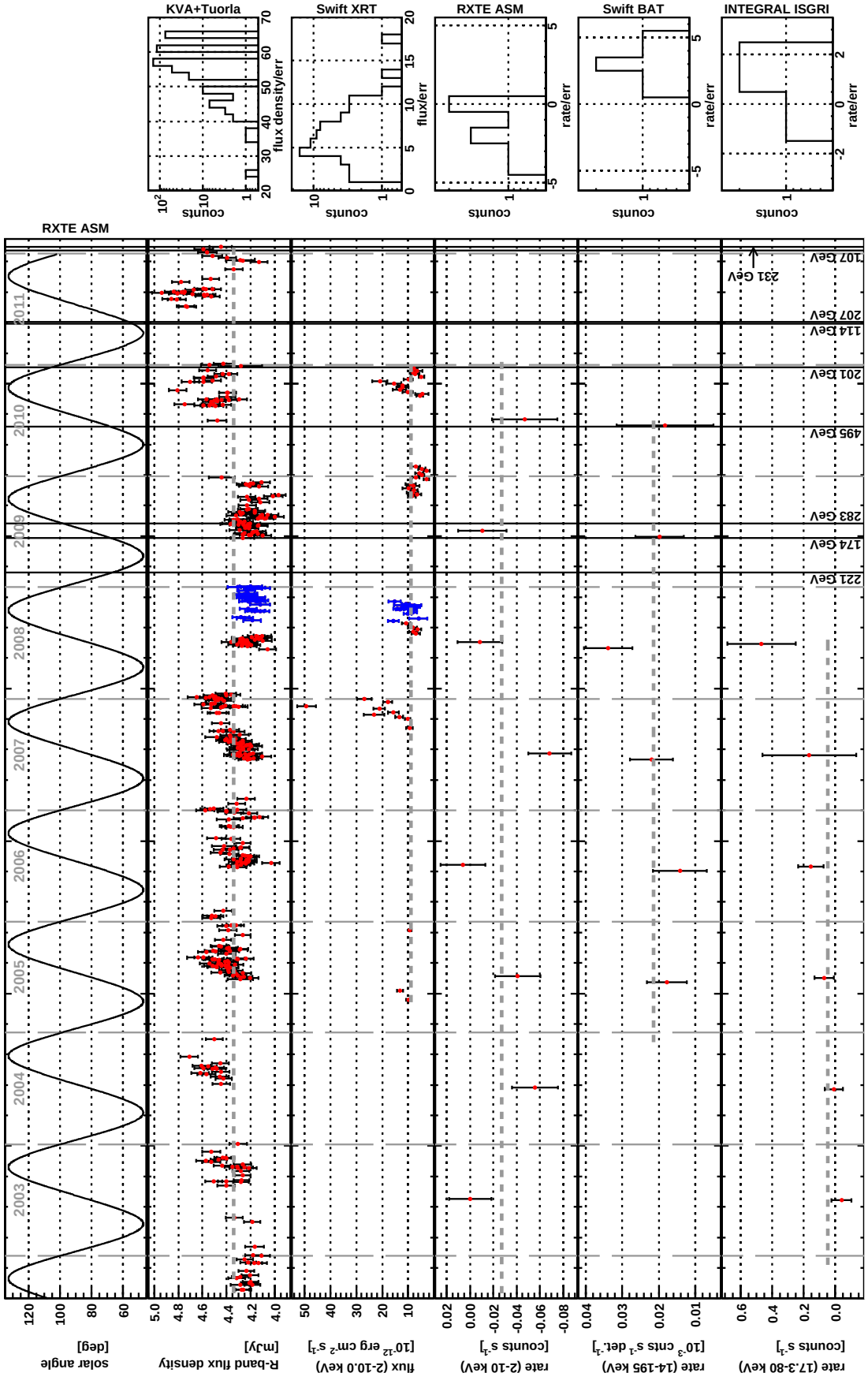

Figure E.15: Same as Figure 6.41 but with year-wise binning for *RXTE* ASM, *Swift* BAT and *INTEGRAL* ISGRI. Instead of the radio observations, the solar angle of *RXTE* ASM is shown.

E.3.3 Correlation Plots

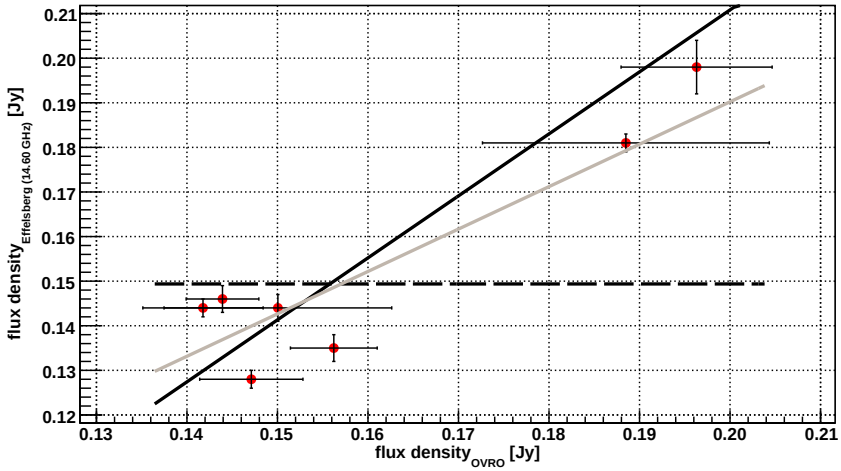

Figure E.16: The flux density at 15.0 GHz measured by OVRO from 1ES 2344+514 as a function of the Effelsberg 14.60 GHz flux density. For Effelsberg, only statistical errors have been used in this case. The black dashed line represents a fit with a constant (χ^2/d.o.f. = 464.6/6), the black solid line gives a linear fit (χ^2/d.o.f. = 12.8/5 with a slope of (1.39 ± 0.25) Jy per Jy). A likelihood ratio test prefers the linear fit with 98.9 %. The grey solid line is denoting a linear fit going through the origin of ordinates, given by a slope of (0.951 ± 0.017) Jy per Jy (χ^2/d.o.f. = 17.2/6).

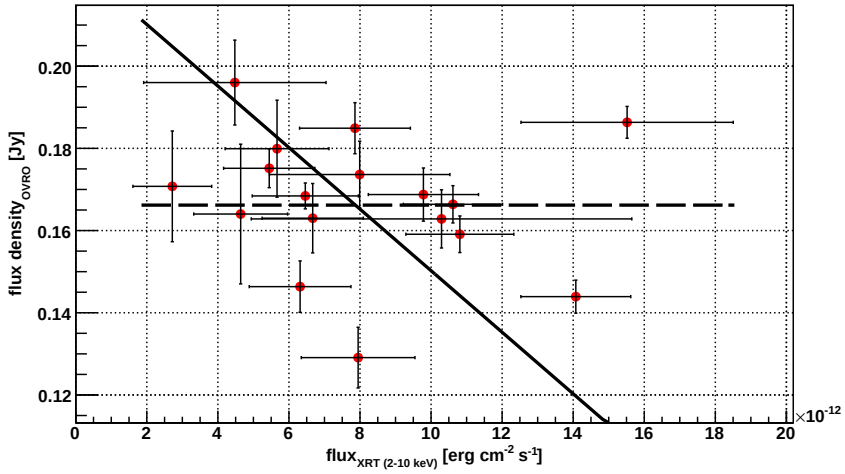

Figure E.17: The flux density at 15.0 GHz measured by OVRO from 1ES 2344+514 as a function of the *Swift* XRT integral flux between 2 and 10 keV. Only data pairs with a time difference < 0.9 days have been considered. OVRO data with an error $\gtrsim 0.02$ Jy have not been used. The dashed line represents a fit with a constant (χ^2/d.o.f. = 120.0/16), the solid line gives a linear fit (χ^2/d.o.f. = 46.0/15 with a slope of $-(7.5 \pm 1.2) \cdot 10^9$ Jy per erg cm^{-2} s^{-1}).

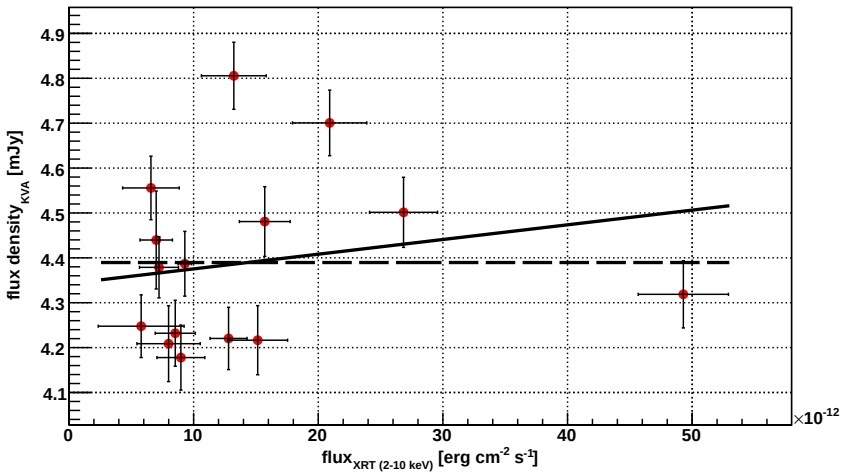

Figure E.18: The R-band flux density measured by KVA from 1ES 2344+514 as a function of the *Swift* XRT integral flux between 2 and 10 keV. Only data pairs with a time difference < 0.9 days have been considered. The dashed line represents a fit with a constant (χ^2/d.o.f. = 92.1/14), the solid line gives a linear fit (χ^2/d.o.f. = 90.0/13 with a slope of $(3.3 \pm 0.8) \cdot 10^9$ mJy per erg cm^{-2} s^{-1}).

List of Figures

List of Tables

Bibliography

Abdo, A. A., Ackermann, M., Agudo, I., *et al.*: *Fermi Large Area Telescope and Multi-wavelength Observations of the Flaring Activity of PKS 1510-089 between 2008 September and 2009 June.* ApJ, **721**, 1425 (2010a)

Abdo, A. A., Ackermann, M., Agudo, I., *et al.*: *The Spectral Energy Distribution of Fermi Bright Blazars.* ApJ, **716**, 30 (2010b)

Abdo, A. A., Ackermann, M., Ajello, M., *et al.*: *Bright Active Galactic Nuclei Source List from the First Three Months of the Fermi Large Area Telescope All-Sky Survey.* ApJ, **700**, 597 (2009a)

Abdo, A. A., Ackermann, M., Ajello, M., *et al.*: *Fermi Observations of TeV-Selected Active Galactic Nuclei.* ApJ, **707**, 1310 (2009b)

Abdo, A. A., Ackermann, M., Ajello, M., *et al.*: *A change in the optical polarization associated with a γ-ray flare in the blazar 3C279.* Nature, **463**, 919 (2010c)

Abdo, A. A., Ackermann, M., Ajello, M., *et al.*: *Fermi Large Area Telescope First Source Catalog.* ApJS, **188**, 405 (2010d)

Abdo, A. A., Ackermann, M., Ajello, M., *et al.*: *The First Catalog of Active Galactic Nuclei Detected by the Fermi Large Area Telescope.* ApJ, **715**, 429 (2010e)

Abdo, A. A., Ackermann, M., Ajello, M., *et al.*: *Fermi Gamma-ray Space Telescope Observations of the Gamma-ray Outburst from 3C454.3 in November 2010.* ApJ, **733**, L26 (2011a)

Abdo, A. A., Ackermann, M., Ajello, M., *et al.*: *Fermi Large Area Telescope Observations of Markarian 421: The Missing Piece of its Spectral Energy Distribution.* ApJ, **736**, 131 (2011b)

Abdo, A. A., Ackermann, M., Ajello, M., *et al.*: *Gamma-Ray Flares from the Crab Nebula.* Science, **331**, 739 (2011c)

Abdo, A. A., Ackermann, M., Ajello, M., *et al.*: *Insights into the High-energy γ-ray Emission of Markarian 501 from Extensive Multifrequency Observations in the Fermi Era.* ApJ, **727**, 129 (2011d)

Abdo, A. A., Ackermann, M., Ajello, M., *et al.*: *Multi-wavelength Observations of the Flaring Gamma-ray Blazar 3C 66A in 2008 October.* ApJ, **726**, 43 (2011e)

Abramowski, A., Acero, F., Aharonian, F., *et al.*: *HESS J1943+213: a candidate extreme BL Lacertae object.* A&A, **529**, A49 (2011a)

Abramowski, A., Acero, F., Aharonian, F., *et al.*: *Simultaneous multi-wavelength campaign on PKS 2005-489 in a high state.* A&A, **533**, A110 (2011b)

Abramowski, A., Acero, F., Aharonian, F., *et al.*: *A multiwavelength view of the flaring state of PKS 2155-304 in 2006.* A&A, **539**, A149 (2012a)

Abramowski, A., Acero, F., Aharonian, F., *et al.*: *Discovery of hard-spectrum γ-ray emission from the BL Lacertae object 1ES 0414+009.* A&A, **538**, A103 (2012b)

Abramowski, A., Acero, F., Aharonian, F., *et al.*: *The 2010 Very High Energy γ-Ray Flare and 10 Years of Multi-wavelength Observations of M 87.* ApJ, **746**, 151 (2012c)

Acciari, V., Aliu, E., Arlen, T., *et al.*: *Discovery of Very High Energy Gamma-ray Radiation from the BL Lac 1ES 0806+524.* ApJ, **690**, L126 (2009a)

Acciari, V. A., Aliu, E., Arlen, T., *et al.*: *Radio Imaging of the Very-High-Energy γ-Ray Emission Region in the Central Engine of a Radio Galaxy.* Science, **325**, 444 (2009b)

Acciari, V. A., Aliu, E., Arlen, T., *et al.*: *Veritas Observations of a Very High Energy γ-Ray Flare From the Blazar 3C 66A.* ApJ, **693**, L104 (2009c)

Acciari, V. A., Aliu, E., Arlen, T., *et al.*: *Discovery of Very High Energy Gamma Rays from PKS 1424+240 and Multiwavelength Constraints on Its Redshift.* ApJ, **708**, L100 (2010a)

Acciari, V. A., Aliu, E., Arlen, T., *et al.*: *The Discovery of γ-Ray Emission from the Blazar RGB J0710+591.* ApJ, **715**, L49 (2010b)

Acciari, V. A., Aliu, E., Arlen, T., *et al.*: *Multiwavelength Observations of the Very High Energy Blazar 1ES 2344+514.* ApJ, **738**, 169 (2011a)

Acciari, V. A., Aliu, E., Arlen, T., *et al.*: *TeV and Multi-wavelength Observations of Mrk 421 in 2006-2008.* ApJ, **738**, 25 (2011b)

Acciari, V. A., Aliu, E., Aune, T., *et al.*: *Multiwavelength Observations of a TeV-Flare from W Comae.* ApJ, **707**, 612 (2009d)

Acciari, V. A., Aliu, E., Aune, T., *et al.*: *Simultaneous Multiwavelength Observations of Markarian 421 During Outburst.* ApJ, **703**, 169 (2009e)

Acciari, V. A., Aliu, E., Beilicke, M., *et al.*: *VERITAS Discovery of >200 GeV Gamma-Ray Emission from the Intermediate-Frequency-Peaked BL Lacertae Object W Comae.* ApJ, **684**, L73 (2008)

Acciari, V. A., Arlen, T., Aune, T., *et al.*: *Spectral Energy Distribution of Markarian 501: Quiescent State Versus Extreme Outburst.* ApJ, **729**, 2 (2011c)

Acero, F., Aharonian, F., Akhperjanian, A. G., *et al.*: *Detection of Gamma Rays from a Starburst Galaxy.* Science, **326**, 1080 (2009)

Acero, F., Aharonian, F., Akhperjanian, A. G., *et al.*: *PKS 2005-489 at VHE: four years of monitoring with HESS and simultaneous multi-wavelength observations.* A&A, **511**, A52 (2010)

Ackermann, M., Ajello, M., Allafort, A., *et al.*: *The Radio/Gamma-Ray Connection in Active Galactic Nuclei in the Era of the Fermi Large Area Telescope.* ApJ, **741**, 30 (2011a)

Ackermann, M., Ajello, M., Allafort, A., *et al.*: *The Second Catalog of Active Galactic Nuclei Detected by the Fermi Large Area Telescope.* ApJ, **743**, 171 (2011b)

Ackermann, M., Ajello, M., Allafort, A., *et al.*: *The imprint of the extragalactic background light in the gamma-ray spectra of blazars.* Science, **338**, 1190 (2012)

Actis, M., Agnetta, G., Aharonian, F., *et al.*: *Design concepts for the Cherenkov Telescope Array CTA: an advanced facility for ground-based high-energy gamma-ray astronomy.* Experimental Astronomy, **32**, 193 (2011)

Agudo, I., Marscher, A. P., Jorstad, S. G., *et al.*: *On the Location of the γ-Ray Outburst Emission in the BL Lacertae Object AO 0235+164 Through Observations Across the Electromagnetic Spectrum.* ApJ, **735**, L10 (2011)

Aharonian, F., Akhperjanian, A., Beilicke, M., *et al.*: *Is the giant radio galaxy M 87 a TeV gamma-ray emitter?* A&A, **403**, L1 (2003)

Aharonian, F., Akhperjanian, A., Beilicke, M., *et al.*: *Observations of 54 Active Galactic Nuclei with the HEGRA system of Cherenkov telescopes.* A&A, **421**, 529 (2004)

Aharonian, F., Akhperjanian, A. G., Anton, G., *et al.*: *Discovery of Very High Energy γ-Ray Emission from Centaurus a with H.E.S.S.* ApJ, **695**, L40 (2009a)

Aharonian, F., Akhperjanian, A. G., Anton, G., *et al.*: *Simultaneous multiwavelength observations of the second exceptional γ-ray flare of PKS 2155-304 in July 2006.* A&A, **502**, 749 (2009b)

Aharonian, F., Akhperjanian, A. G., Anton, G., *et al.*: *Simultaneous Observations of PKS 2155-304 with HESS, Fermi, RXTE, and Atom: Spectral Energy Distributions and Variability in a Low State.* ApJ, **696**, L150 (2009c)

Aharonian, F., Akhperjanian, A. G., Aye, K.-M., *et al.*: *Discovery of VHE gamma rays from PKS 2005-489.* A&A, **436**, L17 (2005a)

Aharonian, F., Akhperjanian, A. G., Barres de Almeida, U., *et al.*: *Discovery of VHE γ-rays from the distant BL Lacertae 1ES 0347-121.* A&A, **473**, L25 (2007a)

Aharonian, F., Akhperjanian, A. G., Barres de Almeida, U., *et al.*: *New constraints on the mid-IR EBL from the HESS discovery of VHE γ-rays from 1ES 0229+200.* A&A, **475**, L9 (2007b)

Aharonian, F., Akhperjanian, A. G., Barres de Almeida, U., *et al.*: *Discovery of VHE γ-rays from the high-frequency-peaked BL Lacertae object RGB J0152+017.* A&A, **481**, L103 (2008)

Aharonian, F., Akhperjanian, A. G., Bazer-Bachi, A. R., *et al.*: *Multi-wavelength observations of PKS 2155-304 with HESS.* A&A, **442**, 895 (2005b)

Aharonian, F., Akhperjanian, A. G., Bazer-Bachi, A. R., *et al.*: *A low level of extragalactic background light as revealed by γ-rays from blazars.* Nature, **440**, 1018 (2006a)

Aharonian, F., Akhperjanian, A. G., Bazer-Bachi, A. R., *et al.*: *Evidence for VHE γ-ray emission from the distant BL Lac PG 1553+113.* A&A, **448**, L19 (2006b)

Aharonian, F., Akhperjanian, A. G., Bazer-Bachi, A. R., *et al.*: *An Exceptional Very High Energy Gamma-Ray Flare of PKS 2155-304.* ApJ, **664**, L71 (2007c)

Aharonian, F. A.: *TeV gamma rays from BL Lac objects due to synchrotron radiation of extremely high energy protons.* New A, **5**, 377 (2000)

Aharonian, F. A., Akhperjanian, A. G., Barrio, J. A., *et al.*: *The time averaged TeV energy spectrum of MKN 501 of the extraordinary 1997 outburst as measured with the stereoscopic Cherenkov telescope system of HEGRA.* A&A, **349**, 11 (1999)

Albert, J., Aliu, E., Anderhub, H., *et al.*: *Discovery of Very High Energy Gamma Rays from 1ES 1218+30.4.* ApJ, **642**, L119 (2006a)

Albert, J., Aliu, E., Anderhub, H., *et al.*: *Discovery of Very High Energy γ-Rays from Markarian 180 Triggered by an Optical Outburst.* ApJ, **648**, L105 (2006b)

Albert, J., Aliu, E., Anderhub, H., *et al.*: *Discovery of Very High Energy γ-Ray Emission from the Low-Frequency-peaked BL Lacertae Object BL Lacertae.* ApJ, **666**, L17 (2007a)

Albert, J., Aliu, E., Anderhub, H., *et al.*: *Discovery of Very High Energy γ-Rays from 1ES 1011+496 at $z = 0.212$.* ApJ, **667**, L21 (2007b)

Albert, J., Aliu, E., Anderhub, H., *et al.*: *MAGIC Upper Limits on the Very High Energy Emission from Gamma-Ray Bursts.* ApJ, **667**, 358 (2007c)

Albert, J., Aliu, E., Anderhub, H., *et al.*: *Observation of Very High Energy γ-Rays from the AGN 1ES 2344+514 in a Low Emission State with the MAGIC Telescope.* ApJ, **662**, 892 (2007d)

Albert, J., Aliu, E., Anderhub, H., *et al.*: *Variable Very High Energy γ-Ray Emission from Markarian 501.* ApJ, **669**, 862 (2007e)

Albert, J., Aliu, E., Anderhub, H., *et al.*: *Very high energy gamma-ray observations during moonlight and twilight with the MAGIC telescope.* ArXiv Astrophysics e-prints, astro-ph:0702475 (2007f)

Albert, J., Aliu, E., Anderhub, H., *et al.*: *FADC signal reconstruction for the MAGIC telescope.* Nuclear Instruments and Methods in Physics Research A, **594**, 407 (2008a)

Albert, J., Aliu, E., Anderhub, H., *et al.*: *Probing quantum gravity using photons from a flare of the active galactic nucleus Markarian 501 observed by the MAGIC telescope.* Physics Letters B, **668**, 253 (2008b)

Albert, J., Aliu, E., Anderhub, H., *et al.*: *Systematic Search for VHE Gamma-Ray Emission from X-Ray-bright High-Frequency BL Lac Objects.* ApJ, **681**, 944 (2008c)

Albert, J., Aliu, E., Anderhub, H., *et al.*: *Very-High-Energy gamma rays from a Distant Quasar: How Transparent Is the Universe?* Science, **320**, 1752 (2008d)

Albert, J., Aliu, E., Anderhub, H., *et al.*: *VHE γ-Ray Observation of the Crab Nebula and its Pulsar with the MAGIC Telescope.* ApJ, **674**, 1037 (2008e)

Aleksić, J., Alvarez, E. A., Antonelli, L. A., *et al.*: *Detection of very-high energy γ-ray emission from <ASTROBJ>NGC 1275</ASTROBJ> by the MAGIC telescopes.* A&A, **539**, L2 (2012a)

Aleksić, J., Alvarez, E. A., Antonelli, L. A., *et al.*: *Discovery of VHE γ-ray emission from the BL Lacertae object B3 2247+381 with the MAGIC telescopes.* A&A, **539**, A118 (2012b)

Aleksić, J., Alvarez, E. A., Antonelli, L. A., *et al.*: *Discovery of VHE γ-rays from the blazar 1ES 1215+303 with the MAGIC telescopes and simultaneous multi-wavelength observations.* A&A, **544**, A142 (2012c)

Aleksić, J., Alvarez, E. A., Antonelli, L. A., *et al.*: *Mrk 421 active state in 2008: the MAGIC view, simultaneous multi-wavelength observations and SSC model constrained.* A&A, **542**, A100 (2012d)

Aleksić, J., Alvarez, E. A., Antonelli, L. A., *et al.*: *Performance of the MAGIC stereo system obtained with Crab Nebula data.* Astroparticle Physics, **35**, 435 (2012e)

Aleksić, J., Anderhub, H., Antonelli, L. A., *et al.*: *MAGIC TeV gamma-ray observations of Markarian 421 during multiwavelength campaigns in 2006.* A&A, **519**, A32 (2010a)

Aleksić, J., Antonelli, L. A., Antoranz, P., & Asensio, M.: *in preparation, to be submitted to* A&A (2013)

Aleksić, J., Antonelli, L. A., Antoranz, P., *et al.*: *Detection of Very High Energy γ-ray Emission from the Perseus Cluster Head-Tail Galaxy IC 310 by the MAGIC Telescopes.* ApJ, **723**, L207 (2010b)

Aleksić, J., Antonelli, L. A., Antoranz, P., *et al.*: *MAGIC Discovery of Very High Energy Emission from the FSRQ PKS 1222+21.* ApJ, **730**, L8 (2011a)

Aleksić, J., Antonelli, L. A., Antoranz, P., *et al.*: *MAGIC Observations and multiwavelength properties of the quasar 3C 279 in 2007 and 2009.* A&A, **530**, A4 (2011b)

Aleksić, J., Antonelli, L. A., Antoranz, P., *et al.*: *The Simultaneous Low State Spectral Energy Distribution of 1ES 2344+514 from Radio to Very High Energies.* ArXiv Astrophysics e-prints, astro-ph:1211.2608 (2012f)

Aliu, E., Anderhub, H., Antonelli, L. A., *et al.*: *Observation of Pulsed γ-Rays Above 25 GeV from the Crab Pulsar with MAGIC.* Science, **322**, 1221 (2008)

Aliu, E., Anderhub, H., Antonelli, L. A., *et al.*: *Discovery of a Very High Energy Gamma-Ray Signal from the 3C 66A/B Region.* ApJ, **692**, L29 (2009a)

Aliu, E., Anderhub, H., Antonelli, L. A., *et al.*: *Improving the performance of the single-dish Cherenkov telescope MAGIC through the use of signal timing.* Astroparticle Physics, **30**, 293 (2009b)

Aliu, E., Archambault, S., Arlen, T., *et al.*: *Discovery of High-energy and Very High Energy γ-Ray Emission from the Blazar RBS 0413.* ApJ, **750**, 94 (2012a)

Aliu, E., Archambault, S., Arlen, T., *et al.*: *Multiwavelength Observations of the AGN 1ES 0414+009 with VERITAS, Fermi-LAT, Swift-XRT, and MDM.* ApJ, **755**, 118 (2012b)

Aliu, E., Aune, T., Beilicke, M., *et al.*: *Multiwavelength Observations of the Previously Unidentified Blazar RX J0648.7+1516.* ApJ, **742**, 127 (2011)

Aller, M. F., Aller, H. D., & Hughes, P. A.: *Radio-Band Observations of Blazar Variability. In* H. R. Miller, K. Marshall, J. R. Webb, & M. F. Aller (editors), *Blazar Variability Workshop II: Entering the GLAST Era*, volume 350 of *Astronomical Society of the Pacific Conference Series*, 25 (2006)

Anderhub, H., Antonelli, L. A., Antoranz, P., *et al.*: *Discovery of very High Energy γ-Rays from the Blazar S5 0716+714.* ApJ, **704**, L129 (2009a)

Anderhub, H., Antonelli, L. A., Antoranz, P., *et al.*: *Simultaneous Multiwavelength Observation of Mkn 501 in a Low State in 2006.* ApJ, **705**, 1624 (2009b)

Anderhub, H., Backes, M., Biland, A., *et al.*: *FACT - The first Cherenkov telescope using a G-APD camera for TeV gamma-ray astronomy.* Nuclear Instruments and Methods in Physics Research A, **639**, 58 (2011)

Angel, J. R. P. & Stockman, H. S.: *Optical and infrared polarization of active extragalactic objects.* ARA&A, **18**, 321 (1980)

Angelakis, E., Fuhrmann, L., Marchili, N., Krichbaum, T. P., & Zensus, J. A.: *Monitoring the radio spectra of selected blazars in the Fermi-GST era . The Effelsberg 100-m telescope covering the cm band.* Mem. Soc. Astron. Italiana, **79**, 1042 (2008)

Angelakis, E., Fuhrmann, L., Nestoras, I., *et al.*: *Unification and physical interpretation of the radio spectra variability patterns in Fermi blazars and jet emission from NLSy1s.* ArXiv Astrophysics e-prints, astro-ph:1205.1961 (2012)

Antón, S. & Browne, I. W. A.: *The recognition of blazars and the blazar spectral sequence.* MNRAS, **356**, 225 (2005)

Antonucci, R.: *Unified models for active galactic nuclei and quasars.* ARA&A, **31**, 473 (1993)

Arlen, T., Aune, T., Beilicke, M., *et al.*: *Rapid TeV Gamma-Ray Flaring of BL Lacertae.* ArXiv Astrophysics e-prints, astro-ph:1211.3073 (2012)

Arshakian, T. G., León-Tavares, J., Böttcher, M., *et al.*: *Radio-optical-gamma-ray properties of MOJAVE AGN detected by Fermi/LAT.* A&A, **537**, A32 (2012)

Atwood, W. B., Abdo, A. A., Ackermann, M., *et al.*: *The Large Area Telescope on the Fermi Gamma-Ray Space Telescope Mission.* ApJ, **697**, 1071 (2009)

Augusto, P., Wilkinson, P. N., & Browne, I. W. A.: *Flat-spectrum radio sources with kpc-scale structure.* MNRAS, **299**, 1159 (1998)

Baczko, A.-K.: *Calibration and imaging of GMVA observations of NGC1052.* Bachelor thesis, Dr. Remeis Sternwarte Bamberg, Friedrich-Alexander-Universität Erlangen-Nürnberg, Universität Würzburg (2012)

Barth, A. J., Ho, L. C., & Sargent, W. L. W.: *The Black Hole Masses and Host Galaxies of BL Lacertae Objects.* ApJ, **583**, 134 (2003)

Barthel, P. D.: *Is every quasar beamed?* ApJ, **336**, 606 (1989)

Bartko, H., Goebel, F., Mirzoyan, R., Pimpl, W., & Teshima, M.: *Tests of a prototype multiplexed fiber-optic ultra-fast FADC data acquisition system for the MAGIC telescope.* Nuclear Instruments and Methods in Physics Research A, **548**, 464 (2005)

Bassani, L., Landi, R., Malizia, A., *et al.*: *IGR J22517+2218=MG3 J225155+2217: A New Gamma-Ray Lighthouse in the Distant Universe.* ApJ, **669**, L1 (2007)

Bastieri, D., Bettini, M., Bigongiari, C., *et al.*: *A two-level pattern trigger for the MAGIC telescope.* Nuclear Instruments and Methods in Physics Research A, **461**, 521 (2001)

Becherini, Y., Behera, B., Biteau, J., *et al.*: *New AGNs discovered by H.E.S.S.* ArXiv Astrophysics e-prints, astro-ph:1105.5243 (2011)

Becherini, Y., Boisson, C., & Cerruti, M.: *Discovery of the most distant BL Lacertae at very high energies with H.E.S.S. In 5th International Symposium on High-Energy Gamma-Ray Astronomy* (2012)

Benbow, W. & for the VERITAS Collaboration: *Highlights of the VERITAS Blazar Observation Program.* ArXiv Astrophysics e-prints, astro-ph:1110.0038 (2011)

Berger, K.: *Overview of the results from extra-galactic observations with the MAGIC telescopes. In International Cosmic Ray Conference*, volume 8 of *International Cosmic Ray Conference*, 167 (2011)

Biland, A., Garczarczyk, M., Anderhub, H., & et al.: *The Active Mirror Control of the MAGIC Telescopes. In International Cosmic Ray Conference*, volume 3 of *International Cosmic Ray Conference*, 1353–1356 (2008)

Blandford, R. D. & Königl, A.: *Relativistic jets as compact radio sources.* ApJ, **232**, 34 (1979)

Blandford, R. D. & Payne, D. G.: *Hydromagnetic flows from accretion discs and the production of radio jets.* MNRAS, **199**, 883 (1982)

Blandford, R. D. & Znajek, R. L.: *Electromagnetic extraction of energy from Kerr black holes.* MNRAS, **179**, 433 (1977)

Błażejowski, M., Blaylock, G., Bond, I. H., *et al.*: *A Multiwavelength View of the TeV Blazar Markarian 421: Correlated Variability, Flaring, and Spectral Evolution.* ApJ, **630**, 130 (2005)

Błażejowski, M., Sikora, M., Moderski, R., & Madejski, G. M.: *Comptonization of Infrared Radiation from Hot Dust by Relativistic Jets in Quasars.* ApJ, **545**, 107 (2000)

Bloom, S. D. & Marscher, A. P.: *An Analysis of the Synchrotron Self-Compton Model for the Multi–Wave Band Spectra of Blazars.* ApJ, **461**, 657 (1996)

Blümer, J., Engel, R., & Hörandel, J. R.: *Cosmic rays from the knee to the highest energies.* Progress in Particle and Nuclear Physics, **63**, 293 (2009)

Böttcher, M., Hivick, B., Dashti, J., *et al.*: *Optical Spectral Variability of the Very High Energy Gamma-ray Blazar 1ES 1011+496.* ApJ, **725**, 2344 (2010)

Böttcher, M. & Reimer, A.: *Modeling the Multiwavelength Spectra and Variability of BL Lacertae in 2000.* ApJ, **609**, 576 (2004)

Breeveld, A. A., Landsman, W., Holland, S. T., *et al.*: *An Updated Ultraviolet Calibration for the Swift/UVOT. In* J. E. McEnery, J. L. Racusin, & N. Gehrels (editors), *American Institute of Physics Conference Series*, volume 1358 of *American Institute of Physics Conference Series*, 373–376 (2011)

Bretz, T.: *Observations of the Active Galactic Nucleus 1ES 1218+304 with the MAGIC-telescope.* Ph.D. thesis, Bayerische Julius-Maximilians-Universität Würzburg (2006)

Bretz, T. & Dorner, D.: *MARS-The Cherenkov Observatory edition. In* F. A. Aharonian, W. Hofmann, & F. Rieger (editors), *American Institute of Physics Conference Series*, volume 1085 of *American Institute of Physics Conference Series*, 664–667 (2008)

Bretz, T., Dorner, D., Wagner, R., & MAGIC Collaboration: *The Tracking System of the MAGIC Telescope. In International Cosmic Ray Conference*, volume 5 of *International Cosmic Ray Conference*, 2943 (2003)

Bretz, T., Dorner, D., Wagner, R. M., & Sawallisch, P.: *The drive system of the major atmospheric gamma-ray imaging Cherenkov telescope.* Astroparticle Physics, **31**, 92 (2009)

Bridle, A. H. & Perley, R. A.: *Extragalactic Radio Jets.* ARA&A, **22**, 319 (1984)

Brinkmann, W., Papadakis, I. E., Raeth, C., Mimica, P., & Haberl, F.: *XMM-Newton timing mode observations of Mrk 421.* A&A, **443**, 397 (2005)

Britzen, S., Kam, V. A., Witzel, A., *et al.*: *Non-radial motion in the TeV blazar S5 0716+714. The pc-scale kinematics of a BL Lacertae object.* A&A, **508**, 1205 (2009)

Britzger, D., Carmona, E., Majumdar, P., *et al.*: *Studies of the Influence of Moonlight on Observations with the MAGIC Telescope.* ArXiv Astrophysics e-prints, astro-ph:0907.0973 (2009)

Browne, I. W. A.: *Is it possible to turn an elliptical radio galaxy into a BL Lac object?* MNRAS, **204**, 23P (1983)

Buehler, R., Scargle, J. D., Blandford, R. D., *et al.*: *Gamma-Ray Activity in the Crab Nebula: The Exceptional Flare of 2011 April.* ApJ, **749**, 26 (2012)

Caccianiga, A. & Marchã, M. J. M.: *The CLASS blazar survey: testing the blazar sequence.* MNRAS, **348**, 937 (2004)

Carini, M. T., Barnaby, D., Mattox, J. R., *et al.*: *Blazar variability studies with the 1.3m Robotically Controlled Telescope and the automated 0.6m Bell Observatory telescope.* Astronomische Nachrichten, **325**, 646 (2004)

Casandjian, J.-M. & Grenier, I. A.: *A revised catalogue of EGRET γ-ray sources.* A&A, **489**, 849 (2008)

Catanese, M., Akerlof, C. W., Badran, H. M., *et al.*: *Discovery of Gamma-Ray Emission above 350 GeV from the BL Lacertae Object 1ES 2344+514.* ApJ, **501**, 616 (1998)

Cerruti, M., Zech, A., Boisson, C., & Inoue, S.: *A mixed lepto-hadronic scenario for PKS 2155-304.* ArXiv Astrophysics e-prints, astro-ph:1210.5024 (2012)

Chadwick, P. M., Lyons, K., McComb, T. J. L., *et al.*: *PKS 2155-304 - a source of VHE gamma-rays.* Astroparticle Physics, **11**, 145 (1999)

Chen, L. & Bai, J. M.: *Implications for the Blazar Sequence and Inverse Compton Models from Fermi Bright Blazars.* ApJ, **735**, 108 (2011)

Chen, X., Fossati, G., Liang, E., & Böttcher, M.: *X-ray Time Lags in TeV Blazars.* Journal of Astrophysics and Astronomy, **32**, 185 (2011)

Coffey, D.: *The enigma of jets and outflows from young stars.* ArXiv Astrophysics e-prints, astro-ph:1112.2508 (2011)

Costamante, L.: *A Warning on the GeV-TeV Connection in Blazars.* ArXiv Astrophysics e-prints, astro-ph:1208.0810 (2012)

Costamante, L. & Ghisellini, G.: *TeV candidate BL Lac objects.* A&A, **384**, 56 (2002)

Costamante, L., Ghisellini, G., Giommi, P., *et al.*: *Extreme synchrotron BL Lac objects. Stretching the blazar sequence.* A&A, **371**, 512 (2001)

Cutri, R. M., Skrutskie, M. F., van Dyk, S., *et al.*: *2MASS All Sky Catalog of point sources.* (2003)

D'Ammando, F., Pucella, G., Raiteri, C. M., *et al.*: *AGILE detection of a rapid γ-ray flare from the blazar PKS 1510-089 during the GASP-WEBT monitoring.* A&A, **508**, 181 (2009)

De Lotto, B.: *The MAGIC telescopes: performance, results and future perspectives. In Topics in Astroparticle and Underground Physics* (2011)

Dermer, C. D., Finke, J. D., Krug, H., & Böttcher, M.: *Gamma-Ray Studies of Blazars: Synchro-Compton Analysis of Flat Spectrum Radio Quasars.* ApJ, **692**, 32 (2009)

Dermer, C. D. & Razzaque, S.: *Acceleration of Ultra-high-energy Cosmic Rays in the Colliding Shells of Blazars and Gamma-ray Bursts: Constraints from the Fermi Gamma-ray Space Telescope.* ApJ, **724**, 1366 (2010)

Dermer, C. D. & Schlickeiser, R.: *Model for the High-Energy Emission from Blazars.* ApJ, **416**, 458 (1993)

Dermer, C. D., Schlickeiser, R., & Mastichiadis, A.: *High-energy gamma radiation from extragalactic radio sources.* A&A, **256**, L27 (1992)

Doeleman, S. S., Fish, V. L., Schenck, D. E., *et al.*: *Jet-Launching Structure Resolved Near the Supermassive Black Hole in M87.* Science, **338**, 355 (2012)

Domínguez, A., Primack, J. R., Rosario, D. J., *et al.*: *Extragalactic background light inferred from AEGIS galaxy-SED-type fractions.* MNRAS, **410**, 2556 (2011)

Donato, D., Ghisellini, G., Tagliaferri, G., & Fossati, G.: *Hard X-ray properties of blazars.* A&A, **375**, 739 (2001)

Donato, D., Gliozzi, M., Sambruna, R. M., & Pesce, J. E.: *Chandra observations of the X-ray environment of BL Lacs.* A&A, **407**, 503 (2003)

Donato, D., Sambruna, R. M., & Gliozzi, M.: *Six years of BeppoSAX observations of blazars: A spectral catalog.* A&A, **433**, 1163 (2005)

Donea, A.-C. & Biermann, P. L.: *The Structure of Accretion Flow at the Base of Jets in AGN.* PASA, **19**, 125 (2002)

Donnarumma, I., Vittorini, V., Vercellone, S., *et al.*: *The June 2008 Flare of Markarian 421 from Optical to TeV Energies.* ApJ, **691**, L13 (2009)

Dorner, D., Nilsson, K., & Bretz, T.: *A method to correct IACT data for atmospheric absorption due to the Saharan Air Layer.* A&A, **493**, 721 (2009)

Dwek, E. & Krennrich, F.: *The Extragalactic Background Light and the Gamma-ray Opacity of the Universe.* ArXiv Astrophysics e-prints, astro-ph:1209.4661 (2012)

Edelson, R. A. & Krolik, J. H.: *The discrete correlation function - A new method for analyzing unevenly sampled variability data.* ApJ, **333**, 646 (1988)

Elvis, M., Plummer, D., Schachter, J., & Fabbiano, G.: *The Einstein Slew Survey.* ApJS, **80**, 257 (1992)

Engel, R., Heck, D., & Pierog, T.: *Extensive Air Showers and Hadronic Interactions at High Energy.* Annual Review of Nuclear and Particle Science, **61**, 467 (2011)

Fanaroff, B. L. & Riley, J. M.: *The morphology of extragalactic radio sources of high and low luminosity.* MNRAS, **167**, 31P (1974)

Fazio, G. G. & Stecker, F. W.: *Predicted High Energy Break in the Isotropic Gamma Ray Spectrum: a Test of Cosmological Origin.* Nature, **226**, 135 (1970)

Fitzpatrick, E. L.: *Correcting for the Effects of Interstellar Extinction.* PASP, **111**, 63 (1999)

Foschini, L.: *Jets (relativistic and non) in astrophysics.* ArXiv Astrophysics e-prints, astro-ph:1003.4212 (2010)

Fossati, G., Buckley, J. H., Bond, I. H., *et al.*: *Multiwavelength Observations of Markarian 421 in 2001 March: An Unprecedented View on the X-Ray/TeV Correlated Variability.* ApJ, **677**, 906 (2008)

Fossati, G., Maraschi, L., Celotti, A., Comastri, A., & Ghisellini, G.: *A unifying view of the spectral energy distributions of blazars.* MNRAS, **299**, 433 (1998)

Franceschini, A., Rodighiero, G., & Vaccari, M.: *Extragalactic optical-infrared background radiation, its time evolution and the cosmic photon-photon opacity.* A&A, **487**, 837 (2008)

Fuhrmann, L., Zensus, J. A., Krichbaum, T. P., Angelakis, E., & Readhead, A. C. S.: *Simultaneous Radio to (Sub-) mm-Monitoring of Variability and Spectral Shape Evolution of potential GLAST Blazars. In* S. Ritz, P. Michelson, & C. A. Meegan (editors), *The First GLAST Symposium*, volume 921 of *American Institute of Physics Conference Series*, 249–251 (2007)

Garczarczyk, M., Merck, M., Danielyan, V., *et al.*: *The Active Mirror Control of the MAGIC Telescope. In International Cosmic Ray Conference*, volume 5 of *International Cosmic Ray Conference*, 2935 (2003)

Gaur, H., Gupta, A. C., Lachowicz, P., & Wiita, P. J.: *Detection of Intra-day Variability Timescales of Four High-energy Peaked Blazars with XMM-Newton.* ApJ, **718**, 279 (2010)

Gaur, H., Gupta, A. C., Strigachev, A., *et al.*: *Optical flux and spectral variability of blazars.* MNRAS, **425**, 3002 (2012a)

Gaur, H., Gupta, A. C., Strigachev, A., *et al.*: *Quasi-simultaneous two-band optical variability of the blazars 1ES 1959+650 and 1ES 2344+514.* MNRAS, **420**, 3147 (2012b)

Gaur, H., Gupta, A. C., & Wiita, P. J.: *Multiwavelength Variability of the Blazars Mrk 421 and 3C 454.3 in the High State.* AJ, **143**, 23 (2012c)

Gehrels, N., Chincarini, G., Giommi, P., *et al.*: *The Swift Gamma-Ray Burst Mission.* ApJ, **611**, 1005 (2004)

Georganopoulos, M., Finke, J. D., & Reyes, L. C.: *A Method for Setting Upper Limits to the Extragalactic Background Light with Fermi-lat and TeV Observations of Blazars.* ApJ, **714**, L157 (2010)

Georganopoulos, M. & Kazanas, D.: *Decelerating Flows in TeV Blazars: A Resolution to the BL Lacertae-FR I Unification Problem.* ApJ, **594**, L27 (2003)

Ghirlanda, G., Ghisellini, G., Tavecchio, F., Foschini, L., & Bonnoli, G.: *The radio-γ-ray connection in Fermi blazars.* MNRAS, **413**, 852 (2011)

Ghisellini, G.: *Extreme blazars.* Astroparticle Physics, **11**, 11 (1999)

Ghisellini, G.: *Electron-positron pairs in blazar jets and γ-ray loud radio galaxies.* MNRAS, **424**, L26 (2012)

Ghisellini, G., Celotti, A., Fossati, G., Maraschi, L., & Comastri, A.: *A theoretical unifying scheme for gamma-ray bright blazars.* MNRAS, **301**, 451 (1998)

Ghisellini, G., Della Ceca, R., Volonteri, M., *et al.*: *Chasing the heaviest black holes of jetted active galactic nuclei.* MNRAS, **405**, 387 (2010a)

Ghisellini, G., Foschini, L., Tavecchio, F., & Pian, E.: *On the 2007 July flare of the blazar 3C 454.3.* MNRAS, **382**, L82 (2007)

Ghisellini, G. & Madau, P.: *On the origin of the gamma-ray emission in blazars.* MNRAS, **280**, 67 (1996)

Ghisellini, G., Maraschi, L., & Tavecchio, F.: *The Fermi blazars' divide.* MNRAS, **396**, L105 (2009)

Ghisellini, G. & Tavecchio, F.: *Rapid variability in TeV blazars: the case of PKS2155-304.* MNRAS, **386**, L28 (2008a)

Ghisellini, G. & Tavecchio, F.: *The blazar sequence: a new perspective.* MNRAS, **387**, 1669 (2008b)

Ghisellini, G., Tavecchio, F., & Chiaberge, M.: *Structured jets in TeV BL Lac objects and radiogalaxies. Implications for the observed properties.* A&A, **432**, 401 (2005)

Ghisellini, G., Tavecchio, F., Foschini, L., & Ghirlanda, G.: *The transition between BL Lac objects and flat spectrum radio quasars.* MNRAS, **414**, 2674 (2011)

Ghisellini, G., Tavecchio, F., Foschini, L., *et al.*: *General physical properties of bright Fermi blazars.* MNRAS, **402**, 497 (2010b)

Ghisellini, G., Tavecchio, F., Foschini, L., *et al.*: *Blue Fermi flat spectrum radio quasars.* MNRAS, **425**, 1371 (2012)

Giannios, D., Uzdensky, D. A., & Begelman, M. C.: *Fast TeV variability in blazars: jets in a jet.* MNRAS, **395**, L29 (2009)

Giommi, P., Barr, P., Pollock, A. M. T., Garilli, B., & Maccagni, D.: *A study of BL Lacertae-type objects with Exosat. I - Flux correlations, luminosity variability, and spectral variability.* ApJ, **356**, 432 (1990)

Giommi, P., Capalbi, M., Fiocchi, M., *et al.*: *A Catalog of 157 X-ray Spectra and 84 Spectral Energy Distributions of Blazars Observed with BeppoSAX. In* P. Giommi, E. Massaro, & G. Palumbo (editors), *Blazar Astrophysics with BeppoSAX and Other Observatories*, 63 (2002)

Giommi, P., Massaro, E., Padovani, P., *et al.*: *ROXA J081009.9+384757.0: a 10^{47} erg s^{-1} blazar with hard X-ray synchrotron peak or a new type of radio loud AGN?* A&A, **468**, 97 (2007)

Giommi, P., Padovani, P., & Perlman, E.: *Detection of exceptional X-ray spectral variability in the TeV BL Lac 1ES 2344+514.* MNRAS, **317**, 743 (2000)

Giommi, P., Padovani, P., Polenta, G., *et al.*: *A simplified view of blazars: clearing the fog around long-standing selection effects.* MNRAS, **420**, 2899 (2012a)

Giommi, P., Polenta, G., Lähteenmäki, A., *et al.*: *Simultaneous Planck, Swift, and Fermi observations of X-ray and γ-ray selected blazars.* A&A, **541**, A160 (2012b)

Giroletti, M., Giovannini, G., Taylor, G. B., & Falomo, R.: *A Sample of Low-Redshift BL Lacertae Objects. I. The Radio Data.* ApJ, **613**, 752 (2004)

Gliozzi, M., Sambruna, R. M., Jung, I., *et al.*: *Long-Term X-Ray and TeV Variability of Mrk 501.* ApJ, **646**, 61 (2006)

Gómez, J. L. & Steffen, W.: *Agujeros negros supermasivos.* Investigación y Ciencia, **396**, 30 (2009)

Gopal-Krishna, Goyal, A., Joshi, S., *et al.*: *Rapid optical variability of TeV blazars.* MNRAS, **416**, 101 (2011)

Gould, R. J. & Schréder, G. P.: *Opacity of the Universe to High-Energy Photons.* Physical Review, **155**, 1408 (1967)

Greiner, J., Mannheim, K., Aharonian, F., *et al.*: *GRIPS - Gamma-Ray Imaging, Polarimetry and Spectroscopy.* Experimental Astronomy, **34**, 551 (2012)

Grupen, C.: *Astroteilchenphysik: Das Universum im Licht der kosmischen Strahlung.* Springer (2000)

Hartman, R. C., Bertsch, D. L., Bloom, S. D., *et al.*: *The Third EGRET Catalog of High-Energy Gamma-Ray Sources.* ApJS, **123**, 79 (1999)

Heck, D., Knapp, J., Capdevielle, J. N., Schatz, G., & Thouw, T.: *CORSIKA: a Monte Carlo code to simulate extensive air showers.* (1998)

Hillas, A. M.: *Cerenkov light images of EAS produced by primary gamma. In* F. C. Jones (editor), *International Cosmic Ray Conference*, volume 3 of *International Cosmic Ray Conference*, 445–448 (1985)

Hofmann, W.: *Very High Energy gamma-ray emission from AP Lib detected by H.E.S.S.* The Astronomer's Telegram, **2743**, 1 (2010a)

Hofmann, W.: *Very high energy gamma-ray emission from SHBL J001355.9-185406 detected by HESS.* The Astronomer's Telegram, **3007**, 1 (2010b)

Hofmann, W. & Fegan, S.: *H.E.S.S. and Fermi-LAT discovery of VHE and HE emission from blazar 1ES 0414+009.* The Astronomer's Telegram, **2293**, 1 (2009)

Högbom, J. A.: *Aperture Synthesis with a Non-Regular Distribution of Interferometer Baselines.* A&AS, **15**, 417 (1974)

Höhne-Mönch, D.: *Steady-state emission of blazars at very high energies.* Ph.D. thesis, Bayerische Julius-Maximilians-Universität Würzburg (2010)

Horan, D., Acciari, V. A., Bradbury, S. M., *et al.*: *Multiwavelength Observations of Markarian 421 in 2005-2006.* ApJ, **695**, 596 (2009)

Horan, D. & VERITAS Collaboration: *Observations of 1H1426+428 with the Whipple 10 m imaging atmospheric Cherenkov telescope. In International Cosmic Ray Conference*, volume 7 of *International Cosmic Ray Conference*, 2622 (2001)

Hovatta, T., Lister, M. L., Aller, M. F., *et al.*: *MOJAVE: Monitoring of Jets in Active Galactic Nuclei with VLBA Experiments. VIII. Faraday Rotation in Parsec-scale AGN Jets.* AJ, **144**, 105 (2012)

Hovatta, T., Nieppola, E., Tornikoski, M., *et al.*: *Long-term radio variability of AGN: flare characteristics.* A&A, **485**, 51 (2008)

Hovatta, T., Tornikoski, M., Lainela, M., *et al.*: *Statistical analyses of long-term variability of AGN at high radio frequencies.* A&A, **469**, 899 (2007)

Huarte-Espinosa, M., Frank, A., & Blackman, E.: *Laboratory experiments and simulations on jets.* ArXiv Astrophysics e-prints, astro-ph:1111.4223 (2011)

Inoue, S.: *Origin of ultra-high energy cosmic rays in the era of Auger and Telescope Array.* Journal of Physics Conference Series, **120**, 6, 062001 (2008)

Jones, T. W., O'dell, S. L., & Stein, W. A.: *Physics of Compact Nonthermal Sources. I. Theory of Radiation Processes.* ApJ, **188**, 353 (1974)

Karlsson, N. & for the VERITAS collaboration: *Discovery of VHE Gamma-ray Emission from the Starburst Galaxy M82.* ArXiv Astrophysics e-prints, astro-ph:0912.3807 (2009)

Karouzos, M., Britzen, S., Witzel, A., Zensus, J. A., & Eckart, A.: *Deconstructing blazars: A different scheme for jet kinematics in flat-spectrum AGN.* A&A, **537**, A112 (2012)

Kataoka, J., Takahashi, T., Makino, F., *et al.*: *Variability Pattern and the Spectral Evolution of the BL Lacertae Object PKS 2155-304.* ApJ, **528**, 243 (2000)

Kaufmann, S., Wagner, S. J., Tibolla, O., & Hauser, M.: *1ES 0229+200: an extreme blazar with a very high minimum Lorentz factor.* A&A, **534**, A130 (2011)

Kellermann, K. I., Sramek, R., Schmidt, M., Shaffer, D. B., & Green, R.: *VLA observations of objects in the Palomar Bright Quasar Survey.* AJ, **98**, 1195 (1989)

Kharb, P., Gabuzda, D., & Shastri, P.: *Parsec-scale magnetic field structures in HEAO-1 BL Lacs.* MNRAS, **384**, 230 (2008)

Kharb, P., Lister, M. L., & Cooper, N. J.: *Extended Radio Emission in MOJAVE Blazars: Challenges to Unification.* ApJ, **710**, 764 (2010)

Kirk, J. G., Rieger, F. M., & Mastichiadis, A.: *Particle acceleration and synchrotron emission in blazar jets.* A&A, **333**, 452 (1998)

Kneiske, T. M., Bretz, T., Mannheim, K., & Hartmann, D. H.: *Implications of cosmological gamma-ray absorption. II. Modification of gamma-ray spectra.* A&A, **413**, 807 (2004)

Kneiske, T. M. & Dole, H.: *A lower-limit flux for the extragalactic background light.* A&A, **515**, A19 (2010)

Kollgaard, R. I., Wardle, J. F. C., Roberts, D. H., & Gabuzda, D. C.: *Radio constraints on the nature of BL Lacertae objects and their parent population.* AJ, **104**, 1687 (1992)

Komissarov, S. S.: *Magnetic acceleration of relativistic jets.* Mem. Soc. Astron. Italiana, **82**, 95 (2011)

Königl, A.: *Relativistic jets as X-ray and gamma-ray sources.* ApJ, **243**, 700 (1981)

Krawczynski, H., Hughes, S. B., Horan, D., *et al.*: *Multiwavelength Observations of Strong Flares from the TeV Blazar 1ES 1959+650.* ApJ, **601**, 151 (2004)

Krennrich, F., Bond, I. H., Bradbury, S. M., *et al.*: *Discovery of Spectral Variability of Markarian 421 at TeV Energies.* ApJ, **575**, L9 (2002)

Krennrich, F., Dwek, E., & Imran, A.: *Constraints on Energy Spectra of Blazars based on Recent EBL Limits from Galaxy Counts.* ApJ, **689**, L93 (2008)

Lafferty, G. D. & Wyatt, T. R.: *Where to stick your data points: The treatment of measurements within wide bins.* Nuclear Instruments and Methods in Physics Research A, **355**, 541 (1995)

Lähteenmäki, A. & Valtaoja, E.: *Total Flux Density Variations in Extragalactic Radio Sources. III. Doppler Boosting Factors, Lorentz Factors, and Viewing Angles for Active Galactic Nuclei.* ApJ, **521**, 493 (1999)

Lamer, G., Brunner, H., & Staubert, R.: *ROSAT observations of BL Lacertae objects.* A&A, **311**, 384 (1996)

Landt, H. & Bignall, H. E.: *On the relationship between BL Lacertae objects and radio galaxies.* MNRAS, **391**, 967 (2008)

Landt, H., Padovani, P., Giommi, P., Perri, M., & Cheung, C. C.: *A Search for Synchrotron X-Ray Emission in Radio Quasars.* ApJ, **676**, 87 (2008)

Larsson, S., Fuhrmann, L., Weiss, A., *et al.*: *APEX sub-mm monitoring of gamma-ray blazars.* ArXiv Astrophysics e-prints, astro-ph:1206.3799 (2012)

Laurent-Muehleisen, S. A., Kollgaard, R. I., Ciardullo, R., *et al.*: *Radio-loud Active Galaxies in the Northern ROSAT All-Sky Survey. III. New Spectroscopic Identifications from the RASS-Green Bank BL Lacertae Survey.* ApJS, **118**, 127 (1998)

Laurent-Muehleisen, S. A., Kollgaard, R. I., Feigelson, E. D., Brinkmann, W., & Siebert, J.: *The RGB Sample of Intermediate BL Lacertae Objects.* ApJ, **525**, 127 (1999)

Leahy, D. A. & Tian, W. W.: *The HI absorption distance of HESS J1943+213 favours its extragalactic nature.* A&A, **539**, A128 (2012)

Lebrun, F., Leray, J. P., Lavocat, P., *et al.*: *ISGRI: The INTEGRAL Soft Gamma-Ray Imager.* A&A, **411**, L141 (2003)

Lefa, E., Rieger, F. M., & Aharonian, F.: *Formation of Very Hard Gamma-Ray Spectra of Blazars in Leptonic Models.* ApJ, **740**, 64 (2011)

Letessier-Selvon, A. & Stanev, T.: *Ultrahigh energy cosmic rays.* Reviews of Modern Physics, **83**, 907 (2011)

Levine, A. M., Bradt, H., Cui, W., *et al.*: *First Results from the All-Sky Monitor on the Rossi X-Ray Timing Explorer.* ApJ, **469**, L33 (1996)

Levinson, A.: *On the Origin of Rapid Flares in TeV Blazars.* ApJ, **671**, L29 (2007)

Li, T.-P. & Ma, Y.-Q.: *Analysis methods for results in gamma-ray astronomy.* ApJ, **272**, 317 (1983)

Lichti, G. G., Bottacini, E., Ajello, M., *et al.*: *INTEGRAL observations of the blazar Mrk 421 in outburst. Results of a multi-wavelength campaign.* A&A, **486**, 721 (2008)

Lister, M. L., Aller, H. D., Aller, M. F., *et al.*: *MOJAVE: Monitoring of Jets in Active Galactic Nuclei with VLBA Experiments. V. Multi-Epoch VLBA Images.* AJ, **137**, 3718 (2009a)

Lister, M. L., Cohen, M. H., Homan, D. C., *et al.*: *MOJAVE: Monitoring of Jets in Active Galactic Nuclei with VLBA Experiments. VI. Kinematics Analysis of a Complete Sample of Blazar Jets.* AJ, **138**, 1874 (2009b)

Liu, X., Song, H.-G., Liu, J., *et al.*: *Radio observations of the first three-months of Fermi AGN at 4.8 GHz.* Research in Astronomy and Astrophysics, **12**, 147 (2012a)

Liu, X., Song, H.-G., Marchili, N., *et al.*: *Intra-day variability observations of S5 0716+714 over 4.5 years at 4.8 GHz.* A&A, **543**, A78 (2012b)

Lobanov, A. P.: *Ultracompact jets in active galactic nuclei.* A&A, **330**, 79 (1998)

Majumdar, P., Moralejo, A., Bigongiari, C., Blanch, O., & Sobczynska, D.: *Monte Carlo simulation for the MAGIC telescope. In International Cosmic Ray Conference*, volume 5 of *International Cosmic Ray Conference*, 203 (2005)

Malkov, M. A. & O'C Drury, L.: *Nonlinear theory of diffusive acceleration of particles by shock waves.* Reports on Progress in Physics, **64**, 429 (2001)

Mankuzhiyil, N., Ansoldi, S., Persic, M., & Tavecchio, F.: *The Environment and Distribution of Emitting Electrons as a Function of Source Activity in Markarian 421.* ApJ, **733**, 14 (2011)

Mankuzhiyil, N., Ansoldi, S., Persic, M., *et al.*: *Emitting Electrons and Source Activity in Markarian 501.* ApJ, **753**, 154 (2012)

Mannheim, K.: *The proton blazar.* A&A, **269**, 67 (1993)

Mannheim, K. & Biermann, P. L.: *Gamma-ray flaring of 3C 279 - A proton-initiated cascade in the jet?* A&A, **253**, L21 (1992)

Maraschi, L., Foschini, L., Ghisellini, G., Tavecchio, F., & Sambruna, R. M.: *Testing the blazar spectral sequence: X-ray-selected blazars.* MNRAS, **391**, 1981 (2008a)

Maraschi, L., Ghisellini, G., & Celotti, A.: *A jet model for the gamma-ray emitting blazar 3C 279.* ApJ, **397**, L5 (1992)

Maraschi, L., Ghisellini, G., Tavecchio, F., Foschini, L., & Sambruna, R. M.: *The Spectral Sequence of Blazars – Status and Perspectives.* International Journal of Modern Physics D, **17**, 1457 (2008b)

Maraschi, L. & Tavecchio, F.: *The Jet-Disk Connection and Blazar Unification.* ApJ, **593**, 667 (2003)

Mariotti, M.: *Discovery of Very High Energy gamma-ray emission from 1FGL J2001.1+4351 by MAGIC.* The Astronomer's Telegram, **2753**, 1 (2010a)

Mariotti, M.: *MAGIC detects a VHE flare from 4C +21.35 (PKS 1222+21).* The Astronomer's Telegram, **2684**, 1 (2010b)

Mariotti, M.: *MAGIC detects VHE gamma-ray emission from IC 310.* The Astronomer's Telegram, **2510**, 1 (2010c)

Mariotti, M.: *Discovery of Very High Energy Gamma-Ray Emission from 1ES 1215+303 by MAGIC.* The Astronomer's Telegram, **3100**, 1 (2011a)

Mariotti, M.: *MAGIC discovers VHE gamma-ray emission from the blazar 1ES 1727+502.* The Astronomer's Telegram, **3774**, 1 (2011b)

Mariotti, M.: *VHE detection of the blazar 1ES 0033+595 by MAGIC.* The Astronomer's Telegram, **3719**, 1 (2011c)

Mariotti, M. & MAGIC Collaboration: *Discovery of Very High Energy Gamma-Ray Emission from B3 2247+381 by MAGIC.* The Astronomer's Telegram, **2910**, 1 (2010a)

Mariotti, M. & MAGIC Collaboration: *Discovery of Very High Energy Gamma-Ray Emission from NGC1275 by MAGIC.* The Astronomer's Telegram, **2916**, 1 (2010b)

Marscher, A. P.: *Relativistic Jets in Active Galactic Nuclei. In* P. A. Hughes & J. N. Bregman (editors), *Relativistic Jets: The Common Physics of AGN, Microquasars, and Gamma-Ray Bursts*, volume 856 of *American Institute of Physics Conference Series*, 1–22 (2006)

Marscher, A. P.: *The Core of a Blazar Jet. In* T. A. Rector & D. S. De Young (editors), *Extragalactic Jets: Theory and Observation from Radio to Gamma Ray*, volume 386 of *Astronomical Society of the Pacific Conference Series*, 437 (2008)

Marscher, A. P.: *Multi-waveband Variations of Blazars during Gamma-ray Outbursts.* ArXiv Astrophysics e-prints, astro-ph:1201.5402 (2012)

Marscher, A. P. & Gear, W. K.: *Models for high-frequency radio outbursts in extragalactic sources, with application to the early 1983 millimeter-to-infrared flare of 3C 273.* ApJ, **298**, 114 (1985)

Marscher, A. P., Jorstad, S. G., D'Arcangelo, F. D., *et al.*: *The inner jet of an active galactic nucleus as revealed by a radio-to-γ-ray outburst.* Nature, **452**, 966 (2008)

Marscher, A. P., Jorstad, S. G., Larionov, V. M., *et al.*: *Probing the Inner Jet of the Quasar PKS 1510-089 with Multi-Waveband Monitoring During Strong Gamma-Ray Activity.* ApJ, **710**, L126 (2010)

Massaro, E., Giommi, P., Leto, C., *et al.*: *Roma-BZCAT: a multifrequency catalogue of blazars.* A&A, **495**, 691 (2009)

Massaro, F., Tramacere, A., Cavaliere, A., Perri, M., & Giommi, P.: *X-ray spectral evolution of TeV BL Lacertae objects: eleven years of observations with BeppoSAX, XMM-Newton and Swift satellites.* A&A, **478**, 395 (2008)

Mastichiadis, A. & Kirk, J. G.: *Variability in the synchrotron self-Compton model of blazar emission.* A&A, **320**, 19 (1997)

Matsuoka, M., Kawasaki, K., Ueno, S., *et al.*: *The MAXI Mission on the ISS: Science and Instruments for Monitoring All-Sky X-Ray Images.* PASJ, **61**, 999 (2009)

Mazin, D.: *Highlights from MAGIC. In 5th International Symposium on High-Energy Gamma-Ray Astronomy* (2012)

McCall, M. L. & Armour, M.-H.: *Extinction of Galaxies by the Milky Way: Bringing R Out of Obscurity. In* R. C. Kraan-Korteweg, P. A. Henning, & H. Andernach (editors), *Mapping the Hidden Universe: The Universe behind the Mily Way - The Universe in HI*, volume 218 of *Astronomical Society of the Pacific Conference Series*, 1–58381 (2000)

Meyer, E. T., Fossati, G., Georganopoulos, M., & Lister, M. L.: *From the Blazar Sequence to the Blazar Envelope: Revisiting the Relativistic Jet Dichotomy in Radio-loud Active Galactic Nuclei.* ApJ, **740**, 98 (2011)

Meyer, M.: *Observations of a systematic selected sample of high frequency peaked BL Lac objects with the MAGIC telescope.* Ph.D. thesis, Bayerische Julius-Maximilians-Universität Würzburg (2008)

Meyer, M., Raue, M., Mazin, D., & Horns, D.: *Limits on the extragalactic background light in the Fermi era.* A&A, **542**, A59 (2012)

Mirabel, I. F.: *Relativistic jets in the universe.* New A Rev., **47**, 471 (2003)

Mücke, A. & Protheroe, R. J.: *Modeling the April 1997 flare of Mkn 501. In* B. L. Dingus, M. H. Salamon, & D. B. Kieda (editors), *American Institute of Physics Conference Series*, volume 515 of *American Institute of Physics Conference Series*, 149–153 (2000)

Mücke, A., Protheroe, R. J., Engel, R., Rachen, J. P., & Stanev, T.: *BL Lac objects in the synchrotron proton blazar model.* Astroparticle Physics, **18**, 593 (2003)

Müller, C., Kadler, M., Ojha, R., *et al.*: *Dual-frequency VLBI study of Centaurus A on sub-parsec scales. The highest-resolution view of an extragalactic jet.* A&A, **530**, L11 (2011)

Murase, K., Dermer, C. D., Takami, H., & Migliori, G.: *Blazars as Ultra-high-energy Cosmic-ray Sources: Implications for TeV Gamma-Ray Observations.* ApJ, **749**, 63 (2012)

Nakagawa, A., Edwards, P. G., Murata, Y., Wajima, K., & Modaka, T.: *VSOP Observations of the Gamma-Ray Sources J1733-1304, J1625-2527, and J1015+4926.* PASJ, **57**, 295 (2005)

Nalewajko, K., Giannios, D., Begelman, M. C., Uzdensky, D. A., & Sikora, M.: *Radiative properties of reconnection-powered minijets in blazars.* MNRAS, **413**, 333 (2011)

Nalewajko, K., Sikora, M., Madejski, G. M., *et al.*: *Herschel PACS and SPIRE Observations of Blazar PKS 1510-089: A Case for Two Blazar Zones.* ApJ, **760**, 69 (2012)

Napier, P. J.: *VLBA Design. In* J. A. Zensus, P. J. Diamond, & P. J. Napier (editors), *Very Long Baseline Interferometry and the VLBA*, volume 82 of *Astronomical Society of the Pacific Conference Series*, 59 (1995)

Nieppola, E., Hovatta, T., Tornikoski, M., *et al.*: *Long-Term Variability of Radio-Bright BL Lacertae Objects.* AJ, **137**, 5022 (2009)

Nieppola, E., Tornikoski, M., Lähteenmäki, A., *et al.*: *37 GHz Observations of a Large Sample of BL Lacertae Objects.* AJ, **133**, 1947 (2007)

Nieppola, E., Tornikoski, M., & Valtaoja, E.: *Spectral energy distributions of a large sample of BL Lacertae objects.* A&A, **445**, 441 (2006)

Nieppola, E., Tornikoski, M., Valtaoja, E., *et al.*: *Correlation between Fermi/LAT gamma-ray and 37 GHz radio properties of northern AGN averaged over 11 months.* A&A, **535**, A69 (2011)

Nieppola, E., Valtaoja, E., Tornikoski, M., Hovatta, T., & Kotiranta, M.: *Blazar sequence - an artefact of Doppler boosting.* A&A, **488**, 867 (2008)

Nilsson, K., Pasanen, M., Takalo, L. O., *et al.*: *Host galaxy subtraction of TeV candidate BL Lacertae objects.* A&A, **475**, 199 (2007)

Nilsson, K., Pursimo, T., Takalo, L. O., *et al.*: *Two-dimensional Photometric Decomposition of the TeV BL Lacertae Objects Markarian 421, Markarian 501, and 1ES 2344+514.* PASP, **111**, 1223 (1999)

Nishiyama, T.: *Detection of a new TeV gamma-ray source of BL Lac object 1ES 1959+650. In International Cosmic Ray Conference*, volume 3 of *International Cosmic Ray Conference*, 370 (1999)

Nolan, P. L., Abdo, A. A., Ackermann, M., *et al.*: *Fermi Large Area Telescope Second Source Catalog.* ApJS, **199**, 31 (2012)

Ojha, R., Kadler, M., Böck, M., *et al.*: *TANAMI: tracking active galactic nuclei with austral milliarcsecond interferometry . I. First-epoch 8.4 GHz images.* A&A, **519**, A45 (2010)

Ong, R.: *VERITAS Discovery of VHE Gamma-Ray Emission from BL Lac object RGB J0710+591.* The Astronomer's Telegram, **1941**, 1 (2009a)

Ong, R. A.: *Discovery of VHE Gamma-Ray Emission from the Fermi-LAT Source 1ES 0502+675.* The Astronomer's Telegram, **2301**, 1 (2009b)

Ong, R. A.: *Discovery of VHE Gamma-Ray Emission from the Fermi-LAT Source PKS 1424+240.* The Astronomer's Telegram, **2084**, 1 (2009c)

Ong, R. A.: *VERITAS discovery of a new VHE Gamma-ray Source, VER J0521+211.* The Astronomer's Telegram, **2260**, 1 (2009d)

Ong, R. A.: *Discovery of Very High Energy Gamma-ray Emission from the Blazar 1ES 1440+122.* The Astronomer's Telegram, **2786**, 1 (2010)

Ong, R. A. & Fortin, P.: *Discovery of High-Energy Gamma-Ray Emission from the BL Lac Object RBS 0413.* The Astronomer's Telegram, **2272**, 1 (2009)

Ong, R. A., VERITAS Collaboration, Paneque, D., & Fermi Large Area Telescope: *VERITAS Discovery of Very High-Energy Gamma-Ray Emission from 1FGL J0648.8+1516.* The Astronomer's Telegram, **2486**, 1 (2010)

Orr, M. R., Krennrich, F., & Dwek, E.: *Strong New Constraints on the Extragalactic Background Light in the Near- to Mid-infrared.* ApJ, **733**, 77 (2011)

Padovani, P.: *A statistical analysis of complete samples of BL Lacertae objects.* A&A, **256**, 399 (1992)

Padovani, P.: *The blazar sequence: validity and predictions.* Ap&SS, **309**, 63 (2007)

Padovani, P., Costamante, L., Ghisellini, G., Giommi, P., & Perlman, E.: *BeppoSAX Observations of Synchrotron X-Ray Emission from Radio Quasars.* ApJ, **581**, 895 (2002)

Padovani, P. & Giommi, P.: *The connection between x-ray- and radio-selected BL Lacertae objects.* ApJ, **444**, 567 (1995)

Padovani, P. & Giommi, P.: *The ROSAT X-ray spectra of BL Lacertae objects.* MNRAS, **279**, 526 (1996)

Padovani, P., Giommi, P., & Rau, A.: *The discovery of high-power high synchrotron peak blazars.* MNRAS, **422**, L48 (2012)

Padovani, P., Perlman, E. S., Landt, H., Giommi, P., & Perri, M.: *What Types of Jets Does Nature Make? A New Population of Radio Quasars.* ApJ, **588**, 128 (2003)

Paneque, D., Gebauer, H. J., Lorenz, E., & Mirzoyan, R.: *A method to enhance the sensitivity of photomultipliers for Air Cherenkov Telescopes by applying a lacquer that scatters light.* Nuclear Instruments and Methods in Physics Research A, **518**, 619 (2004)

Perlman, E. S., Stocke, J. T., Schachter, J. F., *et al.*: *The Einstein Slew Survey Sample of BL Lacertae Objects.* ApJS, **104**, 251 (1996)

Pian, E.: *X-ray Variability of Blazars.* PASA, **19**, 49 (2002)

Pian, E., Foschini, L., Beckmann, V., *et al.*: *INTEGRAL observations of the blazar 3C 454.3 in outburst.* A&A, **449**, L21 (2006)

Pian, E., Vacanti, G., Tagliaferri, G., *et al.*: *BeppoSAX Observations of Unprecedented Synchrotron Activity in the BL Lacertae Object Markarian 501.* ApJ, **492**, L17 (1998)

Pichel, A.: *Highlights from the Whipple 10-m Blazar Monitoring Program.* ArXiv Astrophysics e-prints, astro-ph:0908.0010 (2009)

Piner, B. G. & Edwards, P. G.: *The Parsec-Scale Structure and Jet Motions of the TeV Blazars 1ES 1959+650, PKS 2155-304, and 1ES 2344+514.* ApJ, **600**, 115 (2004)

Piner, B. G., Pant, N., & Edwards, P. G.: *The Parsec-Scale Jets of the TeV Blazars H1426+428, 1ES 1959+650, and PKS 2155-304: 2001-2004.* ApJ, **678**, 64 (2008)

Piner, B. G., Pant, N., & Edwards, P. G.: *The Jets of TeV Blazars at Higher Resolution: 43 GHz and Polarimetric VLBA Observations from 2005 to 2009.* ApJ, **723**, 1150 (2010)

Poole, T. S., Breeveld, A. A., Page, M. J., *et al.*: *Photometric calibration of the Swift ultraviolet/optical telescope.* MNRAS, **383**, 627 (2008)

Punch, M., Akerlof, C. W., Cawley, M. F., *et al.*: *Detection of TeV photons from the active galaxy Markarian 421.* Nature, **358**, 477 (1992)

Quinn, J., Akerlof, C. W., Biller, S., *et al.*: *Detection of Gamma Rays with $E > 300$ GeV from Markarian 501.* ApJ, **456**, L83 (1996)

Raiteri, C. M., Villata, M., Bruschini, L., *et al.*: *Another look at the BL Lacertae flux and spectral variability. Observations by GASP-WEBT, XMM-Newton, and Swift in 2008-2009.* A&A, **524**, A43 (2010)

Raiteri, C. M., Villata, M., Larionov, V. M., *et al.*: *A new activity phase of the blazar <ASTROBJ>3C 454.3</ASTROBJ>. Multifrequency observations by the WEBT and XMM-Newton in 2007-2008.* A&A, **491**, 755 (2008)

Rani, B., Gupta, A. C., Strigachev, A., *et al.*: *Short-term flux and colour variations in low-energy peaked blazars.* MNRAS, **404**, 1992 (2010)

Raue, M., Behera, B., Charbonnier, A., *et al.*: *H.E.S.S. discovers VHE emission from the Fermi LAT source PKS 0447-439.* The Astronomer's Telegram, **2350**, 1 (2009)

Raue, M. & Mazin, D.: *EBL studies with ground-based VHE gamma-ray detectors: Current status and potential of next-generation instruments.* ArXiv Astrophysics e-prints, astro-ph:1106.4384 (2011)

Ravasio, M., Tagliaferri, G., Ghisellini, G., & Tavecchio, F.: *Observing Mkn 421 with XMM-Newton: The EPIC-PN point of view.* A&A, **424**, 841 (2004)

Rector, T. A., Gabuzda, D. C., & Stocke, J. T.: *The Radio Structure of High-Energy-Peaked BL Lacertae Objects.* AJ, **125**, 1060 (2003)

Rector, T. A. & Stocke, J. T.: *The Properties of the Radio-Selected 1 Jy Sample of BL Lacertae Objects.* AJ, **122**, 565 (2001)

Reinthal, R., Lindfors, E. J., Mazin, D., *et al.*: *Connection Between Optical and VHE Gamma-ray Emission in Blazar Jets.* Journal of Physics Conference Series, **355**, 1, 012013 (2012)

Richards, J. L., Max-Moerbeck, W., Pavlidou, V., *et al.*: *Blazars in the Fermi Era: The OVRO 40 m Telescope Monitoring Program.* ApJS, **194**, 29 (2011)

Richter, S. & Spanier, F.: *a Spatially Resolved SSC Shock-In Model.* International Journal of Modern Physics Conference Series, **8**, 392 (2012)

Riegel, B., Bretz, T., Dorner, D., Berger, K., & Höhne, D.: *A systematic study of the interdependence of IACT image parameters. In International Cosmic Ray Conference*, volume 5 of *International Cosmic Ray Conference*, 215 (2005)

Rolke, W. A., López, A. M., & Conrad, J.: *Limits and confidence intervals in the presence of nuisance parameters.* Nuclear Instruments and Methods in Physics Research A, **551**, 493 (2005)

Rügamer, S.: *Systematische Studien der Verwendung der Zeitstruktur von Luftschauern zur Reduktion des Untergrundes in MAGIC-Daten.* Diploma thesis, Bayerische Julius-Maximilians-Universität Würzburg (2006)

Rügamer, S., Angelakis, E., Bastieri, D., *et al.*: *MAGIC and Multi-Wavelength Observations of Mrk 180 and 1ES 2344+514 in 2008.* ArXiv Astrophysics e-prints, astro-ph:1109.6808 (2011)

Rüger, M., Spanier, F., & Mannheim, K.: *Spectral modelling of 1 ES 1218+30.4.* MNRAS, **401**, 973 (2010)

Sambruna, R. M., Barr, P., Giommi, P., *et al.*: *The X-ray spectra of blazars observed with EXOSAT.* ApJ, **434**, 468 (1994)

Sambruna, R. M., Donato, D., Ajello, M., *et al.*: *Swift Burst Alert Telescope, Fermi Large Area Telescope, and the Blazar Sequence.* ApJ, **710**, 24 (2010)

Sambruna, R. M., Maraschi, L., & Urry, C. M.: *On the Spectral Energy Distributions of Blazars.* ApJ, **463**, 444 (1996)

Sato, R., Kataoka, J., Takahashi, T., *et al.*: *Suzaku Observation of the TeV Blazar 1ES 1218+304: Clues on Particle Acceleration in an Extreme TeV Blazar.* ApJ, **680**, L9 (2008)

Scarpa, R., Urry, C. M., Falomo, R., Pesce, J. E., & Treves, A.: *The Hubble Space Telescope Survey of BL Lacertae Objects. I. Surface Brightness Profiles, Magnitudes, and Radii of Host Galaxies.* ApJ, **532**, 740 (2000)

Schlafly, E. F. & Finkbeiner, D. P.: *Measuring Reddening with Sloan Digital Sky Survey Stellar Spectra and Recalibrating SFD.* ApJ, **737**, 103 (2011)

Schmidt, M.: *3C 273 : A Star-Like Object with Large Red-Shift.* Nature, **197**, 1040 (1963)

Schroedter, M., Badran, H. M., Buckley, J. H., *et al.*: *A Very High Energy Gamma-Ray Spectrum of 1ES 2344+514.* ApJ, **634**, 947 (2005)

Shakura, N. I. & Sunyaev, R. A.: *Black holes in binary systems. Observational appearance.* A&A, **24**, 337 (1973)

Sikora, M., Begelman, M. C., Madejski, G. M., & Lasota, J.-P.: *Are Quasar Jets Dominated by Poynting Flux?* ApJ, **625**, 72 (2005)

Sikora, M., Begelman, M. C., & Rees, M. J.: *Comptonization of diffuse ambient radiation by a relativistic jet: The source of gamma rays from blazars?* ApJ, **421**, 153 (1994)

Sikora, M., Moderski, R., & Madejski, G. M.: *3C 454.3 Reveals the Structure and Physics of Its "Blazar Zone".* ApJ, **675**, 71 (2008)

Sillanpää, A., Haarala, S., Valtonen, M. J., Sundelius, B., & Byrd, G. G.: *OJ 287 - Binary pair of supermassive black holes.* ApJ, **325**, 628 (1988)

Silverman, J. D., Green, P. J., Barkhouse, W. A., *et al.*: *Comoving Space Density of X-Ray-selected Active Galactic Nuclei.* ApJ, **624**, 630 (2005)

Sokolovsky, K. V., Kovalev, Y. Y., Lobanov, A. P., *et al.*: *Constraining the magnetic field in the parsec-scale jets of the brightest Fermi blazars with multifrequency VLBI observations.* ArXiv Astrophysics e-prints, astro-ph:1001.2591 (2010a)

Sokolovsky, K. V., Kovalev, Y. Y., Lobanov, A. P., *et al.*: *Constraints on the gamma-ray emitting region in blazars from multi-frequency VLBI measurements.* ArXiv Astrophysics e-prints, astro-ph:1006.3084 (2010b)

Sokolovsky, K. V., Kovalev, Y. Y., Pushkarev, A. B., & Lobanov, A. P.: *A VLBA survey of the core shift effect in AGN jets. I. Evidence of dominating synchrotron opacity.* A&A, **532**, A38 (2011)

Sowards-Emmerd, D., Romani, R. W., & Michelson, P. F.: *The Gamma-Ray Blazar Content of the Northern Sky.* ApJ, **590**, 109 (2003)

Spada, M., Ghisellini, G., Lazzati, D., & Celotti, A.: *Internal shocks in the jets of radio-loud quasars.* MNRAS, **325**, 1559 (2001)

Stawarz, Ł., Aharonian, F., Kataoka, J., *et al.*: *Dynamics and high-energy emission of the flaring HST-1 knot in the M 87 jet.* MNRAS, **370**, 981 (2006)

Stecker, F. W., Baring, M. G., & Summerlin, E. J.: *Blazar γ-Rays, Shock Acceleration, and the Extragalactic Background Light.* ApJ, **667**, L29 (2007)

Steinbring, T.: *Bestimmung des Kerr-Parameters des zentralen Schwarzen Lochs in BL Lacerate Objekten.* Master thesis, Universität Würzburg (2012)

Stern, B. E. & Poutanen, J.: *Radiation from relativistic jets in blazars and the efficient dissipation of their bulk energy via photon breeding.* MNRAS, **383**, 1695 (2008)

Stocke, J. T., Morris, S. L., Gioia, I. M., *et al.*: *The Einstein Observatory Extended Medium-Sensitivity Survey. II - The optical identifications.* ApJS, **76**, 813 (1991)

Striani, E., Tavani, M., Piano, G., *et al.*: *The Crab Nebula Super-flare in 2011 April: Extremely Fast Particle Acceleration and Gamma-Ray Emission.* ApJ, **741**, L5 (2011)

Strübig, C.: *Long Term Studies of the Crab Nebula at Very High Energies.* Diploma thesis, Bayerische Julius-Maximilians-Universität Würzburg (2009)

Superina, G., Benbow, W., Boutelier, T., & et al.: *Discovery of VHE gamma-rays from the BL Lac object PKS 0548-322 with H.E.S.S. In International Cosmic Ray Conference*, volume 3 of *International Cosmic Ray Conference*, 913–916 (2008)

Swordy, S.: *Discovery of >100 GeV Gamma-ray Emission from the Blazar 3C66A by VERITAS.* The Astronomer's Telegram, **1753**, 1 (2008a)

Swordy, S.: *VERITAS discovers TeV gamma rays from W Comae.* The Astronomer's Telegram, **1422**, 1 (2008b)

Swordy, S.: *VERITAS discovers VHE gamma rays from BL Lac 1ES0806+524.* The Astronomer's Telegram, **1415**, 1 (2008c)

Tagliaferri, G., Foschini, L., Ghisellini, G., *et al.*: *Simultaneous Multiwavelength Observations of the Blazar 1ES 1959+650 at a Low TeV Flux.* ApJ, **679**, 1029 (2008)

Takahashi, T., Tashiro, M., Madejski, G., *et al.*: *ASCA Observation of an X-Ray/TeV Flare from the BL Lacertae Object Markarian 421.* ApJ, **470**, L89 (1996)

Tanaka, Y. T., Stawarz, Ł., Thompson, D. J., *et al.*: *Fermi Large Area Telescope Detection of Bright γ-Ray Outbursts from the Peculiar Quasar 4C +21.35.* ApJ, **733**, 19 (2011)

Tavani, M., Barbiellini, G., Argan, A., *et al.*: *The AGILE Mission.* A&A, **502**, 995 (2009)

Tavani, M., Bulgarelli, A., Vittorini, V., *et al.*: *Discovery of Powerful Gamma-Ray Flares from the Crab Nebula.* Science, **331**, 736 (2011)

Tavecchio, F., Ghisellini, G., Ghirlanda, G., Foschini, L., & Maraschi, L.: *TeV BL Lac objects at the dawn of the Fermi era.* MNRAS, **401**, 1570 (2010)

Tavecchio, F., Maraschi, L., & Ghisellini, G.: *Constraints on the Physical Parameters of TeV Blazars.* ApJ, **509**, 608 (1998)

Tavecchio, F., Maraschi, L., Pian, E., *et al.*: *Theoretical Implications from the Spectral Evolution of Markarian 501 Observed with BeppoSAX.* ApJ, **554**, 725 (2001)

Teräsranta, H. & Valtaoja, E.: *Brightness temperatures and viewing angles for extragalactic radio sources: A test of unification schemes for active galactic nuclei.* A&A, **283**, 51 (1994)

Teshima, M. & MAGIC Collaboration: *MAGIC discovers VHE gamma ray emission from the blazar S50716+714.* The Astronomer's Telegram, **1500**, 1 (2008)

Tluczykont, M., Götting, N., Heinzelmann, G., & HEGRA Collaboration: *Observations of 54 Active Galactic Nuclei with the HEGRA Cherenkov Telescopes. In International Cosmic Ray Conference*, volume 5 of *International Cosmic Ray Conference*, 2547 (2003)

Tramacere, A., Giommi, P., Massaro, E., *et al.*: *SWIFT observations of TeV BL Lacertae objects.* A&A, **467**, 501 (2007)

Tramacere, A., Giommi, P., Perri, M., Verrecchia, F., & Tosti, G.: *Swift observations of the very intense flaring activity of Mrk 421 during 2006. I. Phenomenological picture of electron acceleration and predictions for MeV/GeV emission.* A&A, **501**, 879 (2009)

Tueller, J., Baumgartner, W. H., Markwardt, C. B., *et al.*: *The 22 Month Swift-BAT All-Sky Hard X-ray Survey.* ApJS, **186**, 378 (2010)

Unwin, S. C., Wehrle, A. E., Urry, C. M., *et al.*: *Inverse Compton X-ray emission from the superluminal quasar 3C 345.* ApJ, **432**, 103 (1994)

Urry, C. M. & Padovani, P.: *Unified Schemes for Radio-Loud Active Galactic Nuclei.* PASP, **107**, 803 (1995)

Čerenkov, P. A.: *Visible Radiation Produced by Electrons Moving in a Medium with Velocities Exceeding that of Light.* Physical Review, **52**, 378 (1937)

Valtonen, M. J., Lehto, H. J., Nilsson, K., *et al.*: *A massive binary black-hole system in OJ287 and a test of general relativity.* Nature, **452**, 851 (2008)

Vaughan, S., Edelson, R., Warwick, R. S., & Uttley, P.: *On characterizing the variability properties of X-ray light curves from active galaxies.* MNRAS, **345**, 1271 (2003)

Villata, M., Raiteri, C. M., Larionov, V. M., *et al.*: *The correlated optical and radio variability of <ASTROBJ>BL Lacertae</ASTROBJ>. WEBT data analysis 1994-2005.* A&A, **501**, 455 (2009)

Voges, W., Aschenbach, B., Boller, T., *et al.*: *The ROSAT all-sky survey bright source catalogue.* A&A, **349**, 389 (1999)

Wagner, R.: *Monitoring of bright, nearby Active Galactic Nuclei with the MAGIC telescopes. In International Cosmic Ray Conference*, volume 8 of *International Cosmic Ray Conference*, 143 (2011)

Wagner, R. M.: *Measurement of very high energy gamma-ray emission from four blazars using the MAGIC telescope and a comparative blazar study.* Ph.D. thesis, Technische Universität München (2006)

Wagner, S. J.: *Detection of VHE Gamma-ray Emission from a Type 1 Quasar. In High Energy Astrophysics Division* (2010)

Weekes, T.: *Very High Energy Gamma Ray Astronomy.* Series in Astronomy and Astrophysics Series. Taylor & Francis Group (2003)

Weekes, T. C., Cawley, M. F., Fegan, D. J., *et al.*: *Observation of TeV gamma rays from the Crab nebula using the atmospheric Cerenkov imaging technique.* ApJ, **342**, 379 (1989)

Wehrle, A. E., Pian, E., Urry, C. M., *et al.*: *Multiwavelength Observations of a Dramatic High-Energy Flare in the Blazar 3C 279.* ApJ, **497**, 178 (1998)

Weidinger, M.: *Variabilität entlang der Blazar-Sequenz - Hinweise auf die Zusammensetzung relativistischer Ausflüsse Aktiver Galaxienkerne.* Ph.D. thesis, Bayerische Julius-Maximilians-Universität Würzburg (2011)

Weidinger, M. & Spanier, F.: *Modelling the variability of 1ES1218+30.4.* A&A, **515**, A18 (2010)

Weidinger, M. & Spanier, F.: *Variability along the Blazar-Sequence - Hints for extragalactic Cosmic Rays?* ArXiv Astrophysics e-prints, astro-ph:1109.1975 (2011)

Wielebinski, R., Junkes, N., & Grahl, B. H.: *The Effelsberg 100-m Radio Telescope: Construction and Forty Years of Radio Astronomy.* Journal of Astronomical History and Heritage, **14**, 3 (2011)

Winkler, C., Courvoisier, T. J.-L., Di Cocco, G., *et al.*: *The INTEGRAL mission.* A&A, **411**, L1 (2003)

Wolter, A., Beckmann, V., Ghisellini, G., Tavecchio, F., & Maraschi, L.: *The Hard Synchrotron X–ray Spectrum of the TeV BL Lac 1ES 1426+428. In* T. A. Rector & D. S. De Young (editors), *Extragalactic Jets: Theory and Observation from Radio to Gamma Ray*, volume 386 of *Astronomical Society of the Pacific Conference Series*, 302 (2008)

Wood, K. S., Meekins, J. F., Yentis, D. J., *et al.*: *The HEAO A-1 X-ray source catalog.* ApJS, **56**, 507 (1984)

Wu, X.-B., Liu, F. K., & Zhang, T. Z.: *Supermassive black hole masses of AGNs with elliptical hosts.* A&A, **389**, 742 (2002)

Zacharopoulou, O., Khangulyan, D., Aharonian, F. A., & Costamante, L.: *Modeling the Hard TeV Spectra of Blazars 1ES 0229+200 and 3C 66A with an Internal Absorption Scenario.* ApJ, **738**, 157 (2011)

Zhang, J., Liang, E.-W., Zhang, S.-N., & Bai, J. M.: *Radiation Mechanisms and Physical Properties of GeV-TeV BL Lac Objects.* ApJ, **752**, 157 (2012)

Zubovas, K. & Nayakshin, S.: *Fermi bubbles in the Milky Way: the closest AGN feedback laboratory courtesy of Sgr A*?* MNRAS, **424**, 666 (2012)

List of Publications

Publications with Major Personal Contribution

Papers in Refereed Journals

1. Sato, R., Kataoka, J., Takahashi, T., *et al.*:
Suzaku Observation of the TeV Blazar 1ES 1218+304: Clues on Particle Acceleration in an Extreme TeV Blazar. 2008, ApJ, **680**, L9

2. Ushio, M., Tanaka, T., Madejski, G., *et al.*:
Suzaku Wide Band Analysis of the X-Ray Variability of TeV Blazar Mrk 421 in 2006. 2009, ApJ, **699**, 1964

3. Acciari, V. A., Aliu, E., Aune, T., *et al.* (The VERITAS and MAGIC collaborations):
Simultaneous Multiwavelength Observations of Markarian 421 During Outburst. 2009, ApJ, **703**, 169[4]

4. Anderhub, H., Antonelli, L. A., Antoranz, P., *et al.* (The MAGIC collaboration):
Simultaneous Multiwavelength Observation of Mkn 501 in a Low State in 2006. 2009, ApJ, **705**, 1624

5. Aleksić, J., Anderhub, H., Antonelli, L. A., *et al.* (The MAGIC collaboration):
MAGIC TeV gamma-ray observations of Markarian 421 during multiwavelength campaigns in 2006. 2010, A&A, **519**, A32

6. Aleksić, J., Antonelli, L. A., Antoranz, P., *et al.* (The MAGIC collaboration and the *Fermi*-LAT, AGILE and F-GAMMA team):
The Simultaneous Low State Spectral Energy Distribution of 1ES 2344+514 from Radio to Very High Energies. submitted to A&A

- Aleksić, J., Antonelli, L. A., Antoranz, P., *et al.* (The MAGIC collaboration and the AGILE team):
Working title: Multi-Wavelength Observations of the Blazar 1ES 1011+496 in Spring 2008. in preparation

- Aleksić, J., Antonelli, L. A., Antoranz, P., *et al.* (The MAGIC collaboration and the AGILE team):
Working title: Multi-Wavelength Observations of Mrk 180. in preparation

[4]Note that due to a programming mistake, the first author of this paper forgot one power of energy when converting the VHE differential fluxes to νF_ν. An erratum to the paper is in preparation.

Conference Contributions

Talks

1. Rügamer, S.:
Überblick über das MAGIC-Teleskop. 2005, Astroteilchenschule Obertrubach-Bärnfels, Germany

2. Rügamer, S., Hayashida, M. (for the MAGIC collaboration), Costamante, L., Horns, D. (for the H.E.S.S. collaboration), Takahashi, T., Kataoka, J., Sato, R.:
Wide Range Multifrequency Observations of Northern TeV Blazars. 2008, Frühjahrstagung der Deutschen Physikalischen Gesellschaft, Freiburg, Germany (presented by Berger, K.)

3. Rügamer, S., Bretz, T., Dorner, D.:
Upgrade of the Würzburg Data Center. 2008, Frühjahrstagung der Deutschen Physikalischen Gesellschaft, Freiburg, Germany (presented by Berger, K.)

4. Rügamer, S., Oya, I., Wagner, R., Contreras, J. L. (for the MAGIC collaboration):
MAGIC observations of Mkn 421 during multi-frequency campaigns in 2006. 2009, Frühjahrstagung der Deutschen Physikalischen Gesellschaft, München, Germany

5. Rügamer, S., Oya, I., Hayashida, M., Mazin, D., Wagner, R., Contreras, J. L., Bretz, T. (for the MAGIC collaboration):
MAGIC Multi-Wavelength Observations of VHE Blazars in 2006. 2009, 31st International Cosmic Ray Conference, Łódź, Poland

6. Rügamer, S. (for the MAGIC collaboration):
The MAGIC View of Active Galactic Nuclei in Gamma-Rays. 2010, Frühjahrstagung der Deutschen Physikalischen Gesellschaft, Bonn, Germany

7. Rügamer, S.:
The MAGIC Extragalactic Sky. 2010, Workshop "The High Energy Universe", Würzburg, Germany

8. Rügamer, S. (for the MAGIC collaboration):
MAGIC and Multi-Wavelength Observations of 1ES 1011+49.6 and Mrk 180. 2011, Frühjahrstagung der Deutschen Physikalischen Gesellschaft, Karlsruhe, Germany

9. Rügamer, S. (for the MAGIC collaboration):
MAGIC and Multi-Wavelength Observations of Mrk 180 and 1ES 2344+514 in 2008. 2011, 32nd International Cosmic Ray Conference, Beijing, China (presented by Storz, J.)

10. Rügamer, S. (for the MAGIC collaboration):
Multi-Wavelength Observations of Mrk 180 and 1ES 2344+514. 2012, Frühjahrstagung der Deutschen Physikalischen Gesellschaft, Göttingen, Germany

Poster Presentations

1. Rügamer, S., Hayashida, M., Mazin, D., Firpo, R., Mannheim, K., Teshima, M. (for the MAGIC collaboration), Horns, D., Costamante, L., Schwarzburg, S., Wagner, S. (for the H.E.S.S. collaboration), Takahashi, T., Kataoka, J., Madejski, G., Ushio, M. (for the Suzaku team), Lindfors, E., Takalo, L. (for the KVA team):
Wide Range Multifrequency Observations of Northern TeV Blazars. 2007, "Cosmic Matter" conference, Würzburg, Germany

2. Satalecka, K., Rügamer, S. (for the MAGIC collaboration):
Highlights of the MAGIC AGN Research Program. 2010, "Astroteilchenphysik in Deutschland", Zeuthen, Germany

3. Rügamer, S. (for the MAGIC collaboration), Angelakis, E. (for the F-GAMMA program), Bastieri, D. (on behalf of the *Fermi*-LAT team), Dorner, D., Kovalev, Y. Y. (for the RATAN team), Lähteenmäki, A., Lindfors, E., Pittori, C. (on behalf of the AGILE team), Reinthal, R., Sokolovsky, K. V., Stamerra, A., Ungerechts, H. (on behalf of the IRAM team):
MAGIC and Multi-Frequency Observations of three HBLs in 2008. 2011, 3rd Fermi Symposium, Rome, Italy

Conference Proceedings

1. Meyer, M., Bretz, T., Dorner, D., et al. (The MAGIC collaboration):
Systematic search for VHE gamma-ray emission from X-ray bright high-frequency peaked BL Lac objects. 2007, Astronomische Nachrichten, **328**, 621

2. Rügamer, S., Hayashida, M., Mazin, D., et al. (The MAGIC and H.E.S.S. collaborations and the Suzaku and KVA team):
Wide Range Multifrequency Observations of Northern TeV Blazars. 2007, Astronomische Nachrichten, **328**, 623

3. Sato, R., Kataoka, J., Takahashi, T., et al. (The MAGIC collaboration):
Suzaku observation of TeV blazar 1ES 1218+304: clues on particle acceleration in an extreme TeV blazar. 2008, proceedings of the Workshop on Blazar Variability across the Electromagnetic Spectrum, Palaiseau, France.

4. Hayashida, M., Rügamer, S., Mazin, D., et al. (The MAGIC collaboration):
Wide-range multiwavelength observations of northern TeV blazars with MAGIC/HESS, Suzaku and KVA. 2008, proceedings of the 30th International Cosmic Ray Conference, Mérida, Mexico, Vol. **3**, 1029

5. Sato, R., Kataoka, J., Takahashi, T., et al. (The MAGIC collaboration):
Suzaku observation of TeV blazar the 1ES 1218+304: clues on particle acceleration in an extreme TeV blazar. 2008, American Institute of Physics Conference Series, **1085**, 447

6. Rügamer, S., Oya, I., Hayashida, M., et al. (The MAGIC collaboration): *MWL observations of VHE blazars in 2006.* 2009, proceedings of the 31st International Cosmic Ray Conference, Łódź, Poland. arXiv:0907.0551

7. Leonardo, E., Bose, D., Mankuzhiyil, N., et al. (The MAGIC collaboration): *Multiwavelength observation of the blazar 1ES 1426+428 in May-June 2008.* 2009, proceedings of the 31st International Cosmic Ray Conference, Łódź, Poland. arXiv:0907.0959

8. Sato, R., Kataoka, J., Takahashi, T., et al. (The MAGIC collaboration): *Suzaku observation of TeV blazar the 1ES 1218+304: clues on particle acceleration in an extreme TeV blazar.* 2010, proceedings on the 3rd Suzaku Conference, Otaru, Japan, p. 28

9. Reinthal, R., Rügamer, S., Lindfors, E. J., et al. (The MAGIC collaboration): *Multi-wavelength Observations of HBL object 1ES 1011+496 in Spring 2008.* 2011, proceedings of the 32nd International Cosmic Ray Conference, Bejing, China. arXiv:1109.6504

10. Rügamer, S., Angelakis, E., Bastieri, D., et al. (The MAGIC collaboration, the F-GAMMA program and the *Fermi*-LAT, RATAN, MOJAVE, AGILE and IRAM team): *MAGIC and Multi-Wavelength Observations of Mrk 180 and 1ES 2344+514 in 2008.* 2011, proceedings of the 32nd International Cosmic Ray Conference, Bejing, China. arXiv:1109.6808

11. Rügamer, S., Angelakis, E., Bastieri, D., et al. (The MAGIC collaboration, the F-GAMMA program and the *Fermi*-LAT, RATAN, AGILE and IRAM team): *MAGIC and Multi-Wavelength Observations of three HBLs in 2008.* 2011, proceedings of the 3rd Fermi Symposium. arXiv:1110.6341

12. Reinthal, R., Rügamer, S., Lindfors, E. J., et al. (The MAGIC collaboration and the AGILE team): *Multi-wavelength Observations of the HBL 1ES 1011+496 in Spring 2008.* 2012, Journal of Physics Conference Series, **355**, 012017

MAGIC Collaboration Publications

1. Albert, J., Aliu, E., Anderhub, H., et al. (The MAGIC collaboration): *MAGIC Observations of Very High Energy γ-Rays from HESS J1813-178.* 2006, ApJ, **637**, L41

2. Albert, J., Aliu, E., Anderhub, H., et al. (The MAGIC collaboration): *Observation of Gamma Rays from the Galactic Center with the MAGIC Telescope.* 2006, ApJ, **638**, L101

3. Albert, J., Aliu, E., Anderhub, H., et al. (The MAGIC collaboration): *Observation of Very High Energy Gamma-Ray Emission from the Active Galactic Nucleus 1ES 1959+650 Using the MAGIC Telescope.* 2006, ApJ, **639**, 761

4. Albert, J., Aliu, E., Anderhub, H., et al. (The MAGIC collaboration): *Flux Upper Limit on Gamma-Ray Emission by GRB 050713a from MAGIC Telescope Observations.* 2006, ApJ, **641**, L9

5. Albert, J., Aliu, E., Anderhub, H., et al. (The MAGIC collaboration): *Discovery of Very High Energy Gamma Rays from 1ES 1218+30.4.* 2006, ApJ, **642**, L119

6. Albert, J., Aliu, E., Anderhub, H., et al. (The MAGIC collaboration): *Observation of VHE Gamma Radiation from HESS J1834-087/W41 with the MAGIC Telescope.* 2006, ApJ, **643**, L53

7. Albert, J., Aliu, E., Anderhub, H., et al. (The MAGIC collaboration): *Variable Very-High-Energy Gamma-Ray Emission from the Microquasar LS I +61 303.* 2006, Science, **312**, 1771

8. Albert, J., Aliu, E., Anderhub, H., et al. (The MAGIC collaboration): *Discovery of Very High Energy γ-Rays from Markarian 180 Triggered by an Optical Outburst.* 2006, ApJ, **648**, L105

9. Albert, J., Aliu, E., Anderhub, H., et al. (The MAGIC collaboration): *Detection of Very High Energy Radiation from the BL Lacertae Object PG 1553+113 with the MAGIC Telescope.* 2007, ApJ, **654**, L119

10. Albert, J., Aliu, E., Anderhub, H., et al. (The MAGIC collaboration): *First Bounds on the Very High Energy γ-Ray Emission from Arp 220.* 2007, ApJ, **658**, 245

11. Albert, J., Aliu, E., Anderhub, H., et al. (The MAGIC collaboration): *Observation of Very High Energy γ-Rays from the AGN 1ES 2344+514 in a Low Emission State with the MAGIC Telescope.* 2007, ApJ, **662**, 892

12. Albert, J., Aliu, E., Anderhub, H., et al. (The MAGIC collaboration): *Observations of Markarian 421 with the MAGIC Telescope.* 2007, ApJ, **663**, 125

13. Albert, J., Aliu, E., Anderhub, H., et al. (The MAGIC collaboration): *Discovery of Very High Energy Gamma Radiation from IC 443 with the MAGIC Telescope.* 2007, ApJ, **664**, L87

14. Albert, J., Aliu, E., Anderhub, H., et al. (The MAGIC collaboration): *Very High Energy Gamma-Ray Radiation from the Stellar Mass Black Hole Binary Cygnus X-1.* 2007, ApJ, **665**, L51

15. Albert, J., Aliu, E., Anderhub, H., et al. (The MAGIC collaboration): *Discovery of Very High Energy γ-Ray Emission from the Low-Frequency-peaked BL Lacertae Object BL Lacertae.* 2007, ApJ, **666**, L17

16. Albert, J., Aliu, E., Anderhub, H., et al. (The MAGIC collaboration): *MAGIC Upper Limits on the Very High Energy Emission from Gamma-Ray Bursts.* 2007, ApJ, **667**, 358

17. Albert, J., Aliu, E., Anderhub, H., et al. (The MAGIC collaboration): *Discovery of Very High Energy γ-Rays from 1ES 1011+496 at z = 0.212.* 2007, ApJ, **667**, L21

18. Albert, J., Aliu, E., Anderhub, H., et al. (The MAGIC collaboration): *The MAGIC Project: Contributions to ICRC 2007.* 2007, arXiv:0709.3763

19. Albert, J., Aliu, E., Anderhub, H., et al. (The MAGIC collaboration): *Observation of VHE γ-rays from Cassiopeia A with the MAGIC telescope.* 2007, A&A, **474**, 937

20. Albert, J., Aliu, E., Anderhub, H., et al. (The MAGIC collaboration): *Variable Very High Energy γ-Ray Emission from Markarian 501.* 2007, ApJ, **669**, 862

21. Albert, J., Aliu, E., Anderhub, H., et al. (The MAGIC collaboration): *Constraints on the Steady and Pulsed Very High Energy Gamma-Ray Emission from Observations of PSR B1951+32/CTB 80 with the MAGIC Telescope.* 2007, ApJ, **669**, 1143

22. Albert, J., Aliu, E., Anderhub, H., et al. (The MAGIC collaboration): *Unfolding of differential energy spectra in the MAGIC experiment.* 2007, Nuclear Instruments and Methods in Physics Research A, **583**, 494

23. Albert, J., Aliu, E., Anderhub, H., et al. (The MAGIC collaboration): *VHE γ-Ray Observation of the Crab Nebula and its Pulsar with the MAGIC Telescope.* 2008, ApJ, **674**, 1037

24. Albert, J., Aliu, E., Anderhub, H., et al. (The MAGIC collaboration): *MAGIC Observations of the Unidentified γ-Ray Source TeV J2032+4130.* 2008, ApJ, **675**, L25

25. Albert, J., Aliu, E., Anderhub, H., et al. (The MAGIC collaboration): *Implementation of the Random Forest method for the Imaging Atmospheric Cherenkov Telescope MAGIC.* 2008, Nuclear Instruments and Methods in Physics Research A, **588**, 424

26. Albert, J., Aliu, E., Anderhub, H., et al. (The MAGIC collaboration): *Upper Limit for γ-Ray Emission above 140 GeV from the Dwarf Spheroidal Galaxy Draco.* 2008, ApJ, **679**, 428

27. Tagliaferri, G., Foschini, L., Ghisellini, G., et al. (The MAGIC collaboration): *Simultaneous Multiwavelength Observations of the Blazar 1ES 1959+650 at a Low TeV Flux.* 2008, ApJ, **679**, 1029

28. Albert, J., Aliu, E., Anderhub, H., et al. (The MAGIC collaboration): *Very-High-Energy gamma rays from a Distant Quasar: How Transparent Is the Universe?.* 2008, Science, **320**, 1752

29. Albert, J., Aliu, E., Anderhub, H., et al. (The MAGIC collaboration):
Systematic Search for VHE Gamma-Ray Emission from X-Ray-bright High-Frequency BL Lac Objects. 2008, ApJ, **681**, 944

30. Albert, J., Aliu, E., Anderhub, H., et al. (The MAGIC collaboration):
Multiwavelength (Radio, X-Ray, and γ-Ray) Observations of the γ-Ray Binary LS I +61 303. 2008, ApJ, **684**, 1351

31. Albert, J., Aliu, E., Anderhub, H., et al. (The MAGIC collaboration):
Very High Energy Gamma-Ray Observations of Strong Flaring Activity in M87 in 2008 February. 2008, ApJ, **685**, L23

32. Aliu, E., Anderhub, H., Antonelli, L. A., et al. (The MAGIC collaboration):
First Bounds on the High-Energy Emission from Isolated Wolf-Rayet Binary Systems. 2008, ApJ, **685**, L71

33. Albert, J., Aliu, E., Anderhub, H., et al. (The MAGIC collaboration):
FADC signal reconstruction for the MAGIC telescope. 2008, Nuclear Instruments and Methods in Physics Research A, **594**, 407

34. Albert, J., Aliu, E., Anderhub, H., et al. (The MAGIC collaboration):
Probing quantum gravity using photons from a flare of the active galactic nucleus Markarian 501 observed by the MAGIC telescope. 2008, Physics Letters B, **668**, 253

35. Aliu, E., Anderhub, H., Antonelli, L. A., et al. (The MAGIC collaboration):
Observation of Pulsed γ-Rays Above 25 GeV from the Crab Pulsar with MAGIC. 2008, Science, **322**, 1221

36. Albert, J., Aliu, E., Anderhub, H., et al. (The MAGIC collaboration):
MAGIC observations of PG 1553+113 during a multiwavelength campaign in July 2006. 2009, A&A, **493**, 467

37. Aliu, E., Anderhub, H., Antonelli, L. A., et al. (The MAGIC collaboration):
Improving the performance of the single-dish Cherenkov telescope MAGIC through the use of signal timing. 2009, Astroparticle Physics, **30**, 293

38. Donnarumma, I., Vittorini, V., Vercellone, S., et al. (The AGILE team and MAGIC and VERITAS collaborations):
The June 2008 Flare of Markarian 421 from Optical to TeV Energies. 2009, ApJ, **691**, L13

39. Aliu, E., Anderhub, H., Antonelli, L. A., et al. (The MAGIC collaboration):
Discovery of a Very High Energy Gamma-Ray Signal from the 3C 66A/B Region. 2009, ApJ, **692**, L29

40. Albert, J., Aliu, E., Anderhub, H., et al. (The MAGIC collaboration):
Periodic Very High Energy γ-Ray Emission from LS I +61°303 Observed with the MAGIC Telescope. 2009, ApJ, **693**, 303

41. Anderhub, H., Antonelli, L. A., Antoranz, P., et al. (The MAGIC collaboration): *MAGIC upper limits to the VHE gamma-ray flux of 3C 454.3 in high emission state.* 2009, A&A, **498**, 83

42. Aliu, E., Anderhub, H., Antonelli, L. A., et al. (The MAGIC collaboration): *Upper Limits on the VHE Gamma-Ray Emission from the Willman 1 Satellite Galaxy with the Magic Telescope.* 2009, ApJ, **697**, 1299

43. Anderhub, H., Antonelli, L. A., Antoranz, P., et al. (The MAGIC collaboration): *MAGIC Collaboration: Contributions to the 31st International Cosmic Ray Conference (ICRC 2009).* 2009, arXiv:0907.0843

44. Acciari, V. A., Aliu, E., Arlen, T., et al. (The VERITAS collaboration, the VLBA 43 GHz M 87 monitoring team and the H.E.S.S. and MAGIC collaborations): *Radio Imaging of the Very-High-Energy γ-Ray Emission Region in the Central Engine of a Radio Galaxy.* 2009, Science, **325**, 444

45. Anderhub, H., Antonelli, L. A., Antoranz, P., et al. (The MAGIC collaboration): *Search for VHE γ-ray Emission from the Globular Cluster M13 with the Magic Telescope.* 2009, ApJ, **702**, 266

46. Anderhub, H., Antonelli, L. A., Antoranz, P., et al. (The MAGIC collaboration): *Discovery of very High Energy γ-Rays from the Blazar S5 0716+714.* 2009, ApJ, **704**, L129

47. Seta, H., Isobe, N., Tashiro, M. S., et al. (The MAGIC collaboration): *Suzaku and Multi-Wavelength Observations of OJ 287 during the Periodic Optical Outburst in 2007.* 2009, PASJ, **61**, 1011

48. Anderhub, H., Antonelli, L. A., Antoranz, P., et al. (The MAGIC collaboration): *Correlated X-Ray and Very High Energy Emission in the Gamma-Ray Binary LS I +61 303.* 2009, ApJ, **706**, L27

49. Sitarek, J., Aleksic, J., Antonelli, L. A., et al. (The MAGIC collaboration): *Observations of AGNs with the MAGIC telescopes..* 2010, 38th COSPAR Scientific Assembly, **38**, 2241

50. de Cea Del Pozo, E., Anderhub, H., Antonelli, L. A., et al. (The MAGIC collaboration): *Supernova remnants and pulsar wind nebulae as seen by the MAGIC Cherenkov Telescope.* 2010, 38th COSPAR Scientific Assembly, **38**, 2737

51. Aleksić, J., Antonelli, L. A., Antoranz, P., et al. (The MAGIC collaboration): *MAGIC Gamma-ray Telescope Observation of the Perseus Cluster of Galaxies: Implications for Cosmic Rays, Dark Matter, and NGC 1275.* 2010, ApJ, **710**, 634

52. Anderhub, H., Antonelli, L. A., Antoranz, P., et al. (The MAGIC collaboration): *Search for Very High Energy Gamma-ray Emission from Pulsar-Pulsar Wind Nebula Systems with the MAGIC Telescope.* 2010, ApJ, **710**, 828

53. Aleksić, J., Anderhub, H., Antonelli, L. A., et al. (The MAGIC collaboration): *Simultaneous multi-frequency observation of the unknown redshift blazar PG 1553+113 in March-April 2008.* 2010, A&A, **515**, A76

54. Aleksić, J., Anderhub, H., Antonelli, L. A., et al. (The MAGIC collaboration): *MAGIC observation of the GRB 080430 afterglow.* 2010, A&A, **517**, A5

55. Aleksić, J., Antonelli, L. A., Antoranz, P., et al. (The MAGIC collaboration): *Magic Constraints on γ-ray Emission from Cygnus X-3.* 2010, ApJ, **721**, 843

56. Aleksić, J., Antonelli, L. A., Antoranz, P., et al. (The MAGIC collaboration): *Detection of Very High Energy γ-ray Emission from the Perseus Cluster Head-Tail Galaxy IC 310 by the MAGIC Telescopes.* 2010, ApJ, **723**, L207

57. Aleksić, J., Antonelli, L. A., Antoranz, P., et al. (The MAGIC collaboration): *Search for an extended VHE γ-ray emission from Mrk 421 and Mrk 501 with the MAGIC Telescope.* 2010, A&A, **524**, A77

58. Aleksić, J., Antonelli, L. A., Antoranz, P., et al. (The MAGIC collaboration): *MAGIC Upper Limits for Two Milagro-detected Bright Fermi Sources in the Region of SNR G65.1+0.6.* 2010, ApJ, **725**, 1629

59. Aleksić, J., Antonelli, L. A., Antoranz, P., et al. (The MAGIC collaboration): *Observations of the Blazar 3C 66A with the Magic Telescopes in Stereoscopic Mode.* 2011, ApJ, **726**, 58

60. Abdo, A. A., Ackermann, M., Ajello, M., et al. (The *Fermi*-LAT, MAGIC and VERITAS collaborations): *Insights into the High-energy γ-ray Emission of Markarian 501 from Extensive Multifrequency Observations in the Fermi Era.* 2011, ApJ, **727**, 129

61. Acciari, V. A., Arlen, T., Aune, T., et al. (The VERITAS and MAGIC collaborations): *Spectral Energy Distribution of Markarian 501: Quiescent State Versus Extreme Outburst.* 2011, ApJ, **729**, 2

62. Aleksić, J., Antonelli, L. A., Antoranz, P., et al. (The MAGIC collaboration): *Gamma-ray Excess from a Stacked Sample of High- and Intermediate-frequency Peaked Blazars Observed with the MAGIC Telescope.* 2011, ApJ, **729**, 115

63. Aleksić, J., Antonelli, L. A., Antoranz, P., et al. (The MAGIC collaboration): *MAGIC Discovery of Very High Energy Emission from the FSRQ PKS 1222+21.* 2011, ApJ, **730**, L8

64. Aleksić, J., Antonelli, L. A., Antoranz, P., et al. (The MAGIC collaboration): *MAGIC Observations and multiwavelength properties of the quasar 3C 279 in 2007 and 2009.* 2011, A&A, **530**, A4

65. Aleksić, J., Alvarez, E. A., Antonelli, L. A., et al. (The MAGIC collaboration): *Searches for dark matter annihilation signatures in the Segue 1 satellite galaxy with the MAGIC-I telescope.* 2011, J. Cosmology Astropart. Phys., **6**, 35

66. Aleksić, J., Alvarez, E. A., Antonelli, L. A., et al. (The MAGIC collaboration): *A Search for Very High Energy Gamma-Ray Emission from Scorpius X-1 with the Magic Telescopes.* 2011, ApJ, **735**, L5

67. Abdo, A. A., Ackermann, M., Ajello, M., et al. (The *Fermi*-LAT and MAGIC collaborations): *Fermi Large Area Telescope Observations of Markarian 421: The Missing Piece of its Spectral Energy Distribution.* 2011, ApJ, **736**, 131

68. Aleksić, J., Alvarez, E. A., Antonelli, L. A., et al. (The MAGIC collaboration): *Observations of the Crab Pulsar between 25 and 100 GeV with the MAGIC I Telescope.* 2011, ApJ, **742**, 43

69. Aleksić, J., Alvarez, E. A., Antonelli, L. A., et al. (The MAGIC collaboration): *MAGIC contributions to the 32nd International Cosmic Ray Conference.* 2011, arXiv:1111.0879

70. Aleksić, J., Alvarez, E. A., Antonelli, L. A., et al. (The MAGIC collaboration): *Performance of the MAGIC stereo system obtained with Crab Nebula data.* 2012, Astroparticle Physics, **35**, 435

71. Aleksić, J., Alvarez, E. A., Antonelli, L. A., et al. (The MAGIC collaboration): *Detection of the γ-Ray Binary LS I +61°303 in a Low-flux State at Very High Energy γ-Rays with the MAGIC Telescopes in 2009.* 2012, ApJ, **746**, 80

72. Abramowski, A., Acero, F., Aharonian, F., et al. (The H.E.S.S. MAGIC and VERITAS collaborations): *The 2010 Very High Energy γ-Ray Flare and 10 Years of Multi-wavelength Observations of M 87.* 2012, ApJ, **746**, 151

73. Aleksić, J., Alvarez, E. A., Antonelli, L. A., et al. (The MAGIC collaboration): *Discovery of VHE γ-ray emission from the BL Lacertae object B3 2247+381 with the MAGIC telescopes.* 2012, A&A, **539**, A118

74. Aleksić, J., Alvarez, E. A., Antonelli, L. A., et al. (The MAGIC collaboration): *Detection of very-high energy γ-ray emission from <ASTROBJ>NGC 1275</ASTROBJ> by the MAGIC telescopes.* 2012, A&A, **539**, L2

75. Aleksić, J., Alvarez, E. A., Antonelli, L. A., et al. (The MAGIC collaboration): *PG 1553+113: Five Years of Observations with MAGIC.* 2012, ApJ, **748**, 46

76. Aleksić, J., Alvarez, E. A., Antonelli, L. A., et al. (The MAGIC collaboration): *Phase-resolved energy spectra of the Crab pulsar in the range of 50-400 GeV measured with the MAGIC telescopes.* 2012, A&A, **540**, A69

77. Aleksić, J., Alvarez, E. A., Antonelli, L. A., et al. (The MAGIC collaboration): *Morphological and spectral properties of the W51 region measured with the MAGIC telescopes.* 2012, A&A, **541**, A13

78. Aleksić, J., Alvarez, E. A., Antonelli, L. A., et al. (The MAGIC collaboration): *Constraining cosmic rays and magnetic fields in the Perseus galaxy cluster with TeV observations by the MAGIC telescopes.* 2012, A&A, **541**, A99

79. Aleksić, J., Alvarez, E. A., Antonelli, L. A., et al. (The MAGIC collaboration): *Mrk 421 active state in 2008: the MAGIC view, simultaneous multi-wavelength observations and SSC model constrained.* 2012, A&A, **542**, A100

80. Aleksić, J., Alvarez, E. A., Antonelli, L. A., et al. (The MAGIC collaboration): *Detection of VHE γ-Rays from HESS J0632+057 during the 2011 February X-Ray Outburst with the MAGIC Telescopes.* 2012, ApJ, **754**, L10

81. Aleksić, J., Alvarez, E. A., Antonelli, L. A., et al. (The MAGIC collaboration): *High zenith angle observations of PKS 2155-304 with the MAGIC-I telescope.* 2012, A&A, **544**, A75

82. Aleksić, J., Alvarez, E. A., Antonelli, L. A., et al. (The MAGIC collaboration): *MAGIC observations of the giant radio galaxy M 87 in a low-emission state between 2005 and 2007.* 2012, A&A, **544**, A96

83. Aleksić, J., Alvarez, E. A., Antonelli, L. A., et al. (The MAGIC collaboration): *Discovery of VHE γ-rays from the blazar 1ES 1215+303 with the MAGIC telescopes and simultaneous multi-wavelength observations.* 2012, A&A, **544**, A142

84. Aleksić, J., Antonelli, L. A., Antoranz, P., et al. (The MAGIC collaboration): *Observations of the magnetars 4U 0142+61 and 1E 2259+586 with the MAGIC telescopes.* 2013, A&A, **549**, A23

Abbreviations and Acronyms

1FGL	First ***F**ermi* **G**amma-ray **L**AT (First *Fermi*-LAT catalog of γ-ray sources)
1LAC	First **L**AT **A**GN **C**atalog
2FGL	Second ***F**ermi* **G**amma-ray **L**AT (Second *Fermi*-LAT catalog)
2LAC	Second **L**AT **A**GN **C**atalog
AGILE	**A**strorivelatore **G**amma ad **I**mmagini **Le**ggero
AGN	**A**ctive **G**alactic **N**ucleus
ASM	(*RXTE*) **A**ll-**S**ky **M**onitor
BAT	(*Swift*) **B**urst **A**lert **T**elescope
BH	**B**lack **H**ole
BL Lac	**BL Lac**ertae object
BLR	**B**road-**L**ine **R**egion
c.l.	**c**onfidence **l**evel
CMT	**C**arlsberg **M**eridian **T**elescope
CoG	**C**enter **o**f **G**ravity
CR	**C**osmic **R**ay
CrAO	**Cr**imean **A**strophysical **O**bservatory
DSS	**D**igitized **S**ky **S**urvey
DT	**D**iscriminator **T**hreshold
EBL	**E**xtragalactic **B**ackground **L**ight
EGRET	**E**nergetic **G**amma-**R**ay **E**xperiment **T**elescope
EC	**E**xternal **C**ompton
F-GAMMA	***F**ermi* **G**amma-ray space telescope **A**GN **M**ulti-frequency **M**onitoring **A**lliance
FOV	**F**ield **O**f **V**iew
FR-I/-II	**F**anaroff-**R**iley type I/II
FSRQ	**F**lat **S**pectrum **R**adio **Q**uasar
HBL	**H**igh-frequency peaked **BL** **L**acertae object

HE	**H**igh **E**nergy
HEGRA	**H**igh **E**energy **G**amma-**R**ay **A**stronomy
HERG	**H**igh **E**xcitation **R**adio **G**alaxy
IACT	**I**maging **A**ir **C**herenkov **T**elescope
IC	**I**nverse **C**ompton
IBL	**I**ntermediate-frequency peaked **B**L **L**acertae object
IRAM	**I**nstitut de **R**adioastronomie **M**illimétrique
INTEGRAL	**INTE**rnational **G**amma-**R**ay **A**strophysics **L**aboratory
ISGRI	*INTEGRAL* **S**oft **G**amma-**R**ay **I**mager
kpc	**k**ilo **p**arse**c**
KVA	**K**ungliga **V**etenskaps**A**kademien (Royal Swedish Academy of Sciences)
LAT	**L**arge **A**rea **T**elescope
LBL	**L**ow-frequency peaked **B**L **L**acertae object
LERG	**L**ow **E**xcitation **R**adio **G**alaxy
MAGIC	**M**ajor **A**tmospheric **G**amma-ray **I**maging **C**herenkov
mas	**m**illi **a**rc-**s**econd
MAXI	**M**onitor of **A**ll-sky **X**-ray **I**mage
MC	**M**onte-**C**arlo
MOJAVE	**M**onitoring **O**f **J**ets in **A**ctive galactic nuclei with **V**LBA **E**xperiments
Mpc	**M**ega **p**arse**c**
MUX	**MU**ltiple**X**ed FADC (flash analog-to-digital converter)
MW	**M**ulti-**W**avelength
NASA	**N**ational **A**eronautics and **S**pace **A**dministration
NED	**N**ASA/IPAC **E**xtragalactic **D**atabase
NIR	**N**ear **I**nfra**R**ed
NLR	**N**arrow-**L**ine **R**egion
NVSS	**N**RAO **V**LA **S**ky **S**urvey
OVRO	**O**wens **V**alley **R**adio **O**bservatory
pc	**p**arse**c**
PCA	(*RXTE*) **P**roportional **C**ounter **A**rray
phe	**ph**oto-**e**lectron
PSF	**P**oint **S**pread **F**unction
RATAN-600	**R**adio **A**stronomical **T**elescope **A**cademy **N**auk 600

RMS	**R**oot **M**ean **S**quare
RXTE	**R**ossi **X**-ray **T**iming **E**xplorer
SED	**S**pectral **E**nergy **D**istribution
SSC	**S**ynchrotron **S**elf-**C**ompton
XRT	(*Swift*) **X**-**R**ay **T**elescope
UL	**U**pper **L**imit
UVOT	(*Swift*) **U**ltra**V**iolet/**O**ptical **T**elescope
VERITAS	**V**ery **E**nergetic **R**adiation **I**maging **T**elescope **A**rray **S**ystem
VHE	**V**ery **H**igh **E**nergy
VLA	**V**ery **L**arge **A**rray
VLBA	**V**ery **L**ong **B**aseline **A**rray
VLBI	**V**ery **L**ong **B**aseline **I**nterferometry

Acknowledgements

Official The author greatly thanks the Metsähovi Radio Observatory for courtesy of the 37 GHz data. The KVA data were provided by the Tuorla Blazar Monitoring Program. This work made use of public data provided by the Owens Valley Radio Observatory 40-m Blazar Monitoring Program.

This publication makes use of data products from the Two Micron All Sky Survey, which is a joint project of the University of Massachusetts and the Infrared Processing and Analysis Center/California Institute of Technology, funded by the National Aeronautics and Space Administration and the National Science Foundation.

This research has made use of NASA's Astrophysics Data System.

Part of this work is based on archival data, software or on-line services provided by the ASI Science Data Center (ASDC).

This research has made use of SAOImage DS9, developed by Smithsonian Astrophysical Observatory.

This research has made use of the MAXI data provided by RIKEN, JAXA and the MAXI team.

This research has made use of data from the MOJAVE database that is maintained by the MOJAVE team (Lister *et al.* 2009a).

This research has made use of the NASA/IPAC Extragalactic Database (NED) which is operated by the Jet Propulsion Laboratory, California Institute of Technology, under contract with the National Aeronautics and Space Administration.

This research has made use of the SIMBAD database, operated at CDS, Strasbourg, France.

I gratefully acknowledge the support by Elitenetzwerk Bayern and Research Training Group 1147 "Theoretical Astrophysics and Particle Physics" of Deutsche Forschungsgemeinschaft. This work was funded by the BMBF and DFG.

Private First I want to thank Prof. Dr. Karl Mannheim for the possibility to work on this interesting and challenging doctoral thesis and the possibility of working on the topic at the chair of astronomy of the university of Würzburg. Without his constant support this work would not have been possible.

Further sincere thanks goes to my colleagues at the chair of astronomy, foremost Dr. Thomas Bretz for the development and improvements of the MARS analysis software as well as his professional help in all programming issues. In that line I also greatly acknowledge Dr. Daniela Dorner for the setup and administration of the automatic analysis and data base. I had an enjoyable time and many very interesting discussions thanks to Karsten Berger, Dominik Elsässer, Daniel Höhne-Mönch und Markus Meyer, being great friends and always supporting me. I am also greatly thanksful to Matthias Weidinger,

Felix Spanier, Michael Rüger and Stephan Richter for answering willingly all my questions on blazar theory and others, as well as Andreas Vetter, Andreas Klein, Aleksander Paravac und Urs Ganse for technical support in terms of computing and administration as well a our chair secretaries Mrs. Heyder and Mrs. Kuhns. Furthermore my warmest thanks to Prof. Dr. Matthias Kadler for an ever open ear, sharing his time and his great advice.

Many thanks go to my dear colleagues in the MAGIC collaboration, sharing their knowledge with me. It was a pleasure to work with Elina Lindfors, Daniel Mazin, Robert Wagner, Antonio Stamerra, Fabrizio Tavecchio, Malwina Üllenbeck, Elisa Prandini. Special and warmest thanks go to Daniela Hadasch and Michael Backes. Thanks to all of the MAGIC collaboration for maintaining such a great instrument. Not to forget the great support and constant replies on my frequent questions from the other instrument teams, foremost, Emmanouil Angelakis, Denis Bastieri, Wayne Baumgartner, Mike Carini, Neil Gehrels, Yuri Kovalev, Felicia Kraus, Hans Krimm, Anne Lähteenmäki, Francesco Longo, Miguel-Angel Perez-Torres, Joey Richards, Kirill Sokolovsky, and Jörn Wilms.

Last but not least thanks to everybody that I forgot. I was working in a large and great community over many years, and for sure have forgotten to express my deepest thankfulness to some of my colleagues.

Last but not least my deepest thanks to my mother and her husband, my sisters and their families as well as my large family and friends for their continuous support and their understanding. Without you this work would not have been possible. And, of course, heartily thanks to my little witch.

Eigenständigkeitserklärung

Hiermit versichere ich an Eides statt, die Dissertation eigenständig angefertigt und keine anderen als die angegebenen Quellen und Hilfsmittel benutzt zu haben.

Würzburg, den 21. Dezember 2012

.....
Stefan Rügamer